SUSTAINABLE CATALYTIC PRODUCTION OF BIO-BASED HETEROATOM-CONTAINING COMPOUNDS - VOLUME II

EDITED BY: Hu Li, Song Yang and Yaqiong Su
PUBLISHED IN: Frontiers in Chemistry

frontiers Research Topics

About Frontiers

Frontiers is more than just an open-access publisher of scholarly articles: it is a pioneering approach to the world of academia, radically improving the way scholarly research is managed. The grand vision of Frontiers is a world where all people have an equal opportunity to seek, share and generate knowledge. Frontiers provides immediate and permanent online open access to all its publications, but this alone is not enough to realize our grand goals.

Frontiers Journal Series

The Frontiers Journal Series is a multi-tier and interdisciplinary set of open-access, online journals, promising a paradigm shift from the current review, selection and dissemination processes in academic publishing. All Frontiers journals are driven by researchers for researchers; therefore, they constitute a service to the scholarly community. At the same time, the Frontiers Journal Series operates on a revolutionary invention, the tiered publishing system, initially addressing specific communities of scholars, and gradually climbing up to broader public understanding, thus serving the interests of the lay society, too.

Dedication to Quality

Each Frontiers article is a landmark of the highest quality, thanks to genuinely collaborative interactions between authors and review editors, who include some of the world's best academicians. Research must be certified by peers before entering a stream of knowledge that may eventually reach the public - and shape society; therefore, Frontiers only applies the most rigorous and unbiased reviews.
Frontiers revolutionizes research publishing by freely delivering the most outstanding research, evaluated with no bias from both the academic and social point of view. By applying the most advanced information technologies, Frontiers is catapulting scholarly publishing into a new generation.

What are Frontiers Research Topics?

Frontiers Research Topics are very popular trademarks of the Frontiers Journals Series: they are collections of at least ten articles, all centered on a particular subject. With their unique mix of varied contributions from Original Research to Review Articles, Frontiers Research Topics unify the most influential researchers, the latest key findings and historical advances in a hot research area! Find out more on how to host your own Frontiers Research Topic or contribute to one as an author by contacting the Frontiers Editorial Office: frontiersin.org/about/contact

SUSTAINABLE CATALYTIC PRODUCTION OF BIO-BASED HETEROATOM-CONTAINING COMPOUNDS - VOLUME II

Topic Editors:
Hu Li, Guizhou University, China
Song Yang, Guizhou University, China
Yaqiong Su, Xi'an Jiaotong University, China

Table of Contents

Editorial: Sustainable catalytic production of bio-based heteroatom-containing compounds — volume II

Jinshu Huang[1], Hu Li[1]*, Yaqiong Su[2] and Song Yang[1]*

[1]State Key Laboratory Breeding Base of Green Pesticide and Agricultural Bioengineering, Key Laboratory of Green Pesticide and Agricultural Bioengineering, Ministry of Education, State-Local Joint Laboratory for Comprehensive Utilization of Biomass, Center for R&D of Fine Chemicals, Guizhou University, Guiyang, China, [2]School of Chemistry, Xi'an Key Laboratory of Sustainable Energy Materials Chemistry, State Key Laboratory of Electrical Insulation and Power Equipment, Xi'an Jiaotong University, Xi'an, China

Editorial on the Research Topic
Sustainable Catalytic Production of Bio-Based Heteroatom-Containing Compounds — Volume II

Fossil-based heteroatom-containing compounds are crucial core scaffolds or key intermediates in a wide range of pharmaceutical molecules, fiber dyes and printing ink (Li et al., 2019a; Wu et al., 2020; Wu et al., 2021), which can also be directly used as solvents, surfactants, and so on (Li et al., 2019b; Wu et al., 2019; Xu et al., 2019). However, mainly owing to the dependence and overuse of fossil source, the environmental pollution/ deterioration and greenhouse effect are becoming increasingly prominent. In this regard, sustainability is deemed as a key parameter for the future of producing heteroatom-containing compounds and environmental enhancement, which not only requires the replacement of the fossil fuel feedstocks by other renewable resources (e.g., non-food biomass), but also needs the adoption of circular utilisation methods to prevent leakage of any ingredient into the environment (Iglesias et al., 2020).

This Research Topic is Volume II of a series, and here we present a collection of original research and review articles (20 papers in total) with topics on green and sustainable chemistry, including catalytic conversion of biomass feedstocks (Liu et al., Zhu et al., Liu et al., Zhang et al. , Sun et al., Yao et al., Zhou et al., Zhao et al., Yang et al., and Zhou et al.), biodiesel production (Wu et al., Zhang et al., and Liu et al.), and green synthesis of heteroatom-containing bioactive compounds and functional materials (Wang et al., Pan et al., Chen et al., Pan et al., Zhang et al., and Bao et al.). Also, the Research Topic provides interesting insights into the green photocatalysis of organic pollutants (Zhang et al.).

Original research paper of Zhou et al. reports the controllable preparation of three kinds of Fe-based composite catalysts with different Fe loadings for efficient hydrogen production from

biomass steam gasification. When the mass fraction of loading is 10%, Fe species are well dispersed on the carrier, affording a high gas yield of 60.4% (with 42.2% hydrogen proportion). Zhang et al. use glycerol waste to comparatively evaluate the ameliorative effect on lignocellulose under microwave or conventional heating method. During fast pyrolysis, levoglucosan produced from microwave-treated samples (32.9%) was far more selective than the conventional heating group (18.8%), and the content of aldehydes (high toxicity to the downstream fermentation) after glycerol waste and microwave pretreatment was decreased by 2.5 times compared with the untreated counterpart. In addition to directly using raw biomass resources, simple sugars like fructose can be efficiently converted to 5-hydroxymethylfurfural (up to 82% yield) by dehydration over a stable Ti-doped SBA-15 catalyst in DMSO at 140°C for 1 h (Zhu et al.), or to 5-ethoxymethylfurfural (80.4% yield) by cascade dehydration-etherification using a UIO-66-SO_3H catalyst in ethanol under the same thermal conditions (Zhao et al.). Zhang et al. manufacture a biomass-based solid acid catalyst (SiO_2@Cs-SO_3H) with a large specific surface area (21.82 m^2/g) and acidity (3.47 mmol/g) using renewable chitosan as raw material through sulfonation procedure under relatively mild conditions, which is active for esterification of oleic acid and methanol to produce biodiesel (98.2% yield).

The work of Chen et al. reports an unprecedented inactivation process of the indanol-derived NHC catalysts bearing N-C_6F_5 groups, giving an unexpected multi-cyclic complex product from the 3-component reaction with 1-methylcyclopropyl-carbaldehyde, 2,2,2-trifluoroacetophenone and the NHC catalyst. Pan et al. develop an acid-catalyzed 2-alkylation of indole molecules catalyzed by traceless HI, and 2,3-disubstituted indole molecules bearing congested tertiary carbon centers are obtained in moderate to good yields. Some functional catalytic materials such as hierarchical porous SAPO-34 (Wang et al.), bimetallic Zn-Zr metal-organic framework (Zhang et al.), and graphene oxide-silver nanoparticles composite (Bao et al.) are prepared in sustainable ways, and found to be efficient for the synthesis of value-added chemicals (e.g., 4,6-dimethyldibenzothiophene) or degradation of organic pollutants.

This Research Topic features several review articles with distinct scopes (Liu et al., Sun et al., Zhou et al., Yang et al., Yao et al., Liu et al., Wu et al., Liu et al., Pan et al., and Zhang et al.). Liu et al. review the application of recyclable heterogeneous non-noble Zr/Hf-containing catalysts (e.g., Zr/Hf-containing metal oxides, supported materials, zeolites, metal organic frameworks, metal organic hybrids) with acid-base bifunctionality for catalytic transfer hydrogenation using the safe liquid hydrogen donor, with emphasis on evaluating the reaction mechanisms and conversion pathways. In a more detailed manner, the research progress of catalytic synthesis of γ-valerolactone from furfural by Zr/Hf-based catalysts is reviewed by Sun et al., and the effects and regulation approaches of Lewis acid-base and Brønsted acid sites in the catalysts on each steps in the reaction process are discussed. Zhou et al. reveal the significance and potential of using titanate nanotubes-based materials as sustainable and environmentally benign solid catalysts/supports for synthesis of various bio-based chemicals, such as glycerol-derived solketal, jet fuel range alkanes precursors, biomass-derived esters, aldehydes, and aromatic compounds. Yang et al. propose the research development trend for improving the institutional mechanism of the utilization of crop straw resources, strengthening technology research and development, exploring the economic model of green cycle agriculture, accelerating the construction of the industrial system, and designing new paths of resource utilization in multiple ways. Yao et al. mainly review some latest studies about the conversion of cellulose to 5-hydroxymethylfurfural catalyzed by solid acids with Brønsted and/or Lewis acidic sites, such as sulfonated solid acids, carbon-based acids, and zeolites. Liu et al. summarize the mechanisms of several important processes of producing 5-ethoxymethylfurfural from lignocellulosic biomass-derived sugars and the research progress of the developed acid catalysts. In addition, advancements in tobacco (*Nicotiana tabacum L.*) seed oils (Wu et al.) and lipid extraction from microalgae using green solvents (Liu et al.) for biodiesel production are also collected. For some structurally somplex natural products such as sex pheromones (Pan et al.), and momilactones and related 9β-H pimarane skeleton (Zhang et al.), the recent advances in their synthetic strategies with the involved challenges are overviewed.

We wish this Research Topic attracts interested colleagues, enlightening more eco-friendly and sustainable synthetic procedures, shedding light on renewed catalytic strategies and routes developed for the production of bio-based heteroatom-containing compounds, and providing enthusiasm in research and studies. Enjoy its reading!

Author contributions

All authors listed have made a substantial, direct, and intellectual contribution to the work, and approved it for publication.

Acknowledgments

Conflict of interest

The authors declare that the research was conducted in the absence of any commercial or financial relationships that could be construed as a potential conflict of interest.

Publisher's note

All claims expressed in this article are solely those of the authors and do not necessarily represent those of their affiliated organizations, or those of the publisher, the editors and the reviewers. Any product that may be evaluated in this article, or claim that may be made by its manufacturer, is not guaranteed or endorsed by the publisher.

References

Iglesias, J., Martínez-Salazar, I., Maireles-Torres, P., Alonso, D. M., Mariscal, R., and Granados, M. L. (2020). Advances in catalytic routes for the production of carboxylic acids from biomass: A step forward for sustainable polymers. *Chem. Soc. Rev.* 49 (16), 5704–5771. doi:10.1039/d0cs00177e

Li, H., Guo, H., Su, Y., Hiraga, Y., Fang, Z., Hensen, E. J., et al. (2019a). N-formyl-stabilizing quasi-catalytic species afford rapid and selective solvent-free amination of biomass-derived feedstocks. *Nat. Commun.* 10 (1), 699. doi:10.1038/s41467-019-08577-4

Li, H., Wu, H., Zhang, H., Su, Y., Yang, S., and Hensen, E. J. (2019b). A facile direct route to N-(un) substituted lactams by cycloamination of oxocarboxylic acids without external hydrogen. *ChemSusChem* 12 (16), 3778–3784. doi:10.1002/cssc.201901780

Wu, H., Dai, W., Saravanamurugan, S., Li, H., and Yang, S. (2019). Quasi-catalytic approach to N-unprotected lactams via transfer hydro-amination/cyclization of biobased keto acids. *ACS Sustain. Chem. Eng.* 7 (12), 10207–10213. doi:10.1021/acssuschemeng.9b00412

Wu, H., Yu, Z., Li, Y., Xu, Y., Li, H., and Yang, S. (2020). Hot water-promoted catalyst-free reductive cycloamination of (bio-) keto acids with HCOONH$_4$ toward cyclic amides. *J. Supercrit. Fluids* 157, 104698. doi:10.1016/j.supflu.2019.104698

Wu, H., Li, H., and Fang, Z. (2021). Hydrothermal amination of biomass to nitrogenous chemicals. *Green Chem.* 23 (18), 6675–6697. doi:10.1039/d1gc02505h

Xu, Y., Long, J., Zhao, W., Li, H., and Yang, S. (2019). Efficient transfer hydrogenation of nitro compounds to amines enabled by mesoporous N-stabilized Co-Zn/C. *Front. Chem.* 7, 590. doi:10.3389/fchem.2019.00590

Recyclable Zr/Hf-Containing Acid-Base Bifunctional Catalysts for Hydrogen Transfer Upgrading of Biofuranics: A Review

Yixuan Liu[1†], Xixi Liu[2†], Mingrui Li[1], Ye Meng[1], Jie Li[1], Zehui Zhang[2] and Heng Zhang[1]*

[1]State Key Laboratory Breeding Base of Green Pesticide and Agricultural Bioengineering, Key Laboratory of Green Pesticide and Agricultural Bioengineering, Ministry of Education, State-Local Joint Laboratory for Comprehensive Utilization of Biomass, Center for Research and Development of Fine Chemicals, Guizhou University, Guiyang, China, [2]Key Laboratory of Catalysis and Materials Sciences of the Ministry of Education, South-Central University for Nationalities, Wuhan, China

The massive burning of a large amount of fossil energy has caused a lot of serious environmental issues (e.g., air pollution and climate change), urging people to efficiently explore and valorize sustainable alternatives. Biomass is being deemed as the only organic carbon-containing renewable resource for the production of net-zero carbon emission fuels and fine chemicals. Regarding this, the selective transformation of high-oxygen biomass feedstocks by catalytic transfer hydrogenation (CTH) is a very promising strategy to realize the carbon cycle. Among them, the important Meerwein-Ponndorf-Verley (MPV) reaction is believed to be capable of replacing the traditional hydrogenation strategy which generally requires high-pressure H_2 and precious metals, aiming to upgrade biomass into downstream biochemical products and fuels. Employing bifunctional heterogeneous catalysts with both acidic and basic sites is needed to catalyze the MPV reaction, which is the key point for domino/cascade reaction in one pot that can eliminate the relevant complicated separation/purification step. Zirconium (Zr) and hafnium (Hf), belonging to transition metals, rich in reserves, can demonstrate similar catalytic efficiency for MPV reaction as that of precious metals. This review introduced the application of recyclable heterogeneous non-noble Zr/Hf-containing catalysts with acid-base bifunctionality for CTH reaction using the safe liquid hydrogen donor. The corresponding catalysts were classified into different types including Zr/Hf-containing metal oxides, supported materials, zeolites, metal-organic frameworks, metal-organic hybrids, and their respective pros and cons were compared and discussed comprehensively. Emphasis was placed on evaluating the bifunctionality of catalytic material and the key role of the active site corresponding to the structure of the catalyst in the MPV reaction. Finally, a concise summary and prospect were also provided centering on the development and suggestion of Zr/Hf-containing acid-base bifunctional catalysts for CTH.

Keywords: transfer hydrogenation, meerwein-ponndorf-verley reaction, Zr/Hf-containing catalyst, acid-base bifunctionality, biomass conversion
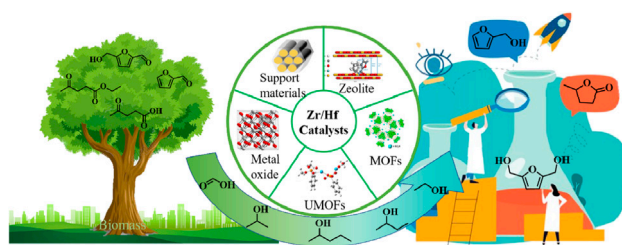
GRAPHIC ABSTRACT |

This review introduced the application of recyclable heterogeneous non-noble Zr/Hf-containing catalysts with acid-base bifunctionality for CTH reaction using the safe liquid hydrogen donor. The corresponding catalysts were classified into different types including Zr/Hf-containing metal oxides, supported materials, zeolites, metal organic frameworks, metal organic hybrids, and their respective pros and cons were compared and discussed comprehensively. Emphasis was placed on evaluating the bifunctionality of catalytic material and the key role of active site corresponding to the structure of the catalyst in the MPV reaction.

INTRODUCTION

The large-scale exploitation of fossil-based resources exists alongside environmental deterioration like global warming, acid rain, and air pollution (Tripathi et al., 2016; Valderrama Rios et al., 2018; Ahmad et al., 2019; Brauer et al., 2021; Schwarzman et al., 2021). On the eve of the "26th United Nations Climate Change Conference" in 2021, more than 230 major journals around the world jointly published an editorial to warn global leaders to act immediately for climate change (Atwoli et al., 2021). These serious problems compel humans to seek renewable and clean resources for the sustainable supply of fuels and chemicals (Zhang et al., 2020; Khan et al., 2021; Osman et al., 2021; Rode et al., 2021; Wu et al., 2021; Yu et al.,

2021; Zantye et al., 2021; Zhang et al., 2021a). Biomass acts as the only organic carbon-containing source on earth that mainly contains carbon, hydrogen, and oxygen species (Wang et al., 2014b; Han et al., 2019; Spinelli et al., 2019; Zhu et al., 2019; Pattnaik et al., 2021). Biomass energy is ubiquitous, rich, renewable, and sustainable and its main sources are firewood, wood waste, agricultural straw, livestock manure, sugar crop waste, municipal waste with sewage, and aquatic plants, respectively (Li et al., 2018a; Luo et al., 2019; Abomohra et al., 2020; Sudarsanam et al., 2020; Wu et al., 2020). Compared with other renewable energy sources, it has unique advantages in terms of the reuse of waste resources and the production of fuels and high-value chemicals. It is highly valued in many aspects such as scientific research, politics, and the economy (Wu et al., 2018a; Mathimani and Mallick, 2019; Welch et al., 2021; Tan et al., 2022). There is a significant long-term two-way causal relationship between biomass energy consumption and economic growth (Ajmi and Inglesi-Lotz, 2020; Sabyrzhan et al., 2021). Hence, biomass has broad application potential in the future production and life of mankind (Kumar et al., 2015; Gawade et al., 2016; Hu et al., 2017; Liu et al., 2021c). However, compared to the desired products especially for fuels or fuel additives, biomass-derived feedstocks generally possess higher oxygen content (Prasomsri et al., 2013; Liao et al., 2014; Li et al., 2020a; Li et al., 2020b; Wang et al., 2020a). It is still necessary to further process the biomass feedstock to upgrade its functional groups (Dabros et al., 2018; Li et al., 2019b; Iglesias et al., 2020
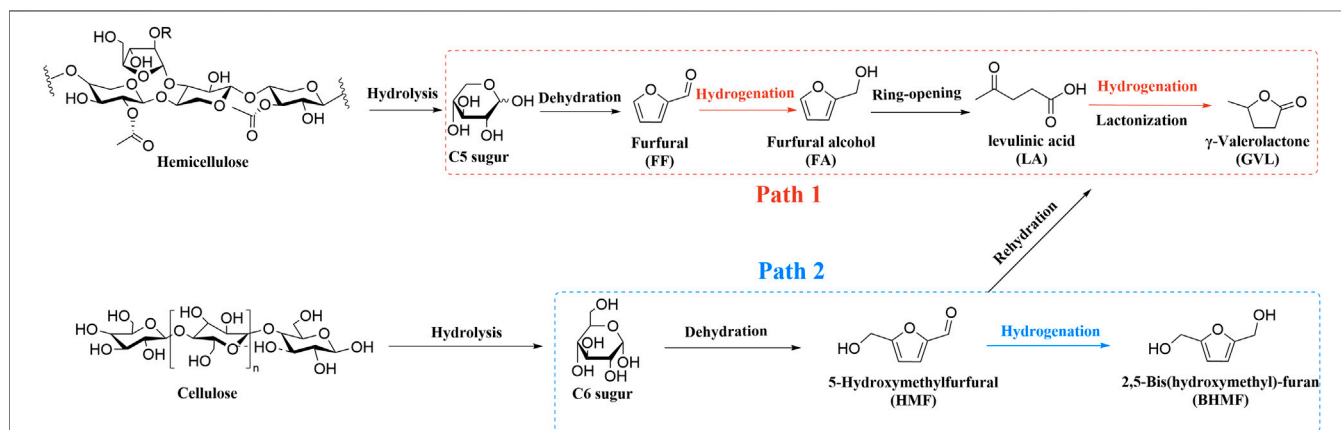
SCHEME 1 | A common pathway for upgrading cellulose and hemicellulose.
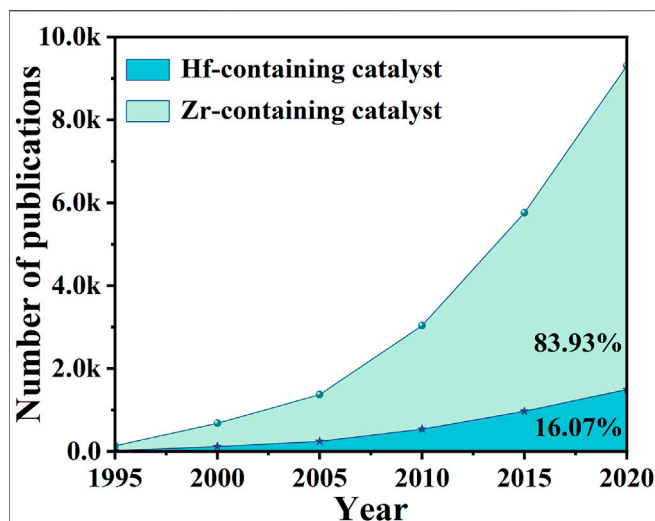
FIGURE 1 | Comparison of the number of publications on Zr-containing catalysts and Hf-containing catalysts. Source: web of science (a search carried out in November 2021).

Tan et al., 2021). In the field of biomass upgrading, the most widely used approach is to convert biomass (e.g., cellulose and hemicellulose) into a series of furan compounds *via* cascade reactions (**Scheme 1**) (Zhou and Zhang, 2016; Liu et al., 2019; Chen et al., 2021b). Among furan compounds, γ-valerolactone (GVL) is recognized as a kind of versatile chemical building block (Liu et al., 2021a; Kerkel et al., 2021; Delgado et al., 2022). It's a green organic solvent and can also be used as a precursor for the manufacture of liquid fuels (Huang et al., 2018; Crabtree, 2019). 5-Hydroxymethylfurfural (HMF) has various furan rings coupled with the hydroxyl and aldehyde groups present at the exocyclic carbon atoms (Chen et al., 2018; Zhang et al., 2021b; Sarkar et al., 2021). It can be converted to levulinic acid (LA) and further produced GVL. or it can be converted to 2,5-bis(hydroxymethyl)furan (BHMF) through another route. (Kou et al., 2016; Priecel et al., 2018; Li and Jiang, 2019). Therefore, the main conversion path of this article is the production of furan compounds such as GVL and BHMF.

Many reactions are involved in these processes, such as dehydration, hydrogenation, ring-opening (Yang et al., 2017b; Iriondo et al., 2017; Solanki and Rode, 2019). But the key speed-determining step is transfer hydrogenation via the Meerwein-Ponndorf-Verley (MPV) reduction reaction, which is also called indirect catalytic transfer hydrogenation (CTH) (Singh et al., 2015; Li et al., 2018c; Shao et al., 2021). Different kinds of alcohols can be used as H-donors in relatively mild conditions, achieving efficient catalysis performance for CTH reaction of the carbonyl group of α, β-unsaturated aldehyde/ketone (Mondelli et al., 2020). Therefore, the C=O bond is hydrogenated while retaining the C=C bond (Wu et al., 2018b; Li et al., 2018d; Jin et al., 2019; Liu et al., 2021d). Heterogeneous catalysts were wildly used in MPV reduction reactions, which can be easily recycled and also can effectively reduce industrial production costs (Santana and Krische, 2021; Pan et al., 2022). It goes without saying that the choice of materials is of great importance for the

relevant catalytic system. In contrast to the indirect hydrogenation via MPV reaction using alcohol as a hydrogen donor (H-donor), there is another direct hydrogenation reaction in CTH that uses precious metals and H_2. Although precious metals (*e.g.*, Ru, Pd, Ir, Pt) were widely studied for direct CTH, the prices were not suitable for industrialization (Tuteja et al., 2014; Brethauer and Studer, 2015; Cao et al., 2017; Wang T. et al., 2020). On the other hand, non-noble metals (*e.g.*, Fe, Co, Cu, Ni) were restricted because of relatively low activity and/or product selectivity (Hu et al., 2019a; Zhang et al., 2019b; Shi et al., 2019; Jiang et al., 2020). These disadvantages have prompted scientists to explore alternative catalysts, which can balance economy and high selectivity (Yin and Shen, 2020). Thus, researchers discovered that transition metal carbides have similar properties with Pt metal (Pang et al., 2019). Since transition metals have both metallic and acidic properties, they can be used as effective catalysts for the upgrading of oxygen-containing compounds derived from biomass (Choi et al., 2011; Heard et al., 2016; Gonell et al., 2017; Wagner et al., 2021). It has good corrosion resistance and is not easily corroded by general acid-base aqueous solutions (Sullivan et al., 2016; Wei et al., 2021). Among the transition metals, Zr and Hf metals with similar properties have set off a wave of research craze in the field of CTH (Champness, 2011; Li et al., 2016a; B et al., 2018). **Figure 1** shows that from 1995 to 2021, the number of articles published on Zr-based catalysts in 2020 is even 5 times than that of Hf-based catalysts. Although the metals of the fourth subgroup have similar properties, the research of Hf-based catalysts in this field is far from enough, which is also a trend and direction of future exploration.

There are some relevant reviews about biomass conversion and CTH reaction. For example, a comprehensive review of bifunctional catalysts to convert biomass into biofuels was proposed by Li et al. (2016a). What's more, some reviews focused on the production of GVL from lignocellulosic biomass, (Tang et al., 2014b; Ye et al., 2020) and other studies paid attention to the mechanism and interface effects of heterogeneous CTH (Gilkey and Xu, 2016; Liu et al., 2021b). However, as far as we know, there is no review of the application of transition metal Zr/Hf catalysts used for the synthesis of biofuranics compounds. In this review, the target is to selectively discuss the latest developments of various types of Zr/Hf-containing catalysts through MPV reduction to upgrade biomass-derived feedstocks. It will focus on exploring the specific mechanism of the catalysts' active site (Lewis/Brønsted acid and base) in each biomass upgrading reaction. Finally, some opportunities and challenges faced by CTH for efficiently converting biomass into fuels or high-value chemicals have also been prospected appropriately.

ZR/HF-CONTAINING METAL OXIDE CATALYSTS

Zr has excellent high-temperature resistance, and its melting point is as high as 2,700°C. Even if it is heated to 1900°C, it will still not react with molten Al, Fe, Ni, Pt, and other metals.

TABLE 1 | Zr/Hf-based metal oxide catalysts.

Entry	Substrate	Catalyst	Condition	H-donor	Product	Conv. (%)	Yield (%)	References
1	LA/FA	Ag–Ni/ZrO$_2$	220°C, 5 h	Water	GVL	100	99	Hengne et al. (2014)
2	LA	HCl/ZrO (OH)$_2$	240°C, 2 h	2-BuOH	GVL	99.9	92.4	Tang et al. (2015)
3	LA	Cu–ZrO$_2$	200°C, 5 h	Water	GVL	100	99.9	Hengne and Rode, (2012)
4	ML	Cu–ZrO$_2$	200°C, 5 h	Methanol	GVL	95	92	Hengne and Rode, (2012)
5	ML	Ni/ZrO$_2$	90°C, 20 h	2-PrOH	GVL	100	92	Sakakibara et al. (2019)
6	ML	Cu/ZrOCO$_3$	180°C, 7 h	2-PrOH	GVL	99	89.79	Ma et al. (2020)
7	EL	ZrO(OH)$_2 \cdot x$H$_2$O	240°C, 1 h	EtOH	GVL	89.1	75.3	Tang et al. (2014a)
8	EL	ZrO$_2$-B$_2$O$_3$	200°C, 4 h	2-PrOH	GVL	95.1	88.5	He et al. (2016a)
9	EL	ZrO$_2$	250°C, 3 h	EtOH	GVL	95.5	81.5	Tang et al. (2013)
10	EL	Al$_7$Zr$_3$-300	220°C, 4 h	2-PrOH	GVL	95.5	83.2	He et al. (2016b)
11	EL	ZrFeO$_x$	270°C, 3 h	EtOH	GVL	94.2	87.2	Li et al. (2015)
12	EL	Zr$_5$Ni$_5$	200°C, 3 h	2-PrOH	GVL	97.2	95.2	Li et al. (2016b)
13	EL	Ti/Zr	180°C, 6 h	2-PrOH	GVL	100	90.1	Yang T. et al. (2017)
14	BL	ZrO$_2$	150°C, 16 h	2-BuOH	GVL	99.9	84.7	Chia and Dumesic (2011)
15	FF	Zr(OH)$_4$@CoFe$_2$O$_4$	160°C, 4 h	2-PrOH	FA	95.4	92.6	Hou et al. (2021)
16	FF	HfO(OH)$_2 \cdot x$H$_2$O	180°C, 8 h	2-PrOH	GVL	100	64.2	Li M. et al. (2021)
17	HMF	ZrO(OH)$_2$	150°C, 2.5 h	EtOH	BHMF	94.1	88.9	Hao et al. (2016)

SCHEME 2 | Two pathways for the conversion of LA and its esters to GVL.
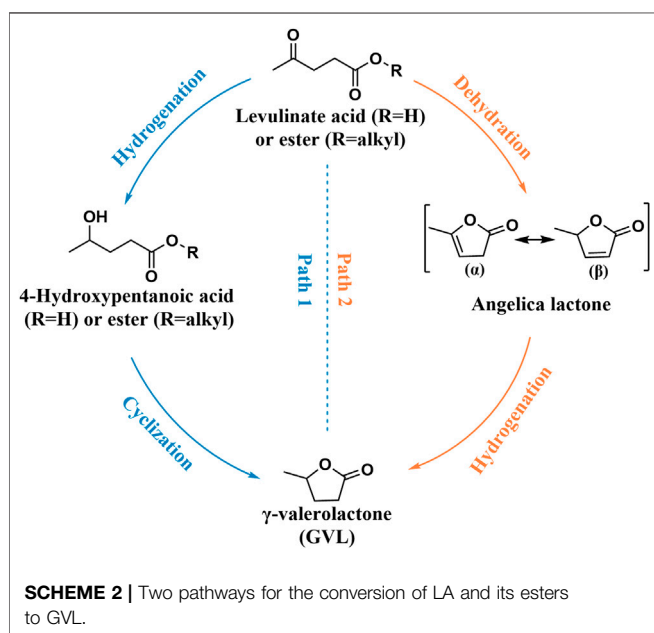
Commercial zirconium oxide (ZrO$_2$) has been used in the nuclear energy industry, national defense industry, electronic components, ceramic carbon powder, along with high-temperature resistant materials, etc. (Ishikawa et al., 2017). Among them, ZrO$_2$ was also used in the field of catalysis due to its excellent chemical stability and high surface chemical activity (Liu et al., 2002; Zhu et al., 2004; Gonell et al., 2017). As a typical weak acid-base bifunctional material, ZrO$_2$ and HfO$_2$ have exceptional catalytic performance in CTH reaction (Paniagua et al., 2021). In Zr/Hf-containing metal oxide catalysts, as shown in **Table 1**, the main researches in recent years are classified and summarized according to the reaction substrate.

LA and its Esters as Substrates
LA as a Substrate

LA was listed as one of the 12 high-value chemicals from biomass by the U.S. DE (Bogale et al., 2019). It was considered as a significant platform compound for the synthesis of organic chemicals (Hu et al., 2021; Tian et al., 2021). In general, there are usually two reaction pathways of heterogeneous catalysis in the production of GVL using LA and its esters [e.g., methyl levulinate (ML), ethyl levulinate (EL), butyl levulinate (BL)] as substrates. These two reaction pathways mainly depend on the controlled reaction conditions and the catalyst used during the reaction (**Scheme 2**) (Dutta et al., 2019). In path 1, hydrogenation reaction is prone to occur at lower temperatures to promote the conversion of LA to 4-hydroxyvaleric acid under the water phase system, which is then dehydrated to GVL under the action of a catalyst. In path 2, LA is first dehydrated to form angelica lactone at higher temperatures, which is then hydrogenated to obtain GVL. In short, hydrogen and dehydration can occur either way. But under different control reaction conditions, the sequence of these two processes will change, accordingly.

Ag–Ni/ZrO$_2$ catalyst has attracted researchers' attention due to its magnetic properties that are easy to separate (Hengne et al., 2014). The two metals play a synergistic effect in the transformation of LA and furfuryl alcohol (FA) (1:1) mixture to GVL. It also proved that Ag–Ni/ZrO$_2$ has a comprehensive scope of applications in the one-pot CTH of biomass-derived C3 to C6 molecules, with relatively high conversion and selectivity (>80%) (entry 1 of **Table 1**). In addition to using high-purity synthetic chemicals as substrates, researchers were further required to explore some methods that can be closer to biomass raw materials to produce GVL. Tang et al. developed an *in-situ* catalyst generation system to produce GVL (Tang et al., 2015). The system can decompose the HCl/ZrO(OH)$_2$ catalyst in LA and 2-butanol (2-BuOH) solution autonomously and then a 2-BuOH *in-situ* H-donor was employed to catalyze the cyclization of LA esterification to GVL. The highlight of this

system was that crude LA can be directly used to produce GVL. The crude LA was extracted from the acid hydrolysis of cellulose (47.8% yield), and flowed into 2-BuOH. Finally, 2-BuOH was used to extract LA and FA from the cellulose hydrolysate (90.2% v. s. 15.1%), as depicted in entry 2 of **Table 1**. Even in the presence of humin after use, a GVL yield of 82.0% can be successfully obtained. In addition, when investigating the influence of solvent, it was found that the GVL yield of 2-BuOH was much lower than that of 2-Propanol (2-PrOH) (27.5% vs. 62%) at 200°C because the steric effect of 2-BuOH was stronger than 2-PrOH. Continue to increase the temperature to 240°C, the steric effect of 2-BuOH can be overcome, and the yield can be increased to 84.5%. According to Derjaguin–Landau–Verwey–Overbeek (DLVO) theory, the principle of the catalysts agglomeration phenomenon was speculated. That was, the absorbed LA and H-donors enhanced the electrostatic repulsion between the $ZrO(OH)_2$ particles formed *in situ*, thereby preventing further agglomeration in 2-BuOH. In other words, the dispersibility and morphology of $ZrO(OH)_2$ particles that played a key catalytic role mainly depended on the solvent and the substrate. Most $Cu-ZrO_2$ catalysts were prepared by co-precipitation with mixed precursors (entry 3 of **Table 1**) (Hengne and Rode, 2012). Its excellent catalytic performance should be attributed to its strong surface acidity. The effective active component in the catalytic hydrogenation process was the reduced Cu particles dispersed on the catalyst surface. The introduction of Cu into the tetragonal ZrO_2 lattice can enhance the adhesion of these particles as well as make them dispersed. It can also enhance the number of acid sites, among which Lewis acid was also determined to enhance the transfer hydrogenation activity. Changing the starting material from LA to ML and the H-donor from water to methanol, $Cu-ZrO_2$ still had a very objective activity (entry 4 of **Table 1**).

ML as a Substrate

Ni/ZrO_2 was also used to convert ML and LA to GVL, which were catalyzed and reacted to test the active materials (Sakakibara et al., 2019). It was concluded that the Ni contributed to the hydrogenation of ML and LA, and the Zr contributed to the lactonization of the hydrogenated product. Under relatively mild conditions of 90°C, the GVL yield reached 92% (entry 5 of **Table 1**). But the disadvantage was that the reaction time was as long as 20 h. It is well known that GVL can be directly hydrogen transfer catalyzed by $ZrOCO_3$. Further studies by Ma et al. found that using $ZrOCO_3$ as a carrier, the introduction of Cu/Cu^+ can increase the CTH activity (entry 6 of **Table 1**) (Ma et al., 2020). And $Cu/ZrOCO_3$ can also further convert GVL into 1,4-Pentanediol (1,4-PDO) through the MPV reaction. This may be caused by the coordination effect between the Cu and the acid-base sites of the carrier. Cu vacancy (Cu^0) and Cu ion (Cu^+) were formed after *in-situ* reduction. Cu^+ can be used as Lewis acid to adsorb and activate the C=O group through the electron lone oxygen atom pair. Alcohol can be excited to become an activated metal hydride on the Cu^0 surface, and then attack the activated C=O group to form an O-H group. $ZrOCO_3$ was an amphoteric catalyst, which can also promote the MPV reaction through six-membered ring intermediates. In

addition, amphoteric carriers (such as $Al(OH)_3$ and $ZrOCO_3$) contained more acid-base sites than basic carriers (such as $Mg_2(OH)_2CO_3$ and ferric hydroxide), demonstrating a better catalytic activity accordingly.

EL as a Substrate

EL was used to prepare GVL through CTH. Tang et al. used $ZrO(OH)_2 \cdot xH_2O$ catalyst to obtain 89.1% EL conversion and 75.3% GVL yield in ethanol (EtOH) under 240°C for 1 h (entry 7 of **Table 1**) (Tang et al., 2014a). First, EtOH was adsorbed on the surface of the catalyst and dissociated into the corresponding alkoxide. EL obtained two hydrogen atoms from EtOH to obtain the intermediate ethyl 4-hydroxypentanoate (4-HPE). Then 4-HPE underwent intramolecular transesterification to obtain the final product GVL. But there was another reaction path, 4-HPE and EtOH were etherified to produce by-product 4-ethoxypentanoate (4-EPE). Self-aldol condensation may occur between EL, GVL, and aldehyde dehydrogenated from EtOH, and the formation of trace by-products can be ignored in the system. Doping boric acid in Zr-containing catalysts can increase its acid content, but the traditional wet impregnation method was difficult to control the leaching of the boron component during the reaction. Therefore, He et al. used the sol-gel method to improve the synthesis of the mesoporous Zr/boron mixed oxides catalyst (He et al., 2016a). $ZrOCl_2 \cdot 8H_2O$ and boric acid were stirred at 40°C for 3 h and then transferred to an oven to evaporate the solvent for 4 h after sonication. After drying at 80°C for 1 day, it was calcined at 450°C for 6 h. In general, the preparation process was relatively simple. With this amorphous material catalyst, 95.1% EL conversion and 88.5% GVL yield were obtained at 200°C for 4 h (entry 8 of **Table 1**). As the boron content increased, the surface area, acid density, and alkali density of the mesoporous material improved correspondingly. Nonetheless, adding too much boron to ZrO_2 will reduce the alkali density and inhibit the alkalinity of the catalyst. However, ZrO_2 catalyst still existed the disadvantage of high temperature or long time during the reaction (entry 9 of **Table 1**) (Tang et al., 2013). To address this issue, Al-Zr mixed metal catalysts were prepared by the co-precipitation method (He et al., 2016b). $ZrOCl_2 \cdot 8H_2O$ and $Al(NO_3)_3 \cdot 9H_2O$ were dissolved in deionized water, and then an aqueous ammonia solution (25–28%) was added dropwise. Next, the solution underwent a series of methods such as pH adjustment, aging, drying, and calcination to obtain the target solid catalyst. It was found that when Al was added to ZrO_2, the surface area was enlarged and the number of effective acid and base sites of the catalyst was increased. With 2-PrOH as the H-donor and solvent, the EL conversion was 95.5% and the GVL yield was 83.2% at 220°C (entry 11 of **Table 1**). Both formic acid and LA can be obtained from sugars in an equimolar ratio were found by Li et al. Therefore, if FA is used as an H-donor and LA is used as a substrate to synthesize GVL, it is obviously a reasonable system. Nano-FeZrO$_X$ materials have also been reported to have magnetic recyclable properties. The acid-base bifunctional catalysts of superparamagnetism were synthesized through the reaction of

solvent heat treatment and hydrolysis condensation. Upon using EtOH as H-donor, effective conversion of EL to GVL was successfully conducted. A series of FeZrO$_x$ catalysts with different Fe-Zr ratios were prepared (entry 11 of **Table 1**) (Li et al., 2015). It was found that ZrFeO (1:3)-300 with Fe$_3$O$_4$ covered by a ZrO$_2$ layer had an appropriate distribution of acid-base sites as well as a medium surface area and pore size. The yield of GVL can be reached as high as 87.2% (3 h, 230°C). In addition, the catalyst containing Zr and Fe can also be combined with the solid acid HY2.6 to directly convert sugar into GVL, with a yield of 44.7%. To be specific, Ni(NO$_3$)$_2$ 6H$_2$O and ZrOCl$_2$ 8H$_2$O were used to synthesize magnetic Ni-Zr nanocatalysts for the conversion of various biomass derivatives (Li et al., 2016b). This hydrogen-reduced magnetic Zr$_5$Ni$_5$ nanoparticles (<20 nm) catalyzed EL to produce GVL (95.2% yield) within 3 h at 200°C (entry 12 in **Table 1**). Surprisingly, the system can also catalyze the conversion of fructose, glucose, cellobiose, and carboxymethyl cellulose into GVL and EL in one pot, with a total yield of 69.5, 60.1, 56.0, and 51.5%, respectively. And ICP-OES detected that only 0.3 wt% Ni and 0.5% Zr were immersed in 2-PrOH. The very small amount of immersion can clearly explain the heterogeneity of the catalyst and the nature of easy recycling. In addition, the nano-catalyst was combined with the solid acid HY6, the catalyst was easily attracted by the permanent magnet because of its magnetic properties. The used catalyst was washed 3 times with EtOH and dried, and it can be reused more than 5 times. In addition, the catalyst can be recovered by more than 89–93%, which is very suitable from an economic and convenient point of view.

Also using EL as a substrate, Yang et al. developed a microsphere Ti/Zr porous oxide catalyst through a sol-gel process combined with solvent heat treatment (Yang et al., 2017a). With hexadecyl amine (HDA) as the directing agent, the catalysts (TixZry) with different Ti/Zr molar ratios that have −Zr−O−Zr− network were developed. This not only allowed the mixed oxide to have adjustable porosity and large surface area but also enhanced its acidity and alkalinity. Compared to the amorphous structure of commercial titanium oxide (TiO$_2$) and ZrO$_2$, Ti/Zr oxides were spherical. Experiments and tests showed that Ti$_2$Zr$_8$ had the largest surface area (385 m^2/g), appropriate acidity (1.12 mmol/g), and alkalinity (0.46 mmol/g), which was the best option. In general, if there was a base in the reaction system, the reaction activity will be improved. The increase in reactivity benefited from the ability to accept hydroxyl protons from the H-donor. There were also many sources of bases, which can be organic ligands, solvent molecules, or dissolved alkaline substances. The catalyst can be reused at least 6 times, and it can still obtain almost complete EL conversion and GVL yield of greater than 84.4% (entry 13 of **Table 1**). BL was also one of the common LA and its esters (entry 14 of **Table 1**) (Chia and Dumesic, 2011).

FF (Furfural) as a Substrate

For the conversion of FF to FA, the hollow core-shell magnetic catalyst named Zr(OH)$_4$@CoFe$_2$O$_4$, was developed and employed for CTH (entry 15 of **Table 1**) (Hou et al., 2021). Firstly, 2-PrOH

was adsorbed on the surface of Zr(OH)$_4$ and interacted with Lewis acid sites (Zr^{4+}) and base sites (O^{2-}) to form metal alkoxide. Then, the O atom on the carbonyl group of FF was activated by Zr^{4+}. A typical six-membered ring transition state was formed. Then hydride transfer from alkoxide to the carbonyl group of FF was accomplished. Finally, the newly formed FA was desorbed from the surface of the catalyst along with acetone, and the active site of Zr^{4+} was re-exposed for the next run.

One-pot conversion of FF to GVL can use commercial HfCl$_4$ as a catalyst (Li et al., 2021b). With 2-PrOH as H-donor, the yield of GVL reached 65.5% in 8 h at 180°C (entry 16 of **Table 1**). During the reaction, HfCl$_4$ is hydrolyzed *in situ* to produce HfO(OH)$_2$ xH$_2$O (medium Lewis basic) and HCl (strong Brønsted acid). Together with the Lewis acid site (Hf^{4+}), they play a synergistic effect in the cascade reaction process, which is significantly improved the catalytic activity. HfCl$_4$ provides Lewis acid site (Hf^{4+}), while HfO(OH)$_2$·xH$_2$O and HCl were gradually *in situ* generated by the HfCl$_4$ hydrolysis in 2-PrOH due to the presence of residual water to provide Lewis base site (O^{2-}) and Brønsted acid site (HCl), respectively. 1) The carbonyl group of FF was adsorbed on the Lewis acid site (Hf^{4+}), and 2-PrOH with the oxygen and hydrogen atom of the hydroxyl group were respectively adsorbed to the Lewis acidic Hf^{4+} and the Lewis basic oxo-ion site. Then, a six-membered ring transition state was formed to complete the transfer hydrogenation process. FF was converted to Furfuryl Alcohol (FA), at the same time the 2-PrOH was transformed to acetone. 2) FA reacting with 2-PrOH was catalyzed by Lewis acid sites to form isopropyl furfuryl ether (FE) by etherification reaction. 3) The conversion of IPL to isopropyl 4-hydroxyvalerate (4-HPE) via transfer hydrogenation was similar to that of FF to FA, which was also catalyzed by the Lewis acid-base site (Hf^{4+}-O^{2-}). 4) 4-HPE undergone cyclization reaction to produce equivalent GVL was conducted in the presence of acid sites. In addition, the recycled catalysts can effectively catalyze the conversion of FF to FA after being calcined (2-PrOH as H-donor and the yield is 60.5% at 170°C for 1.5 h).

HMF as a Substrate

CTH mechanism of HMF on ZrO(OH)$_2$ was shown in **Scheme 3** (Hao et al., 2016). The carbonyl oxygen of HMF coordinated with the alkoxide a to form a six-membered ring transition state b on Zr species. The hydride was transferred from the alkoxide to the carbonyl of HMF in b. Meanwhile, the new carbonyl (aldehyde) dissociated and released the intermediate c. Then another EtOH coordinated with it to form d. At the end, the newly reduced carbonyl (BHMF) dissociated to regenerate the alkoxide a. The BHMF yield of 88.9% can be achieved by reacting for 2.5 h at 150°C (entry 17 of **Table 1**).

The mechanism by which Zr-containing metal oxides catalyze the completion of transfer hydrogenation of carbonyl compounds via MPV reduction reaction is shown in **Scheme 4**. First, the alcohol is absorbed by the Lewis acid sites in the catalyst to form the corresponding alkoxide (Gonell et al., 2017). Then, the carbonyl group combines with the alkoxide to produce a six-membered ring transition state (Injongkol et al., 2017). Finally, a coordinated hydrogen transfer occurs
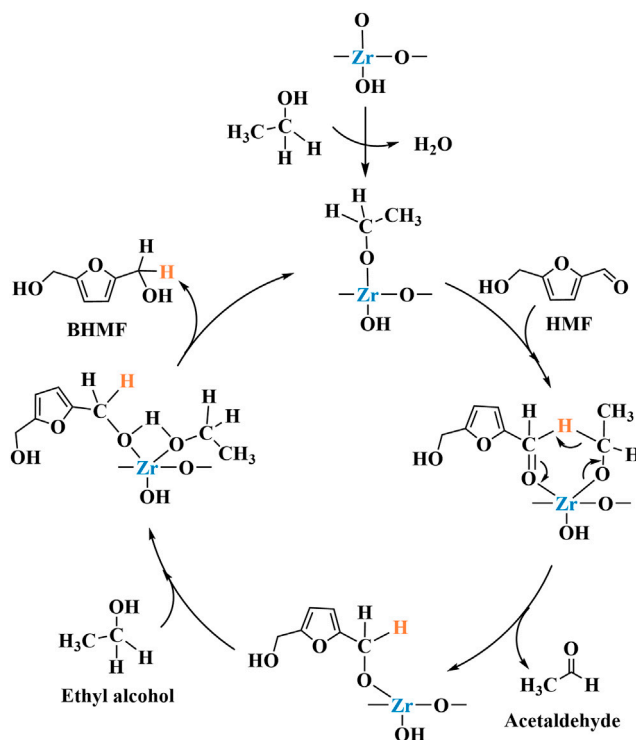
SCHEME 3 | The mechanism for the CTH of HMF into BHMF over $ZrO(OH)_2$ (Hao et al., 2016).
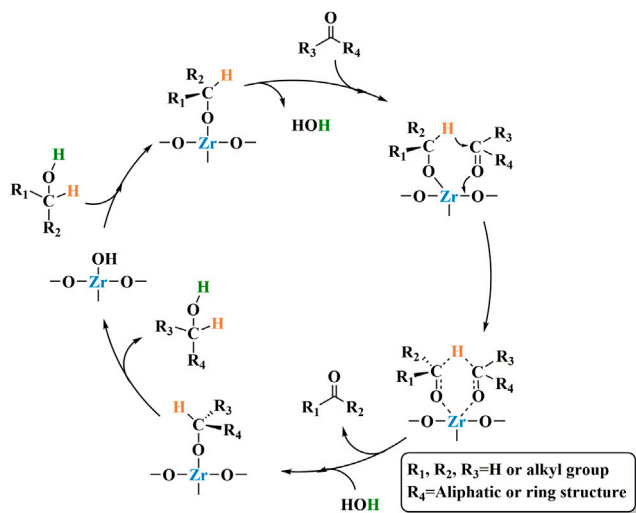
SCHEME 4 | General reaction mechanism of hydrated ZrO_2.

between the activated carbonyl compound and the alkoxide. process. At the same time, the obtained new carbonyl chemical substance ketone is released. Finally, another alcohol molecule participates in the reaction to generate the target product and the starting alkoxide.

ZR/HF-CONTAINING SUPPORTED MATERIAL CATALYSTS

The carrier material usually uses mesoporous molecular sieves, which generally have relatively large specific surface areas, large

TABLE 2 | Zr/Hf-containing supported material catalysts.

Entry	Substrate	Catalyst	Condition	H-donor	Product	Conv. (%)	Yield	References
1	LA	ZrO_2/SBA-15	150°C, 2 h	2-PrOH	GVL	99	83	Kuwahara et al. (2014)
2	ML	ZrO_2/SBA-15	150°C, 2 h	2-PrOH	GVL	98	88	Kuwahara et al. (2014)
3	ML	ZrO_2(10)/SBA-15	150°C, 3 h	2-PrOH	GVL	99.5	91	Kuwahara et al. (2017)
4	EL	ZrO_2/SBA-15	150°C, 2 h	2-PrOH	GVL	86	81	Kuwahara et al. (2014)
5	EL	Chitosan–Hf	160°C, 8 h	2-PrOH	GVL	100	97	Wang T. et al. (2020)
6	EL	Chitosan–Zr	160°C, 8 h	2-PrOH	GVL	100	97	Wang T. et al. (2020)
7	FF	ZrO_2-SBA-15	170°C, 7 h	2-PrOH	GVL	99	37	Iglesias et al. (2018)
8	FF	Fe_3O_4/ZrO_2@ MCM-41	150°C, 24 h	2-PrOH	GVL	99.3	80.8	Gao et al. (2021)
9	FF	TPA-ZrO_2-SBA-15	170°C, 11 h	2-PrOH	GVL	100	81	Srinivasa Rao et al. (2021)
10	FF	Zr-SBA-15	110°C, 6 h	2-PrOH	FA	63	40	Iglesias et al. (2015)

pore sizes, along with regular pore structures (Taniya et al., 2010). Mesoporous molecular sieves are regarded as good shape-selective catalysts and have better catalytic activity and selectivity than zeolite molecular sieves when organic macromolecular substances participate (Shen et al., 2014). In addition, the pore size can be continuously adjusted in the range of 2–50 nm, and the pores and the large and silan-rich surface (up to 2000 m^2/g) are easy to modify (Gao et al., 2021a). Mesoporous molecular sieves are often used as carriers to load or dope transition metal (e.g., Zr and Hf) elements and rare earth elements into their frameworks, surfaces, or pores. There is no doubt that mesoporous materials have also shown their talents in the field of biomass catalytic upgrading (**Table 2**).

LA and its Esters as Substrates

Using LA as a reaction substrate, ZrO_2 was supported on typical hexagonal mesoporous Si, such as Mobil Composition of Matter-41 (MCM-41) and Santa Barbara Amorphous-15 (SBA-15) (entry 1, 2, 4 in **Table 2**) prepared by Kuwahara et al. (2014). The silicon carrier itself is inactive, and the reaction kinetics demonstrated that the pore size of mesoporous Si had little effect on the catalytic activity. However, it was possible to increase the CTH reaction activity by expanding the surface area of the oxide support carrier, which can change the local structure of the Zr species. Specifically, the high surface area of Si support provided a surface environment that was suitable for the introduction of highly dispersed low-coordination Zr. The loss of used catalytic activity was due to the strong adsorption of organic residues on the catalyst surface. This prevented the next batch of organic substrates from entering the Zr active site. Similar catalysts have also been reported, and the conversion and yield have been further improved (entry 3 of **Table 2**) (Kuwahara et al., 2017). For the conversion of EL to GVL, using biopolymer chitosan as a support to prepare the efficient Zr-containing catalyst (chitosan–Zr) was developed by Wang et al. (2020c). Chitosan is derived from the diacylation of chitin (Synowiecki and Al-Khateeb, 2003). The world's marine ecosystems produce about 1,600 million tons of chitin each year (Aydın and Aksoy, 2009). And it was the second kind of abundant biopolymer in nature after cellulose, but they were underutilized. Many–NH2 and–OH groups exist in the chitosan, which means it has a strong chelating ability for M$^+$. The conversion rate of the relevant

catalysts containing Zr or Hf can reach 100%, and the corresponding yield was 97% (entries 5 and 6 of **Table 2**). Undoubtedly, it was a wise strategy to use biomass-derived chemicals to prepare catalysts for the efficient valorization of biomass feedstocks.

FF as a Substrate

Using FF as the starting substrate, the same material had been studied with different Zr coatings of ZrO_2 using wet chemical methods (entry 7 of **Table 2**) (Iglesias et al., 2018). The first type was related to the strong acid position on the interface with Si. Another type of highly dispersed t-ZrO_2 crystals that were ubiquitous in the second and third layers was related to the position of the weak acid. This catalyst was used for the cascade reaction of FF to GVL. In addition, pyridine titration experiments during vacuum and 2-PrOH soaking were also carried out, proving that the Lewis acidity of all ZrO_2 monolayer thicknesses dominated the key role. A single ZrO_2 monolayer had a few Brønsted acid sites. And this may be related to residual surface silanol. The etherification and isomerization of FA to EL reduced the reaction rate. Fe_3O_4/ZrO_2@MCM-41 was tailored by the impregnation of ZrO_2 on mesoporous MCM-41 support coated by Fe_3O_4. It could efficiently catalyze the cascade reaction in terms of conversion of FF to GVL (entry 8 of **Table 2**) (Gao et al., 2021). The introduction of these two substances did not change the original ordered hexagonal framework of MCM-41. The incorporation of Fe_3O_4 was a simple way to adjust its acidity. The kinetic study demonstrated higher activation energy for the LA-to-GVL step (86.9 kJ/mol) than that of FF transfer hydrogenation (35.0 kJ/mol) and that of subsequent alcoholysis process (51.0 kJ/mol). The catalyst could be fully recovered and reused because of its excellent magnetic property. By Zr K-edge XAFS analysis, it can be seen that the Zr^{4+} oxide species anchored on the silica surface in a low-coordination state played the most important role in the reaction. Another application of this catalyst was the conversion of FF and 2-methylfuran (2-MF) to diesel precursors through the hydroxyalkylation/alkylation (HAA) reaction (Luo et al., 2018). The mesoporous catalyst was prepared by using ZrO_2 and phosphotungstic acid (TPA) on the inside and outside of the pores of SBA-15 (Srinivasa Rao et al., 2018) (entry 9 of **Table 2**). It has also been reported that Zr-SBA-15 performs average in

TABLE 3 | Zr/Hf-containing zeolite catalysts.

Entry	Substrate	Catalyst	Condition	H-donor	Product	Conv. (%)	Yield (%)	References
1	LA	Zr-Beta/Al-MFI-ns	120°C, 11 h	2-BuOH	GVL	100	96	Bui et al. (2013)
2	ML	Hf-Beta	160°C, -	2-BuOH	GVL	80	76.8	Luo et al. (2014)
3	EL	Zr-beat-100	150°C, 10 h	2-PrOH	GVL	100	96	Wang J. et al. (2014)
4	BL	(Zr)SSIE-beta	230°C, 24 h	2-BuOH	GVL	85	76	Antunes et al. (2016)
5	FF	Zr/Al-β-TUD1	120°C, -	2-BuOH	GVL	85	76	Antunes et al. (2016)
6	FF	Zr-HY/Al-HY	120°C, 5 h	2-PrOH	GVL	95	85	Zhang H. et al. (2019)
7	FF	Zr-Al-Beta	120°C, 3 h	2-PrOH	FA	99.6	97.3	Gao et al. (2020)

FIGURE 2 | The model of the spatial limitation of the coordination of the catalyst and the substrate in the pore channel [copyright from Zhang et al. (2019a)].
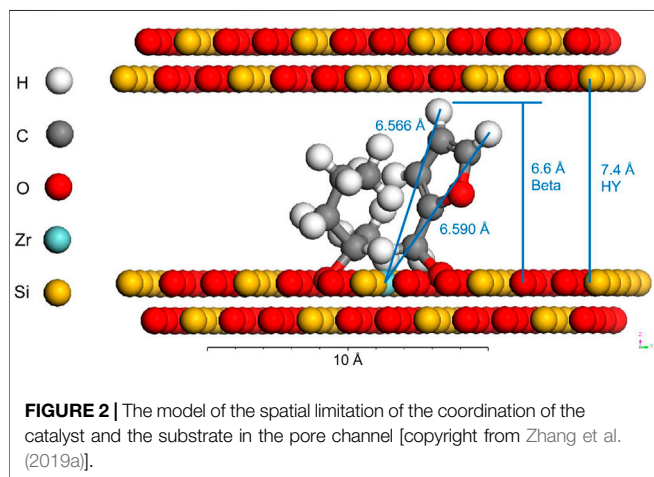
transforming FF to FA (Iglesias et al., 2015). However, it has excellent performance when reducing cyclic ketones with secondary alcohols. After the reaction, the corresponding alcohol yield was as high as 99% (entry 10 of **Table 2**).

ZR/HF-CONTAINING ZEOLITE CATALYSTS

Zeolite is a kind of nanoporous aluminosilicate crystal (Chai et al., 2021; Mardiana et al., 2022). Because of its regular pore structure and adjustable acidity, it is widely used in adsorption, separation, and catalysis (Sushkevich et al., 2014; Koreniuk et al., 2015; Wang et al., 2016c; Kim et al., 2020). The support material mainly uses mesoporous molecular sieves, which are used to provide templates to increase the stability and surface area of the catalyst, while zeolite will coordinate with the metal and form new bonds. As we all know, the catalytic activity of a molecular sieve is closely related to its unique acidity (Ramanathan et al., 2008; Melero et al., 2018; Cho et al., 2020). Usually, the acidity of zeolite is mostly affected by the isostructural substitution of Al^{3+} by Si^{4+} in the framework. This can create an imbalance of negative charges in the crystal lattice, and the concomitant exchangeable cations can make up for this imbalance (such as H^+, Na^+, K^+). When protons are connected to oxygen atoms

that are connected to silicon and Al atoms, the local charge transfer weakens and lengthens the O-H bond. In turn, this enhances the strength of its Brønsted acidity (Melero et al., 2017). The final result of these bonding interactions is that the local environment determines the type and intensity distribution of acidic sites. After a long-term research, scientists have found that if the concentration of substituted tetrahedral atoms does not exceed a certain threshold, Brønsted acid sites can show a constant acid strength which is suitable for adsorption and catalysis (Hernández et al., 2016). Therefore, the high intrinsic catalytic activity of zeolite is mainly derived from the excellent stability of the transition state in the nanopore confinement. **Table 3** compares the catalytic effects of several different Zr/Hf-containing zeolite catalysts with the substrate as the classification standard.

LA and its Esters as Substrates

The reaction system of converting LA to GVL can use Zr-Beta and MFI topological structure nano-layer aluminosilicate (Al-MFI-ns) as the bicatalyst (entry 1 of **Table 3**) (Bui et al., 2013). Both of these steps resulted in the oxidation of the H-donor, which can be separated from the product. And it can be regenerated under mild gas-phase conditions and was directly put into use next time. It was noteworthy that this process can be achieved with cheap catalysts (e.g., Ni or Cu). Moreover, the combined catalysts can also convert hemicellulose to GVL. This also provides a new potential process for the transformation of pentoses to GVL.

The process of reducing ML to GVL by Lewis acid catalyst based on relevant kinetic parameters was described Luo et al. (2014). The reaction sequence and the rate of the mechanism were calculated. And the kinetic parameters of Ti, Sn, Zr, and Hf β-catalysts at different temperatures were analyzed (entry 2 of **Table 3**). Although the selectivity of GVL was over 94%, the turnover rate of these three zeolite catalysts was different during the MPV reaction process, and the Hf β catalyst had the highest activity. It is confirmed that the stronger the Lewis acid of the catalyst is, the more stable the six-membered ring transition state of the rate-limiting CTH step can be achieved (Assary et al., 2013). Kinetic studies were carried out by changing the H-donor (primary alcohol and secondary alcohol), proving that reducing the chain length of the alcohol did not affect the Ea.

TABLE 4 | Zr/Hf-containing MOF catalysts.

Entry	Substrate	Catalyst	Condition	H-donor	Product	Conv. (%)	Yield (%)	References
1	LA	ZrF-MOF	200°C, 2 h	2-PrOH	GVL	98	96	Yun et al. (2019)
2	LA	HPW@ MOF-808	160°C, 6 h	2-PrOH	GVL	99	87	Li et al. (2021a)
3	ML	UiO-66-S60	140°C, 9 h	2-BuOH	GVL	98	80	Kuwahara et al. (2016)
4	EL	UiO-66(Zr)	200°C, 2 h	2-PrOH	GVL	100	92.7	Valekar et al. (2016)
5	EL	Hf-MOF	120°C, 8 h	2-PrOH	GVL	99	94	Rojas-Buzo et al. (2018)
6	FF	DUT-67(Hf)	180°C, 24 h	2-PrOH	GVL	100	87.1	Li et al. (2019c)
7	FF	M-MOF-808	30°C, 24 h	2-PrOH	FA	94.2	90	Valekar et al. (2020)
8	FF	P/Zr-MOFs	200°C, 2 h	2-PrOH	FA	96.1	96	Wang Y. et al. (2020)

EL was catalytically reduced to GVL by Zr-Beta zeolite. A small amount of Zr (Si/Zr ~75–200) was incorporated into the zeolite (Wang et al. (2014a). The Zr-Beta zeolite catalyst with isolated Zr atoms with Lewis acidity was prepared (entry 3 of **Table 3**). Density functional theory (DFT) calculation studies showed that Zr^{4+} was located in unique crystallographic positions of zeolite. To test its industrialization potential, the catalyst effect was further tested in the batch reactors and continuous flow reactors. Through the investigation of the mechanism, it was found that Brønsted acid sites can cause other side reactions. For example, the production of hemiacetals, pentenes, and their isomers reduced the selectivity to GVL.

FF as a Substrate

TUD-1 mixed with Zr/Al and zeolite β-type silicate catalyst was prepared and used for a series of conversion of FF (entry 4 and 5 of **Table 3**) (Antunes et al., 2016). Using 2-BuOH as an H-donor, a stepwise kinetic modeling study was successfully carried out. The effection of catalysts materials on intermediates selectivity was revealed. It was found that the Zr site played a decisive role in the reduction of FF to FA and levulinate (LE) to GVL. It was proved that the coexistence of Al sites can promote the acid catalysis step, involving the process of FA to alkyl furfuryl ethers (FEs), LEs, angelica lactones (AnLs), and LA, respectively. A similar combination also used the catalysts of Zr-HY (Lewis acid) and Al-HY (Brønsted acid) (Zhang et al. (2019a). The Zr-containing zeolite is prepared by a post-synthesis method (entry 6 of **Table 3**). Zr was added after the dealumination of the parent Al-containing zeolite. However, the model shown in **Figure 2** exhibits that there is a certain dimensional limitation in the coordination of FF and 2-PrOH at the Zr Lewis acidic site in the pore channel. Besides, active sites of Zr-Al-Beta zeolites can be changed by mild alkaline treatment (e.g., LiOH, NaOH, KOH) (Gao et al., 2020). It is worth mentioning that alkaline treatment can improve recalcitrance to deactivation and coking, which is beneficial for the recycling of the catalyst.

For the CTH conversion of FF to FA. 2-PrOH as the H-donor over cation-exchanged Lewis acidic BEA zeolite was calculated by DFT (Prasertsab et al., 2018). The catalytic activity of tetravalent metal centers (Sn, Zr, and Hf) substituted into BEA. It found that in the order Zr ≥ Hf > Sn, based on Ea.

In short, the binding capacity of the Hf-zeolite molecular sieve was better than that of the Zr-zeolite molecular sieve. This is because the activation energy of the Zr-zeolite reaction was lower when the Hf-zeolite molecular sieve catalyzed the reaction (Injongkol et al., 2017). The Zr-zeolite catalyst played an important role in the combination of stone and Zr/Hf to form the Lewis acid center, which was believed to constitute the active site of the catalyst. Moreover, it was further determined that this would play an important role in the adsorption and activation of the reactants. The Lewis acid site combined with the carbonyl group to activate the unsaturated C=O double bond, and finally formed the alcohol compound product.

ZR/HF-CONTAINING METAL-ORGANIC FRAMEWORK CATALYSTS

The term MOF was introduced in 1995 and was now widely accepted (Furukawa et al., 2013). It was a kind of coordination polymer material with good crystal form (Wang et al., 2016a; Goetjen et al., 2020). MOF catalysts have been developed successfully in the application of renewable energy and environmental fields, which have good design capabilities (Zhang et al., 2017; Lin et al., 2021; Mautschke and Llabres, 2021). Highly adjustable porosity and specific surface area, high density of accessible metal sites were the fascinating part of this material (Rui et al., 2021). The microporous zeolite material has diffusion limitations. But the MOF has a mesopore with a diameter of about 9.8 nm, facilitating the full diffusion and mixing of the various substances in the reaction. In terms of BET surface area, zeolite is about 200–500 $m^2 g^{-1}$, while MOF is about 1,000–10000 $m^2 g^{-1}$ (Dhakshinamoorthy et al., 2011). Generally, the surface area and porosity of MOF were much higher than those of zeolite, but the chemical and thermal stability of MOFs are not as good as that of zeolite. Zr/Hf-containing MOFs catalysts can be seen everywhere in the field of the transfer hydrogenation of biomass-based carbonyl compounds. **Table 4** summarizes the reaction conditions and yields of some excellent Zr/Hf-containing MOF catalysts for the conversion of biomass-based chemicals.

SCHEME 5 | Possible reaction mechanism for CTH process of levulinate esters to produce GVL over UiO-66-S$_x$ catalyst and its structure diagram [Copyright from Kuwahara et al. (2016)].
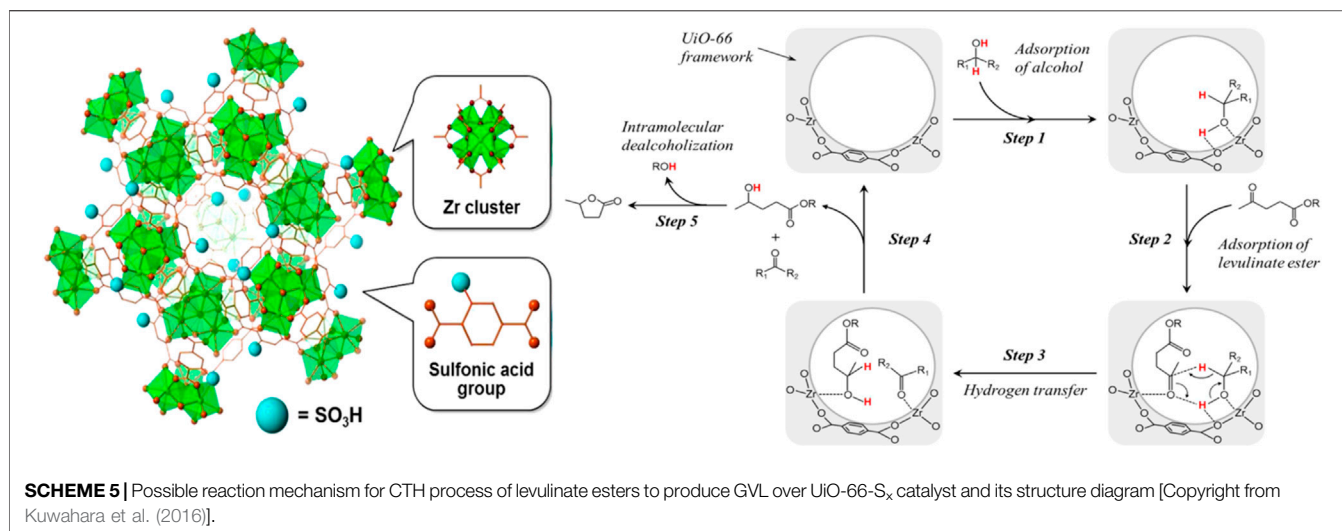
LA and its Esters as Substrates

For the reaction of LA to GVL, Yun et al. avoided most of the toxic solvent dimethylformamide (DMF) which were typically used in the preparation of Zr polysulfide catalysts (Yun et al., 2019). Instead, they prepared the catalyst ZrF with fumaric acid and ZrCl$_4$ in water. In particular, they also used monocarboxylic acids as regulators, which affected the formation and morphology of aquatic zirconia, but did not affect its crystal structure and acidity. ZrF was adjusted with formic acid, acetic acid, and propionic acid, obtaining F-ZrF, A-ZrF, and P-ZrF, respectively. As a comparison, W-ZrF synthesized directly in water without a regulator and D-ZrF prepared in DMF in a traditional mode were also established. The order of particle size is F-ZrF (270 nm) >A-ZrF (130 nm) >P-ZrF (55 nm) >D-ZrF (25 nm). The size of ZrF was related to the molecular weight of the monocarboxylic acid. A regulator with a relatively low molecular weight can obtain ZrF with larger particle size and less excessive aggregation, which is beneficial for catalysis. W-ZrF without modifier did not have a good granular shape but existed in the form of a large block. Among them, at 200°C in 2 h, ZrF prepared by formic acid showed a 98% conversion of LA and 96% yield of GVL (entry 1 of **Table 4**).

HPW@MOF-808 was fabricated via a facile impregnation method with H$_3$PW$_{12}$O$_{40}$ and Zr-based MOF (Li et al., 2021a). Although MOF-808 had good activity in CTH reaction, its Brønsted acidity did not meet the requirements. Therefore, adding HPW (strong Brønsted acid) can effectively promote the esterification of LA with 2-PrOH and the subsequent lactonization reaction. Besides, MOF-808 had high acid resistance, which can exist stably in HCl and its cavity was large enough to encapsulate HPW. The yield of GVL can be obtained by reacting at 160°C for 6 h (entry 2 of **Table 4**)., and the yield can be increased by 5% when the temperature was increased by 20°C. The dipping method for HPW@MOF-808 was relatively simple, but the preparation of MOF-808 was nearly a week, the process was complicated and time-consuming.

Expanding the starting material from LA to its ester, MOF material catalyst (e.g., sulfonic acid-functionalized UiO-66) also performed well (entry 3 of **Table 4**) (Kuwahara et al., 2016). UiO-66(Zr) is comprised of 12-coordinated Zr$_6$O$_4$(OH)$_4$ clusters connected with 1,4-benzene dicarboxylate (BDC) linkers (Hu et al., 2016). Due to the very strong force between Zr-O, UiO-66(Zr) material has good water and thermal stability, and the structure can be maintained stably for a long time in a solution of pH = 1–11 (Shearer et al., 2014). Observing **Scheme 5**, it can be seen that each Zr-O cluster is 12-fold connected to adjacent clusters through a benzene dicarboxylate linker, and stacked together (Kuwahara et al., 2016). Correspondingly, it was confirmed that by FT-IR analysis, the Zr-O cluster only coordinated with the carboxylic acid oxygen atom, but not the sulfonated oxygen atom. With the increased degree of substitution of the sulfonic acid ligand, the XRD intensity and N$_2$ adsorption capacity of the microporous solid decreased significantly. In other words, the crystallinity and surface area of MOF materials decreased with the increase of sulfonic acid ligands, defects or irregular connections, and catalyst activity increased. Lewis basic sites (Zr$_6$O$_4$(OH)$_4$ cluster) catalyzed the CTH reaction of LA and its esters (entry 3 of **Table 4**). Brønsted-acid site (-SO$_3$H) promoted continuous intramolecular dealcoholization. The acid-base sites were arranged adjacent to each other in the confined nanospace, and had a synergistic effect on the entire reaction.

A variety of Zr-containing MOFs with different ligands were prepared for the conversion of EL to GVL (Valekar et al., 2016). UiO-66(Zr) showed good catalytic activity (92.7% GVL yield) at a high temperature (200°C), as shown in entry 4 of **Table 4**. In contrast, MOF-808 has been shown to produce GVL (85% yield) quickly at a moderate reaction temperature (130°C). It is worth mentioning that the latter also performed well in open systems using solvent reflux. In addition, through acid-base modification of the BDC ligand, the changes in its structure and catalytic effect were studied. It was found that the -COOH functional group can provide additional acidity, but the surface area and pore volume of the material have a considerable loss, and the presence of the -NH$_2$ group in the ligand provided additional alkalinity to the material, and the surface area loss was small. This was due to the
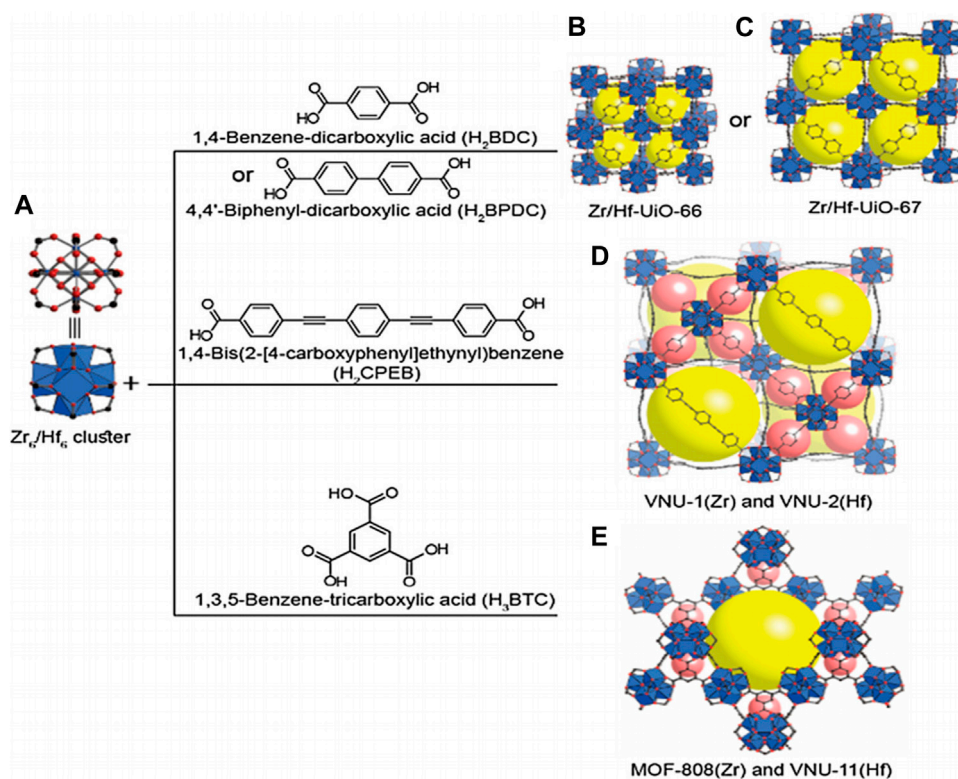
SCHEME 6 | (A). Zr_6/Hf_6 cluster. UiO-type MOF structures of **(B)** Zr/Hf-UiO-66 and **(C)** Zr-, Hf-UiO-67. Interpenetrated structure **(D)** of VNU-1(Zr) and VNU-2(Hf). **(E)** Structures of MOF-808 (Zr) and VNU-11(Hf). Color code: C, black; O, red; Zr or Hf, blue; cages, yellow and purple [Copyright from Nguyen et al. (2019)].

smaller size of the -NH$_2$ group compared to the -COOH group. The order of pore size and EL conversion and GVL yield showed consistency, that was UiO-66(Zr)-COOH (25% EL conversion, 13.9% GVL yield) < UiO-66(Zr)-NH$_2$ (99% EL conversion, 64.6% IPL yield) < UiO-66(Zr) (100% EL conversion, 92.7% GVL yield). The low catalytic efficiency of UiO-66 (Zr)-COOH was because EL only reacted on its surface or diffused slowly into its narrow pores. On the contrary, when UiO-66(Zr)-NH$_2$ was used, almost all EL was converted, but the main by-product IPL was produced. This proved that UiO-66(Zr) functionalized with -NH$_2$ will preferentially undergo transesterification with excess 2-PrOH. Similar conversion and yield have been obtained in other work using the same substrate (entry 4 of **Table 4**) (Rojas-Buzo et al., 2018).

Using EL as the starting substrate, it can be directly converted to GVL through transfer hydrogenation. Sergio et al. prepared a series of materials such as UiO-66 and MOF-808, using formic acid as a modulator (Rojas-Buzo et al., 2018). The latter can be converted into GVL to obtain 100% FF conversion and 97% yield (2 h, 100°C), as shown in entry 5 of **Table 4**. Compared to UiO-66 (pore size 6Å), MOF-808 has a wider pore structure (pore size 14 Å), which allows the conversion of larger substrates (Mautschke and Llabres, 2021). In the cascade reaction, the combination of Hf-MOF-808 with Al-Beta catalyst was used, and a 51% yield was obtained after 6 h of reaction (entry 5 of **Table 4**). Hf-MOF-808 showed excellent activity and specific

selectivity in hydrogenating carbonyl compounds through the CTH strategy because of its poor crystallinity, defects, large specific surface, and abundant Lewis acid-base sites. By using DFT calculations on the mechanism of MPV reaction, Lin et al. found that carbonyl compounds (e.g., ketones and alcohols) filled the defects of Hf-MOF (Lin et al., 2021). Lewis acid with Hf as the center can coordinate with the oxygen of the substrate molecule, and form a six-membered ring transition state. But other reactive groups with insufficient hardness or large steric hindrance (e.g., -NO$_2$, C=C, -CN) were difficult to coordinate with Hf, which was difficult to play a catalytic role. This also explained why Hf-MOF materials have specific selectivity for reducing carbonyl groups.

FF as a Substrate

For the reaction of FF to GVL, DUT-67 (Hf) performed well. All Hf^{4+} contained in the Hf$_6$O$_8$ cluster of 12-linked UiO-66(Hf) was saturated, so it is difficult to introduce SO$_4^{2-}$ through a post-synthetic modification method (Li et al., 2019c). In contrast, each Hf cluster of DUT-67 (Hf) is 8 times connected to the 2,5-thiophenedicarboxylic acid (H$_2$TDC) linker (Bon et al., 2013). An inorganic acid (H$_2$SO$_4$) can be added to introduce Brønsted acid sites. The optimal ratio of sulfated DUT-67(Hf) can convert 100% of FF and undergo a cascade reaction (180°C for 20 h) to finally obtain 84.9% GVL (entry 6 of **Table 4**). However, the preparation process of the catalyst was very complicated and time-consuming, which was a challenge for the promotion of large-scale use.

TABLE 5 | Zr/Hf-containing metal-organic hydride catalysts.

Entry	Substrate	Catalyst	Condition	H- donor	Product	Conv. (%)	Yield (%)	References
1	LA	Hf-DTMP	140°C, 3 h	2-BuOH	GVL	98.7	96.9	Hu L. et al. (2019)
2	LA	Zr-BDB	130°C, 3 h	2-PrOH	GVL	99.7	97.2	Song et al. (2021)
3	ML	Zr-BDB	130°C, 4 h	2-PrOH	GVL	99.7	98.4	Song et al. (2021)
4	EL	Zr-BDB	130°C, 6 h	2-PrOH	GVL	99.5	98.7	Song et al. (2021)
5	EL	PPOA-Hf	160°C, 6 h	2-PrOH	GVL	100	85	Wu W. et al. (2018)
6	EL	HA-Zr	150°C, 24 h	2-PrOH	GVL	100	88.3	Xiao et al. (2017)
7	EL	Zr-SRf	150°C, 7 h	2-PrOH	GVL	92.4	92	Zhang et al. (2018)
8	EL	Zr-PhyA	200°C, 1 h	2-PrOH	GVL	100	98.5	Song et al. (2015b)
9	EL	Hf-ATMP	150°C, 4 h	2-PrOH	GVL	95	86	Xie et al. (2016)
10	EL	Zr–CA	150°C, 4 h	2-PrOH	GVL	100	96.9	Xue et al. (2016)
11	EL	FDCA-Hf	160°C, 4 h	2-PrOH	GVL	100	98	Li et al. (2018b)
12	EL	Zr-TMPA	160 °C, 8 h	2-PrOH	GVL	100	96.2	Xie et al. (2017)
13	EL	Zr-HBA	150°C, 4 h	2-PrOH	GVL	100	94.4	Song et al. (2015a)
14	EL	Hf-OFR	150°C, 9 h	2-PrOH	GVL	91	86	Chen et al. (2021a)
15	EL	Hf-GO	150°C, 5 h	2-PrOH	GVL	95.5	87.7	Li et al. (2020c)
16	EL	Hf-GO	150°C, 5 h	2-PrOH	GVL	54.8	54.7	Li et al. (2020c)
17	EL	Hf-DTMP	140°C, 3 h	2-BuOH	GVL	97.63	96.2	Hu L. et al. (2019)
18	BL	Zr-BDB	130°C, 6 h	2-PrOH	GVL	81.4	77.2	Song et al. (2021)
19	BL	ZrPO-1.00	210°C, 2 h	2-PrOH	GVL	98.1	95.7	Li et al. (2017)
20	FF	ZrPN	140°C, 2 h	2-PrOH	FA	98	98	Li et al. (2016c)
21	FF	Zr-LS	100°C, 1 h	2-PrOH	FA	97.5	96	Zhou et al. (2019b)
22	FF	Zr-LS	80°C, 3 h	2-PrOH	FA	99	90	Zhou et al. (2019b)
23	FF	PhP-Hf	120°C, 2 h	2-PrOH	FA	99.2	97.6	Li et al. (2019a)
24	FF	Zr-HAs	50°C, 15 h	2-PrOH	FA	97.4	96.9	Sha et al. (2017)
25	FF	Hf–TA	70°C, 3 h	2-PrOH	FA	100	99	Wang X. et al. (2020)
26	FF	Hf-DTMP	130°C, 3 h	2-BuOH	FA	99.9	98.5	Hu et al. (2019b)
27	FF	HPW/Zr-β	160°C, 24 h	2-PrOH	GVL	100	68	Winoto et al. (2019)
28	HMF	Hf-DTMP	100°C, 2 h	2-BuOH	BMHF	99	90	Hu et al. (2019b)
29	HMF	MZCCP	130°C, 4 h	2-BuOH	DHMF	83.9	64.2	Hu et al. (2018)

In the classic reaction of FF to FA under mild conditions, three Zr-molybdenum compounds (UiO-66, UiO-67, and DUT-52) with the same ligand-metal node coordination but different porous properties were compared. It was proved that the metal node connectivity was more important than high porosity when the Zr-porous membrane material underwent a CTH reaction (Valekar et al., 2020). In addition, the synthesis of an M-MOF-808 material has also been optimized, which can also obtain a 94.2% FF conversion and 90% FA yield after reacting at 40°C for 24 h (entry 7 of **Table 4**). Low-temperature conditions provided novel ideas for new applications of low-grade waste heat. P/Zr-MOF catalysts were prepared by $(NH_4)_2HPO_4$ pyrolysis approach starting from Zr-MOFs (Wang Y. et al., 2020). P/Zr-MOFs compared with Zr-MOFs, a part of O–Zr–O in the MOFs was phosphated to form O–Zr–P and P–Zr–P, in which Zr–P possessed stronger Lewis acidity and basicity than those of Zr–O. The increase of reaction temperature and time was conducive to the CTH of FF. However, too high a reaction temperature will result in a decrease in the conversion of FF. Meanwhile, too long reaction time will lead to side reactions of excessive hydrogenation and hydrogenolysis, resulting in a decrease in the selectivity of FA (entry 8 of **Table 4**).

In a word, Zr/Hf-containing MOFs exhibited good chemical, thermal, and mechanical stability due to the strong bond between Zr/Hf and oxygen and their high coordination number. **Scheme 6** clearly shows the proposed structure of MOFs built from 12-connected and 6-connected Zr_6/Hf_6 clusters coordinated with ditopic and tritopic carboxylate linkers, respectively (Nguyen et al., 2019).

ZR/HF-CONTAINING METAL-ORGANIC HYDRIDE CATALYSTS

Metal-organic hydride materials have also been known as unconventional MOF (UMOF) (Gagnon et al., 2012; Goetjen et al., 2020). Compared with the MOF material with good crystal form, Metal-organic hydrides are polymer with an amorphous structure but have good stability and more accessible sites. The organometallic coordination polymerization catalyst has high catalytic activity and good molecular tailoring (Wang et al., 2016b; Liu et al., 2021e). By adjusting the microstructure of catalysts, such as the substituents of the ligand, the coordination atom, and the electronic and three-dimensional environment of the coordination center, the molecular design and assembly of the polymer can be realized at the molecular level (Erickson et al., 2015; Hu et al., 2018; Liu et al., 2019; Peng et al., 2021). In this way, the physical properties of polymers can be controlled, and various polymers with novel functions and stereoisomers can be obtained (Asghari and Yoshida, 2006; Dutta et al., 2012; Jain et al., 2015; Zhou et al., 2019a). **Table 5** summarizes the reaction conditions and yields of some excellent Zr/Hf-containing metal-organic hydride catalysts for the conversion of biomass-based chemicals.

LA and its Esters as Substrates

Using LA as a substrate, a new type of organic zirconium borate (Zr-BDB) was developed by Song et al. to convert it to GVL (Song et al., 2021). 1,4-Benzodiboric acid (BDB) and $ZrOCl_2.8H_2O$ were synthesized by a solvothermal method in DMF (entry 1 of

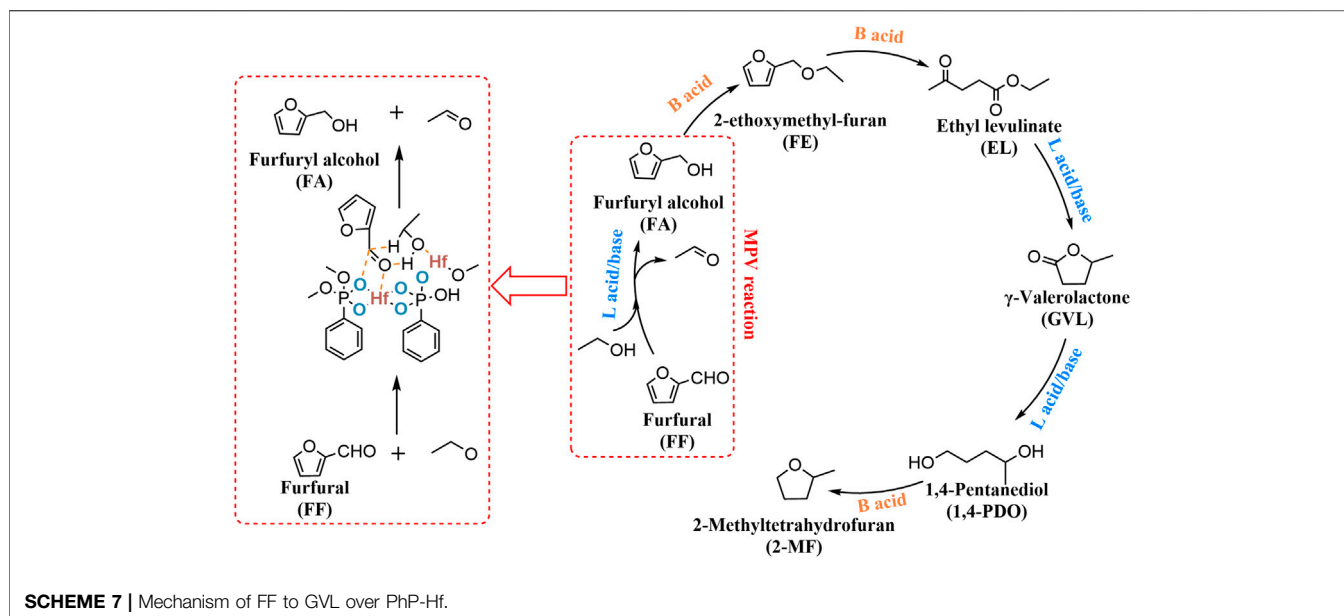**SCHEME 7 |** Mechanism of FF to GVL over PhP-Hf.

Table 5). As a Lewis acid, BDB can coordinate with and activate the hydroxyl group in alcohol. At the same time, Zr was combined to activate the carbon group, achieving the purpose of synergistically catalyzing the MPV reaction. The yields of different substrates (ML > EL > BL) to GVL were due to the increased steric hindrance from methyl to butyl.

In the system of EL to GVL, there were many different catalysts, such as Zr-BDB, PPOA-Hf, HA-Zr, Zr-SRf, Zr-PhyA, Hf-ATMP, Zr–CA, 2,5-furandicarboxylic acid (FDCA)-Hf, Zr-TMPA, Zr-HBA, Hf-OFR, Hf-GO, Hf-DTMP (entry 4–17 of **Table 5**). All of them were coordinated by different organic ligands. Hf-OFR was prepared by the oxytetracycline fermentation broth residue (OFR), which is an abundant solid waste in the fermentation industry (Chen et al., 2021a). It is beneficial for both pharmaceutical wastes and bio-based resources. Hazardous and tricky to treat. EL was completely converted to obtain GVL with a yield of 85% (160°C, 6 h) by PPOA-Hf catalyst (Wu et al., 2018b). Ea was estimated at approximately 53 kJ/mol, which was relatively lower than other catalysts. The layered metal phosphonate-phosphate hybrid can be used for ion exchange. Using humic acid (HAs) as a raw material to synthesize Zr-containing catalyst (Zr-HA) was proposed (Xiao et al., 2017). HAs are an important part of lignite (typical low-rank coal) with abundant reserves. This low-rank coal is usually only used as a low-quality fuel. If it can be applied to fine chemical catalysts, it will be a new method to realize the classification and clean utilization of coal. Similarly, HA and the solid residues (SR) after HA extraction from lignite were used to prepare Zr-SRf catalyst (Zhang et al., 2018). Compared to the previous study, this work had greatly shortened the reaction time (7 h V.S. 24 h) and improved the selectivity (83% V.S. 99.5%). Besides, graphene oxide (GO) is rich in acidic carboxyl groups and phenolic hydroxyl groups (Palermo et al., 2016; Karthik et al., 2021). Through the coordination of Hf^{4+}/Zr^{4+} with the carboxyl

group in graphene oxide, Hf-GO, and Zr-GO catalysts were constructed (Li et al., 2020c).

There are not many studies on BL as the substrate, and zirconium phosphates were used in this reaction (Li et al., 2017). The BL conversion at 2 h was 98.1%, and the GVL yield was 95.7% (entry 19 of **Table 5**). Compared with ZrO_2, the binding energies of Zr3d and O1s of all ZrPO-X materials were significantly increased. This was due to the introduction of phosphorus, leading to the decrease of Zr electron density and the increase of surface hydroxyl groups.

FF as a Substrate

For the conversion of FF to FA, a template-free method to synthesize various heterogeneous acid–base bifunctional nitrogen-containing alkyltriphosphonate-metal hybrids (MPN) catalysts were synthesized by Li et al. (Li et al., 2016c). The organotriphosphate-zirconium hybrid (ZrPN) mainly focused on the CTH reactions of biomass-derived carbonyl compounds to alcohols and aldoses to ketoses (entry 20 of **Table 5**). Through calculation, the rate constant of ZrPN at 100°C was $3.6 \times 10^{-3} s^{-1}$, which was 12 times than that of ZrO_2. The Ea of ZrPN and ZrO_2 were 70.5 and 79.1 kJ/mol, respectively. Both two proved the superior performance of the Zr N-Alkyltriphosphate nanohybrid from the perspective of reaction kinetics. It's worth paying high attention that the intramolecular CTH of C3−C6 aldoses to the corresponding ketoses in water was also studied. Generally, Al-zeolites can not catalyze glucose isomerization due to the weakening of Lewis acid sites existing in water. In contrast, Lewis acid sites in ZrPN can not be hampered by water, which showed excellent potential in CTH reaction. In another word, ZrPN can be extrapolated to other similar lignocellulose-derived substrates for upgrading biomass.

The conversion of FF can also be achieved by simply assembling lignosulfonate and $ZrCl_4$ to form a Zr-containing polyphenol biopolymer catalyst under hydrothermal conditions (entry 22 of **Table 5**) (Zhou et al., 2019b). Lignosulfonate has a sulfonic acid

group and can be used as an alkali-free acidic site. Therefore, dangerous sulfonation can be avoided. Catalytic experiments were also carried out with 18 typical aldehydes and ketones in the traditional chemical industry as substrates. It proved that Lignosulfonate-based catalysts had good universality and application potential. Different proportions of phenylphosphonic acid (PhP) and Hf were used to prepare the acid-base bifunctional nano-hybrid catalyst PhP-Hf, which can convert FF to FA (entry 23 of **Table 5**) (Li et al., 2019a). The catalyst had a moderate acid-base site and acidity. PhP-Hf was weaker than that of HfO_2, but it also promoted the reaction. Acid (Hf^{4+}) and base (O^{2-}) sites had a synergistic effect on the CTH reaction of FF to FA. The base sites facilitated the adsorption and dissociation of 2-PrOH on the catalyst, and the aldehyde group was activated by Hf^{4+}. Then the six-membered ring transition state was formed *in situ* and completed the hydrogen transfer. And the Ea was calculated at about 60.8 kJ/mol.

The Hf-TA catalyst was synthesized in DMF with naturally occurring tannic acid (TA) as a ligand to coordinate with $HfCl_4$. (Wang et al., 2020d). The advantage of this method was that renewable and natural resources were used to construct an efficient and environmentally friendly Hf-containing catalyst, and the preparation process was simple. Although the general catalyst can only be recycled about 5 times, the catalytic effectiveness of the 10th used catalyst was better than the first time. It was further confirmed by FT-IR spectra, showing that the residual DMF in the pore structure of the catalyst was gradually replaced by 2-PrOH during the reuse process. This would facilitate contact with more active sites, increasing the MPV activity. Under the relatively mild reaction conditions (70°C, 3 h), a high yield of 99.0% of FA can be obtained (entry 25 of **Table 5**). Zirconium phosphonate The materials synthesized by the coordination of organic acids and zirconium were widely used in the biomass-based conversion. Zr-containing catalysts such as Zr-HAs, Zr-DTMP, HPW/Zr-β (entries 24, 26, 27 of **Table 5**) also can be used in similar systems from FF to FA or GVL. By regulating the ratio of organic phosphonate and inorganic phosphate with the center of Zr metal (Silbernagel et al., 2016), further optimization of the MPV reduction reaction system could be successfully carried out. The specific active sites required for each step of FF to GVL were shown in **Scheme 7**. Lewis acid/base sites were responsible for the MPV reduction (FF to FA, and EL to GVL), while Brønsted acid sites exhibited key effects on the etherification reaction (FA to FE) and ring-opening reaction (FE to EL).

HMF as a Substrate

Converting HMF to BHMF is also a significant path for biomass-derived conversion. A new Hf-based metal-organic coordination polymer (Hf-DTMP) was assembled by $HfCl_4$ and diethylene triaminepenta (methylene phosphonic acid) (DTMP) (Hu et al., 2019b). The mechanism was that 2-BuOH, and HMF were first adsorbed on catalyst. Subsequently, 2-BuOH was dissociated into the active H and alkoxide by O^{2-}. Meanwhile, the carbonyl group of HMF was activated by Hf^{4+}. Then, a six-membered intermediate was generated by the dissociated alcohol and carbonyl group with Hf^{4+}-O^{2-}. Finally, BHMF was eventually

formed *via* CTH (entry 28 of **Table 5**). In contrast, the magnetic catalysts (MZCCP) synthesized by $ZrCl_4$, cyanuric acid (CA), and Fe_3O_4 did not have an advantage in terms of yield (90% V.S. 64.2%) (entry 29 of **Table 5**) (Hu et al., 2018).

CONCLUSION AND PERSPECTIVES

Mountains of researches proved that CTH is a significant strategy to transform biomass-based substrates into chemical platform products and fuel precursors of high value. Zr/Hf can be supported on other materials or coordinated/coupled with them to form Zr/Hf-containing materials, of which they can play a significant role in CTH that is similar to noble metal catalysis. In this review, the catalytic effects and mechanisms of different types of Zr/Hf-containing catalysts are discussed. Various kinds of materials demonstrate different properties and preparation methods. Zr/Hf-containing oxides are relatively inexpensive and easily available. However, their basic sites are not strong and are easily affected by solvents, and the corresponding reaction activity is not ideal. Supported catalysts containing Zr/Hf can use existing templates to enhance stability and increase surface area. The zeolite catalysts are prone to be affected by the hydroxyl groups on Si, and the acidic enhancement of Lewis can effectively fix the metal and coordinate. The MOF catalysts generally have a good crystal form and spatial structure. However, the preparation process of these three catalysts is complicated and the relevant precursors are expensive, which is not suitable to apply from an economic point of view. Relatively speaking, the preparation steps of metal-organic hybrid materials are simpler and the time is shorter, which have abundant sources and room for expansion.

To establish a mature industrialization system, economic benefits and environmental impacts should be taken into account. In other words, the preparation and reaction process of the catalyst should be as simple and time-saving as possible. Also, the consumption of raw materials and energy should be low. Correspondingly, the purity and quality of the obtained product should be high. The problem at this stage is that there are seasonal differences in the availability of biomass raw materials, and the competitiveness of economic benefits is not very strong. As the saying goes, there is no useless waste, only misplaced resources. How to convert this huge amount of useless waste into resources that can replace the heavily polluting traditional energy and generate economic benefits is a problem that needs to be tackled on the road to green development. And this depends on the joint efforts of scientific researchers, enterprises, and the government, respectively. We still need to propose a new solid acid catalyst design strategy. 1) Using non-precious metal materials and green solvents to achieve a win-win situation for the economy and environmental protection. 2) Increasing the density of acid and base sites accessible to the catalyst. 3) Controlling the ratio of Lewis/Brønsted acid sites. 4) Developing more functional group synergistic catalysis. 5) Modulating the wettability of the catalyst surface together with increasing its water resistance. 6) Simplifying the catalyst preparation process, reducing the preparation cost, and controlling the energy consumption of each link accurately.

AUTHOR CONTRIBUTIONS

FUNDING

REFERENCES

Abomohra, A. E.-F., Elsayed, M., Esakkimuthu, S., El-Sheekh, M., and Hanelt, D. (2020). Potential of Fat, Oil and Grease (Fog) for Biodiesel Production: A Critical Review on the Recent Progress and Future Perspectives. *Prog. Energ. Combustion Sci.* 81, 100868. doi:10.1016/j.pecs.2020.100868

Ahmad, S. F. K., Md Ali, U. F., and Isa, K. M. (2019). Compilation of Liquefaction and Pyrolysis Method Used for Bio-Oil Production from Various Biomass: A Review. *Environ. Eng. Res.* 25, 18–28. doi:10.4491/eer.2018.419

Ajmi, A. N., and Inglesi-Lotz, R. (2020). Biomass Energy Consumption and Economic Growth Nexus in OECD Countries: A Panel Analysis. *Renew. Energ.* 162, 1649–1654. doi:10.1016/j.renene.2020.10.002

Antunes, M. M., Lima, S., Neves, P., Magalhães, A. L., Fazio, E., Neri, F., et al. (2016). Integrated Reduction and Acid-Catalysed Conversion of Furfural in Alcohol Medium Using Zr,Al-Containing Ordered Micro/mesoporous Silicates. *Appl. Catal. B: Environ.* 182, 485–503. doi:10.1016/j.apcatb.2015.09.053

Asghari, F. S., and Yoshida, H. (2006). Dehydration of Fructose to 5-hydroxymethylfurfural in Sub-critical Water over Heterogeneous Zirconium Phosphate Catalysts. *Carbohydr. Res.* 341, 2379–2387. doi:10.1016/j.carres.2006.06.025

Assary, R. S., Curtiss, L. A., and Dumesic, J. A. (2013). Exploring Meerwein-Ponndorf-Verley Reduction Chemistry for Biomass Catalysis Using a First-Principles Approach. *ACS Catal.* 3, 2694–2704. doi:10.1021/cs400479m

Atwoli, L., Baqui, A. H., Benfield, T., Bosurgi, R., Godlee, F., Hancocks, S., et al. (2021). Call for Emergency Action to Limit Global Temperature Increases, Restore Biodiversity, and Protect Health. *Med. J. Aust.* 215, 210–212. doi:10.5694/mja2.51221

Aydın, Y. A., and Aksoy, N. D. (2009). Adsorption of Chromium on Chitosan: Optimization, Kinetics and Thermodynamics. *Chem. Eng. J.* 151, 188–194. doi:10.1016/j.cej.2009.02.010

Bogale, T. F., Gul, I., Wang, L., Deng, J., Chen, Y., Majerić-Elenkov, M., et al. (2019). Biodegradation of 1,2,3-trichloropropane to Valuable (S)-2,3-dcp Using a One-Pot Reaction System. *Catalysts* 10, 3. doi:10.3390/catal10010003

Bon, V., Senkovska, I., Baburin, I. A., and Kaskel, S. (2013). Zr- and Hf-Based Metal-Organic Frameworks: Tracking Down the Polymorphism. *Cryst. Growth Des.* 13, 1231–1237. doi:10.1021/cg301691d

Brauer, M., Casadei, B., Harrington, R. A., Kovacs, R., Sliwa, K., Davaakhuu, N., et al. 2021). Taking a Stand against Air Pollution - the Impact on Cardiovascular Disease. *Eur. Heart J.* 42, 1460–1463. doi:10.1093/eurheartj/ehaa1025

Brethauer, S., and Studer, M. H. (2015). Biochemical Conversion Processes of Lignocellulosic Biomass to Fuels and Chemicals - a Review. *Chimia* 69, 572–581. doi:10.2533/chimia.2015.572

Bui, L., Luo, H., Gunther, W. R., and Román-Leshkov, Y. (2013). Domino Reaction Catalyzed by Zeolites with Brønsted and Lewis Acid Sites for the Production of γ-Valerolactone from Furfural. *Angew. Chem. Int. Ed.* 52, 8022–8025. doi:10.1002/anie.201302575

Cao, W., Luo, W., Ge, H., Su, Y., Wang, A., and Zhang, T. (2017). UiO-66 Derived Ru/ZrO2@C as a Highly Stable Catalyst for Hydrogenation of Levulinic Acid to γ-valerolactone. *Green. Chem.* 19, 2201–2211. doi:10.1039/c7gc00512a

Chai, Y., Dai, W., Wu, G., Guan, N., and Li, L. (2021). Confinement in a Zeolite and Zeolite Catalysis. *Acc. Chem. Res.* 54, 2894–2904. doi:10.1021/acs.accounts.1c00274

Champness, N. R. (2011). The Future of Metal-Organic Frameworks. *Dalton Trans.* 40, 10311–10315. doi:10.1039/c1dt11184a

Chen, S., Wojcieszak, R., Dumeignil, F., Marceau, E., and Royer, S. (2018). How Catalysts and Experimental Conditions Determine the Selective Hydroconversion of Furfural and 5-hydroxymethylfurfural. *Chem. Rev.* 118, 11023–11117. doi:10.1021/acs.chemrev.8b00134

Chen, Y., Yao, X., Wang, X., Zhang, X., Zhou, H., He, R., et al. (2021). Direct Use of the Solid Waste from Oxytetracycline Fermentation Broth to Construct Hf-Containing Catalysts for Meerwein-Ponndorf-Verley Reactions. *RSC Adv.* 11, 13970–13979. doi:10.1039/d1ra01738a

Chen, Y., Zhang, L., Yang, Y., Pang, B., Xu, W., Duan, G., et al. (2021). Recent Progress on Nanocellulose Aerogels: Preparation, Modification, Composite Fabrication, Applications. *Adv. Mater.* 33, 2005569. doi:10.1002/adma.202005569

Chia, M., and Dumesic, J. A. (2011). Liquid-phase Catalytic Transfer Hydrogenation and Cyclization of Levulinic Acid and its Esters to γ-valerolactone over Metal Oxide Catalysts. *Chem. Commun.* 47, 12233–12235. doi:10.1039/c1cc14748j

Cho, H. J., Kim, D., and Xu, B. (2020). Selectivity Control in Tandem Catalytic Furfural Upgrading on Zeolite-Encapsulated Pt Nanoparticles through Site and Solvent Engineering. *ACS Catal.* 10, 4770–4779. doi:10.1021/acscatal.0c00472

Choi, J. H., Mao, Y., and Chang, J. P. (2011). Development of Hafnium Based High-K Materials-A Review. *Mater. Sci. Eng. R: Rep.* 72, 97–136. doi:10.1016/j.mser.2010.12.001

Crabtree, R. H. (2019). Transfer Hydrogenation with Glycerol as H-Donor: Catalyst Activation, Deactivation and Homogeneity. *ACS Sustain. Chem. Eng.* 7, 15845–15853. doi:10.1021/acssuschemeng.9b00228

Dabros, T. M. H., Stummann, M. Z., Høj, M., Jensen, P. A., Grunwaldt, J.-D., Gabrielsen, J., et al. (2018). Transportation Fuels from Biomass Fast Pyrolysis, Catalytic Hydrodeoxygenation, and Catalytic Fast Hydropyrolysis. *Prog. Energ. Combustion Sci.* 68, 268–309. doi:10.1016/j.pecs.2018.05.002

Delgado, J., Vasquez Salcedo, W. N., Bronzetti, G., Casson Moreno, V., Mignot, M., Legros, J., et al. (2022). Kinetic Model Assessment for the Synthesis of γ-valerolactone from N-Butyl Levulinate and Levulinic Acid Hydrogenation over the Synergy Effect of Dual Catalysts Ru/C and Amberlite IR-120. *Chem. Eng. J.* 430, 133053. doi:10.1016/j.cej.2021.133053

Dhakshinamoorthy, A., Alvaro, M., Corma, A., and Garcia, H. (2011). Delineating Similarities and Dissimilarities in the Use of Metal Organic Frameworks and Zeolites as Heterogeneous Catalysts for Organic Reactions. *Dalton Trans.* 40, 6344–6360. doi:10.1039/c1dt10354g

Dutta, A., Patra, A. K., Dutta, S., Saha, B., and Bhaumik, A. (2012). Hierarchically Porous Titanium Phosphate Nanoparticles: An Efficient Solid Acid Catalyst for Microwave Assisted Conversion of Biomass and Carbohydrates into 5-hydroxymethylfurfural. *J. Mater. Chem.* 22, 14094. doi:10.1039/c2jm30623a

Dutta, S., Yu, I. K. M., Tsang, D. C. W., Ng, Y. H., Ok, Y. S., Sherwood, J., et al. (2019). Green Synthesis of Gamma-Valerolactone (Gvl) through Hydrogenation of Biomass-Derived Levulinic Acid Using Non-noble Metal Catalysts: A Critical Review. *Chem. Eng. J.* 372, 992–1006. doi:10.1016/j.cej.2019.04.199

Erickson, K. A., Stelmach, J. P. W., Mucha, N. T., and Waterman, R. (2015). Zirconium-catalyzed Amine Borane Dehydrocoupling and Transfer Hydrogenation. *Organometallics* 34, 4693–4699. doi:10.1021/acs.organomet.5b00415

Furukawa, H., Cordova, K. E., O'Keeffe, M., and Yaghi, O. M. (2013). The Chemistry and Applications of Metal-Organic Frameworks. *Science* 341, 1230444. doi:10.1126/science.1230444

Gagnon, K. J., Perry, H. P., and Clearfield, A. (2012). Conventional and Unconventional Metal-Organic Frameworks Based on Phosphonate Ligands: Mofs and Umofs. *Chem. Rev.* 112, 1034–1054. doi:10.1021/cr2002257

Gao, G., Jiang, Z., and Hu, C. (2021). Selective Hydrogenation of the Carbonyls in Furfural and 5-hydroxymethylfurfural Catalyzed by Ptni alloy Supported on SBA-15 in Aqueous Solution under Mild Conditions. *Front. Chem.* 9, 759512. doi:10.3389/fchem.2021.759512

Gao, L., Li, G., Sheng, Z., Tang, Y., and Zhang, Y. (2020). Alkali-metal-ions Promoted Zr-Al-Beta Zeolite with High Selectivity and Resistance to Coking in

the Conversion of Furfural toward Furfural Alcohol. *J. Catal.* 389, 623–630. doi:10.1016/j.jcat.2020.07.002

Gao, X., Yu, X., Peng, L., He, L., and Zhang, J. (2021). Magnetic Fe3O4 Nanoparticles and ZrO2-Doped Mesoporous MCM-41 as a Monolithic Multifunctional Catalyst for γ-valerolactone Production Directly from Furfural. *Fuel* 300, 120996. doi:10.1016/j.fuel.2021.120996

Gawade, A. B., Tiwari, M. S., and Yadav, G. D. (2016). Biobased Green Process: Selective Hydrogenation of 5-Hydroxymethylfurfural to 2,5-Dimethyl Furan under Mild Conditions Using Pd-Cs2.5H0.5PW12O40/K-10 Clay. *ACS Sustain. Chem. Eng.* 4, 4113–4123. doi:10.1021/acssuschemeng.6b00426

Gilkey, M. J., and Xu, B. (2016). Heterogeneous Catalytic Transfer Hydrogenation as an Effective Pathway in Biomass Upgrading. *ACS Catal.* 6, 1420–1436. doi:10.1021/acscatal.5b02171

Goetjen, T. A., Liu, J., Wu, Y., Sui, J., Zhang, X., Hupp, J. T., et al. (2020). Metal-organic Framework (Mof) Materials as Polymerization Catalysts: A Review and Recent Advances. *Chem. Commun.* 56, 10409–10418. doi:10.1039/d0cc03790g

Gonell, F., Boronat, M., and Corma, A. (2017). Structure-reactivity Relationship in Isolated Zr Sites Present in Zr-Zeolite and ZrO2 for the Meerwein-Ponndorf-Verley Reaction. *Catal. Sci. Technol.* 7, 2865–2873. doi:10.1039/c7cy00567a

Han, X., Guo, Y., Liu, X., Xia, Q., and Wang, Y. (2019). Catalytic Conversion of Lignocellulosic Biomass into Hydrocarbons: A Mini Review. *Catal. Today* 319, 2–13. doi:10.1016/j.cattod.2018.05.013

Hao, W., Li, W., Tang, X., Zeng, X., Sun, Y., Liu, S., et al. (2016). Catalytic Transfer Hydrogenation of Biomass-Derived 5-hydroxymethyl Furfural to the Building Block 2,5-bishydroxymethyl Furan. *Green. Chem.* 18, 1080–1088. doi:10.1039/c5gc01221j

He, J., Li, H., Liu, Y., Zhao, W., Yang, T., Xue, W., et al. (2016a). Catalytic Transfer Hydrogenation of Ethyl Levulinate into γ -valerolactone over Mesoporous Zr/B Mixed Oxides. *J. Ind. Eng. Chem.* 43, 133–141. doi:10.1016/j.jiec.2016.07.059

He, J., Li, H., Lu, Y.-M., Liu, Y.-X., Wu, Z.-B., Hu, D.-Y., et al. (2016b). Cascade Catalytic Transfer Hydrogenation-Cyclization of Ethyl Levulinate to γ-valerolactone with Al-Zr Mixed Oxides. *Appl. Catal. A: Gen.* 510, 11–19. doi:10.1016/j.apcata.2015.10.049

Heard, C. J., Hu, C., Skoglundh, M., Creaser, D., and Grönbeck, H. (2016). Kinetic Regimes in Ethylene Hydrogenation over Transition-Metal Surfaces. *ACS Catal.* 6, 3277–3286. doi:10.1021/acscatal.5b02708

Hengne, A. M., Malawadkar, A. V., Biradar, N. S., and Rode, C. V. (2014). Surface Synergism of an Ag-Ni/ZrO2 Nanocomposite for the Catalytic Transfer Hydrogenation of Bio-Derived Platform Molecules. *RSC Adv.* 4, 9730–9736. doi:10.1039/c3ra46495d

Hengne, A. M., and Rode, C. V. (2012). Cu-ZrO2 Nanocomposite Catalyst for Selective Hydrogenation of Levulinic Acid and its Ester to γ-valerolactone. *Green. Chem.* 14, 1064–1072. doi:10.1039/c2gc16558a

Hernández, B., Iglesias, J., Morales, G., Paniagua, M., López-Aguado, C., García Fierro, J. L., et al. (2016). One-pot cascade Transformation of Xylose into γ-valerolactone (GVL) over Bifunctional Brønsted-Lewis Zr-Al-Beta Zeolite. *Green. Chem.* 18, 5777–5781. doi:10.1039/c6gc01888b

Hou, P., Ma, M., Zhang, P., Cao, J., Liu, H., Xu, X., et al. (2021). Catalytic Transfer Hydrogenation of Furfural to Furfuryl Alcohol Using Easy-To-Separate Core-Shell Magnetic Zirconium Hydroxide. *New J. Chem.* 45, 2715–2722. doi:10.1039/d0nj05638c

Hu, D., Xu, H., Wu, Z., Zhang, M., Zhao, Z., Wang, Y., et al. (2021). Noble Metal-free Hierarchical ZrY Zeolite Efficient for Hydrogenation of Biomass-Derived Levulinic Acid. *Front. Chem.* 9, 725175. doi:10.3389/fchem.2021.725175

Hu, F., Wang, Y., Xu, S., Zhang, Z., Chen, Y., Fan, J., et al. (2019). Efficient and Selective Ni/Al2O3-C Catalyst Derived from Metal-Organic Frameworks for the Hydrogenation of Furfural to Furfuryl Alcohol. *Catal. Lett.* 149, 2158–2168. doi:10.1007/s10562-019-02766-y

Hu, L., Dai, X., Li, N., Tang, X., and Jiang, Y. (2019). Highly Selective Hydrogenation of Biomass-Derived 5-hydroxymethylfurfural into 2,5-bis(hydroxymethyl)furan over an Acid-Base Bifunctional Hafnium-Based Coordination Polymer Catalyst. *Sustain. Energ. Fuels* 3, 1033–1041. doi:10.1039/c8se00545a

Hu, L., Li, T., Xu, J., He, A., Tang, X., Chu, X., et al. (2018). Catalytic Transfer Hydrogenation of Biomass-Derived 5-hydroxymethylfurfural into 2,5-dihydroxymethylfuran over Magnetic Zirconium-Based Coordination Polymer. *Chem. Eng. J.* 352, 110–119. doi:10.1016/j.cej.2018.07.007

Hu, L., Yang, M., Xu, N., Xu, J., Zhou, S., Chu, X., et al. (2017). Selective Transformation of Biomass-Derived 5-hydroxymethylfurfural into 2,5-dihydroxymethylfuran via Catalytic Transfer Hydrogenation over Magnetic Zirconium Hydroxides. *Korean J. Chem. Eng.* 35, 99–109. doi:10.1007/s11814-017-0238-3

Hu, Z., Peng, Y., Gao, Y., Qian, Y., Ying, S., Yuan, D., et al. (2016). Direct Synthesis of Hierarchically Porous Metal-Organic Frameworks with High Stability and Strong Brønsted Acidity: The Decisive Role of Hafnium in Efficient and Selective Fructose Dehydration. *Chem. Mater.* 28, 2659–2667. doi:10.1021/acs.chemmater.6b00139

Huang, R., Cui, Q., Yuan, Q., Wu, H., Guan, Y., and Wu, P. (2018). Total Hydrogenation of Furfural over Pd/Al2O3 and Ru/ZrO2 Mixture under Mild Conditions: Essential Role of Tetrahydrofurfural as an Intermediate and Support Effect. *ACS Sustain. Chem. Eng.* 6, 6957–6964. doi:10.1021/acssuschemeng.8b00801

Iglesias, J., Martínez-Salazar, I., Maireles-Torres, P., Martin Alonso, D., Mariscal, R., and López Granados, M. (2020). Advances in Catalytic Routes for the Production of Carboxylic Acids from Biomass: A Step Forward for Sustainable Polymers. *Chem. Soc. Rev.*, 49, 5704–5771. doi:10.1039/d0cs00177e

Iglesias, J., Melero, J. A., Morales, G., Paniagua, M., Hernández, B., Osatiashtiani, A., et al. (2018). ZrO2-SBA-15 Catalysts for the One-Pot cascade Synthesis of GVL from Furfural. *Catal. Sci. Technol.* 8, 4485–4493. doi:10.1039/c8cy01121d

Iglesias, J., Melero, J., Morales, G., Moreno, J., Segura, Y., Paniagua, M., et al. (2015). Zr-SBA-15 Lewis Acid Catalyst: Activity in Meerwein Ponndorf Verley Reduction. *Catalysts* 5, 1911–1927. doi:10.3390/catal5041911

Injongkol, Y., Maihom, T., Treesukul, P., Sirijaraensre, J., Boekfa, B., and Limtrakul, J. (2017). Theoretical Study on the Reaction Mechanism of Hydrogenation of Furfural to Furfuryl Alcohol on lewis Acidic Bea Zeolites: Effects of Defect Structure and Tetravalent Metals Substitution. *Phys. Chem. Chem. Phys.* 19, 24042–24048. doi:10.1039/c7cp04229a

Iriondo, A., Mendiguren, A., Güemez, M. B., Requies, J., and Cambra, J. F. (2017). 2,5-DMF Production through Hydrogenation of Real and Synthetic 5-HMF over Transition Metal Catalysts Supported on Carriers with Different Nature. *Catal. Today* 279, 286–295. doi:10.1016/j.cattod.2016.02.019

Ishikawa, S., Jones, D. R., Iqbal, S., Reece, C., Morgan, D. J., Willock, D. J., et al. (2017). Identification of the Catalytically Active Component of Cu-Zr-O Catalyst for the Hydrogenation of Levulinic Acid to γ-valerolactone. *Green. Chem.* 19, 225–236. doi:10.1039/c6gc02598f

Jain, A., Shore, A. M., Jonnalagadda, S. C., Ramanujachary, K. V., and Mugweru, A. (2015). Conversion of Fructose, Glucose and Sucrose to 5-Hydroxymethyl-2-Furfural over Mesoporous Zirconium Phosphate Catalyst. *Appl. Catal. A: Gen.* 489, 72–76. doi:10.1016/j.apcata.2014.10.020

Jiang, S., Li, F., Huang, J., Wang, Y., Lu, S., Li, P., et al. (2020). Catalytic Transfer Hydrogenation of Furfural over Magnetic Carbon-Encapsulated CoO@C Catalyst. *Chemistryselect* 5, 9883–9892. doi:10.1002/slct.202002269

Jin, W., Pastor-Pérez, L., Shen, D., Sepúlveda-Escribano, A., Gu, S., and Ramirez Reina, T.(2019).Catalytic Upgrading of Biomass Model Compounds: Novel Approaches and Lessons Learnt from Traditional Hydrodeoxygenation - a Review .ChemCatChem 11 ,924 -960.doi:10.1002/cctc.201801722

Karthik, V., Selvakumar, P., Senthil Kumar, P., Vo, D.-V. N., Gokulakrishnan, M., Keerthana, P., et al. (2021). Graphene-based Materials for Environmental Applications: A Review. *Environ. Chem. Lett.* 19, 3631–3644. doi:10.1007/s10311-021-01262-3

Kerkel, F., Markiewicz, M., Stolte, S., Müller, E., and Kunz, W. (2021). The green Platform Molecule Gamma-Valerolactone - Ecotoxicity, Biodegradability, Solvent Properties, and Potential Applications. *Green. Chem.* 23, 2962–2976. doi:10.1039/d0gc04353b

Khan, K., Tareen, A. K., Iqbal, M., Shi, Z., Zhang, H., and Guo, Z. (2021). Novel Emerging Graphdiyne Based Two Dimensional Materials: Synthesis, Properties and Renewable Energy Applications. *Nano Today* 39, 101207. doi:10.1016/j.nantod.2021.101207

Kim, K. D., Kim, J., Teoh, W. Y., Kim, J.-C., Huang, J., and Ryoo, R. (2020). Cascade Reaction Engineering on Zirconia-Supported Mesoporous MFI Zeolites with Tunable Lewis-Brønsted Acid Sites: a Case of the One-Pot Conversion of Furfural to γ-valerolactone. *RSC Adv.* 10, 35318–35328. doi:10.1039/d0ra06915a

Koreniuk, A., Maresz, K., and Mrowiec-Białoń, J. (2015). Supported Zirconium-Based Continuous-Flow Microreactor for Effective Meerwein-Ponndorf-Verley

Reduction of Cyclohexanone. *Catal. Commun.* 64, 48–51. doi:10.1016/j.catcom.2015.01.021

Kou, H., Luo, W., Huang, Z., Sang, G., Hu, C., Chen, C., et al. (2016). Effects of Temperature and Hydrogen Pressure on the Activation Behavior of Zrco. *Int. J. Hydrogen Energ.* 41, 10811–10818. doi:10.1016/j.ijhydene.2016.05.011

Kumar, A., Kumar, N., Baredar, P., and Shukla, A. (2015). A Review on Biomass Energy Resources, Potential, Conversion and Policy in india. *Renew. Sustain. Energ. Rev.* 45, 530–539. doi:10.1016/j.rser.2015.02.007

Kuwahara, Y., Kaburagi, W., and Fujitani, T. (2014). Catalytic Conversion of Levulinic Acid and its Esters to γ-Valerolactone over Silica-Supported Zirconia Catalysts. *Bcsj* 87, 1252–1254. doi:10.1246/bcsj.20140205

Kuwahara, Y., Kaburagi, W., Osada, Y., Fujitani, T., and Yamashita, H. (2017). Catalytic Transfer Hydrogenation of Biomass-Derived Levulinic Acid and its Esters to γ-valerolactone over ZrO 2 Catalyst Supported on SBA-15 Silica. *Catal. Today* 281, 418–428. doi:10.1016/j.cattod.2016.05.016

Kuwahara, Y., Kango, H., and Yamashita, H. (2016). Catalytic Transfer Hydrogenation of Biomass-Derived Levulinic Acid and its Esters to γ-Valerolactone over Sulfonic Acid-Functionalized UiO-66. *ACS Sustain. Chem. Eng.* 5, 1141–1152. doi:10.1021/acssuschemeng.6b02464

Li, F., France, L. J., Cai, Z., Li, Y., Liu, S., Lou, H., et al. (2017). Catalytic Transfer Hydrogenation of Butyl Levulinate to γ-valerolactone over Zirconium Phosphates with Adjustable Lewis and Brønsted Acid Sites. *Appl. Catal. B: Environ.* 214, 67–77. doi:10.1016/j.apcatb.2017.05.013

Li, H., Dai, M., Dai, S., and Dong, X. (2018a). Current Status and Environment Impact of Direct Straw Return in china's Cropland - a Review. *Ecotoxicology Environ. Saf.* 159, 293–300. doi:10.1016/j.ecoenv.2018.05.014

Li, H., Fang, Z., Smith, R. L., and Yang, S. (2016a). Efficient Valorization of Biomass to Biofuels with Bifunctional Solid Catalytic Materials. *Prog. Energ. Combustion Sci.* 55, 98–194. doi:10.1016/j.pecs.2016.04.004

Li, H., Fang, Z., and Yang, S. (2016a). Direct Catalytic Transformation of Biomass Derivatives into Biofuel Component γ-Valerolactone with Magnetic Nickel-Zirconium Nanoparticles. *Chempluschem* 81, 135–142. doi:10.1002/cplu.201500492

Li, H., Fang, Z., and Yang, S. (2015). Direct Conversion of Sugars and Ethyl Levulinate into γ-Valerolactone with Superparamagnetic Acid-Base Bifunctional ZrFeOx Nanocatalysts. *ACS Sustain. Chem. Eng.* 4, 236–246. doi:10.1021/acssuschemeng.5b01480

Li, H., Guo, H., Fang, Z., Aida, T. M., and Smith, R. L. (2020a). Cycloamination Strategies for Renewable N-Heterocycles. *Green. Chem.* 22, 582–611. doi:10.1039/c9gc03655e

Li, H., He, J., Riisager, A., Saravanamurugan, S., Song, B., and Yang, S. (2016c). Acid-Base Bifunctional Zirconium N-Alkyltriphosphate Nanohybrid for Hydrogen Transfer of Biomass-Derived Carboxides. *ACS Catal.* 6, 7722–7727. doi:10.1021/acscatal.6b02431

Li, H., Li, Y., Fang, Z., and Smith, R. L. (2019a). Efficient Catalytic Transfer Hydrogenation of Biomass-Based Furfural to Furfuryl Alcohol with Recyclable Hf-Phenylphosphonate Nanohybrids. *Catal. Today* 319, 84–92. doi:10.1016/j.cattod.2018.04.056

Li, H., Wang, C., Xu, Y., Yu, Z., Saravanamurugan, S., Wu, Z., et al. (2020b). Heterogeneous (de)chlorination-enabled control of reactivity in the liquid-phase synthesis of furanic biofuel from cellulosic feedstock. *Green. Chem.* 22, 637–645. doi:10.1039/c9gc04092g

Li, H., Wu, H., Zhang, H., Su, Y., Yang, S., and Hensen, E. J. M. (2019b). A Facile Direct Route to N -(Un)substituted Lactams by Cycloamination of Oxocarboxylic Acids without External Hydrogen. *Chemsuschem* 12, 3778–3784. doi:10.1002/cssc.201901780

Li, H., Yang, T., and Fang, Z. (2018b). Biomass-derived Mesoporous Hf-Containing Hybrid for Efficient Meerwein-Ponndorf-Verley Reduction at Low Temperatures. *Appl. Catal. B: Environ.* 227, 79–89. doi:10.1016/j.apcatb.2018.01.017

Li, H., Zhao, W., Dai, W., Long, J., Watanabe, M., Meier, S., et al. (2018). Noble Metal-free Upgrading of Multi-Unsaturated Biomass Derivatives at Room Temperature: Silyl Species Enable Reactivity. *Green. Chem.* 20, 5327–5335. doi:10.1039/c8gc02934b

Li, H., Zhao, W., Saravanamurugan, S., Dai, W., He, J., Meier, S., et al. (2018). Control of Selectivity in Hydrosilane-Promoted Heterogeneous Palladium-Catalysed Reduction of Furfural and Aromatic Carboxides. *Commun. Chem.* 1. doi:10.1038/s42004-018-0033-z

Li, J., Zhao, S., Li, Z., Liu, D., Chi, Y., and Hu, C. (2021). Efficient Conversion of Biomass-Derived Levulinic Acid to γ-Valerolactone over Polyoxometalate@Zr-

Based Metal-Organic Frameworks: The Synergistic Effect of Brønsted and Lewis Acidic Sites. *Inorg. Chem.* 60, 7785–7793. doi:10.1021/acs.inorgchem.1c00185

Li, M., Liu, Y., Lin, X., Tan, J., Yang, S., and Li, H. (2021). One-step Upgrading of Bio-Based Furfural to γ-valerolactone via HfCl4-Mediated Bifunctional Catalysis. *RSC Adv.* 11, 35415–35424. doi:10.1039/d1ra05637a

Li, W., Cai, Z., Li, H., Shen, Y., Zhu, Y., Li, H., et al. (2019). Hf-based Metal Organic Frameworks as Bifunctional Catalysts for the One-Pot Conversion of Furfural to γ-valerolactone. *Mol. Catal.* 472, 17–26. doi:10.1016/j.mcat.2019.04.010

Li, X., Du, Z., Wu, Y., Zhen, Y., Shao, R., Li, B., et al. (2020). A Novel Hafnium-Graphite Oxide Catalyst for the Meerwein-Ponndorf-Verley Reaction and the Activation Effect of the Solvent. *RSC Adv.* 10, 9985–9995. doi:10.1039/c9ra10795a

Li, X., and Jiang, J. (2019). Molecular Design of Chiral Zirconium Metal-Organic Frameworks for Asymmetric Transfer Hydrogenation of Imines. *Catal. Sci. Technol.* 9, 4888–4897. doi:10.1039/c9cy00770a

Liao, Y., Liu, Q., Wang, T., Long, J., Ma, L., and Zhang, Q. (2014). Zirconium Phosphate Combined with Ru/C as a Highly Efficient Catalyst for the Direct Transformation of Cellulose to C6 Alditols. *Green. Chem.* 16, 3305–3312. doi:10.1039/c3gc42444h

Lin, Y., Bu, Q., Xu, J., Liu, X., Zhang, X., Lu, G.-P., et al. (2021). Hf-MOF Catalyzed Meerwein−Ponndorf−Verley (MPV) Reduction Reaction: Insight into Reaction Mechanism. *Mol. Catal.* 502, 111405. doi:10.1016/j.mcat.2021.111405

Liu, C., Wei, L., Yin, X., Pan, X., Hu, J., Li, N., et al. (2021). Synthesis of Furfural from Xylan in γ-valerolactone/molten Salt Hydrate Biphasic System. *Chem. Eng. J.* 425, 130608. doi:10.1016/j.cej.2021.130608

Liu, C., Xu, G., Hu, A., Xie, Y., and Wang, H. (2019). Porous Zirconium Hydroxyphosphonoacetate: Catalyst for Conversion of Furfural into Furfuryl Alcohol. *Chemistryselect* 4, 8000–8006. doi:10.1002/slct.201901612

Liu, K., Qin, R., and Zheng, N. (2021). Insights into the Interfacial Effects in Heterogeneous Metal Nanocatalysts toward Selective Hydrogenation. *J. Am. Chem. Soc.* 143, 4483–4499. doi:10.1021/jacs.0c13185

Liu, S. H., Jaenicke, S., and Chuah, G. K. (2002). Hydrous Zirconia as a Selective Catalyst for the Meerwein-Ponndorf-Verley Reduction of Cinnamaldehyde. *J. Catal.* 206, 321–330. doi:10.1006/jcat.2001.3480

Liu, S., Meng, Y., Li, H., and Yang, S. (2021). Hierarchical Porous mil-101(Cr) Solid Acid-Catalyzed Production of Value-Added Acetals from Biomass-Derived Furfural. *Polymers* 13, 3498. doi:10.3390/polym13203498

Liu, X., Yin, B., Zhang, W., Yu, X., Du, Y., Zhao, S., et al. (2021). Catalytic Transfer Hydrogenolysis of Glycerol over Heterogeneous Catalysts: A Short Review on Mechanistic Studies. *Chem. Rec.* 21, 1792–1810. doi:10.1002/tcr.202100037

Liu, Y., Chen, D., Li, M., Zhang, H., and Li, H. (2021). Catalytic Stereoselective Conversion of Biomass-Derived 4'-Methoxypropiophenone to Trans-anethole with a Bifunctional and Recyclable Hf-Based Polymeric Nanocatalyst. *Polymers* 13, 2808. doi:10.3390/polym13162808

Luo, H. Y., Consoli, D. F., Gunther, W. R., and Román-Leshkov, Y. (2014). Investigation of the Reaction Kinetics of Isolated Lewis Acid Sites in Beta Zeolites for the Meerwein-Ponndorf-Verley Reduction of Methyl Levulinate to γ-valerolactone. *J. Catal.* 320, 198–207. doi:10.1016/j.jcat.2014.10.010

Luo, Y.-J., Zhou, Y.-H., and Huang, Y.-B. (2018). A New lewis Acidic Zr Catalyst for the Synthesis of Furanic Diesel Precursor from Biomass Derived Furfural and 2-methylfuran. *Catal. Lett.* 149, 292–302. doi:10.1007/s10562-018-2599-6

Luo, Y., Li, Z., Li, X., Liu, X., Fan, J., Clark, J. H., et al. (2019). The Production of Furfural Directly from Hemicellulose in Lignocellulosic Biomass: A Review. *Catal. Today* 319, 14–24. doi:10.1016/j.cattod.2018.06.042

Ma, M., Yan, X., Hou, P., Cao, J., Liu, H., Xu, X., et al. (2020). One-Pot Transfer Hydrogenation of Methyl Levulinate into Valerolactone and 1,4-pentanediol over In Situ Reduced Cu/ZrOCO3 in 2-PrOH. *Chemistryselect* 5, 924–930. doi:10.1002/slct.201904480

Mardiana, S., Azhari, N. J., Ilmi, T., and Kadja, G. T. M. (2022). Hierarchical Zeolite for Biomass Conversion to Biofuel: A Review. *Fuel* 309, 122119. doi:10.1016/j.fuel.2021.122119

Mathimani, T., and Mallick, N. (2019). A Review on the Hydrothermal Processing of Microalgal Biomass to Bio-Oil - Knowledge Gaps and Recent Advances. *J. Clean. Prod.* 217, 69–84. doi:10.1016/j.jclepro.2019.01.129

Mautschke, H. H., and Llabrés i Xamena, F. X. (2021). One-Step Chemo-, Regio- and Stereoselective Reduction of Ketosteroids to Hydroxysteroids over Zr-

Containing MOF-808 Metal-Organic Frameworks. *Chem. Eur. J.* 27, 10766–10775. doi:10.1002/chem.202100967

Melero, J. A., Morales, G., Iglesias, J., Paniagua, M., and López-Aguado, C. (2018). Rational Optimization of Reaction Conditions for the One-Pot Transformation of Furfural to γ-Valerolactone over Zr-Al-Beta Zeolite: Toward the Efficient Utilization of Biomass. *Ind. Eng. Chem. Res.* 57, 11592–11599. doi:10.1021/acs.iecr.8b02475

Melero, J. A., Morales, G., Iglesias, J., Paniagua, M., López-Aguado, C., Wilson, K., et al. (2017). Efficient One-Pot Production of γ-valerolactone from Xylose over Zr-Al-Beta Zeolite: Rational Optimization of Catalyst Synthesis and Reaction Conditions. *Green. Chem.* 19, 5114–5121. doi:10.1039/c7gc01969f

Mondelli, C., Gözaydın, G., Yan, N., and Pérez-Ramírez, J. (2020). Biomass Valorisation over Metal-Based Solid Catalysts from Nanoparticles to Single Atoms. *Chem. Soc. Rev.* 49, 3764–3782. doi:10.1039/d0cs00130a

Nguyen, L. H. T., Nguyen, T. T. T., Tran, P. H., Kawazoe, Y., Le, H. M., and Doan, T. L. H. (2019). Zr and Hf-Metal-Organic Frameworks: Efficient and Recyclable Heterogeneous Catalysts for the Synthesis of 2-arylbenzoxazole via Ring Open Pathway Acylation Reaction. *J. Catal.* 374, 110–117. doi:10.1016/j.jcat.2019.04.023

Osman, A. I., Mehta, N., Elgarahy, A. M., Al-Hinai, A., Al-Muhtaseb, A. a. H., and Rooney, D. W. (2021). Conversion of Biomass to Biofuels and Life Cycle Assessment: A Review. *Environ. Chem. Lett.* 19, 4075–4118. doi:10.1007/s10311-021-01273-0

Palermo, V., Kinloch, I. A., Ligi, S., and Pugno, N. M. (2016). Nanoscale Mechanics of Graphene and Graphene Oxide in Composites: A Scientific and Technological Perspective. *Adv. Mater.* 28, 6232–6238. doi:10.1002/adma.201505469

Pan, H., Xia, Q., Li, H., Wang, Y., Shen, Z., Wang, Y., et al. (2022). Direct Production of Biodiesel from Crude euphorbia Lathyris L. Oil Catalyzed by Multifunctional Mesoporous Composite Materials. *Fuel* 309, 122172. doi:10.1016/j.fuel.2021.122172

Pang, J., Sun, J., Zheng, M., Li, H., Wang, Y., and Zhang, T. (2019). Transition Metal Carbide Catalysts for Biomass Conversion: A Review. *Appl. Catal. B: Environ.* 254, 510–522. doi:10.1016/j.apcatb.2019.05.034

Paniagua, M., Morales, G., Melero, J. A., Iglesias, J., López-Aguado, C., Vidal, N., et al. (2021). Understanding the Role of Al/Zr Ratio in Zr-Al-Beta Zeolite: Towards the One-Pot Production of Gvl from Glucose. *Catal. Today* 367, 228–238. doi:10.1016/j.cattod.2020.04.025

Pattnaik, F., Tripathi, S., Patra, B. R., Nanda, S., Kumar, V., Dalai, A. K., et al. (2021). Catalytic Conversion of Lignocellulosic Polysaccharides to Commodity Biochemicals: A Review. *Environ. Chem. Lett.* 19, 4119–4136. doi:10.1007/s10311-021-01284-x

Peng, Q., Wang, H., Xia, Y., and Liu, X. (2021). One-pot Conversion of Furfural to Gamma-Valerolactone in the Presence of Multifunctional Zirconium Alizarin Red S Hybrid. *Appl. Catal. A: Gen.* 621, 118203. doi:10.1016/j.apcata.2021.118203

Prasertsab, A., Maihom, T., Probst, M., Wattanakit, C., and Limtrakul, J. (2018). Furfural to Furfuryl Alcohol: Computational Study of the Hydrogen Transfer on lewis Acidic Bea Zeolites and Effects of Cation Exchange and Tetravalent Metal Substitution. *Inorg. Chem.* 57, 6599–6605. doi:10.1021/acs.inorgchem.8b00741

Prasomsri, T., Nimmanwudipong, T., and Román-Leshkov, Y. (2013). Effective Hydrodeoxygenation of Biomass-Derived Oxygenates into Unsaturated Hydrocarbons by Moo3 Using Low H2 Pressures. *Energy Environ. Sci.* 6, 1732–1738. doi:10.1039/c3ee24360e

Priecel, P., Endot, N. A., Carà, P. D., and Lopez-Sanchez, J. A. (2018). Fast Catalytic Hydrogenation of 2,5-hydroxymethylfurfural to 2,5-dimethylfuran with Ruthenium on Carbon Nanotubes. *Ind. Eng. Chem. Res.* 57, 1991–2002. doi:10.1021/acs.iecr.7b04715

Ramanathan, A., Castro Villalobos, M. C., Kwakernaak, C., Telalovic, S., and Hanefeld, U. (2008). Zr-TUD-1: A lewis Acidic, Three-Dimensional, Mesoporous, Zirconium-Containing Catalyst. *Chem. Eur. J.* 14, 961–972. doi:10.1002/chem.200700725

Rode, A., Carleton, T., Delgado, M., Greenstone, M., Houser, T., Hsiang, S., et al. (2021). Estimating a Social Cost of Carbon for Global Energy Consumption. *Nature* 598, 308–314. doi:10.1038/s41586-021-03883-8

Rojas-Buzo, S., García-García, P., and Corma, A. (2018). Catalytic Transfer Hydrogenation of Biomass-Derived Carbonyls over Hafnium-Based Metal-Organic Frameworks. *Chemsuschem* 11, 432–438. doi:10.1002/cssc.201701708

Rui, T., Lu, G.-P., Zhao, X., Cao, X., and Chen, Z. (2021). The Synergistic Catalysis on Co Nanoparticles and Conx Sites of Aniline-Modified Zif Derived Co@ncs for Oxidative Esterification of HMF. *Chin. Chem. Lett.* 32, 685–690. doi:10.1016/j.cclet.2020.06.027

Sabyrzhan, A., Balgimbekova, G., and Shestak, V. (2021). Economic and Legal Regulation of the Use and Development of Renewable Energy Sources. *Int. Environ. Agreements* 21, 595–610. doi:10.1007/s10784-021-09532-9

Sakakibara, K., Endo, K., and Osawa, T. (2019). Facile Synthesis of γ-valerolactone by Transfer Hydrogenation of Methyl Levulinate and Levulinic Acid over Ni/ZrO2. *Catal. Commun.* 125, 52–55. doi:10.1016/j.catcom.2019.03.021

Santana, C. G., and Krische, M. J. (2021). From Hydrogenation to Transfer Hydrogenation to Hydrogen Auto-Transfer in Enantioselective Metal-Catalyzed Carbonyl Reductive Coupling: Past, Present, and Future. *ACS Catal.* 11, 5572–5585. doi:10.1021/acscatal.1c01109

Sarkar, C., Paul, R., Chandra Shit, S., Trinh, Q. T., Koley, P., Rao, B. S., et al. (2021). Navigating Copper-Atom-Pair Structural Effect inside a Porous Organic Polymer Cavity for Selective Hydrogenation of Biomass-Derived 5-hydroxymethylfurfural. *ACS Sustain. Chem. Eng.* 9, 2136–2151. doi:10.1021/acssuschemeng.0c07594

Schwarzman, M., Schildroth, S., Bhetraratana, M., Alvarado, Á., and Balmes, J. (2021). Raising Standards to Lower Diesel Emissions. *Science* 371, 1314–1316. doi:10.1126/science.abf8159

Sha, Y., Xiao, Z., Zhou, H., Yang, K., Song, Y., Li, N., et al. (2017). Direct Use of Humic Acid Mixtures to Construct Efficient Zr-Containing Catalysts for Meerwein-Ponndorf-Verley Reactions. *Green. Chem.* 19, 4829–4837. doi:10.1039/c7gc01925d

Shao, Y., Li, Q., Dong, X., Wang, J., Sun, K., Zhang, L., et al. (2021). Cooperation between Hydrogenation and Acidic Sites in Cu-Based Catalyst for Selective Conversion of Furfural to γ-valerolactone. *Fuel* 293, 120457. doi:10.1016/j.fuel.2021.120457

Shearer, G. C., Chavan, S., Ethiraj, J., Vitillo, J. G., Svelle, S., Olsbye, U., et al. (2014). Tuned to Perfection: Ironing Out the Defects in Metal-Organic Framework UiO-66. *Chem. Mater.* 26, 4068–4071. doi:10.1021/cm501859p

Shen, S., Chen, J., Koodali, R. T., Hu, Y., Xiao, Q., Zhou, J., et al. (2014). Activation of MCM-41 Mesoporous Silica by Transition-Metal Incorporation for Photocatalytic Hydrogen Production. *Appl. Catal. B: Environ.* 150-151, 138–146. doi:10.1016/j.apcatb.2013.12.014

Shi, D., Yang, Q., Peterson, C., Lamic-Humblot, A.-F., Girardon, J.-S., Griboval-Constant, A., et al. (2019). Bimetallic Fe-Ni/SiO2 Catalysts for Furfural Hydrogenation: Identification of the Interplay between Fe and Ni during Deposition-Precipitation and thermal Treatments. *Catal. Today* 334, 162–172. doi:10.1016/j.cattod.2018.11.041

Silbernagel, R., Martin, C. H., and Clearfield, A. (2016). Zirconium(iv) Phosphonate-Phosphates as Efficient Ion-Exchange Materials. *Inorg. Chem.* 55, 1651–1656. doi:10.1021/acs.inorgchem.5b02555

Singh, J., Suhag, M., and Dhaka, A. (2015). Augmented Digestion of Lignocellulose by Steam Explosion, Acid and Alkaline Pretreatment Methods: A Review. *Carbohydr. Polym.* 117, 624–631. doi:10.1016/j.carbpol.2014.10.012

Solanki, B. S., and Rode, C. V. (2019). Selective Hydrogenation of 5-HMF to 2,5-DMF over a Magnetically Recoverable Non-noble Metal Catalyst. *Green. Chem.* 21, 6390–6406. doi:10.1039/c9gc03091c

Song, J., Hua, M., Huang, X., Visa, A., Wu, T., Fan, H., et al. (2021). Highly Efficient Meerwein-Ponndorf-Verley Reductions over a Robust Zirconium-Organoboronic Acid Hybrid. *Green. Chem.* 23, 1259–1265. doi:10.1039/d0gc04179c

Song, J., Wu, L., Zhou, B., Zhou, H., Fan, H., Yang, Y., et al. (2015). A New Porous Zr-Containing Catalyst with a Phenate Group: an Efficient Catalyst for the Catalytic Transfer Hydrogenation of Ethyl Levulinate to γ-valerolactone. *Green. Chem.* 17, 1626–1632. doi:10.1039/c4gc02104e

Song, J., Zhou, B., Zhou, H., Wu, L., Meng, Q., Liu, Z., et al. (2015). Porous Zirconium-Phytic Acid Hybrid: A Highly Efficient Catalyst for Meerwein-Ponndorf-Verley Reductions. *Angew. Chem. Int. Ed.* 54, 9399–9403. doi:10.1002/anie.201504001

Spinelli, R., Visser, R., Björheden, R., and Röser, D. (2019). Recovering Energy Biomass in Conventional forest Operations: A Review of Integrated Harvesting Systems. *Curr. For. Rep* 5, 90–100. doi:10.1007/s40725-019-00089-0

Srinivasa Rao, B., Krishna Kumari, P., Dhana Lakshmi, D., and Lingaiah, N. (2018). One Pot Selective Transformation of Biomass Derived Chemicals towards Alkyl

Levulinates over Titanium Exchanged Heteropoly Tungstate Catalysts. *Catal. Today* 309, 269–275. doi:10.1016/j.cattod.2017.05.040

Srinivasa Rao, B., Yogita Dhana Lakshmi, D., Dhana Lakshmi, D., Kumari, P. K., and Lingaiah, N. 2021). Influence of Metal Oxide and Heteropoly Tungstate Location in Mesoporous Silica towards Catalytic Transfer Hydrogenation of Furfural to γ-valerolactone. *Sustain. Energ. Fuels* 5, 3719–3728. doi:10.1039/d1se00340b

Sudarsanam, P., Li, H., and Sagar, T. V. (2020). TiO2-Based Water-Tolerant Acid Catalysis for Biomass-Based Fuels and Chemicals. *ACS Catal.* 10, 9555–9584. doi:10.1021/acscatal.0c01680

Sullivan, M. M., Chen, C.-J., and Bhan, A. (2016). Catalytic Deoxygenation on Transition Metal Carbide Catalysts. *Catal. Sci. Technol.* 6, 602–616. doi:10.1039/c5cy01665g

Sushkevich, V. L., Ivanova, I. I., Tolborg, S., and Taarning, E. (2014). Meerwein-Ponndorf-Verley-Oppenauer Reaction of Crotonaldehyde with Ethanol over Zr-Containing Catalysts. *J. Catal.* 316, 121–129. doi:10.1016/j.jcat.2014.04.019

Synowiecki, J., and Al-Khateeb, N. A. (2003). Production, Properties, and Some New Applications of Chitin and its Derivatives. *Crit. Rev. Food Sci. Nutr.* 43, 145–171. doi:10.1080/10408690390826473

Tan, J., Li, Y., Tan, X., Wu, H., Li, H., and Yang, S. (2021). Advances in Pretreatment of Straw Biomass for Sugar Production. *Front. Chem.* 9, 696030. doi:10.3389/fchem.2021.696030

Tan, X., Zhang, H., Li, H., and Yang, S. (2022). Electrovalent Bifunctional Acid Enables Heterogeneously Catalytic Production of Biodiesel by (Trans) esterification of Non-edible Oils. *Fuel* 310, 122273. doi:10.1016/j.fuel.2021.122273

Tang, X., Chen, H., Hu, L., Hao, W., Sun, Y., Zeng, X., et al. (2014a). Conversion of Biomass to γ-valerolactone by Catalytic Transfer Hydrogenation of Ethyl Levulinate over Metal Hydroxides. *Appl. Catal. B: Environ.* 147, 827–834. doi:10.1016/j.apcatb.2013.10.021

Tang, X., Hu, L., Sun, Y., Zhao, G., Hao, W., and Lin, L. (2013). Conversion of Biomass-Derived Ethyl Levulinate into γ-valerolactone via Hydrogen Transfer from Supercritical Ethanol over a ZrO2 Catalyst. *RSC Adv.* 3, 10277. doi:10.1039/c3ra41288a

Tang, X., Zeng, X., Li, Z., Hu, L., Sun, Y., Liu, S., et al. (2014b). Production of γ-valerolactone from Lignocellulosic Biomass for Sustainable Fuels and Chemicals Supply. *Renew. Sustain. Energ. Rev.* 40, 608–620. doi:10.1016/j.rser.2014.07.209

Tang, X., Zeng, X., Li, Z., Li, W., Jiang, Y., Hu, L., et al. (2015). *In Situ* Generated Catalyst System to Convert Biomass-Derived Levulinic Acid to γ-Valerolactone. *ChemCatChem* 7, 1372–1379. doi:10.1002/cctc.201500115

Taniya, K., Izumi, A., Ichihashi, Y., and Nishiyama, S. (2010). Influence of Preparation Methods of Supported Zr Oxide Catalysts for Meerwein-Ponndorf-Verlay Reduction of Acetophenone. *Msf* 658, 420–423. doi:10.4028/www.scientific.net/msf.658.420

Tian, Y., Zhang, F., Wang, J., Cao, L., and Han, Q. (2021). A Review on Solid Acid Catalysis for Sustainable Production of Levulinic Acid and Levulinate Esters from Biomass Derivatives. *Bioresour. Techn.* 342, 125977. doi:10.1016/j.biortech.2021.125977

Tripathi, M., Sahu, J. N., and Ganesan, P. (2016). Effect of Process Parameters on Production of Biochar from Biomass Waste through Pyrolysis: A Review. *Renew. Sustain. Energ. Rev.* 55, 467–481. doi:10.1016/j.rser.2015.10.122

Tuteja, J., Nishimura, S., and Ebitani, K. (2014). Base-free Chemoselective Transfer Hydrogenation of Nitroarenes to Anilines with Formic Acid as Hydrogen Source by a Reusable Heterogeneous Pd/ZrP Catalyst. *RSC Adv.* 4, 38241–38249. doi:10.1039/c4ra06174h

Valderrama Rios, M. L., González, A. M., Lora, E. E. S., and Almazán del Olmo, O. A. (2018). Reduction of Tar Generated during Biomass Gasification: A Review. *Biomass and Bioenergy* 108, 345–370. doi:10.1016/j.biombioe.2017.12.002

Valekar, A. H., Cho, K.-H., Chitale, S. K., Hong, D.-Y., Cha, G.-Y., Lee, U.-H., et al. (2016). Catalytic Transfer Hydrogenation of Ethyl Levulinate to γ-valerolactone over Zirconium-Based Metal-Organic Frameworks. *Green. Chem.* 18, 4542–4552. doi:10.1039/c6gc00524a

Valekar, A. H., Lee, M., Yoon, J. W., Kwak, J., Hong, D.-Y., Oh, K.-R., et al. (2020). Catalytic Transfer Hydrogenation of Furfural to Furfuryl Alcohol under Mild Conditions over Zr-MOFs: Exploring the Role of Metal Node Coordination and Modification. *ACS Catal.* 10, 3720–3732. doi:10.1021/acscatal.9b05085

Wagner, M., Meyer, B., Setvin, M., Schmid, M., and Diebold, U. (2021). Direct Assessment of the Acidity of Individual Surface Hydroxyls. *Nature* 592, 722–725. doi:10.1038/s41586-021-03432-3

Wang, A., Sudarsanam, P., Xu, Y., Zhang, H., Li, H., and Yang, S. (2020). Functionalized Magnetic Nanosized Materials for Efficient Biodiesel Synthesis via Acid-Base/enzyme Catalysis. *Green. Chem.* 22, 2977–3012. doi:10.1039/d0gc00924e

Wang, C., Liu, X., Keser Demir, N., Chen, J. P., and Li, K. (2016). Applications of Water Stable Metal-Organic Frameworks. *Chem. Soc. Rev.* 45, 5107–5134. doi:10.1039/c6cs00362a

Wang, F., Yuan, Z., Liu, B., Chen, S., and Zhang, Z. (2016). Catalytic Oxidation of Biomass Derived 5-hydroxymethylfurfural (HMF) over Ru Iii -incorporated Zirconium Phosphate Catalyst. *J. Ind. Eng. Chem.* 38, 181–185. doi:10.1016/j.jiec.2016.05.001

Wang, J., Jaenicke, S., and Chuah, G.-K. (2014). Zirconium-Beta Zeolite as a Robust Catalyst for the Transformation of Levulinic Acid to γ-valerolactone via Meerwein-Ponndorf-Verley Reduction. *RSC Adv.* 4, 13481–13489. doi:10.1039/c4ra01120a

Wang, T., He, J., and Zhang, Y. (2020). Production of γ-Valerolactone from One-Pot Transformation of Biomass-Derived Carbohydrates over Chitosan-Supported Ruthenium Catalyst Combined with Zeolite ZSM-5. *Eur. J. Org. Chem.* 2020, 1611–1619. doi:10.1002/ejoc.201901704

Wang, T., Xu, H., He, J., and Zhang, Y. (2020). MPV Reduction of Ethyl Levulinate to γ-valerolactone by the Biomass-Derived Chitosan-Supported Zr Catalyst. *New J. Chem.* 44, 14686–14694. doi:10.1039/d0nj02667k

Wang, X., Hao, J., Deng, L., Zhao, H., Liu, Q., Li, N., et al. (2020). The Construction of Novel and Efficient Hafnium Catalysts Using Naturally Existing Tannic Acid for Meerwein-Ponndorf-Verley Reduction. *RSC Adv.* 10, 6944–6952. doi:10.1039/c9ra10317a

Wang, Y., Huang, J., Lu, S., Li, P., Xia, X., Li, C., et al. (2020). Phosphorus-modified Zirconium Metal Organic Frameworks for Catalytic Transfer Hydrogenation of Furfural. *New J. Chem.* 44, 20308–20315. doi:10.1039/d0nj04285d

Wang, Y., Lewis, J. D., and Román-Leshkov, Y. (2016). Synthesis of Itaconic Acid Ester Analogues via Self-Aldol Condensation of Ethyl Pyruvate Catalyzed by Hafnium Bea Zeolites. *ACS Catal.* 6, 2739–2744. doi:10.1021/acscatal.6b00561

Wang, Y., Tong, X., Yan, Y., Xue, S., and Zhang, Y. (2014). Efficient and Selective Conversion of Hexose to 5-hydroxymethylfurfural with Tin-Zirconium-Containing Heterogeneous Catalysts. *Catal. Commun.* 50, 38–43. doi:10.1016/j.catcom.2014.02.023

Wei, J., Jiang, L., Huang, M., Wu, Y., and Chen, S. (2021). Intrinsic Defect Limit to the Growth of Orthorhombic HfO 2 and (Hf,Zr)O 2 with Strong Ferroelectricity: First-Principles Insights. *Adv. Funct. Mater.* 31, 2104913. doi:10.1002/adfm.202104913

Welch, A. J., Digdaya, I. A., Kent, R., Ghougassian, P., Atwater, H. A., and Xiang, C. (2021). Comparative Technoeconomic Analysis of Renewable Generation of Methane Using Sunlight, Water, and Carbon Dioxide. *ACS Energ. Lett.* 6, 1540–1549. doi:10.1021/acsenergylett.1c00174

Winoto, H. P., Fikri, Z. A., Ha, J.-M., Park, Y.-K., Lee, H., Suh, D. J., et al. (2019). Heteropolyacid Supported on Zr-Beta Zeolite as an Active Catalyst for One-Pot Transformation of Furfural to γ-valerolactone. *Appl. Catal. B: Environ.* 241, 588–597. doi:10.1016/j.apcatb.2018.09.031

Wu, H., Dai, W., Saravanamurugan, S., Li, H., and Yang, S. (2020). Endogenous X-C O Species Enable Catalyst-free Formylation Prerequisite for CO2 Reductive Upgrading. *Green. Chem.* 22, 5822–5832. doi:10.1039/d0gc02142c

Wu, H., Liu, Y., Li, H., and Yang, S. (2018). Rapid and Efficient Conversion of Bio-Based Sugar to 5-hydroxymethylfurfural Using Amino-Acid Derived Catalysts. *Energy Sourc. A: Recovery, Utilization, Environ. Effects* 40, 2632–2639. doi:10.1080/15567036.2018.1505982

Wu, H., Zhang, L.-L., Wang, J., Jiang, Y., Li, H., Sudarsanam, P., et al. (2021). Room-temperature Quasi-Catalytic Hydrogen Generation from Waste and Water. *Green. Chem.* 23, 7528–7533. doi:10.1039/d1gc02722k

Wu, W., Li, Y., Li, H., Zhao, W., and Yang, S. (2018). Acid-Base Bifunctional Hf Nanohybrids Enable High Selectivity in the Catalytic Conversion of Ethyl Levulinate to γ-Valerolactone. *Catalysts* 8, 264. doi:10.3390/catal8070264

Xiao, Z., Zhou, H., Hao, J., Hong, H., Song, Y., He, R., et al. (2017). A Novel and Highly Efficient Zr-Containing Catalyst Based on Humic Acids for the Conversion of Biomass-Derived Ethyl Levulinate into Gamma-Valerolactone. *Fuel* 193, 322–330. doi:10.1016/j.fuel.2016.12.072

Xie, C., Song, J., Zhou, B., Hu, J., Zhang, Z., Zhang, P., et al. (2016). Porous Hafnium Phosphonate: Novel Heterogeneous Catalyst for Conversion of Levulinic Acid and Esters into γ-Valerolactone. *ACS Sustain. Chem. Eng.* 4, 6231–6236. doi:10.1021/acssuschemeng.6b02230

Xie, Y., Li, F., Wang, J., Wang, R., Wang, H., Liu, X., et al. (2017). Catalytic Transfer Hydrogenation of Ethyl Levulinate to γ-valerolactone over a Novel Porous Zirconium Trimetaphosphate. *Mol. Catal.* 442, 107–114. doi:10.1016/j.mcat.2017.09.011

Xue, Z., Jiang, J., Li, G., Zhao, W., Wang, J., and Mu, T. (2016). Zirconium-cyanuric Acid Coordination Polymer: Highly Efficient Catalyst for Conversion of Levulinic Acid to γ-valerolactone. *Catal. Sci. Technol.* 6, 5374–5379. doi:10.1039/c5cy02215k

Yang, T., Li, H., He, J., Liu, Y., Zhao, W., Wang, Z., et al. (2017). Porous Ti/Zr Microspheres for Efficient Transfer Hydrogenation of Biobased Ethyl Levulinate to γ-Valerolactone. *ACS Omega* 2, 1047–1054. doi:10.1021/acsomega.6b00469

Yang, Y., Liu, Q., Li, D., Tan, J., Zhang, Q., Wang, C., et al. (2017). Selective Hydrodeoxygenation of 5-hydroxymethylfurfural to 2,5-dimethylfuran on Ru-MoOx/C Catalysts. *RSC Adv.* 7, 16311–16318. doi:10.1039/c7ra00605e

Ye, L., Han, Y., Feng, J., and Lu, X. (2020). A Review about Gvl Production from Lignocellulose: Focusing on the Full Components Utilization. *Ind. Crops Prod.* 144, 112031. doi:10.1016/j.indcrop.2019.112031

Yin, K., and Shen, Y. (2020). Theoretical Insights into CO2 Hydrogenation to HCOOH over FexZr1-xO2 Solid Solution Catalyst. *Appl. Surf. Sci.* 528, 146926. doi:10.1016/j.apsusc.2020.146926

Yu, Z., Li, Z., Zhang, L., Zhu, K., Wu, H., Li, H., et al. (2021). A Substituent- and Temperature-Controllable NHC-Derived Zwitterionic Catalyst Enables CO2 Upgrading for High-Efficiency Construction of Formamides and Benzimidazoles. *Green. Chem.* 23, 5759–5765. doi:10.1039/d1gc01897c

Yun, W.-C., Yang, M.-T., and Lin, K.-Y. A. (2019). Water-born Zirconium-Based Metal Organic Frameworks as green and Effective Catalysts for Catalytic Transfer Hydrogenation of Levulinic Acid to γ-valerolactone: Critical Roles of Modulators. *J. Colloid Interf. Sci.* 543, 52–63. doi:10.1016/j.jcis.2019.02.036

Zantye, M. S., Arora, A., and Hasan, M. M. F. (2021). Renewable-integrated Flexible Carbon Capture: A Synergistic Path Forward to Clean Energy Future. *Energ. Environ. Sci.* 14, 3986–4008. doi:10.1039/d0ee03946b

Zhang, B., Hao, J., Sha, Y., Zhou, H., Yang, K., Song, Y., et al. (2018). Utilization of lignite Derivatives to Construct Zr-Based Catalysts for the Conversion of Biomass-Derived Ethyl Levulinate. *Fuel* 217, 122–130. doi:10.1016/j.fuel.2017.12.064

Zhang, H., Li, H., Wang, A., Xu, C., and Yang, S. (2020). Progress of Catalytic Valorization of Bio-Glycerol with Urea into Glycerol Carbonate as a Monomer for Polymeric Materials. *Adv. Polym. Techn.* 2020, 1, 17. doi:10.1155/2020/7207068

Zhang, H., Nai, J., Yu, L., and Lou, X. W. (2017). Metal-organic-framework-based Materials as Platforms for Renewable Energy and Environmental Applications. *Joule* 1, 77–107. doi:10.1016/j.joule.2017.08.008

Zhang, H., Yang, W., Roslan, I. I., Jaenicke, S., and Chuah, G.-K. (2019). A Combo Zr-HY and Al-HY Zeolite Catalysts for the One-Pot cascade Transformation of Biomass-Derived Furfural to γ-valerolactone. *J. Catal.* 375, 56–67. doi:10.1016/j.jcat.2019.05.020

Zhang, H., Zhang, L.-L., Tan, X., Li, H., and Yang, S. (2021). Catalytic High-Yield Biodiesel Production from Fatty Acids and Non-food Oils over a Magnetically Separable Acid Nanosphere. *Ind. Crops Prod.* 173, 114126. doi:10.1016/j.indcrop.2021.114126

Zhang, S., Liu, Y., Yang, S., and Li, H. (2021). Catalytic Upgrading of Bio-Based 5-Hydroxymethylfurfural to 2,5-Dimethylfuran with Non-Noble Metals, *Energy Technol.*, 9. 2100653. doi:10.1002/ente.202100653

Zhang, X., Han, M., Liu, G., Wang, G., Zhang, Y., Zhang, H., et al. (2019). Simultaneously High-Rate Furfural Hydrogenation and Oxidation Upgrading on Nanostructured Transition Metal Phosphides through Electrocatalytic Conversion at Ambient Conditions. *Appl. Catal. B: Environ.* 244, 899–908. doi:10.1016/j.apcatb.2018.12.025

Zhou, P., and Zhang, Z. (2016). One-pot Catalytic Conversion of Carbohydrates into Furfural and 5-hydroxymethylfurfural. *Catal. Sci. Technol.* 6, 3694–3712. doi:10.1039/c6cy00384b

Zhou, S., Dai, F., Chen, Y., Dang, C., Zhang, C., Liu, D., et al. (2019). Sustainable Hydrothermal Self-Assembly of Hafnium-Lignosulfonate Nanohybrids for Highly Efficient Reductive Upgrading of 5-hydroxymethylfurfural. *Green. Chem.* 21, 1421–1431. doi:10.1039/c8gc03710h

Zhou, S., Dai, F., Xiang, Z., Song, T., Liu, D., Lu, F., et al. (2019). Zirconium-lignosulfonate Polyphenolic Polymer for Highly Efficient Hydrogen Transfer of Biomass-Derived Oxygenates under Mild Conditions. *Appl. Catal. B: Environ.* 248, 31–43. doi:10.1016/j.apcatb.2019.02.011

Zhu, Y., Li, Z., and Chen, J. (2019). Applications of Lignin-Derived Catalysts for green Synthesis. *Green. Energ. Environ.* 4, 210–244. doi:10.1016/j.gee.2019.01.003

Zhu, Y., Liu, S., Jaenicke, S., and Chuah, G. (2004). Zirconia Catalysts in Meerwein-Ponndorf-Verley Reduction of Citral. *Catal. Today* 97, 249–255. doi:10.1016/j.cattod.2004.07.002

Effective Dehydration of Fructose Over Stable Ti-Doped SBA-15 Catalysts

Yutong Zhu[1], Xiaofei Xu[1], Jian He[1,2], Jie Guo[1,2] and Ke Song[1,2]*

[1]Key Laboratory of Hunan Forest Products and Chemical Industry Engineering, Jishou University, Zhangjiajie, China, [2]College of Chemistry and Chemical Engineering, Jishou University, Jishou, China

High-effective synthesis of 5-hydroxymethylfurfural (HMF) from carbohydrates is an interesting reaction among biomass valorization. The as-synthesized Ti-SBA-15 catalysts with mesoporous structures showed high catalytic efficiency for the conversion of fructose to HMF. Ti-SBA-15 catalysts with different Si/Ti ratios were characterized by characterization techniques such as elemental analysis, XRD, TEM, N_2 adsorption–desorption, NH_3-TPD, and pyridine-FTIR. The acidity of Ti-SBA-15 catalysts could be tuned by altering addition amount of titanium. The effects of reaction conditions, including reaction time, temperature, and amount of catalyst, on the conversions of fructose and the yields of HMF were also investigated. It is found that Ti-SBA-15 catalysts whose Si/Ti ratio is 120 gave the best yields of HMF, which demonstrated 100% conversion of fructose with a maximum HMF yield of 82% at 140°C after 1 h. In addition, its catalytic performance was retained after 5 recycles in fructose conversion reaction, proving its good catalytic stability.

Keywords: 5-hydroxymethylfurfural, fructose, SBA-15, dehydration, heterogeneous catalysis

INTRODUCTION

Petroleum-based energy shortage and environmental pollution have become global issues due to over-reliance on finite fossil fuels, which caused considerable search for alternatives to the limited fossil resources to efficiently supply of energy and chemicals (Yue et al., 2016). Biomass, a renewable organic carbon sources, has great potential to substitute fossil re-sources for the production of fuels and chemicals because it is abundant and easily available. The conversion of biomass into energy and chemicals generally begins with the conversion of biomass into platform molecules. Consequently, various bio-based molecules (e.g., HMF, lactic acid, 2,5-furandicarboxylic acid, and levulinic acid) are yielded from biomass, which serve as important starting feedstocks for synthesis of fuels and chemicals (Bozell and Petersen, 2010; Sudarsanam et al., 2018; Jing et al., 2019; Ma et al., 2020). HMF has attracted researchers' interest as a prospective biorefinery intermediate and precursor for medicines, polymer monomers, and fuels. Because of its furan ring structure with one aldehyde and one alcohol group, HMF is regarded as a major platform compound among biomass-derived compounds. The special chemical structure character of HMF makes it very active (**Figure 1**) to be converted into a series of compounds including polymer precursors [2,5-furan dicarboxylic acid and bis-2,5-(hydroxymethyl)furan], liquid fuel precursor, and fuel additives (5-acetoxymethyl-2-furaldehyde, N,N-dimethylformamide, and n-hexane) as well as other platform chemicals (levulinic acid and γ-valerolactone).

FIGURE 1 | Reaction pathway of dehydration of fructose into HMF and illustrations for HMF application.
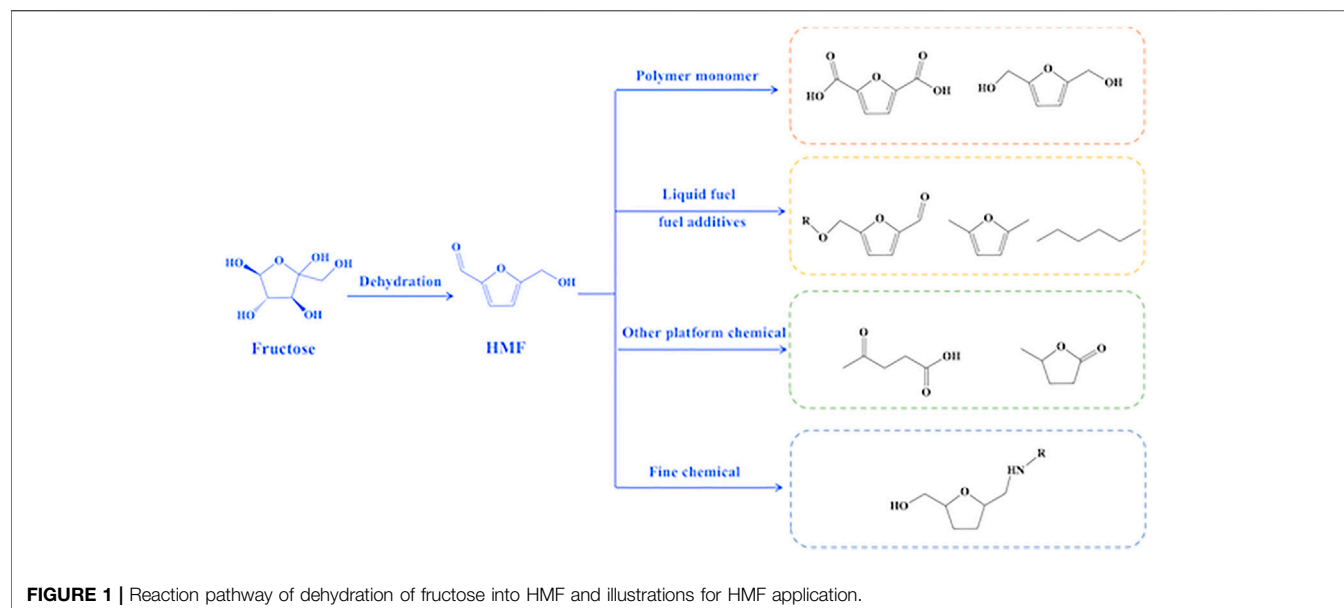
Currently, in the studies of HMF production, fructose, glucose, and cellulose are often used as the feedstocks (Tzeng et al., 2019). Complex carbohydrates, such as cellulose, can be transformed to HMF in three steps: cellulose hydrolysis to glucose, glucose isomerization to fructose, and fructose dehydration to HMF. The final step of these carbohydrates conversion into HMF is the dehydration of fructose to HMF. Thus, high-effective synthesis of HMF from fructose will lay the foundation for biomass-to-HMF transformation (Jiménez-Morales et al., 2014). Actually, fructose is considered as the most efficient and common raw material for HMF synthesis, which allows higher yields of HMF to be obtained (Zhang et al., 2017) because its fructofuranoic structure is more reactive to dehydration (Wang et al., 2019). Generally, dehydration of fructose into HMF is an acid-catalyzed reaction and many homogeneous acid catalysts, such as the easily available mineral acids [H_2SO_4 (Zuo et al., 2017), HCl (Zuo et al., 2017), H_3PO_4 (Ray et al., 2011), CH_3COOH (Thananatthanachon and Rauchfuss, 2010), etc.] and salts [$AlCl_3$ (Zuo et al., 2017), $CrCl_3$ (Yong et al., 2008), $ZnCl_2$ (Zuo et al., 2017), etc.], have been studied in dehydration of fructose to produce HMF. The above mentioned homogeneous catalytic systems, however, usually suffer from corrosivity and difficulty in catalysts separation and reuse (Zhang et al., 2020).

Recently, various heterogeneous catalysts such as metal oxides (DaVià et al., 2017), zeolites (Nie et al., 2020), resins (Qi et al., 2009; Atanda et al., 2015), metal phosphates (Dibenedetto et al., 2016), and heteropoly acids (Gomes et al., 2017) have been successfully developed for dehydration of fructose into HMF, in order to avert the issues associated with using homogeneous catalysts. Although excellent results are obtained, those catalysts encounter some issues including small specific surface area [e.g., resin, $S_{BET} < 50 \, m^2/g$], non-adjustable pore structure, and heteropoly acids (such as $H_3PW_{12}O_{40}$ (Gomes et al., 2017))

dissolved to some extent in DMSO and low active (e.g., metal oxide catalysts). As a result, it is critical to develop an effective, low-cost, and hydrothermally stable catalyst for conversion of carbohydrate to HMF.

SBA-15 mesoporous silica materials, featured with high surface area, relatively large and tunable pore size, as well as facile surface functionalization properties, have been widely applied in catalysis fields (Wang et al., 2019). Another feature of this material is that the mesoporous channels are linked by microporous channels (Wróblewska et al., 2018). It has superior hydrothermal properties and acid resistance when compared to other materials in this group, such as MCM-41. The unique molecular structure and mesoporous structure render SBA-15 mesoporous molecular sieves to serve as an attractive catalysts/catalyst carriers through improved mass transport diffusion during reactions (Agarwal et al., 2018). Up to now, various SBA-15-based catalysts, such as Fe-grafted SBA-15 (Nozaki et al., 2002), Co-substituted SBA-15 (Cui et al., 2010), single-site SBA-15 supported zirconium (Xu et al., 2015), molybdenum on SBA-15 (Azofra et al., 2018), and Ti-substituted mesoporous SBA-15 (Yu Y. et al., 2020), have been successfully developed. Meanwhile, the metal modified SBA-15 catalysts have been widely applied in various reactions, such as epoxidation, hydrogen generation, selective hydrogenation, dye degradation, ethanol oxidation, water splitting, soot combustion, and esterification. Especially, titanium-based catalysts such as $TiO_2/Nb_2O_5.nH_2O$ and phosphated TiO_2 (P-TiO_2) have attracted much attention in the conversion of carbohydrates to HMF owing to their outstanding catalytic performance (DaVià et al., 2017; Rao et al., 2019; Huang et al., 2020). Zhang et al. (2019) used Al_2O_3-TiO_2 Modified Sulfonated Carbon as a catalyst to catalyze the conversion of glucose dehydration to HMF and obtained 57.4% yield at

130°C. In those established catalytic systems, Ti^{4+} served as the Lewis acid sites for carbohydrates dehydration. Based on mesoporous SBA-15 with improved mass-transport diffusion and Ti^{4+} with strong Lewis acidity, we envision that mesoporous SBA-15 modified with Ti^{4+} will exhibit excellent catalytic performance for synthesis of HMF from fructose dehydration.

Herein, we demonstrated that Ti-SBA-15 solid acid prepared by a facile thermal synthesis method could facilitate the dehydration of fructose to produce HMF. Characteristic analysis of Ti-SBA-15 from XRD and TEM revealed that Ti groups were successfully doped into SBA-15 without the destruction of mesoporous structure. Meanwhile, the acidic properties (type, strength, and amount) of various Ti-SBA-15 samples were also investigated by pyridine-FTIR and NH_3-TPD analysis. Various reaction parameters including reaction time, reaction temperature, and catalyst amount were investigated to explore the optimized reaction conditions. In particular, 100% fructose conversion with 82% HMF yield was obtained over Ti-SBA-15 (120) catalyst in DMSO under mild reaction conditions (140°C, 1 h). Furthermore, the catalytic performance of Ti-SBA-15 (120) in the fructose-to-HMF conversion was retained after fifth recycles, clearly suggesting its high stability.

MATERIALS AND METHODS

Chemicals

Fructose (98%–102%) was purchased from the Sinopharm Chemical Reagent Co., Ltd. 5-Hydroxymethylfurfural (HMF, 97%), P123 ($EO_{20}PO_{70}EO_{20}$), tetraethyl orthosilicate ($SiO_2 \geq 28.4\%$), HCl (36%–38%), titanium (IV) chloride (98%), and dimethyl sulfoxide (DMSO, 99.5%) were purchased from Shanghai Titan Scientific Co., Ltd. All chemicals were used as supplied without any further purification. Besides, deionized water (DI water, 18.2 MΩ cm) used in this work was prepared using a water purification system (Heal Force, Shanghai Shengke Equipment Co., Ltd.).

Preparation of Ti-SBA-15

The preparation procedure of Ti-SBA-15 was similar to the previously reported literature (Lin et al., 2018). In a typical process, 2 g of Pluronic P123 was dissolved in 60 ml of 2 mol/L hydrochloric acid and 15 ml H_2O at 40°C under stirring for 12 h. Then, 11.2, 5.6, or 2.8 ml of titanium chloride (0.5 mol/L) was added followed by 4.2 ml of tetraethylorthosilicate to yield a Si/Ti of 30, 60, and 120. The mixture was stirred at 40°C for 5 h and subsequently hydrothermally treated at 100°C for another 24 h. The solid product was collected by filtration, washing several times with deionized water, and dried at 100°C overnight before calcined at 550°C in air for 6 h to remove the organic template. The resultant materials prepared with different amounts of titanium (IV) are denoted as Ti-SBA-15(x), where x represents the Si/Ti atomic ratio used in the reaction.
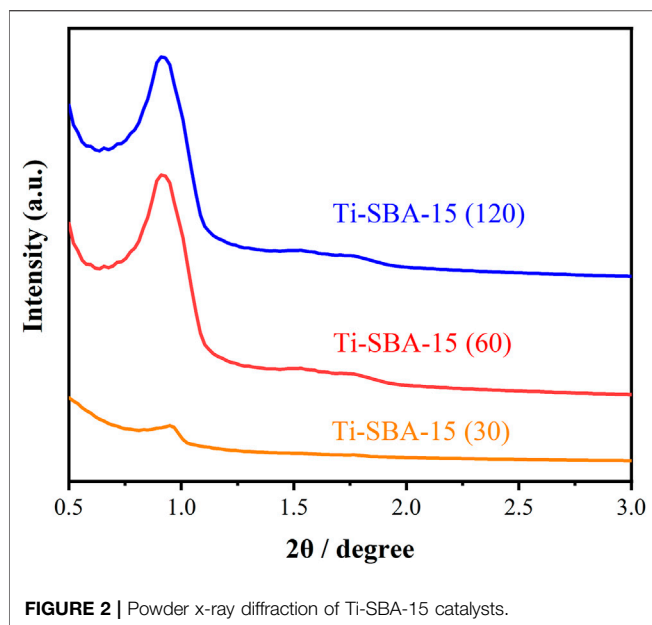
Catalyst Characterization

The small-angle XRD diffraction patterns (0.5–5°) of as-prepared materials were collected with a Bruker D8 power diffractometer using Cu-Kα radiation (40 kV, 40 mA), at a scan rate of 0.5° min^{-1}. TEM (Thermo Fisher Talos F200X) at 200 kV was used to examine the catalyst morphology. Nitrogen adsorption–desorption isotherms of as-prepared materials were measured on a Micro for TriStar II Plus 2.02 at −196°C. The samples were heated in a vacuum at 120°C for 6 h before the measurements to remove moisture and volatile impurities. On the basis of the desorption data, the surface area was calculated using the BET method while the Barrett–Joyner–Holanda (BJH) method was used to calculate the pore size distribution. To determine the total acidity of catalysts, the NH_3-TPD (temperature programmed desorption) was performed in an AutoChemII analyzer. The sample tube was filled with 0.1 g of catalysts and heated at 350°C for 1 h in a helium environment. After cooling to 50°C, the samples were subjected to NH_3/He (10%) mixed gas flow for 1 h. Then, the physisorbed NH_3 was removed by changing the gas flow to helium for 1 h at 50°C. The TPD was then measured at a heating rate of 10°C min^{-1} (maximum desorption temperature was 550°C). Pyridine-IR data were collected using a PerkinElmer Frontier FT-IR spectrometer, with 64 scans at an effective resolution of 1 cm^{-1}. A sample of 10 mg was pressed into a self-supporting wafer. The samples were pretreated at 350°C under vacuum prior to adsorption and then cooled to room temperature when pyridine vapor was introduced into the cell. At 150°C, the samples were heated in a vacuum, and the spectra were recorded at room temperature. The Ti content in the catalysts and filtrate after removal of Ti-SBA-15(120) was measured by ICP-OES.

Catalytic Test

All fructose dehydration experiments were carried out in a 15-ml pressure tube with magnetic stirring. In a typical reaction, fructose (0.1 g) was mixed with Ti-SBA-15 at different mass ratios (1:1–20:1), followed by 10 ml of DMSO. The reactor was sealed and immersed in a heated at different temperatures (110–170°C) oil bath with stirring at a speed of 500 rpm for 0.5–5 h (Yu X et al., 2020). Time zero was established when the reactor was immersed in the oil bath. After the reaction, the liquid phases were passed through a 0.45-μm filter, and products in both aqueous and organic phases were analyzed by a high-performance liquid chromatography (HPLC).

HPLC analysis was performed using a Shimadzu liquid chromatography system fitted with a UV detector (SPD-16) and a Refractive Index (RI) detector (RID-20A), respectively. Fructose conversion was quantified with a Cosmosil packed column of D-sugars (4.6 mm, I.D. × 250 mm) and RI detector (RID-20A), using acetonitrile and water (3:1, v/v) as mobile phase at 30°C with a flow rate of 1 ml/min. HMF was monitored with a Cosmosil C18-AR-II packed column (4.6 mm, I.D × 150 mm), using a mobile phase consisting of methanol and water with phosphoric acid (20:80) at a flow rate

FIGURE 2 | Powder x-ray diffraction of Ti-SBA-15 catalysts.

of 1 ml/min, with a UV detector (SPD-16) and the column temperature was 30°C.

RESULTS AND DISCUSSION

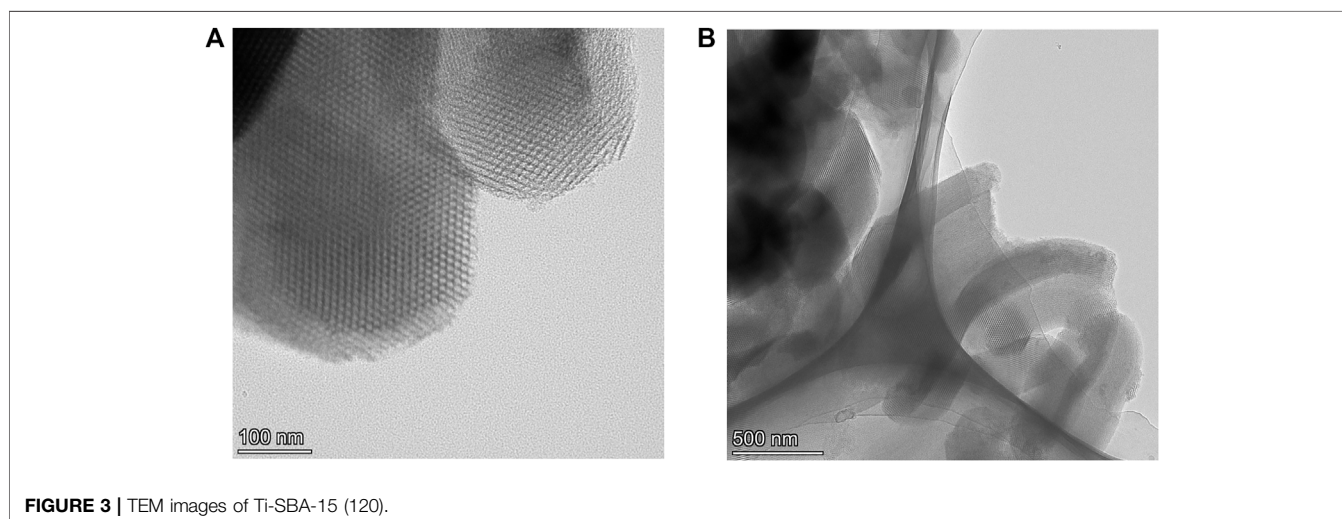### Catalyst Characterization of Ti-SBA-15 Catalysts

The low-angle XRD patterns of Ti-SBA-15(30), Ti-SBA-15(60), and Ti-SBA-15(120) catalysts are shown in **Figure 2**. The materials of Ti-SBA-15(60) and Ti-SBA-15(120) exhibit a very strong peak at about $2\theta = 1.0°$, which is attributed to the (100) plane of the SBA-15 material. Another two weak peaks between 1.5° and 2.0° are ascribed to the (110) and (200) planes, respectively. The results indicated that the Ti-SBA-15 catalysts possessed a two-dimensional hexagonal mesoporous structure
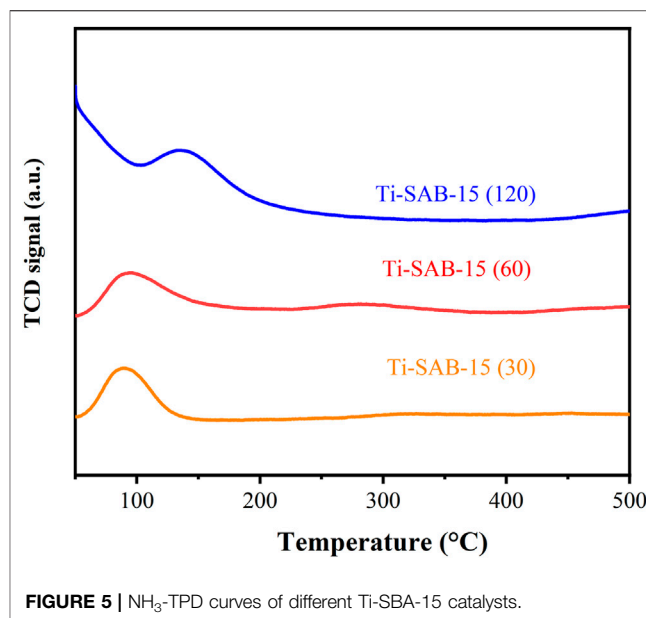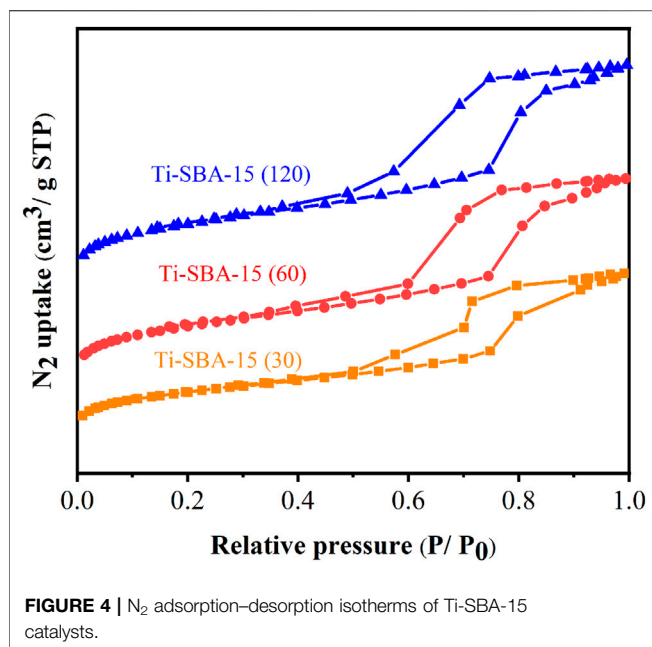
with well ordered. The presence of those peaks confirms that the hexagonal mesoporous structure is also maintained after Ti group incorporation. In contrast, in the case of XRD patterns of Ti-SBA-15(30), a weak peak of the (100) plane is clearly observed while the peaks assigned to the (110) and (200) plane are not observed, indicating the partly collapsing of the mesoporous structure of SBA-15. The low-angle XRD patterns of Ti-SBA-15 catalysts showed that the intensity of all diffraction peaks gradually decreased with increasing Ti content, suggesting a decrease of long-distance order.

The TEM images of Ti-SBA-15(120) are presented in **Figure 3**. It shows the highly ordered hexagonal arrangement of the channels and clearly demonstrates the retention of the periodic structure. The prepared Ti-SBA-15(120) sample preserved with one-dimensional channels, indicating a 2D hexagonal (p6mm) mesostructure, which is consistent with XRD results, also similar to those reported in the literature (Yu Y.et al., 2020).

The textural properties of the Ti-SBA-15(30), Ti-SBA-15(60), and Ti-SBA-15(120) catalysts were studied by nitrogen physisorption at 77 K (**Figure 4**), and the detailed data about textural properties of all catalysts are summarized in **Table 1**. For all samples, the adsorption branch of the isotherms presented two adsorption phenomena, wherein the adsorption of nitrogen at low relative pressure ($P/P_0 < 0.1$) mainly occurred by monolayer adsorption on micropores, while the samples showed a capillary condensation step at relative pressure at $0.6 < P/P_0 < 0.8$. The obtained results clearly indicate the presence of the mesopores within Ti-SBA-15 catalysts. The N_2 adsorption–desorption curves of all Ti-SBA-15 catalysts displayed type IV isotherms, which is characteristic of typical mesoporous molecular sieves (**Figure 4**). This finding is also in well accordance with XRD spectrum analysis. As shown in **Table 1**, the BET surface area and total pore volume of the as-prepared materials significantly increased from 696 to 967 m^2/g and 0.95–1.29 cm^3/g, respectively, with the decrease of Ti content.

The acid concentration of the Ti-SBA-15 samples was determined by temperature-programmed desorption of ammonia

FIGURE 3 | TEM images of Ti-SBA-15 (120).

FIGURE 4 | N_2 adsorption–desorption isotherms of Ti-SBA-15 catalysts.

FIGURE 5 | NH_3-TPD curves of different Ti-SBA-15 catalysts.

(**Figure 5** and **Table 2**, entries 1–5). It is clear that all of the Ti-SBA-15 catalysts mainly possessed weak (<300°C) and moderate acid sites (300–500°C), and the acid density of all catalysts increases with the decrease of Ti content. It is also worth noting that Ti-SBA-15(120) has the highest concentration of acid sites (1.32 mmol/g) than the others. The Ti-SBA-15(120) catalyst has higher weak acidity than other catalysts. The weak acid amount of Ti-SBA-15 samples decreased with decreasing the Si/Ti ratio (or increasing titanium contents) from 120 to 30. As more Ti is introduced, the proportion of medium acidic sites gradually increases, while the proportion of weak acidic sites gradually decreases, which indicates that Ti is introduced as a moderate acidic site. The Ti content of Ti-SBA-15(30), Ti-SBA-15(60), and Ti-SBA-15(120) was 16.56%, 3.11%, and 0.16%, respectively (**Table 1**). The results show that the measured values inevitably deviate from the calculated values, indicating that not all Ti species enter the molecular sieves.

To learn more about the acidic nature of Ti-SBA-15 catalysts, the pyridine-FTIR spectra were collected as shown in **Figure 6**. The band at 1,590 cm^{-1} in **Figure 6** corresponds to the physical adsorption of weak Lewis acid sites (Ravi et al., 2020). The characteristic bands at 1,450 and 1,623 cm^{-1} belonging to pyridine bounded to the strong Lewis acid sites are observed in all Ti-SBA-15 samples, demonstrating that the as-prepared Ti-

SBA-15 catalysts possessed Lewis acid sites (Yu Y.et al., 2020). The bands at 1,545 cm^{-1} with low intensity corresponding to Brönsted acid sites were also clearly observed for Ti-SBA-15(60) and Ti-SBA-15(30) catalysts, suggesting the presence of a small amount of Brönsted acid sites within the Ti-SBA-15(30) and Ti-SBA-15(60) materials. Furthermore, the band at 1,490 cm^{-1} attributed to pyridine adsorption on both Lewis and Brönsted acid sites were also observed for all Ti-SBA-15 samples as exhibited in **Figure 6**. These results showed that Ti-SBA-15(60) and Ti-SBA-15(30) samples had a large amount of Lewis acid sites along with a small amount of Brönsted acid sites. For as-prepared Ti-SBA-15 samples, the TiO_4 units of the hydrated surface titanium species on SBA-15 might be connected by Ti–O–Si bonds (Sudarsanam et al., 2020). As the structure of surface titanium species is reversible during hydration and dehydration, these titanium species possess little Brönsted acidity (Peng et al., 2017). The absence of Brönsted acid sites in Ti-SBA-15(120) is due to the low content of titanium (**Table 2**, entries 6).

Equation Dehydration of Fructose Into HMF Over Different Catalysts

The catalytic performances of Ti-SBA-15 catalysts with different Si/Ti ratios and without catalyst in catalyzing

TABLE 1 | Physio-chemical properties of catalysts.

Entry	Catalyst	BET surface area (m^2 g^{-1})[a]	Pore volume (cm^3 g^{-1})[a]	Pore size (nm)[a]	Ti content (wt%)[b]
1	Ti-SBA-15 (30)	696	0.95	5.50	16.56
2	Ti-SBA-15 (60)	937	1.22	5.21	3.11
3	Ti-SBA-15 (120)	967	1.29	5.36	0.16

[a]BET, surface area, pore volume, and pore size were measured by N_2-adsorption–desorption.
[b]Ti content was determined by ICP-OES.

TABLE 2 | Acid strength, type, and density of Ti-SBA-15.

Entry	Catalyst	Acid strength distribution (%) [a]		Total acid density (mmol/g) [a]	L/(L+B) [b]
		<300°C	300–500°C		
1	Ti-SBA-15 (30)	58.5	41.5	0.53	0.92
2	Ti-SBA-15 (60)	69.6	30.4	0.70	0.868
3	Ti-SBA-15 (120)	100	0	1.32	1

[a]Acid strength distribution and total acid density were measured by NH_3-TPD.
[b]L/(L + B) was determined by Pyridine-IR.
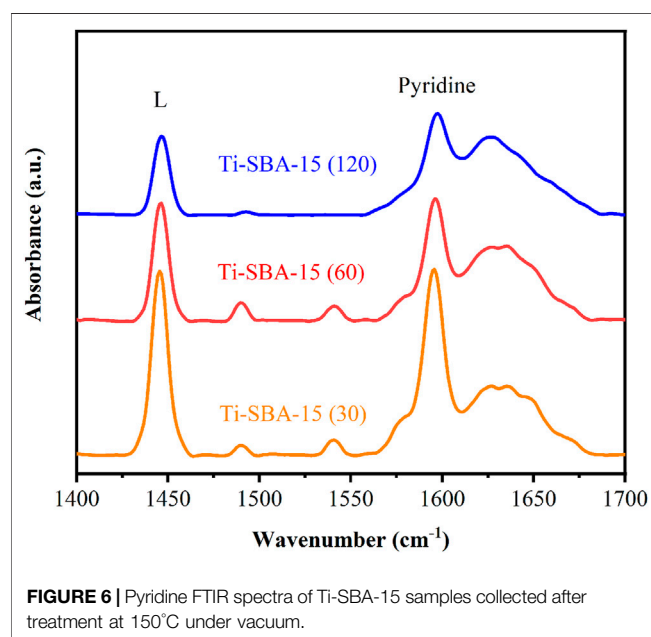
FIGURE 6 | Pyridine FTIR spectra of Ti-SBA-15 samples collected after treatment at 150°C under vacuum.

TABLE 3 | Influence of Si/Ti ratio on fructose conversion, and HMF yield over Ti-SBA-15 catalysts (reaction conditions: 0.1 g fructose, 0.01 g catalysts, 140°C, 1 h, 10 ml DMSO).

Catalyst	Fructose conversion (%)	HMF yield (%)
Without catalyst	100	57
Ti-SBA-15 (30)	100	76
Ti-SBA-15 (60)	100	79
Ti-SBA-15 (120)	100	82

dehydration of fructose are summarized in **Table 3**. Only 57% yield of HMF was obtained in the blank experiment, far inferior to HMF yield (82%) obtained with the Ti-SBA-15(120) catalyst, which clearly demonstrated the high activity of the Ti-SBA-15(120) catalyst. All the catalysts demonstrated high conversion rate to fructose (100%) under the reaction conditions. As the amount of Ti in the catalyst increased, the reactivity diminished for fructose dehydration. The highest HMF yield (82%) was obtained over Ti-SBA-15(120). The yield from the different catalysts did not vary greatly for 1 h in our study. In order to find the activity difference among the as-prepared catalysts, we have

lowered the reaction temperature and shortened the reaction time. Note that high temperature with a short time (130°C for 20 min) showed a significant difference in HMF yield. As shown in the **Supplementary Table S2**, The Ti-SBA-15(120) catalyst gave the greatest HMF yield of about 9%. There was almost no HMF production when the experiment was carried out in the presence of Ti-SBA-15(30) or Ti-SBA-15(60) catalysts (only 1 and 2%). It was observed that Ti-SBA-15(120) showed the highest activity among the different catalysts employed in this reaction. The excellent catalytic performance of Ti-SBA-15(120) was associated to its high surface area, large pore size, and high pore volume. Therefore, we chose the Ti-SBA-15(120) catalyst for the following investigation.

Effect of Reaction Time, Temperature, and Amount of Catalyst

In accordance with the initial catalysts screening above, Ti-SBA-15(120) was the most effective catalyst for fructose dehydration reaction. Thus, the effect of the reaction time and temperature on fructose-to-HMF conversion was examined with Ti-SBA-15(120) as catalysts and the results are shown in **Figure 7**. **Figure 7A** shows that the fructose was almost completely consumed at 140°C after 30 min. The yield of HMF increased remarkably with the reaction time from 0.5 to 1 h. However, the yield of HMF showed a decreased trend when the time was extended to 5 h owing to the production of by-products (e.g., humins and levulinic acid). So, the optimal reaction time was chosen as 1 h.

The effect of reaction temperature (110–170°C) on dehydration of fructose into HMF over Ti-SBA-15(120) catalyst was examined as shown in **Figure 7B**. Obviously, the yield of HMF was strongly influenced by the reaction temperature. For example, the yield of HMF increased with the increase of reaction temperature, and an 82% yield of HMF with 100% fructose conversion was acquired at 140°C after 1 h. At a higher temperature (150, 160, and 170°C), the yield of HMF was lower than that obtained at 140°C. Moreover, the high temperature results in more by-products derived from further degradation of HMF (Zhao et al., 2011; Wang et al., 2019). The optimal reaction temperature and reaction time were thus 140°C and 1 h, respectively.

The catalyst dosage is also an important factor affecting hydrolysis processes, so it is necessary to explore the effect of Ti-SBA-15(120) dosage on the dehydration of fructose. The
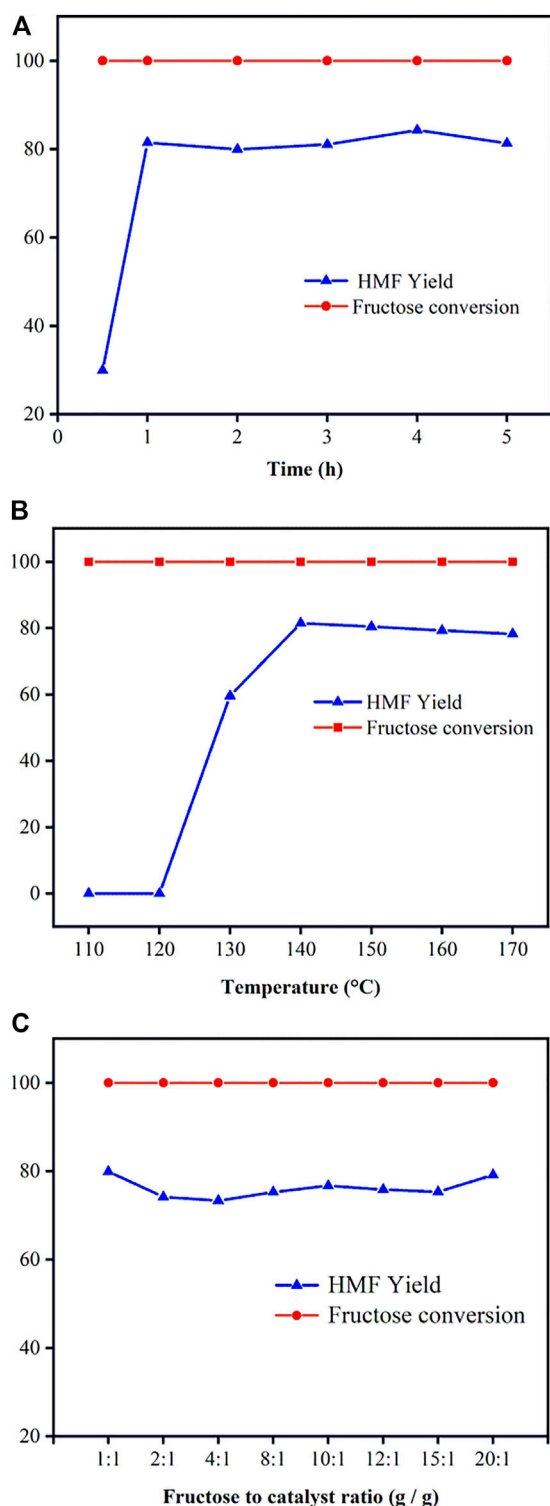
FIGURE 7 | Dependence of fructose (0.1 g) conversion yield and yield for HMF **(A)** effect of reaction time; **(B)** effect of reaction temperature; **(C)** effect of catalyst dosage [reaction conditions: **(A)** 0.1 g fructose, 0.01 g catalysts, 140°C, 10 ml DMSO; **(B)** 0.1 g fructose, 0.01 g catalysts, 1 h, 10 ml DMSO; **(C)** 0.1 g fructose, 140°C, 1 h, 10 ml DMSO].

effect of Ti-SBA-15 dosage on the dehydration of fructose over the Ti-SBA-15(120) catalyst is shown in **Figure 7C**. When the Ti-SBA-15(120) dosage is 0.005 g (mass ratio of fructose/catalyst is 20:1), the Lewis acid sites were already saturated for the hydrolysis of fructose. Further increase in the amount of Ti-SBA-15 dosage from 0.005 to 0.1 g (mass ratio of fructose/catalyst from 20:1 to 1:1) showed no significant increase in the HMF yield, which may be attributed to the formation of the side products (e.g., humins), which probably stemmed from polymerization of HMF in the presence of a high amount of the catalyst loading (Girisuta et al., 2006). So, the optimal mass ratio for fructose and Ti-SBA-15 is 20:1.

Catalyst Stability

Heterogeneous catalysts with high stability are critical for the advancement of aqueous phase biomass processing. The catalytic stability of the Ti-SBA-15(120) catalyst was investigated in the conversion of fructose to HMF in 10 ml of DMSO (140°C, 1 h). After the reaction was completed, the reused catalyst was collected by centrifugation, washed three times with DMSO and acetone in ultrasonic (5 min), dried at 100°C for 2 h, and then calcined at 550°C for 3 h, before being used for the next run under the same reaction conditions. Ti-SBA-15(120) recycle test results are shown in **Figure 8**. The HMF yield remained at 80% in the fifth cycle, indicating that the catalyst can be recycled effectively without losing catalytic activity, strongly demonstrating the high stability of the Ti-SBA-15(120) catalyst for fructose dehydration.

In addition, XRD patterns and N_2 adsorption–desorption isotherms of fresh and used Ti-SBA-15(120) catalysts have been compared as shown in **Supplementary Figures S1, S2**. N_2 adsorption–desorption analysis shows that there is a slight
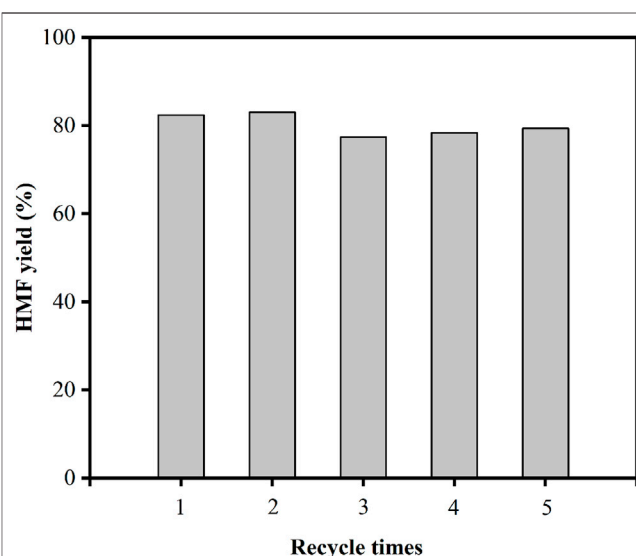

FIGURE 8 | Cycle use of Ti-SBA-15 (120) catalyst for fructose conversion reaction (reaction conditions: 0.1 g fructose, 0.01 g catalysts, 10 ml DMSO, 140°C, 1 h).

discrepancy in BET surface area (967–735 m^2/g) and pore volume (1.29–1.07 cm^3/g) between fresh and used Ti-SBA-15(120) (**Supplementary Table S1**). The used Ti-SBA-15(120) catalyst kept its original mesoporous structure (**Supplementary Figure S1**). The reusability experiments have shown that Ti-SBA-15(120) was a stable and efficient catalyst for the synthesis of HMF. Furthermore, we also determined the Ti concentration in the filtrate after removing the catalyst using ICP-OES. The Ti species leaching during the reaction was extremely minimal (<0.00002%); thus, the active species leaching during the reaction is negligible. These results further proved the good stability of Ti-SBA-15(120) in the hydrolysis of fructose to HMF.

CONCLUSION

The Ti-SBA-15 catalyst that we developed is an efficient catalyst for the production of HMF from fructose. Characterization results revealed that the addition of Ti into SBA-15 materials had no obvious influence on its pristine mesoporous structure. The Ti-SBA-15 also had a high surface area, large pore size, and high pore volume. Ti-SBA-15(120) proved to be highly active to HMF, and a high yield of HMF of 82% was obtained by the hydrolysis of fructose in DMSO. Consecutive use of Ti-SBA-15(120) demonstrated that, after the fifth cycle, the activity loss is not significant in the conversion of fructose-based substrates to HMF. Ti-SBA-15 exhibited better activity and stability.

DATA AVAILABILITY STATEMENT

The original contributions presented in the study are included in the article/**Supplementary Material**, further inquiries can be directed to the corresponding author.

AUTHOR CONTRIBUTIONS

KS and YZ: conceptualization. KS and JH: methodology. YZ: validation. All authors: formal analysis. KS: investigation. JG and KS: resources. YZ and XX: data curation. YZ and XX: writing—original draft preparation. KS and YZ: writing—review and editing. YZ and XX: visualization. JG: supervision. KS: project administration. KS: funding acquisition.

SUPPLEMENTARY MATERIAL

The Supplementary Material for this article can be found online at: https://www.frontiersin.org/articles/10.3389/fchem.2021.817417/full#supplementary-material

REFERENCES

Agarwal, B., Kailasam, K., Sangwan, R. S., and Elumalai, S. (2018). Traversing the History of Solid Catalysts for Heterogeneous Synthesis of 5-hydroxymethylfurfural from Carbohydrate Sugars: A Review. *Renew. Sust. Energ. Rev.* 82, 2408–2425. doi:10.1016/j.rser.2017.08.088

Atanda, L., Silahua, A., Mukundan, S., Shrotri, A., Torres-Torres, G., Beltramini, J., et al. (2015). Catalytic Behaviour of TiO2-ZrO2 Binary Oxide Synthesized by Sol-Gel Process for Glucose Conversion to 5-Hydroxymethylfurfural. *RSC Adv* 5, 80346–80352. doi:10.1039/C5RA15739K

Azofra, L. M., Morlanés, N., Poater, A., Samantaray, M. K., Vidjayacoumar, B., Albahily, K., et al. (2018). Single-Site Molybdenum on Solid Support Materials for Catalytic Hydrogenation of N2-into-NH3. *Angew. Chem. Int. Ed.* 57, 15812–15816. doi:10.1002/anie.201810409

Bozell, J. J., and Petersen, G. R. (2010). Technology Development for the Production of Biobased Products from Biorefinery Carbohydrates-The US Department of Energy's "Top 10" Revisited. *Green. Chem.* 12, 539–554. doi:10.1039/B922014C

Cui, H., Zhang, Y., Qiu, Z., Zhao, L., and Zhu, Y. (2010). Synthesis and Characterization of Cobalt-Substituted SBA-15 and its High Activity in Epoxidation of Styrene with Molecular Oxygen. *Appl. Catal. B: Environ* 101, 45–53. doi:10.1016/j.apcatb.2010.09.003

DaVià, L., Recchi, C., Gonzalez-Yañez, E. O., Davies, T. E., and Lopez-Sanchez, J. A. (2017). Visible Light Selective Photocatalytic Conversion of Glucose by TiO2. *Appl. Catal. B: Environ.* 202, 281–288. doi:10.1016/j.apcatb.2016.08.035

Dibenedetto, A., Aresta, M., Bitonto, L., and Pastore, C. (2016). Organic Carbonates: Efficient Extraction Solvents for the Synthesis of HMF in Aqueous Media with Cerium Phosphates as Catalysts. *ChemSusChem* 9, 118–125. doi:10.1002/cssc.201501181

Girisuta, B., Janssen, L. P. B. M., and Heeres, H. J. (2006). A Kinetic Study on the Decomposition of 5-hydroxymethylfurfural into Levulinic Acid. *Green. Chem.* 8, 701–709. doi:10.1039/B518176C

Gomes, F. N. D. C., Mendes, F. M. T., and Souza, M. M. V. M. (2017). Synthesis of 5-hydroxymethylfurfural from Fructose Catalyzed by Phosphotungstic Acid. *Catal. Today* 279, 296–304. doi:10.1016/j.cattod.2016.02.018

Huang, F., Jiang, T., Xu, X., Chen, L., Laurenczy, G., Fei, Z., et al. (2020). A TiO2/Nb2O5·nH2O Heterojunction Catalyst for Conversion of Glucose into 5-hydroxymethylfurfural in Water. *Catal. Sci. Technol.* 10, 7857–7864. doi:10.1039/D0CY01601B

Jiménez-Morales, I., Teckchandani-Ortiz, A., Santamaría-González, J., Maireles-Torres, P., and Jiménez-López, A. (2014). Selective Dehydration of Glucose to 5-Hydroxymethylfurfural on Acidic Mesoporous Tantalum Phosphate. *Appl. Catal. B: Environ.* 144, 22–28. doi:10.1016/j.apcatb.2013.07.002

Jing, Y., Guo, Y., Xia, Q., Liu, X., and Wang, Y. (2019). Catalytic Production of Value-Added Chemicals and Liquid Fuels from Lignocellulosic Biomass. *Chem* 5, 2520–2546. doi:10.1016/j.chempr.2019.05.022

Lin, Y.-C., Chang, C.-C., Sung, K.-H., Lee, J. F., and Cheng, S. (2018). Importance of Solvents in Preparing Highly Active Ti-SBA-15 Catalysts by Grafting Method. *Microporous Mesoporous Mater.* 272, 276–285. doi:10.1016/j.micromeso.2018.06.046

Ma, Y., Tan, W., Wang, J., Xu, J., Wang, K., and Jiang, J. (2020). Liquefaction of Bamboo Biomass and Production of Three Fractions Containing Aromatic Compounds. *J. Bioresources Bioproducts* 5, 114–123. doi:10.1016/j.jobab.2020.04.005

Nie, Y., Hou, Q., Bai, C., Qian, H., Bai, X., and Ju, M. (2020). Transformation of Carbohydrates to 5-hydroxymethylfurfural with High Efficiency by Tandem Catalysis. *J. Clean. Prod.* 274, 123023. doi:10.1016/j.jclepro.2020.123023

Nozaki, C., Lugmair, C. G., Bell, A. T., and Tilley, T. D. (2002). Synthesis, Characterization, and Catalytic Performance of Single-Site Iron(III) Centers

on the Surface of SBA-15 Silica. *J. Am. Chem. Soc.* 124, 13194–13203. doi:10.1021/ja020388t

Peng, K., Li, X., Liu, X., and Wang, Y. (2017). Hydrothermally Stable Nb-SBA-15 Catalysts Applied in Carbohydrate Conversion to 5-hydroxymethyl Furfural. *Mol. Catal.* 441, 72–80. doi:10.1016/j.mcat.2017.04.034

Qi, X., Watanabe, M., Aida, T. M., and Smith, R. L., Jr (2009). Efficient Process for Conversion of Fructose to 5-Hydroxymethylfurfural with Ionic Liquids. *Green. Chem.* 11, 1327–1331. doi:10.1039/B905975J

Rao, K. T. V., Souzanchi, S., Yuan, Z., and Xu, C. (2019). One-pot Sol-Gel Synthesis of a Phosphated TiO2 Catalyst for Conversion of Monosaccharide, Disaccharides, and Polysaccharides to 5-Hydroxymethylfurfural. *New J. Chem.* 43, 12483–12493. doi:10.1039/C9NJ01677E

Ravi, S., Choi, Y., and Choe, J. K. (2020). Achieving Effective Fructose-To-5-Hydroxymethylfurfural Conversion via Facile Synthesis of Large Surface Phosphate-Functionalized Porous Organic Polymers. *Appl. Catal. B: Environ.* 271, 118942–118954. doi:10.1016/j.apcatb.2020.118942

Ray, D., Mittal, N., and Chung, W.-J. (2011). Phosphorous Pentoxide Mediated Synthesis of 5-HMF in Ionic Liquid at Low Temperature. *Carbohydr. Res.* 346, 2145–2148. doi:10.1016/j.carres.2011.08.006

Sudarsanam, P., Li, H., and Sagar, T. V. (2020). TiO2-Based Water-Tolerant Acid Catalysis for Biomass-Based Fuels and Chemicals. *ACS Catal.* 10, 9555–9584. doi:10.1021/acscatal.0c01680

Sudarsanam, P., Zhong, R., Van den Bosch, S., Coman, S. M., Parvulescu, V. I., and Sels, B. F. (2018). Functionalised Heterogeneous Catalysts for Sustainable Biomass Valorisation. *Chem. Soc. Rev.* 47, 8349–8402. doi:10.1039/c8cs00410b

Thananatthanachon, T., and Rauchfuss, T. B. (2010). Efficient Route to Hydroxymethylfurans from Sugars via Transfer Hydrogenation. *ChemSusChem* 3, 1139–1141. doi:10.1002/cssc.201000209

Tzeng, T.-W., Bhaumik, P., and Chung, P.-W. (2019). Understanding the Production of 5-hydroxymethylfurfural (HMF) from Chitosan Using Solid Acids. *Mol. Catal.* 479, 110627–110633. doi:10.1016/j.mcat.2019.110627

Wang, L., Zhang, L., Li, H., Ma, Y., and Zhang, R. (2019). High Selective Production of 5-hydroxymethylfurfural from Fructose by Sulfonic Acid Functionalized SBA-15 Catalyst. *Composites B: Eng.* 156, 88–94. doi:10.1016/j.compositesb.2018.08.044

Wróblewska, A., Miądlicki, P., Sreńscek-Nazzal, J., Sadłowski, M., Koren, Z. C., and Michalkiewicz, B. (2018). Alpha-pinene Isomerization over Ti-SBA-15 Catalysts Obtained by the Direct Method: The Influence of Titanium Content, Temperature, Catalyst Amount and Reaction Time. *Microporous Mesoporous Mater.* 258, 72–82. doi:10.1016/j.micromeso.2017.09.007

Xu, W., Yu, B., Zhang, Y., Chen, X., Zhang, G., and Gao, Z. (2015). Single-site SBA-15 Supported Zirconium Catalysts. Synthesis, Characterization and toward Cyanosilylation Reaction. *Appl. Surf. Sci.* 325, 227–234. doi:10.1016/j.apsusc.2014.11.064

Yong, G., Zhang, Y., and Ying, J. Y. (2008). Efficient Catalytic System for the Selective Production of 5-Hydroxymethylfurfural from Glucose and Fructose. *Angew. Chem. Int. Ed.* 47, 9345–9348. doi:10.1002/anie.200803207

Yu, X., Chu, Y., Zhang, L., Shi, H., Xie, M., Peng, L., et al. (2020). Adjacent Acid Sites Cooperatively Catalyze Fructose to 5-hydroxymethylfurfural in a New, Facile Pathway. *J. Energ. Chem.* 47, 112–117. doi:10.1016/j.jechem.2019.11.020

Yu, Y., Li, F., Zang, Z., Xu, L., and Liu, G. (2020). Highly Efficient Selective Oxidation of 2-methylnaphthalene to Vitamin K3 over Mesoporous Al/Ti-SBA-15 Catalysts: The Effect of Acid Sites and Textural Property. *Mol. Catal.* 495, 111158–111171. doi:10.1016/j.mcat.2020.111158

Yue, C., Li, G., Pidko, E. A., Wiesfeld, J. J., Rigutto, M., and Hensen, E. J. M. (2016). Dehydration of Glucose to 5-Hydroxymethylfurfural Using Nb-Doped Tungstite. *ChemSusChem* 9, 2421–2429. doi:10.1002/cssc.201600649

Zhang, L., Xi, G., Chen, Z., Qi, Z., and Wang, X. (2017). Enhanced Formation of 5-HMF from Glucose Using a Highly Selective and Stable SAPO-34 Catalyst. *Chem. Eng. J.* 307, 877–883. doi:10.1016/j.cej.2016.09.003

Zhang, T., Wei, H., Xiao, H., Li, W., Jin, Y., Wei, W., et al. (2020). Advance in Constructing Acid Catalyst-Solvent Combinations for Efficient Transformation of Glucose into 5-Hydroxymethylfurfural. *Mol. Catal.* 498, 111254–111275. doi:10.1016/j.mcat.2020.111254

Zhang, Y., Wang, J., Wang, J., Wang, Y., Wang, M., Cui, H., et al. (2019). Al 2 O 3 - TiO 2 Modified Sulfonated Carbon with Hierarchically Ordered Pores for Glucose Conversion to 5-HMF. *ChemistrySelect* 4, 5724–5731. doi:10.1002/slct.201901084

Zhao, Q., Wang, L., Zhao, S., Wang, X., and Wang, S. (2011). High Selective Production of 5-hydroxymethylfurfural from Fructose by a Solid Heteropolyacid Catalyst. *Fuel* 90, 2289–2293. doi:10.1016/j.fuel.2011.02.022

Zuo, M., Le, K., Li, Z., Jiang, Y., Zeng, X., Tang, X., et al. (2017). Green Process for Production of 5-hydroxymethylfurfural from Carbohydrates with High Purity in Deep Eutectic Solvents. *Ind. Crops Prod.* 99, 1–6. doi:10.1016/j.indcrop.2017.01.027

Advancements in Tobacco (*Nicotiana tabacum* L.) Seed Oils for Biodiesel Production

Shengjiang Wu[1†], Chuanchuan Gao[2†], Hu Pan[3], Kesu Wei[1], Delun Li[1], Kai Cai[1]* and Heng Zhang[4]*

[1]Guizhou Academy of Tobacco Science, Upland Flue-cured Tobacco Quality and Ecology Key Laboratory, CNTC, Guiyang, China, [2]Guizhou Tobacco Quality Supervision and Test Station, Guiyang, China, [3]College of Biological, Chemical Science and Engineering, Jiaxing University, Jiaxing, China, [4]State Key Laboratory Breeding Base of Green Pesticide and Agricultural Bioengineering, Key Laboratory of Green Pesticide and Agricultural Bioengineering, Ministry of Education, State-Local Joint Laboratory for Comprehensive Utilization of Biomass, Center for Research and Development of Fine Chemicals, Guizhou University, Guiyang, China

With the increasing demand for fossil fuels, decreasing fossil fuel reserves and deteriorating global environment, humanity urgently need to explore new clean and renewable energy to replace fossil fuel resources. Biodiesel, as an environmentally friendly fuel that has attracted considerable attention because of its renewable, biodegradable, and non-toxic superiority, seems to be a solution for future fuel production. Tobacco (*Nicotiana tabacum* L.), an industrial crop, is traditionally used for manufacturing cigarettes. More importantly, tobacco seed is also widely being deemed as a typical inedible oilseed crop for the production of second-generation biodiesel. Advancements in raw material and enhanced production methods are currently needed for the large-scale and sustainable production of biodiesel. To this end, this study reviews various aspects of extraction and transesterification methods, genetic and agricultural modification, and properties and application of tobacco biodiesel, while discussing the key problems in tobacco biodiesel production and application. Besides, the proposals of new ways or methods for producing biodiesel from tobacco crops are presented. Based on this review, we anticipate that this can further promote the development and application of biodiesel from tobacco seed oil by increasing the availability and reducing the costs of extraction, transesterification, and purification methods, cultivating new varieties or transgenic lines with high oilseed contents, formulating scientific agricultural norms and policies, and improving the environmental properties of biodiesel.

Keywords: biodiesel, tobacco seed, inedible oilseed crop, biodiesel property, biotechnology

INTRODUCTION

The industrial revolution results in the widespread use of fossil fuels, which constitute 80% of the energy supply. Additionally, various fossil fuel derivatives are also widely used in the production of industrial and agricultural products. In the past 2 decades, global fossil fuel consumption has continued to grow by 48.7%. According to the reports in 2019, the corresponding consumption reached 136,761 TW-hours (TWh), and oil, natural gas and coal were 53,620, 39,292 and 43,849, respectively (Smil, 2017). The global carbon balance has been broken with massive amounts of CO_2

FIGURE 1 | Schematic illustration of catalytic conversion of liquid biomass into biodiesel.
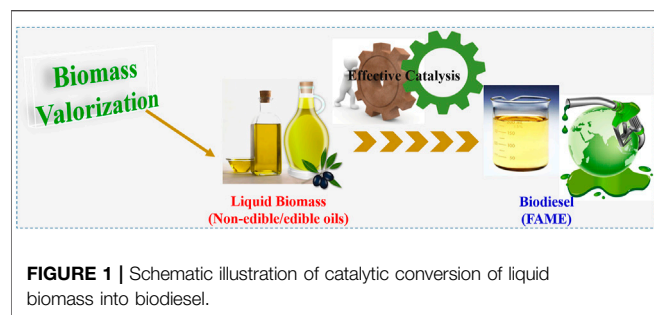
emitted from the use of fossil fuels. The carbon surplus of the atmosphere is the major driving force for the modern global environment and climate change issues such as global warming, extreme weather, etc. (Pao and Tsai, 2010; Pan et al., 2020). To mitigate the negative consequences of excess CO_2 emissions, biofuels derived from waste have been recognized as a substitute for the traditional fossil fuels (Kim et al., 2019). They are carbon neutral, inexpensive and an environmentally friendly and renewable source of energy (Hill et al., 2006). Among the various types of biofuels, biodiesel has been characterized by lower agricultural inputs and more efficient conversion (Hill et al., 2006). Biodiesel has been widely commercialized due to its relatively mature production technology, simple and universal platform (**Figure 1**) (Liu et al., 2019). It is inferred that the global production of biodiesel will reach 46 billion liters in 2025 (Zhang et al., 2017).

Although biodiesel brings many benefits, the key basis of biodiesel production is feedstocks, and feedstocks are determined to play the most important role in the biodiesel value chain. The feedstock should fulfill three main requirements: low production costs, large-scale production and appropriate fatty acid content/composition for biodiesel (Mishra and Goswami, 2018). Moreover, their oil content and composition are highly important indicators, such as the feedstocks rich in monounsaturated fatty acids (MUFAs) are desirable for biodiesel but the composition of the saturated fatty acids (SFAs) is also shown to be of great importance (Stansell, et al., 2012). According to the source of feedstocks, we can categorize them into three biodiesel generations. First-generation biodiesel is currently being widely produced and is extracted from various feedstocks, such as edible rapeseed oil, sunflower oil, palm oil, soybeans, and animal fats. Second- and third-generation biodiesels, only a few of which are close to large-scale commercialization, are extracted from inedible lipid feedstocks such as terrestrial biomass (i.e., breeding crops and transgenic crops) and aquatic biomass (i.e., microalgae and macroalgae) (Vauhkonen et al., 2009; Chung et al., 2020; Mizik and Gyarmati, 2021). However, biodiesel produced from edible oils is more expensive than conventional fossil diesel. Biodiesel has over double the price of diesel fuel. The major economic factor to consider for input costs of biodiesel production is the feedstock, which is about 80% of the total operating cost (Demirbas, 2007). On the other hand, food shortages may occur due to the use of large amounts of edible oils in producing biodiesel, especially in poor countries. These

drawbacks can be overcome by using inedible oils for biodiesel production like *Aleurites trisperma*, bitter almond, *Brucea javanica* seeds, Argemone Mexicana, wild mustard (*Brassica Juncea L.*) seed, and tobacco (*Nicotiana tabacum* L.) seed (Arumugam et al., 2017; Muthukumaran et al., 2017; Jain, 2019; Wang et al., 2019; Adepoju, 2020; Tlili et al., 2020). Generally, tobacco, *Nicotiana tabacum*, which is an annual plant in the Solanaceae family with leaves harvested to manufacture cigarettes, is widespread in China and North and South America, and the leaves are commonly harvested. In recent years, tobacco has been cultivated in approximately 130 countries and covered almost 3.4 million hectares in fields, wherein China alone provides over 40% of the world's production (García-Martínez et al., 2017; Berbe and Matyka, 2020; Wu et al., 2020). It is reported that the *N. tabacum* varieties with the highest seed yields reach 1,171 kg per hectare, which corresponds to 432.9 kg of oil based on an effective oil biosynthesis mechanism for tobacco (Zdremnan and Zdremnan, 2006; García-Martínez et al., 2017). The oil content of tobacco seed often ranges from 30 to 43 wt% and consists mainly of unsaturated fatty acids (Giannelos et al., 2002; Banković-Ilić et al., 2012; Khan et al., 2014; Hu et al., 2020; Rajan et al., 2021). The major fatty acids in tobacco seed oil are stearic acid (2.1–3.3%), palmitic acid (8.72–12.3%), oleic acid (9.97–13.49%), and linoleic acid (64.38–79.0%), respectively (Koiwai et al., 1983; Mukhtar et al., 2007; Tian et al., 2020). As a kind of second-generation biodiesel, tobacco-based biodiesel production is very promising. Therefore, in this review, we elucidate the extraction and transesterification methods, genetic modification, properties and application, and agricultural strategies applied in tobacco biodiesel production, and then discuss the key problems and prospects for biodiesel production from tobacco.

EXTRACTION METHODS OF TOBACCO SEED OIL FOR BIODIESEL PRODUCTION

The tobacco seed oil has been traditionally extracted by mechanical pressing and solvent extraction, mainly with nonpolar solvents. Mechanical pressing, a relatively environmentally friendly extraction method, has been widely applied for the production of high-quality edible oils (Sannino et al., 2017). The whole process includes sample preparation and mechanical pressing stages followed by a solvent extraction procedure to recover the oil located in the press cake (Geow et al., 2021). Seed preparation involving preheating and microwaving destroy or soften the cellular structure of tobacco seeds, which significantly increases the oil yield (Sannino et al., 2017). The pressing equipment parameters including feeding rate, restriction dye diameter, temperature and rotation speed, affect the tobacco seed oil yield. The evaluation of extraction methods in the literature based on the oil yield provided by Soxhlet or accelerated solvent extraction (ASE) due to high oil recovery.

Oil extraction yield obtained from mechanical pressing were usually about 80% (*w/w*) of ASE, but Stanisavljević et al. reported

TABLE 1 | Characteristics of several common methods used in tobacco seed oil extraction.

Methods	Advantages	Disadvantages	Extraction efficiency	Key parameters
Mechanical pressing	Economic, environment friendly, high quality oil and throughput, simple crude oil separation	Lower oil recovery, high power consumption, partial oil left in seed cake	80.28% Sannino et al. (2017).[a], 79.47% Faugno et al. (2016).[a], comparable to Soxhlet extraction Stanisavljević et al. (2009)	Machine type, feeding rate, restriction dye diameter, temperature, rotation speed, seed pretreatment
Soxhlet extraction	High oil recovery, simple operation	Time consuming, consuming organic solvent, complex crude oil separation	100% Stanisavljević et al. (2007b) and Stanisavljević et al. (2009)	Extraction solvent, temperature and time, seed-to-solvent ratio, seed pretreatment
Ultrasonic extraction	Short extraction time, simple and moderate operation	Lower oil recovery, consuming organic solvent, specific equipment, complex crude oil separation	45.81–72.12% Stanisavljević et al. (2009) 78.20% Stanisavljević et al. (2007b)	Ultrasonic power, extraction solvent, temperature and time, seed-to-solvent ratio, seed pretreatment
Accelerated solvent extraction	Short extraction time, high oil recovery, consuming less organic solvent	High operating cost, specific equipment	100% Faugno et al. (2016); Sannino et al. (2017).[a]	Extraction solvent, temperature, time and pressure, static cycle, seed pretreatment
Supercritical fluid extraction	Environment friendly, high quality oil, simple crude oil separation	Lower oil recovery, high operating cost, specific equipment	56.49–78.85% Majdi et al. (2012)	Extraction pressure, temperature and time, modifier type, seed pretreatment
Maceration	Short extraction time, simple and moderate operation	Lowest oil recovery, consuming organic solvent, complex crude oil separation	56.91–57.55% Stanisavljević et al. (2009)	Extraction solvent, temperature and time, seed pretreatment

[a]The ratio of crude oil content obtained from different extraction methods compared to ASE.
"Seed pretreatment"-Seed drying, seed size reduction, seed preheating, seed microwaving, etc.

a higher oil extraction yield, which may be related to pressing equipment type (Stanisavljević et al., 2009; Faugno et al., 2016; Sannino et al., 2017). The characteristics of several common methods used in tobacco seed oil extraction is shown in **Table 1**.

Soxhlet extraction is a classical method for extracting tobacco seed oil with high extraction efficiency (Maestri and Guzmán, 1995; Zlatanov, et al., 2007). Compared with Soxhlet extraction, ASE with a similar oil yield consumed less solvent and time (Faugno et al., 2016; Sannino et al., 2017). However, the milder extraction operations, such as ultrasonic extraction and maceration, showed a lower extraction efficiency (Stanisavljević et al., 2007b and 2009). The solvent extraction efficiency from tobacco seed oil depends on the comminution of the seed, the solvent, the seed-to-solvent ratio, and the extraction time and temperature. Specifically, milling greatly improves extraction efficiency by breaking down tobacco seed cells and augmenting the interfacial area for mass transfer. The oil yield obtained from ground tobacco seeds was shown to be 10 times that of native seeds during ultrasonic extraction, even though the oil yield of tobacco seeds repeatedly grounded was 6 times higher than that of native seed extracted by mechanical pressing (Stanisavljević et al., 2009). Supercritical fluid extraction was also used to extract tobacco seed oil with high recovery and without any residual organic solvents (Stanisavljević et al., 2007b; Majdi et al., 2012; Ashraf-Khorassani et al., 2015). It is worth emphasizing that pressure is the most important factor in supercritical fluid extraction. These extractions of tobacco seed oil mainly focus on laboratory- or small-scale operations. However, application at the industrial scale is still limited to date. Future research should study and develop more
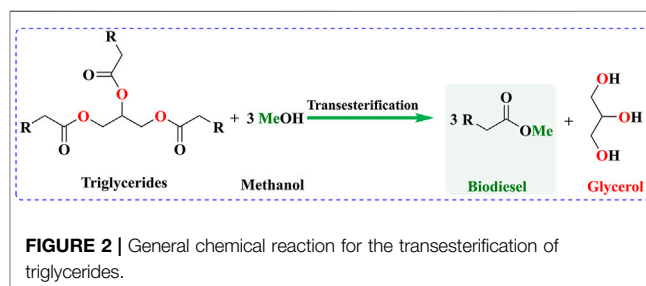
FIGURE 2 | General chemical reaction for the transesterification of triglycerides.

environmentally friendly extraction methods suitable for the large-scale production of tobacco seed oil.

TRANSESTERIFICATION OF BIODIESEL IN TOBACCO SEED OIL

Also known as alcoholysis, transesterification is a process involving the breakage of old ester bonds and the formation of new ester bonds with another alcohol. This process is similar to the mechanism of hydrolysis (Srivastava and Prasad, 2000). Transesterification reactions have been widely applied to convert triglycerides to fatty acid methyl esters or fatty acid ether esters with reduced oil viscosity. The typical reaction with common methanol is shown in **Figure 2** and is also called methanolysis. The transesterification reactions of the process are reversible, and the presence of a suitable catalyst can accelerate the forward conversion reaction. Although acid and enzyme have also been applied in transesterification, base is the most commonly used catalyst and it mainly consists of three steps. These consist of alkoxide formation, nucleophilic attack at

TABLE 2 | Catalysts for the transesterification of tobacco seed oil.

Catalyst types	Catalyst	Oil to MeOH ratio	Time/ min	Catalyst amount, w/w	Temp/ °C	Conversion efficiency, %	Ref
Homogeneous acid/alkali	H_2SO_4	7:1	120	8.1%	65	84.6	Santoso et al. (2021)
	KOH	6:1	10	1.1%			
Homogeneous acid/alkali	H_2SO_4	1:7.5	60	2.5%	65	90.2	Waheed et al. (2015)
	KOH	1:6.09	78	1.1%			
Homogeneous acid/alkali	H_2SO_4	5:1	Total	2.0%	60	92.0	Hariram and Rajan, (2016)
	NaOH	5:1	100	0.7%			
Homogeneous acid/alkali	H_2SO_4	1:18	25–50	2.0%	60	91.0	Veljković et al. (2006)
	KOH	1:6	20–30	1.0%			
Homogeneous acid/alkali	H_2SO_4	1:18	60	1.0%	50–65	82.0–96.0	Motojesi et al. (2017)
	KOH	1:18		1.0%			
or ash	Cocoa pod ash and rice husk ash	1:6		Ash for 2.0%			
Homogeneous alkali	KOH	4:1	—	1.5%	50	—	Karabas et al., 2018
Homogeneous alkali	KOH	5:1	—	1.0%	60	—	Karabas et al. (2016)
Homogeneous alkali	KOH	1:6	80	1.1%	60	> 95.0	Samuel et al. (2020)
Homogeneous alkali	KOH	10:1	5	1.0%	50–60	98.0	Parlak et al. (2009)
Homogeneous alkali	CH_3ONa	1:4–1:8	20	2.0%	70	97.0	Fornasier et al. (2018)
Heterogeneous Acid/alkali	$KHCO_3/Al_2O_3$	1:8	150	3.0% w/w	60	97.1	Anastopoulos et al. (2011)
Noncatalytic with supercritical MeOH	—	1:43	90	—	303	92.8	García-Martínez et al. (2017)

the carbonyl carbon, and the formation of the alkyl ester, which needs to be repeated three times for TGAs. The mechanism of acid-catalyzed transesterification is a little different and consists of carbocation formation, nucleophilic attack of the alcohol, and the formation of the alkyl ester (Ma and Hanna, 1999; Meher et al., 2006). The transesterification process determines the cost and complexity of tobacco seed biodiesel production.

Transesterification efficiency is affected by various critical factors, such as the influence of free fatty acids (FFAs) and water, type and amount of catalyst, the molar ratio of alcohol to oil and type of alcohol, transesterification time and temperature, uniformity of mixing, and whether or not organic co-solvents are used, depending upon reaction conditions. The catalyst chosen is ultimately critical and determines the degree of influence by other factors (Meher et al., 2006). Therefore, research on high-efficiency, low-cost and recyclable catalysts is of high importance.

Transesterification for biodiesel production can be carried out catalytically and non-catalytically under supercritical conditions and enzyme-catalyzed reactions (Leung et al., 2010). Catalytic reactions can also be divided into homogeneous/heterogeneous alkali-catalyzed and homogeneous/heterogeneous acid-catalyzed reactions (Avhad and Marchetti, 2015). The application of transesterification with tobacco seeds is shown in **Table 2**. Generally, the content of FFAs in tobacco seeds is approximately 6% (Stanisavljević et al., 2007a). This high level would result in saponification and then the difficulty in transesterification because the FFA level exceeds 2% (Anguebes-Franseschi et al., 2016). To decrease acid levels, pre-esterification with homogeneous acid could be performed. FFA content was shown to decrease to approximately 1.00% after pre-esterification. This content met the standards for the alkali-catalyzed transesterification process into biodiesel (Murmu et al.,

2017). Compared with other catalysts, alkali catalysts are more commonly used with tobacco seed oil. The common homogeneous and heterogeneous alkalis reported in the literature are KOH, NaOH, CH_3ONa, and $KHCO_3/Al_2O_3$ (Veljković et al., 2006; Parlak et al., 2009; Anastopoulos et al., 2011; Waheed et al., 2015; Hariram and Rajan, 2016; Karabas et al., 2016, 2019; Motojesi et al., 2017; Fornasier et al., 2018; Samuel et al., 2020; Santoso et al., 2021). Due to their low costs and high catalytic capacities, NaOH and KOH are the most commonly used homogeneous alkali catalysts. Moreover, $KHCO_3/Al_2O_3$, a heterogeneous alkali catalyst, can be rapidly separated from the reaction solution with centrifugation or filtration in the subsequent purification process. Moreover, this solid heterogeneous catalyst can simultaneously catalyze transesterification and esterification reactions with little impact from the high contents of FFAs. Thus, these heterogeneous catalysts are very suitable for application with feedstocks containing high FFA contents. However, this reaction often requires a relatively long time because the uniformity of the three-phase transesterification reaction is poor (Kulkarni et al., 2006; Liu et al., 2008). The non-catalytic supercritical method with methanol is also applied in tobacco seed oil conversion to biodiesel. The supercritical transesterification method often requires much higher temperature and pressure in a sealed reactor with an external heater. The transesterification reaction starts during the heating and pressurization period. Compared with the conventional alkali-catalyzed method, this process has advantages in terms of environmental friendliness and ease of purification but requires more energy consumption due to the high temperature and pressure utilized (García-Martínez et al., 2017). Recently, enzyme catalysts for biodiesel production have become increasingly attractive since they do not undergo saponification, and the subsequent purification process is

simple. However, these catalysts are less often used commercially because of relatively long transesterification times and high costs (Moazeni et al., 2019).

ROLE OF BIOTECHNOLOGY IN BIODIESEL PRODUCTION IN TOBACCO SEED OIL

Biotechnology is an important method for improving tobacco seed oil production and accumulation. In recent years, fatty acid and TAG accumulation in tobacco seeds has become a promising way to meet the increasing demand for renewable biofuels (Andrianov et al., 2010; Li et al., 2010; Hernández et al., 2012). The first step of fatty acid synthesis involves acetyl-CoA carboxylase (ACCase) catalysis of the carboxylation of acetyl-CoA to malonyl-CoA (Alonso et al., 2010; Fan et al., 2013). Phosphoenolpyruvate carboxylases (PEPCs) play important roles in fatty acid biosynthesis in seeds of oil plants by regulating carbon partitioning (Fan et al., 2013). During seed oil production and accumulation in oil plants, the increased mRNA level of PEPC indicates a potential role in partitioning carbohydrates to fatty acid biosynthesis (Azocar et al., 2010; Fan et al., 2013). Overexpression of *JcPEPC1* in tobacco results in an increase in PEPC activity and fatty acid content, proving its important role in seed oil biosynthesis (Fan et al., 2013).

During TAG accumulation, diacylglycerol acyltransferases (DGATs) are the final enzymes employed in TAG biosynthesis, and they play a critical role in plant oleaginous seed production (Xu et al., 2014). In particular, overexpression of DGATs was shown to increase the accumulation of TAG in plant seeds (Li et al., 2010; Xu et al., 2014). To date, the *DGAT1*, *DGAT2* and *DGAT3* gene families that encode the DGAT enzymes have been identified in plants (Li et al., 2010; Hernández et al., 2012; Xu et al., 2014). Xu et al. (2014) reported that overexpression of *JcDGAT1* and *JcDGAT2* from *J. curcas* resulted in increases in seed oil contents of 32.8 and 31.8%, respectively, in transgenic tobacco.

Most recently, the CRISPR-Cas9 system has emerged as a programmable and versatile tool for genome editing in a wide variety of organisms (Tian et al., 2020 and 2021). Altering the fatty acid metabolic profile by raising the oleic acid content improves the properties of the biodiesel produced and accumulated from tobacco seed oil. Tobacco *fad2–2* mutant seeds based on CRISPR-Cas9 gene-editing technology showed a sharp increase in oleic acid content from 11% to over 79%, whereas the linoleic acid content dropped from 72 to 7% (Tian et al., 2020). Additionally, lipid accumulation in tobacco seeds was dramatically enhanced by approximately 18 and 15% in two targeted knockout mutant lines, of which the *NtAn1* gene of the *TT8* homolog was created by CRISPR-Cas9 (Tian et al., 2021). Yang et al. (2006) employed a partial coding sequence of a microsomal ω-6 fatty acid desaturase gene (*FAD2*) associated with the first step in polyunsaturated fatty acid biosynthesis to make an hpRNA-producing construct to more specifically silence the endogenous *FAD2* gene, thereby realizing a significant increase in the oleic acid level in tobacco seed lipids. In addition, Zhang L. et al. (2016) stated that the oleic acid

FIGURE 3 | Fatty acid and TAG metabolic pathways in tobacco seeds. ACCase, acetyl-CoA carboxylase; FAS, fatty acid synthase; ACP, acyl carrier protein; FA, fatty acid; FatA/B, acyl-ACP thioesterases; DAG, diacyl-glycerol; TAG, triacylglycerol; PC, phosphatidylcholine; SAD, stearoyl-ACP desaturase; DGAT, diacylglycerol acyltransferase; PDCT, phosphatidylcholine:diacylglycerol cholinephosphotransferase; CPT, CDP-choline:1,2-diacylglycerol cholinephosphotransferase; FAD2, oleoyl desaturase; FAD3, linoleoyl desaturase (Zhang, et al., 2016b; Zhou et al., 2019).

content relative to the content of total seed lipids of transformants was drastically decreased in FAD2-silenced tobacco at a low temperature, and there was a corresponding increase in the content of polyunsaturated fatty acid. The reduction in *DGAT1* transcript levels in transgenic tobacco mediated by hpRNA is correlated with a decrease in oil content of 9–49% in mature seeds of transgenic lines (Zhang et al., 2005).

Identifying important regulatory factors involved in tobacco seed oil biosynthesis may enhance our understanding of the process of oil biosynthesis and improve strategies for increasing oil production. It has also been reported that several transcription factors, such as *LEC1*, *LEC2*, and *FUS3*, are associated with embryo development and seed oil biosynthesis (Chen et al., 2014; Zhang M. et al., 2016). However, many genes, proteins, regulatory factors, and multiple pathways are associated with the processes of tobacco seed oil biosynthesis and accumulation (**Figure 3**), and the molecular mechanisms of fatty acid and TAG biosyntheses are not fully understood (Zhang M. et al., 2016; Zhou et al., 2019).

INFLUENCING FACTORS FOR BIODIESEL PRODUCTION DURING TOBACCO SEED OIL ACCUMULATION

During seed development, the contents of TAG, diacylglycerol, and sterol esters were shown to increase, while those of phosphatidylcholine, phosphatidylethanolamine, phosphatidylinositol, phosphatidylglycerol, monogalactosyldiacylglycerol, digalactosyldiacylglycerol, and sulfoquinovosyldiacylglycerol were shown to decrease, suggesting that the proportions of

TABLE 3 | Comparisons of the properties of TSOBD under different standards.

Parameters	Recommended range			References												
	EN 14214-2012	ASTM D6751-15a	GB25199-2017	He et al. (2021)	Veljković et al. (2006)	Usta, (2005)	Anastopoulos et al. (2011)	Parlak et al. (2012)		Rao et al. (2013c)	Waheed et al. (2015)	Rao et al. (2013a)	Hariram and Rajan, (2016)	Guntur and Prasanthi, (2018)	Karabas et al. (2019)
								KOH	NaOH						
Fatty acid methyl esters content (%)	>96.5	—	>96.5	98.15	—	98.6	—	96.5	97	—	—	—	—	—	96.5
Density (kg/m^3)	860–900	—	820–900	887	882	888.5	917.5	880	860	870	890	870	921	870	880
Flash point (°C)	>101	>130	>130	—	—	165.4	220	>100	152	174	126	—	262	174	135
Water and sediment volume (%)	—	<0.05	—	—	—	—	—	—	—	—	—	—	—	—	—
Sulfur content (mg/kg)	<10	S15 < 15, S50 < 500	S50* < 50, S10* < 10	6	—	8	9	0	0	0	—	—	—	—	—
Carbon residue (%)	<0.30	<0.05	<0.05	—	—	0.029	0.086	0.17	0.17	—	—	—	—	—	0.17
Cetane index	>51	>47	S50* > 49, S10* > 51	51	—	51.6	—	54.5	49	55	—	52	26	35	54.5
Sulfated ash (%)	<0.02	<0.02	<0.02	—	—	0.0004	—	—	—	—	—	—	—	—	—
Water content (mg/kg)	<500	—	<500	368	—	354	570	300	400	—	—	—	—	—	—
Viscosity (mm^2/s)	3.50–5.00	1.9–6.0	1.9–6.0	3.5	5.2	4.23	27.7	4.88	3.5	4.2	3.87	13.7	3.5	4.12	4.88
Total contamination (mg/kg)	<24	—	—	—	—	23.95	—	20	23	—	—	—	—	—	20
Copper strip corrosion (rating)	Class 1	Class 3	Class 1	—	—	Class 1	—	Class 1	Class 1	—	—	—	—	—	Class 1
Oxidation stability (h)	>8	>3	>6	—	—	0.8	—	—	—	—	—	—	—	—	—
Acid value (mg KOH/g)	<0.5	<0.5	<0.5	0.45	0.66	0.30	0.48	—	—	—	0.42	—	0.56	0.49	0.25
Iodine value (g I$_2$/100)	<120	—	—	112	110	136	135	122	118	—	—	—	139	110	122
Linolenic acid methyl ester (%)	<12	—	—	—	—	0.759	—	—	—	—	—	—	—	—	—
Polyunsaturated (≥4 double bonds) methyl esters (%)	<1	—	—	—	—	<0.1	—	—	—	—	—	—	—	—	—
Methanol content (%)	<0.20	<0.20	—	—	—	<0.01	—	0.20	0.18	—	—	—	—	—	—
Monoglyceride content (%)	<0.70	Grade No. 1B < 0.40	<0.80	—	—	0.54	—	0.29	<0.29	—	—	—	—	—	—
Diglyceride content (%)	<0.2	—	—	—	—	0.13	—	0.20	<0.05	—	—	—	—	—	—
Triglyceride content (%)	<0.2	—	—	—	—	0.17	—	0.11	0.11	—	—	—	—	—	—
Free glycerine (%)	<0.02	<0.02	<0.02	—	—	0.002	—	—	—	—	—	—	—	—	—
Total glycerine (%)	<0.25	<0.24	<0.24	—	—	0.23	—	0.02	0.02	—	—	—	—	—	0.02
Phosphorus content (mg/kg)	<4	<10	<10	—	—	4	—	4	<4	—	—	—	—	—	—
Group I metals (Na + K) (mg/kg)	<5	<5	<5	—	—	<5	—	—	—	—	—	—	—	—	—
Group II metals (Ca + Mg) (mg/kg)	<5	<5	<5	—	—	<5	—	—	—	—	—	—	—	—	—
Cold filter plug point (°C)	—	—	—	—	—	-5	—	–7	–10	—	—	—	—	—	—
Gross calorific value (cal/g)	—	—	—	9,510	—	—	—	9,355	9,560	8,958	—	9,078	9,510	7,764	9,355
Pour point (°C)	—	—	—	—	—	—	—	–6	–12	—	—	—	—	—	-6
Distillation temperature (°C)	—	<360	—	—	—	—	—	—	—	—	—	—	—	—	—

"—"-parameters that are not regulated in standards or tests in the literature.
"S15"-a grade of biodiesel meeting ASTM, Specification D6751 and having a sulfur specification of 15 ppm maximum.
"S50"-a grade of biodiesel meeting ASTM, Specification D6751 and having a sulfur specification of 500 ppm maximum.
"S10"-a grade of biodiesel meeting GB25199-2017 and having a sulfur specification of 10 ppm maximum.*
"S50"-a grade of biodiesel meeting GB25199-2017 and having a sulfur specification of 50 ppm maximum.*
"Grade No. 1B"-A special purpose biodiesel blend stock intended for use in middle distillate fuel applications that can be sensitive to the presence of partially reacted glycerides, including those applications requiring good low temperature operability.
"NaOH, and KOH"-Catalysts used in transesterification reaction.

linoleate and linolenate decreased with concomitant increased proportions of stearate and oleate in the phospholipids (Koiwai et al., 1982). The contents of tobacco seed fatty acids in ovaries grown in the greenhouse were more than four-fold higher than those in mature ovaries cultured *in vitro* because of many cultural factors, such as mineral and sugar concentrations, plant hormone interactions, oxygen concentration, and culture temperatures (Toshiake et al., 2006). Lin et al. (2020) were able to increase the seed and oil yields and modify the fatty acid composition of tobacco plants by enhancing the level of nitrogen applied. However, the effects of many influencing factors (such as the ecological environment, heredity, exogenous hormones, etc.) and agricultural strategies (e.g., Fertilization, irrigation, weeding, diseases and pests control) on tobacco seed oil biosynthesis and accumulation associated with biodiesel production have not been revealed.

PROPERTIES AND APPLICATION OF BIODIESEL FROM TOBACCO SEED OIL

Tobacco seed oil cannot be used directly in diesel engines, primarily due to its high viscosity and low heat content (Sharma et al., 2008). Transesterification reaction converts triglycerides into methyl esters to meet the specifications of biodiesel standards. Many countries have implemented national standards to promote biodiesel quality and regulate biodiesel production (Yang et al., 2016). Generally, the evaluation of biodiesel properties is based on ASTM D6751-2015c and BS EN 14214-2012 + A1-2019 standards (BSI, 2019; ASTM D6751-20a, 2020). Biodiesel is characterized by considering its physicalchemical and fuel properties, such as density, kinematic viscosity, cloud and pour point, energy content, cetane index (Ashraful et al., 2014). It is worth emphasizing that carbon chain length and saturation of fatty acids are important factors affecting the properties of biodiesel (Knothe, 2005). Additionally, the fluidity of biodiesel is related to density, kinematic viscosity, and cloud and pour point. The energy content and cetane index influence the production of torque and power. The flashpoint and ignition point are important parameters for evaluating the safety of biodiesel. Biodiesel has relatively low contents of ash, sulfur, and carbon residue; thus, the amount of pollutants emitted is reduced. Biodiesel usually has limited stability and is likely to form polymers that may block the fuel supply system. The amounts of monoglycerides, diglycerides, triglycerides, and free and total glycerine are important indicators of biodiesel purity. The metal ion residues (Na^+, K^+, Ca^{2+}, Mg^{2+}) introduced by catalysts could cause deposition and wear of engine components. Water and methanol contents and acid values may also accelerate erosion of the injection system and increase carbon deposition in engines. An evaluation of the important properties of tobacco seed oil biodiesel (TSOBD) is shown in **Table 3** (Veljković et al., 2006; Anastopoulos et al., 2011; Usta et al., 2011; Parlak et al., 2012; Rao B. S. et al., 2013, 2013c; Waheed et al., 2015; Hariram and Rajan, 2016; Guntur and Prasanthi, 2018; Karabas et al., 2019; He et al., 2021).

Generally, the flashpoint, density, acid value, sulfur content, and carbon residue of TSOBD are within or near the ranges recommended by European standards. Some parameters, such as oxidation stability, cetane index, iodine value, and cold filter plugging point, are correlated with the methyl ester content of TSOBD (Ramos et al., 2008). Variations in these indexes may be explained by the different characteristics of tobacco seeds and the whole biodiesel production process. Tobacco seed oil is rich in unsaturated fatty acids; thus, TSOBD has a higher iodine value and unsatisfactory oxidation stability (Usta et al., 2011), which can also be altered by the type and amount of catalyst used in the transesterification reaction (Parlak et al., 2012). The addition of antioxidants can enhance oxidation stability. TSOBD has a lower energy content and cetane index than fossil diesel, which can be improved by blending with other types of biodiesels or pure diesel (Usta, 2005; Anastopoulos et al., 2011). TSOBD addition can also improve the lubrication of engine fuel systems and extend the operating life of system components (Cesur et al., 2014).

Brake power, brake thermal efficiency (BTE), and brake special fuel consumption (BSFC) are used to evaluate the fuel characteristics of biodiesel (Ashraful et al., 2014). TSOBD blends are compatible with pure diesel uses and can increase combustion efficiency and show relatively high brake power and BTE and low BSFC in most cases. On the other hand, TSOBD blends in diesel engines can reduce CO and SO_2 emissions while slightly increasing NO_x emissions (Usta, 2005; He et al., 2021). The TSOBD mixing ratio (Parlak et al., 2012), injection opening pressure (Hountalas et al., 2003), injection time (Teoh et al., 2015), engine load (He et al., 2021), engine speed (Parlak et al., 2013), engine type (Rao et al., 2013c), and compression ratio (Guntur and Prasanthi, 2018) affect TSOBD blend properties and pollutant emissions. It is worth noting that a fuel blend with a low percentage of TSOBD is more efficient at a higher load than at a partial load (Usta, 2005). Compared to diesel, NO_x emissions are slightly increased due to high temperatures and oxygen levels in the cylinder at relatively high load, but there is no significant difference in NO_x emissions at partial load. In addition, Sharma et al. (2020) examined the impact of engine input parameters on the engine performance using the response surface methodology approach. Low heat rejection diesel engines with relatively high capacities to handle fuels with low calorific values can enhance TSOBD fuel characteristics while also producing more NO_x emissions than conventional engines (Rao N. V. et al., 2013). The NO_x emissions of variable compression ratio diesel engine using TSOBD decreased nearly 50% at 16:1 compression ratio compared to 18:1 compression ratio at half and full load (Guntur and Prasanthi, 2018). In addition, catalysts that convert NO_x into N_2, such as traditional three-way and new developed zeolite-based catalyst, can be introduced to reduce NO_x emissions of diesel engine (Beale et al., 2015).

FUTURE DIRECTIONS

Although mechanical processing gives rise to relatively fast and inexpensive results, the small size of tobacco seeds leads to relatively high requirements for pressing equipment and

pretreatment technology, which can subsequently raise production costs. The advantages of conventional extraction with solvents are low cost, simple equipment, no need for filtration, and high efficiency, but the disadvantages are environmental pollution and the application of high temperatures (Castro and Priego-Capote, 2010). The application of the supercritical fluid extraction process is based on the balance between economic benefits and environmental benefits. Recently, new extraction processes using renewable natural products or nonhazardous solvents have been applied to extractions of grape seed oil and sunflower oil (Sineiro et al., 1998; Passos et al., 2009). Enzyme extraction is an enzyme-assisted aqueous extraction that operates under moderate conditions and provides a high oil yield. In the future, processes for the extraction of tobacco seed oil should combine two or more extraction techniques into a complete process or modify available techniques to enhance oil yields. Moreover, more economical and environmentally friendly extraction processes should be utilized.

The ideal biodiesel transesterification catalyst should have the characteristics of high catalytic capacity, stability, minimal lixiviation, reusability, low cost, recyclability, etc. These are crucial for the selection of appropriate catalysts and reaction conditions in biodiesel production from tobacco seed oil. Heterogeneous catalysts are easy to separate from the reaction mixture, regenerate and reuse. Therefore, heterogeneous catalysts will likely replace traditional homogeneous catalysts for transesterification of tobacco seed oil in the near future. Compared with other transesterification methods, the enzymatic method has the following advantages: the catalyst (i.e., enzyme) is environmentally friendly; the operating conditions are moderate; the quality of the by-product glycerin is high; side effects such as saponification are few; the purity of the final product is high, and the enzyme method allows a relatively high FFA content and proceeds with one step. Hence, the enzymatic production of biodiesel is another important direction for the development of tobacco seed oil use. Although the catalysts for these two methods are relatively slow and expensive, novel heterogeneous and enzymatic catalysis may overcome these drawbacks.

Biotechnology, such as overexpression, silencing, knockout, and editing of genes associated with seed development, plays vital roles in the accumulation and production of tobacco seed oil in the future. Using the mining of genes and proteins involved in tobacco seed oil biosynthesis, the content of tobacco seed oil will be increased through metabolic pathways. Reorganization of acyl flux and coexpression of genes involved in lipid metabolism and TAG production accumulated more than 15% oil (dry weight) in tobacco leaves (Vanhercke et al., 2014). Tobacco seed oil contents differ among different tobacco varieties, so the yield of biodiesel from tobacco seeds can be increased by cultivating high-oil varieties. Additionally, grafting may also be an important way to increase biodiesel yields from tobacco seeds during planting. Strikingly, national policies and

government support will also affect the development and research of tobacco seed oil and leaves for the production of biodiesel.

Recently, many countries have implemented higher standards and requirements for biodiesel fuel characteristics and pollution emissions. Further research should focus on modifications of TSOBD properties to meet diesel standards and assess the efficiency of TSOBD in an experimental engine setup, either alone or blended with diesel. The evaluation of biodiesel should involve all of the parameters specified in standards and provide for a good balance between engine performance and NO_x emissions by optimizing engine operating parameters or designing new diesel engines.

CONCLUSIONS

Tobacco seed is identified as a promising feedstock for sustainable biodiesel production due to its suitable physicochemical composition, higher oil yields, and lower competition with food crops. However, securing sustainable and sufficient amounts of tobacco seed oil for large scale biodiesel production is not achieved yet. The tobacco seed for sustainable biodiesel production is significantly affected by various factors, which could be considered as varieties, cultivation, extraction, transesterification, application etc. Thus, future studies should focus on the higher-oil varieties with biotechnology, high-effective cultivation technique, economical and environmentally friendly extraction methods, novel heterogeneous or enzymatic catalyzed transesterifications and modifications of TSOBD physicochemical properties.

AUTHOR CONTRIBUTIONS

Writing—original draft preparation, SW; Revising—manuscript, CG; Data curation, HP; Figure drawing, KW; Writing—reviewing, DL; Editing, supervision, KC; Writing—reviewing, supervision, HZ. All authors have read and agreed to the published version of the manuscript.

FUNDING

REFERENCES

Adepoju, T. F. (2020). Optimization Processes of Biodiesel Production from Pig and Neem (Azadirachta indica a.Juss) Seeds Blend Oil Using Alternative Catalysts from Waste Biomass. *Ind. Crops Prod.* 149, 112334. doi:10.1016/j.indcrop.2020.112334

Andrianov, V., Borisjuk, N., Pogrebnyak, N., Brinker, A., Dixon, J., Spitsin, S., et al. (2010). Tobacco as a Production Platform for Biofuel: Overexpression ofArabidopsis DGATandLEC2genes Increases Accumulation and Shifts the Composition of Lipids in green Biomass. *Plant Biotechnol. J.* 8, 277–287. doi:10.1111/j.1467-7652.2009.00458.x

Anguebes-Franseschi, F., Córdova-Quiroz, A., Cerón-Bretón, J., Aguilar-Ucan, C., Castillo-Martínez, G., Cerón-Bretón, R., et al. (2016). Optimization of Biodiesel Production from African Crude Palm Oil (Elaeis Guineensis Jacq) with High Concentration of Free Fatty Acids by a Two-step Transesterification Process. *Oje* 06 (1), 13–21. doi:10.4236/oje.2016.61002

Arumugam, A., Thulasidharan, D., and Jegadeesan, G. B. (2018). Process Optimization of Biodiesel Production from Hevea Brasiliensis Oil Using Lipase Immobilized on Spherical Silica Aerogel. *Renew. Energ.* 116, 755–761. doi:10.1016/j.renene.2017.10.021

Ashraf-Khorassani, M., Coleman, W. M., Dube, M. F., Isaac, G., and Taylor, L. T. (2015). Synthesis, Purification, and Quantification of Fatty Acid Ethyl Esters after Trans-esterification of Large Batches of Tobacco Seed Oil. *Btrge. Zur Tabakforschung* 26 (5), 205–213. doi:10.1515/cttr-2015-0008

Ashraful, A. M., Masjuki, H. H., Kalam, M. A., Rizwanul Fattah, I. M., Imtenan, S., Shahir, S. A., et al. (2014). Production and Comparison of Fuel Properties, Engine Performance, and Emission Characteristics of Biodiesel from Various Non-edible Vegetable Oils: A Review. *Energ. Convers. Manage.* 80, 202–228. doi:10.1016/j.enconman.2014.01.037

ASTM D6751-20a (2020). License Agreement, Standard Specification for Biodiesel Fuel Blend Stock (B100) for Middle Distillate Fuels. *ICS Code* 75, 11. doi:10.1520/D6751-20A

Avhad, M. R., and Marchetti, J. M. (2015). A Review on Recent Advancement in Catalytic Materials for Biodiesel Production. *Renew. Sustain. Energ. Rev.* 50, 696–718. doi:10.1016/j.rser.2015.05.038

Awais, M., Musmar, S. e. A., Kabir, F., Batool, I., Rasheed, M. A., Jamil, F., et al. (2020). Biodiesel Production from Melia Azedarach and Ricinus Communis Oil by Transesterification Process. *Catalysts* 10 (4), 427. doi:10.3390/catal10040427

Azócar, L., Ciudad, G., Heipieper, H. J., and Navia, R. (2010). Biotechnological Processes for Biodiesel Production Using Alternative Oils. *Appl. Microbiol. Biotechnol.* 88 (3), 621–636. doi:10.1007/s00253-010-2804-z

Banković-Ilić, I. B., Stamenković, O. S., and Veljković, V. B. (2012). Biodiesel Production from Non-edible Plant Oils. *Renew. Sustain. Energ. Rev.* 16 (6), 3621–3647. doi:10.1016/j.rser.2012.03.002

Beale, A. M., Gao, F., Lezcano-Gonzalez, I., Peden, C. H. F., and Szanyi, J. (2015). Recent Advances in Automotive Catalysis for NOx Emission Control by Small-Pore Microporous Materials. *Chem. Soc. Rev.* 44 (20), 7371–7405. doi:10.1039/c5cs00108k

Berbeć, A. K., and Matyka, M. (2020). Biomass Characteristics and Energy Yields of Tobacco (*Nicotiana Tabacum* L.) Cultivated in Eastern Poland. *Agriculture* 10 (11), 551. doi:10.3390/agriculture10110551

BSI (2019). *BS EN 14214:2012+A1:2019 Liquid Petroleum Products-Fatty Acid Methyl Esters (FAME) for Use in Diesel Engines and Heating Applications-Requirements and Test Methods.* London, United Kingdom: BSI. ICS Code: 75.160.40.

Cesur, İ., Ayhan, V., Parlak, A., Savaş, Ö., and Aydin, Z. (2014). The Effects of Different Fuels on Wear between Piston Ring and Cylinder. *Adv. Mech. Eng.* 6, 503212–503218. doi:10.1155/2014/503212

Chen, M., Xuan, L., Wang, Z., Zhou, L., Li, Z., Du, X., et al. (2014). TRANSPARENT TESTA8 Inhibits Seed Fatty Acid Accumulation by Targeting Several Seed Development Regulators in Arabidopsis. *Plant Physiol.* 165 (2), 905–916. doi:10.1104/pp.114.235507

Chung, C.-c., Zhang, Y., Liu, L., Wang, Y., and Wei, Z. (2020). The Evolution of Biodiesel Policies in China over the Period 2000-2019. *Processes* 8 (8), 948. doi:10.3390/pr8080948

Dean, S. W., Anastopoulos, G., Deligiannis, A., Kalligeros, S., Karonis, D., Zannikos, F., et al. (2010). Synthesis of Biodiesel from Tobacco and Waste Frying Oil Using Heterogeneous KHCO3/Al2O3 Catalyst. *J. ASTM Int.* 7 (3), 293–311. doi:10.1520/JAI102574

Demirbas, A. (2007). Importance of Biodiesel as Transportation Fuel. *Energy Policy* 35 (9), 4661–4670. doi:10.1016/j.enpol.2007.04.003

Fan, Z., Li, J., Lu, M., Li, X., and Yin, H. (2013). Overexpression of Phosphoenolpyruvate Carboxylase from *Jatropha Curcas* Increases Fatty Acid Accumulation in *Nicotiana Tabacum*. *Acta Physiol. Plant* 35, 2269–2279. doi:10.1007/s11738-013-1264-3

Faugno, S., del Piano, L., Crimaldi, M., Ricciardiello, G., and Sannino, M. (2016). Mechanical Oil Extraction of *Nicotiana Tabacum* L. Seeds: Analysis of Main Extraction Parameters on Oil Yield. *J. Agricult Engineer* 47 (3), 142–147. doi:10.4081/jae.2016.539

Fornasier, F., Gomez, J. F. C., Sansone, F. D. C., Schneider, R. D. C. D. S., Costa, A. B. d., Moraes, J. A. R., et al. (2018). Biodiesel Production from Energy Tobacco. *Orbital: Electron. J. Chem.* 10 (2), 123–132. doi:10.17807/orbital.v10i2.1120

García-Martínez, N., Andreo-Martínez, P., Quesada-Medina, J., de los Ríos, A. P., Chica, A., Beneito-Ruiz, R., et al. (2017). Optimization of Non-catalytic Transesterification of Tobacco (Nicotiana Tabacum) Seed Oil Using Supercritical Methanol to Biodiesel Production. *Energ. Convers. Manage.* 131, 99–108. doi:10.1016/j.enconman.2016.10.078

Geow, C. H., Tan, M. C., Yeap, S. P., and Chin, N. L. (2021). A Review on Extraction Techniques and its Future Applications in Industry. *Eur. J. Lipid Sci. Technol.* 123 (4), 2000302. doi:10.1002/ejlt.202000302

Giannelos, P. N., Zannikos, F., Stournas, S., Lois, E., and Anastopoulos, G. (2002). Tobacco Seed Oil as an Alternative Diesel Fuel: Physical and Chemical Properties. *Ind. Crops Prod.* 16 (1), 1–9. doi:10.1016/S0926-6690(02)00002-X

Gowtham Rajan, A., Sivasubramanian, M., Gowthaman, S., and Ramkumar, P. (2021). Investigation of Physical and Chemical Properties of Tobacco Seed Oil Fatty Acid Methyl Ester for Biodiesel Production. *Mater. Today Proc.* 46, 7670–7675. doi:10.1016/j.matpr.2021.02.081

Guntur, R., and Prasanthi, G. (2018). Effect of Compression Ratio on Thermal Characteristics of VCR Diesel Engine Using *Nicotiana Tabacum* L. Seed Oil Methyl Ester. *J. Eng. Sci. Technol.* 13 (3), 558–572.

Hariram, V., and Rajan, A. G. (2016). Extraction of Tobacco (*Nicotiana Tabacum* L.) Seed Oil and Biodiesel Preparation through Two Stage Transesterification. *Res. J. Pharm. Biol. Chem. Sci.* 7 (2), 978–983.

He, A., Hu, L., Zhang, Y., Jiang, Y., Wang, X., Xu, J., et al. (2021). High-Efficiency Catalytic Transfer Hydrogenation of Biomass-Based 5-Hydroxymethylfurfural to 2,5-Bis(hydroxymethyl)furan over a Zirconium-Carbon Coordination Catalyst. *ACS Sustain. Chem. Eng.* 9 (46), 15557–15570. doi:10.1021/acssuschemeng.1c05618

Hernández, M. L., Whitehead, L., He, Z., Gazda, V., Gilday, A., Kozhevnikova, E., et al. (2012). A Cytosolic Acyltransferase Contributes to Triacylglycerol Synthesis in Sucrose-Rescued Arabidopsis Seed Oil Catabolism Mutants. *Plant Physiol.* 160 (1), 215–225. doi:10.1104/pp.112.201541

Hill, J., Nelson, E., Tilman, D., Polasky, S., and Tiffany, D. (2006). Environmental, Economic, and Energetic Costs and Benefits of Biodiesel and Ethanol Biofuels. *Proc. Natl. Acad. Sci.* 103 (30), 11206–11210. doi:10.1073/pnas.0604600103

Hountalas, D. T., Kouremenos, D. A., Binder, K. B., Schwarz, V., and Mavropoulos, G. C. "Effect of Injection Pressure on the Performance and Exhaust Emissions of a Heavy Duty DI Diesel Engine," in Proceedings of the SAE 2003 World Congress & Exhibition, Detroit, Michigan, U.S.A, March 2003. doi:10.4271/2003-01-0340

Hu, L., Wu, Z., Jiang, Y., Wang, X., He, A., Song, J., et al. (2020). Recent Advances in Catalytic and Autocatalytic Production of Biomass-Derived 5-Hydroxymethylfurfural. *Renew. Sustain. Energ. Rev.* 134, 110317. doi:10.1016/j.rser.2020.110317

Jain, S. (2019). "The Production of Biodiesel Using Karanja (Pongamia Pinnata) and Jatropha (Jatropha Curcas) Oil," in *Biomass, Biopolymer-Based Materials, and Bioenerg.* Editors D. Verma, E. Fortunati, S. Jain, and X. Zhang (Sawston, United Kingdom: Woodhead Publishing), 397–408. doi:10.1016/B978-0-08-102426-3.00017-5

Karabas, H., Boran, S., and Yazgan, H. R. (2016). Identification of Process Parameters of Tobacco Seed Oil Methyl Ester by Applied Multi Response Taguchi Technique. *Fresen. Environ. Bull.* 25, 3802–3807.

Karabas, H., Boran, S., and Yazgan, H. R. (2019). Optimization of Production Parameters of Tobacco Seed Oil Methyl Ester Using Multi-Response Taguchi Method and MANOVA. *J. Chem. Soc. Pakistan* 41 (3), 414.

Khan, T. M. Y., Atabani, A. E., Badruddin, I. A., Badarudin, A., Khayoon, M. S., and Triwahyono, S. (2014). Recent Scenario and Technologies to Utilize Non-edible Oils for Biodiesel Production. *Renew. Sustain. Energ. Rev.* 37 (3), 840–851. doi:10.1016/j.rser.2014.05.064

Kim, J.-H., Jung, J.-M., Cho, S.-H., Tsang, Y. F., Wang, C.-H., Lee, J., et al. (2019). Upgrading Bio-Heavy Oil via Esterification of Fatty Acids and Glycerol. *J. Clean. Prod.* 217, 633–638. doi:10.1016/j.jclepro.2019.01.289

Knothe, G. (2005). Dependence of Biodiesel Fuel Properties on the Structure of Fatty Acid Alkyl Esters. *Fuel Process. Technol.* 86 (10), 1059–1070. doi:10.1016/j.fuproc.2004.11.002

Koiwai, A., Suzuki, F., Matsuzaki, T., and Kawashima, N. (1982). Changes in Glycerolipids and Their Fatty Acid Composition during Maturation of Tobacco Seeds. *Phytochemistry* 21 (2), 305–308. doi:10.1016/S0031-9422(00)95256-7

Koiwai, A., Suzuki, F., Matsuzaki, T., and Kawashima, N. (1983). The Fatty Acid Composition of Seeds and Leaves of *Nicotiana* Species. *Phytochemistry* 22 (6), 1409–1412. doi:10.1016/S0031-9422(00)84024-8

Kulkarni, M. G., Gopinath, R., Meher, L. C., and Dalai, A. K. (2006). Solid Acid Catalyzed Biodiesel Production by Simultaneous Esterification and Transesterification. *Green. Chem.* 8 (12), 1056–1062. doi:10.1039/b605713f

Leung, D. Y. C., Wu, X., and Leung, M. K. H. (2010). A Review on Biodiesel Production Using Catalyzed Transesterification. *Appl. Energ.* 87 (4), 1083–1095. doi:10.1016/j.apenergy.2009.10.006

Li, R., Yu, K., Hatanaka, T., and Hildebrand, D. F. (2010). VernoniaDGATs Increase Accumulation of Epoxy Fatty Acids in Oil. *Plant Biotechnol. J.* 8 (2), 184–195. doi:10.1111/j.1467-7652.2009.00476.x

Lin, Y., Kong, D., Wang, Z., Chen, Y., Yang, Z., Wu, C., et al. (2020). Nitrogen Application Modifies the Seed and Oil Yields and Fatty Acid Composition of *Nicotiana Tabacum.* *horts* 55 (12), 1898–1902. doi:10.21273/HORTSCI15335-20

Liu, X., He, H., Wang, Y., Zhu, S., and Piao, X. (2008). Transesterification of Soybean Oil to Biodiesel Using Cao as a Solid Base Catalyst. *Fuel* 87 (2), 216–221. doi:10.1016/j.fuel.2007.04.013

Liu, X., Pan, H., Zhang, H., Li, H., and Yang, S. (2019). Efficient Catalytic Upgradation of Bio-Based Furfuryl Alcohol to Ethyl Levulinate Using Mesoporous Acidic MIL-101(Cr). *ACS Omega* 4, 8390–8399. doi:10.1021/acsomega.9b00480

Luque de Castro, M. D., and Priego-Capote, F. (2010). Soxhlet Extraction: Past and Present Panacea. *J. Chromatogr. A* 1217 (16), 2383–2389. doi:10.1016/j.chroma.2009.11.027

Ma, F., and Hanna, M. A. (1999). Biodiesel Production: a review1Journal Series #12109, Agricultural Research Division, Institute of Agriculture and Natural Resources, University of Nebraska-Lincoln.1. *Bioresour. Technol.* 70 (1), 1–15. doi:10.1016/S0960-8524(99)00025-5

Maestri, D. M., and Guzmán, C. A. (1995). A Comparative Study of Seed Lipid Components of Nicotianeae (Solanaceae). *Biochem. Syst. Ecol.* 23 (2), 201–207. doi:10.1016/0305-1978(95)93850-3

Majdi, S., Barzegar, M., Jabbari, A., and Alikhani, M. A. (2012). Supercritical Fluid Extraction of Tobacco Seed Oil and its Comparison with Solvent Extraction Methods. *J. Agr. Sci. Tech.* 14 (5), 1043–1051. doi:10.1111/j.1744-697X.2012.00258.x

Matsuzaki, T., Iwai, S., and Koiwai, A. (1988). Effects of Temperature on Seed Fatty Acid Composition in Ovary Culture of Tobacco. *Agric. Biol. Chem.* 52 (5), 1283–1285. doi:10.1080/00021369.1988.10868821

Meher, L., Vidyasagar, D., and Naik, S. (2006). Technical Aspects of Biodiesel Production by Transesterification-A Review. *Renew. Sustain. Energ. Rev.* 10 (3), 248–268. doi:10.1016/j.rser.2004.09.002

Mishra, V. K., and Goswami, R. (2018). A Review of Production, Properties and Advantages of Biodiesel. *Biofuels* 9 (2), 273–289. doi:10.1080/17597269.2017.1336350

Mizik, T., and Gyarmati, G. (2021). Economic and Sustainability of Biodiesel Production-A Systematic Literature Review. *Clean. Technol.* 3 (1), 19–36. doi:10.3390/cleantechnol3010002

Moazeni, F., Chen, Y.-C., and Zhang, G. (2019). Enzymatic Transesterification for Biodiesel Production from Used Cooking Oil, A Review. *J. Clean. Prod.* 216, 117–128. doi:10.1016/j.jclepro.2019.01.181

Motojesi, O., Ogunniyi, D. S., and Odetoye, T. E. (2017). *Transesterification of Tobacco Seed Oil Using Some Agricultural Wastes as Catalysts*. Nigeria: Unilorin Institutional Repository.

Mukhtar, A., Ullah, H., and Mukhtar, H. (2007). Fatty Acid Composition of Tobacco Seed Oil and Synthesis of Alkyd Resin. *Chin. J. Chem.* 25 (5), 705–708. doi:10.1002/cjoc.200790132

Murmu, R., Sutar, H., and Patra, S. (2017). Experimental Investigation and Process Optimization of Biodiesel Production from Kusum Oil Using Taguchi Method. *Aces* 07 (4), 464–476. doi:10.4236/aces.2017.74033

Muthukumaran, C., Praniesh, R., Navamani, P., Swathi, R., Sharmila, G., and Manoj Kumar, N. (2017). Process Optimization and Kinetic Modeling of Biodiesel Production Using Non-edible Madhuca Indica Oil. *Fuel* 195, 217–225. doi:10.1016/j.fue1.2017.01.06010.1016/j.fuel.2017.01.060

Pan, H., Liu, Y., Xia, Q., Zhang, H., Guo, L., Li, H., et al. (2020). Synergetic Combination of a Mesoporous Polymeric Acid and a Base Enables Highly Efficient Heterogeneous Catalytic One-Pot Conversion of Crude Jatropha Oil into Biodiesel. *Green. Chem.* 22 (5), 1698–1709. doi:10.1039/C9GC04135D

Pao, H.-T., and Tsai, C.-M. (2010). CO2 Emissions, Energy Consumption and Economic Growth in BRIC Countries. *Energy Policy* 38 (12), 7850–7860. doi:10.1016/j.enpol.2010.08.045

Parlak, A., Ayhan, V., Cesur, İ., and Kökkülünk, G. (2013). Investigation of the Effects of Steam Injection on Performance and Emissions of a Diesel Engine Fuelled with Tobacco Seed Oil Methyl Ester. *Fuel Process. Technol.* 116, 101–109. doi:10.1016/j.fuproc.2013.05.006

Parlak, A., Karabas, H., Ayhan, V., Yasar, H., Soyhan, H. S., and Ozsert, I. (2009). Comparison of the Variables Affecting the Yield of Tobacco Seed Oil Methyl Ester for KOH and NaOH Catalysts. *Energy Fuels* 23 (2), 1818–1824. doi:10.1021/ef800371g

Parlak, A., Karabaş, H., Özsert, I., Ayhan, V., and Cesur, I. (2012). Application of Taguchi's Methods to Investigate Factors Affecting Emissions of a Diesel Engine Running with Tobacco Oil Seed Methyl Ester. *Ijvd* 59 (2/3), 196–211. doi:10.1504/IJVD.2012.048693

Passos, C. P., Yilmaz, S., Silva, C. M., and Coimbra, M. A. (2009). Enhancement of Grape Seed Oil Extraction Using a Cell Wall Degrading Enzyme Cocktail. *Food Chem.* 115 (1), 48–53. doi:10.1016/j.foodchem.2008.11.064

Paula Alonso, A., Dale, V. L., and Shachar-Hill, Y. (2010). Understanding Fatty Acid Synthesis in Developing Maize Embryos Using Metabolic Flux Analysis. *Metab. Eng.* 12 (5), 488–497. doi:10.1016/j.ymben.2010.04.002

Ramos, M. J., Fernández, C. M., Casas, A., Rodríguez, L., and Pérez, Á. (2009). Influence of Fatty Acid Composition of Raw Materials on Biodiesel Properties. *Bioresour. Technol.* 100 (1), 261–268. doi:10.1016/j.biortech.2008.06.039

Rao, B. S., Murthy, P. V. K., Ramjee, E., and Krishna, M. V. S. (2013a). Studies on Exhaust Emissions and Combustion Characteristics of Tobacco Seed Oil in Crude Form and Biodiesel from a High Grade Low Heat Rejection Diesel Engine. *J. Ind. Eng. Res.* 3 (1), 27–36.

Rao, N. V., Krishna, M. V. S. M., and Murthy, P. V. K. (2013b). Effect of Injector Opening Pressure and Injection Timing on Performance Parameters of High-Grade Low Heat Rejection Diesel Engine with Tobacco Seed Oil Based Biodiesel. *Int. J. Recent Technol. Eng.* 2 (4), 70–78.

Rao, N. V., Krishna, M. V. S. M., and Murthy, P. V. K. (2013c). Investigations on Performance Parameters of Ceramic Coated Diesel Engine with Tobacco Seed Oil Biodiesel. *Int. J. Adv. Eng. Technol.* 6 (5), 2286–2300.

Samuel, O. D., Boye, T. E., and Enweremadu, C. C. (2020). Financial and Parametric Study of Biodiesel Production from Hemp and Tobacco Seed Oils in Modified Fruit Blender and Prediction Models of Their Fuel Properties with Diesel Fuel. *Bioresour. Technol. Rep.* 12, 100599. doi:10.1016/j.biteb.2020.100599

Sannino, M., del Piano, L., Abet, M., Baiano, S., Crimaldi, M., Modestia, F., et al. (2017). Effect of Mechanical Extraction Parameters on the Yield and Quality of Tobacco (*Nicotiana Tabacum* L.) Seed Oil. *J. Food Sci. Technol.* 54, 4009–4015. doi:10.1007/s13197-017-2865-4

Santoso, A., Putri, D. E. K., Rusdi, M., Sumari, S., Wijaya, A. R., and Rachman, I. B. (2021). The Effect of Basic Catalyst Concentration on Tobacco Oil Transesterification (Voor-Oogst) Using Ultra-sonic Wave and its Potential as Renewable Energy. *AIP Conf. Proc.* 2330 (1), 070008. doi:10.1063/5.0043406

Sharma, A., Singh, Y., Kumar Singh, N., Singla, A., Chyuan Ong, H., and Chen, W.-H. (2020). Effective Utilization of Tobacco (*Nicotiana Tabaccum*) for Biodiesel Production and its Application on Diesel Engine Using Response Surface Methodology Approach. *Fuel* 273, 117793. doi:10.1016/j.fuel.2020.117793

Sharma, Y. C., Singh, B., and Upadhyay, S. N. (2008). Advancements in Development and Characterization of Biodiesel: A Review. *Fuel* 87 (12), 2355–2373. doi:10.1016/j.fuel.2008.01.014

Sineiro, J., Domı́nguez, H., Núñez, M. J., and Lema, J. M. (1998). Optimization of the Enzymatic Treatment during Aqueous Oil Extraction from sunflower Seeds. *Food Chem.* 61 (4), 467–474. doi:10.1016/S0308-8146(97)00080-0

Smil, V. (2017). *Energy Transitions: Global and National Perspectives*. 2nd ed. Santa Barbara, CA, USA: ABC-CLIO.

Srivastava, A., and Prasad, R. (2000). Triglycerides-based Diesel Fuels. *Renew. Sust. Energ. Rev.* 4 (1), 111–133. doi:10.1016/S1364-0321(99)00013-1

Stanisavljevic, I., Lakicevic, S., Velickovic, D., Lazic, M., and Veljković, V. (2007a). The Extraction of Oil from Tobacco (*Nicotiana Tabacum* L.) Seeds. *CI&CEQ* 13 (1), 41–50. doi:10.2298/CICEQ0701041S

Stanisavljević, I. T., Lazić, M. L., and Veljković, V. B. (2007b). Ultrasonic Extraction of Oil from Tobacco (*Nicotiana Tabacum* L.) Seeds. *Ultrason. Sonochem.* 14 (5), 646–652. doi:10.1016/j.ultsonch.2006.10.003

Stanisavljević, I. T., Veličković, D. T., Todorović, Z. B., Lazić, M. L., and Veljković, V. B. (2009). Comparison of Techniques for the Extraction of Tobacco Seed Oil. *Eur. J. Lipid Sci. Technol.* 111 (5), 513–518. doi:10.1002/ejlt.200800232

Stansell, G. R., Gray, V. M., and Sym, S. D. (2012). Microalgal Fatty Acid Composition: Implications for Biodiesel Quality. *J. Appl. Phycol.* 24, 791–801. doi:10.1007/s10811-011-9696-x

Teoh, Y. H., Masjuki, H. H., Kalam, M. A., and How, H. G. (2015). Effect of Injection Timing and EGR on Engine-Out-Responses of a Common-Rail Diesel Engine Fueled with Neat Biodiesel. *RSC Adv.* 5 (116), 96080–96096. doi:10.1039/C5RA14831F

Tian, Y., Chen, K., Li, X., Zheng, Y., and Chen, F. (2020). Design of High-Oleic Tobacco (Nicotiana Tabacum L.) Seed Oil by CRISPR-Cas9-Mediated Knockout of NtFAD2-2. *BMC Plant Biol.* 20, 233. doi:10.1186/s12870-020-02441-0

Tian, Y., Liu, X., Fan, C., Li, T., Qin, H., Li, X., et al. (2021). Enhancement of Tobacco (*Nicotiana Tabacum* L.) Seed Lipid Content for Biodiesel Production by CRISPR-Cas9-Mediated Knockout of NtAn1. *Front. Plant Sci.* 11, 599474. doi:10.3389/fpls.2020.599474

Usta, N. (2005). An Experimental Study on Performance and Exhaust Emissions of a Diesel Engine Fuelled with Tobacco Seed Oil Methyl Ester. *Energ. Convers. Manage.* 46 (15-16), 2373–2386. doi:10.1016/j.enconman.2004.12.002

Usta, N., Aydoğan, B., Çon, A. H., Uğuzdoğan, E., and Özkal, S. G. (2011). Properties and Quality Verification of Biodiesel Produced from Tobacco Seed Oil. *Energ. Convers. Manage.* 52 (5), 2031–2039. doi:10.1016/j.enconman.2010.12.021

Vanhercke, T., El Tahchy, A., Liu, Q., Zhou, X. R., Shrestha, P., Divi, U. K., et al. (2014). Metabolic Engineering of Biomass for High Energy Density: Oilseed-like Triacylglycerol Yields from Plant Leaves. *Plant Biotechnol. J.* 12 (2), 231–239. doi:10.1111/pbi.12131

Vauhkonen, V., Niemi, S., Hiltunen, E., Salminen, H. J., and Pasila, A. (2009). The First Generation Biodiesel: The Effects of Raw Material on Physical Properties, Oxidation Stability and Emissions. *Int. Conf. Clean Electr. Power* 117–123. doi:10.1109/ICCEP.2009.5212074

Veljkovic, V., Lakicevic, S., Stamenkovic, O., Todorovic, Z., and Lazic, M. (2006). Biodiesel Production from Tobacco (*Nicotiana Tabacum* L.) Seed Oil with A High Content of Free Fatty Acids. *Fuel* 85 (17-18), 2671–2675. doi:10.1016/j.fuel.2006.04.015

Waheed, M. A., Samuel, O. D., Bolaji, B. O., and Dairo, O. U. (2015). *RSM Based Optimization of Biodiesel Production from Tobacco Seed Oil. Renewable Energy and Sustainable Development*. New York: Nova Science Publishers, 85–101.

Wang, A., Li, H., Zhang, H., Pan, H., and Yang, S. (2019). Efficient Catalytic Production of Biodiesel with Acid-Base Bifunctional Rod-like Ca-B Oxides by the Sol-Gel Approach. *Materials* 12, 83. doi:10.3390/ma12010083

Wu, S., Guo, Y., Adil, M. F., Sehar, S., Cai, B., Xiang, Z., et al. (2020). Comparative Proteomic Analysis by Itraq Reveals that Plastid Pigment Metabolism Contributes to Leaf Color Changes in Tobacco (*Nicotiana Tabacum*) during Curing. *Ijms* 21 (7), 2394. doi:10.3390/ijms21072394

Xu, R., Yang, T., Wang, R., and Liu, A. (2014). Characterisation of *DGAT1* and *DGAT2* from *Jatropha Curcas* and Their Functions in Storage Lipid Biosynthesis. *Funct. Plant Biol.* 41 (3), 321–329. doi:10.1071/FP12388

Yang, C., Zhang, B., Zhang, B., Wu, J., Ding, Y., and Wu, Y. (2016). Standards and Protocols for Characterization of Algae-Based Biofuels. *Tr Ren. Energ.* 2 (2), 56–60. doi:10.17737/tre.2016.2.2.0022

Yang, M., Zheng, G., Zhang, F., and Xu, Y. (2006). FAD2-silencing Has Pleiotropic Effect on Polar Lipids of Leaves and Varied Effect in Different Organs of Transgenic Tobacco. *Plant Sci.* 170 (1), 170–177. doi:10.1016/j.plantsci.2005.08.022

Zdremnan, M., and Zdremnan, D. (2006). The Tobacco Oil and its Qualities. *Horticulture* 63, 388–392. doi:10.15835/buasvmcn-hort:1898

Zhang, F.-Y., Yang, M.-F., and Xu, Y.-N. (2005). Silencing of *DGAT1* in Tobacco Causes a Reduction in Seed Oil Content. *Plant Sci.* 169 (4), 689–694. doi:10.1016/j.plantsci.2005.05.019

Zhang, H., Pan, H., and Yang, S. (2017). Upgrading of Cellulose to Biofuels and Chemicals with Acidic Nanocatalysts. *Cnano* 13 (5), 513–527. doi:10.2174/1573413713666170405161546

Zhang, L., Lu, H., Liu, C., Xue, F., Yang, J., Ma, L., et al. (2016a). Lipid Desaturation in Prokaryotic Pathway Abates the High-Oleic Phenotype of FAD2-Silenced Tobacco at Lower Temperature. *J. Plant Biochem. Biotechnol.* 25, 375–381. doi:10.1007/s13562-016-0349-7

Zhang, M., Cao, X., Jia, Q., and Ohlrogge, J. (2016b). FUSCA3activates Triacylglycerol Accumulation in Arabidopsis Seedlings and Tobacco BY2 Cells. *Plant J.* 88 (1), 95–107. doi:10.1111/tpj.13233

Zhou, X.-R., Bhandari, S., Johnson, B. S., Kotapati, H. K., Allen, D. K., Vanhercke, T., et al. (2019). Reorganization of Acyl Flux through the Lipid Metabolic Network in Oil-Accumulating Tobacco Leaves. *Plant Physiol.* 182 (2), 739–755. doi:10.1104/pp.19.00667

Zlatanov, M., Angelova, M., and Antova, G. (2007). Lipid Composition of Tobacco Seeds. *Bulg. J. Agric. Sci.* 13 (5), 539. doi:10.1109/9780470545607.ch54

Catalytic Upgrading of Lignocellulosic Biomass Sugars Toward Biofuel 5-Ethoxymethylfurfural

Xiaofang Liu[†], Dayong Yu[†], Hangyu Luo[‡] and Can Li*

Guizhou Provincial Key Laboratory for Rare Animal and Economic Insects of the Mountainous Region, College of Biology and Environmental Engineering, Guiyang University, Guiyang, China

The conversion of biomass into high-value chemicals through biorefineries is a requirement for sustainable development. Lignocellulosic biomass (LCB) contains polysaccharides and aromatic polymers and is one of the important raw materials for biorefineries. Hexose and pentose sugars can be obtained from LCB by effective pretreatment methods, and further converted into high-value chemicals and biofuels, such as 5-hydroxymethylfurfural (HMF), levulinic acid (LA), γ-valerolactone (GVL), ethyl levulinate (EL), and 5-ethoxymethylfurfural (EMF). Among these biofuels, EMF has a high cetane number and superior oxidation stability. This mini-review summarizes the mechanism of several important processes of EMF production from LCB-derived sugars and the research progress of acid catalysts used in this reaction in recent years. The influence of the properties and structures of mono- and bi-functional acid catalysts on the selectivity of EMF from glucose were discussed, and the effect of reaction conditions on the yield of EMF was also introduced.

Keywords: lignocellulosic biomass, biorefinery, high-value chemicals, biofuels, 5-ethoxymethylfurfural

INTRODUCTION

Extensive use of fossil fuels has caused energy depletion and serious environmental problems (e.g., greenhouse effect and acid rain). It is urgent to develop green renewable energy to replace fossil fuels for a better living environment (Li et al., 2017; Li et al., 2020; Pan et al., 2020). Lignocellulosic biomass (LCB) is a typical renewable energy with an annual global output of approximately 12 billion tons (Abraham et al., 2020). It is mainly composed of a layer of firm lignin-wrapped cellulose and hemicellulose components (Bhatia et al., 2020). Among them, cellulose is a biopolymer linking massive glucose units *via β*-1,4-glycosidic bonds, accounting for 38–50 wt% of LCB (Somerville et al., 2010). Thus, a large amount of glucose can be obtained by hydrolyzing cellulose. There were many researchers focused on the conversion of glucose to high value-added chemicals. Through various catalytic reactions such as dehydration, hydrogenation, hydrolysis, alcoholysis, and etherification, glucose can be turned into high value-added fuels and fine chemicals [e.g., 5-hydroxymethylfurfural (HMF), 5-ethoxymethylfurfural (EMF), levulinic acid (LA), and ethyl levulinate (EL)] (Rackemann and Doherty, 2011; Yang et al., 2012; Climent et al., 2014; Yang et al., 2019).

Furan derivatives like furfural, furfuryl alcohol, HMF, EMF, and 2,5-dimethylfuran have shown great potential in the formation of fine chemicals and alternative fossil fuels (Tong et al., 2010; Liu et al., 2021). Among these furan derivatives, EMF has the advantages for instance a higher boiling point (235℃), superior energy density (30.3 MJ/L) compare with ethanol (23.5 MJ/L), and low flash point (ca. 110℃) (Corma et al., 2007). Therefore, it has been considered one of the excellent choices of fuel additives in the future (Li et al., 2016). When 17 wt% EMF was used as an additive that mixes
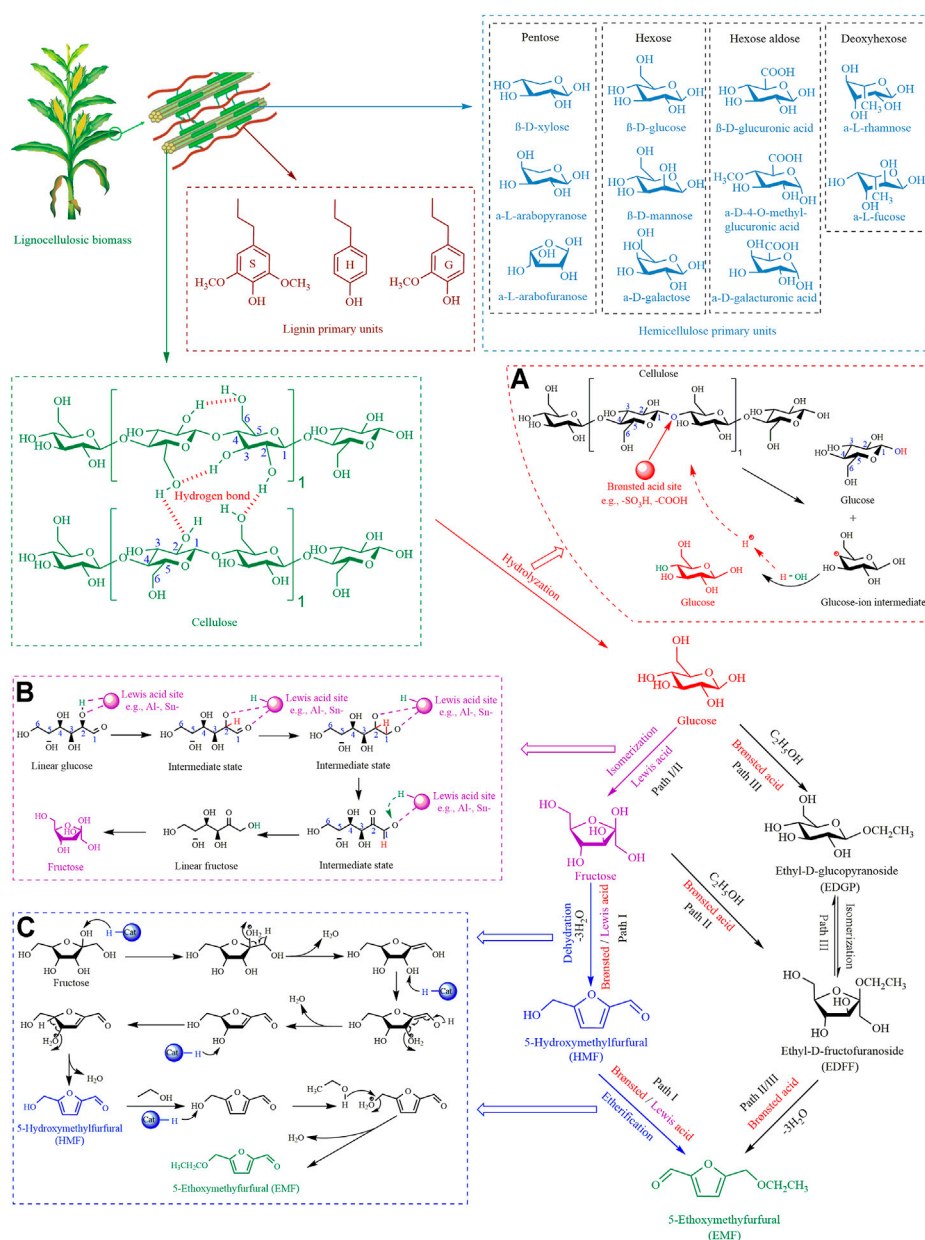
FIGURE 1 | The conversion paths of LCB to EMF. **(A)** Cellulose hydrolysis by Brønsted acid, **(B)** glucose isomerization by Lewis acid, **(C)** the conversion of fructose to EMF.

with fuel in a fuel engine, the engine could run stably and release fewer harmful particles and sulfides (with a 16% reduction in soot) (Mascal and Nikitin, 2008). In addition, EMF has also be used as a reaction substrate for the synthesis of various industrially significant chemicals, such as 5-ethoxymethylfurfuryl alcohol, 2,5-diethoxymethylfuran, and cyclopentenone (Ras et al., 2009; Ras et al., 2010; Bredihhin et al., 2016).

Generally, EMF can be transformed from HMF and ketose (e.g., fructose, inulin, and sucrose) with a satisfactory yield (ca. 70–90%) (Bredihhin et al., 2013; Dai et al., 2019; Hafizi et al., 2020). Yet, the industrial-scale production of EMF was limited by

these high-priced feedstocks. For example, the price of HMF and fructose in Sigma-Aldrich is 12,634 and 205 EUR per kilogram, respectively. However, glucose has a lower price (88 EUR per kilogram in Sigma-Aldrich), which is reasonable to convert glucose into EMF (187 EUR per gram in Sigma-Aldrich). Moreover, the large amount of glucose can be obtained from cheap LCB, which is also a choice for economic and environmental development. At present, relevant reviews have summarized the use of various types of catalysts to convert different raw materials into EMF (Chen B. et al., 2020; Yu et al., 2021). But almost no review focused on the mechanism

of EMF synthesis from glucose to EMF. Hereby, this mini-review introduces the paths and mechanisms of producing EMF from LCB derivatives, with a focus on challenges of the conversion of glucose to EMF. The aim is to provide a feasibility method for maximizing the conversion of LCB into EMF.

THE PREPARATION OF EMF FROM LCB-DERIVED SUGARS

The Synthesis Routes

EMF can be obtained from glucose or cellulose *via* multi-step chemical conversion (Zheng et al., 2021). There are three paths to synthesize EMF from glucose (**Figure 1**). The mainstream Path I uses glucose as the starting material, which is isomerized to produce fructose, then HMF is obtained through fructose dehydration ($-3H_2O$), and finally, HMF is etherified to EMF (Chen et al., 2019). The most important step in this path is the isomerization of glucose, which usually requires the participation of Lewis acid (Lew et al., 2012). There are two other secondary paths with ethyl-D-fructofuranoside (EDFF) as an intermediate transit. Path II is that fructose reacts with ethanol in acidic solution to form EDFF, which is then dehydrated ($-3H_2O$) to produce EMF (Zhang et al., 2018). Path III is glucose and ethanol to generate ethyl-D-glucopyranoside (EDGP) in an acid medium, then isomerized to EDFF, finally dehydrated ($-3H_2O$) to obtain EMF (Zheng et al., 2021). Currently, most EMF is obtained through Path I for the following reasons:

(i) Compare Path I and Path II. The difference is that fructose is more likely to be converted into HMF (Path I) or EDFF (Path II). It has been found that fructose was inclined to be dehydrated to form HMF (Path I) rather than etherified with ethanol to form EDFF (Path II) when Brønsted acid is present (Xiang et al., 2017).

(ii) Compare Path I and Path III. Glucose is usually isomerized to fructose when Brønsted acid and Lewis acid are present at the same time (He et al., 2022). When there is only Brønsted acid in the system, although the DFT calculation results show that the highest energy barriers required for Path I (17.7 kcal/mol) and II (20.8 kcal/mol) are similar, the thermodynamic reaction is more favorable for Path I (Wang et al., 2021). And the intermediate EDGP in Path III is difficult to continue further conversion.

The Synthesis Mechanism

The conversion of cellulose to EMF requires multiple reaction processes, namely cascade reactions. A detailed description of the synthesis mechanism of each step in Path I is shown in **Figure 1**.

Cellulose has a condensed structure (**Figure 1**), and is a high molecular polymer connected by β-1,4-glycosidic bonds and axial hydrogen bonds between numerous glucose monomers (Shrotri et al., 2018). Therefore, the hydrolysis of cellulose in the first step of Path I is a major obstacle that needs to be overcome. Many studies have shown that Brønsted acid can destroy the β-1,4-glycosidic bonds of cellulose (Zeng and Pan, 2020). As shown in **Figure 1A**, firstly, the oxygen atom of the β-1,4-glycosidic bond is attacked by the proton of the Brønsted acid site. Then the C-O bond between the two glucose molecules is broken for releasing glucose and glucose-ion intermediate. Finally, the hydroxyl group

from water binds to the exposed carbon of glucose-ion intermediate to form glucose. And the free protons from water participate in the next hydrolysis reaction.

The second step in Path I, the isomerization of glucose into fructose, is the most important step in determining the yield of EMF. Many studies have indicated that glucose transforms into fructose *via* Lewis acid sites (Li et al., 2014; Rajabbeigi et al., 2014). As shown in **Figure 1B**, the C_1-O_5 bond of glucose is broken by Lewis acid and forms a linear glucose molecule. The oxygen atoms of C_1 and C_2 on linear glucose coordinate with the Lewis acid center. Subsequently, the hydrogen on C_2 is transferred to C_1, which realizes the aldehyde-ketone conversion between C_1 and C_2 to form linear fructose. Finally, the oxygen of C_2 is linked with C_5 to form a fructose molecule by C-C bond.

The third step is that fructose generates HMF by dehydration of three H_2O molecules under acidic conditions. Firstly, the hydroxyl group on C_2 is protonated to release the first H_2O, and C=C is formed between C_1 and C_2. Then, the hydroxyl group on C_3 is protonated to release the second H_2O. Meanwhile, the C=C bond between C_1 and C_2 is broken, the aldehyde group is formed at the C_1, and C=C is formed between C_2 and C_3. Finally, the hydroxyl group on C_4 is protonated to release the third H_2O, and C=C is formed between C_4 and C_5 to get HMF. After that, HMF is etherified to EMF with ethanol existence (**Figure 1C**).

THE FACTORS IMPACTING THE YIELD OF EMF FROM LCB-DERIVED SUGARS

Many LCB-derived sugars and compounds have been used to convert into EMF, such as cellulose, cellobiose, and glucose. The EMF yield from these substrates has displayed the order of glucose > cellobiose > cellulose > LCB (Li et al., 2016; Guo et al., 2018). In general, only moderate or low EMF yields can be obtained from these raw materials which are due to the different number of reaction steps. For example, HMF as a feedstock (high EMF yield) just needs one step, but cellulose (low EMF yield) needs four steps. Meanwhile, the lengthy chemical reaction process increased more by-products or humins (Zheng et al., 2021). Therefore, many studies were devoted to developing more efficient catalytic systems, which can obtain more satisfactory EMF yields from glucose or glucose-based carbohydrates (Guo et al., 2017; Guo et al., 2018; Karnjanakom et al., 2020; He et al., 2022). Some catalysts and reaction conditions for obtaining EMF from LCB-derived sugars were summarized in **Table 1**.

Monofunctional Acid Catalysts

Currently, many monofunctional (Brønsted or Lewis) acid catalysts are designed to catalyze the synthesis of EMF from glucose, including H_2SO_4 (Xu et al., 2017), metal salts (Liu et al., 2013), SO_3H-based catalyst (Liu and Zhang, 2013), and ionic liquid (Guo et al., 2017). From the perspective of the synthesis routes, theoretically, when only Brønsted acid exists, using glucose as substrates hardly produces EMF. Yet, many studies had found that in the presence of Brønsted acid, a spot of EMF could be detected using glucose (7.46% yield), cellobiose (19.8% yield), and cellulose (3.05% yield) as raw materials (De et al., 2012;

TABLE 1 | EMF from LCB-derived sugars *via* different catalysts and reaction systems.

Entry	Feedstock	Catalyst	Brønsted acid	Lewis acid	Solvent	Reaction conditions	Yield/ %	Ref.
1	Glucose	H_2SO_4	-SO_3H	—	Ethanol	200°C, 90 min	7.5	Xu et al. (2017)
2	Glucose	[BMIM][HSO_4]	-SO_3H	—	Ethanol	130°C, 20 min	8.0	Guo et al. (2017)
3	Glucose	$AlCl_3$	—	Al-	Ethanol	100°C, 11 h	38.4	Liu et al. (2013)
4	Corn Stover	USY	Al-O(H)-Si	Al-	Ethanol/THF (v/v = 1:1)	168°C, 2.9 h	21.8	Chen et al. (2019)
5	Glucose	DeAl-H-β	Al-O(H)-Si	Al-	Ethanol	125°C, 10 h	41.0	Li et al. (2016)
6	Glucose	MFI-Sn/Al	Al-O(H)-Si	Sn-/Al-	Ethanol	140°C, 9 h	44.0	Bai et al. (2018)
7	Glucose	BFC-3	-SO_3H	Cr-	Ethanol/THF (v/v = 3:2)	100°C, 10 h	48.1	Chen et al. (2020a)
8	Cellobiose	BFC-3	-SO_3H	Cr-	Ethanol/THF (v/v = 3:2)	100°C, 10 h	37.1	Chen et al. (2020b)
9	Glucose	Zr-Sn-Fe-Al-O-S	-SO_3H	Zr-/Sn-/Fe-/Al-	Ethanol	160°C, 12 h	0.7	He et al. (2022)
10	Glucose	Zr-Sn-Fe-Al-O-S	-SO_3H	Zr-/Sn-/Fe-/Al-	Ethanol/DMSO (v/v = 9:1)	160°C, 4 h	3.9	He et al. (2022)
11	Glucose	Zr-Sn-Fe-Al-O-S	-SO_3H	Zr-/Sn-/Fe-/Al-	Ethanol/DMSO (v/v = 9:1)	160°C, 12 h	7.9	He et al. (2022)
12	Glucose	Zr-Sn-Fe-Al-O-S	-SO_3H	Zr-/Sn-/Fe-/Al-	Ethanol/DMSO (v/v = 3:1)	160°C, 12 h	14.3	He et al. (2022)
13	Glucose	Zr-Sn-Fe-Al-O-S	-SO_3H	Zr-/Sn-/Fe-/Al-	Ethanol/DMSO (v/v = 1:1)	160°C, 12 h	33.1	He et al. (2022)
14	Glucose	Zr-Sn-Fe-Al-O-S	-SO_3H	Zr-/Sn-/Fe-/Al-	Ethanol/DMSO (v/v = 1:3)	160°C, 12 h	12.4	He et al. (2022)
15	Glucose	Zr-Sn-Fe-Al-O-S	-SO_3H	Zr-/Sn-/Fe-/Al-	Ethanol/DMSO (v/v = 1:1)	140°C, 12 h	18.8	He et al. (2022)
16	Glucose	Zn-S-C	-SO_3H	Zn-	Ethanol/THF (v/v = 1:1)	Ultrasonic system: 98°C, 47 min	80.9	Karnjanakom et al. (2020)
17	Cellobiose	Zn-S-C	-SO_3H	Zn-	Ethanol/THF (v/v = 1:1)	Ultrasonic system: 98°C, 47 min	74.6	Karnjanakom et al. (2020)
18	Glucose	Zn-SO_3H-GR-carbon	-SO_3H	Zn-	Ethanol/THF (v/v = 1:2)	Ultrasonic system: 106°C, 72 min	86.3	Karnjanakom and Maneechakr, (2019a)
19	Glucose	Al-SC	-SO_3H	Al-	Ethanol/THF (v/v = 1:1)	Ultrasonic system: 106°C, 72 min	84.4	Karnjanakom and Maneechakr, (2019b)
20	Glucose	Zn-SC	-SO_3H	Zn-	Ethanol/THF (v/v = 1:1)	Ultrasonic system: 106°C, 72 min	85.1	Karnjanakom and Maneechakr, (2019b)

Guo et al., 2017; Xu et al., 2017). One possible reason for this is that glucose formed a bit intermediate 3-deoxyglucosone in Brønsted acid, which is then dehydrated to form HMF, and finally etherified to EMF (Jadhav et al., 2011; Jadhav et al., 2012). In addition, Brønsted acid and protonated ethanol ($[C_2H_5OH_2]^+$) can open the ring of glucose to form intermediate 1,2-enediol then isomerizes to fructose, which makes it possible to produce EMF in the next step (Guo et al., 2017; Wang et al., 2021). When there is only Lewis acid in the system, a moderate EMF yield (10–40%) can be obtained from glucose (Dutta et al., 2012; Liu et al., 2013; Tan et al., 2017). In the presence of a single Lewis acid, the possible reason for the failure to obtain high EMF yield is that the Lewis acid cannot provide H^+, resulting in the low $[C_2H_5OH_2]^+$ concentration in the system which limits the fructose dehydration and subsequent etherification steps. Meanwhile, the EMF yields obtained by catalyzing glucose with different types of metal salts were quite different. Such as metal chlorides $AlCl_3$ and $CrCl_3$ could obtain 11.2 and 15.2% EMF yields, respectively. However, with metal sulfates $Al_2(SO_4)_3$, $CuSO_4$, $Fe_2(SO_4)_3$, and $Cr_2(SO_4)_3$ as catalysts, the reaction system hardly detected EMF, but more EDGP (ca. 80% yield) was detected (Yu et al., 2017). Thus, the metal chloride is more

conducive to the isomerization of glucose, while the metal sulfate is more inclined to promote the etherification of glucose. Overall, the monofunctional acid catalysts cannot obtain satisfactory EMF yield from glucose. Whereas, the developed bifunctional acid catalysts with Brønsted-Lewis acids can obtain high EMF yield from glucose.

Bifunctional Acid Catalysts

Generally, zeolite molecular sieve catalysts contain Brønsted acid species Al-O(H)-Si (framework four-coordinate aluminum), and Lewis acid species Al- (framework three-coordinate aluminum) can be obtained after high-temperature dealumination (Xin et al., 2019). For example, ultra-stable Y zeolite (USY) and β zeolite (H-β) after high-temperature dealumination were used to catalyze the synthesis of EMF from glucose and obtained 39.5 and 41% EMF yields, respectively (Li et al., 2016; Zheng et al., 2021). In addition, zeolite can also be modified to obtain better EMF yield. Introducing Lewis acid species Sn- and Al- into zeolite to obtain MFI-Sn/Al (Bai et al., 2018) or simultaneously introduce H_4[$Si(W_3O_{10})_4$] and $SnCl_4$ (Brønsted-Lewis acids) into zeolite to obtain SBA-15 (Srinivasa Rao et al., 2020). These catalysts could obtain EMF with medium yield from glucose. A soft template

HIPE was utilized to support the sulfonic acid group and Cr^{3+} to synthesize BFC-3 catalyst, which could be used to catalyze glucose and cellobiose and obtain 48.1 and 37.1% EMF yields, respectively (Chen et al., 2020a). Furthermore, glycerol and glucose were sulfonated into carbon spheres, then introduced into Zn- to prepare Zn-SO$_3$H-GR-carbon (Karnjanakom and Maneechakr, 2019a) and Zn-S-C (Karnjanakom et al., 2020). Both of them can obtain amazing EMF yields from glucose (86.3 and 80.9%).

Bifunctional acid catalysts have great differences in catalytic performance. Using the same Brønsted acid and different Lewis acids to prepare various catalysts, the yields of EMF obtained from glucose were different. For example, the sulfonated carbon (SC) was doped with different metal species (Zn-, Al-, and Ni-), which exhibits different catalytic performances (Karnjanakom and Maneechakr, 2019b). When EMF was selectively produced from glucose, Zn-SC, Al-SC, and Ni-SC provided yields of 85.1, 84.4, and 32.8%, respectively. The reason for the difference is that the acidity provided by specie Ni- is lower than Zn- and Al-. A recent study also confirmed that the type of Lewis acids affects the yield of EMF (He et al., 2022). Meanwhile, this study found that the performance of the catalyst was also affected by the number of metal species in it. Specifically, the more types of metals contained in the catalyst, the better the catalytic efficiency. In addition, choosing a suitable ratio of Brønsted/Lewis acid can improve the selectivity of EMF (Srinivasa Rao et al., 2020). For the ratio of strong/weak acid, when the weak acid accounts for more, it is harmful to glucose isomerization, fructose dehydration, and HMF etherification, resulting in lower EMF selectivity. On the contrary, when more strong acids are present in the system, the generated EMF can be turned into EL by a ring-opening reaction or converted into humins (He et al., 2022). Therefore, the ratio of Brønsted/Lewis and strong/weak acids in the bifunctional acid catalysts are also critical for obtaining EMF from glucose.

Reaction Conditions

The selectivity of EMF is also affected by the reaction conditions, such as temperature, time, ultrasound, and co-solvent.

Obtaining EMF from glucose usually requires a higher temperature and longer reaction time (Srinivasa Rao et al., 2020; Wang et al., 2021). However, continuously increasing the reaction temperature and time leads to the decrease in the yield of EMF, which is due to the unstable EMF and easily converted to EL under high temperature and long time (Zheng et al., 2021). During the conversion of glucose to EMF, water may be produced due to dehydration and etherification, which makes the hydrolysis of HMF into LA inevitable in this system (Wang et al., 2021). Since the polar co-solvent limits the conversion of HMF to LA (Morales et al., 2017), such as dimethyl sulfoxide (DMSO), tetrahydrofuran (THF), and GVL, many studies add co-solvents to this system, which significantly inhibited the production of EL (Yu et al., 2018). The amount of co-solvent also affects the yield of EMF. With the increase of co-solvent ratio, the yield of EMF first increased and then decreased, while the yield of EL continued to decrease and HMF continued to increase (He et al., 2022). The increase of

EMF can be attributed to the inhibition of the conversion of EMF to EL. Then adding too much co-solvent can reduce the amount of EMF, which is attributed to the decrease of ethanol content in the system to limit the etherification of HMF into EMF (Chen et al., 2020b). Besides, several studies have shown that ultrasonic assistance can form cavitation bubbles in the system and promote bond breakage, which can promote the reaction to a certain extent (Karnjanakom and Maneechakr, 2019b). The ultrasound assistance can greatly reduce the requirement of temperature and time from glucose to high yield EMF, such as 98°C for 47 min obtained 80.9% yield (Karnjanakom et al., 2020) and 106°C for 72 min obtained 86.3% yield (Karnjanakom and Maneechakr, 2019a). Therefore, EMF can be generated rapidly under mild conditions.

CONCLUSION

The richness, versatility, and accessibility of LCB are the reasons for its advantages in the field of sustainable energy conversion. The mechanisms and technologies of EMF production from LCB-derived sugars in recent years were reviewed. These studies aim to develop more efficient catalysts and reaction systems to increase the yield of EMF.

Glucose as a typical LCB-derived sugar is used to synthesize EMF. It is mainly through path I (**Figure 1**) to synthesize EMF. In general, it shows low EMF yield when used monofunctional acid catalysts. The key to this problem is attributed to the glucose isomerization step (corresponding to Lewis acid) and low concentration of $[C_2H_5OH_2]^+$ (corresponding to Brønsted acid). Yet, the developed bifunctional (Brønsted-Lewis) acid catalysts can effectively solve this problem, which can obtain satisfactory EMF yields from glucose. Meanwhile, the species of Lewis acids, ratio of Brønsted/Lewis acids, and ratio of strong/weak acids in the bifunctional acid catalysts have decisive effects on EMF yield. In addition, the optimization of reaction conditions has also made efforts in EMF yield. The suitable time, temperature, and a certain concentration of co-solvent can provide upside space for the selectivity of EMF.

PERSPECTIVES

Although there are some technological breakthroughs in obtaining high EMF yield from glucose, high yield EMF has not been found directly from LCB. However, studies based on glucose can provide feasible strategies for direct conversion of LCB to obtain high EMF in the future. Firstly, the bifunctional acid solid catalysts were given priority in the choice of catalysts, and the catalysts can adjust the type and quantity of acid. Secondly, it is also crucial to select appropriate co-solvents and reaction conditions. Although the ultrasound-assisted method showed excellent effects, it is not suitable for large-scale industries. Therefore, it is of great significance to develop an efficient catalyst strategy to convert LCB into EMF under mild conditions.

AUTHOR CONTRIBUTIONS

FUNDING

REFERENCES

Abraham, A., Mathew, A. K., Park, H., Choi, O., Sindhu, R., Parameswaran, B., et al. (2020). Pretreatment Strategies for Enhanced Biogas Production from Lignocellulosic Biomass. *Bioresour. Technology.* 301, 122725. doi:10.1016/j.biortech.2019.122725

Bai, Y., Wei, L., Yang, M., Chen, H., Holdren, S., Zhu, G., et al. (2018). Three-Step Cascade over a Single Catalyst: Synthesis of 5-(ethoxymethyl)Furfural from Glucose over a Hierarchical Lamellar Multi-Functional Zeolite Catalyst. *J. Mater. Chem. A.* 6, 7693–7705. doi:10.1039/c8ta01242c

Bhatia, S. K., Jagtap, S. S., Bedekar, A. A., Bhatia, R. K., Patel, A. K., Pant, D., et al. (2020). Recent Developments in Pretreatment Technologies on Lignocellulosic Biomass: Effect of Key Parameters, Technological Improvements, and Challenges. *Bioresour. Technology.* 300, 122724. doi:10.1016/j.biortech.2019.122724

Bredihhin, A., Mäeorg, U., and Vares, L. (2013). Evaluation of Carbohydrates and Lignocellulosic Biomass from Different wood Species as Raw Material for the Synthesis of 5-bromomethyfurfural. *Carbohydr. Res.* 375, 63–67. doi:10.1016/j.carres.2013.04.002

Bredihhin, A., Vares, L., and Luiga, S. (2016). Application of 5-ethoxymethylfurfural (EMF) for the Production of Cyclopentenones. *Synthesis.* 48, 4181–4188. doi:10.1055/s-0035-1562790

Chen, B., Xu, G., Zheng, Z., Wang, D., Zou, C., and Chang, C. (2019). Efficient Conversion of Corn stover into 5-ethoxymethylfurfural Catalyzed by Zeolite USY in Ethanol/THF Medium. *Ind. Crops Prod.* 129, 503–511. doi:10.1016/j.indcrop.2018.12.027

Chen, B., Yan, G., Chen, G., Feng, Y., Zeng, X., Sun, Y., et al. (2020). Recent Progress in the Development of Advanced Biofuel 5-ethoxymethylfurfural. *BMC Energy* 2, 1–13. doi:10.1186/s42500-020-00012-5

Chen, Y., Guan, W., Zhang, Y., Yan, C., Li, B., Wei, Y., et al. (2020a). One-pot Synthesis of the Biofuel 5-ethoxymethylfurfural from Carbohydrates Using a Bifunctional Catalyst Prepared through a Pickering HIPE Template and Pore-Filled Strategy. *Energy Fuels.* 34, 14264–14274. doi:10.1021/acs.energyfuels.0c02942

Chen, Y., Peng, L., Zhang, J., and He, L. (2020b). Synergy of Al2(SO4)3 and H3PO4 in Co-Solvents Converts Starch to 5-Ethoxymethylfurfural. *Catal. Commun.* 137, 105947. doi:10.1016/j.catcom.2020.105947

Climent, M. J., Corma, A., and Iborra, S. (2014). Conversion of Biomass Platform Molecules into Fuel Additives and Liquid Hydrocarbon Fuels. *Green. Chem.* 16, 516. doi:10.1039/c3gc41492b

Corma, A., Iborra, S., and Velty, A. (2007). Chemical Routes for the Transformation of Biomass into Chemicals. *Chem. Rev.* 107, 2411–2502. doi:10.1021/cr050989d

Dai, J., Liu, Z., Hu, Y., Liu, S., Chen, L., Qi, T., et al. (2019). Adjusting the Acidity of Sulfonated Organocatalyst for the One-Pot Production of 5-ethoxymethylfurfural from Fructose. *Catal. Sci. Technol.* 9, 483–492. doi:10.1039/c8cy02010h

De, S., Dutta, S., and Saha, B. (2012). One-pot Conversions of Lignocellulosic and Algal Biomass into Liquid Fuels. *ChemSusChem.* 5, 1826–1833. doi:10.1002/cssc.201200031

Dutta, S., De, S., Alam, M. I., Abu-Omar, M. M., and Saha, B. (2012). Direct Conversion of Cellulose and Lignocellulosic Biomass into Chemicals and Biofuel with Metal Chloride Catalysts. *J. Catal.* 288, 8–15. doi:10.1016/j.jcat.2011.12.017

Guo, H., Duereh, A., Hiraga, Y., Aida, T. M., Qi, X., and Smith, R. L. (2017). Perfect Recycle and Mechanistic Role of Hydrogen Sulfate Ionic Liquids as Additive in Ethanol for Efficient Conversion of Carbohydrates into 5-ethoxymethylfurfural. *Chem. Eng. J.* 323, 287–294. doi:10.1016/j.cej.2017.04.111

Guo, H., Duereh, A., Hiraga, Y., Qi, X., and Smith, R. L. (2018). Mechanism of Glucose Conversion into 5-ethoxymethylfurfural in Ethanol with Hydrogen Sulfate Ionic Liquid Additives and a Lewis Acid Catalyst. *Energy Fuels.* 32, 8411–8419. doi:10.1021/acs.energyfuels.8b00717

Hafizi, H., Walker, G., Iqbal, J., Leahy, J. J., and Collins, M. N. (2020). Catalytic Etherification of 5-Hydroxymethylfurfural into 5-Ethoxymethyfurfural over Sulfated Bimetallic SO42–/Al-Zr/KIT-6, a Lewis/Brønsted Acid Hybrid Catalyst. *Mol. Catal.* 496, 111176. doi:10.1016/j.mcat.2020.111176

He, Y., Zhang, L., Liu, Y., Yi, S., Yu, H., Zhu, Y., et al. (2022). Sulfated Complex Metal Oxides Solid Acids with Dual Brønsted-Lewis Acidic Property for Production of 5-Ethoxymethylfurfural from Biomass-Derived Carbohydrates. *Chem. Eng. J.* 429, 132279. doi:10.1016/j.cej.2021.132279

Jadhav, H., Pedersen, C. M., Sølling, T., and Bols, M. (2011). 3-Deoxy-glucosone Is an Intermediate in the Formation of Furfurals from D-Glucose. *ChemSusChem.* 4, 1049–1051. doi:10.1002/cssc.201100249

Jadhav, H., Taarning, E., Pedersen, C. M., and Bols, M. (2012). Conversion of D-Glucose into 5-hydroxymethylfurfural (HMF) Using Zeolite in [Bmim]Cl or Tetrabutylammonium Chloride (TBAC)/CrCl2. *Tetrahedron Lett.* 53, 983–985. doi:10.1016/j.tetlet.2011.12.059

Karnjanakom, S., and Maneechakr, P. (2019a). Designs of Linear-Quadratic Regression Models for Facile Conversion of Carbohydrate into High Value (5-(ethoxymethyl)furan-2-Carboxaldehyde) Fuel Chemical. *Energ. Convers. Management.* 196, 410–417. doi:10.1016/j.enconman.2019.06.015

Karnjanakom, S., and Maneechakr, P. (2019b). Novelty Catalytic Transformation of Sugar over Excellent Biphasic-Heterogeneous Reaction System. *Catal. Commun.* 130, 105767. doi:10.1016/j.catcom.2019.105767

Karnjanakom, S., Phanthong, P., Bayu, A., Maneechakr, P., Samart, C., Kongparakul, S., et al. (2020). Facile *In Situ* 5-EMF Synthesis and Extraction Processes from Catalytic Conversion of Sugar under Sustainable Long-Life Cycle. *ACS Sustainable Chem. Eng.* 8, 14867–14876. doi:10.1021/acssuschemeng.0c04517

Lew, C. M., Rajabbeigi, N., and Tsapatsis, M. (2012). One-pot Synthesis of 5-(ethoxymethyl)furfural from Glucose Using Sn-BEA and Amberlyst Catalysts. *Ind. Eng. Chem. Res.* 51, 5364–5366. doi:10.1021/ie2025536

Li, G., Pidko, E. A., and Hensen, E. J. M. (2014). Synergy between Lewis Acid Sites and Hydroxyl Groups for the Isomerization of Glucose to Fructose over Sn-Containing Zeolites: A Theoretical Perspective. *Catal. Sci. Technol.* 4, 2241–2250. doi:10.1039/c4cy00186a

Li, H., Riisager, A., Saravanamurugan, S., Pandey, A., Sangwan, R. S., Yang, S., et al. (2017). Carbon-increasing Catalytic Strategies for Upgrading Biomass into Energy-Intensive Fuels and Chemicals. *ACS Catal.* 8, 148–187. doi:10.1021/acscatal.7b02577

Li, H., Saravanamurugan, S., Yang, S., and Riisager, A. (2016). Direct Transformation of Carbohydrates to the Biofuel 5-ethoxymethylfurfural by Solid Acid Catalysts. *Green. Chem.* 18, 726–734. doi:10.1039/c5gc01043h

Li, H., Wang, C., Xu, Y., Yu, Z., Saravanamurugan, S., Wu, Z., et al. (2020). Heterogeneous (de)Chlorination-Enabled Control of Reactivity in the LIquid-Phase Synthesis of Furanic Biofuel From Cellulosic Feedstock. *Green. Chem.* 22, 637–645. doi:10.1039/c9gc04092g

Liu, B., Zhang, Z., Huang, K., and Fang, Z. (2013). Efficient Conversion of Carbohydrates into 5-ethoxymethylfurfural in Ethanol Catalyzed by AlCl3. *Fuel.* 113, 625–631. doi:10.1016/j.fuel.2013.06.015

Liu, B., and Zhang, Z. (2013). One-pot Conversion of Carbohydrates into 5-ethoxymethylfurfural and Ethyl D-Glucopyranoside in Ethanol Catalyzed by a Silica Supported Sulfonic Acid Catalyst. *RSC Adv.* 3, 12313. doi:10.1039/c3ra41043a

Liu, S., Meng, Y., Li, H., and Yang, S. (2021). Hierarchical Porous MIL-101(Cr) Solid Acid-Catalyzed Production of Value-Added Acetals from Biomass-Derived Furfural. *Polymers.* 13, 3498. doi:10.3390/polym13203498

Mascal, M., and Nikitin, E. B. (2008). Direct, High-Yield Conversion of Cellulose into Biofuel. *Angew. Chem.* 120, 8042–8044. doi:10.1002/anie.200801594

Morales, G., Paniagua, M., Melero, J. A., and Iglesias, J. (2017). Efficient Production of 5-ethoxymethylfurfural from Fructose by Sulfonic Mesostructured Silica Using DMSO as Co-solvent. *Catal. Today.* 279, 305–316. doi:10.1016/j.cattod.2016.02.016

Pan, H., Li, H., Zhang, H., Wang, A., and Yang, S. (2020). Functional Nanomaterials-Catalyzed Production of Biodiesel. *Cnano.* 16, 376–391. doi:10.2174/1573413715666190411142820

Rackemann, D. W., and Doherty, W. O. (2011). The Conversion of Lignocellulosics to Levulinic Acid. *Biofuels, Bioprod. Bioref.* 5, 198–214. doi:10.1002/bbb.267

Rajabbeigi, N., Torres, A. I., Lew, C. M., Elyassi, B., Ren, L., Wang, Z., et al. (2014). On the Kinetics of the Isomerization of Glucose to Fructose Using Sn-Beta. *Chem. Eng. Sci.* 116, 235–242. doi:10.1016/j.ces.2014.04.031

Ras, E.-J., Maisuls, S., Haesakkers, P., Gruter, G.-J., and Rothenberg, G. (2009). Selective Hydrogenation of 5-ethoxymethylfurfural over Alumina-Supported Heterogeneous Catalysts. *Adv. Synth. Catal.* 351, 3175–3185. doi:10.1002/adsc.200900526

Ras, E.-J., McKay, B., and Rothenberg, G. (2010). Understanding Catalytic Biomass Conversion Through Data Mining. *Top. Catal.* 53, 1202–1208. doi:10.1007/s11244-010-9563-z

Shrotri, A., Kobayashi, H., and Fukuoka, A. (2018). Cellulose Depolymerization over Heterogeneous Catalysts. *Acc. Chem. Res.* 51, 761–768. doi:10.1021/acs.accounts.7b00614

Somerville, C., Youngs, H., Taylor, C., Davis, S. C., and Long, S. P. (2010). Feedstocks for Lignocellulosic Biofuels. *Science.* 329, 790–792. doi:10.1126/science.1189268

Srinivasa Rao, B., Dhana Lakshmi, D., Krishna Kumari, P., Rajitha, P., and Lingaiah, N. (2020). Dehydrative Etherification of Carbohydrates to 5-ethoxymethylfurfural over SBA-15-Supported Sn-Modified Heteropolysilicate Catalysts. *Sustainable Energ. Fuels.* 4, 3428–3437. doi:10.1039/d0se00509f

Tan, J., Liu, Q., Chen, L., Wang, T., Ma, L., and Chen, G. (2017). Efficient Production of Ethyl Levulinate from Cassava over Al2(SO4)3 Catalyst in Ethanol-Water System. *J. Energ. Chem.* 26, 115–120. doi:10.1016/j.jechem.2016.08.004

Tong, X., Ma, Y., and Li, Y. (2010). Biomass into Chemicals: Conversion of Sugars to Furan Derivatives by Catalytic Processes. *Appl. Catal. A: Gen.* 385, 1–13. doi:10.1016/j.apcata.2010.06.049

Wang, S., Chen, Y., Jia, Y., Xu, G., Chang, C., Guo, Q., et al. (2021). Experimental and Theoretical Studies on Glucose Conversion in Ethanol Solution to 5-ethoxymethylfurfural and Ethyl Levulinate Catalyzed by a Brønsted Acid. *Phys. Chem. Chem. Phys.* 23, 19729–19739. doi:10.1039/d1cp02986j

Xiang, B., Wang, Y., Qi, T., Yang, H.-Q., and Hu, C.-W. (2017). Promotion Catalytic Role of Ethanol on Brønsted Acid for the Sequential Dehydration-Etherification of Fructose to 5-ethoxymethylfurfural. *J. Catal.* 352, 586–598. doi:10.1016/j.jcat.2017.06.031

Xin, S., Wang, Q., Xu, J., Chu, Y., Wang, P., Feng, N., et al. (2019). The Acidic Nature of "NMR-Invisible" Tri-Coordinated Framework Aluminum Species in Zeolites. *Chem. Sci.* 10, 10159–10169. doi:10.1039/c9sc02634g

Xu, G., Chen, B., Zheng, Z., Li, K., and Tao, H. (2017). One-pot Ethanolysis of Carbohydrates to Promising Biofuels: 5-ethoxymethylfurfural and Ethyl Levulinate. *Asia-pac. J. Chem. Eng.* 12, 527–535. doi:10.1002/apj.2095

Yang, F., Tang, J., Ou, R., Guo, Z., Gao, S., Wang, Y., et al. (2019). Fully Catalytic Upgrading Synthesis of 5-ethoxymethylfurfural from Biomass-Derived 5-hydroxymethylfurfural over Recyclable Layered-Niobium-Molybdate Solid Acid. *Appl. Catal. B: Environ.* 256, 117786. doi:10.1016/j.apcatb.2019.117786

Yang, Y., Hu, C.-w., and Abu-Omar, M. M. (2012). Conversion of Carbohydrates and Lignocellulosic Biomass into 5-hydroxymethylfurfural Using AlCl3·6H2O Catalyst in a Biphasic Solvent System. *Green. Chem.* 14, 509–513. doi:10.1039/c1gc15972k

Yu, D., Liu, X., Jiang, J., Liu, Y., Tan, J., Li, H., et al. (2021). Catalytic Synthesis of the Biofuel 5-ethoxymethylfurfural (EMF) from Biomass Sugars. *J. Chem.* 2021, 1–16. doi:10.1155/2021/9015481

Yu, X., Gao, X., Peng, L., He, L., and Zhang, J. (2018). Intensified 5-ethoxymethylfurfural Production from Biomass Components over Aluminum-Based Mixed-Acid Catalyst in Co-solvent Medium. *ChemistrySelect* .3, 13391–13399. doi:10.1002/slct.201803059

Yu, X., Gao, X., Tao, R., and Peng, L. (2017). Insights into the Metal Salt Catalyzed 5-ethoxymethylfurfural Synthesis from Carbohydrates. *Catalysts.* 7, 182. doi:10.3390/catal7060182

Zeng, M., and Pan, X. (2020). Insights into Solid Acid Catalysts for Efficient Cellulose Hydrolysis to Glucose: Progress, Challenges, and Future Opportunities. *Catal. Rev.* 1, 1–46. doi:10.1080/01614940.2020.1819936

Zhang, J., Dong, K., Luo, W., and Guan, H. (2018). Catalytic Upgrading of Carbohydrates into 5-ethoxymethylfurfural Using SO3H Functionalized Hyper-Cross-Linked Polymer Based Carbonaceous Materials. *Fuel.* 234, 664–673. doi:10.1016/j.fuel.2018.07.060

Zheng, Z., Wang, C., Chen, Y., Wang, S., Guo, Q., Chang, C., et al. (2021). One-pot Efficient Conversion of Glucose into Biofuel 5-ethoxymethylfurfural Catalyzed by Zeolite Solid Catalyst. *Biomass Conv. Bioref.*, 1–12. doi:10.1007/s13399-021-01660-1

2-Alkylation of 3-Alkyindoles With Unactivated Alkenes

Xuling Pan *, Qian Liu and Yingling Nong

State Key Laboratory Breeding Base of Green Pesticide and Agricultural Bioengineering, Key Laboratory of Green Pesticide and Agricultural Bioengineering Ministry of Education, Guizhou University, Guiyang, China

An acid-catalyzed 2-alkylation of indole molecules is developed. Only catalytic amount of the commercially available, inexpensive and traceless HI is used as the sole reaction promoter. 2,3-Disubstituted indole molecules bearing congested tertiary carbon centers are afforded as the final products in moderate to excellent yields.

Keywords: metal-free, acid catalysis, atom economy, indole-2-alkylation, alkene

INTRODUCTION

Indole and its derivatives are versatile molecules and have found significant applications in biological and medicinal research (Ma et al., 2016) (**Figure 1A**). For example, the indole derivative neoechinulin A has been isolated from *P. griseofulvum* and *Aspergillus sp.* and shown significant cytotoxic activity against P388 cells (Ma et al., 2016). Typrostatin A and B can be obtained from *A. fumigatus*, which is present in the sea sediment and the *Ficus* carica in both Japan and China. They have exhibited excellent antiphytopathogenic activity and have been used in the investigation of novel anti-tumor reagents (Ma et al., 2016). Therefore, the development of simple and efficient methods for functionalization of indole molecules is attractive and important to both scientific research and drug manufacturing.

Indole can be functionalized at each position around its aromatic structure through various transformations. Traditionally, the C3-positions of indole molecules have been widely used as nucleophiles to react with a variety of electrophiles in both enantioselective (Austin and MacMillan et al., 2002; Zhou and Tang et al., 2002; Evans et al., 2005; Wang et al., 2006; Terada et al., 2007; Bandini et al., 2009; Joucla and Djakovitch et al., 2009; Bartoli et al., 2010) and non-chiral fashion (Bartoli et al., 2005; Kimura et al., 2005; Moran et al., 2006; Kusurkar et al., 2008; Lerch et al., 2014). Transition metals, amines and Lewis acids are frequently used as effective catalysts for these reactions. The C2-positions of the *N*-protected indoles can undergo transition metal-catalyzed alkylations (Doyle et al., 2010; Johansen and Kerr et al., 2010; Jiao and Bach et al., 2011; Pan et al., 2012; Lin et al., 2013; Yoshino et al., 2013; Su et al., 2014; Soni et al., 2018; Wang and Wang, 2021), arylations (Lane and Sames, 2004; Wang et al., 2005; Deprez et al., 2006; Lebrasseur and Larrosa et al., 2008; Phipps et al., 2008; Yang et al., 2008; Ackermann and Lygin, 2011; Sauermann et al., 2011; Li et al., 2016; Yang and Shi, 2018), alkenylations (Nakao et al., 2006; Maehara et al., 2008; Ding and Yoshikai, 2012; Li et al., 2013a; Li et al., 2013b; Liang et al., 2014; Schramm et al., 2015; Wong et al., 2015; Zhang W et al., 2015; Zhou et al., 2016), alkynylations (Yang et al., 2010; Tolnai et al., 2013; Sauermann et al., 2015; Zhang Z Z et al., 2015; Kong et al., 2016), aminations (Sun et al., 2014; Sun et al., 2015) and thiolation reactions (Gensch et al., 2016). A directing group is generally required to be installed on the *N* atom of the indole molecule for the C2-functional group introductions in these transformations. In contrast, intermolecular reactions for direct functionalization of the C2-positions of the unprotected indoles have been relatively less developed (**Figure 1B**). Success within this direction includes the transition metal-catalyzed indole C2-alkylations with alkyl halides (Straathof et al., 2014;

FIGURE 1 | Bioactive Indole Derivatives bearing C2-Substituents and C2-Functionalizations of Unprotected Indoles.

Shao et al., 2015; Yang et al., 2015) and alkenes (Weng et al., 2016; Zhou et al., 2017; Bai et al., 2020) (**Figure 1B**, eq. 1 and eq. 2). Melchiorre (Kandukuri et al., 2015) and co-workers

have disclosed the formation of the electron donor-acceptor (EDA) complex between indoles and electron-deficient benzylbromides and reported a metal-free photo-catalyzed

TABLE 1 | Optimization of reaction conditions.[a]

Entry	Acid	Solvent	Equiv	Yield (%)[b]
1	HCl	CH_2Cl_2	0.3	21
2	HBr	CH_2Cl_2	0.3	87
3	HI	CH_2Cl_2	0.3	92
4	H_2SO_4	CH_2Cl_2	0.3	30
5	TsOH	CH_2Cl_2	0.3	74
6	TFA	CH_2Cl_2	0.3	27
7	CH_3CO_2H	CH_2Cl_2	0.3	0
8	HI	EtOAc	0.3	80
9	HI	hexane	0.3	73
10	HI	toluene	0.3	88
11	HI	H_2O/DMF/THF/CH_3OH/MTBE	0.3	0
12	HI	CH_2Cl_2	0.2	94
13	HI	CH_2Cl_2	0.1	93
14	HI	CH_2Cl_2	0.05	67
15[c]	HI	CH_2Cl_2	0.1	94

[a]Reaction conditions: unless otherwise stated, the reaction of 3-methylindole **1a** (0.11 mmol), 1,1-diphenylethene **2a** (0.10 mmol) and HI (0.01 mmol) was carried out at 30°C in CH_2Cl_2 (1.0 ml) for 12 h.
[b]Isolated yield of **3a**.
[c]at 25°C.
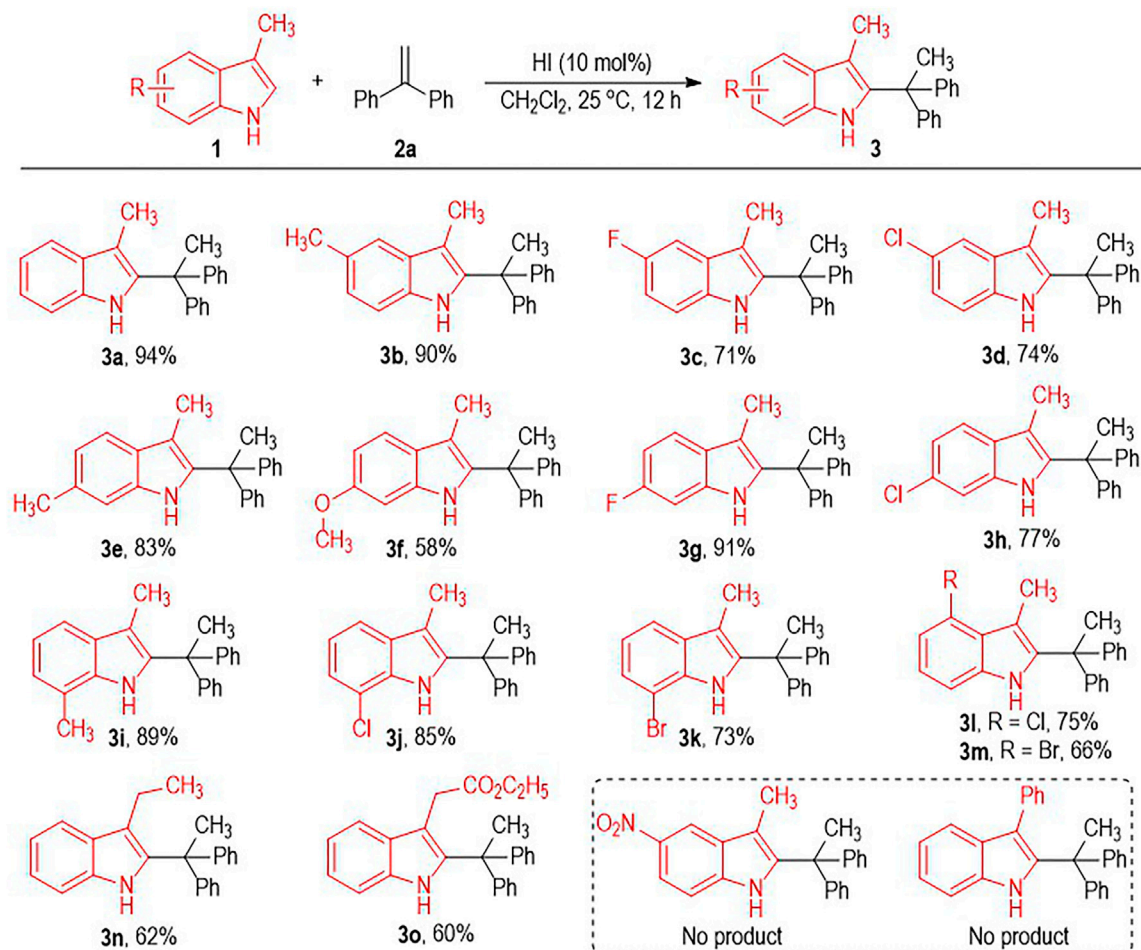
SCHEME 1 | Scope of Indoles **1**.[a]. [a] Reaction conditions as stated in **Table 1**, entry 15. Yields are isolated yields after purification by column chromatography.
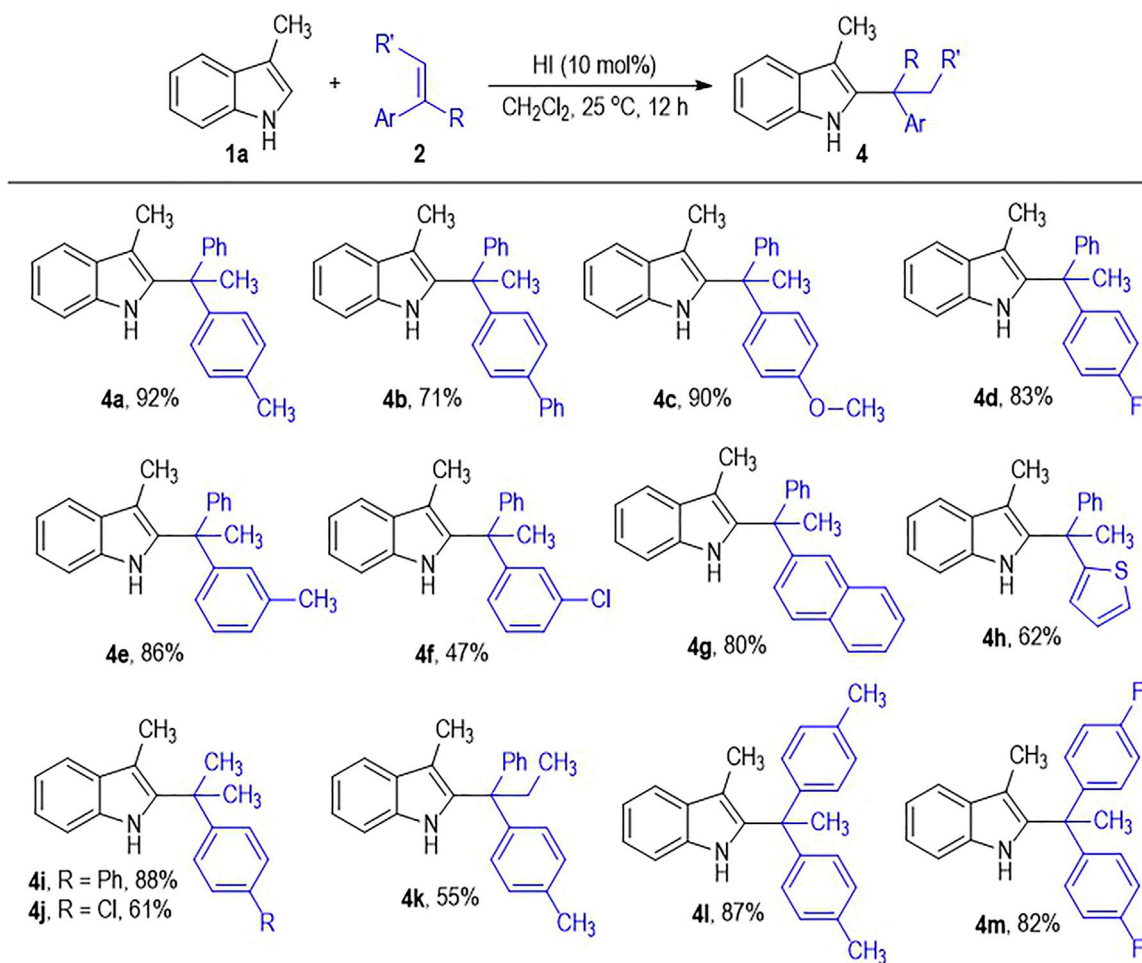
SCHEME 2 | Scope of Alkenes **2**.[a]. [a] Reaction conditions as stated in **Table 1**, entry 15. Yields are isolated yields after purification by column chromatography.

direct indole C2-alkylation *via* formation of this EDA complex (eq. 3). Zhang (Wang et al., 2016) and co-workers reported in 2016 the organic semiconductor-catalyzed, visible light-promoted indole C2-alkylation with 2-bromomalanates (eq. 4). Recently, Glorius (James et al., 2019) and co-workers used the pyridinium salt as the EDA complex acceptor and realized the indole C2-alkylation reaction under basic conditions with white light irradiation (eq. 5). To the best of our knowledge, the direct and metal-free C2-alkylation of indoles with unactivated alkenes has not been disclosed.

Herein, we report an acid-promoted regioselective C2-alkylation reaction of unprotected indoles **1** (**Figure 1C**). Unactivated alkenes **2** are used as the alkylation reagent, with no sacrificing atoms or functional groups lost during this transformation. The use of EDA acceptors can be avoided in this protocol. A traceless and inexpensive HI is used in a catalytic amount as the sole reaction catalyst. The C2-branched alkylation products **3** or **4** bearing a tertiary carbon center are afforded in excellent regioselective fashion with good to excellent isolated yields. The reaction features excellent atom-economy and C2-regioselectivity.

The reaction was initially carried out by using 3-methylindole **1a** and 1,1-diphenylethene **2a** as the substrates in dichloromethane under the catalysis of different organic and inorganic acids (**Table 1**, entries 1–7). To our delight, the indole C2-branched alkylation product **3a** can be obtained in promising yields with a variety of strong acids after stirring at 30°C for 12 h (entries 1–6). The target product of **3a** could be afforded in 21% yield in the presence of 30 mol% of HCl acid (entry 1). The yield of **3a** could be dramatically improved to 87% when switching the HCl into HBr (entry 2). Gratifyingly, the product **3a** was obtained in 92% yield when using HI as the acid catalyst (entry 3). Other organic or inorganic acids gave the desired product **3a** in lower yields (entries 4–6). Notably, the reaction could not happen when using acetic acid as the reaction catalyst, which is probably due to its weak acidity (entry 7). A diversity of organic solvents could be used as the reaction mediate (entries 8–11). For example, the reaction went on smoothly in the solvents of EtOAc, hexane and toluene, with the desired product **3a** afforded in good yields (entries 8–10). However, solvents with high polarities such as H_2O, DMF,
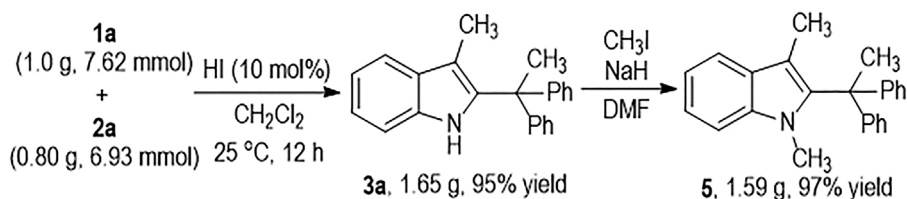
SCHEME 3 | Gram-Scale Synthesis of **3a** and Its Synthetic Transformation.

THF, CH₃OH and MTBE could not be used for this transformation (entry 11). The amount of the HI catalyst could be decreased to 0.1 mol% without obvious erosion of the product yield (entries 12–13). Further decreasing the amount of the HI to 0.05 mol% resulted in significant loss of the yield (entry 14). The reaction temperature could also be decreased to 25°C with the desired product of **3a** afforded in an even higher yield (entry 15).

Having identified the optimal reaction condition for the HI-induced indole C2-alkylation, we next evaluated the scope of this transformation using indole substrates **1** bearing different substituents (**Scheme 1**). Both electron-donating and electron-withdrawing substituents are well tolerated on the benzene rings of the indole structure, with the target C2-alkylated indole products afforded in moderate to excellent yields (**Scheme 1**, **3a** to **3m**). We also examined the effect of the substitution position of the C5 with NO₂ group, but gave no desired product. The C3-methyl group on the indole molecule can be changed into other alkyl groups, with the desired C2-alkylated indole products afforded in a bit lower yields (e.g., **3n** to **3o**). However, switching the C3-methyl group on the reaction substrates into a C3-phenyl group resulted in no formation of the target product.

The alkene substrates **2** can also tolerate diverse substituents and substitution patterns (**Scheme 2**). Various substituents can be introduced to the *para-* and *meta-* positions of the phenyl rings on **2a**, with the corresponding products afforded in good to excellent yields (**Scheme 2**, **4a** to **4f**). However, installing substituents on the *ortho-* position of the phenyl rings on **2a** leads to no formation of the desired products, which is probably due to the substantially increased steric hindrance during the C2-branched product formation process. One of the phenyl rings on **2a** can be switched into a naphthyl or a thiophenyl group with retention of the good to excellent product yields (**4g** to **4h**). To our delight, one of the two aryl groups on the alkene substrates can be replaced by a methyl group without much erosion on the product yield (**4i** to **4j**). It is worth noting that the internal alkene of 1,1-diphenylpropene also works well in this photo-induced indole C2-alkylation process, with the target product **4k** afforded in 55% yield. It is not surprising that the 1,1-diarylethenes bearing two substituted phenyl groups generally give the desired indole C2-branched alkylation products in excellent yields (**4l** to **4m**).

The HI-induced C2-alkylation reaction of the 3-methylindole **1a** with **2a** can be carried out at Gram scales to give the functionalized indole product **3a** in an excellent yield (**Scheme 3**). The indole NH group on **3a** can be efficiently protected by

CH₃I and the *N*-methylindole product **5** can be afforded in almost quantitative yield.

CONCLUSION

In summary, we have disclosed a metal-free reaction for the synthesis of 2-alkylation of 3-alkylindole derivatives. 1,1-Disubstituted alkenes are used as the alkylation reagent with the C2-branched alkylated indole products afforded in generally good to excellent yields with excellent Markovnikov regioselectivity. A catalytic amount of the commercially available and inexpensive HI is used as the sole reaction catalyst. Further investigations towards the applications of the C2-functionalized indole molecules are in progress in our laboratory.

DATA AVAILABILITY STATEMENT

The original contributions presented in the study are included in the article/**Supplementary Material**, further inquiries can be directed to the corresponding author.

AUTHOR CONTRIBUTIONS

XP conducted most of the experiments. QL and YN participated in some of the experiments. XP conceptualized and directed the whole project. XP drafted the manuscript. All of the authors contributed in scientific discussions.

FUNDING

SUPPLEMENTARY MATERIAL

The Supplementary Material for this article can be found online at: https://www.frontiersin.org/articles/10.3389/fchem.2022.860764/full#supplementary-material

REFERENCES

Ackermann, L., and Lygin, A. V. (2011). Ruthenium-Catalyzed Direct C-H Bond Arylations of Heteroarenes. *Org. Lett.* 13, 3332–3335. doi:10.1021/ol2010648

Austin, J. F., and MacMillan, D. W. C. (2002). Enantioselective Organocatalytic Indole Alkylations. Design of a New and Highly Effective Chiral Amine for Iminium Catalysis. *J. Am. Chem. Soc.* 124, 1172–1173. doi:10.1021/ja017255c

Bai, J.-F., Zhao, L., Wang, F., Yan, F., Kano, T., Maruoka, K., et al. (2020). Organocatalytic Formal (3 + 2) Cycloaddition toward Chiral Pyrrolo[1,2-A] indoles via Dynamic Kinetic Resolution of Allene Intermediates. *Org. Lett.* 22, 5439–5445. doi:10.1021/acs.orglett.0c01812

Bandini, M., and Eichholzer, A. (2009). Catalytic Functionalization of Indoles in a New Dimension. *Angew. Chem. Int. Edition* 48, 9608–9644. doi:10.1002/anie.200901843

Bartoli, G., Bencivenni, G., and Dalpozzo, R. (2010). Organocatalytic Strategies for the Asymmetric Functionalization of Indoles. *Chem. Soc. Rev.* 39, 4449–4465. doi:10.1039/b923063g

Bartoli, G., Bosco, M., Giuli, S., Giuliani, A., Lucarelli, L., Marcantoni, E., et al. (2005). Efficient Preparation of 2-Indolyl-1-Nitroalkane Derivatives Employing Nitroalkenes as Versatile Michael Acceptors: New Practical Linear Approach to Alkyl 9H-β-Carboline-4-Carboxylate. *J. Org. Chem.* 70, 1941–1944. doi:10.1021/jo048776w

Deprez, N. R., Kalyani, D., Krause, A., and Sanford, M. S. (2006). Room Temperature Palladium-Catalyzed 2-Arylation of Indoles. *J. Am. Chem. Soc.* 128, 4972–4973. doi:10.1021/ja060809x

Ding, Z., and Yoshikai, N. (2012). Mild and Efficient C2-Alkenylation of Indoles with Alkynes Catalyzed by a Cobalt Complex. *Angew. Chem. Int. Ed.* 51, 4698–4701. doi:10.1002/anie.201200019

Doyle, M. P., Duffy, R., Ratnikov, M., and Zhou, L. (2010). Catalytic Carbene Insertion into C–H Bonds. *Chem. Rev.* 110, 704–724. doi:10.1021/cr900239n

Evans, D. A., Fandrick, K. R., and Song, H.-J. (2005). Enantioselective Friedel−Crafts Alkylations of α,β-Unsaturated 2-Acyl Imidazoles Catalyzed by Bis(oxazolinyl)pyridine−Scandium(III) Triflate Complexes. *J. Am. Chem. Soc.* 127, 8942–8943. doi:10.1021/ja052433d

Gensch, T., Klauck, F. J. R., and Glorius, F. (2016). Cobalt-Catalyzed C–H Thiolation through Dehydrogenative Cross-Coupling. *Angew. Chem. Int. Ed.* 55, 11287–11291. doi:10.1002/anie.201605193

James, M. J., Strieth-Kalthoff, F., Sandfort, F., Klauck, F. J. R., Wagener, F., and Glorius, F. (2019). Visible-Light-Mediated Charge Transfer Enables C–C Bond Formation with Traceless Acceptor Groups. *Chem. Eur. J.* 25, 8240–8244. doi:10.1002/chem.201901397

Jiao, L., and Bach, T. (2011). Palladium-Catalyzed Direct 2-Alkylation of Indoles by Norbornene-Mediated Regioselective Cascade C-H Activation. *J. Am. Chem. Soc.* 133, 12990–12993. doi:10.1021/ja2055066

Johansen, M. B., and Kerr, M. A. (2010). Direct Functionalization of Indoles: Copper-Catalyzed Malonyl Carbenoid Insertions. *Org. Lett.* 12, 4956–4959. doi:10.1021/ol1020948

Joucla, L., and Djakovitch, L. (2009). Transition Metal-Catalysed, Direct and Site-Selective N1-, C2- or C3-Arylation of the Indole Nucleus: 20 Years of Improvements. *Adv. Synth. Catal.* 351, 673–714. doi:10.1002/adsc.200900059

Kandukuri, S. R., Bahamonde, A., Chatterjee, I., Jurberg, I. D., Escudero-Adán, E. C., and Melchiorre, P. (2015). X-Ray Characterization of an Electron Donor-Acceptor Complex that Drives the Photochemical Alkylation of Indoles. *Angew. Chem. Int. Ed.* 54, 1485–1489. doi:10.1002/anie.201409529

Kimura, M., Futamata, M., Mukai, R., and Tamaru, Y. (2005). Pd-Catalyzed C3-Selective Allylation of Indoles with Allyl Alcohols Promoted by Triethylborane. *J. Am. Chem. Soc.* 127, 4592–4593. doi:10.1021/ja0501161

Kong, L., Yu, S., Tang, G., Wang, H., Zhou, X., and Li, X. (2016). Cobalt(III)-Catalyzed C-C Coupling of Arenes with 7-Oxabenzonorbornadiene and 2-Vinyloxirane via C-H Activation. *Org. Lett.* 18, 3802–3805. doi:10.1021/acs.orglett.6b01806

Kusurkar, R. S., Alkobati, N. A. H., Gokule, A. S., and Puranik, V. G. (2008). Use of the Pictet-Spengler Reaction for the Synthesis of 1,4-Disubstituted-1,2,3,4-Tetrahydro-β-Carbolines and 1,4-Disubstituted-β-Carbolines: Formation of γ-carbolines. *Tetrahedron* 64, 1654–1662. doi:10.1016/j.tet.2007.12.008

Lane, B. S., and Sames, D. (2004). Direct C−H Bond Arylation: Selective Palladium-Catalyzed C2-Arylation of N-Substituted Indoles. *Org. Lett.* 6, 2897–2900. doi:10.1021/ol0490072

Lebrasseur, N., and Larrosa, I. (2008). Room Temperature and Phosphine Free Palladium Catalyzed Direct C-2 Arylation of Indoles. *J. Am. Chem. Soc.* 130, 2926–2927. doi:10.1021/ja710731a

Lerch, S., Unkel, L. N., and Brasholz, M. (2014). Tandem Organocatalysis and Photocatalysis: An Anthraquinone-Catalyzed Indole-C3-Alkylation/Photooxidation/1,2-Shift Sequence. *Angew. Chem. Int. Ed.* 53, 6558–6562. doi:10.1002/anie.201402920

Li, B., Ma, J., Xie, W., Song, H., Xu, S., and Wang, B. (2013b). Regioselective C2 Oxidative Olefination of Indoles and Pyrroles through Cationic Rhodium(III)-Catalyzed CH Bond Activation. *Chem. Eur. J.* 19, 11863–11868. doi:10.1002/chem.201301987

Li, B., Ma, J., Xie, W., Song, H., Xu, S., and Wang, B. (2013a). Ruthenium-Catalyzed Regioselective C2 Alkenylation of Indoles and Pyrroles via C-H Bond Functionalization. *J. Org. Chem.* 78, 9345–9353. doi:10.1021/jo401579m

Li, T., Wang, Z., Qin, W.-B., and Wen, T.-B. (2016). Rhodium-Catalyzed/Copper-Mediated Selective C2 Alkynylation of Indoles and C1 Alkynylation of Carbazoles Withγ-Substitutedtert-Propargyl Alcohols. *ChemCatChem* 8, 2146–2154. doi:10.1002/cctc.201600218

Liang, L., Fu, S., Lin, D., Zhang, X.-Q., Deng, Y., Jiang, H., et al. (2014). Ruthenium(II)-Catalyzed Direct Addition of Indole/Pyrrole C2-H Bonds to Alkynes. *J. Org. Chem.* 79, 9472–9480. doi:10.1021/jo501460h

Lin, Q., Chu, L., and Qing, F.-L. (2013). Direct Introduction of Ethoxycarbonyldifluoromethyl-Group to Heteroarenes with Ethyl Bromodifluoroacetate via Visible-Light Photocatalysis. *Chin. J. Chem.* 31, 885–891. doi:10.1002/cjoc.201300411

Ma, Y.-M., Liang, X.-A., Kong, Y., and Jia, B. (2016). Structural Diversity and Biological Activities of Indole Diketopiperazine Alkaloids from Fungi. *J. Agric. Food Chem.* 64, 6659–6671. doi:10.1021/acs.jafc.6b01772

Maehara, A., Tsurugi, H., Satoh, T., and Miura, M. (2008). Regioselective C–H Functionalization Directed by a Removable Carboxyl Group: Palladium-Catalyzed Vinylation at the Unusual Position of Indole and Related Heteroaromatic Rings. *Org. Lett.* 10, 1159–1162. doi:10.1021/ol8000602

Moran, J., Suen, T., and Beauchemin, A. M. (2006). Photoinduced 1,4-Additions of Indoles to Enones. *J. Org. Chem.* 71, 676–679. doi:10.1021/jo0521044

Nakao, Y., Kanyiva, K. S., Oda, S., and Hiyama, T. (2006). Hydroheteroarylation of Alkynes under Mild Nickel Catalysis. *J. Am. Chem. Soc.* 128, 8146–8147. doi:10.1021/ja0623459

Pan, S., Ryu, N., and Shibata, T. (2012). Ir(I)-Catalyzed C-H Bond Alkylation of C2-Position of Indole with Alkenes: Selective Synthesis of Linear or Branched 2-Alkylindoles. *J. Am. Chem. Soc.* 134, 17474–17477. doi:10.1021/ja308742x

Phipps, R. J., Grimster, N. P., and Gaunt, M. J. (2008). Cu(II)-Catalyzed Direct and Site-Selective Arylation of Indoles under Mild Conditions. *J. Am. Chem. Soc.* 130, 8172–8174. doi:10.1021/ja801767s

Sauermann, N., González, M. J., and Ackermann, L. (2015). Cobalt(III)-Catalyzed C-H Alkynylation with Bromoalkynes under Mild Conditions. *Org. Lett.* 17, 5316–5319. doi:10.1021/acs.orglett.5b02678

Schramm, Y., Takeuchi, M., Semba, K., Nakao, Y., and Hartwig, J. F. (2015). Anti-Markovnikov Hydroheteroarylation of Unactivated Alkenes with Indoles, Pyrroles, Benzofurans, and Furans Catalyzed by a Nickel-N-Heterocyclic Carbene System. *J. Am. Chem. Soc.* 137, 12215–12218. doi:10.1021/jacs.5b08039

Shao, C., Shi, G., Zhang, Y., Pan, S., and Guan, X. (2015). Palladium-Catalyzed C-H Ethoxycarbonyldifluoromethylation of Electron-Rich Heteroarenes. *Org. Lett.* 17, 2652–2655. doi:10.1021/acs.orglett.5b01024

Soni, V., Sharma, D. M., and Punji, B. (2018). Nickel-Catalyzed Regioselective C(2)−H Difluoroalkylation of Indoles with Difluoroalkyl Bromides. *Chem. Asian J.* 13, 2516–2521. doi:10.1002/asia.201800504

Straathof, N. J. W., Gemoets, H. P. L., Wang, X., Schouten, J. C., Hessel, V., and Noël, T. (2014). Rapid Trifluoromethylation and Perfluoroalkylation of Five-Membered Heterocycles by Photoredox Catalysis in Continuous Flow. *ChemSusChem* 7, 1612–1617. doi:10.1002/cssc.201301282

Su, Y.-M., Hou, Y., Yin, F., Xu, Y.-M., Li, Y., Zheng, X., et al. (2014). Visible Light-Mediated C-H Difluoromethylation of Electron-Rich Heteroarenes. *Org. Lett.* 16, 2958–2961. doi:10.1021/ol501094z

Sun, B., Yoshino, T., Matsunaga, S., and Kanai, M. (2015). A Cp*CoI2-Dimer as a Precursor for Cationic Co(iii)-Catalysis: Application to C-H Phosphoramidation of Indoles. *Chem. Commun.* 51, 4659–4661. doi:10.1039/C4CC10284C

Sun, B., Yoshino, T., Matsunaga, S., and Kanai, M. (2014). Air-Stable Carbonyl(pentamethylcyclopentadienyl)cobalt Diiodide Complex as a Precursor for Cationic (Pentamethylcyclopentadienyl)Cobalt(III) Catalysis: Application for Directed C-2 Selective CH Amidation of Indoles. *Adv. Synth. Catal.* 356, 1491–1495. doi:10.1002/adsc.201301110

Terada, M., and Sorimachi, K. (2007). Enantioselective Friedel–Crafts Reaction of Electron-Rich Alkenes Catalyzed by Chiral Brønsted Acid. *J. Am. Chem. Soc.* 129, 292–293. doi:10.1021/ja0678166

Tolnai, G. L., Ganss, S., Brand, J. P., and Waser, J. (2013). C2-Selective Direct Alkynylation of Indoles. *Org. Lett.* 15, 112–115. doi:10.1021/ol3031389

Wang, L., Huang, W., Li, R., Gehrig, D., Blom, P. W. M., Landfester, K., et al. (2016). Structural Design Principle of Small-Molecule Organic Semiconductors for Metal-free, Visible-Light-Promoted Photocatalysis. *Angew. Chem. Int. Ed.* 55, 9783–9787. doi:10.1002/anie.201603789

Wang, X., Lane, B. S., and Sames, D. (2005). Direct C-Arylation of Free (NH)-Indoles and Pyrroles Catalyzed by Ar–Rh(III) Complexes Assembled *In Situ*. *J. Am. Chem. Soc.* 127, 4996–4997. doi:10.1021/ja050279p

Wang, Y.-Q., Song, J., Hong, R., Li, H., and Deng, L. (2006). Asymmetric Friedel–Crafts Reaction of Indoles with Imines by an Organic Catalyst. *J. Am. Chem. Soc.* 128, 8156–8157. doi:10.1021/ja062700v

Wang, Z., and Wang, C. (2021). Manganese/NaOPh Co-catalyzed C2-Selective C-H Conjugate Addition of Indoles to α,β-unsaturated Carbonyls. *Green. Synth. Catal.* 2, 66–69. doi:10.1016/j.gresc.2021.01.010

Weng, J.-Q., Fan, R.-J., Deng, Q.-M., Liu, R.-R., Gao, J.-R., and Jia, Y.-X. (2016). Enantioselective Friedel-Crafts Alkylation Reactions of 3-Substituted Indoles with Electron-Deficient Alkenes. *J. Org. Chem.* 81, 3023–3030. doi:10.1021/acs.joc.6b00123

Wong, M. Y., Yamakawa, T., and Yoshikai, N. (2015). Iron-Catalyzed Directed C2-Alkylation and Alkenylation of Indole with Vinylarenes and Alkynes. *Org. Lett.* 17, 442–445. doi:10.1021/ol503395g

Yang, L., Zhao, L., and Li, C.-J. (2010). Palladium-Catalyzed Direct Oxidative Heck-Cassar-Sonogashira Type Alkynylation of Indoles with Alkynes under Oxygen. *Chem. Commun.* 46, 4184–4186. doi:10.1039/c0cc00014k

Yang, Q.-Q., Marchini, M., Xiao, W.-J., Ceroni, P., and Bandini, M. (2015). Visible-Light-Induced Direct Photocatalytic Carboxylation of Indoles with CBr4/MeOH. *Chem. Eur. J.* 21, 18052–18056. doi:10.1002/chem.201503787

Yang, S.-D., Sun, C.-L., Fang, Z., Li, B.-J., Li, Y.-Z., and Shi, Z.-J. (2008). Palladium-Catalyzed Direct Arylation of (Hetero)Arenes with Aryl Boronic Acids. *Angew. Chem. Int. Ed.* 47, 1473–1476. doi:10.1002/anie.200704619

Yang, Y., and Shi, Z. (2018). Regioselective Direct Arylation of Indoles on the Benzenoid Moiety. *Chem. Commun.* 54, 1676–1685. doi:10.1039/c7cc08752g

Yoshino, T., Ikemoto, H., Matsunaga, S., and Kanai, M. (2013). Cp*CoIII-Catalyzed C2-Selective Addition of Indoles to Imines. *Chem. Eur. J.* 19, 9142–9146. doi:10.1002/chem.201301505

Zhang, W., Wei, J., Fu, S., Lin, D., Jiang, H., and Zeng, W. (2015). Highly Stereoselective Ruthenium(II)-Catalyzed Direct C2-Syn-Alkenylation of Indoles with Alkynes. *Org. Lett.* 17, 1349–1352. doi:10.1021/ol503618m

Zhang, Z.-Z., Liu, B., Wang, C.-Y., and Shi, B.-F. (2015). Cobalt(III)-Catalyzed C2-Selective C-H Alkynylation of Indoles. *Org. Lett.* 17, 4094–4097. doi:10.1021/acs.orglett.5b02038

Zhou, J., and Tang, Y. (2002). Sidearm Effect: Improvement of the Enantiomeric Excess in the Asymmetric Michael Addition of Indoles to Alkylidene Malonates. *J. Am. Chem. Soc.* 124, 9030–9031. doi:10.1021/ja026936k

Zhou, X., Fan, Z., Zhang, Z., Lu, P., and Wang, Y. (2016). Construction of Pyrrolo [1,2-*a*]Indoles *via* Cobalt(III)-Catalyzed Enaminylation of 1-(Pyrimidin-2-Yl)-1*h*-Indoles with Ketenimines and Subsequent Base-Promoted Cyclization. *Org. Lett.* 18, 4706–4709. doi:10.1021/acs.orglett.6b02353

Zhou, Z., Li, Y., Gong, L., and Meggers, E. (2017). Enantioselective 2-Alkylation of 3-Substituted Indoles with Dual Chiral Lewis Acid/Hydrogen-Bond-Mediated Catalyst. *Org. Lett.* 19, 222–225. doi:10.1021/acs.orglett.6b03500

Cascade Upgrading of Biomass-Derived Furfural to γ-Valerolactone Over Zr/Hf-Based Catalysts

Wenjuan Sun[1]*, Haifeng Li[1], Xiaochen Wang[2] and Anqiu Liu[2]*

[1]School of Chemistry and Materials Science, Ludong University, Yantai, China, [2]School of Energy Materials and Chemical Engineering, Hefei University, Hefei, China

Biomass feedstocks are promising candidates of renewable clean energy. The development and utilization of biological energy is in line with the concept of sustainable development and circular economy. As an important platform chemical, γ-valerolactone (GVL) is often used as green solvent and biofuel additive. Regarding this, the efficient synthesis of GVL from biomass derivative furfural (FF) has attracted wide attention recently, However, suitable catalyst with appropriate acid-base sites is required due to the complex reaction progress. In this *Mini Review*, the research progress of catalytic synthesis of GVL from furfural by Zr/Hf-based catalysts was reviewed. The different effects of Lewis acid-base and Brønsted acid sites in the catalysts on each steps in the reaction process were discussed firstly. Then the effects of regulation of acid-base sites in the catalysts was also studied. Finally, the advantages and challenges of Zr/Hf-based catalysts in FF converted to GVL system were proposed.

Keywords: biomass, furfural, γ-valerolactone, Zr/Hf-based catalysts, active site regulation

INTRODUCTION

Although the exploration and utilization of fossil energy promote the development of human society, it also causes nonnegligible harm to the environment, which makes people focus on available energy to reduce dependence on fossil energy (Roman-Leshkov et al., 2007; Luterbacher et al., 2014; Zhang et al., 2019). Biomass, as the only renewable organic carbon source, has received extensive attention due to its abundance, cheapness, and availability (Li et al., 2014; Zhao et al., 2019; Li H. et al., 2020). A variety of valuable compounds (e.g., xylose, furfural, furfuryl alcohol, levulinic acid and its esters, and γ-valerolactone) can be obtained from biomass (Liu et al., 2015; Li F. et al., 2017; Li H. et al., 2017; Lingaiah, 2018; Li et al., 2019a; Luo et al., 2019). Among them, γ-valerolactone (GVL) has excellent physical and chemical properties such as high boiling point (207°C), low melting point (31°C), and low toxicity (LD$_{50}$ = 8,800 mg/kg). It can be used as a green organic solvent in a variety of reactions, and has broad application prospects in the organic synthesis, biorefinery, and food industry (Yan et al., 2015; Ye et al., 2020b). In addition, GVL can be further converted into various valerate esters (these have been identified as new generation biofuels), which can be used to synthesize various biomass-based liquid fuels (Yu et al., 2019).

In recent years, the related research on the synthesis of GVL mainly focuses on the direct hydrogenation or catalytic transfer hydrogenation (CTH) with levulinic acid and its esters as substrates. Both noble metal (Ru, Rh, Pt, Pd, Au) catalysts and non-precious metal (Ni, Cu, Co.)
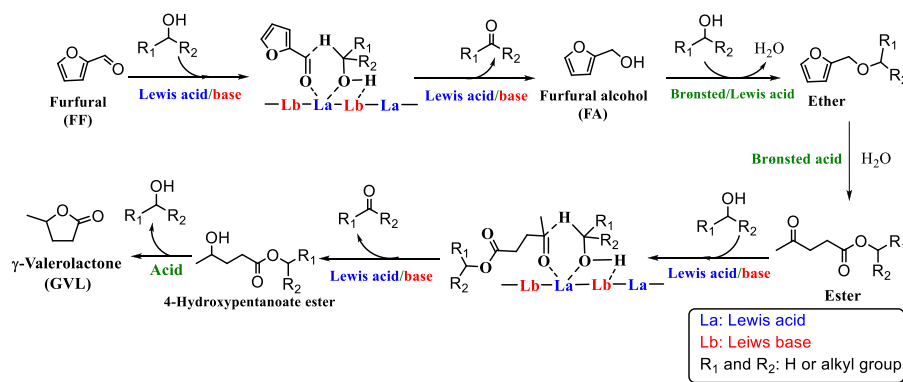
FIGURE 1 | Possible reaction mechanism for the cascade conversion of biomass-derived furfural (FF) to γ-valerolactone (GVL).

catalystshave been used for the hydrogenation of LA to GVL (Yuan et al., 2013; Luo et al., 2014; Molleti et al., 2018). Obregon et al. studied the liquid phase hydrogenation of LA on Ni/Al2O3, after reacting at 250°C and 6.5 MPa H2 pressure for 2 h, The yiled of GVL reached 92%I. (Obregon et al., 2014). Although high yield was achieved by hydrogenation, however, the use of pressur-ized-hydrogen gas is often associated with potential explosion hazard, so the transfer hydrogenation strategy for the synthesis of GVL from LA has been developed. Numerous sup-ported Ru, Pd, Ni, and Cu catalysts were investigated to this reaction (Dutta et al., 2019; Ye et al., 2020b). Fu et al. firstly reported an non-precious skeletal Ni catalyst which could effective catalyze the reaction with i-PrOH as H-donor at room temperature over 9 h (Yang, et al., 2013). In addition, different hydrogen donors such as formic acid, hydrosilicon and alcohol have been exploited for this transformation, compare to other H-donors, the secure, safe and easily operated alcohol not only can act as H-donor, but also can serve as a solvent, furthermore, it can enhance the selec-tivity in the hydrogenation process, too(He et al., 2020a).Compared with levulinic acid, furfural (FF) is more available from biomass feedstocks, so the researchers considered FF directly as a feedstock for GVL production (Bui et al., 2013).

The conversion of FF to GVL requires a series of cascade reactions (**Figure 1**) such as CTH, etherification, ring-opening, partial hydrogenation, and cyclization reaction (Zhu et al., 2016). Such complex reaction processes require higher performance catalysts. Therefore, it is necessary to fully consider both the structure and acid-base properties of the catalyst to improve the catalyst activity. Since Zr/Hf-based catalysts show excellent catalytic performance in CTH reactions and are more economical than precious metals, more and more researchers applied them to the reaction of converting GVL from FF (Li et al., 2016; Wu et al., 2018; Zhou et al., 2019a; Wang et al., 2019).

At present, some excellent reviews are related to the synthesis of GVL, but most of these reviews focus on the synthesis of GVL with levulinic acid and its esters as the substrate (Dutta et al., 2019; Ye et al., 2020b). In this mini-review, the latest progress in the design of high-performance Zr/Hf-based catalysts for GVL production from FF. Some variables affecting the design of Zr/Hf-based catalysts such as the regulation of active sites of catalysts

and the physical and chemical properties of catalysts were summarized. In addition, the reaction parameters in regulating conversion efficiency was discussed, providing insights for the development of efficient, economic, and sustainable catalytic systems that would be important for future research.

EFFECTS OF CATALYST PROPERTIES ON THE SYNTHESIS OF GVL FROM FF

In the system of FF for the synthesis of GVL, Zr/Hf-based catalysts showed good performance, as shown in **Table 1**. Zhu et al. first used Au/ZrO$_2$ (providing Lewis acid-base sites) with ZSM-5 (providing Brønsted acid sites) to catalyze the conversion of FF to GVL (Zhu et al., 2016). The experimental results showed that when Au/ZrO$_2$ was used as the catalyst, FF was almost completely converted to furfuryl alcohol (FA) (99.0% yield) rather than GVL. Similarly, no GVL was detected when only ZSM-5 was used as the catalyst. These results showed that the presence of both Lewis acid-base and Brønsted acid sites in the catalyst was necessary to successfully catalyze the conversion of FF to GVL. Rojas-Buzo et al. found that the prepared Hf-MOF-808 catalyst could successfully catalyze the CTH reaction of FF to FA and levulinic acid to obtain GVL, but could not directly catalyze the synthesis of GVL from FF(Rojas-Buzo et al., 2018). However, when the Hf-MOF-808/Al-β zeolite (containing Brønsted acid sites) combined catalyst was applied to this reaction, a good 75% yield of GVL was obtained at 120°C for 48 h. This result strongly shows that Brønsted acid is crucial to the ring-opening process involved in the conversion of FA to levulinate in this reaction process. Although combined catalyst system could improve the reaction yield, the catalyst preparation process becomes complicated and the production cost increases. To simplify the preparation process of the catalyst and increase reaction yield of GVL, the exploration of bifunctional catalysts containing both Lewis and Brønsted acid sites has attracted more and more attention. Bui et al. first used the physical mixture of Zr-Beta and mesoporous Al-MFI zeolite as Lewis acid and Brønsted acid catalysts to convert FF into GVL in one-pot (Bui et al., 2013). Later, Iglesias et al. synthesized a bifunctional catalyst containing

TABLE 1 | Catalytic production of γ-valerolactone (GVL) from furfural (FF)over Zr/Hf-based catalysts.

Entry	Catalysts	Acidity (mmol/ g)	L/B	H-donor	Adjustment of active sites	Reaction conditions	GVL yield (%)	Ref
1	Zr-Beta + Al-MFI-ns	--	--	2-butanol	Lewis acid site and Brønsted acid site are independent of each other, which can adjust the content and strength of	120°C, 48 h	78	Bui et al. (2013)
2	Au/ZrO2+ZSM-5	--	--	2-propanol	Lewis acid and Brønsted acid in the catalyst respectively	120°C, 30 h	80.4	Zhu et al. (2016)
3	Hf-MOF 808+Al-β zeolite	--	--	2-propanol		120°C, 48 h	75	Rojas-Buzo et al. (2018)
4	ZrO2-SBA-15(2)	0.32	0.08	2-propanol	With the increase of the number of ZrO2 film layers supported on the surface of SBA-15, the strength of Lewis acid in the catalyst increases, while the strength of Brønsted acid decreases	170°C, 7 h	37	Iglesias et al. (2018)
5	Zr-KIT-5	1.86	6.5	2-propanol	Change the loading of Zr in the catalyst	180°C, 6 h	40.1	He et al. (2020b)
6	HZ-ZrP 1-5	0.87	4.1	2-propanol	Change the ratio of zeolite and NH4H2PO4 in the catalyst	185°C, 18 h	64.2	Ye et al. (2020a)
7	HPW/Zr-Beta	0.78	3.2	2-propanol	Use different acid treatment catalysts	160°C, 24 h	68	Winoto et al. (2019)
8	20%Zr-5%T-zeolite	1.67	1.53	2-propanol	Adjust the ratio of TPA and Zr in the catalyst	170°C, 10 h	90	Srinivasa Rao et al. (2019)
9	DUT-67(Hf)-0.06	1.28	--	2-propanol	Treatment of DUT-67-(Hf) with different concentrations of sulfuric acid	180°C, 8 h	70.7	Li et al. (2019b)
10	FM-Zr-ARS	0.55	0.23	2-propanol	Modification of the catalyst with formic acid	160°C, 8 h	72.4	Peng et al. (2021)
11	ZPS-1.0	--	3.25	2-propanol	Change the amount of Zr in the catalyst	150°C, 18 h	80.4	Li et al. (2021c)

both Lewis acid and Brønsted acid by loading ZrO_2 on SBA-15 zeolite (Iglesias et al., 2018). The catalyst can control the strength of Lewis acid and Brønsted acid by changing the number of ZrO_2 layers. Kinetic studies showed that the strength of Lewis acid in the catalyst had an important influence on the distribution of products. Strong Lewis acid sites promote etherification and isomerization of FA rather than MPV reduction. Srinivasa Rao et al. used the impregnation method to load different proportions of ZrO_2 and phosphotungstic acid (TPA) on β-zeolite to further study the effect of Lewis/Brønsted acid content in the catalyst on the yield of GVL (Srinivasa Rao et al., 2021). The experimental results show that more Brønsted acid sites and fewer Lewis acid sites in the catalyst are more conducive to the production of levulinic acid ester rather than GVL. Therefore, the key to obtain high yield GVL is to control the Lewis acid-base and Brønsted acid sites with appropriate strength and number of bifunctional catalysts. Very recently, Tan et al. synthesised a variety of novel coordination organophosphate–Hf polymers from vinylphosphonic acid (VPA), p-toluenesulfonic acid (p-TSA), and HfCl. Specifically, VPA–Hf(1 : 1.5)-0.5 with an appropriate L/B acid ratio of 5.3 and was found to exhibit superior performance in the one-step conversion of furfural (FF) to γ-valerolactone (GVL) in a high yield of 81.0%, with a turnover frequency of 5.0 h^{-1}. (Tan et al., 2022).

Zeolite with a complex microporous structure has an open framework with regular pore size and appropriate size, which is conducive to mass transfer and is easy to adjust acidity (Wang et al., 2017; Wang et al., 2020; Peng et al., 2020; Chai et al., 2021). Since zeolite has these unique advantages, the existing catalysts for FF conversion to GVL are mostly prepared with various

zeolites as supporter. These catalysts mainly change the content of Lewis acid sites in the catalysts by changing the metal loading, and different kinds and concentrations of acids are used to control the content of Brønsted acid in the catalysts (Srinivasa Rao et al., 2019; Winoto et al., 2019; He et al., 2020a; Ye et al., 2020a). He et al. adjusted the content of Lewis/Brønsted acid in the catalyst by adding different amounts of $ZrOCl_2 \cdot 8H_2O$(He et al., 2020b). The more Zr is loaded in the catalyst, the higher the molar ratio of Lewis acid to Brønsted acid is. NH$_3$-TPD results showed that with the increase of Zr loading in the catalyst, the total number of acid sites in the catalyst increased gradually. But excessive Zr loading will produce zirconia clusters, which will reduce the activity of the catalyst. Li et al. treated the catalyst by soaking DUT-67 (Hf) in different concentrations of sulfuric acid solution to change the content of Brønsted acid (Li W. et al., 2019). The results showed that with the increase of sulfuric acid concentration, the total content of acid sites in the catalyst increased continuously, but excessive Brønsted acid in the catalyst would lead to side reactions, which decreased the yield of GVL. SrinivasaRao et al. loaded phosphotungstic acid (TPA) and ZrO_2 with different contents inside and outside the pores of SBA-15, respectively (Srinivasa Rao et al., 2021). Under the premise of keeping the total Lewis acid content in the catalyst unchanged, the molar ratio of Lewis acid to Brønsted acid in the catalyst was adjusted by controlling the amount of ZrO_2 and TPA. The catalyst showed excellent catalytic activity, and the yield of GVL reached 90% at 170°C for 10 h.

In addition to using zeolite as a carrier, bifunctional materials prepared with ligands base on biomass derivatives are also applied to the conversion of FF to GVL. Using alizarin red S

(ARS) as the ligand, Peng et al. synthesized FM-Zr-ARS catalyst by a simple hydrothermal method (Peng et al., 2021). The sulfonic acid group contained in ARS can acted as Brønsted acid for the ring-opening reaction, however, it cannot effectively regulate the relative content of different active sites in the catalyst. As a key step in the conversion of FF to GVL, CTH reaction is generally completed through a six-membered ring transition state. Lewis acid sites are usually used to activate H on the aldehyde group and C connected with the alcohol hydroxyl group. Lewis base sites are mainly used to activate the alcohol hydroxyl group, making H easier to remove. Finally, the transfer hydrogenation process is completed through the six-membered ring transition state (Li et al., 2018; Zhou et al., 2019b; Li et al., 2019c). Jarinya et al. found that Hf-UiO-66 has lower activation energy (13.5 kcal/molvs 14.9 kcal/mol) than Zr-UiO-66 based on density functional theory (DFT)(Sittiwong et al., 2021). It is due toHf having stronger Lewis acidity, Hf has better performance than Zr in CTH reaction under the same preparation conditions (Luo et al., 2014; Xie et al., 2016; Injongkol et al., 2017; Li X. et al., 2020). Tan et al. prepared a new coordination organic phosphate-Hf polymer VPA-Hf(1:1.5)-0.5, which showed good activity for one-pot cascade conversion of FF to GVL. By controlling the ratio of vinyl phosphoric acid, p-toluenesulfonic acid and HfCl$_4$, the content of Lewis acid sites and B acid sites can be accurately adjusted, and the E factor value (0.19) shows that the conversion process mediated by the catalyst is ecologically friendly.

EFFECT OF REACTION PARAMETERS

The reaction can be carried out under mild conditions (120°C) when combined catalysts were used (**Table 1**). For bifunctional catalysts containing both Lewis acid and Brønsted acid, although the preparation of the catalyst is simpler and the cost is reduced, a higher reaction temperature (150–180°C) is often required to ensure the sufficient progress of the reaction. This may due to the independent active sites can also effectively reduce the adverse effects of steric hindrance in the reaction process, so the reaction can be carried out under mild conditions. However, the disadvantages such as excessively long reaction time and more tedious catalyst preparation process cannot be ignored. The key CTH reactions in the reaction process are completed by MPV reduction reaction, and more green and safe alcohols are usually used as H-donors to avoid the use of dangerous high-pressure H$_2$and corrosive formic acid. In general, the β-H of secondary alcohols is easier to be removed from the transition state, so the hydrogen supply capacity of secondary alcohols is stronger than that of primary alcohols (Elsayed et al., 2020; Li J. et al., 2021). However, the steric hindrance of secondary alcohols will gradually increase with the extension of the carbon chain, and excessive steric hindrance is not conducive to the formation of stable transition states, thereby reducing the hydrogen supply capacity (Li M. et al., 2021; Li W. et al., 2021). Therefore, due to the small steric hindrance, 2-propanol was used as the H-donor to prepare GVL in most cases. In addition, the reusability of the catalyst is also an important aspect to evaluate the catalytic system. However, humus is usually formed during the reaction, which not only affects the carbon balance of the reaction

system but also reduces the activity of the catalyst during recycling. Usually, calcination can remove the humus attached to the catalyst and restore the activity of the catalyst (Iglesias et al., 2018; Ye et al., 2020a; Tang et al., 2021). In addition, the catalyst may also have active site leaching during recycling, and it needs to be treated with acid before being put into the next recycling (Li W. et al., 2019).

CONCLUSION AND OUTLOOK

GVL is an important biomass derivative, which can be used as green solvents and biofuels. Highly efficient cascade conversion of FF to GVL presents great challenges due to complex reaction processes and high requirements for catalyst performance. In this mini-review, the influence of the catalyst preparation process on catalyst activity was reviewed, and the reaction parameters such as temperature and H- donor were also discussed. The acid-base properties of the catalyst have a great influence on its catalytic performance. The Lewis acid-base sites in the catalyst are mainly used to catalyze the CTH reaction, and the crucial ring-opening reaction needs to be carried out in the presence of Brønsted acid sites. There is no doubt that higher acid content in the catalyst can provide more active sites, but the imbalance of Lewis acid and Brønsted acid ratio can easily lead to undesirable side reactions. It may lead to carbon imbalance and GVL yield reduction, while the formation of humus attached to the catalyst will reduce the reusability of the catalyst.

Renewable biomass-based carbonaceous support catalysts have great potential for the green synthesis of GVL. Organic hybrid materials have proved to have good activity for CTH reaction, but the Brønsted acid sites are usually not sufficient to catalyze the ring-opening reaction. Therefore, how to improve the strength of Brønsted acid while ensuring the stability of the catalyst structure is the challenge that must be overcome for its application for FF synthesis to GVL. In addition, the accurate control of the strength and content of each active site in the catalyst can better control the reaction process, which is crucial to improving the yield of GVL. Due to the strong Lewis acidity of Zr/Hf materials, Zr/Hf-Based Catalysts showed high performance in the reaction of convert FF to GVL. However, most of the exiting catylic system still suffered from high temperature as well as not so excellent yield, so it is still a challegen to design novel and effecient catalyst for this reaction.

AUTHOR CONTRIBUTIONS

WS and AL organized and original draft the manuscript; HL and XW contributed to reviewing and supervising part of the manuscript.

FUNDING

REFERENCES

Bui, L., Luo, H., Gunther, W. R., and Román-Leshkov, Y. (2013). Domino Reaction Catalyzed by Zeolites with Brønsted and Lewis Acid Sites for the Production of γ-Valerolactone from Furfural. *Angew. Chem. Int. Ed.* 52, 8022–8025. doi:10.1002/anie.201302575

Chai, Y., Dai, W., Wu, G., Guan, N., and Li, L. (2021). Confinement in a Zeolite and Zeolite Catalysis. *Acc. Chem. Res.* 54, 2894–2904. doi:10.1021/acs.accounts.1c00274

Dutta, S., Yu, I. K. M., Tsang, D. C. W., Ng, Y. H., Ok, Y. S., Sherwood, J., et al. (2019). Green Synthesis of Gamma-Valerolactone (GVL) through Hydrogenation of Biomass-Derived Levulinic Acid Using Non-noble Metal Catalysts: A Critical Review. *Chem. Eng. J.* 372, 992–1006. doi:10.1016/j.cej.2019.04.199

Elsayed, I., Jackson, M. A., and Hassan, E. B. (2020). Hydrogen-Free Catalytic Reduction of Biomass-Derived 5-Hydroxymethylfurfural into 2,5-Bis(hydroxymethyl)furan Using Copper-Iron Oxides Bimetallic Nanocatalyst. *ACS Sustain. Chem. Eng.* 8, 1774–1785. doi:10.1021/acssuschemeng.9b05575

He, J., Li, H., Xu, Y., and Yang, S. (2020a). Dual Acidic Mesoporous KIT Silicates Enable One-Pot Production of γ-valerolactone from Biomass Derivatives via cascade Reactions. *Renew. Energ.* 146, 359–370. doi:10.1016/j.renene.2019.06.105

He, J., Xu, Y., Yu, Z., Li, H., Zhao, W., Wu, H., et al. (2020b). ZrOCl2 as a Bifunctional and *In Situ* Precursor Material for Catalytic Hydrogen Transfer of Bio-Based Carboxides. *Sustain. Energ. Fuels* 4, 3102–3114. doi:10.1039/c9se01313j

Iglesias, J., Melero, J. A., Morales, G., Paniagua, M., Hernández, B., Osatiashtiani, A., et al. (2018). ZrO2-SBA-15 Catalysts for the One-Pot cascade Synthesis of GVL from Furfural. *Catal. Sci. Technol.* 8, 4485–4493. doi:10.1039/c8cy01121d

Injongkol, Y., Maihom, T., Treesukul, P., Sirijaraensr, J., Boekfa, B., and Limtrakul, J. (2017). Theoretical Study on the Reaction Mechanism of Hydrogenation of Furfural to Furfuryl Alcohol on Lewis Acidic BEA Zeolites: Effects of Defect Structure and Tetravalent Metals Substitution. *Phys. Chem. Chem. Phys.* 19, 24042–24048. doi:10.1039/c7cp04229a

Li, F., France, L. J., Cai, Z., Li, Y., Liu, S., Lou, H., et al. (2017a). Catalytic Transfer Hydrogenation of Butyl Levulinate to γ-valerolactone over Zirconium Phosphates with Adjustable Lewis and Brønsted Acid Sites. *Appl. Catal. B: Environ.* 214, 67–77. doi:10.1016/j.apcatb.2017.05.013

Li, H., Bhadury, P. S., Riisager, A., and Yang, S. (2014). One-pot Transformation of Polysaccharides via Multi-Catalytic Processes. *Catal. Sci. Technol.* 4, 4138–4168. doi:10.1039/c4cy00711e

Li, H., Guo, H., Fang, Z., Aida, T. M., and Smith, R. L. (2020a). Cycloamination Strategies for Renewable N-Heterocycles. *Green. Chem.* 22, 582–611. doi:10.1039/C9GC03655E

Li, H., Guo, H., Su, Y., Hiraga, Y., Fang, Z., Hensen, E. J. M., et al. (2019a). N-formyl-stabilizing Quasi-Catalytic Species Afford Rapid and Selective Solvent-free Amination of Biomass-Derived Feedstocks. *Nat. Commun.* 10, 699. doi:10.1038/s41467-019-08577-4

Li, H., He, J., Riisager, A., Saravanamurugan, S., Song, B., and Yang, S. (2016). Acid-Base Bifunctional Zirconium N-Alkyltriphosphate Nanohybrid for Hydrogen Transfer of Biomass-Derived Carboxides. *ACS Catal.* 6, 7722–7727. doi:10.1021/acscatal.6b02431

Li, H., Li, Y., Fang, Z., and Smith, R. L. (2019c). Efficient Catalytic Transfer Hydrogenation of Biomass-Based Furfural to Furfuryl Alcohol with Recyclable Hf-Phenylphosphonate Nanohybrids. *Catal. Today* 319, 84–92. doi:10.1016/j.cattod.2018.04.056

Li, H., Yang, T., and Fang, Z. (2018). Biomass-derived Mesoporous Hf-Containing Hybrid for Efficient Meerwein-Ponndorf-Verley Reduction at Low Temperatures. *Appl. Catal. B: Environ.* 227, 79–89. doi:10.1016/j.apcatb.2018.01.017

Li, H., Zhao, W., and Fang, Z. (2017b). Hydrophobic Pd Nanocatalysts for One-Pot and High-Yield Production of Liquid Furanic Biofuels at Low Temperatures. *Appl. Catal. B: Environ.* 215, 18–27. doi:10.1016/j.apcatb.2017.05.039

Li, J., Zhao, S., Li, Z., Liu, D., Chi, Y., and Hu, C. (2021a). Efficient Conversion of Biomass-Derived Levulinic Acid to γ-Valerolactone over Polyoxometalate@Zr-Based Metal-Organic Frameworks: The Synergistic Effect of Brønsted and

Lewis Acidic Sites. *Inorg. Chem.* 60, 7785–7793. doi:10.1021/acs.inorgchem.1c00185

Li, M., Liu, Y., Lin, X., Tan, J., Yang, S., and Li, H. (2021b). One-step Upgrading of Bio-Based Furfural to γ-valerolactone via HfCl4-Mediated Bifunctional Catalysis. *RSC Adv.* 11, 35415–35424. doi:10.1039/d1ra05637a

Li, W., Cai, Z., Li, H., Shen, Y., Zhu, Y., Li, H., et al. (2019b). Hf-based Metal Organic Frameworks as Bifunctional Catalysts for the One-Pot Conversion of Furfural to γ-valerolactone. *Mol. Catal.* 472, 17–26. doi:10.1016/j.mcat.2019.04.010

Li, W., Li, M., Liu, H., Jia, W., Yu, X., Wang, S., et al. (2021c). Domino Transformation of Furfural to γ-valerolactone over SAPO-34 Zeolite Supported Zirconium Phosphate Catalysts with Tunable Lewis and Brønsted Acid Sites. *Mol. Catal.* 506, 111538. doi:10.1016/j.mcat.2021.111538

Li, X., Du, Z., Wu, Y., Zhen, Y., Shao, R., Li, B., et al. (2020b). A Novel Hafnium-Graphite Oxide Catalyst for the Meerwein-Ponndorf-Verley Reaction and the Activation Effect of the Solvent. *RSC Adv.* 10, 9985–9995. doi:10.1039/c9ra10795a

Lingaiah, N. (2018). One Pot Selective Transformation of Biomass Derived Chemicals towards Alkyl Levulinates over Titanium Exchanged Heteropoly Tungstate Catalysts. *Catal. Today* 309, 269–275. doi:10.1016/j.cattod.2017.05.040

Liu, J., Li, H., Liu, Y.-C., Lu, Y.-M., He, J., Liu, X.-F., et al. (2015). Catalytic Conversion of Glucose to 5-hydroxymethylfurfural over Nano-Sized Mesoporous Al2O3-B2o3 Solid Acids. *Catal. Commun.* 62, 19–23. doi:10.1016/j.catcom.2015.01.008

Luo, H. Y., Consoli, D. F., Gunther, W. R., and Román-Leshkov, Y. (2014). Investigation of the Reaction Kinetics of Isolated Lewis Acid Sites in Beta Zeolites for the Meerwein-Ponndorf-Verley Reduction of Methyl Levulinate to γ-valerolactone. *J. Catal.* 320, 198–207. doi:10.1016/j.jcat.2014.10.010

Luo, Y., Li, Z., Li, X., Liu, X., Fan, J., Clark, J. H., et al. (2019). The Production of Furfural Directly from Hemicellulose in Lignocellulosic Biomass: A Review. *Catal. Today* 319, 14–24. doi:10.1016/j.cattod.2018.06.042

Luterbacher, J. S., Rand, J. M., Alonso, D. M., Han, J., Youngquist, J. T., Maravelias, C. T., et al. (2014). Nonenzymatic Sugar Production from Biomass Using Biomass-Derived γ-Valerolactone. *Science* 343, 277–280. doi:10.1126/science.1246748

Molleti, J., Tiwari, M. S., and Yadav, G. D. (2018). Novel Synthesis of Ru/OMS Catalyst by Solvent-free Method: Selective Hydrogenation of Levulinic Acid to γ-valerolactone in Aqueous Medium and Kinetic Modelling. *Chem. Eng. J.* 334, 2488–2499. doi:10.1016/j.cej.2017.11.125

Obregón, I., Corro, E., Izquierdo, U., Requies, J., and Arias, P. L. (2014). Levulinic Acid Hydrogenolysis on Al2O3-Based Ni-Cu Bimetallic Catalysts. *Chin. J. Catal.* 35, 656–662. doi:10.1016/S1872-2067(14)60051-6

Peng, P., Gao, X.-H., Yan, Z.-F., and Mintova, S. (2020). Diffusion and Catalyst Efficiency in Hierarchical Zeolite Catalysts. *Natl. Sci. Rev.* 7, 1726–1742. doi:10.1093/nsr/nwaa184

Peng, Q., Wang, H., Xia, Y., and Liu, X. (2021). One-pot Conversion of Furfural to Gamma-Valerolactone in the Presence of Multifunctional Zirconium Alizarin Red S Hybrid. *Appl. Catal. A: Gen.* 621, 118203. doi:10.1016/j.apcata.2021.118203

Rojas-Buzo, S., García-García, P., and Corma, A. (2018). Catalytic Transfer Hydrogenation of Biomass-Derived Carbonyls over Hafnium-Based Metal-Organic Frameworks. *ChemSusChem* 11, 432–438. doi:10.1002/cssc.201701708

Román-Leshkov, Y., Barrett, C. J., Liu, Z. Y., and Dumesic, J. A. (2007). Production of Dimethylfuran for Liquid Fuels from Biomass-Derived Carbohydrates. *Nature* 447, 982–985. doi:10.1038/nature05923

Sittiwong, J., Boonmark, S., Nunthakitgoson, W., Maihom, T., Wattanakit, C., and Limtrakul, J. (2021). Density Functional Investigation of the Conversion of Furfural to Furfuryl Alcohol by Reaction with I-Propanol over UiO-66 Metal-Organic Framework. *Inorg. Chem.* 60, 4860–4868. doi:10.1021/acs.inorgchem.0c03764

Srinivasa Rao, B., Krishna Kumari, P., Koley, P., Tardio, J., and Lingaiah, N. (2019). One Pot Selective Conversion of Furfural to γ-valerolactone over Zirconia Containing Heteropoly Tungstate Supported on β-zeolite Catalyst. *Mol. Catal.* 466, 52–59. doi:10.1016/j.mcat.2018.12.024

Srinivasa Rao, B., Yogita, D., Dhana Lakshmi, P. K., and Lingaiah, N. (2021). Influence of Metal Oxide and Heteropoly Tungstate Location in Mesoporous

Silica towards Catalytic Transfer Hydrogenation of Furfural to γ-valerolactone. *Sustain. Energ. Fuels* 5, 3719–3728. doi:10.1039/d1se00340b

Tan, J., Liu, Y., Li, M., Li, H., and Yang, S. (2022). One-step Catalytic Upgrading of Bio-Based Furfural to γ-valerolactone Actuated by Coordination Organophosphate-Hf Polymers. *Sustain. Energ. Fuels* 6, 484–501. doi:10.1039/D1SE01476E

Tang, B., Li, S., Song, W.-C., Li, Y., and Yang, E.-C. (2021). One-pot Transformation of Furfural into γ-valerolactone Catalyzed by a Hierarchical Hf-Al-USY Zeolite with Balanced Lewis and Brønsted Acid Sites. *Sustain. Energ. Fuels* 5, 4724–4735. doi:10.1039/d1se00942g

Wang, T., Hu, A., Xu, G., Liu, C., Wang, H., and Xia, Y. (2019). Porous Zr-Thiophenedicarboxylate Hybrid for Catalytic Transfer Hydrogenation of Bio-Based Furfural to Furfuryl Alcohol. *Catal. Lett.* 149, 1845–1855. doi:10.1007/s10562-019-02748-0

Wang, Y., Wu, Q., Meng, X., and Xiao, F.-S. (2017). Insights into the Organotemplate-free Synthesis of Zeolite Catalysts. *Engineering* 3, 567–574. doi:10.1016/j.eng.2017.03.029

Winoto, H. P., Fikri, Z. A., Ha, J.-M., Park, Y.-K., Lee, H., Suh, D. J., et al. (2019). Heteropolyacid Supported on Zr-Beta Zeolite as an Active Catalyst for One-Pot Transformation of Furfural to γ-valerolactone. *Appl. Catal. B: Environ.* 241, 588–597. doi:10.1016/j.apcatb.2018.09.031

Wu, W., Li, Y., Li, H., Zhao, W., and Yang, S. (2018). Acid–Base Bifunctional Hf Nanohybrids Enable High Selectivity in the Catalytic Conversion of Ethyl Levulinate to γ-Valerolactone. *Catalysts* 8, 264–278. doi:10.3390/catal8070264

Xie, C., Song, J., Zhou, B., Hu, J., Zhang, Z., Zhang, P., et al. (2016). Porous Hafnium Phosphonate: Novel Heterogeneous Catalyst for Conversion of Levulinic Acid and Esters into γ-Valerolactone. *ACS Sustain. Chem. Eng.* 4, 6231–6236. doi:10.1021/acssuschemeng.6b02230

Yan, K., Yang, Y., Chai, J., and Lu, Y. (2015). Catalytic Reactions of Gamma-Valerolactone: A Platform to Fuels and Value-Added Chemicals. *Appl. Catal. B: Environ.* 179, 292–304. doi:10.1016/j.apcatb.2015.04.030

Yang, Z., Huang, Y.-B., Guo, Q.-X., and Fu, Y. (2013). RANEY Ni Catalyzed Transfer Hydrogenation of Levulinate Esters to γ-valerolactone at Room Temperature. *Chem. Commun.* 49, 5328–5330. doi:10.1039/c3cc40980e

Ye, L., Han, Y., Bai, H., and Lu, X. (2020a). HZ-ZrP Catalysts with Adjustable Ratio of Brønsted and Lewis Acids for the One-Pot Value-Added Conversion of Biomass-Derived Furfural. *ACS Sustain. Chem. Eng.* 8, 7403–7413. doi:10.1021/acssuschemeng.0c01259

Ye, L., Han, Y., Feng, J., and Lu, X. (2020b). A Review about GVL Production from Lignocellulose: Focusing on the Full Components Utilization. *Ind. Crops Prod.* 144, 112031. doi:10.1016/j.indcrop.2019.112031

Yu, Z., Lu, X., Liu, C., Han, Y., and Ji, N. (2019). Synthesis of γ-valerolactone from Different Biomass-Derived Feedstocks: Recent Advances on Reaction Mechanisms and Catalytic Systems. *Renew. Sustain. Energ. Rev.* 112, 140–157. doi:10.1016/j.rser.2019.05.039

Yuan, J., Li, S.-S., Yu, L., Liu, Y.-M., Cao, Y., He, H.-Y., et al. (2013). Copper-based Catalysts for the Efficient Conversion of Carbohydrate Biomass into γ-valerolactone in the Absence of Externally Added Hydrogen. *Energy Environ. Sci* 6, 3308–3313. doi:10.1039/c3ee40857d

Zhang, H., Li, H., Hu, Y., Venkateswara Rao, K. T., Xu, C., and Yang, S. (2019). Advances in Production of Bio-Based Ester Fuels with Heterogeneous Bifunctional Catalysts. *Renew. Sustain. Energ. Rev.* 114, 109296. doi:10.1016/j.rser.2019.109296

Zhao, W., Chi, X., Li, H., He, J., Long, J., Xu, Y., et al. (2019). Eco-friendly Acetylcholine-Carboxylate Bio-Ionic Liquids for Controllable N-Methylation and N-Formylation Using Ambient CO2 at Low Temperatures. *Green. Chem.* 21, 567–577. doi:10.1039/c8gc03549k

Zhou, S., Dai, F., Chen, Y., Dang, C., Zhang, C., Liu, D., et al. (2019a). Sustainable Hydrothermal Self-Assembly of Hafnium-Lignosulfonate Nanohybrids for Highly Efficient Reductive Upgrading of 5-hydroxymethylfurfural. *Green. Chem.* 21, 1421–1431. doi:10.1039/c8gc03710h

Zhou, S., Dai, F., Xiang, Z., Song, T., Liu, D., Lu, F., et al. (2019b). Zirconium-lignosulfonate Polyphenolic Polymer for Highly Efficient Hydrogen Transfer of Biomass-Derived Oxygenates under Mild Conditions. *Appl. Catal. B: Environ.* 248, 31–43. doi:10.1016/j.apcatb.2019.02.011

Zhu, S., Xue, Y., Guo, J., Cen, Y., Wang, J., and Fan, W. (2016). Integrated Conversion of Hemicellulose and Furfural into γ-Valerolactone over Au/ZrO2 Catalyst Combined with ZSM-5. *ACS Catal.* 6, 2035–2042. doi:10.1021/acscatal.5b02882

Dual Utilization of Lignocellulose Biomass and Glycerol Waste to Produce Fermentable Levoglucosan via Fast Pyrolysis

Yingchuan Zhang[1,2,3,4], Feixiang Xu[3], Fenglin Chen[5], Yanru Zhang[1], Yaxiang Wu[3] and Liqun Jiang[2,3]*

[1]State Key Laboratory of Utilization of Woody Oil Resource, Hunan Academy of Forestry, Changsha, China, [2]Institute of Biological and Medical Engineering, Guangdong Academy of Sciences, Guangzhou, China, [3]Guangzhou Institute of Energy Conversion, Chinese Academy of Sciences, Guangzhou, China, [4]Department of Chemistry, The University of Hong Kong, Hong Kong SAR, China, [5]College of Biology, Hunan University, Changsha, China

Glycerol waste was combined with microwave to pretreat lignocellulose before fast pyrolysis. After pretreatment, most alkali and alkaline earth metals (87.9%) and lignin (52.6%) were removed, and a higher crystallinity was obtained. Comparatively, glycerol waste combined with microwave was proven to be more efficient than glycerol with conventional heating. During fast pyrolysis, higher content of levoglucosan in glycerol waste–pretreated products (27.5%) was obtained, compared with those pretreated by pure glycerol (18.8%) and untreated samples (5.8%). Production of fermentative toxic aldehyde and phenol by-products was also inhibited after glycerol waste treatment. Following mechanistic study had validated that microwave in glycerol waste solvent could effectively ameliorate structure and components of lignocellulose while selectively removing lignin. Notably, under the optimal condition, the levoglucosan content in pyrolytic products was enhanced significantly from 5.8% to 32.9%. In short, this study provided an archetype to dually utilize waste resources for ameliorating lignocellulose structure and precisely manipulating complex fast pyrolysis.

Keywords: lignocellulose biomass, glycerol waste, microwave pretreatment, levoglucosan, fast pyrolysis

INTRODUCTION

Because of the global energy and environmental issues, development of environment-friendly technology for utilizing sustainable resources is urgently needed (Shen et al., 2019; Qian et al., 2021). Lignocellulose, as a predominant natural carbon source with a worldwide distribution, can potentially provide versatile carbohydrate resources. A traditional way of valorizing lignocellulose is to hydrolyze it to fermentable sugars by enzymes or acids and then convert those into valued chemicals via large-scale fermentation (Clomburg et al., 2017), whereas technical limitations, such as a tedious and expensive process and a low yield of fermentable products versus uncontrollable by-products, restrict the viability of industrial intermediation of lignocellulose (Lin and Lu, 2021).

Emerging in recent years, pyrolysis harnesses the thermochemical power to unleash numerous energy-hindered chemical reactions. As a widely used pyrolysis technology, fast pyrolysis is typically performed under temperature of 500°C–750°C with a rapid heating rate (100°C/s–500°C/s) and a short residence time (<2 s), which greatly expand its applications for a quick and efficient thermal

process. For its utilization in lignocellulose conversion, it has been reported that fast pyrolysis of cellulose can yield up to 70.1 wt %-concentrated commercial levoglucosan for further fermentation (Kwon et al., 2007). As an intriguing anhydride form of glucose, levoglucosan can be easily fermented to a variety of chemicals by both prokaryotic and eukaryotic enzymes or bioreactors and next fermented to ethanol, lipids, and itaconic acid (Jabareen et al., 2021). The economics of fast pyrolysis technology to obtain fermentable intermediates from biomass and further conversion has been evaluated to be competent with traditional direct enzymatic and acid hydrolysis (Vivek et al., 2017).

To further enhance the performance of lignocellulose-derived intermediates for fermentation, an efficient production of levoglucosan is of great significance during fast pyrolysis. Levoglucosan can be formed by cleavage of β-1,4-glycosidic bonds in cellulose under homolytic, heterolytic, or concerted mechanism (Jiang et al., 2017). Unfortunately, release of this anhydride sugar via fast pyrolysis is hindered by the intrinsic obstructive structure of lignocellulose in biomass. A reality is that production of levoglucosan from lignocellulose is far more difficult than pure crystalline cellulose. Many studies have shown that both metal ashes and lignin components in natural lignocellulose could impede the thermo-induced destabilization of obstructive structure and promote the fast pyrolysis of lignocellulose to generate small molecule compounds such as ketones and aldehydes instead of levoglucosan (Zhang et al., 2015; Maduskar et al., 2018). Besides, extra separation and purification for removing these by-products are necessary before fermentation, as C1-C3 aldehydes have been proven with capacity of inhibiting hydrolytic enzymes and killing microorganisms (Zaldivar et al., 1999; Xie et al., 2016). To solve this problem, various pretreatment methods have been developed to ameliorate the component and structure of lignocellulose for the following selective pyrolysis. In general, they can be classified as physical methods (by grinding or high-energy radiation), chemical methods (via acid/alkali or oxidative treatment), and hybrid methods (such as steam explosion hydrothermal and organosolv treatment) (Jiang et al., 2019). Among all hybrid methods are notably highlighted because of its simple and flexible process, excellent and selective amelioration, and cheap and sustainable possibility. A key problem, however, is the choice of chemical solvent to bridge the physical process, where a large range from acid–base to ionic liquids have been explored and indeed achieved different valorization effects.

Disposal of glycerol waste is a long-term perplexing environmental issue, with toilsome degradation contrary to its wide use in medicine, cosmetics, and other fields (Anitha et al., 2016). Compositionally, 70% to 98% in glycerol waste is glycerin, along with low extent of fatty acids, methyl esters, fatty acids, alcohols, and inorganic salts. Its high boiling point and hydrophobicity consequently hinder a thorough decomposition and degradation. Recently, a novel reutilization method using glycerol to pretreat lignocellulose under atmospheric pressure followed by fast pyrolysis has been developed, where selective and enhanced production of levoglucosan has been achieved (Jiang

et al., 2017; Jiang et al., 2020). Glycerol provided an excellent thermal medium when pretreating lignocellulose; external heating is necessary for ameliorating its obstacle structure. Recently, it has also been reported that a biomass hydrolysis approach that dilutes acid-catalyzed glycerol pretreatment can significantly enhance the production of microbial oils by removing lignin-degradation products (Hassanpour et al., 2020).

With regard to thermal conversion compared with traditional methods, mild microwave can effectively destroy the recalcitrant structure of lignocellulose due to volumetric heating and selective penetration (Hu and Wen, 2008). In microwave process, high-frequency reciprocation of dipole molecules can go inside the heated materials to generate the internal frictional heat that quickly raises the intrinsic temperature (**Figure 1**). Unfortunately, dried lignocellulose is not prone to microwave energy due to the poor dielectric properties and shakable components. It has been illustrated that cotreatment with glycerol with a high boiling point and hydrophobicity can handle the dielectric nature of lignocellulose, thus improving the pretreatment effects (Zhou et al., 2017).

Herein, obstinate lignocellulose (reed rod) was soaked with glycerol waste and then cotreated under different conditions for amelioration before fast pyrolysis. The consequent structural and componential changes and following fast pyrolytic reactions were extensively investigated. Production of levoglucosan and small molecule compounds with capacity to inhibit fermentation was systematically quantified and compared. Mechanism behind these effects was revealed via elemental, componential, and crystallinity analysis. These studies provided an insight into the precise manipulation of fast pyrolysis of lignocellulose via glycerol waste and microwave pretreatment.

MATERIALS AND METHODS

Materials
Reed rod was collected from Hunan province, China. Before use, it was pulverized to 60–80 mesh and then dried at 105°C to obtain constant weight. Glycerol was obtained from Tianjin Yongda Chemical Reagent Co., Ltd. Other agents were purchased from Sigma–Aldrich (Shanghai). Glycerol waste was prepared in laboratory by transesterification of soybean oil and methanol with the catalyst of sodium silicate ($Na_2SiO_3·9H_2O$). Methanol was mixed with soybean oil and catalyst at mole ratios of 15:1 and 40:1, respectively. The reaction was performed at 65°C for 3 h. The components of glycerol waste had been reported in previous literature (Jiang et al., 2017).

Pretreatment Procedure
Microwave treatment was executed in microwave reactor (MCR-3, Guangzhou Xingshuo Instrument Co., Ltd., China). Reed rod and glycerol were added to a 250-mL flat-bottomed double-necked flask at a solid–liquid ratio of 1:20 (wt/wt) and well-mixed with a glass rod. To prevent the volatilization of glycerol, a reflux device was connected. PW-220 and PW-160 represented microwave treatment with glycerol at 220°C and 160°C for 6 min, whereas BW-160 referred to microwave treatment with glycerol
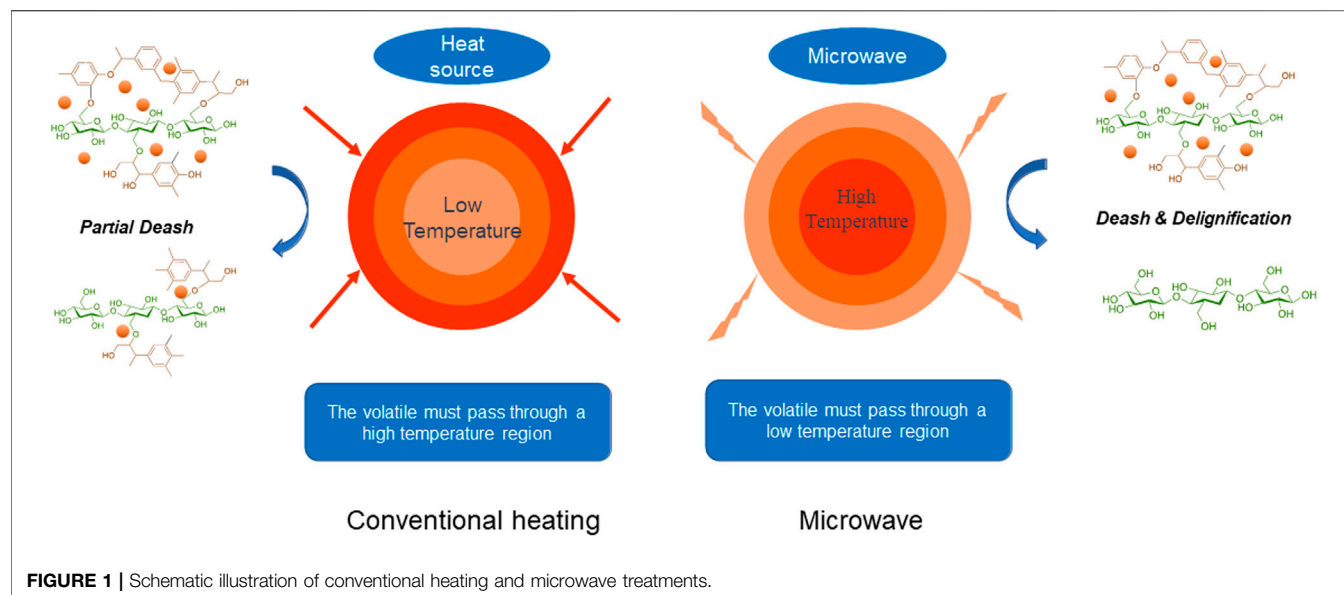
FIGURE 1 | Schematic illustration of conventional heating and microwave treatments.

waste at 160°C for 6 min. Heating treatment was performed in an oil bath. Similarly, glycerol and reed rod were mixed thoroughly before pretreatment. PY-160 and BY-160 represented oil bath treatment with glycerol and glycerol waste heated at 160°C for 6 min, respectively.

After pretreatment, the residual glycerol and soluble substances in the reed rod sample were thoroughly washed with deionized water. The solid residue was collected by vacuum filtration and then dried with a vacuum freeze dryer. The recovery rate of pretreated solid samples was evaluated as follows:

$$\text{Recovery rate}\,(\text{wt\%}) = \frac{\text{solid mass after treatment}}{\text{solid mass before treatment}} \times 100\% \quad (1)$$

Elemental and Componential Analysis

Elemental analyzer (Vario EL cube; Elementar, Germany) was used to determine the content of the main organic elements (C, H, N) in lignocellulose. Content of alkali and alkaline earth metals (AAEMs) was detected by an inductively coupled plasma emission spectrometer (OPTIMA 8000DV; PerkinElmer, United States). Components of cellulose and hemicellulose were quantified according to the technical report issued by the National Renewable Energy Laboratory using Sugar Column (Aminex HPX-87P) using **formulas (2)** and **(3)** (Sluiter et al., 2004). Lignin content was measured by detecting the absorbance of the liquid phase portion under $\lambda = 320$ nm and weighing the insoluble ash after burning. The content of lignin was defined as the sum of acid-soluble and acid-insoluble lignin parts. To demonstrate the removing effect of pretreatment, a component removal rate was introduced, and its definition is shown in **formula (4)**

$$\text{Cellulose content}\,(\text{wt\%}) = \frac{\text{Glucose conc.}\,(\text{g/L}) \times 0.90 \times \text{liquid volume}\,(\text{L})}{\text{Biomass total mass}\,(\text{g})} \times 100\%$$

$$(2)$$

Hemiellulose content (wt%)

$$= \frac{\text{Xylose conc.}\,(\text{g/L}) \times 0.88 \times \text{liquid volume}\,(\text{L})}{\text{Biomass total mass}\,(\text{g})} \times 100\% \quad (3)$$

$$\text{Removal rate}\,(\%) = \frac{m_1 C_1 - m_2 C_2}{m_1 C_1} \times 100\% \quad (4)$$

where m_1 and m_2 are the sample mass before and after hydrolysis, respectively. Similarly, C_1 and C_2 refer to the content of specific component before and after hydrolysis, respectively.

Crystallinity Analysis

The crystallinity of samples was analyzed by X-ray diffractometer (PANalytical V.B., Holland) with Cu radiation ($\lambda = 1.54$Å). The tube voltage and current of the diffractometers were 40 kV and 40 mA. The scanned range of the 2θ angle for X-ray was 5° to 45°. The crystallinity was calculated according to **formula (5)**.

$$\text{CrI}\,(\%) = \frac{I_{002} - I_{am}}{I_{002}} \times 100\% \quad (5)$$

where CrI and I_{002} represent the crystallinity index, I_{002} refers to the peak intensity ($2\theta = 22°$) representative for crystalline and amorphous cellulose, and I_{am} refers to the peak intensity ($2\theta = 18°$) for amorphous cellulose.

Fast Pyrolysis

Fast pyrolysis was performed with semi-batch CDS reactor (Pyroprobe 5200; CDS Analytical, United States) in duplicate. Reaction temperature was set at 500°C, and heating rate was $20\,\text{K}\cdot\text{ms}^{-1}$. High-purity helium was set at 20 mL/min to sweep the fast pyrolyzed volatiles through a 300°C transmission line into the gas chromatography–mass spectrometry (GC-MS) system (GC-7890A, MS-5975C; Agilent Technologies, United States) for separation. Specifically, pyrolysis volatiles were separated by DB-1701 capillary column. GC oven temperature was set to be maintained at 40°C for 3 min and then increased from 40°C to

TABLE 1 | Organic elemental analysis of different sample.

Sample	C (wt%)	H (wt%)	N (wt%)	C/H
Untreated	46.4	5.8	0.1	8.0
PW-220	45.3	6.3	ND	7.2
PW-160	46.0	6.1	ND	7.5
PY -160	46.7	6.1	ND	7.7
BW-160	45.8	6.3	ND	7.3
BY -160	46.1	6.1	ND	7.6

ND, means not detected.

280°C at a rate of 5°C/min and finally at 280°C for 8 min. Mass spectrometer parameters include ion source temperature of 230°C, quadrupole temperature of 150°C, ion source energy of 70 eV, and a scan range (m/z) of 29 to 450 amu. The relative content of compounds was calculated according to **formula (6)**.

$$\text{Relative content (\%)} = \frac{\text{Area of specific compound}}{\text{Total area of all compounds}} \times 100\%$$

(6)

RESULTS AND DISCUSSION

Elemental Analysis

Content of three dominant organic elements in lignocellulose is shown in **Table 1**. In untreated sample, contents of C (46.4 wt%), H (5.8 wt%), and N (0.1 wt%) were detected, where C/H ratio was calculated as 8.0. In pretreated samples, C (45.3–46.7 wt%), H (6.1–6.3 wt%), and N (0.0 wt%) were given, consequently with a dropped C/H ratio to 7.2 to 7.7. It had been reported that C/H ratio in lignin was much higher than those in cellulose and hemicellulose (11.1 compared with 7.5 and 7.2) (Maduskar et al., 2018). Furthermore, microwave and glycerol waste condition was found to be more effective in reducing the organic element contents and C/H ratio than heating and pure glycerol (7.7 vs. 7.3). This discrimination was inferred with relation to the polar nature of glycerol waste to preferably absorb AAEMs ions, derived from the multicomponent of carboxylic acids and metals.

As for AAEMs, it has been reported that these metals were contained massively in natural biomass and had a significant catalytic effect on the pyrolytic reaction that consequently influenced the product distribution. Content of AAEMs is shown in **Table 2**. In untreated biomass, contents of K, Ca,
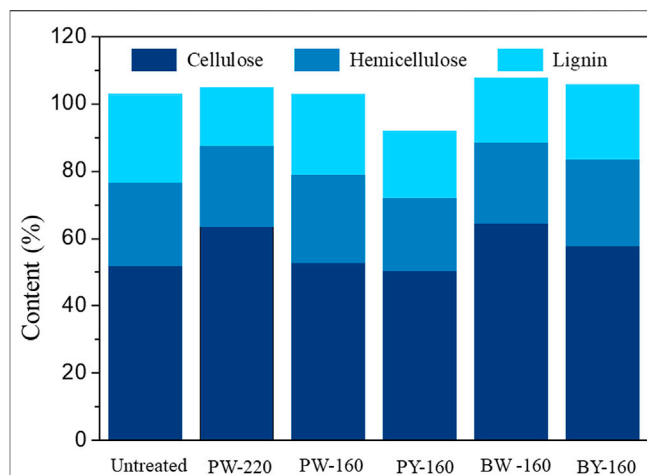
FIGURE 2 | Content of major components after different pretreatment.

Na, and Mg were 3,396.2, 1,055.8, 543.2, and 231.2 mg/kg (kg is the unit of biomass), respectively, and the overall value was 5,226.4 mg/kg. After glycerol treatment, the overall value was decreased to 1,154.9 to 1,903.2 mg/kg with a removal rate of 63.6% to 77.9%. Comparatively, in glycerol waste–pretreated samples, it was decreased more effectively, with 635.8 to 702.0 mg/kg with removal by 86.6% to 87.8%. Furthermore, as the heating temperature was lifted to 220°C, an optimal removal of AAEMs was found with an absolute removal of K up to 97.3% to 99.4%.

Content of AAEMs had a huge impact on the yield of levoglucosan, as trace existence of AAEMs could inhibit the pathway to form levoglucosan while promoting its competitive reaction for the generation of small molecular compounds (Kuzhiyil et al., 2012; Lindstrom et al., 2019). In detail, the levoglucosan formation depended on cleavage of bonds between cellulose units, but during the competitive reaction, the pyranose rings in each monomer were intrinsically opened (Patwardhan et al., 2010). It has been found that AAEMs potentially generate coordinate complex with hydroxyl groups located at the ortho-positions in pyranose rings, leading to its structural stabilization and conversely antagonizing the production of levoglucosan (Shaik et al., 2013). Among AAEMs, K was reported to be the most effective factor to inhibit production of anhydride sugars (Patwardhan et al., 2010). In glycerol waste–treated samples, it was efficiently

TABLE 2 | Inorganic elemental analysis of different samples.

Samples	AAEMs (mg/kg)					Removal rate (%)
	K	Ca	Na	Mg	Total	
Untreated	3,396.2	1,055.8	543.2	231.2	5,226.4	—
PW-220	70.8	656.6	353.5	74.0	1,154.9	77.9
PW-160	59.6	976.0	424.2	143.6	1,603.4	69.3
PY-160	20.7	1,309.7	386.2	186.6	1,903.2	63.6
BW-160	91.0	230.1	353.9	27.0	702.0	86.6
BY-160	66.2	222.2	322.1	25.3	635.8	87.8

FIGURE 3 | Removal rates of major components after different pretreatment.

FIGURE 4 | X-ray diffraction spectra of lignocellulose samples after different pretreatment.
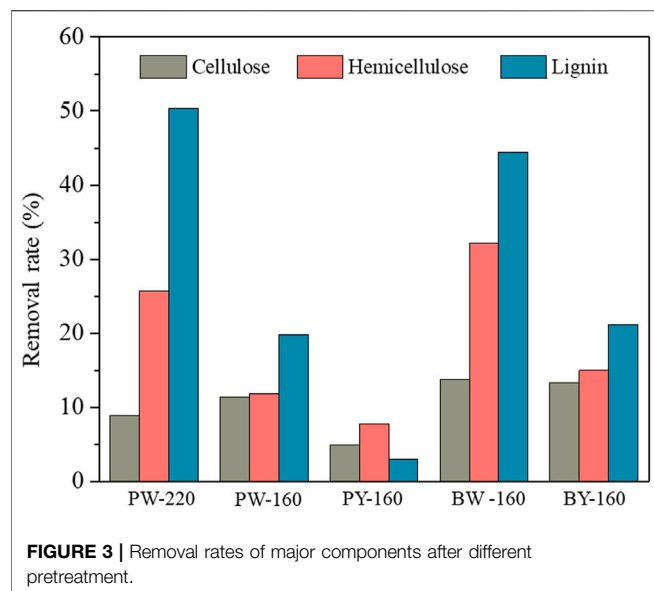
removed compared with other AAEMs, which confirmed the fundamental for the power of glycerol pretreatment to enhance levoglucosan production.

Componential Analysis

Calculated recovery rates of pretreated biomass variously were from 72.9 to 99.0 wt%, which validated the analytical confidence. Distribution of three cellulose, hemicellulose, and lignin in different samples is demonstrated in **Figure 2**. Despite an overall removal effect of three components after pretreatment, the most significantly removed component was lignin, which dropped from 26.4% in natural biomass to 17.1% to 23.8% in pretreated samples and achieved the lowest content in PW-220 sample treated with glycerol waste and microwave. To intuitively compare the removal effect of different pretreatment, componential proportions with recovery rates are shown in **Figure 3**. For PW-220, cellulose and hemicellulose were removed only by 2.0% to 10.5% and 4.6% to 29.5% compared with lignin by 52.6%. After comparing the removal rates in samples treated at 160°C, it was found that the removal of lignin was more efficient in glycerol waste–treated samples than those with pure glycerol treatment. This was probably due to the complex component in glycerol waste, which could facilitate the dissolution of hydrophobic aromatic lignin. According to previous research, glycerol waste derived from biodiesel had a peculiar composition of (Z, Z)-9,12-octadecadienoic acid, n-hexadecenoic acid, and 4-methyl-2-pentanol, which are intermiscible with lignin and also alkaline metals (Wu et al., 2019). In addition, higher temperature was found to favor the delignification in lignocellulose. These results were also consistent with C/H ratio change revealed in previous elemental analysis. It has been reported that removal of lignin could significantly increase the yield of levoglucosan due to the enhanced relative content of cellulose (Miura et al., 2001). Simultaneously, chemical linkages between cellulose–hemicellulose and cellulose–lignin had a profound
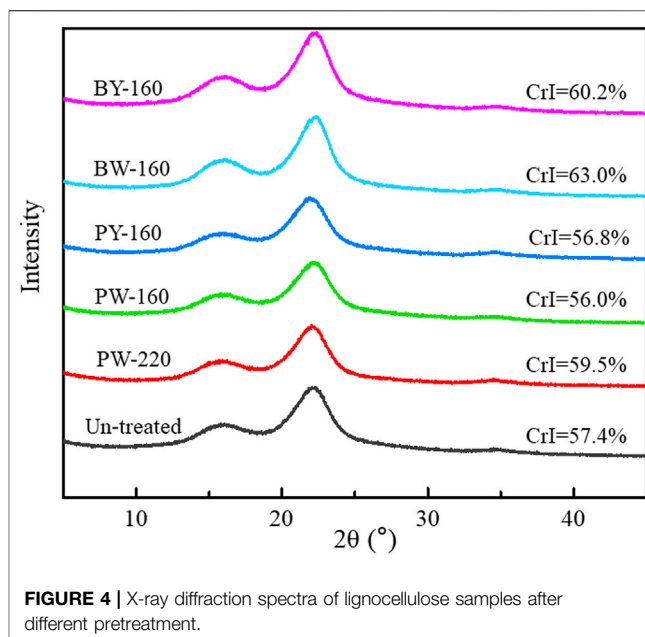
impact on the distribution of pyrolytic products in varying degrees. These covalent bonds between cellulose and lignin would significantly inhibit the production of levoglucosan, instead of promoting the generation of small molecule compounds (Hosoya et al., 2007).

Crystallinity Analysis

X-ray diffraction spectra of lignocellulose before and after glycerol treatment are shown in **Figure 4**. Effects on crystallinity were reported to correlate with both the components and structure of raw material, as well as the treatment conditions including times, temperatures, and ratios of aqueous/solid segments (Jiang et al., 2019). As a referable index of pyrolysate distribution, the crystallinity of biomass was increased from 57.4% to 63.0% after glycerol treatment. The maximum peak was achieved in BW-160 that was treated by glycerol waste with microwave. Notably, an efficient removal of lignin and hemicellulose in this sample aforementioned was consistent with its high crystallinity (Maduskar et al., 2018). In brief, enhancement on crystallinity by microwave was found to be more effective than oil bath heating, and higher temperature favored this effect.

The improvement of crystallinity was attributed to the selective removal of amorphous lignin and hemicellulose segments, simultaneously conserving the crystalline cellulose by glycerol waste with hydrophobic interactions. As levoglucosan was sourced from the cellulose, a conserved crystalline structure could significantly profit its release. As reported, cellulose type I (with a higher crystallinity) tended to be transferred to levoglucosan more efficiently, whereas cellulose with a lower crystallinity favored the conversion to carbonyl compounds or 5-methyl furfural (Mukarakate et al., 2016). Consistent with previous study, microwave was remarkable in removing amorphous components, superior to traditional thermal

TABLE 3 | Relative content of major pyrolytic products from different samples.

Retention time (min)	Compounds	Relative content (%)					
		Untreated	PW-220	PW-160	PY-160	BW-160	BY-160
4.8	Methyl glyoxal	1.8	3.2	3.6	3.4	3.1	3.1
7.0	Acetaldehyde, hydroxy-	4.3	3.5	2.9	2.6	5.3	3.3
8.2	Acetic acid	3.8	0.7	2.9	3.5	0.7	1.5
12.3	Acetic acid, methyl ester	1.5	0.6	1.6	1.4	0.4	0.7
14.3	Furfural	1.3	1.3	1.4	1.5	1.8	1.7
15.7	2(3H)-furanone, 5-methyl-	0.1	0.1	0.1	0.1	0.1	0.1
15.8	2-Furanmethanol	0.3	0.1	0.1	0.2	0.3	0.2
18.0	1,2-Cyclopentanedione	1.7	0.9	1.0	1.1	1.3	1.2
19.7	2(5H)-furanone	0.6	0.2	0.3	0.3	0.6	0.4
22.0	Phenol	0.8	0.2	0.3	0.4	0.3	0.3
22.5	Phenol, 2-methoxy-	1.7	0.5	0.8	0.9	0.8	0.8
24.4	p-Cresol	0.3	0.5	0.6	0.7	0.5	0.5
25.5	Creosol	0.6	0.4	0.6	0.6	0.7	0.5
26.9	Phenol, 4-ethyl-	0.3	0.1	0.3	0.3	0.2	0.3
28.3	2,3-Anhydro-D-mannosan	0.4	0.1	0.6	0.7	0.4	0.6
28.7	1,4:3,6-Dianhydro-α-D-glucopyranose	0.4	0.4	0.3	0.4	0.4	0.4
29.2	Benzofuran, 2,3-dihydro-	8.4	2.8	6.5	6.7	3.1	7.0
29.3	2-Methoxy-4-vinylphenol	3.7	1.8	2.8	3.1	1.9	2.6
30.3	5-Hydroxymethylfurfural	0.2	0.7	0.5	0.6	1.0	0.8
30.7	Phenol, 2,6-dimethoxy-	3.1	0.7	1.3	1.5	1.3	1.5
32.9	3,5-Dimethoxy-4-hydroxytoluene	0.8	0.5	0.8	0.8	0.8	0.8
36.5	(E)-2,6-dimethoxy-4-(prop-1-en-1-yl)-phenol	1.9	1.0	1.7	1.7	1.5	1.5
38.6	Levoglucosan	5.8	32.9	21.5	18.8	27.5	23.0
39.6	Benzaldehyde, 4-hydroxy-3,5-dimethoxy-	0.7	0.2	0.4	0.5	0.4	0.4
41.7	1,6-Anhydro-β-D-glucofuranose	0.2	1.2	0.5	0.5	0.8	0.8

FIGURE 5 | Product distribution for fast pyrolysis of different samples.
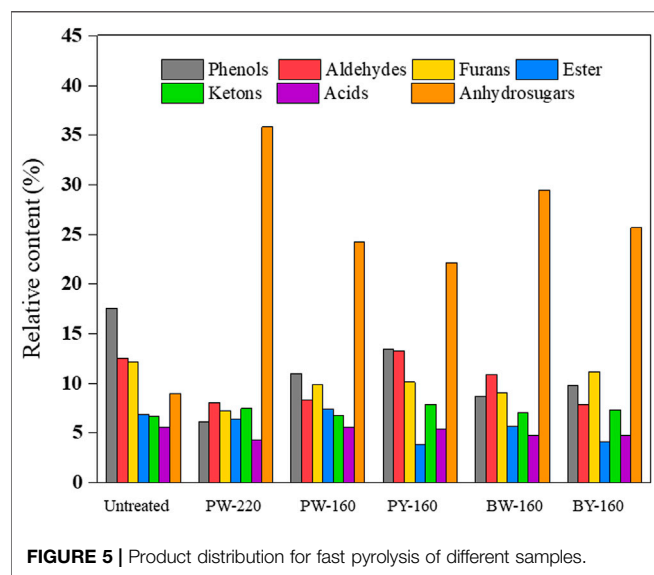
conduction way (Shi et al., 2011). This study also mentioned that removal of amorphous components could improve the pyrolytic yield of levoglucosan, which was demonstrated in the following analysis.

Fast Pyrolysis

Pyrolytic products consisted of several organic compounds from C1 to C5 (listed in **Table 3**). Up to 100 compounds identified by GC-MS were divided into seven groups (acids, esters, furans,

aldehydes, ketones, phenols, and anhydrosugars) in **Figure 5**. There was no apparent change in the product repertoire after different pretreatment. However, the proportion of phenols in pyrolytic products declined from 17.6% to a minimum of 6.2% in glycerol and microwave-treated samples. More detailed, phenol, 2-methoxy-4-vinyl phenol, 2,6-dimethoxy- phenol, and 4-((1E)-3-hydroxy-1-propenyl)-2-methoxy phenol exhibited a decrease of 50% compared with untreated sample. This decrease was attributed to the removal of lignin, as aromatic network was destroyed and removed by glycerol waste. The lowest proportion of phenols in pyrolytic products was achieved in PW-220, which was in accordance with the componential and elemental analysis. Production of fermentative toxic aldehydes was also inhibited, from 4.3% in untreated to minimum 2.6% after glycerol pretreatment. Besides, there was a slight decrease in the production of acids (5.6% before pretreatment and the lowest in PW-220 as 4.3% after pretreatment), especially acetic acid, which had a decrease up to 81.6%. In contrast, an increase in acids such as adenosine and N6-phenylacetic acid was observed conversely. The content of anhydrosugars accounted for 9.0% in untreated sample and 22.2% to 35.9% in pretreated samples. Notably, the production of 1,6-anhydro-β-D-glucofuranose (0.2–1.2%) was negligible as compared with levoglucosan, which constituted the major component of anhydrosugars. Bearing pyrolysis, the content of levoglucosan was only 5.8% in the untreated sample, which was disappointingly less than lignin derivative 2,3-dihydro-benzofuran with content of 8.4%. After glycerol treatment, the latter dropped to 2.8% while significantly raising the generation of levoglucosan. Its content in pyrolytic products was increased by 5.7-fold in PW-220

(32.9%). By comparing PW-220 and PW-160, it could be found that an upper temperature was crucial, with an enhancement of 11.4% in the levoglucosan yield using microwave. Looking back to the elemental and componential analysis, both an effective removal of lignin and AAEMs at high temperatures contributed to this boosted yield. Furthermore, it was found that glycerol waste was more beneficial to the production of levoglucosan. Under the same condition, the pyrolytic yield from glycerol waste–pretreated samples was 27.5% than 21.5% from pure glycerol-treated samples. A similar trend was observed in oil bath–heated samples, as 23.0% came from glycerol waste samples compared with 18.8% pretreated by pure glycerol. There was a noticeable difference in the production of levoglucosan between treatment using microwave and oil bath. After the pure/crude glycerol pretreatment, relative content of levoglucosan from samples heated by microwave was 21.5%/27.5%, compared with 18.8%/23.0% in the oil bath–heated samples. It was concluded that the removal of lignin derived from glycerol was further enhanced by microwave.

Considering all effects mentioned previously, enhanced pyrolytic production of levoglucosan could be explained as (1) the catalytic effect on promoting competitive reactions against levoglucosan production was prohibited with the removal of AAEMs; (2) relative abundance of lignin was increased due to the selective removal of lignin; and (3) the thermal stability was improved with increased crystallinity of reactants (Wu et al., 2019). These effects consequently decreased the conversion of cellulose into small molecule compounds and promoted the formation of levoglucosan. Besides, reactions responsible for the productions of aldehydes were inhibited, which could favor the following fermentation process. This could maximally improve the fermentability of anhydrosugars from pyrolysis, leading to an economical downstream to further valorize biomass products.

CONCLUSION

In this work, glycerol waste was comparatively used to evaluate the ameliorative effect on lignocellulose under microwave or conventional heating method, and the following fast pyrolysis was comprehensively assessed. In elemental, componential, and crystallinity analysis, lignocellulose pretreated by glycerol waste was found to be ameliorated thoroughly. Intriguingly, during fast pyrolysis, production of levoglucosan from microwave-treated samples (32.9%) was far more selective than conventional heating group (18.8%). Furthermore, content of aldehydes with high toxicity to the downstream fermentation was decreased to 2.5 times the untreated after glycerol waste and microwave pretreatment. In summary, this work provided an elaborate insight into the precise manipulation of fast pyrolysis of lignocellulose via glycerol waste and microwave treatment and could provoke more novel approaches to ameliorating lignocellulose in the future.

DATA AVAILABILITY STATEMENT

The original contributions presented in the study are included in the article/supplementary material, further inquiries can be directed to the corresponding author.

AUTHOR CONTRIBUTIONS

YZ and YW performed the experiment and analysed the data. LJ provided the financial support and the supervision. YZ and FC provided the biomass resource and partial experimental instruments. All authors wrote and improved the manuscript.

FUNDING

REFERENCES

Anitha, M., Kamarudin, S. K., and Kofli, N. T. (2016). The Potential of Glycerol as a Value-Added Commodity. *Chem. Eng. J.* 295, 119–130. doi:10.1016/j.cej.2016.03.012

Clomburg, J. M., Crumbley, A. M., and Gonzalez, R. (2017). Industrial Biomanufacturing: The Future of Chemical Production. *Science* 355, aag0804. doi:10.1126/science.aag0804

Hassanpour, M., Abbasabadi, M., Strong, J., Gebbie, L., Te'o, V. S. J., O'Hara, I. M., et al. (2020). Scale-up of Two-step Acid-Catalysed Glycerol Pretreatment for Production of Oleaginous Yeast Biomass from Sugarcane Bagasse by Rhodosporidium Toruloides. *Bioresour. Tech.* 313, 123666. doi:10.1016/j.biortech.2020.123666

Hosoya, T., Kawamoto, H., and Saka, S. (2007). Cellulose-hemicellulose and Cellulose-Lignin Interactions in wood Pyrolysis at Gasification Temperature. *J. Anal. Appl. Pyrolysis* 80, 118–125. doi:10.1016/j.jaap.2007.01.006

Hu, Z., and Wen, Z. (2008). Enhancing Enzymatic Digestibility of Switchgrass by Microwave-Assisted Alkali Pretreatment. *Biochem. Eng. J.* 38, 369–378. doi:10.1016/j.bej.2007.08.001

Jabareen, L., Maruthapandi, M., Saravanan, A., and Gedanken, A. (2021). Effective Degradation of Cellulose by Microwave Irradiation in Alkaline Solution. *Cellulose* 28, 11275–11285. doi:10.1007/s10570-021-04274-y

Jiang, L.-Q., Fang, Z., Zhao, Z.-L., Zheng, A.-Q., Wang, X.-B., and Li, H.-B. (2019). Levoglucosan and its Hydrolysates via Fast Pyrolysis of Lignocellulose for Microbial Biofuels: A State-Of-The-Art Review. *Renew. Sust. Energ. Rev.* 105, 215–229. doi:10.1016/j.rser.2019.01.055

Jiang, L.-q., Wu, Y.-x., Wu, N.-n., Zhong, H. q., Zhang, Y.-c., Zhao, Z.-l., et al. (2020). Selective Saccharification of Microwave-Assisted Glycerol Pretreated Corncobs via Fast Pyrolysis and Enzymatic Hydrolysis. *Fuel* 265, 116965. doi:10.1016/j.fuel.2019.116965

Jiang, L., Wu, N., Zheng, A., Wang, X., Liu, M., Zhao, Z., et al. (2017). Effect of Glycerol Pretreatment on Levoglucosan Production from Corncobs by Fast Pyrolysis. *Polymers* 9, 599. doi:10.3390/polym9110599

Kuzhiyil, N., Dalluge, D., Bai, X., Kim, K. H., and Brown, R. C. (2012). Pyrolytic Sugars from Cellulosic Biomass. *ChemSusChem* 5, 2228–2236. doi:10.1002/cssc.201200341

Kwon, G.-J., Kim, D.-Y., Kimura, S., and Kuga, S. (2007). Rapid-cooling, Continuous-Feed Pyrolyzer for Biomass Processing: Preparation Of Levoglucosan From Cellulose and Starch. *J. Anal. Appl. Pyrolysis* 80, 1–5. doi:10.1016/j.jaap.2006.12.012

Lin, C.-Y., and Lu, C. (2021). Development Perspectives of Promising Lignocellulose Feedstocks for Production of Advanced Generation Biofuels: A Review. *Renew. Sust. Energ. Rev.* 136, 110445. doi:10.1016/j.rser.2020.110445

Lindstrom, J. K., Proano-Aviles, J., Johnston, P. A., Peterson, C. A., Stansell, J. S., and Brown, R. C. (2019). Competing Reactions Limit Levoglucosan Yield during Fast Pyrolysis of Cellulose. *Green. Chem.* 21, 178–186. doi:10.1039/c8gc03461c

Maduskar, S., Maliekkal, V., Neurock, M., and Dauenhauer, P. J. (2018). On the Yield of Levoglucosan from Cellulose Pyrolysis. *ACS Sust. Chem. Eng.* 6, 7017–7025. doi:10.1021/acssuschemeng.8b00853

Miura, M., Kaga, H., Yoshida, T., and Ando, K. (2001). Microwave Pyrolysis of Cellulosic Materials for the Production of Anhydrosugars. *J. Wood Sci.* 47, 502–506. doi:10.1007/BF00767906

Mukarakate, C., Mittal, A., Ciesielski, P. N., Budhi, S., Thompson, L., Iisa, K., et al. (2016). Influence of crystal Allomorph and Crystallinity on the Products and Behavior of Cellulose during Fast Pyrolysis. *ACS Sust. Chem. Eng.* 4, 4662–4674. doi:10.1021/acssuschemeng.6b00812

Patwardhan, P. R., Satrio, J. A., Brown, R. C., and Shanks, B. H. (2010). Influence of Inorganic Salts on the Primary Pyrolysis Products of Cellulose. *Bioresour. Tech.* 101, 4646–4655. doi:10.1016/j.biortech.2010.01.112

Qian, L., Xu, F., Liu, S., Lv, G., Jiang, L., Su, T., et al. (2021). Selective Production of Levoglucosenone by Catalytic Pyrolysis of Cellulose Mixed with Magnetic Solid Acid. *Cellulose* 28, 7579–7592. doi:10.1007/s10570-021-04010-6

Shaik, S. M., Sharratt, P. N., and Tan, R. B. H. (2013). Influence of Selected mineral Acids and Alkalis on Cellulose Pyrolysis Pathways and Anhydrosaccharide Formation. *J. Anal. Appl. Pyrolysis* 104, 234–242. doi:10.1016/j.jaap.2013.07.010

Shen, X.-J., Wen, J.-L., Mei, Q.-Q., Chen, X., Sun, D., Yuan, T.-Q., et al. (2019). Facile Fractionation of Lignocelluloses by Biomass-Derived Deep Eutectic Solvent (DES) Pretreatment for Cellulose Enzymatic Hydrolysis and Lignin Valorization. *Green. Chem.* 21, 275–283. doi:10.1039/c8gc03064b

Shi, J., Pu, Y., Yang, B., Ragauskas, A., and Wyman, C. E. (2011). Comparison of Microwaves to Fluidized Sand Baths for Heating Tubular Reactors for Hydrothermal and Dilute Acid Batch Pretreatment of Corn stover. *Bioresour. Tech.* 102, 5952–5961. doi:10.1016/j.biortech.2011.03.027

Sluiter, A., Hames, B., Ruiz, R. O., Scarlata, C., Sluiter, J., Templeton, D., et al. (2004). Determination of Structural Carbohydrates and Lignin in Biomass. *Biomass Anal. Technol. Team Lab. Anal. Proced.*, 1–14.

Vivek, N., Sindhu, R., Madhavan, A., Anju, A. J., Castro, E., Faraco, V., et al. (2017). Recent Advances in the Production of Value Added Chemicals and Lipids Utilizing Biodiesel Industry Generated Crude Glycerol as a Substrate - Metabolic Aspects, Challenges and Possibilities: An Overview. *Bioresour. Tech.* 239, 507–517. doi:10.1016/j.biortech.2017.05.056

Wu, Y., Jiang, L., Lin, Y., Qian, L., Xu, F., Lang, X., et al. (2019). Novel Crude Glycerol Pretreatment for Selective Saccharification of Sugarcane Bagasse via Fast Pyrolysis. *Bioresour. Tech.* 294, 122094. doi:10.1016/j.biortech.2019.122094

Xie, R., Tu, M., and Elder, T. (2016). Substituent Effect of Phenolic Aldehyde Inhibition on Alcoholic Fermentation by *Saccharomyces cerevisiae*. *Energy Fuels* 30, 3078–3084. doi:10.1021/acs.energyfuels.5b03034

Zaldivar, J., Martinez, A., and Ingram, L. O. (1999). Effect of Selected Aldehydes on the Growth and Fermentation of ethanologenic*Escherichia Coli*. *Biotechnol. Bioeng.* 65, 24–33. doi:10.1002/(sici)1097-0290(19991005)65:1<24:aid-bit4>3.0.co;2-2

Zhang, J., Choi, Y. S., Yoo, C. G., Kim, T. H., Brown, R. C., and Shanks, B. H. (2015). Cellulose-hemicellulose and Cellulose-Lignin Interactions during Fast Pyrolysis. *ACS Sust. Chem. Eng.* 3, 293–301. doi:10.1021/sc500664h

Zhou, M., Eberhardt, T. L., Cai, B., Hse, C.-Y., and Pan, H. (2017). Dynamic Dielectric Properties of a Wood Liquefaction System Using Polyethylene Glycol and Glycerol. *ACS Sust. Chem. Eng.* 5, 1123–1131. doi:10.1021/acssuschemeng.6b02447

Synthesis of Hierarchical Porous SAPO-34 and Its Catalytic Activity for 4,6-Dimethyldibenzothiophene

Hua-Qin Wang[1], Yun-Qi Cui[1], Ya-Long Ding[1]*, Mei Xiang[2], Pei Yu[1] and Rong-Qiang Li[1]*

[1]College of Chemistry and Pharmaceutical Engineering, Huanghuai University, Zhumadian, China, [2]School of Chemical Engineering and Materials, Changzhou Institute of Technology, Changzhou, China

Zeolite SAPO-34 has been widely used in the industry because of its special pore structure and wide distribution of acid sites in the pore channel. However, traditional SAPO-34 with a small pore size suffers from carbon deposition and deactivation in catalytic reactions, and its inability to catalytically convert bulky organic molecules limits its industrial application. Meanwhile, impurities of SAPO-5, which have weak acidity leading to rapid catalyst deactivation, appear in SAPO-34 zeolite. Therefore, it is of great significance to synthesize SAPO-34 zeolite with a mesoporous pore structure, which can significantly improve the transfer of molecules in zeolites. In this paper, SAPO-34 zeolite with a hierarchical pore structure was synthesized, and its hydrodesulfurization performance for 4,6-dimethyldibenzothiophene (4,6-DMDBT) was studied in a fixed bed reactor. The characteristic results show that BET-specific surface area, micropore volume, and mesoporous volume of synthesized SAPO-34 are $754 \, m^2 \, g^{-1}$, 0.25, and $0.23 \, cm^3 \, g^{-1}$ respectively, and the pore size is mainly concentrated at 4 nm. The catalytic conversion of 4,6-DMDMT with Co- and Mo-supported SAPO-34 is about 83%, which is much higher than the catalytic performance of Al_2O_3.

Keywords: hierarchical, zeolite, SAPO-34, material and process optimization, 4,6-dimethyldibenzothiophene (4,6-DMDBT)

INTRODUCTION

Aluminophosphate (AlPO) zeolite is composed of alternating AlO_4 and PO_4 tetrahedrons (Wilson et al., 1982), and has no Bronsted acidity due to the absence of exchangeable electric charge in its framework. Compared with the silicoaluminite zeolite, AlPO zeolite has rich diverse varieties and strong adjustability (Rakoczy et al., 1999), but the small pore size limits its application in the catalytic conversion of bulky organic molecules (Carreon et al., 2008). In the synthesis of silica alumina zeolites, the introduction of a mesoporous structure using surfactant as a structure directing agent (SDA) makes it possible to synthesize mesoporous AlPO zeolite. In 1993, Czametzki first synthesized mesoporous AlPO zeolite with weak catalytic ability because of charge neutrality or weak acidity of the zeolite framework (Kranshaar-Czametzki et al., 1993). The type of mesoporous aluminophosphate zeolite varies with synthesis conditions. The formation of layered mesoporous $AlPO_4$ is more favorable at higher crystallization temperature and the initial solution containing SiO_4. Tiemann et al. firstly reported the synthesis of mesoporous layered aluminum phosphate material SCS-22, but the mesoporous layered structure collapsed easily during material roasting process (Tiemann and Fröba, 2001). Afterwards, Fu et al. synthesized layered mesoporous aluminum phosphate material by using long-chain alkylammonium bromide $[C_nH_{2n+1}(CH_3)_3]NBr$ (Fu et al.,

1995). Kimura et al. found that pure layered and hexagonal mesoporous zeolite can be synthesized by using hexadecyl ammonium chloride as SDA (Kimura et al., 1999).

As for the absence of acidity resulting from lack of exchangeable electric charge in framework, doping other atoms into the framework of aluminophosphate zeolites is one of the effective methods to improve the catalytic activity of zeolites. Zhao et al. firstly used the synthesis method of mesoporous aluminophosphate zeolite (AlPO) in a mesoporous silicoaluminophosphate zeolite field and found that the strong ion pairing effect between sodium ions and aluminum phosphate species was harmful to the formation of a mesoporous structure (Zhao et al., 1997; Luan et al., 1998). Compared with mesoporous silicon materials, mesoporous phosphorous aluminum materials started late, and there are few reports on their applications, but their excellent catalytic activity and the easy introduction of metal atoms have attracted the special attention of researchers. For example, mesoporous Fe-AlPO can efficiently catalyze the oxidation of cyclohexane under neutral conditions, and the catalyst has a long service life. Mesoporous Co-AlPO has high selectivity for the hydrogenation of nitro and carbonyl compounds. Cr-AlPO and Ti-AlPO zeolites have high catalytic activity for the oxidation of cyclohexane and the alkyl substitution of carbonyl compounds under neutral conditions, respectively.

With the introduction of Si atoms into the framework of aluminophosphate zeolites where Si atoms can enter the framework of zeolites by substituting Al or P atoms, named SAPO zeolites (Lok et al., 1984; Chen et al., 1999; Arstad and Kolboe, 2001), the acidity and catalytic performance have been greatly improved as a result of the presence of exchangeable electric charges, though the thermal stability of the zeolites decreased (Numpilai et al., 2021). Like mesoporous aluminosilicate zeolites, mesoporous SAPO zeolites have potential applications in the fields of catalyst, drug delivery, and gas and liquid adsorption, and have important application value in the fields of chemical industry, biotechnology, and environmental energy, among others (Song et al., 2001; Hwang et al., 2016). SAPO-34 is a member of a series of SAPO zeolites, where eight-membered rings in the crystal are linked into an ellipsoidal cavity. The crystal structure of SAPO-34 is similar to that of chabazite, belonging to the CHA structure, and the regularly arranged cages form three-dimensional channels with 8-ring openings of 0.34 nm (Chen et al., 2007; Tian et al., 2015; Jiang et al., 2021; Lin et al., 2021). SAPO-34 crystal has high hydrothermal stability, and its special eight-membered ring pore structure can effectively inhibit the formation of aromatics, and has a high selectivity for light olefins, up to 90% (Hwang et al., 2019).

Traditional microporous SAPO-34 is favored by researchers because of its high catalytic activity, high selectivity, and good hydrothermal stability in MTO reaction (Liang, et al., 2021). However, traditional SAPO-34 has a small pore size and is prone to carbon deposition and deactivation in catalytic reaction of bulky organic molecules, which cannot meet the needs of the development of the chemical industry (Zhong et al., 2017; Kim et al., 2021; Zhang et al., 2021). To cope with these shortcomings,

several strategies have been developed to improve the diffusion limitation of SAPO-34, such as synthesis of nano-sized mesopore-containing SAPO-34 (Yang et al., 2014; Sun et al., 2018; Mi et al., 2021). Hierarchical porous SAPO-34 can be synthesized by post-treatment, such as acid or alkali treatment, in which the skeleton cations were removed selectively. Besides, the hierarchical porous SAPO-34 can also be synthesized by using a hard template method, which often refers to the application of mesoporous carbon particles or carbon nanotubes, and a soft template method, which refers to the use of organo-silane, surfactants, and polymers (Schmidt et al., 2012; Rimaz et al., 2016; Varzaneh et al., 2016). Although some researchers reported the synthesis of mesoporous SAPO-34 (Li et al., 2014; Shi et al., 2021), the expensive long-chain amines used in the synthesis method seriously hindered its industrial application (Sun et al., 2021; Xuan et al., 2021). In this paper, hierarchical porous SAPO-34 was synthesized by using diethylamine (DEA) and morpholine as SDA, silicone quaternary ammonium salt $\{[(C_2H_5O)_3SiC_3H_6N^+(CH_3)_2C_{18}H_{37}]Br\}$ as mesoporous SDA, and phosphoric acid, pseudo boehmite, and silica sol as phosphorus source, aluminum source, and silicon source, respectively. The effects of the amount of DEA and morpholine, phosphoric acid, silica sol, and silicone quaternary ammonium salt on the synthetic products were investigated. The hydrodesulfurization of 4,6-dimethyl dibenzothiophene (4,6-DMDBT), which is difficult to remove from diesel fraction, was studied in a fixed bed reactor with hierarchical porous SAPO-34-supported Co and Mo metal sulfide as catalysts.

EXPERIMENTAL SECTION

Synthesis of Microporous SAPO-34
Synthesis of Microporous SAPO-34 Using Organic Silicon Source and Organic Aluminum Source
The solution composed of a certain amount of DEA and tetraethyl orthosilicate (TEOS) was added into another solution that contained a certain amount of phosphoric acid (H_3PO_4, 85 wt%) and aluminum isopropoxide solution, and the material ratio of the final white mushy mixture was 1.0 Al_2O_3:1.0 P_2O_5:0.6 SiO_2:2.0 DEA:50 H_2O, and then the mixture was transferred into an autoclave lined with polytetrafluoroethylene. After the autoclave was kept at 200°C for 48 h, products obtained were filtered, dried at 120°C for 12 h, and roasted at 550°C for 4 h to remove organic SDA. The obtained white powder was microporous SAPO-34, labeled as SAPO-34-M1.

Synthesis of Microporous SAPO-34 Using Inorganic Silicon Source and Inorganic Aluminum Source
Some phosphoric acid (H_3PO_4, 85%) was added dropwise into a certain amount of pseudo boehmite solution, and stirred at room temperature for 2 h. Then, some silica sol is added to the system, followed by the addition of a certain amount of DEA. In the process of dropping DEA, the reaction system thickened first, then diluted, and finally showed a white mushy mixture with the

same material ratio as 1.0 Al_2O_3:1.0 P_2O_5:0.6 SiO_2:2.0 DEA: 50 H_2O. Subsequent treatment is the same as synthesis of microporous SAPO-34 using organic silicon source and organic aluminum source, and the obtained white powder was also microporous SAPO-34, labeled as SAPO-34-M2.

Synthesis of Hierarchical Porous SAPO-34

Except for the fact that a certain amount of mesoporous SDA $\{[(C_2H_5O)_3SiC_3H_6N^+(CH_3)_2C_{18}H_{37}]Br\}$ was added into the synthesis system before the addition of DEA, the other synthesis steps are the same as the synthesis of microporous SAPO-34 using inorganic silicon source and inorganic aluminum source. The obtained white powder was hierarchical porous SAPO-34, labeled as HSAPO-34.

Preparation of Catalysts

The zeolite sample was soaked with solution of ammonia solution of $(NH_4)_2MoO_4$, $Co(NO_3)_2$, and complexing agent EDTA by equal volume impregnation method. The impregnated sample was kept at room temperature for 12 h, then at 100°C for 12 h, and then pressed and ground to particles whose diameter was between 0.245 and 0.350 mm. Subsequently, the sample was heated to 400°C in H_2S atmosphere and maintained for 3 h to obtain the corresponding catalyst.

Characterization and Catalytic Performance of SAPO-34

The x-ray powder diffraction (XRD) of SAPO-34 was carried out on a RIGAKU ultimate V diffractometer, and the ray emission source was Cu Target Kα. The radiation tube voltage and current are 40 kV and 40 mA, respectively. The scanning speed is $2°\cdot min^{-1}$, and the scanning range is 5–40°. The N_2 adsorption–desorption isotherm of SAPO-34 was characterized on a micromeritics ASAP2020 analyzer at liquid nitrogen temperature. The sample was pretreated under vacuum at 350°C for 10 h before analysis. The specific surface area of the sample was calculated by the Barrett–Emmett–Teller (BET) method, and the pore size distribution was calculated by the Barrett–Joyner–Halenda (BJH) method. The scanning electron microscopy (SEM) image was obtained from JSM-600, and the sample was ground with agate mortar and sprayed with gold before the test.

The catalytic performance of catalyst was conducted on a fixed bed reactor. A small amount of quartz cotton is padded at the bottom of the fixed bed reactor to prevent the catalyst from flowing out of the constant temperature zone of the reactor. The prepared catalyst is mixed with quartz sand with the same size of 0.245–0.350 mm, so that the catalyst can be well dispersed, so as to prevent the catalyst from aggregation and from making contact with the reactant efficiently during the reaction process. After the mixture of catalyst and quartz sand is loaded into the reactor, a small amount of quartz sand and quartz cotton are successively loaded on the top of the reactor, which can stabilize the flow speed of the reaction mixture in the reaction process. 4,6-Dimethyldibenzothiophene was dissolved in decahydronaphthalene to prepare a solution with a mass fraction of 4,6-DMDBT of 0.5 wt% as reaction mixture, and
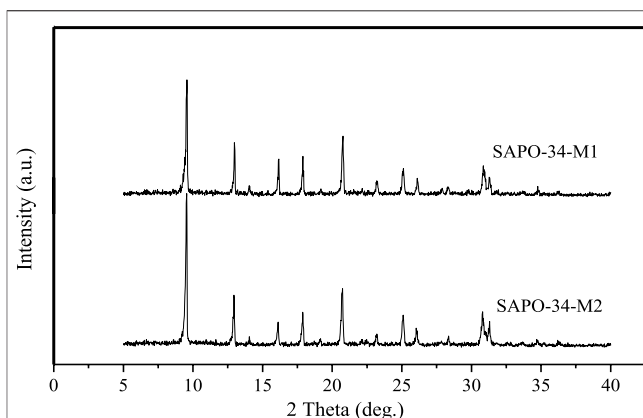
FIGURE 1 | Comparison of XRD pattern of SAPO-34-M1 and SAPO-34-M2.

hydrodesulfurization reaction was carried out at 290°C and 5.0 MPa. Meanwhile, γ-Al_2O_3 was also used as the catalyst support for the same catalytic reaction.

RESULTS AND DISCUSSION

Characterization of SAPO-34 Zeolite
X-Ray Diffraction
Effects of Different Raw Materials
The main raw materials for the synthesis of SAPO-34 are silicon source, aluminum source, and phosphoric acid. Fu Ye et al. studied SAPO-34 prepared with different silicon and aluminum sources and found that the zeolite synthesized with inorganic silicon and aluminum sources has the highest crystallinity, while the zeolite synthesized with organic silicon and aluminum sources has the lowest crystallinity, and the effect of silicon source on crystallinity is smaller than that of the aluminum source (Fu et al., 2001). Popova et al. further studied the effect of SAPO-34 samples synthesized from different silicon and aluminum sources on MTO reaction, and experimental results showed that the samples synthesized from organic silicon and aluminum sources inactivated faster in the reaction (Popova et al., 1998). In contrast, the samples synthesized from inorganic silicon and aluminum sources had better crystallinity and higher stability. Herein, **Figure 1** shows the comparison of XRD patterns of SAPO-34-M1 and SAPO-34-M2 with the same material ratio as 1.0 Al_2O_3:1.0 P_2O_5:0.6 SiO_2:2.0 DEA:50 H_2O, which were synthesized from organic silicon and aluminum sources (TEOS and aluminum isopropoxide) and inorganic silicon and aluminum sources (silica sol and pseudo boehmite), respectively. SAPO-34-M2 is taken as the reference and its crystallinity is assumed to be 100%; the relative crystallinity of SAPO-34-M1 is calculated to be 95%. This result shows that SAPO-34-M2 synthesized from an inorganic silicon source (silica sol) and an inorganic aluminum source (pseudo boehmite) also has high crystallinity.

Influence of Material Ratio
In the synthesis of SAPO-34, the material ratio has a great influence on the type of molecular sieve of the synthetic

FIGURE 2 | Different XRD patterns of SAPO-34 zeolites synthesized with different silico content when inorganic silicon source (silica sol) and inorganic aluminum source (pseudo boehmite) are used.

FIGURE 3 | XRD patterns of SAPO-34 samples synthesized with different SDA.
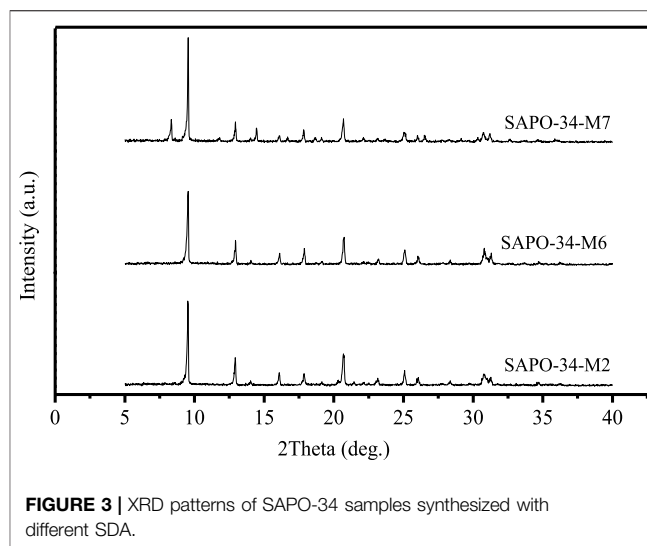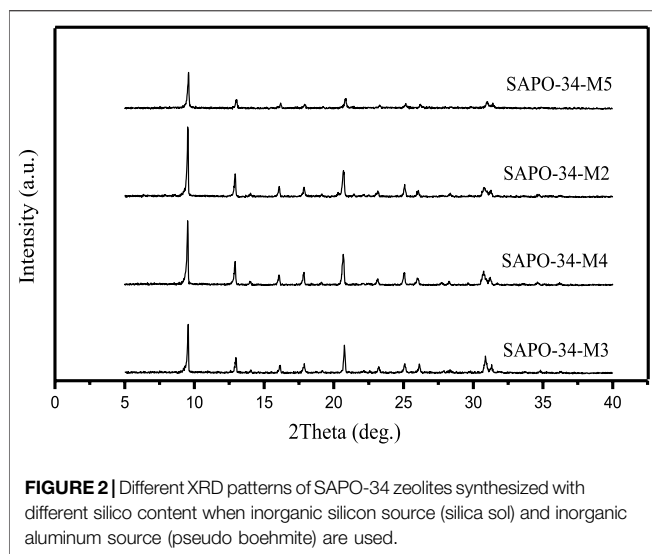
product. Li et al. pointed out that when the molar ratio of phosphorus to aluminum in the synthetic system is greater than 1, the synthetic product is mainly phosphoaluminate; when this molar ratio is less than 1, a series of SAPO-34 zeolite can be synthesized (Li et al., 1987). It is also pointed out that when TEAOH/P_2O_5 in the system is 2.0–3.0, the synthetic product is pure SAPO-34, and the increase of the amount of TEAOH is beneficial to the synthesis of SAPO-34. Even when the silicon source, aluminum source, phosphorus source, and SDA are the same, different types of SAPO zeolite, such as SAPO-11, SAPO -31, SAPO-34, and SAPO-41, can be synthesized when the material ratio is different. **Figure 2** is the XRD pattern of SAPO-34 zeolites synthesized with DEA as SDA when the silicon content in the material was different. The material compositions of each sample were as follows:

1.0 Al_2O_3:1.0 P_2O_5:0.1 SiO_2:2.0 DEA:50 H_2O (SAPO-34-M3).
1.0 Al_2O_3:1.0 P_2O_5:0.3 SiO_2:2.0 DEA:50 H_2O (SAPO-34-M4).
1.0 Al_2O_3:1.0 P_2O_5:0.6 SiO_2:2.0 DEA:50 H_2O (SAPO-34-M2).
1.0 Al_2O_3:1.0 P_2O_5:1.0 SiO_2:2.0 DEA:50 H_2O (SAPO-34-M5).

The calculation shows that the crystallinity of the sample is as follows: SAPO-34-M2 (100%) > B (95%) > A (94%) > D (79%). When the silicon content in the material is small (A and B), the crystallinity of the sample is equivalent to C, and when the silicon content in the material increases to a certain extent, the crystallinity (D) of the sample decreases.

Effects of Different SDA

The type and amount of SDA are crucial to the formation of the crystal structure, because SDA not only guides the formation of the crystal structure, but also controls the distribution of silicon atoms on zeolite skeleton to a certain extent. Li et al. used the mixture of triethylamine (TEA) and DEA as SDA, the crystallinity of synthesized SAPO-34 was lower than that obtained by DEA alone, and the crystallinity of SAPO-34 decreased with the increase in the amount of TEA in the mixed SDA (Li et al., 2005). However, the specific surface area and pore volume of SAPO-34 zeolite synthesized with DEA as

FIGURE 4 | The XRD spectra of SAPO-34 samples synthesized at different crystallization temperatures and times.
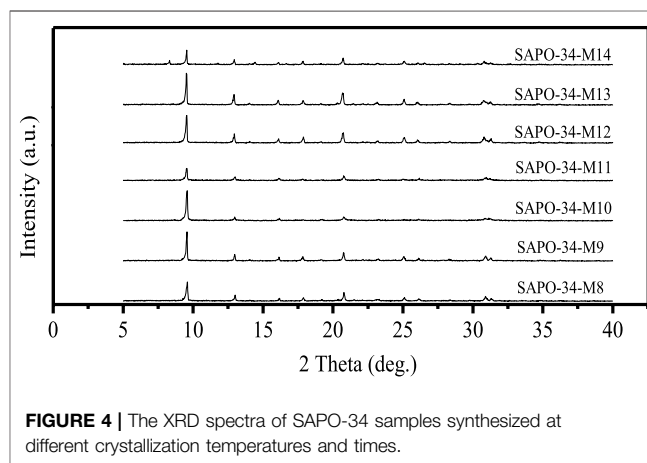
SDA alone are lower than those synthesized with TEA as SDA alone. **Figure 3** shows the XRD patterns of SAPO-34 zeolite synthesized with DEA (SAPO-34-M2), morpholine (SAPO-34-M6), and TEAOH (SAPO-34-M7) as SDA. It can be seen that when DEA was used as SDA, the crystallinity of the product is the highest. In contrast, the crystallinity of the product decreases when morpholine (MOR) is used as SDA, and when TEAOH is used as SDA, the heterophase of SAPO-5 zeolite appears in the product. Therefore, in this paper, DEA is mainly used as the SDA for the synthesis of SAPO-34 zeolite.

Effect of Crystallization Conditions

The temperature and time of crystallization are important factors affecting the synthesis of all zeolites, because there are obvious differences between the skeletons of different zeolites, and the guiding mechanism of different SDAs is also different. With the increase in crystallization temperature, the induction period in the synthesis of zeolite will be shortened, and the formation and growth of crystals will be accelerated, but excessive crystallization temperature also provides conditions for the formation of the
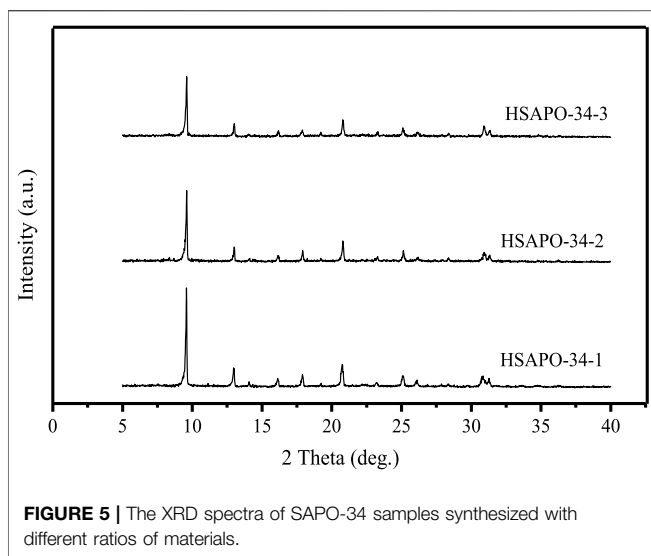
FIGURE 5 | The XRD spectra of SAPO-34 samples synthesized with different ratios of materials.

impure phase of zeolite. **Figure 4** shows the XRD spectra of samples obtained with silica sol and pseudo boehmite as raw materials and a material ratio of 1.0 Al_2O_3:1.0 P_2O_5:0.6 SiO_2:2.0 DEA:50 H_2O at different crystallization temperatures and times: SAPO-34-M8: 150°C–24 h + 200°C–12 h; SAPO-34-M9: 150°C–24 h + 200°C–12 h; SAPO-34-M10: 170°C–24 h + 200°C–24 h; SAPO-34-M11: 180°C–72 h; SAPO-34-M12: 200°C–24 h; SAPO-34-M13: 200°C–48 h; SAPO-34-M14: 200°C–72 h. It can be seen that when crystallization was conducted in two stages (SAPO-34-M8, SAPO-34-M9, and SAPO-34-M10), the170°C of temperature of pre-crystallization (SAPO-34-M10) was better than 150°C (SAPO-34-M8, SAPO-34-M9), and the24 h of crystallization time for the second stage of crystallization is better (SAPO-34-M9). Moreover, when one-step crystallization is used, the crystallinity of obtained SAPO-34 is very low when the crystallization temperature is 180°C (SAPO-34-M11), so the crystallization temperature was raised to 200°C. The results showed that 48 h of crystallization time (SAPO-34-M13) brought about higher crystallinity than 24 h (SAPO-34-M12), but heterophase of SAPO-5 appeared in the product when the crystallization time is extended to 72 h (SAPO-34-M14). In conclusion, the better crystallization condition is 200°C–48 h (SAPO-34-M13).

Given all of those above, the conditions for synthesizing SAPO-34 zeolite with a mesoporous structure are as follows: silica sol and pseudo boehmite are used as inorganic silicon and aluminum sources, phosphoric acid is used as phosphorus source, DEA is used as microporous template, and organosilane DM-3010 is used as mesoporous SDA. The XRD spectra of the obtained HSAPO-34-1 zeolite molecular sieve is shown in **Figure 5**. It can be seen that the sample HSAPO-34-1 has higher crystallinity compared with the other two samples. It is proven that the addition of mesoporous SDA, namely, DM-3010, does not affect the crystallinity of the product (generally, the addition of mesoporous SDA will affect the formation of the zeolite crystal framework and decrease the crystallinity of the obtained sample, even to an amorphous product). The optimal

initial raw material ratios are 1.0 Al_2O_3:0.6 SiO_2:2.0 P_2O_5:3.1 DEA:90 H_2O for HSAPO-34-1, 1.0 Al_2O_3:1.0 SiO_2:1.5 P_2O_5:2.6 DEA:100 H_2O for HSAPO-34-2, and 1.0 Al_2O_3:0.6 SiO_2:1.1 P_2O_5: 2.2 DEA:65 H_2O for HSAPO-34-3. The volume ratio of DM-3010 to silica sol was 1:2 for synthesis of all hierarchical porous SAPO-34 zeolites.

N$_2$ Adsorption–Desorption
The N_2 adsorption–desorption results of HSAPO-34-1, HSAPO-34-2, and HSAPO-34-3 indicate that the existence of a mesoporous structure of HSAPO-34 zeolite and the pore size of HSAPO-34 is mainly concentrated at 4 nm, which provides favorable conditions for the catalytic conversion of a bulky organic molecule, such as 4,6-DMDBT, in the pore channel of zeolite. The texture properties of HSAPO-34-1, HSAPO-34-2, and HSAPO-34-3 are listed in **Table 1**. Compared with HSAPO-34-1, the BET-specific surface area and external surface area of both HSAPO-34-2 and HSAPO-34-3 are almost the same as that of HSAPO-34-1, but the micropore volume and mesopore volume decrease in varying degrees, which may result from the DEA content reduction in raw materials of HSAPO-34-2 and HSAPO-34-3, leading to the decrease in crystallinity and to the decrement of micropore volume of the sample. Besides that, the reduction of silicon content in the raw material reduces the silicon content in zeolite skeleton, which further reduces the interaction of zeolite skeleton and organosilane DM-3010, resulting in the decrement of mesoporous pore volume.

Scanning Electron Microscope
Figure 6 shows the SEM images of HSAPO-34-1, HSAPO-34-2, and HSAPO-34-3. It can be seen that the size of the three samples is uniform, about 2–3 μm. Along with the increase in the mesoporous volume of the samples in the order of HSAPO-34-3, HSAPO-34-2, and HSAPO-34-1, the surface smoothness of the three samples decreases in turn, and the regular cube shape of the samples gradually becomes blurred, which is the result of the increase of mesoporous volume in zeolite skeleton.

Transmission Electron Microscope
Figure 7 shows the TEM images of HSAPO-34-1. We can see many white small bright spots, that is, the mesoporous channel in HSAPO-34-1 with a size of about 5 nm, which is consistent with the N_2 adsorption–desorption results about the pore diameter (4 nm). The TEM images give direct evidence for the existence of a mesoporous structure in HSAPO-34-1.

Catalytic Performance of Hydrodesulfurization
The aim of the hydrodesulfurization process is to catalyze the sulfur-containing compounds in fuel oil at a certain temperature and pressure to convert them into corresponding hydrocarbons and H_2S, so as to reduce the sulfur content in raw materials. The catalyst is the key factor for the efficiency of hydrodesulfurization. At present, Al_2O_3-

TABLE 1 | The texture properties of HSAPO-34-1, HSAPO-34-2, and HSAPO-34-3.

Samples	S_{BET}^{a} (m^2/g)	S_{ext}^{b} (m^2/g)	V_{micro}^{c} (cm^3/g)	V_{meso}^{d} (cm^3/g)
HSAPO-34–1	754	133	0.25	0.23
HSAPO-34–2	758	148	0.20	0.20
HSAPO-34–3	580	165	0.17	0.22

[a]BET, specific surface area.
[b]External surface area (calculated from a pore diameter greater than 2 nm).
[c]Microporous volume (calculated from a pore diameter smaller than 2 nm).
[d]Mesoporous volume (calculated from a pore diameter greater than 2 nm).
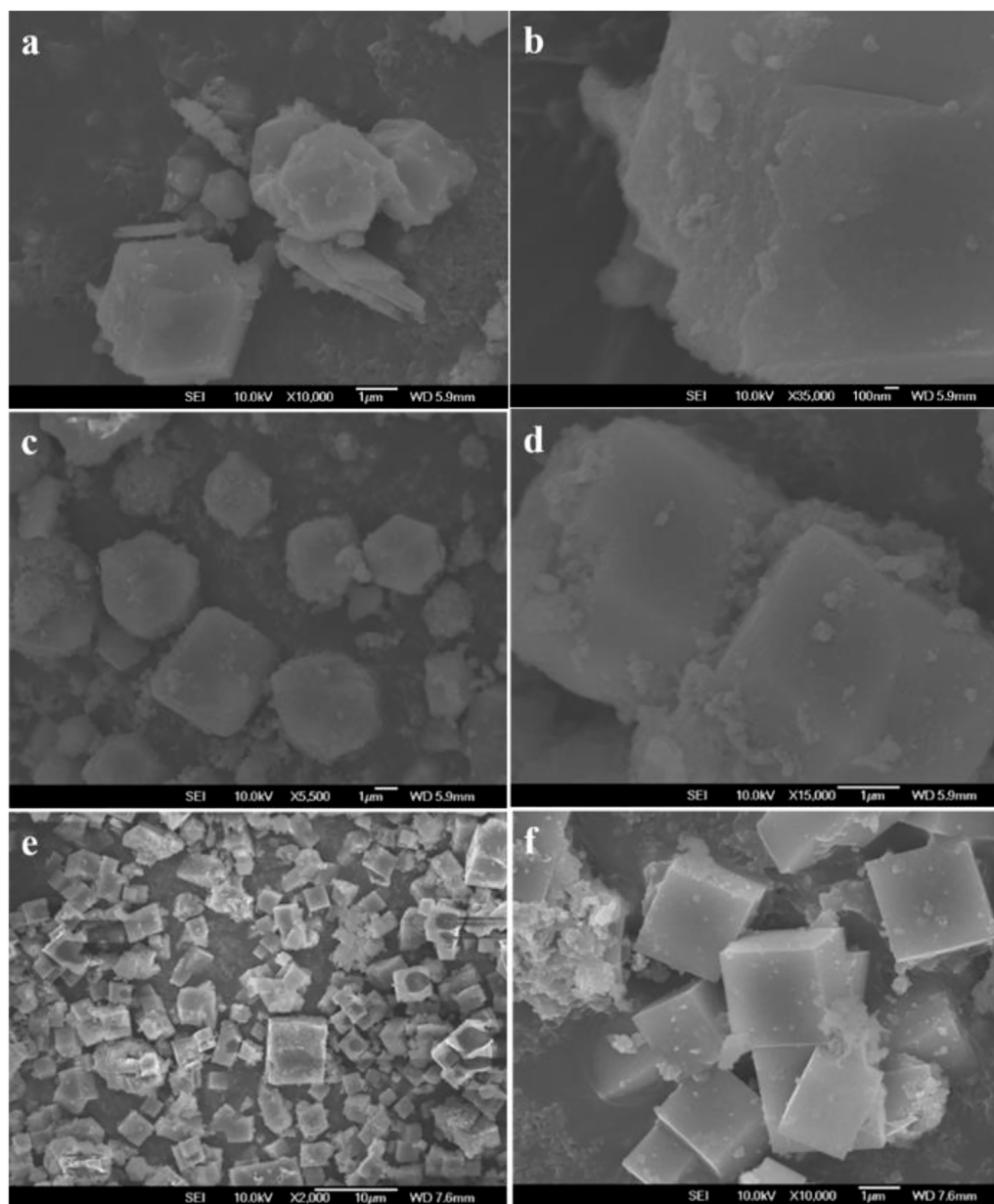
FIGURE 6 | SEM images of HSAPO-34-1 **(A,B)**, HSAPO-34-2 **(C,D)**, and HSAPO-34-3 **(E,F)**.
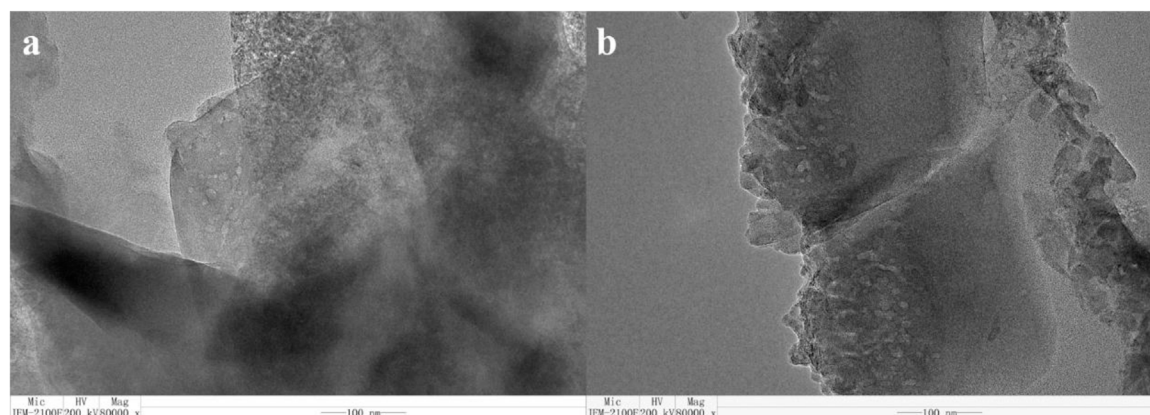
FIGURE 7 | TEM image of HSAPO-34-1.
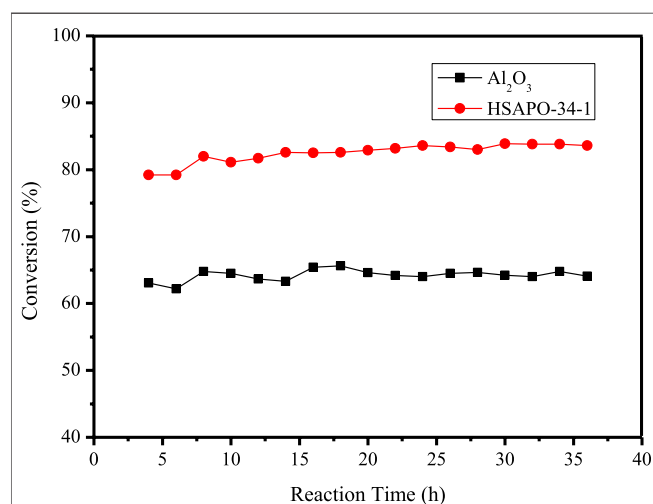
FIGURE 8 | The hydrodesulfurization performance of supported HSAPO-34-1 and Al$_2$O$_3$.

supported metals Co and Mo are widely used in the industry to catalyze the conversion of organic sulfides in fuel oil. However, the surface Al$_2$O$_3$ suffers from the reduction of catalytic activity and instability, and it is difficult to treat macromolecular organic sulfides, such as dibenzothiophene (DBT) and 4,6-dimethyldibenzothiophene (4,6-DMDBT), to deeply affect hydrogenation. Therefore, it is very important to find a more effective carrier to overcome these weaknesses. In this work, a decahydronaphthalene solution of 4,6-DMDBT was used as simulated fuel oil, HSAPO-34-1 was used as carrier, and quantitative metal Co and Mo were loaded to characterize the hydrodesulfurization performance of HSAPO-34-1 at 5.0 MPa and 290°C and compared with the hydrodesulfurization performance of Al$_2$O$_3$ under the same conditions.

The hydrodesulfurization experiment of 4,6-DMDBT was carried out on a fixed bed. The inner diameter of the reactor was 6.5 nm and the length was 50 cm. After loading the

prepared catalyst with a particle size of 0.245–0.350 mm into the reactor, *in situ* reduction with 10% H$_2$–90% N$_2$ mixture was conducted on a fixed bed. The temperature of the reactor was raised from room temperature to 300°C at a speed of 2°C/min and maintained at 300°C for 2 h, and the gas flow speed is 50 ml/min. Then, the reactor temperature and pressure were adjusted to 290°C and 5.0 MPa, and the inlet flow of reaction liquid and the flow rate of H$_2$ were 5 ml/h and 60 ml/h, respectively. The reaction products took samples every 2 h and were detected using an Agilent 7890A GC with FID detector.

Figure 8 shows the hydrodesulfurization performance of 4,6-DMDBT with HSAPO-34-1 and Al$_2$O$_3$ as carriers, respectively. It can be seen that the hydrodesulfurization conversion of 4,6-DMDBT with Al$_2$O$_3$ is about 64%, while the conversion with HSAPO-34-1 is about 83%. It is nearly 20 percentage points higher, which may be due to the medium-strength acid sites generated by the entry of silicon atoms into the skeleton of hierarchical porous HSAPO-34-1. Moreover, hierarchical porous HSAPO-34-1 not only provides larger mesoporous pore volume and pore diameter, but also has the skeleton structure of microporous zeolite, which can provide more active sites.

CONCLUSION

In this work, the effects of different raw materials, material ratios, SDAs, and crystallization conditions on the synthesis of SAPO-34 zeolite were studied. On this basis, SAPO-34 zeolite with a hierarchical porous structure was characterized by XRD, N$_2$ adsorption–desorption, SEM, and TEM. The obtained results prove that the synthesized SAPO-34 zeolite had good crystallinity and micro-mesoporous properties. Subsequently, the synthesized HSAPO-34 zeolite with a hierarchical porous structure was used as the carrier for catalytic hydrodesulfurization of bulky molecule organic sulfide 4,6-DMDBT, and also showed excellent performance. However, some aspects still need to be improved, such as whether SAPO-

34 with a hierarchical porous structure can be synthesized with much cheaper mesoporous SDA. Additionally, the catalytic hydrodesulfurization of bulky molecule organic sulfide and kinetics of hydrodesulfurization with HSAPO-34 supported by different types and amounts of metals still need to be studied in the future.

DATA AVAILABILITY STATEMENT

The original contributions presented in the study are included in the article/Supplementary Material. Further inquiries can be directed to the corresponding authors.

REFERENCES

AUTHOR CONTRIBUTIONS

Y-LD and H-QW: investigation and original draft. Y-QC, MX, and PY: review and editing. R-QL: supervision.

Arstad, B., and Kolboe, S. (2001). The Reactivity of Molecules Trapped within the SAPO-34 Cavities in the Methanol-To-Hydrocarbons Reaction. *J. Am. Chem. Soc.* 123 (33), 8137–8138. doi:10.1021/ja010668t

Carreon, M. A., Li, S., Falconer, J. L., and Noble, R. D. (2008). Alumina-Supported SAPO-34 Membranes for CO2/CH4 Separation. *J. Am. Chem. Soc.* 130 (16), 5412–5413. doi:10.1021/ja801294f

Chen, D., Grønvold, A., Moljord, K., and Holmen, A. (2007). Methanol Conversion to Light Olefins over SAPO-34: Reaction Network and Deactivation Kinetics. *Ind. Eng. Chem. Res.* 46 (12), 4116–4123. doi:10.1021/ie0610748

Chen, D., Moljord, K., Fuglerud, T., and Holmen, A. (1999). The Effect of crystal Size of Sapo-34 on the Selectivity and Deactivation of the MTO Reaction. *Microporous Mesoporous Mater.* 29 (1-2), 191–203. doi:10.1016/S1387-1811(98)00331-X

Fu, G., Fyfe, C. A., Schwieger, W., and Kokotailo, G. T. (1995). Structure Organization of Aluminosilicate Polyanions with Surfactants: Optimization of Al Incorporation in Aluminosilicate Mesostructural Materials. *Angew. Chem. Int. Ed. Engl.* 34 (1314), 1499–1502. doi:10.1002/anie.199514991

Fu, Y., Wang, L., and Tan, Y. (2001). Effects of Crystallization Conditions on the Crystallinity and Catalytic Activity of SAPO-34. *J. South China Univ. Tech. (Natural Sci. Edition)* 29 (4), 30–32.

Hwang, A., Johnson, B. A., and Bhan, A. (2019). Mechanistic Study of Methylbenzene Dealkylation in Methanol-To-Olefins Catalysis on HSAPO-34. *J. Catal.* 369, 86–94. doi:10.1016/j.jcat.2018.10.022

Hwang, A., Prieto-Centurion, D., and Bhan, A. (2016). Isotopic Tracer Studies of Methanol-To-Olefins Conversion over HSAPO-34: the Role of the Olefins-Based Catalytic Cycle. *J. Catal.* 337, 52–56. doi:10.1016/j.jcat.2016.01.021

Jiang, B., Zhao, S., Wang, Y., Wenren, Y., Zhu, Z., Harding, J., et al. (2021). Plasma-enhanced Low Temperature NH3-SCR of NOx over a Cu-Mn/SAPO-34 Catalyst under Oxygen-Rich Conditions. *Appl. Catal. B: Environ.* 286, 119886. doi:10.1016/j.apcatb.2021.119886

Kim, T. H., Gim, M. Y., Hwang, G., Bang, J., and Kim, D. H. (2021). Effects of Ce/Al Molar Ratio in Ce-Incorporated Mesoporous SAPO-34 on the Physicochemical Property and Catalytic Performance in the Selective Production of Light Olefins via Conversion of Chloromethane. *Appl. Catal. A: Gen.* 615, 118061. doi:10.1016/j.apcata.2021.118061

Kimura, T., Sugahara, Y., and Kuroda, K. (1999). Synthesis and Characterization of Lamellar and Hexagonal Mesostructured Aluminophosphates Using Alkyltrimethylammonium Cations as Structure-Directing Agents. *Chem. Mater.* 11 (2), 508–518. doi:10.1021/cm981036h

Kraushaar-Czarnetzki, B., Stork, W. H. J., and Dogterom, R. J. (1993). Novel Aluminophosphate-Based Compounds with a Layered Structure and Intercalation Behavior. *Inorg. Chem.* 32 (23), 5029–5033. doi:10.1021/ic00075a014

Li, H., Liang, J., Wang, R., Liu, Z., and Zhao, S. (1987). Synthesis of Silicoaluminophosphate Zeolite SAPO-34. *Petrochemical Tech.* 16 (5), 340–346.

Li, J., Zhang, F., Li, L., and Shu, X. (2005). Synthesis and Performance of SAPO-34 Molecular Sieve Prepared by Dual-Template Method. *Pet. Process. Petrochemicals* 36 (6), 49–52.

Li, Y., Huang, Y., Guo, J., Zhang, M., Wang, D., Wei, F., et al. (2014). Hierarchical SAPO-34/18 Zeolite with Low Acid Site Density for Converting Methanol to Olefins. *Catal. Today* 233, 2–7. doi:10.1016/j.cattod.2014.03.038

Liang, Y., Gao, B., Zhou, L., Yang, X., Lu, T., Yao, H., et al. (2021). Correction: Rational Construction of Hierarchical SAPO-34 with Enhanced MTO Performance without an Additional Meso/macropore Template. *J. Mater. Chem. A.* 9 (3), 1868. doi:10.1039/D1TA90006D

Lin, Q., Liu, S., Xu, S., Xu, S., Pei, M., Yao, P., et al. (2021). Comprehensive Effect of Tuning Cu/SAPO-34 Crystals Using PEG on the Enhanced Hydrothermal Stability for NH3-SCR. *Catal. Sci. Technol.* 11, 7640–7651. doi:10.1039/D1CY01194D

Lok, B. M., Messina, C. A., Patton, R. L., Gajek, R. T., CannanFlanigen, T. R. E. M., and Flanigen, E. M. (1984). Silicoaluminophosphate Molecular Sieves: Another New Class of Microporous Crystalline Inorganic Solids. *J. Am. Chem. Soc.* 106 (20), 6092–6093. doi:10.1021/ja00332a063

Luan, Z., Zhao, D., He, H., Klinowski, J., and Kevan, L. (1998). Characterization of Aluminophosphate-Based Tubular Mesoporous Molecular Sieves. *J. Phys. Chem. B* 102 (7), 1250–1259. doi:10.1021/jp973109a

Mi, Y., Li, G., Zheng, Y., Luo, Y., Liu, W., Li, Z., et al. (2021). Insights into Novel Mesoporous Cu-SAPO-34 with Enhanced deNOx Performance for Diesel Emission Control. *Microporous Mesoporous Mater.* 323, 111245. doi:10.1016/j.micromeso.2021.111245

Numpilai, T., Kahadit, S., Witoon, T., Ayodele, B. V., Cheng, C. K., Siri-Nguan, N., et al. (2021). CO2 Hydrogenation to Light Olefins over In2O3/SAPO-34 and Fe-Co/K-Al2O3 Composite Catalyst. *Top. Catal.* 64 (15), 316–327. doi:10.1007/s11244-021-01412-5

Popova, M., Minchev, C., and Kanazirev, V. (1998). Methanol Conversion to Light Alkenes over SAPO-34 Molecular Sieves Synthesized Using Various Sources of Silicon and Aluminium. *Appl. Catal. A: Gen.* 169 (2), 227–235. doi:10.1016/S0926-860X(98)00003-9

Rakoczy, R. A., Ernst, S., Hartmann, M., Traa, Y., and Weitkamp, J. (1999). Synthesis of Large Molecular Sieve Crystals with the AFI (AlPO4-5) Topology. *Catal. Today* 49 (1), 261–266. doi:10.1016/S0920-5861(98)00432-5

Rimaz, S., Halladj, R., and Askari, S. (2016). Synthesis of Hierarchal SAPO-34 Nano Catalyst with Dry Gel Conversion Method in the Presence of Carbon Nanotubes as a Hard Template. *J. Colloid Interf. Sci.* 464, 137–146. doi:10.1016/j.jcis.2015.11.005

Schmidt, F., Paasch, S., Brunner, E., and Kaskel, S. (2012). Carbon Templated SAPO-34 with Improved Adsorption Kinetics and Catalytic Performance in the MTO-Reaction. *Microporous Mesoporous Mater.* 164, 214–221. doi:10.1016/j.micromeso.2012.04.045

Shi, Z., Neurock, M., and Bhan, A. (2021). Methanol-to-olefins Catalysis on HSSZ-13 and HSAPO-34 and its Relationship to Acid Strength. *ACS Catal.* 11 (3), 1222–1232. doi:10.1021/acscatal.0c04011

Song, W., Fu, H., and Haw, J. F. (2001). Supramolecular Origins of Product Selectivity for Methanol-To-Olefin Catalysis on HSAPO-34. *J. Am. Chem. Soc.* 123 (20), 4749–4754. doi:10.1021/ja0041167

Sun, C., Zhao, A., Wang, Y., Wang, Z., Zhao, J., Zhao, T., et al. (2021). Organosilane-assistant Synthesis of Hierarchical SAPO-34 Aggregates with superior MTO Performance. *Microporous Mesoporous Mater.* 310, 110619. doi:10.1016/j.micromeso.2020.110619

Sun, Q., Xie, Z., and Yu, J. (2018). The State-Of-The-Art Synthetic Strategies for SAPO-34 Zeolite Catalysts in Methanol-To-Olefin Conversion. *Natl. Sci. Rev.* 5 (4), 542–558. doi:10.1093/nsr/nwx103

Tian, P., Wei, Y., Ye, M., and Liu, Z. (2015). Methanol to Olefins (MTO): From Fundamentals to Commercialization. *ACS Catal.* 5 (3), 1922–1938. doi:10.1021/acscatal.5b00007

Tiemann, M., and Fröba, M. (2001). Mesostructured Aluminophosphates Synthesized with Supramolecular Structure Directors. *Chem. Mater.* 13 (10), 3211–3217. doi:10.1021/cm0110371

Varzaneh, A. Z., Towfighi, J., Sahebdelfar, S., and Bahrami, H. (2016). Carbon Nanotube Templated Synthesis of Hierarchical SAPO-34 Catalysts with Different Structure Directing Agents for Catalytic Conversion of Methanol to Light Olefins. *J. Anal. Appl. Pyrolysis* 121, 11–23. doi:10.1016/j.jaap.2016.06.007

Wilson, S. T., Lok, B. M., and Flanigen, E. M. (1982). *Crystalline Metallophosphate Compositions.* US Patent, US4310440 A.

Xuan, L., Wang, X., Zhu, Y., and Li, Z. (2021). Synthesis of Low-Silica SAPO-34 at Lower Hydrothermal Temperature by Additional Pressure and its Enhanced Catalytic Performance for Methanol to Olefin. *Microporous Mesoporous Mater.* 323, 111218. doi:10.1016/j.micromeso.2021.111218

Yang, M., Tian, P., Wang, C., Yuan, Y., Yang, Y., Xu, S., et al. (2014). A Top-Down Approach to Prepare Silicoaluminophosphate Molecular Sieve Nanocrystals with Improved Catalytic Activity. *Chem. Commun.* 50 (15), 1845–1847. doi:10.1039/c3cc48264b

Zhang, S., Ming, S., Guo, L., Bian, C., Meng, Y., Liu, Q., et al. (2021). Controlled Synthesis of Cu-Based SAPO-18/34 Intergrowth Zeolites for Selective Catalytic Reduction of NOx by Ammonia. *J. Hazard. Mater.* 414, 125543. doi:10.1016/j.jhazmat.2021.125543

Zhao, D., Luan, Z., and Kevan, L. (1997). Synthesis of Thermally Stable Mesoporous Hexagonal Aluminophosphate Molecular Sieves. *Chem. Commun.* (11), 1009–1010. doi:10.1039/A700965H

Zhong, J., Han, J., Wei, Y., Tian, P., Guo, X., Song, C., et al. (2017). Recent Advances of the Nano-Hierarchical SAPO-34 in the Methanol-To-Olefin (MTO) Reaction and Other Applications. *Catal. Sci. Technol.* 7 (21), 4905–4923. doi:10.1039/C7CY01466J

Conflict of Interest: The authors declare that the research was conducted in the absence of any commercial or financial relationships that could be construed as a potential conflict of interest.

Publisher's Note: All claims expressed in this article are solely those of the authors and do not necessarily represent those of their affiliated organizations, or those of the publisher, the editors and the reviewers. Any product that may be evaluated in this article, or claim that may be made by its manufacturer, is not guaranteed or endorsed by the publisher.

A Highly Effective Biomass-Derived Solid Acid Catalyst for Biodiesel Synthesis Through Esterification

Songdang Zhang[1], Hu Pan[2], Jinshu Huang[1], Yuncong Li[1] and Heng Zhang[1]*

[1]State Key Laboratory Breeding Base of Green Pesticide and Agricultural Bioengineering, Key Laboratory of Green Pesticide and Agricultural Bioengineering, State-Local Joint Laboratory for Comprehensive Utilization of Biomass, Center for Research and Development of Fine Chemicals, Ministry of Education, Guizhou University, Guiyang, China, [2]College of Biological, Chemical Science and Engineering, Jiaxing University, Jiaxing, China

Efficient valorization of renewable liquid biomass for biodiesel production using the desirable biomass-based catalysts is being deemed to be an environmentally friendly process. Herein, a highly active biomass-based solid acid catalyst (SiO_2@Cs-SO_3H) with renewable chitosan as raw material through sulfonation procedure under the relatively mild condition was successfully manufactured. The SiO_2@Cs-SO_3H catalyst was systematically characterized, especially with a large specific surface area (21.82 m^2/g) and acidity (3.47 mmol/g). The catalytic activity of SiO_2@Cs-SO_3H was evaluated by esterification of oleic acid (OA) and methanol for biodiesel production. The best biodiesel yield was acquired by Response Surface Methodology (RSM). The optimized reaction conditions were temperature of 92°C, time of 4.1 h, catalyst dosage of 6.8 wt%, and methanol to OA molar ratio of 31.4, respectively. In this case, the optimal experimental biodiesel yield was found to be 98.2%, which was close to that of the predicted value of 98.4%, indicating the good reliability of RSM employed in this study. Furthermore, SiO_2@Cs-SO_3H also exhibited good reusability in terms of five consecutive recycles with 87.0% biodiesel yield. As such, SiO_2@Cs-SO_3H can be considered and used as a bio-based sustainable catalyst of high-efficiency for biodiesel production.

Keywords: biodiesel, renewable bio-based catalyst, response surface methodology, sulfonation, esterification

1 INTRODUCTION

In today's society, due to the rapid development of industry, the accompanying sharp increase in the consumption of fossil fuels has led to a series of social problems including energy shortages and environmental pollution (Li et al., 2017; Li et al., 2019; Zhao et al., 2019; Hu et al., 2021). Therefore, it is of great significance to develop the renewable bioenergy of huge potential in terms of green and efficiency, aiming to replace the increasingly scarce traditional fossil energy (Liu et al., 2021; Li et al., 2022). Biodiesel, a kind of green and clean energy with low pollutant emission, non-toxic, good renewability and biodegradability, is regarded as a promising alternative to conventional fossil fuels (Atadashi et al., 2013; Pan et al., 2019; Tan et al., 2021). Biodiesel is mainly composed of various fatty acid alkyl esters, which are related to the composition of raw materials (Pan et al., 2018; Wang et al., 2018; Alagumalai et al., 2021). In general, biodiesel can be produced mainly through the transesterification of triglycerides of

edible oil, vegetable oil, and waste edible oil, such as soybean (Hu et al., 2020; Xie et al., 2021b; Zhu et al., 2021), rapeseed (Hájek et al., 2020; Gaidukevič et al., 2021), and *Jatropha curcas* oil (Gutiérrez-López et al., 2021; Laskar et al., 2021), as well as the esterification of free fatty acids (FFAs) such as oleic acid (OA) with methanol. Recently, on account of the merits of microalgae, biodiesel production directly from microalgae oil has also attracted attention (Zhang et al., 2015; Bauer et al., 2017; Abdala et al., 2020). However, considering the issues of cost, environmental pollution, and food safety, producing biodiesel from waste edible oil has gradually become a research hotspot. It is worth noting that although the use of waste edible oil can reduce the relevant process cost and environmental pollution, the high levels of FFA in waste edible oil make its biodiesel technology difficult (Zhang et al., 2019; Bhatia et al., 2020; Shatesh et al., 2020). Therefore, to solve this problem, it is necessary to design a catalyst that can efficiently transform the high levels of FFA feedstock into biodiesel. Usually, the conventional catalysts used widely for biodiesel production are divided into two types, namely homogeneous and heterogeneous groups. Homogeneous catalysts restrict their further development due to the obvious disadvantages including difficult separation, difficult regeneration, and high requirements on experimental equipment (Guldhe et al., 2017; Negm et al., 2019; Li et al., 2020). Hence, heterogeneous catalysts are being regarded as the more extensive way for biodiesel production using low-quality oil feedstocks.

A negative saponification reaction occurs when biodiesel is produced directly from oil with high FFA content under the catalysis of an alkali catalyst. As such, acid pretreatment *via* esterification should be required to reduce acid content, and esterification of FFAs is also deemed as an effective manner to produce biodiesel (Zhang et al., 2017; Xie et al., 2021). To this end, it is a good choice to employ heterogeneous acid catalysts that can effectively catalyze the esterification reactions for the preparation of biodiesel. Solid acid catalysts containing sulfonic acid groups generally showed better catalytic activity for biodiesel production, especially in the esterification of FFAs with methanol. This should

be attributed to the strong acidity of $-SO_3H$ (Liu et al., 2020). Nonetheless, compared with homogeneous catalysts, the heterogeneous acid catalysts usually depict lower catalytic efficiency, of which more stringent reaction conditions are required and the relatively higher catalyst production cost should also be carried out to achieve the desired effect. As a consequence, it is of great importance to developing low-cost and efficient solid acid catalysts that catalyze the esterification of FFAs to produce biodiesel.

With respect to this, biomass-derived catalysts have been widely used in the biodiesel production on account of their advantages of renewability, non-toxic, and environmental protection property. Nevertheless, the common biomass-based catalysts [bagasse (Akinfalabi et al., 2020), rice husk carbon (Chen et al., 2013) and bamboo (Tang and Niu, 2019), etc.] are mainly prepared by carbonization at high temperatures (>300℃) and sulfonation with corrosive sulfuric acid. The as-mentioned protocol usually requires harsh reaction conditions and also brings about pollution to the environment. Consequently, the relatively simple synthesis methods and the more environmentally friendly organic sulfonation reagents should be adopted to manufacture biomass-based catalysts. *p*-Toluenesulfonic acid, a non-oxidizing strong organic acid (one million times more acidic than benzoic acid), is considered to be a better organic sulfonation reagent (Wang et al., 2015).

Chitosan (Cs), the product of natural polysaccharide chitin after the removal of acetyl group, has demonstrated various attractive advantages such as biodegradability, biocompatibility, and non-toxicity. It is widely applied in many fields such as food additives, environmental protection, cosmetics, antimicrobial agent, drug development, and other daily chemical industry (Liu et al., 2015; Dhakshinamoorthy et al., 2021). Cs, as a weakly alkaline polysaccharide, is rich in $-NH_2$ and $-OH$ functional groups and also shows strong modification potential. Therefore, of particular interest is the rational synthesis of biomass-based catalysts from Cs for biodiesel production. Recently, supported solid acid catalysts have shown great application potential in the production of biodiesel owing to
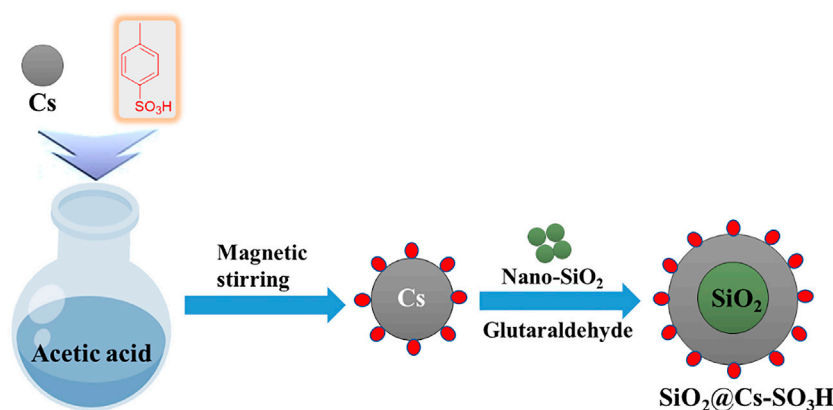
SCHEME 1 | Schematic illustration for the synthesis of $SiO_2@Cs-SO_3H$.

their excellent catalytic performance and strong design ability. With regard to this, nano-SiO_2 is considered an excellent carrier because of its large pore size and specific surface area, along with strong stability even in the acidic media.

In this study, a novel biomass-derived solid acid catalytic material SiO_2@Cs-SO_3H was successfully prepared using p-toluenesulfonic acid as the sulfonation reagent, and nano-SiO_2 as the solid support. The synthetic procedure used in this study was simple, mild, and environmentally friendly. Furthermore, the catalytic performance of SiO_2@Cs-SO_3H was assessed through the esterification of OA and methanol for biodiesel production.

2 MATERIALS AND METHODS

2.1 Materials

Chitosan (>99%, the degree of deacetylation ≥95%), p-toluenesulfonic acid monohydrate (AR, 99%), and methanol (AR, ≥99.7%) were obtained from Chengdu Jinshan Chemical Reagent Co., Ltd. Oleic acid (AR, ≥99%) and nano-SiO_2 were bought from Shanghai Macklin Biochemical Co., Ltd. Acetic acid (AR, ≥99.5%) was supplied by Chongqing Chuandong Chemical Co., Ltd. 50% of glutaraldehyde (AR, ≥99%) was purchased from Tianjin Damao Chemical Reagent Factory. Ethanol (AR, ≥99.5%) and petroleum ether (AR, 60–90°C) were obtained from Tianjin Fuyu Fine Chemical Co., Ltd. KOH (AR, ≥85.0%) was purchased from Shanghai Titan Scientific Co., Ltd.

2.2 Catalyst Preparation

The synthesis diagram of biomass-based solid acid catalyst SiO_2@Cs-SO_3H is shown in **Scheme 1**.

2.2.1 Sulfonation of Chitosan

0.5 g chitosan was added to 50 ml 1 wt% acetic acid solution and stirred magnetically for 10 min at room temperature. Then, 5.7 g p-toluenesulfonic acid monohydrate was added to the chitosan acetic acid solution and strongly stirred until the solid was dissolved.

2.2.2 Preparation of SiO_2 @Cs-SO_3H Catalyst

0.1 g SiO_2 and 1 ml glutaraldehyde were added to the sulfonated chitosan solution followed by stirring at room temperature for 2 h. The resulting solution was then dried overnight at 80°C, and the as-synthesized solid materials were ground and repeatedly washed with anhydrous ethanol until the filtrate became pH = 7. Finally, the so-called catalyst SiO_2@Cs-SO_3H was obtained after being dried at 80°C for 4 h.

2.3 Catalyst Characterization

X-ray diffraction (XRD) was measured by Tongda TD-3500 X-ray diffractometer (Cu Kα radiation) to characterize the crystallinity and structure of the catalyst. The functional groups of the catalyst were determined by KBr compression using Nicolet 360 FT-IR (Fourier-transform infrared apparatus). The thermal stability of the catalyst in the nitrogen

atmosphere was detected by PerkinElmer TGA 47 thermogravimetric analyzer. The ammonia temperature-programmed desorption (NH_3-TPD) measurements were performed on the AutoChem 2920 chemisorption apparatus with a thermal conductivity detector (TCD) to detect the acidity of the catalyst. The Bruner-Emmett-Teller (BET) method and N_2 adsorption-desorption apparatus (ASAP 2460, McMerric Instruments Co., Ltd.) were used to check the physical properties of the catalytic material (specific surface area, pore-volume, and pore diameter, respectively).

2.4 Esterification of Oleic Acid With Methanol

The catalytic performance of SiO_2@Cs-SO_3H was determined by the esterification of oleic acid and methanol for biodiesel synthesis. To be specific, a mixture of 1 g oleic acid (acid value: 200 mg KOH/g), 4.3 ml methanol, and 0.06 g catalyst were added into a 15 ml thick wall pressure tube (Beijing Synthware Glass Instrument Co. Ltd.), and the encapsulated tube was allowed to proceed in an oil bath at 650 rpm using different temperatures for a specific time. After the reaction, petroleum ether was added to extract the reaction products. Finally, the petroleum ether was removed by vacuum distillation. The acid value (AV) of the product was detected by 0.1 M KOH solution titration using phenolphthalein as an indicator (Lin et al., 2021). The yield of biodiesel was determined according to the change of AV before and after oleic acid reaction, and the calculation formula was as follows:

$$\text{Biodiesel Yield}\,(\%) = \frac{AV_0 - AV_1}{AV_0} \times 100\%$$

$$AV_1 = \frac{56.1 \times 0.1 \times V_{KOH}}{m} \qquad (1)$$

Where AV_0 and AV_1 are the acid value of oleic acid and products, respectively; The numbers 56.1 and 0.1 in **Eq. 1** are the relative molecular mass and solution concentration (0.1 mol/L) of KOH, respectively; V_{KOH} is the volume of KOH titrated; m is the mass of the product.

2.5 Response Surface Methodology (RSM)

The factors affecting the esterification of oleic acid with methanol were optimized by the Box-Behnken design (BBD) experiment of RSM. In this process, four factors and three levels were adopted to design the experiment, in which the biodiesel yield was regarded as the response value, and the temperature, time, methanol to oleic acid molar ratio, and the catalyst dosage were served as the main four experimental parameters. Accordingly, a total of 29 experiments were designed in a random order manner. The detailed symbols, names of each parameter, and their ranges and levels are shown in **Table 1**. Moreover, the relationship between response values and parameters was studied by the least square multiple regression method. The second-order polynomial was fitted to establish the model (Kumar and Singh, 2019; Hossain et al., 2021).

TABLE 1 | Experimental parameters and range of response surface methodology optimization.

Independent variables	Symbols	Range and levels		
		−1	0	1
Temperature	A	80	90	100
Time	B	3	4	5
Catalyst dosage	C	4	6	8
Methanol to oleic acid molar ratio	D	25	30	35

$$Y = \beta_0 + \beta_1 A + \beta_2 B + \beta_3 C + \beta_4 D + \beta_5 AB + \beta_6 AC + \beta_7 AD + \beta_8 BC + \beta_9 BD + \beta_{10} CD + \beta_{11} A^2 + \beta_{12} B^2 + \beta_{13} C^2 + \beta_{14} D^2 + \varepsilon$$

(2)

Where Y represents the response prediction value, β_0 refers the intercept term, β_1 to β_{14} are the linear effect coefficient, the quadratic coefficient of the crossover and square effect, and ε implies the error.

Analysis of variance (ANOVA) was used to perform statistical analysis on the model, and the influence of independent experimental variables along with their interactions on the response value (biodiesel yield) was also investigated. The p-value plays a decisive role in the probability error of the model and the significance of each variable. When the p-value is below 0.05%, it indicates that the variable has statistical significance. In addition, a response surface diagram was drawn to demonstrate the influence of the interaction between univariate and bivariate on the yield of biodiesel, and the optimal value was also determined accordingly.

2.6 Reusability

The reusability of $SiO_2@Cs-SO_3H$ was evaluated under the optimal experimental conditions. After the reaction was finished, the catalyst was separated by centrifugation followed by washing with anhydrous ethanol 3 times to remove the impurities attached to the catalyst. After washing, the catalyst was dried in a vacuum drying oven at 80°C for 8 h to remove the solvent. Then, the as-dried recycled catalyst was employed for the next optimization experiment. The recycling process of the catalyst was repeated for five consecutive runs.

3 RESULTS AND DISCUSSION

3.1 Catalyst Characterization

The structure and crystallinity $SiO_2@Cs-SO_3H$ samples were characterized by XRD. As shown in **Figure 1A**, $SiO_2@Cs-SO_3H$ samples showed a broad diffraction peak within the range of $2\theta = 10°–30°$, corresponding to the characteristic peaks of Cs (Ranjani et al., 2019; Sabar et al., 2020). However, the absorption peak of SiO_2 was not highlighted in the figure, which may be due to the amorphous state of nano-SiO_2 (Thangaraj et al., 2019). With respect to this, the existence of SiO_2 was further proved by FT-IR spectroscopy. **Figure 1B** shows the FT-IR spectra of $SiO_2@Cs-SO_3H$ and Cs. The absorption peaks observed in both the two samples at 1,380 cm^{-1} and

1,598 cm^{-1} are attributed to the C-O and N-H functional groups, respectively, and these should be typical characteristic peaks of Cs (Saengprachum et al., 2019). The obvious peaks of $SiO_2@Cs-SO_3H$ at 1,182 cm^{-1} and 1,035 cm^{-1} are derived from the stretching vibration of O=S=O, indicating the successful functionalization of the active sulfonic acid group on the Cs (Nata et al., 2017). Meanwhile, the absorption peaks shown at 1,076 cm^{-1}, 795 cm^{-1}, and 680 cm^{-1} correspond to the anti-symmetrical stretching vibration, symmetrical stretching, and bending of Si-O-Si, respectively (Owoeye et al., 2020). These indicate that the sulfonated chitosan has been successfully coated onto SiO_2.

The thermal stability of the prepared catalyst was studied by TGA analysis. From **Figure 2A**, it can be observed that the weight loss of $SiO_2@Cs-SO_3H$ mainly occurs in two stages. When the temperature is below 205°C, the weight loss of the catalyst determined as 6.95 wt% should be ascribed to the loss of water adsorbed on the catalyst. The second peak existing in the range of 205–540°C (weight loss of 42.97 wt%) was related to the polymeric network decomposition and the formation of carbon materials. However, the mass of the catalyst did not decrease significantly after 540°C, indicating that the carbon material produced gradually became stable. In short, the catalyst showed good thermal stability and it can completely meet the demand of catalytic esterification reaction to produce biodiesel.

NH_3-TPD was used to investigate the relative acidity density and acidic strength of $SiO_2@Cs-SO_3H$. As depicted in **Figure 2B**, the peaks shown in the profile were derived from the desorption of NH_3 at acidic sites on the sample, and the desorption temperature was related to the acid strength of $SiO_2@Cs-SO_3H$. As illustrated in **Figure 2B**, the NH_3-TPD profile shows three peaks within the range of 50–600°C. The peaks in the temperature ranges of 110–200°C, 310–400°C, and 450–520°C correspond to the sites of a weak acid (-OH), medium strong acid (-SO_3H) and strong acid (-SO_3H), respectively. Meanwhile, the measurement result showed that $SiO_2@Cs-SO_3H$ possessed a higher acid density of 3.47 mmol/g, which were superior to the reported sulfonated solid acid catalysts such as SAC (1.50 mmol/g) (Lathiya et al., 2018), ASHC-SO_3H (1.40 mmol/g) (Cao et al., 2021), and PMB-SO_3H (1.92 mmol/g) (Quah et al., 2020). The specific surface area, pore size, and pore volume of the $SiO_2@Cs-SO_3H$ catalyst were measured by BET-BJH, as shown in **Figures 2C,D**. According to the results, the catalyst exhibited a specific surface area of 21.82 m^2/g, a pore volume of 0.022 cm^2/g, and a pore size distribution between 2 and 20 nm. Compared with the sulfonated chitosan catalysts that were reported in the previous literature (Wang et al., 2019; Zhang and Sun, 2020), $SiO_2@Cs-SO_3H$ demonstrated a benign porous structure, implying that $SiO_2@Cs-SO_3H$ will be conducive to esterification for biodiesel synthesis. It is worth mentioning that when nano-SiO_2 with good surface efficiency and large surface area was used as the suitable carrier, of crucial significance was to improve the specific surface area of the catalyst, thus leading to better catalytic performance accordingly.
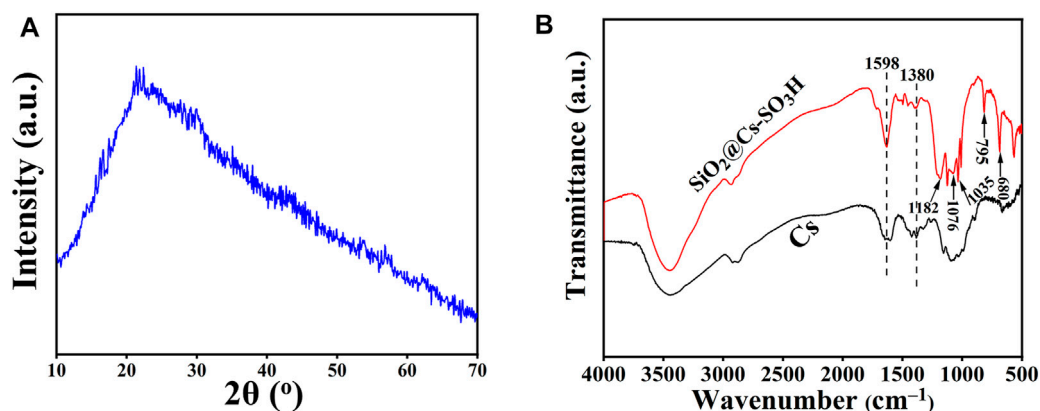
FIGURE 1 | **(A)** XRD spectrum of SiO$_2$@Cs-SO$_3$H, **(B)** FI-IR spectra of Cs and SiO$_2$@Cs-SO$_3$H
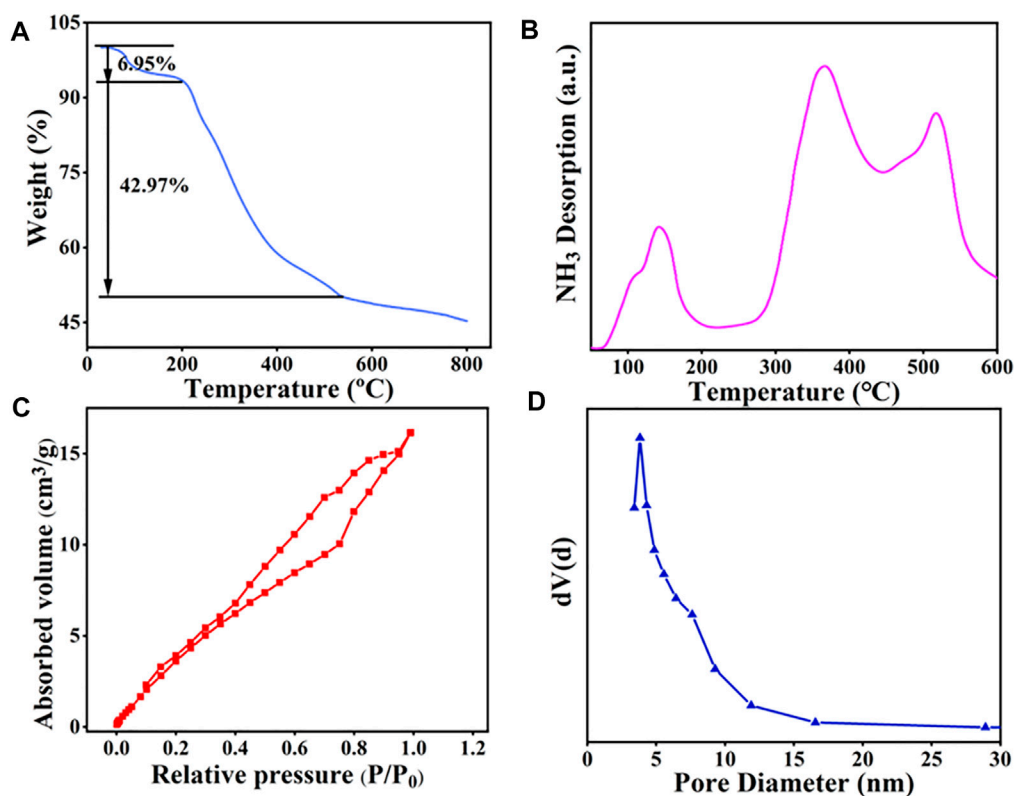
FIGURE 2 | SiO$_2$@Cs-SO$_3$H catalyst diagram of **(A)** TGA, **(B)** NH$_3$-TPD, **(C)** BET, and **(D)** pore size distribution.

3.2 Esterification of Oleic Acid to Biodiesel

The prepared SiO$_2$@Cs-SO$_3$H catalyst from sulfonated chitosan was further applied to catalyze the esterification reaction of oleic acid with methanol for the production of biodiesel. The effects of reaction temperature (70–110°C), reaction time (1–5 h), catalyst dosage (0–8 wt%), and the methanol to OA molar ratio (15/1–35/1) on biodiesel yield were studied by single-factor experiments.

3.2.1 Reaction Temperature

Generally, the reaction temperature is a significant variable affecting the reaction rate in the esterification of OA with methanol (Zhang et al., 2018). As shown in **Figure 3A**, the influence of temperature on the yield of biodiesel was investigated in the temperature range of 70–110°C. It was found that with the temperature rising from 70 to 90°C, the biodiesel yield gradually increased to more than 90%.
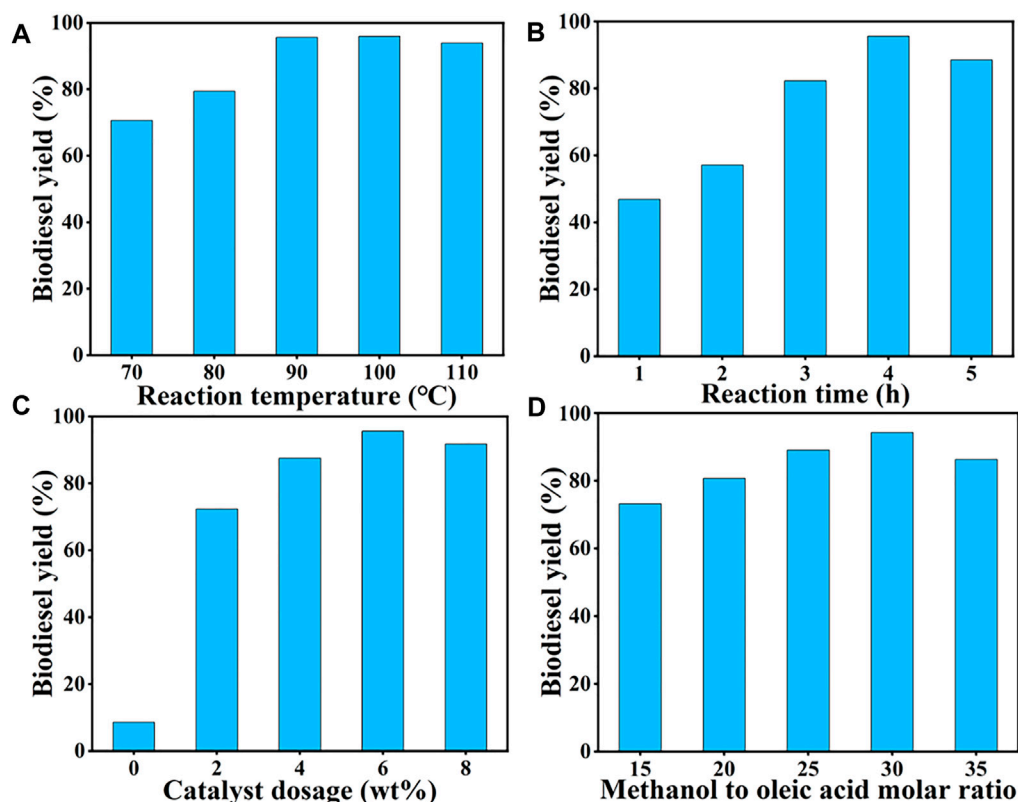
FIGURE 3 | Single-factor optimization of SiO$_2$@Cs-SO$_3$H catalyst for oleic acid esterification reaction: **(A)** reaction temperature, **(B)** reaction time, **(C)** catalyst dosage, and **(D)** methanol to oleic acid molar ratio.

Subsequently, as the temperature continued to rise, the yield of biodiesel decreased slightly, which may be due to the decrease of methanol feedstock caused by the higher temperature. Therefore, 90°C was selected as the appropriate reaction temperature.

3.2.2 Reaction Time
The reaction time also has a certain influence on biodiesel yield. From the point of kinetic, the esterification of OA with methanol requires a certain amount of time for mass transfer to reach an equilibrium state (Pan et al., 2017). **Figure 3B** shows the effect of reaction time on biodiesel yield at 90°C, methanol to OA molar ratio of 30/1, and catalyst dosage of 6 wt %, and the highest yield of 96% was obtained after 4 h of reaction. Thus, 4 h was determined as the optimal reaction time.

3.2.3 Catalyst Dosage
The amount of catalyst is also an important parameter to evaluate its catalytic capacity for OA esterification reaction, wherein the number of active sites is closely related to the yield of biodiesel (Wang et al., 2021). As shown in **Figure 3C**, only 8.57% of the biodiesel yield was obtained without any catalyst. With the increase of catalyst amount from 0 wt% to 6 wt%, the corresponding biodiesel yield reached over 90%. However, when the catalyst amount exceeded 6 wt%, the biodiesel

yield showed a downward trend. This could be explained that since the increase of the catalyst dosage proceeded, the number of catalytic active sites also raised, thus promoting the esterification reaction towards the biodiesel synthesis. It should be noted that too much catalyst would hinder mass transfer between the catalyst and the reactants, slowing down the reaction rate ultimately. Therefore, 6 wt% was selected as the suitable dosage of catalyst.

3.2.4 Methanol to OA Molar Ratio
Apart from the above three factors, the amount of methanol also played a crucial role in the esterification of OA. It is certain that appropriately increasing the amount of alcohol can promote the forward reaction, thus improving the yield of biodiesel accordingly (Xie and Wang, 2021). As shown in **Figure 3D**, the influence of alcohol dosage on biodiesel yield was studied with different molar ratios (15/1–35/1), while remaining the other variables as the same. It was determined that the biodiesel yield showed an upward trend with the increase of molar ratio, of which the highest yield of 95% was observed at 30/1. However, excessive methanol ultra-dilution the concentration of the reaction system and reduces the chance of OA arriving at the catalytic active site, thus reducing the yield of biodiesel. Thus, 30/1 was determined as the appropriate molar ratio.

TABLE 2 | Experimental design and results of oleic acid esterification reaction catalyzed by SiO_2@Cs-SO_3H.

Run	A: Temperature (°C)	B: Time (h)	C: Catalyst dosage (wt%)	D: Methanol to oleic acid molar ratio	Experimental biodiesel yield (%)	Predicted biodiesel yield (%)
1	90	3	4	30	92.64	92.53
2	90	4	6	30	97.33	97.33
3	80	4	6	35	94.77	94.43
4	100	3	6	30	97.34	97.67
5	90	4	4	25	92.96	92.68
6	80	4	4	30	90.24	90.17
7	80	5	6	30	96.44	96.13
8	100	5	6	30	97.17	96.87
9	80	4	6	25	92.66	92.84
10	90	4	8	25	95.23	94.8
11	90	5	6	35	97.98	98.07
12	100	4	6	35	97.54	97.3
13	90	4	6	30	96.34	97.33
14	80	3	6	30	92.27	92.6
15	90	5	4	30	93.49	93.66
16	90	4	4	35	91.59	92.05
17	90	5	6	25	94.50	94.81
18	100	4	8	30	97.27	97.38
19	90	5	8	30	98.15	98.2
20	90	4	6	30	97.82	97.33
21	90	3	6	35	95.26	94.99
22	100	4	4	30	94.85	94.68
23	100	4	6	25	95.51	95.78
24	90	3	6	25	95.20	95.15
25	90	4	6	30	97.54	97.33
26	90	4	8	35	98.14	97.54
27	90	4	6	30	97.62	97.33
28	90	3	8	30	96.82	96.59
29	80	4	8	30	95.88	96.08

3.3 Optimization of Biodiesel Production by RSM

To further optimize the reaction conditions of the SiO_2@Cs-SO_3H catalyzing oleic acid esterification reaction to obtain the best biodiesel yield, we further employed the response surface method to randomly design 29 sets of experiments on the basis of the single-factor experimental results in the previous section. The obtained results and the corresponding predicted values of the above **Eq. 2** are shown in **Table 2**. The specific second-order polynomial equation of the design model based on the predicted response value of the four parameters is depicted in **Eq. 3**.

$$Y = 97.33 + 1.45A + 0.68B + 2.15C + 0.78D - 1.09AB - 0.18AC - 0.02AD + 0.12BC + 0.86BD + 1.09CD - 1.09A^2 - 0.42B^2 - 1.66C^2 - 1.15D^2$$

$$(3)$$

Analysis of variance was performed on the experimental design model as exhibited in **Table 2**, and the corresponding results are presented in **Table 3**. The F and p-value represent the significance of the entire model and the model term respectively. The larger the F value, the more significant the model and the better the fit. The smaller the p-value, the more important the model term is for the response value. In general, the p-value < 0.05 is highly significant of the model variables (Sulaiman et al., 2017). According to the results in **Table 3**, it can be observed that

the reaction parameters including A, B, C, and D can be determined to be highly significant. Meanwhile, for the high F value (45.57) and low p-value (<0.0001) of the model, it can be seen that the selected quadratic polynomial regression model to optimize the yield of biodiesel is significant. The "Lack of Fit F-value" of 0.47 indicates that lack of fit is not significant compared with the pure error, showing that the model fits the experimental data sufficiently. Furthermore, the coefficient of determination R^2 of 97.85% indicates that the obtained model can explain 97.85% of the response variability, indicating that the model has high reliability. The adjusted R^2 of 95.71% and the predicted R^2 of 91.76% are considered to be reasonably consistent because their difference is less than 0.2. Thus, it can be concluded that the fit of the model is more significant. To explain the reliability and applicability of the model, the experimental real value is compared with the predicted value (**Figure 4**). There is a low deviation between the predicted value and the real value. Therefore, these have proven that the quadratic polynomial regression model can match the data well, and the system response is generated within the scope of independent variable research.

Through the three-dimensional surface graph, the influence of the interaction of any two independent variables on biodiesel yield was studied, while the coding values of the other two parameters were kept at zero, as shown in **Figure 5**.

TABLE 3 | ANOVA on the RSM experimental design data.

Source	Sum of squares	Df	Mean square	F value	p-value prob > F	
Model	134.32	14	9.59	45.57	<0.0001	significant
A: Temperature	25.29	1	25.29	120.11	<0.0001	
B: Time	5.6	1	5.6	26.61	0.0001	
C: Catalyst dosage	55.56	1	55.56	263.88	<0.0001	
D: Methanol/OA molar ratio	7.24	1	7.24	34.38	<0.0001	
AB	4.71	1	4.71	22.37	0.0003	
AC	2.59	1	2.59	12.31	0.0035	
AD	0.0016	1	0.0016	0.0076	0.9318	
BC	0.058	1	0.058	0.27	0.6091	
BD	2.92	1	2.92	13.89	0.0023	
CD	4.8	1	4.8	22.78	0.0003	
A^2	7.69	1	7.69	36.55	<0.0001	
B^2	1.17	1	1.17	5.54	0.0337	
C^2	17.91	1	17.91	85.07	<0.0001	
D^2	8.6	1	8.6	40.86	<0.0001	
Residual	2.95	14	0.21			
Lack of Fit	1.6	10	0.16	0.47	0.8455	not significant
Pure Error	1.35	4	0.34			
Cor Total	137.27	28				
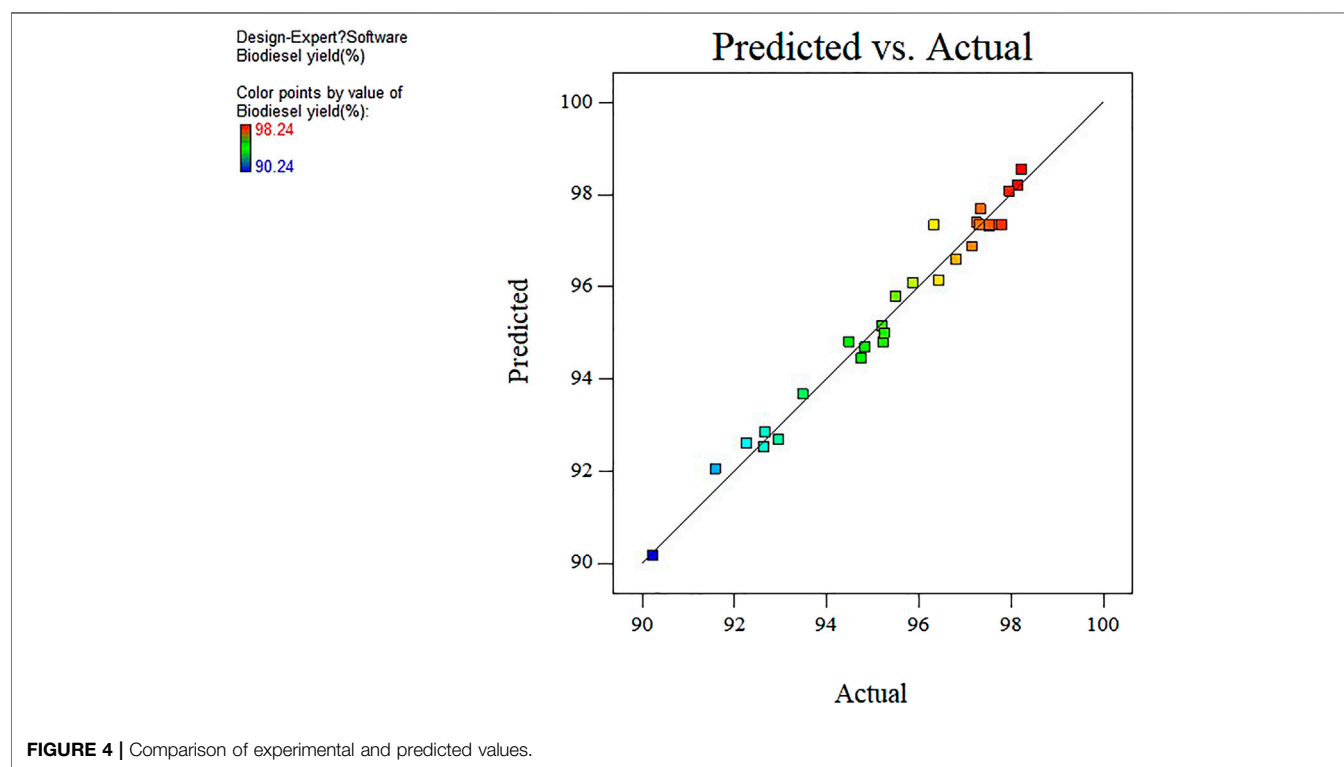
FIGURE 4 | Comparison of experimental and predicted values.

Figure 5A displays the interaction effect of time and temperature, and catalyst dosage was 6 wt% and methanol to oleic acid molar ratio was 30:1. The extension of reaction time shows no significant impact on the yield of biodiesel in the lower reaction temperature range, which may be that the reaction requires a higher temperature to improve the reaction rate (Wang et al., 2018). However, with the increase of the temperature, it can be found that higher biodiesel yield can be reached in a relatively short time, indicating that the influence of reaction temperature on biodiesel yield was more significant than the reaction time. This can also be observed from the higher F value (120.11) of the reaction temperature. **Figure 5B** and **Figure 5C** show the interaction of temperature with catalyst dosage and molar ratio, respectively. For low temperature and catalyst dosage, the biodiesel yield was low. However, when the amount of catalyst and temperature increased, the biodiesel yield
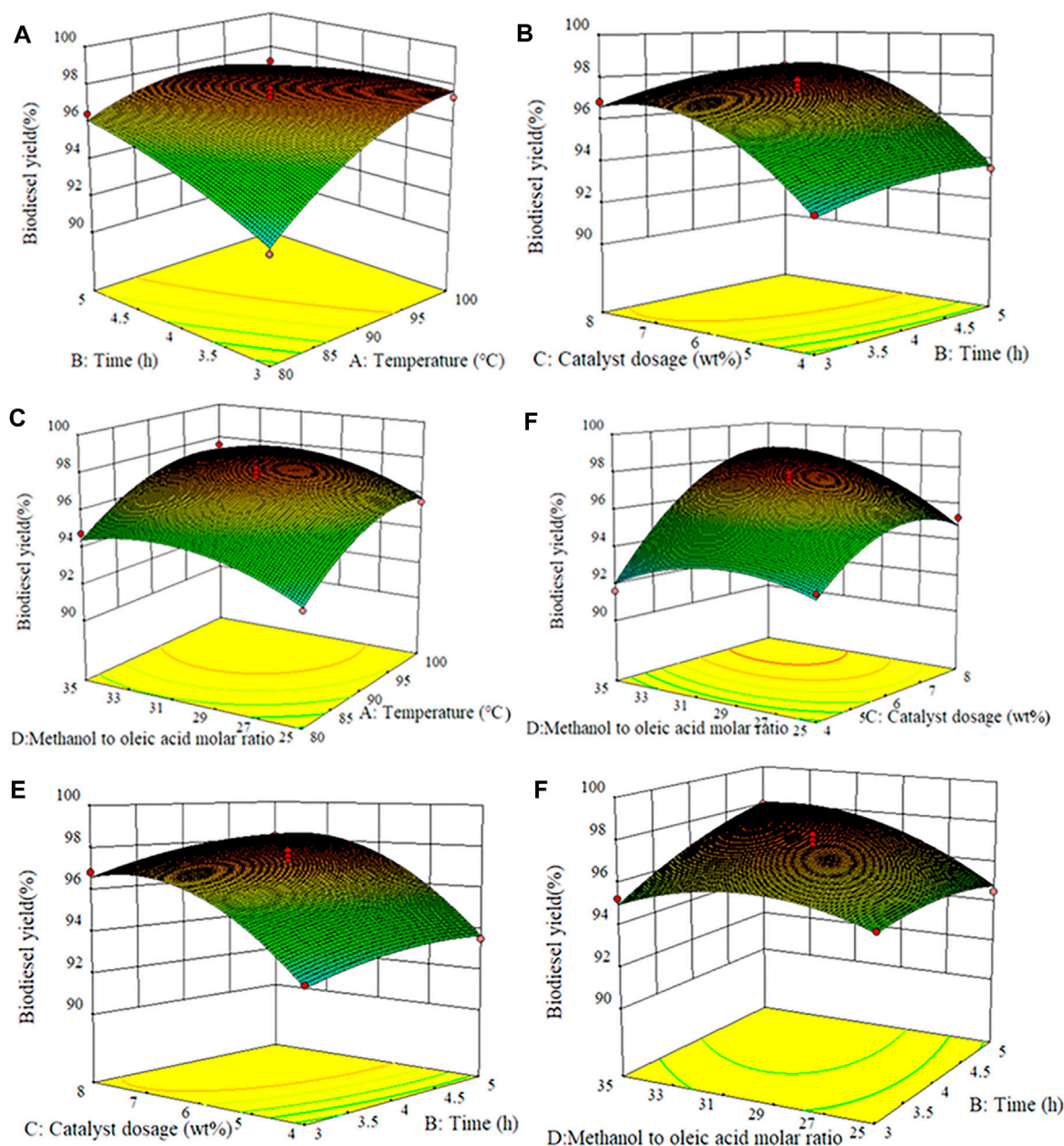
FIGURE 5 | Surface response plots of different experimental variables against biodiesel yield. **(A)** Temperature and time, **(B)** time and catalyst dosage, **(C)** methanol to oleic acid molar ratio and temperature, **(D)** catalyst dosage and methanol to oleic acid molar ratio, **(E)** catalyst dosage and time, and **(F)** methanol to oleic acid molar ratio and time.

gradually moved to the high-value region, and the effect of the catalyst dosage on the yield of biodiesel was greater than that of the reaction temperature. This is attributed to the addition of catalytic active sites that can promote the reaction more effectively and quickly, but a superfluous amount will inversely hinder the mass transfer between substances, slowing down the reaction rate ultimately (Cao et al., 2021). Similarly, **Figure 5C** shows that the biodiesel yield increases with the increase of reaction temperature and the molar ratio of methanol to oleic acid, but when the molar ratio increases to a certain extent, the

biodiesel yield takes on a downtrend. This was because the increase of methanol dosage is conducive to the positive occurrence of the reaction, thus resulting in the improvement of product yield. However, excessive methanol will dilute the concentration of the reaction system, and the inverse reaction rate will be increased with the increase of the number of product esters, both of which are unfavorable for the formation of products (Lim et al., 2020). In addition, compared with the molar ratio, the influence of temperature on the yield of biodiesel was more significant.
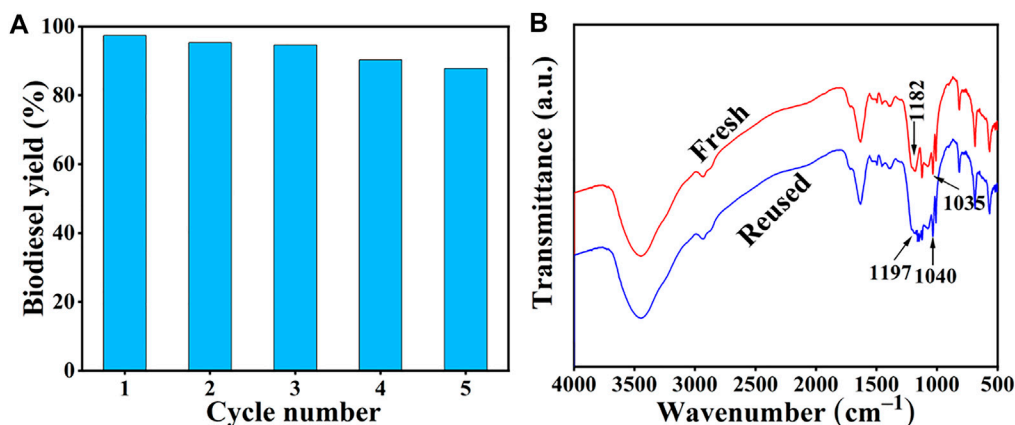
FIGURE 6 | (A) Reusability of SiO$_2$@Cs-SO$_3$H catalyst, **(B)** FI-IR spectra before and after repeated use of SiO$_2$@Cs-SO$_3$H (Methanol to oleic acid molar ratio of 31.4/1, 6.8 wt% and 92°C for 4.1 h).

The conjugate effect of the catalyst amount and methanol/OA molar ratio on biodiesel yield was depicted in **Figure 5D**. The reaction temperature and time were kept at 90°C and 4 h, respectively. It can be seen from **Figure 5D** that the yield of biodiesel was constantly increased with the molar ratio of methanol to oleic acid and catalyst dosage increased. In the esterification reaction, the low molar ratio of methanol to oleic acid is adopted, the increase of catalyst dosage demonstrated a weak effect on the improvement of biodiesel yield. This should be due to the fact that the reversibility of the esterification reaction usually requires a higher methanol/OA molar ratio. However, an excessive amount of methanol will dilute the concentration of catalyst in the whole system, resulting in a decrease in the concentration of active center per unit volume (Nongbe et al., 2017). **Figure 5E** and **Figure 5F** show the interaction of time with the catalyst amount and the molar ratio of methanol to OA, respectively. As mentioned earlier, the biodiesel yield continues to increase with the increment of time, the amount of catalyst, and the molar ratio.

The experimental parameters were optimized according to the RSM to obtain the best biodiesel yield. The optimum conditions were obtained as follows: reaction temperature of 92°C, reaction time of 4.1 h, catalyst dosage of 6.8 wt%, and methanol to oleic acid molar ratio of 31.4/1. Correspondingly, the predicted biodiesel yield was as high as 98.4%. For the effectiveness of the model, the corresponding experiments were conducted under the predicted conditions, and the experimental biodiesel yield of 98.2% was very close to the predicted value, verifying that the model had certain reliability and effectiveness in predicting the biodiesel yield in this study.

3.4 Reusability of Catalyst

Reusability is considered to be an important guideline to assess the performance of the catalyst, and efficient catalyst recycle can also reduce the biodiesel cost, to some extent (Dai et al., 2021). Therefore, we conducted five consecutive reactions under the optimized experimental conditions to determine the reusability of the SiO$_2$@Cs-SO$_3$H catalyst in oleic acid

esterification reaction. The specific steps are as follows: after each reaction, the catalyst obtained through centrifugation was washed 3 times with anhydrous ethanol to remove the impurities attached to the catalyst, and then dried at 80°C to remove the solvent. The dried catalyst was used for the next experiment. The tested results of SiO$_2$@Cs-SO$_3$H catalyst after five recycles are shown in **Figure 6A**, wherein 87.0% biodiesel yield for the fifth recycle can still be reached, showing the relatively good reusability of SiO$_2$@Cs-SO$_3$H. More importantly, **Figure 6B** shows the infrared spectra of the catalysts before and after use, whereas the important absorption peak of the sulfonic acid -SO$_3$H group still exists in the reused catalyst. Nonetheless, the intensity of the absorption peak is relatively weak compared with the fresh catalyst, indicating that part of -SO$_3$H was lost in the recycling process, which may be the reason for the decrease of biodiesel yield.

4 CONCLUSION

Sulfonated chitosan-derived SiO$_2$@Cs-SO$_3$H solid acid catalyst was synthesized by an easy method at room temperature. The SiO$_2$@Cs-SO$_3$H catalyst exhibited a high acidity (3.47 mmol/g) and large specific surface area (21.82 m^2/g), showing high catalytic activity for the esterification of oleic acid and methanol. The reaction temperature, reaction time, catalyst amount, and molar ratio of methanol to oleic acid were optimized and analyzed by RSM to obtain the best biodiesel yield. Accordingly, the ideal reaction conditions were determined: 92°C, 4.1 h, catalyst dosage of 6.8 wt%, and methanol to oleic acid molar ratio of 31.4/1. In this case, the maximum biodiesel yield (98.2%) was obtained. In addition, the catalyst also had good reusability, and the biodiesel yield of 87.0% can still be reached after repeated use of 5 times. In conclusion, the SiO$_2$@Cs-SO$_3$H solid acid catalyst prepared from Cs biomass had excellent catalytic performance for the esterification of FFAs, which shows a good application prospect in the biodiesel production field.

DATA AVAILABILITY STATEMENT

The original contributions presented in the study are included in the article/Supplementary Material, further inquiries can be directed to the corresponding author.

AUTHOR CONTRIBUTIONS

Writing—original draft preparation, SZ. Revising—manuscript, HP. Figure drawing, JH. Data curation, YL. Writing—reviewing, supervision, HZ. All authors have read and agreed to the published version of the manuscript.

FUNDING

REFERENCES

Abdala, E., Nur, O., and Mustafa, M. A. (2020). Efficient Biodiesel Production from Algae Oil Using Ca-Doped ZnO Nanocatalyst. *Ind. Eng. Chem. Res.* 59, 19235–19243. doi:10.1021/acs.iecr.0c04118

Akinfalabi, S.-I., Rashid, U., Ngamcharussrivichai, C., and Nehdi, I. A. (2020). Synthesis of Reusable Biobased Nano-Catalyst from Waste Sugarcane Bagasse for Biodiesel Production. *Environ. Tech. Innovation* 18, 100788. doi:10.1016/j.eti.2020.100788

Alagumalai, A., Mahian, O., Hollmann, F., and Zhang, W. (2021). Environmentally Benign Solid Catalysts for Sustainable Biodiesel Production: A Critical Review. *Sci. Total Environ.* 768, 144856. doi:10.1016/j.scitotenv.2020.144856

Atadashi, I. M., Aroua, M. K., Abdul Aziz, A. R., and Sulaiman, N. M. N. (2013). The Effects of Catalysts in Biodiesel Production: A Review. *J. Ind. Eng. Chem.* 19, 14–26. doi:10.1016/j.jiec.2012.07.009

Bauer, G., Lima, S., Chenevard, J., Sugnaux, M., and Fischer, F. (2017). Biodiesel via *In Situ* Wet Microalgae Biotransformation: Zwitter-type Ionic Liquid Supported Extraction and Transesterification. *ACS Sustain. Chem. Eng.* 5, 1931–1937. doi:10.1021/acssuschemeng.6b02665

Bhatia, S. K., Gurav, R., Choi, T.-R., Kim, H. J., Yang, S.-Y., Song, H.-S., et al. (2020). Conversion of Waste Cooking Oil into Biodiesel Using Heterogenous Catalyst Derived from Cork Biochar. *Bioresour. Tech.* 302, 122872. doi:10.1016/j.biortech.2020.122872

Cao, M., Peng, L., Xie, Q., Xing, K., Lu, M., and Ji, J. (2021). Sulfonated Sargassum Horneri Carbon as Solid Acid Catalyst to Produce Biodiesel via Esterification. *Bioresour. Tech.* 324, 124614. doi:10.1016/j.biortech.2020.124614

Chen, K.-T., Wang, J.-X., Dai, Y.-M., Wang, P.-H., Liou, C.-Y., Nien, C.-W., et al. (2013). Rice Husk Ash as a Catalyst Precursor for Biodiesel Production. *J. Taiwan Inst. Chem. Eng.* 44, 622–629. doi:10.1016/j.jtice.2013.01.006

Dai, Q., Yang, Z., Li, J., Cao, Y., Tang, H., and Wei, X. (2021). Zirconium-based MOFs-Loaded Ionic Liquid-Catalyzed Preparation of Biodiesel from Jatropha Oil. *Renew. Energ.* 163, 1588–1594. doi:10.1016/j.renene.2020.09.122

Dhakshinamoorthy, A., Jacob, M., Vignesh, N. S., and Varalakshmi, P. (2021). Pristine and Modified Chitosan as Solid Catalysts for Catalysis and Biodiesel Production: A Minireview. *Int. J. Biol. Macromolecules* 167, 807–833. doi:10.1016/j.ijbiomac.2020.10.216

Gaidukevič, J., Barkauskas, J., Malaika, A., Jasulaitienė, V., and Kozłowski, M. (2021). Preparation and Characterization of Basic Graphene-Based Catalysts and Their Application in Biodiesel Synthesis. *Appl. Surf. Sci.* 554, 149588. doi:10.1016/j.apsusc.2019.149588

Guldhe, A., Singh, P., Ansari, F. A., Singh, B., and Bux, F. (2017). Biodiesel Synthesis from Microalgal Lipids Using Tungstated Zirconia as a Heterogeneous Acid Catalyst and its Comparison with Homogeneous Acid and Enzyme Catalysts. *Fuel* 187, 180–188. doi:10.1016/j.fuel.2016.09.053

Gutiérrez-López, A. N., Mena-Cervantes, V. Y., García-Solares, S. M., Vazquez-Arenas, J., and Hernández-Altamirano, R. (2021). NaFeTiO4/Fe2O3-FeTiO3 as Heterogeneous Catalyst towards a Cleaner and Sustainable Biodiesel Production from Jatropha Curcas L. Oil. *J. Clean. Prod.* 304, 127106. doi:10.1016/j.jclepro.2021.127106

Hájek, M., Vávra, A., and Mück, J. (2020). Butanol as a Co-solvent for Transesterification of Rapeseed Oil by Methanol under Homogeneous and Heterogeneous Catalyst. *Fuel* 277, 118239. doi:10.1016/j.fuel.2020.118239

Hossain, M., Goni, L. K. M. O., Muntaha, N., Jamal, M. S., Sujan, S. M. A., Ahmed, S., et al. (2021). Box-Behnken Design-Based Optimization for Biodiesel Production from Waste Cooking Oil Using Mahogany (Swietenia Macrophylla) Fruit Shell Derived Activated Carbon as a Heterogeneous Base Catalyst. *Reac Kinet Mech. Cat* 133, 117–138. doi:10.1007/s11144-021-01995-w

Hu, Y., He, Q., and Xu, C. (2021). Catalytic Conversion of Glycerol into Hydrogen and Value-Added Chemicals: Recent Research Advances. *Catalysts* 11, 1455. doi:10.3390/catal11121455

Hu, Y., Qi, L., Tirumala Venkateswara Rao, K., Zhao, B., Li, H., Zeng, Y., et al. (2020). Supercritical Water Gasification of Biocrude Oil from Low-Temperature Liquefaction of Algal Lipid Extraction Residue. *Fuel* 276, 118017. doi:10.1016/j.fuel.2020.118017

Kumar, D., and Singh, B. (2019). BaZrO3 and Cs-BaZrO3 Catalysed Transesterification of Millettia Pinnata Oil and Optimisation of Reaction Variables by Response Surface Box-Behnken Design. *Renew. Energ.* 133, 411–421. doi:10.1016/j.renene.2018.10.037

Laskar, I. B., Changmai, B., Gupta, R., Shi, D., Jenkinson, K. J., Wheatley, A. E. H., et al. (2021). A Mesoporous Polysulfonic Acid-Formaldehyde Polymeric Catalyst for Biodiesel Production from Jatropha Curcas Oil. *Renew. Energ.* 173, 415–421. doi:10.1016/j.renene.2021.04.004

Lathiya, D. R., Bhatt, D. V., and Maheria, K. C. (2018). Synthesis of Sulfonated Carbon Catalyst from Waste orange Peel for Cost Effective Biodiesel Production. *Bioresour. Tech. Rep.* 2, 69–76. doi:10.1016/j.biteb.2018.04.007

Li, H., Guo, H., Fang, Z., Aida, T. M., and Smith, R. L. (2020). Cycloamination Strategies for Renewable N-Heterocycles. *Green. Chem.* 22, 582–611. doi:10.1039/C9GC03655E

Li, H., Li, Y., Fang, Z., and Smith, R. L. (2019). Efficient Catalytic Transfer Hydrogenation of Biomass-Based Furfural to Furfuryl Alcohol with Recyclable Hf-Phenylphosphonate Nanohybrids. *Catal. Today* 319, 84–92. doi:10.1016/j.cattod.2018.04.056

Li, H., Zhao, W., and Fang, Z. (2017). Hydrophobic Pd Nanocatalysts for One-Pot and High-Yield Production of Liquid Furanic Biofuels at Low Temperatures. *Appl. Catal. B: Environ.* 215, 18–27. doi:10.1016/j.apcatb.2017.05.039

Li, Z., Jiang, Y., Li, Y., Zhang, H., Li, H., and Yang, S. (2022). Advances in Diels-Alder/aromatization of Biomass Furan Derivatives towards Renewable Aromatic Hydrocarbons. *Catal. Sci. Technol.* doi:10.1039/D1CY02122B

Lim, S., Yap, C. Y., Pang, Y. L., and Wong, K. H. (2020). Biodiesel Synthesis from Oil palm Empty Fruit bunch Biochar Derived Heterogeneous Solid Catalyst Using 4-benzenediazonium Sulfonate. *J. Hazard. Mater.* 390, 121532. doi:10.1016/j.jhazmat.2019.121532

Lin, X., Li, M., Chen, Z., Li, M., Huang, Y., and Qiu, T. (2021). One-step Fabrication of Polymeric Self-Solidifying Ionic Liquids as the Efficient Catalysts for Biodiesel Production. *J. Clean. Prod.* 292, 125967. doi:10.1016/j.jclepro.2021.125967

Liu, F., Ma, X., Li, H., Wang, Y., Cui, P., Guo, M., et al. (2020). Dilute Sulfonic Acid post Functionalized Metal Organic Framework as a Heterogeneous Acid Catalyst for Esterification to Produce Biodiesel. *Fuel* 266, 117149. doi:10.1016/j.fuel.2020.117149

Liu, J., Li, H., Liu, Y.-C., Lu, Y.-M., He, J., Liu, X.-F., et al. (2015). Catalytic Conversion of Glucose to 5-hydroxymethylfurfural over Nano-Sized Mesoporous Al2O3-B2o3 Solid Acids. *Catal. Commun.* 62, 19–23. doi:10.1016/j.catcom.2015.01.008

Liu, Y., Liu, X., Li, M., Meng, Y., Li, J., Zhang, Z., et al. (2021). Recyclable Zr/Hf-Containing Acid-Base Bifunctional Catalysts for Hydrogen Transfer Upgrading of Biofuranics: A Review. *Front. Chem.* 9, 812331. doi:10.3389/fchem.2021.812331

Nata, I. F., Putra, M. D., Irawan, C., and Lee, C.-K. (2017). Catalytic Performance of Sulfonated Carbon-Based Solid Acid Catalyst on Esterification of Waste Cooking Oil for Biodiesel Production. *J. Environ. Chem. Eng.* 5, 2171–2175. doi:10.1016/j.jece.2017.04.029

Negm, N. A., Betiha, M. A., Alhumaimess, M. S., Hassan, H. M. A., and Rabie, A. M. (2019). Clean Transesterification Process for Biodiesel Production Using Heterogeneous Polymer-Heteropoly Acid Nanocatalyst. *J. Clean. Prod.* 238, 117854. doi:10.1016/j.jclepro.2019.117854

Nongbe, M. C., Ekou, T., Ekou, L., Yao, K. B., Le Grognec, E., and Felpin, F.-X. (2017). Biodiesel Production from palm Oil Using Sulfonated Graphene Catalyst. *Renew. Energ.* 106, 135–141. doi:10.1016/j.renene.2017.01.024

Owoeye, S. S., Jegede, F. I., and Borisade, S. G. (2020). Preparation and Characterization of Nano-Sized Silica Xerogel Particles Using Sodium Silicate Solution Extracted from Waste Container Glasses. *Mater. Chem. Phys.* 248, 122915. doi:10.1016/j.matchemphys.2020.122915

Pan, H., Li, H., Zhang, H., Wang, A., Jin, D., and Yang, S. (2018). Effective Production of Biodiesel from Non-edible Oil Using Facile Synthesis of Imidazolium Salts-Based Brønsted-Lewis Solid Acid and Co-solvent. *Energ. Convers. Manage.* 166, 534–544. doi:10.1016/j.enconman.2018.04.061

Pan, H., Li, H., Zhang, H., Wang, A., and Yang, S. (2019). Acidic Ionic Liquid-Functionalized Mesoporous Melamine-Formaldehyde Polymer as Heterogeneous Catalyst for Biodiesel Production. *Fuel* 239, 886–895. doi:10.1016/j.fuel.2018.11.093

Pan, H., Liu, X., Zhang, H., Yang, K., Huang, S., and Yang, S. (2017). Multi-SO3H Functionalized Mesoporous Polymeric Acid Catalyst for Biodiesel Production and Fructose-To-Biodiesel Additive Conversion. *Renew. Energ.* 107, 245–252. doi:10.1016/j.renene.2017.02.009

Quah, R. V., Tan, Y. H., Mubarak, N. M., Kansedo, J., Khalid, M., Abdullah, E. C., et al. (2020). Magnetic Biochar Derived from Waste palm Kernel Shell for Biodiesel Production via Sulfonation. *Waste Manage.* 118, 626–636. doi:10.1016/j.wasman.2020.09.016

Ranjani, P., Pannipara, M., Al-Sehemi, A. G., Vignesh, A., and kumar, G. G. (2019). Chitosan/sulfonated Graphene Oxide/silica Nanocomposite Membranes for Direct Methanol Fuel Cells. *Solid State Ionics* 338, 153–160. doi:10.1016/j.ssi.2019.05.010

Sabar, S., Abdul Aziz, H., Yusof, N. H., Subramaniam, S., Foo, K. Y., Wilson, L. D., et al. (2020). Preparation of Sulfonated Chitosan for Enhanced Adsorption of Methylene Blue from Aqueous Solution. *Reactive Funct. Polym.* 151, 104584. doi:10.1016/j.reactfunctpolym.2020.104584

Saengprachum, N., Cai, D., Li, M., Li, L., Lin, X., and Qiu, T. (2019). Acidic Chitosan Membrane as an Efficient Catalyst for Biodiesel Production from Oleic Acid. *Renew. Energ.* 143, 1488–1499. doi:10.1016/j.renene.2019.05.101

Shatesh Kumar, K., Shamsuddin, M. R., Farabi, M. S. A., Saiman, M. I., Zainal, Z., and Taufiq-Yap, Y. H. (2020). Production of Methyl Esters from Waste Cooking Oil and Chicken Fat Oil via Simultaneous Esterification and Transesterification Using Acid Catalyst. *Energ. Convers. Manage.* 226, 113366. doi:10.1016/j.enconman.2020.113366

Sulaiman, N. F., Wan Abu Bakar, W. A., and Ali, R. (2017). Response Surface Methodology for the Optimum Production of Biodiesel over Cr/Ca/γ-Al2O3 Catalyst: Catalytic Performance and Physicochemical Studies. *Renew. Energ.* 113, 697–705. doi:10.1016/j.renene.2017.06.007

Tan, X., Sudarsanam, P., Tan, J., Wang, A., Zhang, H., Li, H., et al. (2021). Sulfonic Acid-Functionalized Heterogeneous Catalytic Materials for Efficient Biodiesel Production: A Review. *J. Environ. Chem. Eng.* 9, 104719. doi:10.1016/j.jece.2020.104719

Tang, X., and Niu, S. (2019). Preparation of Carbon-Based Solid Acid with Large Surface Area to Catalyze Esterification for Biodiesel Production. *J. Ind. Eng. Chem.* 69, 187–195. doi:10.1016/j.jiec.2018.09.016

Thangaraj, B., Jia, Z., Dai, L., Liu, D., and Du, W. (2019). Effect of Silica Coating on Fe3O4 Magnetic Nanoparticles for Lipase Immobilization and Their Application for Biodiesel Production. *Arabian J. Chem.* 12, 4694–4706. doi:10.1016/j.arabjc.2016.09.004

Wang, A., Li, H., Pan, H., Zhang, H., Xu, F., Yu, Z., et al. (2018). Efficient and green Production of Biodiesel Catalyzed by Recyclable Biomass-Derived Magnetic Acids. *Fuel Process. Tech.* 181, 259–267. doi:10.1016/j.fuproc.2018.10.003

Wang, A., Zhang, H., Li, H., and Yang, S. (2019). Efficient Production of Methyl Oleate Using a Biomass-Based Solid Polymeric Catalyst with High Acid Density. *Adv. Polym. Tech.*, 2019 2019, 1–11. doi:10.1155/2019/4041631

Wang, S., Xue, Y., Zhao, X., and Yuan, H. (2021). Preparation of a Carbon Microsphere-Based Solid Acid Application to Waste Frying Oil Transesterification. *Diamond Relat. Mater.* 116, 108420. doi:10.1016/j.diamond.2021.108420

Wang, Y., Wang, D., Tan, M., Jiang, B., Zheng, J., Tsubaki, N., et al. (2015). Monodispersed Hollow SO3H-Functionalized Carbon/Silica as Efficient Solid Acid Catalyst for Esterification of Oleic Acid. *ACS Appl. Mater. Inter.* 7, 26767–26775. doi:10.1021/acsami.5b08797

Xie, W., Gao, C., and Li, J. (2021). Sustainable Biodiesel Production from Low-Quantity Oils Utilizing H6PV3MoW8O40 Supported on Magnetic Fe3O4/ZIF-8 Composites. *Renew. Energ.* 168, 927–937. doi:10.1016/j.renene.2020.12.129

Xie, W., and Wang, H. (2021). Grafting Copolymerization of Dual Acidic Ionic Liquid on Core-Shell Structured Magnetic Silica: A Magnetically Recyclable Brönsted Acid Catalyst for Biodiesel Production by One-Pot Transformation of Low-Quality Oils. *Fuel* 283, 118893. doi:10.1016/j.fuel.2020.118893

Xie, W., Xiong, Y., and Wang, H. (2021). Fe3O4-poly(AGE-DVB-GMA) Composites Immobilized with Guanidine as a Magnetically Recyclable Catalyst for Enhanced Biodiesel Production. *Renew. Energ.* 174, 758–768. doi:10.1016/j.renene.2021.04.086

Zhang, H., Li, H., Hu, Y., Venkateswara Rao, K. T., Xu, C., Yang, S., et al. (2019). Advances in Production of Bio-Based Ester Fuels with Heterogeneous Bifunctional Catalysts. *Renew. Sustain. Energ. Rev.* 114, 109296. doi:10.1016/j.rser.2019.109296

Zhang, H., Li, H., Pan, H., Wang, A., Souzanchi, S., Xu, C., et al. (2018). Magnetically Recyclable Acidic Polymeric Ionic Liquids Decorated with Hydrophobic Regulators as Highly Efficient and Stable Catalysts for Biodiesel Production. *Appl. Energ.* 223, 416–429. doi:10.1016/j.apenergy.2018.04.061

Zhang, H., Li, H., Pan, H., Wang, A., Xu, C., and Yang, S. (2017). Magnetically Recyclable Basic Polymeric Ionic Liquids for Efficient Transesterification of *Firmiana Platanifolia* L.F. Oil into Biodiesel. *Energ. Convers. Manage.* 153, 462–472. doi:10.1016/j.enconman.2017.10.023

Zhang, H., Zhou, Q., Chang, F., Pan, H., Liu, X.-F., Li, H., et al. (2015). Production and Fuel Properties of Biodiesel from Firmiana Platanifolia L.F. As a Potential Non-food Oil Source. *Ind. Crops Prod.* 76, 768–771. doi:10.1016/j.indcrop.2015.08.002

Zhang, X., and Sun, J. (2020). Synthesis, Characterization, and Properties of Sulfonated Chitosan for Protein Adsorption. *Int. J. Polym. Sci.* 2020, 1–10. doi:10.1155/2020/9876408

Zhao, W., Chi, X., Li, H., He, J., Long, J., Xu, Y., et al. (2019). Eco-friendly Acetylcholine-Carboxylate Bio-Ionic Liquids for Controllable N-Methylation and N-Formylation Using Ambient CO2 at Low Temperatures. *Green. Chem.* 21, 567–577. doi:10.1039/C8GC03549K

Zhu, Z., Liu, Y., Cong, W., Zhao, X., Janaun, J., Wei, T., et al. (2021). Soybean Biodiesel Production Using Synergistic CaO/Ag Nano Catalyst: Process Optimization, Kinetic Study, and Economic Evaluation. *Ind. Crops Prod.* 166, 113479. doi:10.1016/j.indcrop.2021.113479

Sex Pheromones of the Potato Tuber Moth (*Phthorimaea operculella*)

Huanhuan Pan, Hongyi Zhao, Likun Ai, Jian Huang* and Yang Chen*

State Key Laboratory Breeding Base of Green Pesticide and Agricultural Bioengineering, Key Laboratory of Green Pesticide and Agricultural Bioengineering, Ministry of Education, Research and Development Center for Fine Chemicals, Guizhou University, Guiyang, China

The potato tuber moth (*Phthorimaea operculella*) is a major potato pest. Its sex pheromones contain two chemical structures: 4E,7Z-tridecadiene-1-ol acetate (PTM1) and 4E,7Z,10Z-tridecatriene-1-ol acetate (PTM2). Increasing global consciousness of environmental protection is driving widespread attention to the possible use of these pheromones for sustainable pest management. This review summarizes research on the structure confirmation, field application, and chemical synthesis of the sex pheromones of the potato tuber moth. An efficient synthesis strategy of the two sex pheromones is proposed.

INTRODUCTION

Insect sex pheromones are used in environmentally friendly pest management. A large number of insect sex pheromones have been isolated and identified to control harmful insects in agriculture, horticulture, forestry, and stored products (Shen et al., 2020; Witzgall et al., 2010). Since the beginning of the 21st century, the attention of this field has increased exponentially, and the number of papers and the frequency of citations have increased yearly (**Figure 1I**). According to the statistics of *Web of Sciences in 2022* (Web of Scienece, 2022), the total number of papers on insect sex pheromones has reached 8,828, the H index has reached 146, and the cumulative citation frequency has reached 213,502 times.

Insect sex pheromones have some common characteristics: most of them are aliphatic long-chain olefin compounds that are volatile, they are safe for target organisms and non-target organisms because they have no direct killing effect, and they are mixtures of compounds in specific proportions that show strong specificity and high biological activity.

In China, potatoes play a key role in the national food security strategy and poverty alleviation strategies (Gao et al., 2019b). However, with the continuous expansion of potato planting areas, the occurrence of pests and diseases in production and storage is becoming increasingly severe (Xu et al., 2019). Traditional pests and diseases such as potato bacterial wilt, morning and late blight, and underground pests have been increasing year by year, as have outbreaks of insect pests such as the twenty-eight-star lady beetle (*Henosepilachna vigintioctopunctata*), potato tuber moth (*Phthorimaea operculella*), potato golden nematode (*Globodera rostochiensis*), potato beetle (*Leptinotarsa decemlineata*) and other pests. Changes in planting structure and scale together with global climate change further cause these hazards to spread. The potato tuber moth has developed into an important pest in China's main potato producing areas such as Sichuan, Yunnan, and Guizhou.

The female potato tuber moth (also known as the tobacco leaf miner) lays multiple eggs individually on the ground and in soil crevices at the root of potato stems, near the midrib of the dorsal leaf, or between the petioles and axillary buds. For stored potatoes, adults prefer to lay eggs

FIGURE 1 | I Statistics of the number of research papers on insect sex pheromone from *web of science*. **II** Chemical structure of sex pheromone of potato tuber moth. **III** Synthesis of sex pheromone analogues of potato tuber moth by Fouda in 1975. **IV** Roelofs' synthesis of PTM1 in 1975. **V** Voerman's synthesis of PTM1 in 1978. **VI** Alexakis's synthesis of PTM1 in 1978. VII Nishiyama's synthesis of PTM1 in 1984. **VIII** Yadav's synthesis of PTM1 in 1986.

near the bud eye after the potato nubs are unearthed. In the field, the first-instar larvae start spinning silk after the eggs hatch, generally completing their larval stage in the leaves, and the old larvae fall into the soil to pupate. During the storage period, the larvae mostly enter from the bud eye or the cracked skin and gradually penetrate the potato pieces. After spinning silk the larvae form a worm tunnel (Coll and Gavish, 2000) and can consume much if not all of the potato flesh, causing the tubers to rot and lose their planting and edible value (Xie, 2014).

The early prevention and control of potato tuber moth mainly involve cultural control measures such as planting resistant varieties, deep seeding, and irrigation, but chemical control is still the main control method during potato production. Due to over-reliance on chemical pesticides, potato tuber moths have developed different degrees of resistance to pesticides such as organophosphorus and pyrethroids (Xu et al., 2019; Yan and Gao, 2019). With the gradual enhancement of people's awareness of environmental protection, the research on insect sex pheromones has attracted extensive attention from agricultural biologists and chemists, as they provide a possibility to reduce dependence on

chemical pesticides. This field is gradually becoming a hot spot in the field of sustainable plant protection (Wright, 1964).

STRUCTURE IDENTIFICATION OF THE POTATO TUBER MOTH SEX PHEROMONE

Sexually mature female potato tuber moths were first described to use sex pheromones to attract males in the late 1960s (Adeesan et al., 1969; Ono et al., 1972). Compounds with strong attracting effect were first isolated from female potato tuber moths in 1975 (Fouda et al., 1975). Due to the limitations of structural analysis techniques at that time, only chemical tests, gas chromatography, and mass spectrometry were used to preliminarily determine the pheromone's structure, which was thought to be isomers containing unsaturated double bonds and acetyl ester groups. In the same year, Roelofs (Roelofs et al., 1975) extracted and isolated a compound from the glands of the female potato tuber moth, and its structure (**Figure 1II**:4E,7Z-tridecadien-1-ol acetate (PTM1)) was determined by fine gas chromatography coupled with mass spectrometry, chemical synthesis, and

bioactivity validation. One year later, Yamaoka et al. (1976) isolated the sex pheromones produced by potato tuber moth adults from unmated female moths raised in the laboratory. The results of gas chromatography and mass spectrometry showed that the pheromone was tridecatrienol acetate. They speculated that the pheromone structure was 4,7,10-Tridecatrienoate, but the configuration of its double bond had not been determined. In the same year, Persoons (Persoons et al., 1976) reported the extraction, isolation, structural identification, and field activity of the sex pheromone, and found that it was a mixture of two compounds as shown in **Figure 1II**. These compounds are 4E,7Z-tridecadien-1-ol acetate (PTM1) and 4E,7Z,10Z-tridecatrien-1-ol acetate (PTM2).

Voerman (Voerman et al., 1977) summarized a review on these sex pheromones and the two compounds are mixed in a certain proportion to exert the induction effect.

FIELD APPLICATION OF POTATO TUBER MOTH SEX PHEROMONE

Used in the field for more than 50 years, a variety of effective methods have been developed to measure the population size of potato tuber moths and control their damage to potato crops using sexual inducement technology.

Bacon (Bacon et al., 1976) used eight kinds of tridecene and tridecen-1-ol acetate monomers (including PTM1) or their mixtures to carry out chemical trapping experiments of potato tuber moths in the field, and found that PTM1 obtained the highest number of catches. Persoons (Persoons et al., 1976) found that the mixture of PTM1 and PTM2 had a synergistic effect in a field trapping experiment using mixing ratios from 4:1 to 1:4, but the use of any one of the monomers alone had almost no activity. In 1980, Ei-Garhy (1980) used a mixture of PTM1 and PTM2 sex pheromones smeared on a rubber lure core to capture male potato tuber moths in the field, and found that the environmental temperature and relative humidity had a very significant effect on trapping efficiency. Raman (1982); Raman (1984); Raman (1988) conducted a large number of field trapping activity experiments using PTM1 and PTM2, and found that the mixture of PTM1 and PTM2 was more attractive than PTM1 alone. In 1982, the research group used a mixture of PTM1 and PTM2 in eight different ratio formulations to conduct capture tests and found that the highest capture rate was initially obtained when the ratio of PTM1 to PTM2 was 9:1, 3:1, or 1:1.5. However, after 90 days in the field, the attractiveness of the 9:1 ratio mixture decreased, while the 1:1.5 ratio remained attractive after 90 days. Storage at −5°C for 2 months did not reduce the attractiveness of the mixture. Toth (Toth et al., 1984) studied the response of male potato tuber moths to two sex pheromone components and female crude extracts and found that in wind tunnels and fields, compared with compounds composed of trienes alone, males were better able to localize by a mixture of PTM1 and PTM2 (1:1). The addition of PTM1 reduced the time male moths spent near the pheromone source and the pheromone itself compared to PTM2 alone, also increasing the average number of visits to the source; and male potato tuber moths were also found to have behavioral responses to a mixture of PTM1 and PTM2 (1:1) similar to those elicited by the female crude extract. From 1972 to 2016, Ono (1993); Ono (1994); Ono et al. (1997); Ono and Orita (1986) and Tejima et al. (2013); Tejima et al. (2016) carried out systematic research on the structure and properties of potato tuber moth sex pheromones. In 1986, they found that the ratio of the sex pheromones was affected by temperature. As the feeding temperature increased, PTM2 gradually decreased, but the total amount of sex pheromones did not change. The pupal stage was the most sensitive to temperature changes. Kroschel and Zegarra (Kroschel and Zegarra, 2010; Kroschel and Zegarra, 2013) studied the use of the potato tuber moth pheromones and a single structural pheromone of *Symmetrischema tangolias* combined with the insecticide cyfluthrin to form an attract-kill system, which resulted in 100% mortality in males under laboratory conditions. In field and storage conditions, the trapping method was very effective against potato tuber moths and represents a low-cost control method inducible under storage conditions that can be effectively integrated into potato pest control programs, especially in tropical and subtropical small farming systems. From 2018 to 2019, Gao et al. (2018); Gao et al. (2019a) developed a "comprehensive green control technology for potato tuber moths based on sexual attractants", which integrates a number of prevention and control measures for different stages of potato tuber moth. The application of sexual attractant technology interferes with the normal mating of female adults in the field, and the lack of mating leads to an increase in unviable eggs. After the technology was applied in Qujing, Yunnan, for one to 2 years, the number of potato tuber moths was greatly reduced, and the damage was alleviated.

SYNTHESIS OF POTATO TUBER MOTH SEX PHEROMONE BY PREDECESSORS

So far, the source of potato tuber moth sex pheromone mainly relies on extraction from female insects. Due to the low content in the insect source glands, the separation efficiency is not high, and this source cannot meet the needs of a wide range of field applications. Since the structures of the potato tuber moth sex pheromones (PTM1 and PTM2) were first reported, their structural specificity and remarkable sex-inducing activity have attracted many chemists to attempt the chemical synthesis of these two molecules.

As shown in **Figure 1III**, Fouda et al. (1975) used commercially available tetrahydropyran-protected 6-chloro-1-hexanol as the starting material, and then reacted it with ethynyl lithium to generate compound 4, which was coupled with n-hexene to obtain intermediate 5. Then the elimination reaction took place under the action of phosphorus oxychloride to obtain intermediate 6. The target product 7 (7Z, 9E/Z-tridec-dien-1-ol acetate) was then obtained by catalytic hydrogenation with Pd/C, and the alkyne bond was reduced in parallel with liquid sodium ammonia to obtain the target compound 8 of E-configured olefin (7E, 9E/Z-tridec-dien-1-ol acetate).

In the same year, Roelofs et al. (1975) started their synthesis with a coupling reaction between 4-pentyn-1-ol and vinyl ethyl ether to obtain acetal 9, and propynyl alcohol 10 was gained by reaction with paraformaldehyde and *n*-BuLi. Followed by reduction with LiAlH$_4$, hydroxychlorination under the combined action of MsCl/LiCl/2,4,6-trimethylpyridine to obtain Chloride 11, as illustrated in **Figure 1IV**. Coupling with alkynyl Grignard reagent under the action of CuCl gave compound 12, the protecting group is subsequently removed and alkyne bond was reduced by Lindlar catalyzed stereoselective hydrogenation to obtain Z-configuration double bond. Finally, the terminal primary alcohol hydroxyl group is acetylated to obtain the target compound PTM1.

In 1978, Voerman and Rothschild (1978) used 3-bromo-1-propanol as the starting material, first protected the alcoholic hydroxyl group under the action of dihydropyran to obtain intermediate 14, and then reduced it with propargyl alcohol by Birch to generate alkyne alcohol 15. Then, with *p*-toluenesulfonyl chloride as the halogen source and *n*-butyllithium as the strong base, hydroxychlorination occured to obtain the alkene halogen compound 17, which was then coupled with the alkynyl Grignard reagent to remove the protective group with cuprous chloride to obtain compound 18, as shown in **Figure 1V**. Finally, the target compound PTM1 was obtained by hydroxyacetylation and Raney nickel-catalyzed hydrogenation to reduce the alkynyl group.

The same year, Alexakis et al. (1978) reported the total synthesis route of PTM1. The key step is the ring-opening coupling reaction between an organocopper reagent and an allyl epoxy compound, as illustrated in **Figure 1VI**. This route uses lithium dipentyl ketone as the starting material. First, the key E, Z diene compound 19 is prepared by addition coupling and conjugated ring opening, and then the intermediate 21 is obtained by hydroxy chlorination and alkylation. This is followed by ester reduction and hydroxyacetylation to give the pheromone PTM1.

In 1984, Nishiyama et al. (1984) used the silicon-guided Beckmann fragmentation strategy to develop several new methods for the stereo-controlled synthesis of insect sex pheromones. The key is to construct the E-type double bond through the trimethylsilyl auxiliary region and the stereo-controlled Beckmann rearrangement reaction. This route uses 2-cyclopentenone as the starting material, reacts with trimethylsilyllithium and n-tributyltin hydride in turn, and then reacts with octynyl bromide to obtain compound 22, which is hydrogenated by Lindlar catalyzed to obtain Z-configuration alkene 23, as shown in **Figure 1VII**. Subsequently, it was reacted with hydroxylamine hydrochloride to form oxime acyl ester 24, and then the diene cyano compound 25 was obtained by silicon-promoted Beckmann fragmentation reaction under the action of TMSOTf silicon reagent, and finally potato Tuber moth sex pheromone PTM1 was obtained through two reductions and hydroxyacetylation.

In 1986, Yadav and Reddy (1986), using Z-alkene-1-ol as the starting material, first obtained Z-form alkene chloride 27 by hydroxychlorination, and then reacted with Grignard reagent for carbon chain growth and coupling reaction to obtain alkene benzyl ether 28, as illustrated in **Figure 1VIII**. Subsequent

Birch reduction to remove the benzyl group and hydroxy bromination in two steps produced intermediate 29, which was reacted with 4-pentyn-1-ol prepared with tetrahydrofuroyl chloride through a diionic reaction to obtain primary alkenyl alkyne primary alcohol 30. Finally, Birch reduction of the alkynyl group and primary alcohol hydroxyacetylation completed the total synthesis of PTM1.

In 1990, Nonoshita et al. (1990) developed the use of bulky, sterically hindered diarylmethylaluminum as a key reducing agent for Claisen rearrangement to construct E-form double bonds with high selectivity, as shown in **Figure 2I**. Using 1-heptyne as the starting material, the rearranged precursor allyl vinyl ether 31 was obtained through SN2 reaction, Lindlar reduction, deacetalization, and Grignard reagent coupling and substitution. The Claisen rearrangement reaction occurred under the action of large sterically hindered diarylmethylaluminum 37, and the diene aldehyde with the E configuration was obtained with high stereoselectivity. Finally, the target product PTM1 was obtained through two-step conversion of aldehyde group reduction and primary alcohol acetylation.

In 1995, Hutzinger and Oehlschlager (1995) developed a method for the stereoselective synthesis of Z, E- and 1Z, 4Z-dienes by cross-coupling of allyl substrates with vinyl organometallic reagents, and used this method to synthesize PTM1. The synthetic route uses 3-pentyn-1-ol as the starting material, obtains 4-pentyn-1-ol through the Zipper reaction, and then protects the hydroxyl group to obtain compound 39. The E-configuration olefin 41 was obtained under the action of an organocopper reagent, as illustrated in **Figure 2II**. This is then coupled with allyl chloride under the action of lithium 2-thiophene cyanoate to obtain diolefin 42, and finally the hydroxy THP protecting group is removed and acetylated to obtain the target compound PTM1.

One year later, Vasil'ev and Serebryakov (1996) used 2E, 4E-nonadienal and vinylmagnesium bromide as starting materials, and obtained triene secondary alcohol 33 through the Grignard reaction, and then 1,4-selective reduction of conjugated olefins took place under the action of the aromatic chromium tricarbonyl to generate Z-type olefins 45, as illustrated in **Figure 2III**. Subsequently, Claisen-Johnson rearrangement occurred in the presence of trimethyl orthoacetate and a small amount of propionic acid to obtain (4E, 7Z)-configured diene 46, and finally ester reduction and hydroxyacetylation occurred to obtain the target compound PTM1.

In 1997, Odinokov et al. (1997) started their synthesis with a coupling reaction between propargyl alcohol and 1-bromopentane to build alkynol compounds. Then, under the action of phosphorus tribromide, hydroxy bromination occured to obtain propargyl bromide, which was then prepared into propargyl magnesium bromide Grignard reagent, and a Grignard addition reaction occured with acrolein to obtain the key intermediate 50, as illustrated in **Figure 2IV**. Subsequent intramolecular Claisen rearrangement under the action of triethyl orthoate generated compound 51. Finally, through Raney-Ni catalyzed hydrogenation reduction to 7Z double bond, ester reduction to alcohol, and hydroxyacetylation, two simple transformations achieved the total synthesis of the target PTM1.
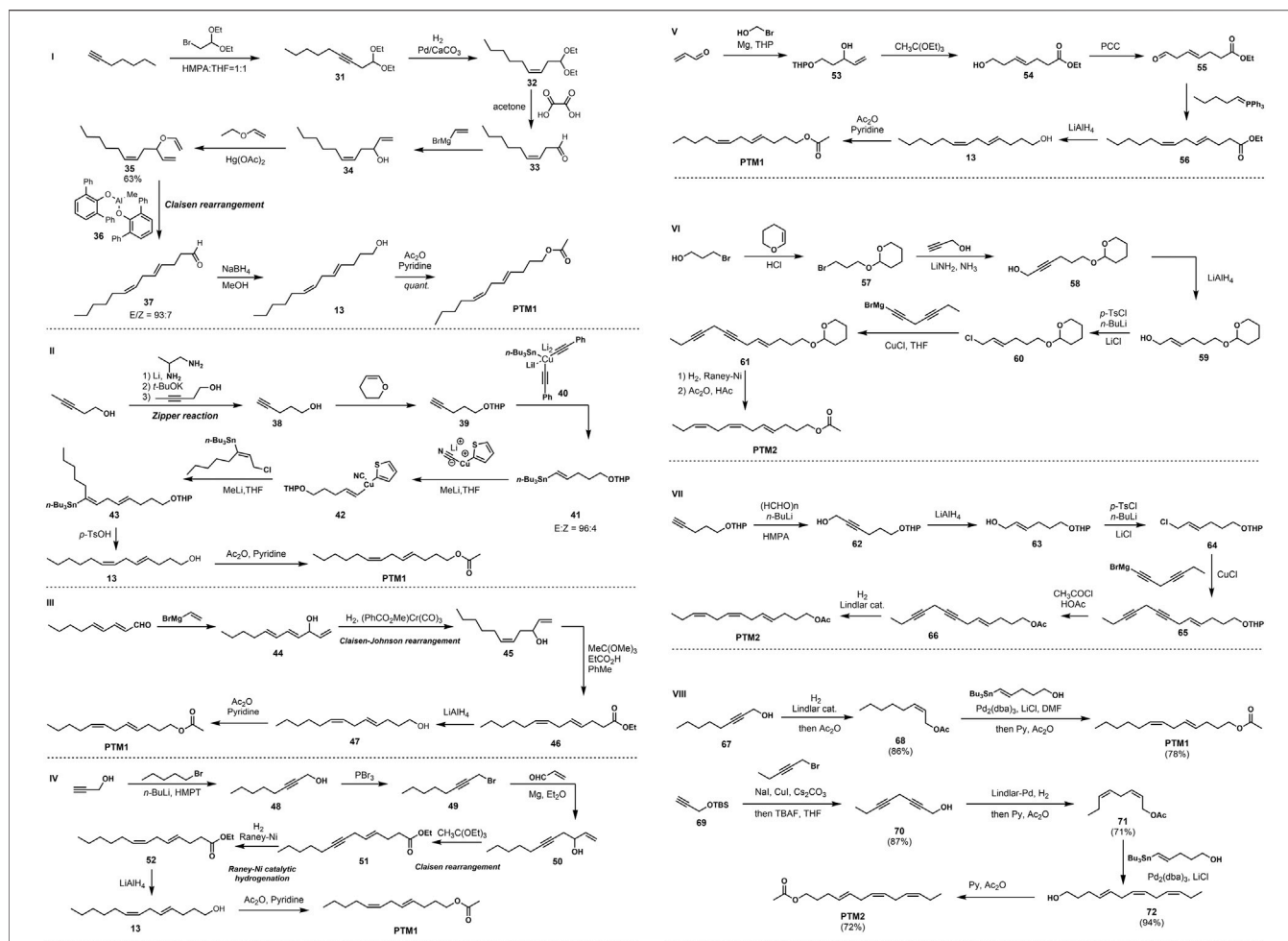
FIGURE 2 | I Nonashita's synthesis of PTM1 via Claisen rearrangement in 1990. II Hutzinger's synthesis of PTM1 in 1995. III Vasil'ev's synthesis of PTM1 in 1996. IV Odiokov's synthesis of PTM1 in 1997. V Vakhidov's synthesis of PTM1 in 2007. VI Voerman's synthesis of PTM2 in 1978. VII Fukami's synthesis of PTM2 in 1978. VIII Our group's synthesis of PTM1 and PTM2 via Stille coupling in 2021.

In 2007, Vakhidov and Musina (2007) reported a new method for the synthesis of PTM1 using the Claisen rearrangement reaction and the Wittig reaction, as shown in **Figure 2V**. Using acrolein and 2-bromoethanol as starting materials, hydroxyaldehyde 53 was first prepared by Grignard reaction, and then intramolecular Claisen rearrangement occurred in the presence of triethyl orthoacetate as THP was simultaneously removed to generate E-form olefin carboxylate 54, followed by PCC oxidation and Wittig reaction to give 55, and finally ester reduction and hydroxyacetylation to achieve the synthesis of PTM1.

There are relatively few synthetic examples of PTM2, with only two cases reported. In 1978, Voerman and Rothschild (1978) completed the synthesis PTM2 adopting the same strategy as shown in **Figure 2VI**. After allyl chloride 60 is prepared, it is coupled with diacetylene under the catalysis of cuprous chloride to obtain 4E-7,10-diacetylene 61, followed by Raney-Ni catalytic hydrogenation to obtain 4E-7Z,10Z-trien-1-ol, and finally acetylation to obtain the target compound PTM2.

That same year, Fukami et al. (1978) used dihydropyran-protected as the starting material, and obtained allyl chloride 64 through chain extension, acetylenic bond reduction, and hydroxyl halogenation, as shown in **Figure 2VII**. This was coupled with a dialkynyl Grignard reagent to obtain 4E-7,10-dialkyne 65, followed by replacement of the hydroxyl protecting group, and finally the synthesis of the potato tuber moth sex pheromone PTM2 by Lindlar hydrogenation reduction.

SYNTHESIS OF POTATO TUBER MOTH SEX PHEROMONE BY OUR GROUP

The difficulty and challenge for PTM1 and PTM2 lie in the high stereoselectivity construction of the double bonds. In the early reports of sporadic synthesis methods, the construction of E and Z double bonds mainly included Grignard reagent coupling, Wittig reaction, etc., but these methods have the defects of low yield and vague selectivity. Based on this, our research group has

carried out research on the synthesis of the potato tuber moth sex pheromones PTM1 and PTM2, as shown in **Figure 2VIII**. The goal was to use Lindlar-catalyzed hydrogenation and Stille coupling as key reactions to realize the construction of Z and E double bonds with high selectivity and yield.

This scheme uses commercial tert-butyldimethyl (2-propynyloxy) silane as the starting material, first reacting it with 1-bromo-2-pentyne and removing the TBS protecting group to give the bisalkynyl compound 70 by TBAF. At the same time, using 2-octyn-1-ol as the starting material, the key intermediates 67 and 70 were obtained by the catalytic hydrogenation of Lindlar and the protection of the primary alcohol by the acetyl group. Subsequently, the construction of the E-type double bond was achieved by Stille coupling under the action of tris(dibenzylideneacetone)dipalladium. Finally, the primary alcohol was acetylated to obtain the target compounds PTM1 and PTM2, with the overall yields of 67 and 42% (Gao et al., 2018).

SUMMARY

Potatoes are harmed by various pests such as potato tuber moth, and the average yield loss can reach 40–45%. However, the acquisition of the sex pheromone of potato tuber moth is mainly obtained from the glands of female moths. This method is inefficient and not enough to support the application of field experiments. The new method developed by our group has low cost, and has important scientific significance and application prospect for realizing the technological production of potato tuber moth sex pheromone.

AUTHOR CONTRIBUTIONS

HP: She reviewed the abstract, introduction, structure identification, field application and synthesis of potato tuber moth sex pheromone, summary and prospect. HZ: She prepared all the scheme and references. LA: He foud the references about YG. JH: He reviewed all literatures and gave significant discussion. YC: He reviewed the synthetic efforts towards potato tuber moth sex pheromone in the past time. He summed up very beautiful reaction schemes.

FUNDING

REFERENCES

Adeesan, C., Tamhankar, A. J., and Rahalkar, G. W. (1969). Sex Pheromone Gland in the Potato Tuberworm Moth, Phthorimaea Operculella1,2. *Ann. Entomol. Soc. America* 62, 670–671. doi:10.1093/aesa/62.3.670

Alexakis, A., Cahiez, G., and Normant, J. F. (1978). Highly Stereoselective Synthesis of the Insect Sex Pheromone of Phthorimaea Operculella and of Propylure. *Tetrahedron Lett.* 19, 2027–2030. doi:10.1016/S0040-4039(01)94740-9

Bacon, O. G., Seiber, J. N., and Kennedy, G. G. (1976). Evaluation of Survey Trapping Techniques for Potato Tuberworm Moths with Chemical Baited Traps1. *J. Econ. Entomol.* 69, 569–572. doi:10.1093/jee/69.5.569

Coll, M., Gavish, S., and Dori, I. (2000). Population Biology of the Potato Tuber Moth, Phthorimaea Operculella (Lepidoptera: Gelechiidae), in Two Potato Cropping Systems in Israel. *Bull. Entomol. Res.* 90, 309–315. doi:10.1017/s0007485300000432

El-Garhy, M. S. (1980). Preliminary Results with Sex Pheromones to Trap Potato Tuber Worm Moths in Saudi Arabia. *Potato Res.* 23, 361–363. doi:10.1007/BF02360675

Fouda, H. G., Seiber, J. N., and Bacon, O. G. (1975). A Potent Sex Attractant for the Potato Tuberworm Moth1. *J. Econ. Entomol.* 68, 423–427. doi:10.1093/jee/68.4.423

Fukami, H., Ishii, S., and Yamaoka, R. (1978). *Bochu Kagaku Kenkyusho*, 7. Japan.

Gao, Y. L., Mei, X., Weng, A., and Yuan, H. (2018). *Potato Tuber Moth Attractant Composition and its Application*. Beijing: CN108077256A.

Gao, Y., Xu, J., Liu, N., Zhou, Q., Ding, X., Zhan, J., et al. (2019a). Current Status and Management Strategies for Potato Insect Pests and Diseases in China. *Plant Prot.* 45, 106–111. doi:10.16688/j.zwbh.2019353

Gao, Y. L., Yan, J., Mei, X., Wang, L., and Ning, J. (2019b). *System Optimized Potato Tuber Moth Attractant Containing Cis-10-Tridecene-1-Ol Acetate and its Application*. Beijing: CN110292043A.

Hutzinger, M. W., and Oehlschlager, A. C. (1995). Stereoselective Synthesis of 1,4-Dienes. Application to the Preparation of Insect Pheromones (3Z,6Z)-Dodeca-3,6-Dien-1-Ol and (4E,7Z)-Trideca-4,7-Dienyl Acetate. *J. Org. Chem.* 60, 4595–4601. doi:10.1021/jo00119a043

Kroschel, J., and Zegarra, O. (2010). Attract-and-kill: a New Strategy for the Management of the Potato Tuber Moths Phthorimaea Operculella (Zeller) and Symmetrischema Tangolias (Gyen) in Potato: Laboratory Experiments towards Optimising Pheromone and Insecticide Concentration. *Pest Manag. Sci.* 66, 490–496. doi:10.1002/ps.1898

Kroschel, J., and Zegarra, O. (2013). Attract-and-kill as a New Strategy for the Management of the Potato Tuber mothsPhthorimaea operculella(Zeller) andSymmetrischema tangolias(Gyen) in Potato: Evaluation of its Efficacy under Potato Field and Storage Conditions. *Pest Manag. Sci.* 69, a–n. doi:10.1002/ps.3483

Nishiyama, H., Sakuta, K., and Itoh, K. (1984). New Stereocontrolled Approach to Some Insect Pheromones via Silicon-Directed Beckmann Fragmentation. *Tetrahedron Lett.* 25, 223–226. doi:10.1016/S0040-4039(00)99845-9

Nonoshita, K., Banno, H., Maruoka, K., and Yamamoto, H. (1990). Organoaluminum-promoted Claisen Rearrangement of Allyl Vinyl Ethers. *J. Am. Chem. Soc.* 112, 316–322. doi:10.1021/ja00157a049

Odinokov, V. N., Vakhidov, R. R., Shakhmaev, R. N., and Zorin, V. V. (1997). Insect Pheromones and Their Analogs LV. Synthesis of trideca-4E, 7Z-Dien-1-YL Acetate-Component of the Sex Pheromone ofPhthorimaea Opercucella. *Chem. Nat. Compd.* 33, 350–352. doi:10.1007/BF02234894

Ono, T., Chouvalitwongporn, P., and Saito, T. (1997). Comparison of the Sex Pheromone System between Japanese and Thai Populations of the Potato Tuberworm Moth, Phthorimaea Operculella (Lepidoptera: Gelechiidae). *Appl. Entomol. Zool.* 32, 514–517. doi:10.1303/aez.32.514

Ono, T. (1993). Effect of Rearing Temperature on Pheromone Component Ratio in Potato Tuberworm moth,Phthorimaea Operculella, (Lepidoptera: Gelechiidae). *J. Chem. Ecol.* 19, 71–81. doi:10.1007/BF00987472

Ono, T. (1994). Effect of Temperature on Biosynthesis of Sex Pheromone Components in Potato Tuberworm moth,Phthorimaea Operculella (Lepidoptera: Gelechiidae). *J. Chem. Ecol.* 20, 2733–2741. doi:10.1007/BF02036204

Ono, T., Iyatomi, K., and Saito, T. (1972). Mating Behavior of the Potato Tuber Moth, Phthorimaea Operculella ZELLER. *Jpn. J. Appl. Entomol. Zoolog.* 16, 51–53. doi:10.1303/jjaez.16.51

Ono, T., and Orita, S. (1986). Field Trapping of the Potato Tuber Moth, Phthorimaea Operculella (Lepidoptera : Gelechiidae), with the Sex Pheromone. *Appl. Entomol. Zool.* 21, 632–634. doi:10.1303/aez.21.632

Persoons, C. J., Voerman, S., Verweil, P. E. J., Ritter, F. J., Nooyen, W. J., and Minks, A. K. (1976). Sex Pheromone of the Potato Tuberworm Moth, Phthorimaea Operculella: Isolation, Identification and Field Evaluation. *Entomol. Exp. Appl.* 20, 289–300. doi:10.1111/j.1570-7458.1976.tb02645.x

Raman, K. V. (1982). Field Trials with the Sex Pheromone of the Potato Tuberworm. *Environ. Entomol.* 11, 367–370. doi:10.1093/ee/11.2.367

Raman, K. V. (1984). Evaluation of a Synthetic Sex Pheromone Funnel Trap for Potato Tuberworm Moths (Lepidoptera: Gelechiidae). *Environ. Entomol.* 13, 61–64. doi:10.1093/ee/13.1.61

Raman, K. V. (1988). Control of Potato Tuber Moth Phthorimaea Operculella with Sex Pheromones in Peru. *Agric. Ecosyst. Environ.* 21, 85–99. doi:10.1016/0167-8809(88)90141-7

Roelofs, W. L., Kochansky, J. P., Carde, R. T., Kennedy, G. G., Henrick, C. A., Labovitz, J. N., et al. (1975). Sex Pheromone of the Potato Tuberworm Moth,. *Life Sci.* 17, 699–705. doi:10.1016/0024-3205(75)90524-X

Shen, S., Cao, S., Zhang, Z., Kong, X., Liu, F., Wang, G., et al. (2020). Evolution of Sex Pheromone Receptors in Dendrolimus Punctatus Walker (Lepidoptera: Lasiocampidae) Is Divergent from Other Moth Species. *Insect Biochem. Mol. Biol.* 122, 103375. doi:10.1016/j.ibmb.2020.103375

Tejima, S., Ono, T., and Sakuma, M. (2013). Aim-then-shoot Anemotaxis Involved in the Hopping Approach of Potato Tuberworm mothPhthorimaea Operculellatoward a Sex Pheromone Source. *Physiol. Entomol.* 38, 292–301. doi:10.1111/phen.12033

Tejima, S., Ono, T., and Sakuma, M. (2016). Antennal Mechanosensors Mediate Sex Pheromone-Induced Upwind Orientation in the Potato Tuberworm Moth. *Physiol. Entomol.* 42, 113–124. doi:10.1111/phen.12180

Toth, M., Bellas, T. E., and Rothschild, G. H. L. (1984). Role of Pheromone Components in Evoking Behavioral Responses from Male Potato Tuberworm moth,Phthorimaea Operculella (Zeller) (Lepidoptera: Gelechiidae). *J. Chem. Ecol.* 10, 271–280. doi:10.1007/BF00987855

Vakhidov, R. R., and Musina, I. N. (2007). Synthesis of 4E,7Z-Tridecadien-1-Ylacetate, a Component of the Phthorimaea Opercucella Sex Pheromone. *Chem. Nat. Compd.* 43, 282–284. doi:10.1007/s10600-007-0105-2

Vasil'ev, A. A., and Serebryakov, E. P. (1996). Simple Synthesis of 4E,7Z-Tridecadien-1-Yl Acetate, a Component of the Sex Pheromone of the Potato Moth Phthorimaea Operculella (Lepidoptera: Gelechiidae). *Izv. Akad. Nauk, Ser. Khim.*, 2350–2353.

Voerman, S., Minks, A. K., and Persoons, C. J. (1977). Elucidation of the Sex Pheromone System of the Potato Tuberworm moth,Phthorimaea Operculella (Zeller) (Lepidoptera, Gelechiidae): a Short Review. *Potato Res.* 20, 123–126. doi:10.1007/bf02360271

Voerman, S., and Rothschild, G. H. L. (1978). Synthesis of the Two Components of the Sex Pheromone System of the Potato Tuberworm moth,Phthorimaea Operculella (Zeller) (Lepidoptera: Gelechiidae) and Field Experience with Them. *J. Chem. Ecol.* 4, 531–542. doi:10.1007/BF00988917

Web of Science (2022). *Statistics of the Number of Research Papers on Insect Sex Pheromone from Web of Science Upto 2022*. Available from: http://webofknowledge.com.

Witzgall, P., Kirsch, P., and Cork, A. (2010). Sex Pheromones and Their Impact on Pest Management. *J. Chem. Ecol.* 36, 80–100. doi:10.1007/s10886-009-9737-y

Wright, R. H. (1964). After Pesticides-What? *Nature* 204, 121–125. doi:10.1038/204121a0

Xie, C. (2014). Integrated Control Techniques of Phthorimaea Operculella (Zeller). *Chin. Potato J.* 28, 235–237.

Xu, J., Zhu, J., Yang, Y., Tang, H., Lü, H., Fan, M., et al. (2019). Status of Major Diseases and Insect Pests of Potato and Pesticide Usage in China. *Scientia Agricultura Sinica* 52, 2800–2808. doi:10.3864/j.issn.0578-1752.2019.16.006

Yadav, J. S., and Reddy, P. S. (1986). Allylation of Grignard Reagents: Its Application for the Synthesis of (4E, 7Z)-4,7-Tridecadienyl Acetate, A Sex Pheromone of Potato Tuberworm Moth. *Synth. Commun.* 16, 1119–1131. doi:10.1080/00397918608056355

Yamaoka, R., Fukami, H., and Ishii, S. (1976). Isolation and identification of the female sex pheromone of the potato tuberworm moth, Phthorimaea operculella (Zeller). *Agric. Biol. Chem.* 40, 1971–1977. doi:10.1080/00021369.1976.10862333

Yan, J., and Gao, Y. (2019). Biology, Ecology and Integrated Management of the Potato Tuber Moth, Phthorimaea Operculella (Lepidoptera: Gelechiidae). *Acta Entomologica Sinica* 62, 1469–1482. doi:10.16380/j.kcxb.2019.12.012

A Synthetic View on Momilactones and Related 9*β*-H Pimarane Skeleton Diterpenoids

Yue Zhang, Mengran Li, Qichang Liu, Jian Huang* and Yang Chen*

State Key Laboratory Breeding Base of Green Pesticide and Agricultural Bioengineering, Key Laboratory of Green Pesticide and Agricultural Bioengineering, Ministry of Education, Research and Development Center for Fine Chemicals, Guizhou University, Guiyang, China

Allelochemicals are secondary metabolites produced from plants and used to prevent and control the invasion of other plants and microorganisms, with broad application prospects in crop protection. Structurally, momilactones belong to 9*β*-H pimarane diterpenoids, one of rice's significant allelochemicals with anti-weeds and antibacterial activity. Rare studies have been reported with the synthesis challenges of the unique 9*β*-H pimarane skeleton. Hence, synthetic strategies of momilactones and related 9*β*-H pimarane skeleton are reviewed from 1984 to 2021.

Keywords: 9*β*-H pimarane, skeleton, momilactones, allelochemical, diterpenoids

INTRODUCTION

Modern genetic evidence and recent studies have shown that momilactones are among the most active allelochemicals (Lin et al., 2019) and play a key role in allelopathy and resistance induction in rice (Okada et al., 2016). In 1973, momilactone A (**1**) and momilactone B (**2**) were isolated from *Oryza sativa* L. by Kato (Kato et al., 1973), firstly identified as new growth inhibitors. They have significant bioactivities, including weeds elimination in paddy fields and antimicrobial activity, especially toward *Pyricularia oryzae* Cav. (Jiang et al., 2016). However, the natural content of momilactones could not meet further research needs. Synthetic approaches to yield these natural products seem to attract synthetic chemists (Mohan et al., 1996). Kato (Kato et al., 1977) determined the stereochemical configuration of momilactone A by X-ray single-crystal diffraction as 9*β*-H. Momilactone A has continuous chiral centers with a *trans-syn-cis* tricyclic skeleton named 9*β*-H pimaranes, as shown in **Figure 1**, characterized in the family compounds (Zhao et al., 2018). Moreover, the *trans-syn-cis* tricyclic ring and the stereochemistry at C-9 led to significant challenges in synthesizing these molecules. In the early stage (Deslongchamps and Germain, 1999), the construction of the 9*β*-H-pimarane skeleton commonly had drawn the attention of scientists devoted to the synthesis of momilactones and related diterpenoids.

9*β*-H-pimarane diterpenoids are featured with the *trans-syn-cis* tricyclic skeleton and *β*-configuration of the proton at C-9. Such studies have been reported to investigate their abundant biological activities (Xu et al., 2021). **Figure 1** shows that the known (9*β*-H)-pimarane related diterpenoids can be classified into (9*β*-H)-pimarane (**1–4**, **6–18**), 16-*nor*-(9*β*-H)-pimarane (**28**), 17-*nor*-(9*β*-H)-pimarane (**19–27**), 19-*nor*-(9*β*-H)-pimarane (**5**), and 15,16,17-tri*nor*-(9*β*-H)-pimarane derivatives (**29–33**). Among the momilactone family, momilactones A and B were obtained from moss *Hypnum plumaeforme* by Nozaki (Nozaki et al., 2007). Momilactones C (**3**), F (**4**), and E (**5**) found from the hulls (Liu et al., 2012), leaves, and roots of rice (Cho et al., 2015). Strictly speaking, momilactone E belongs to 19-*nor*-(9*β*-H)-pimarane, and momilactone D possesses the 9*β*-OH, which could not be classified as (9*β*-H)-pimarane. These natural products

FIGURE 1 | 9β-H-Pimarane related diterpenoids and the 9β-H pimarane skeleton.
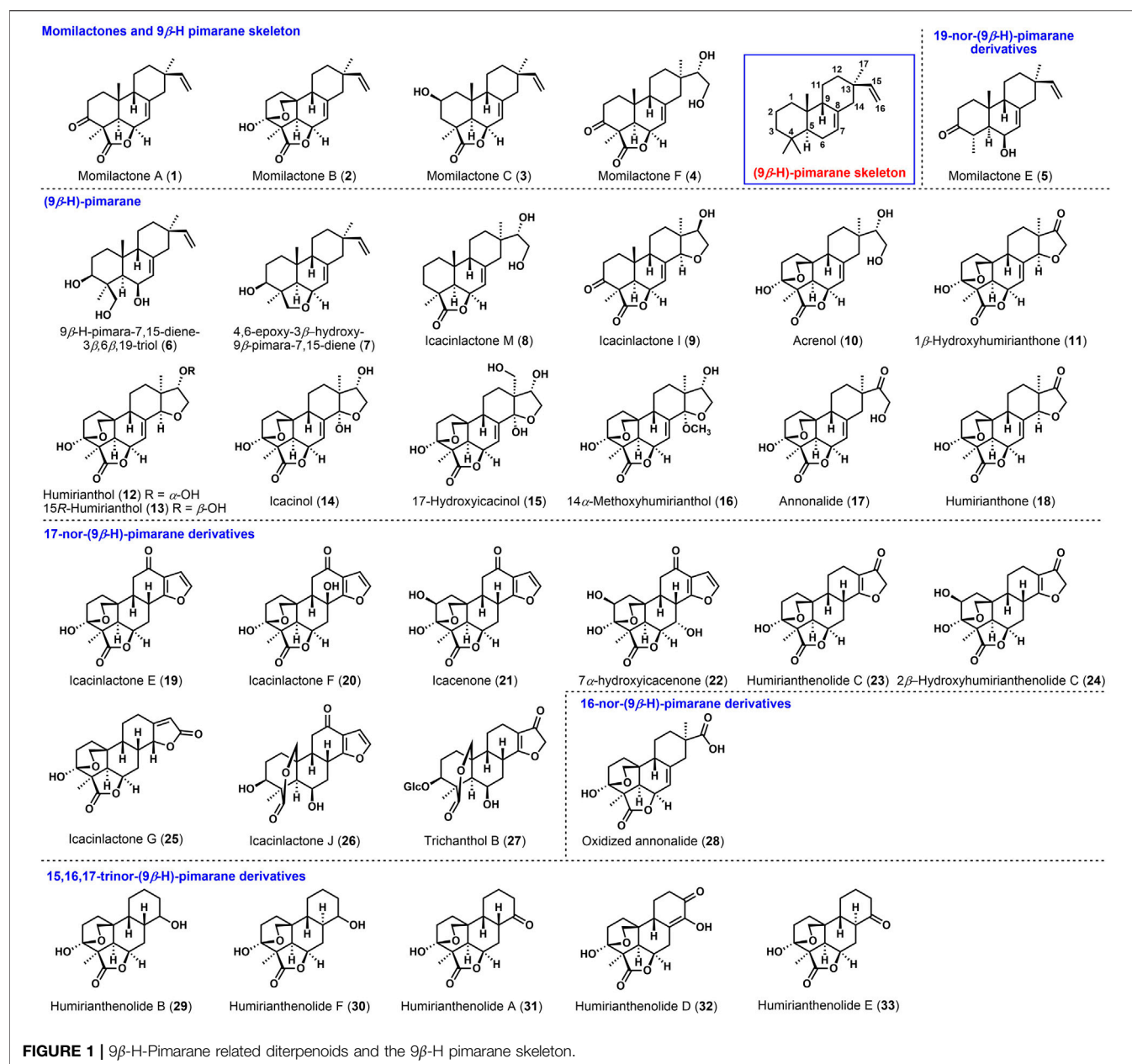
exhibited inhibition of weeds and antibacterial activities (Tsunakawa et al., 1976). Momilactone B had the most efficient, currently known bioactivity (Dayan et al., 2009).

For example, (9β-H)-pimaranes, 4,6-epoxy-3β-hydroxy-9β-pimara-7,15-diene (**7**), and 9β-H-pimara-7,15-diene-3β,6β,19-triol (**6**) (Horie et al., 2015) were isolated from the rice husks of *Oryza sativa* L. The anti-fungal activities on *Magnaporthe grisea* (Li et al., 2014) have been investigated. Icacinlactone M (**8**), 14α-methoxyhumirianthol (**16**), and annonalide (**17**) were found from *Icacina oliviformis* (Zhao et al., 2015a) for the first time (Sun et al., 2021). Besides (Graebner et al., 2000), humirianthol (**12**) (Li et al., 2020), icacinol (**14**), 17-hydroxyicacinol (**15**), 14α-methoxyhumirianthol (**16**), and annonalide (**17**) showed

cytotoxic activities (Onakpa et al., 2014) toward human cancer cell lines. These compounds were also obtained from the tuber of *Icacina oliviformis* (Zhou et al., 2020). Cytotoxic humirianthone (**18**) and 15R-humirianthol (**13**) were found from the lianas in the Suriname rainforest (Adou et al., 2005). The 17-*nor*-(9β-H)-pimarane derivates (Zhao et al., 2015b), humirianthenolide C (**23**), 2β-hydroxyhumirianthenolide C (**24**), icacenone (**21**), 7α-hydroxyicacenone (**22**), and icacinlactone E-J (**19**, **20**, **25**, **26**) with cytotoxic activities (Guo et al., 2016) were isolated from the tubers of *Icacina trichantha* (Zhao et al., 2015a). 7α-Hydroxyicacenone (**22**), icacenone (**21**), and trichanthol B (**27**) (Xu et al., 2021) might also be considered for antimicrobial activities (On'Okoko et al., 1985).

SCHEME 1 | De Groot's first synthesis of (±)-4,4-dinor-(9β-H)-pimara-7,15-diene in 1984.
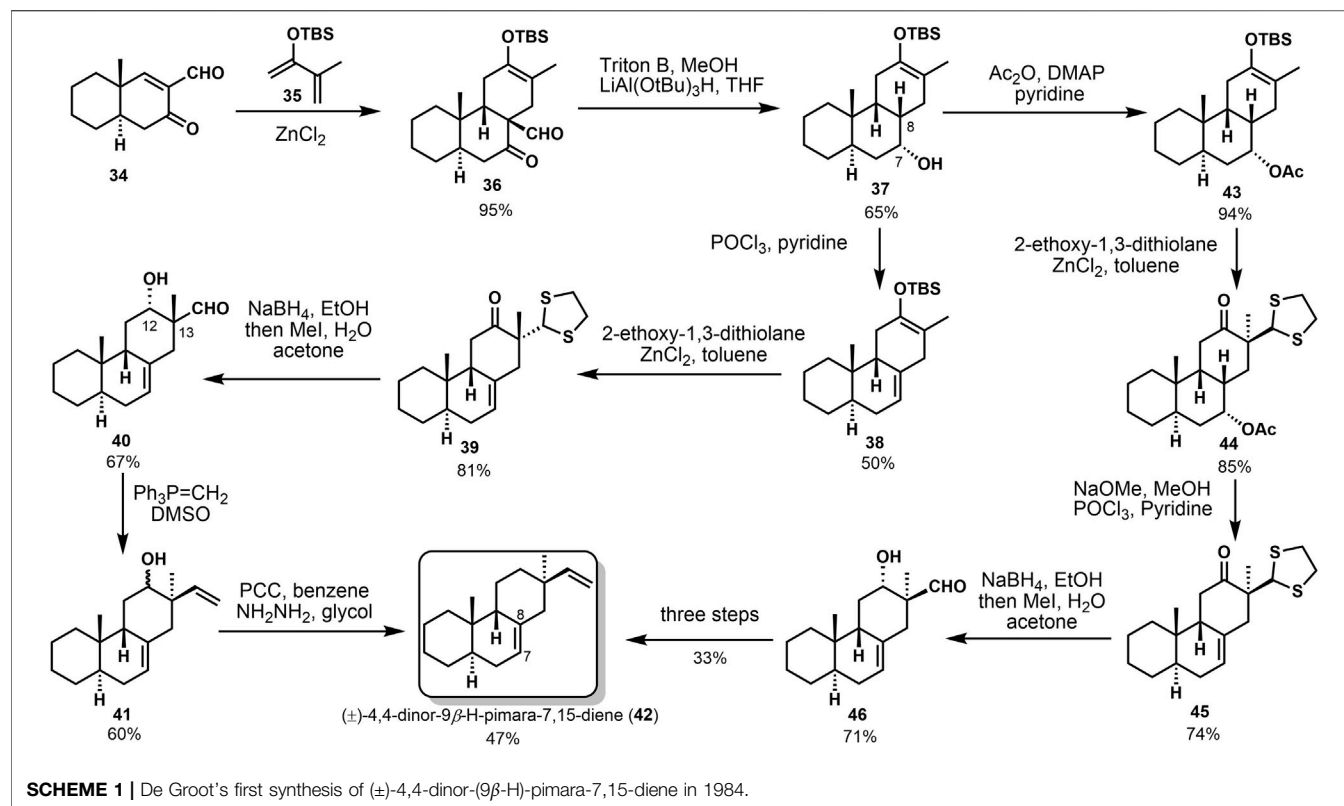
Humirianthenolides A, B, D, E, and F (**29–33**) were separated from the tuber of *Humirianthera rupestris*, known as the 15,16,17-tri*nor*-(9β-H)-pimarane derivates (Zoghbi et al., 1981). Oxidized annonalide (**28**) was identified as 16-*nor*-(9β-H)-pimarane derivates. Most of the above compounds exhibited biological activities such as plant growth inhibition, anti-fungal activity (Shen et al., 2020), and cytotoxicity (Zhou et al., 2020). Given the broad biological activities, the chemical syntheses of 9β-H-pimarane diterpenoids are significant, although there was only one total synthesis of (±)-momilactone A reported by Germain and Deslongchamps Germain and Deslongchamps (2002). This review covers the recent synthetic approaches to momilactones and related 9β-H-pimarane skeleton.

SYNTHETIC STUDIES TOWARD 9β-H PIMARANE SKELETON DITERPENOIDS

A few synthetic strategies about 9β-H-pimarane skeleton molecules had been described for the challenging framework, especially the continuous chiral centers. It would be difficult to accomplish the *trans-syn-cis* tricyclic with stereoselectivity.

In 1984, Sicherer-Roetman (Sicherer-Roetman et al., 1984) described the synthesis of model compound (±)-4,4-dinor-(9β-H)-pimara-7,15-diene **42**, possessing the *trans-syn-cis* skeleton and α-methyl and β-vinyl groups at C-13. The transannular Diels–Alder strategy had been used to construct the core tricyclic system, as shown in **Scheme 1**. Product **36** was obtained by the Diels–Alder reaction of

ketone formaldehyde **34** and o-diolefin **35** under the catalysis of ZnCl₂; the step provided that *cis*-adduct **36** was deformylated in the presence of triton B and then hydrogenated with LiAl(O*t*Bu)₃H to obtain sole reduction product **37**. From this point on, compound **42** could be provided by two different strategies. First, compound **37** was dehydrated in POCl₃ and pyridine to yield dienolsilane **38**. Then, dithioacetal **39** was obtained with 2-ethoxy-1,3-dithiolan, and *cis*-β-hydroxyaldehyde **40** was afforded by reduction and hydrolysis. They got β-vinyl product **41** through a Wittig reaction of compound **40**. Considerable epimerization occurred at C-12 and C-13, a handful of the α-vinyl product was detected. Finally, oxidation of **41** and Wolff–Kishner reduction of the carbonyl gave compound **42** at 47% yield. The second approach protected the hydroxyl group to afford acetyl ester **43**. Alkene intermediate **45** was afforded through the alkylation, hydrolyzation, and dehydration, followed by reduction and hydrolyzation. With compound **46** in hand, epimerization also occurred, resulting in a single β-vinyl product. The target compound **42** is finally transformed under the same conditions as the first route.

The stereoselective synthesis of (±)-4,4-dinor-9β-H-pimara-7,15-diene (**42**) was accomplished by Sicherer-Roetman Sicherer-Roetman et al. (1985). Initially Meyer (Meyer et al. 1975) formed the *trans-syn-cis* tricyclic product **50** with formyl enone **34** and tert-butyl 3-oxopentanoate **49** (**Scheme 2A**). Formylation and dehydrogenation of decalone **47** provided the starting compound **34**. To investigate the alkylation of **50** and get β-vinyl group at C-13, they prepared trimethylsilyl enol ether **53** after reduction, but product **53** would hydrolyze rapidly. Then they obtained **54** from

SCHEME 2 | De Groot's second synthesis of (±)-4,4-dinor-(9β-H)-pimara-7,15-diene in 1985.
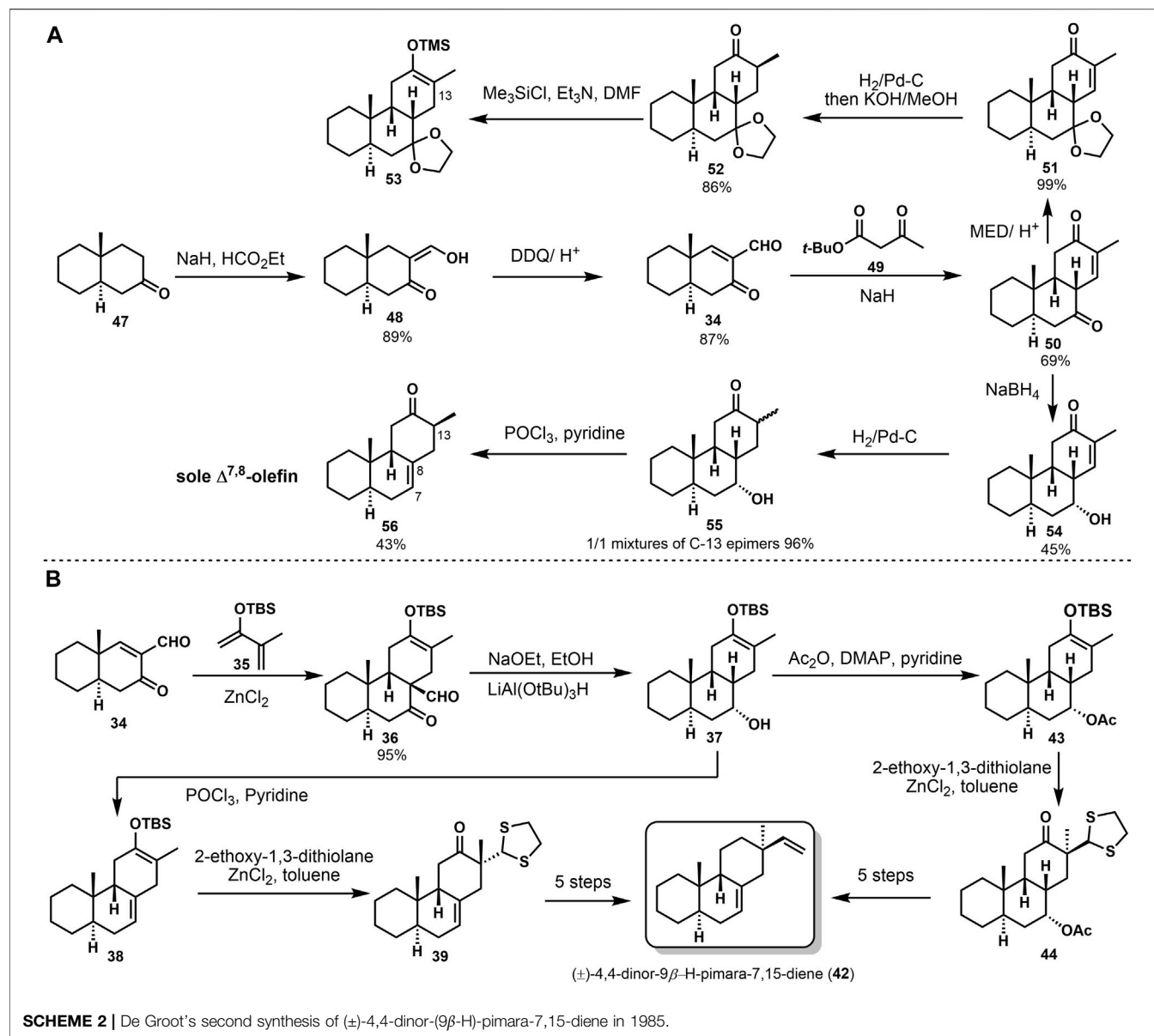
50 with the presence of NaBH₄. Product **54** could be treated through hydrogenation and elimination to get **56**. Elimination of **55** only provided the Δ⁷,⁸-olefin in 43% yield. Another approach was based on the Diels–Alder reaction. They obtained regiospecific silyl enol ether **36** and provided the desired stereochemistry at C-9. Deformylation of product **36** and reduction with lithium tri-tert-butoxy aluminum hydride gave alcohol **37**. Then, product **37** was converted into model compound (±)-4,4-dinor-(9β-H)-pimara-7,15-diene (**42**) *via* several transformations (**Scheme 2B**). These conversions were reported in 1984 by Sicherer-Roetman (Sicherer-Roetman et al., 1984).

(±)-9β-H-pimara-7,19-diene (**64**) was seen as one of the intermediates in the biosynthesis of photoalexines in rice. It possessed the A, B, C ring system of momilactones. In 1989,

Jansen (Jansen et al., 1989) reported the synthesis of (±)-9β-H-pimara-7,19-diene (**64**). They followed their previous syntheses to carry out a Diels–Alder reaction between enone aldehyde **57** and 2-(tert-butyldimethylsilyloxy)-3-methyl-1,3-butadiene **35**. Through deformylation and hydrogenation, with the hydroxyl group being protected, 7α-acetoxy compound **60** was provided. Stereoselective alkylation of the silyl enol ether **60** with CH₂CHClSPh, followed by oxidation and elimination of the sulfoxide group, gained the desired vinyl product **62**. The carbonyl was removed during the Wolff–Kishner reduction of **62**. Finally, (±)-9β-H-pimara-7,19-diene (**64**) gave a 28% overall yield (**Scheme 3**).

The synthetic challenge of 9β-H pimarane skeleton could be to create the 9,10-*syn* configuration (Feilner et al., 2021). Several synthetic approaches have been accomplished (Feilner et al.,

SCHEME 3 | De Groot's synthesis of (±)-(9β-H)-pimara-7,19-diene in 1989.

SCHEME 4 | Coates's synthesis of (−)-(9β-H)-pimara-7,15-diene in 1992.

SCHEME 5 | Yajiama's synthesis of (±)-3β-hydroxy-9β-pimara-7,15-diene in 2011.
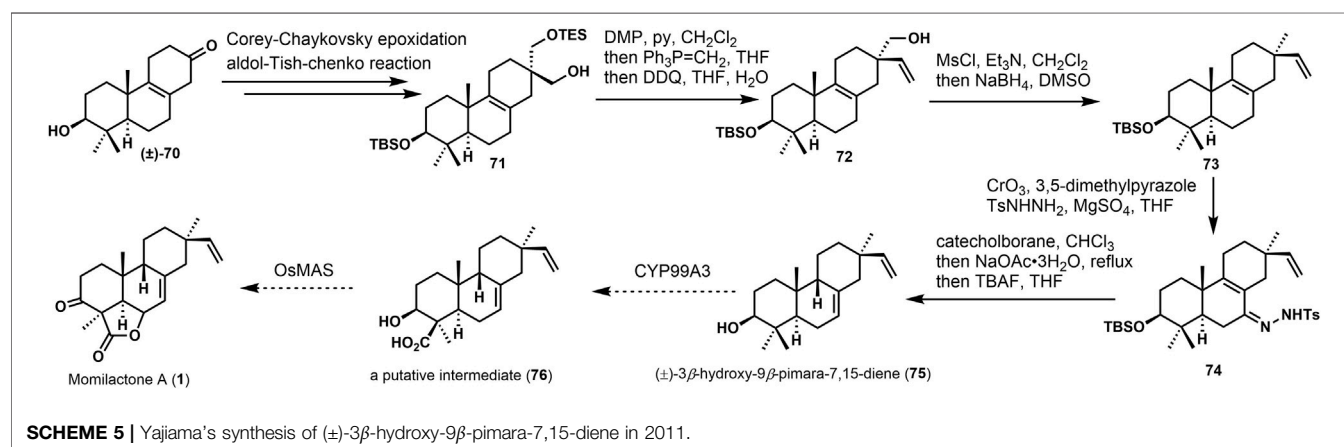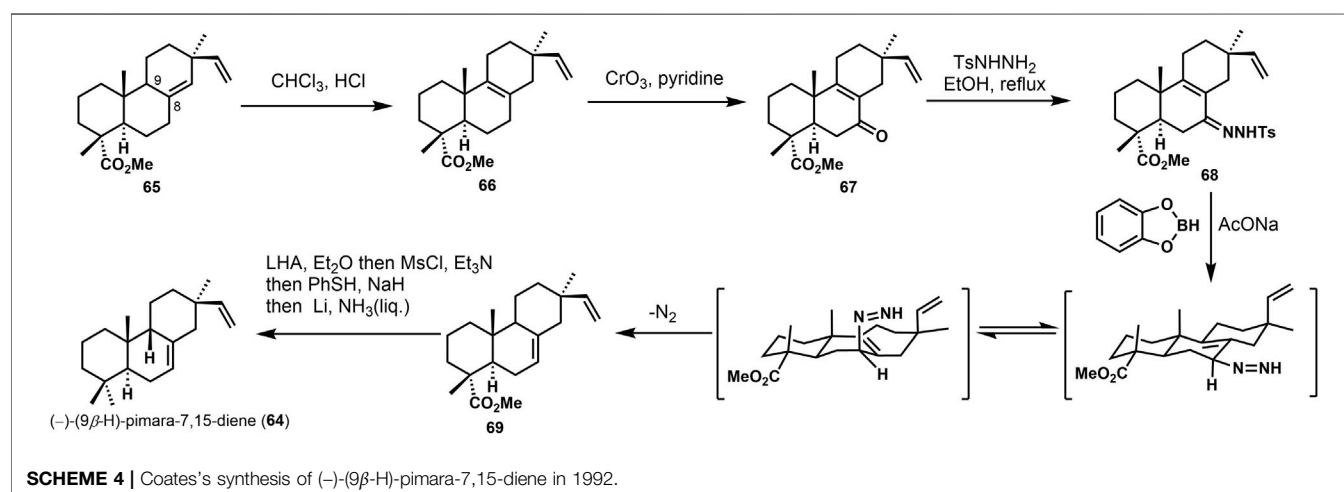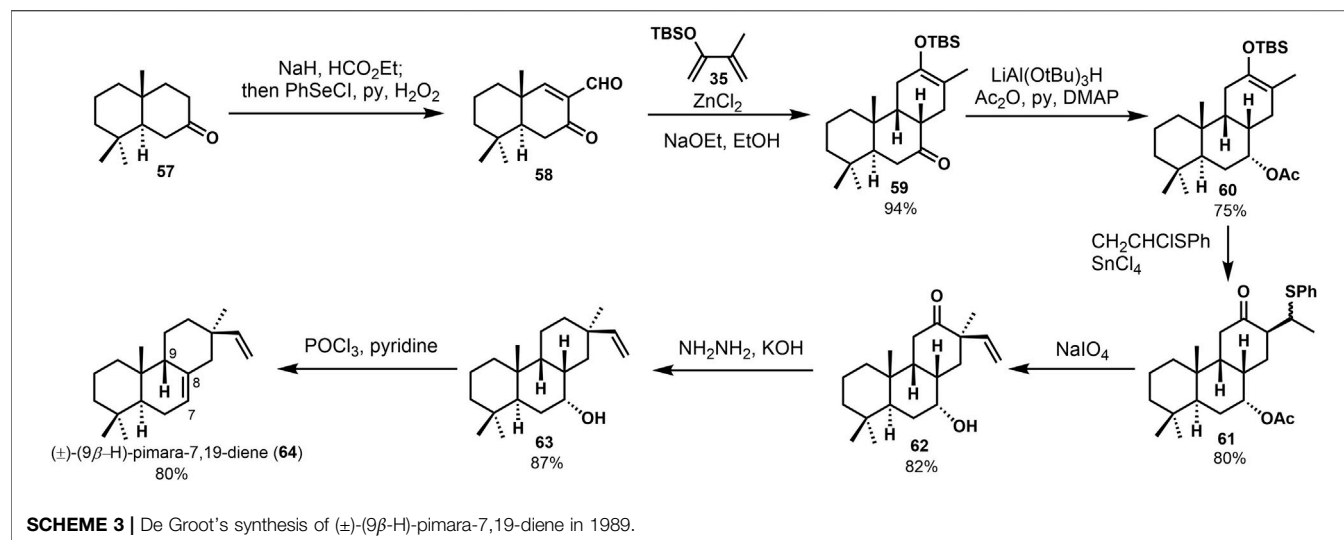
2020) to construct the stereochemistry at C-9,10 by Michael addition, lithium-ammonia reduction (Yu and Yu, 2015), and Diels–Alder reaction (Deslongchamps et al., 2014). Some of these strategies would gain the 9,10-*trans* products, inconsistent with the desired goal. In 1992, the 9,10-*syn* stereochemistry was accomplished via catechol borane reduction by Coates (Chu and Coates, 1992). As

SCHEME 6 | Coates's synthesis of (+)-9,10-*syn*-copalol in 1992.

SCHEME 7 | Nakada's stereoselective approach to *tran-syn-cis* tricyclic system in 2014.
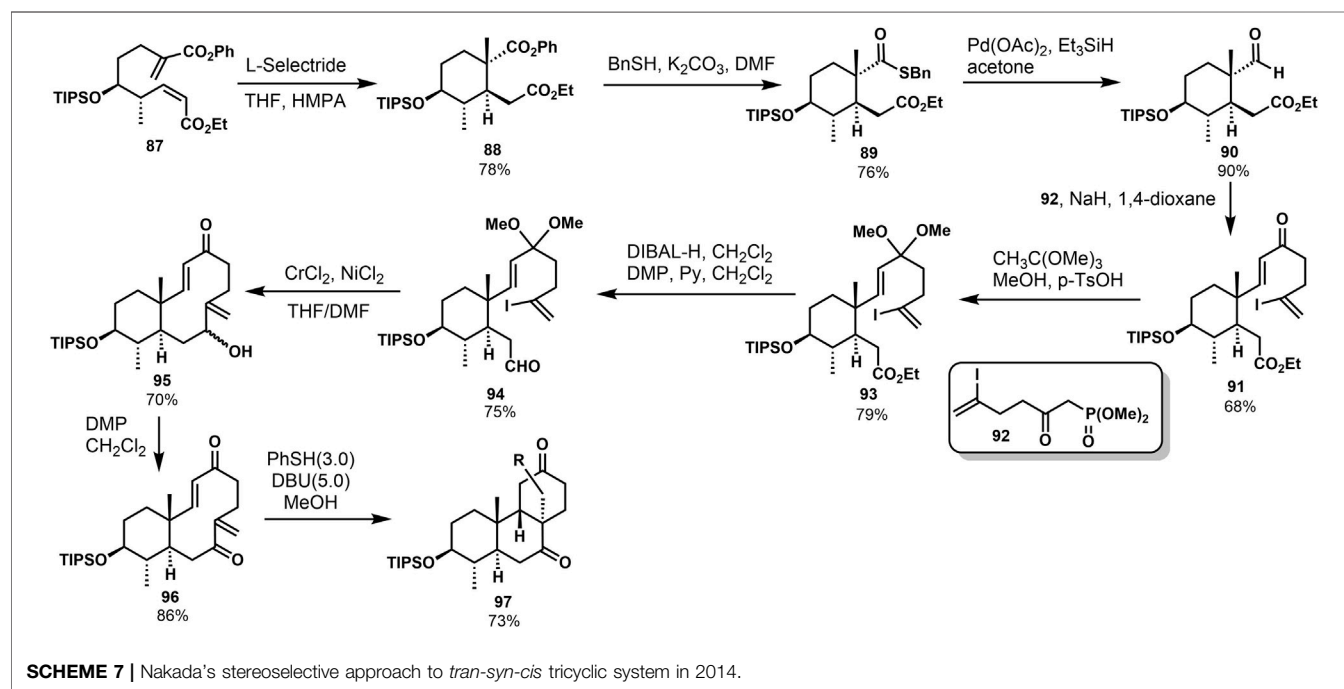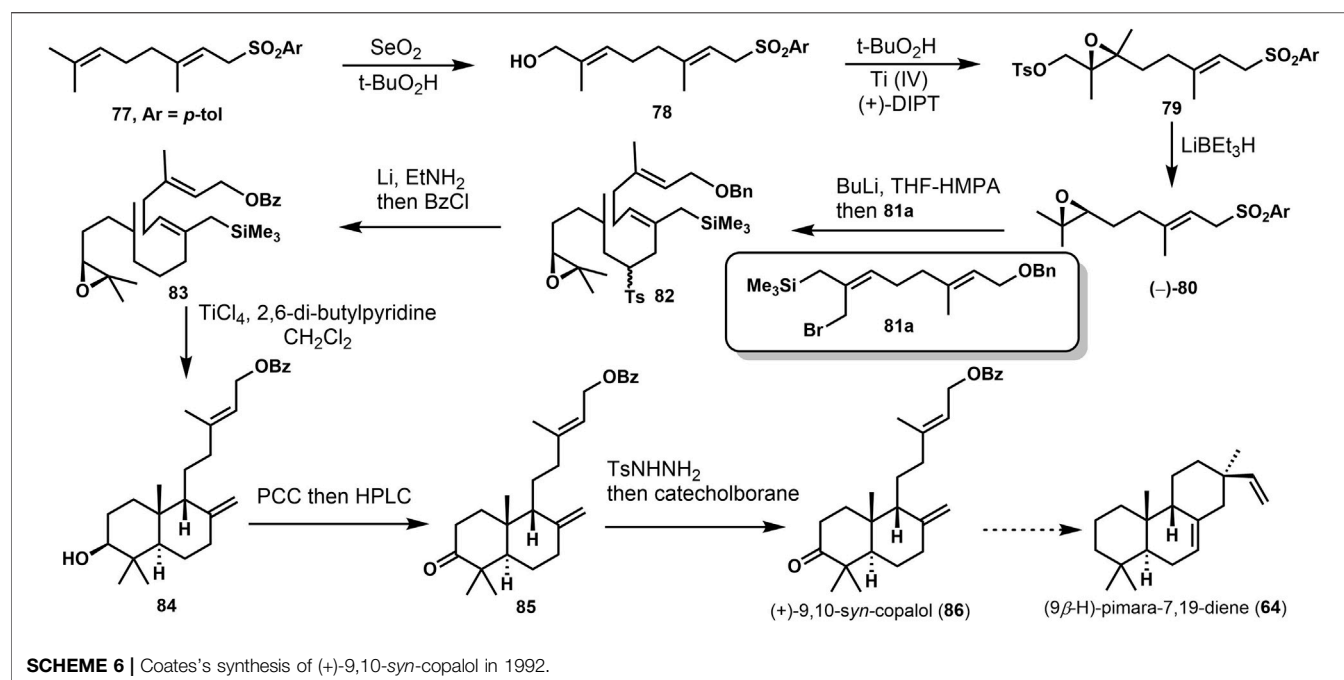
shown in **Scheme 4**, the unsaturated compound **66** was obtained from **65** by isomerization to its Δ^8 isomer with HCl/CHCl$_3$. Regioselective allylic oxidation of **66** provided ketene **67**. It was refluxed with *p*-toluene sulfonyl hydrazine in ethanol to obtain tosylhydrazone **68** and treated with catechol borane and sodium acetate. Double bond isomerization rearrangement was used, and $\Delta7,8$-olefin **69** was obtained. Subsequently, the 4α-ester group of compound **69** was reduced by lithium aluminum-hydrogen to yield

primary alcohol, and hydroxyl was protected after removing the methyl sulfonyl and fulguration. Finally, the target product (−)-(9β-H)-pimara-7,15-diene (**64**) was obtained by desulphurization with liquid lithium ammonia.

Yajiama (Yajiama et al., 2011) investigated the synthesis of (±)-3β-hydroxy-9β-pimara-7,15-diene (**75**). The core skeleton was constructed via Hutchins allyldiazene rearrangement (Chu and Coates, 1992). In **Scheme 5**, the approach started from the known

ketone (±)−**70**, and **71** was gained *via* several transformations in good yield. Then, the hydroxyl group was oxidized. After the Witting olefination and deprotection, vinyl product **72** was obtained. The hydroxyl group of **72** was removed to get the desired derivative **73**. It possesses β-vinyl groups at C-13. After reducing **74** by catechol borane, under the presence of sodium acetate, the desired 9,10-*syn* tricyclic compound (±)−3α-hydroxy-9β-pimara-7,15-diene (**75**) was provided, which was considered a putative intermediate of momilactones and other diterpene phytoalexins in rice. It can be converted into **76** and momillactone A (**1**). In these syntheses, it

furnished the configuration of the C-13 quaternary center using a stereoselective approach, and 9,10-*syn* tricyclic skeleton was constructed *via* rearrangement. This methodology would also apply to the synthesis of 9β-H pimaranes.

Yee and Coates (Yee and Coates, 1992) accomplished the synthesis of 9,10-*syn*-Copalol (**86**). In **Scheme 6**, the approach was started from **77** *via* Riley oxidation and Sharpless epoxidation under the presence of $TiCl_4$. A conversion was performed to remove the hydroxyl group with $LiBEt_3H$. Then, **82** was provided *via* lithiation and alkylation with (E, Z)-8-bromo-9-

SCHEME 8 | Deslongchamps's total synthesis of (±)-momillactone A in 2002.
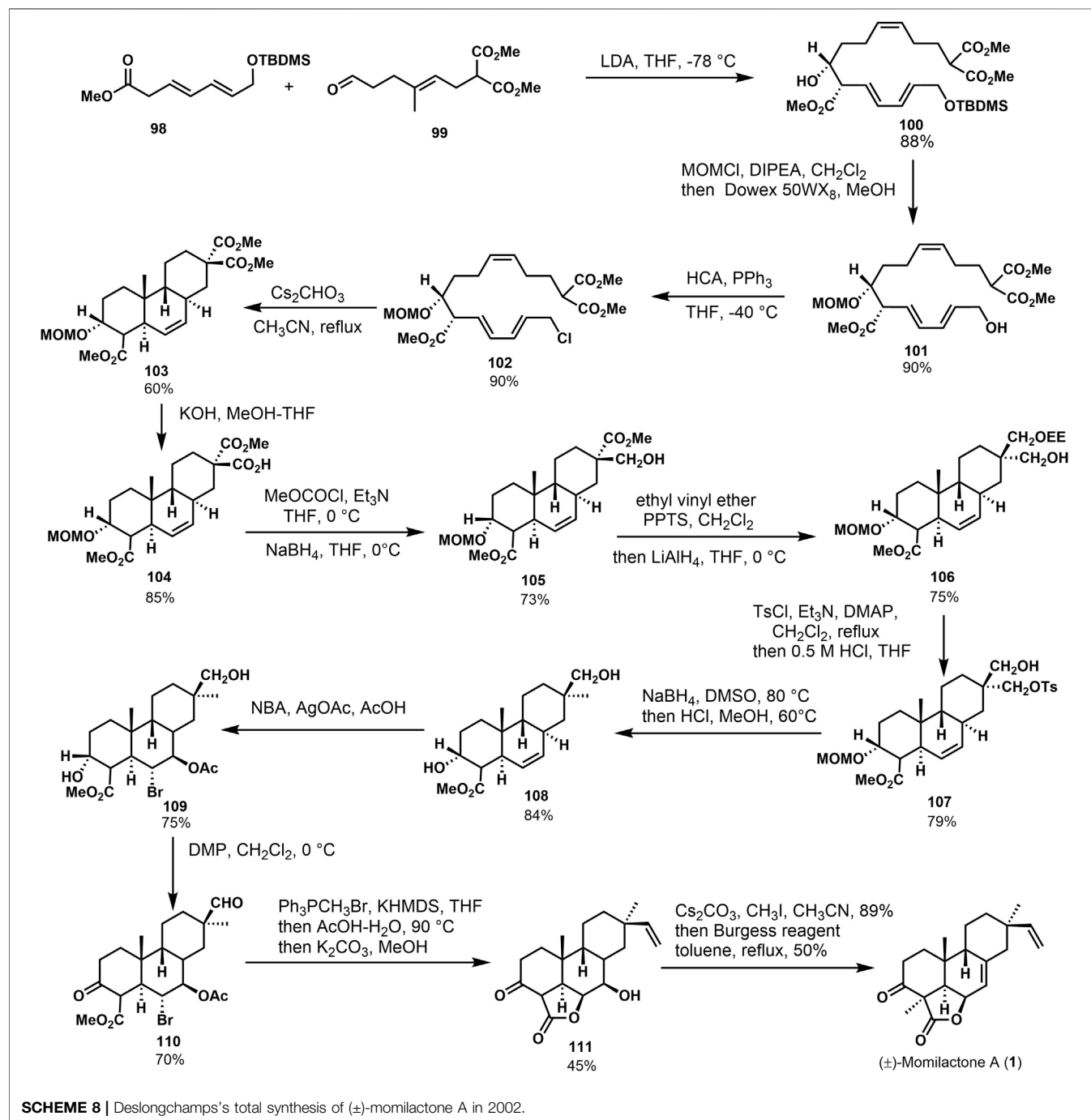
(trimethylsilyl) geranyl benzyl ethers (**81a**). Selective reductive cleavage of the toluenesulfonyl and protected benzyl group produced the tandem cyclization precursor **83**. Lewis acid treatment (TiCl₄) of **83** afforded the stereorandom bicyclizations **84** and its diastereoisomers. Then, mixtures were oxidized and separated to get **85**. (+)-9,10-*syn*-copalol (**86**) was offered through the reduction with catecholborane. It could be converted to (9β-H)-pimaran-7,19-diene **64**) *via* another tandem cyclization.

Fusidane triterpenes are a relatively small family of natural steroidal antibiotics, including fusidine, helvolic acid, and fusidic acid. These compounds have a unique chair-boat-chair ABC tricyclic ring system seen as a sort of 9β-pimara skeleton (Caron and Deslongchamps, 2010). In 2014, the intermolecular/transannular Michael reaction was first applied to the synthesis of ABC-ring in fusidane triterpenes by Fujii and Nakada (Fujii and Nakada, 2014). In **Scheme 7**, they developed the stereoselective intramolecular Michael reaction of compound **87** with L-Selectride to provide compound **88** (**Scheme 7**). Compound **88** was performed with benzyl thiol and potassium carbonate affording the benzyl thioester **89**. It was then converted to aldehyde **90** by Fukuyama reduction. Enone **91** was prepared *via* HWE reaction of aldehyde **90** and keto phosphonate **92**. The dimethyl acetal **93** was afforded from **91**, followed by reduction, and Dess–Martin oxidation gave aldehyde **94**. The intramolecular Cr-mediated reaction of compound **94** was optimized when the reaction was performed in THF/DMF mixture, offering sole product **95** (70%). After that, oxidation of compound **95** provided the *bis*-enone **96**, the substrate for intermolecular/transannular Michael reaction cascade. Then, they carried out the reaction of compound **96** under several conditions. Annulation product **97** was formed when thiophenol and DBU were used in methanol at 0 °C in a 73% yield.

Germain and Deslongchamps (Germain and Deslongchamps, 2002) accomplished the first total synthesis of (±)-momilactone A (**1**) *via* a Diels–Alder reaction (Germain and Deslongchamps, 1999). **Scheme 8** shows that the condensation was accomplished from conjugated olefins **98** and vinylaldehydes **99** with 88% yield to give diethylisomers **100**. Subsequently, MOM ether was obtained from **100** *via* the protection, followed by selective desilication of primary hydroxyl ether to obtain compound **102**. *Trans-syn-trans* tricyclic compound **103** was offered by Diels–Alder reaction with stereoselectivity under reflux in cesium carbonate acetonitrile solution. In a word, a series of conversions of **100** provided the diastereoisomer **103** in the chair-boat-chair configuration, which is consistent with (±)-momilactone A (**1**). The target product was obtained

through linear strategy transformation starting from intermediate **103**. Malonate compound **103** underwent partial hydrolysis and several functional group transformations to afford intermediate **104**. Then, the double bond addition was performed under the action of NBS and silver acetate to obtain bromoacetate **109** with high stereoselectivity, followed by the Dess–Martin oxidation and Wittig reaction to obtain the alkenone. Under the condition of acetic acid-water, intramolecular esterification was performed. Moreover, the hydrolysis of acetyl ester was carried out to obtain hydroxylolactone **111**. Then, the target product (±)-momilactone A (**1**) was obtained by the carbonyl *α*-methylation and dehydration of lactone.

SUMMARY AND FURTHER PROSPECTS

Some synthetic strategies have been reported about the construction of the 9β-H piamarane skeleton, such as Diels–Alder reaction, Michael addition, and catechol borane reduction. They carried out the syntheses of the skeleton and the intermediates in natural products using simple procedures. The asymmetric totals synthesis of 9β-H piamaranes has not been reported so far. A new approach must be applied to the natural products in 9β-H pimaranes.

AUTHOR CONTRIBUTIONS

YZ collected and organized all literature about 9β-H pimarane diterpenoids and reviewed for abstract, introduction, some 9β-H pimarane skeleton, and momilactones syntheses. ML prepared all the scheme and references, summary, and further prospects. QL reviewed Coates's synthesis of (9β-H)-pimara-7,15-diene and De Groot's first synthesis of 4,4-dinor-(9β-H)-pimara-7,15-diene. JH reviewed all literature and gave significant discussion. YC reviewed the synthetic efforts towards 9β-H pimarane diterpenoids in the past three decades. He summed up very beautiful reaction schemes.

FUNDING

REFERENCES

Adou, E., Williams, R. B., Schilling, J. K., Malone, S., Meyer, J., Wisse, J. H., et al. (2005). Cytotoxic Diterpenoids from Two Lianas from the Suriname Rainforest. *Bioorg. Med. Chem.* 13, 6009–6014. doi:10.1016/j.bmc.2005.07.026

Caron, P.-Y., and Deslongchamps, P. (2010). Versatile Strategy to Access Tricycles Related to Quassinoids and Triterpenes. *Org. Lett.* 12, 508–511. doi:10.1021/ol902711b

Cho, J.-G., Cha, B.-J., Min Lee, S., Shrestha, S., Jeong, R.-H., Sung Lee, D., et al. (2015). Diterpenes from the Roots ofOryza sativaL. And Their Inhibition Activity on NO Production in LPS-Stimulated RAW264.7 Macrophages. *Chem. Biodiversity* 12, 1356–1364. doi:10.1002/cbdv.201400239

Chu, M., and Coates, R. M. (1992). Partial Synthesis of 9,10-Syn-Diterpenes via Tosylhydrazone Reduction: (-)-(9β)-Pimara-7,15-Diene and (-)-(9β)-isopimaradiene. *J. Org. Chem.* 57, 4590–4597. doi:10.1021/jo00043a013

Das G.B. Zoghbi, M., F. Roque, N., and Gottlieb, H. E. (1981). Humirianthenolides, New Degraded Diterpenoids from Humirianthera Rupestris. *Phytochemistry* 20, 1669–1673. doi:10.1016/S0031-9422(00)98552-2

Dayan, F. E., Cantrell, C. L., and Duke, S. O. (2009). Natural Products in Crop protection. *Bioorg. Med. Chem.* 17, 4022–4034. doi:10.1016/j.bmc.2009.01.046

Deslongchamps, P., and Germain, J. (1999). Transannular Diels-Alder Approach to the Synthesis of Momilactone A. *Tetrahedron Lett.* 40, 4051–4054. doi:10.1016/S0040-4039(99)00669-3

Feilner, J. M., Plangger, I., Wurst, K., and Magauer, T. (2021). Bifunctional Polyene Cyclizations: Synthetic Studies on Pimarane Natural Products. *Chem. Eur. J.* 27, 12410–12421. doi:10.1002/chem.202101926

Feilner, J. M., Wurst, K., and Magauer, T. (2020). A Transannular Polyene Tetracyclization for Rapid Construction of the Pimarane Framework. *Angew. Chem. Int. Ed.* 59, 12436–12439. doi:10.1002/anie.202003127

Fujii, T., and Nakada, M. (2014). Stereoselective Construction of the ABC-Ring System of Fusidane Triterpenes via Intermolecular/transannular Michael Reaction cascade. *Tetrahedron Lett.* 55, 1597–1601. doi:10.1016/j.tetlet.2014.01.071

Germain, J., and Deslongchamps, P. (2002). Total Synthesis of (±)-Momilactone A. *J. Org. Chem.* 67, 5269–5278. doi:10.1021/jo025873l

Germain, J., and Deslongchamps, P. (1999). Transannular Diels-Alder Approach to the Synthesis of Momilactone A. *Tetrahedron Lett.* 40, 4051–4054. doi:10.1016/S0040-4039(99)00669-3

Graebner, I. B., Mostardeiro, M. A., Ethur, E. M., Burrow, R. A., Dessoy, E. C. S., and Morel, A. F. (2000). Diterpenoids from Humirianthera Ampla. *Phytochemistry* 53, 955–959. doi:10.1016/S0031-9422(99)00585-3

Guo, B., Onakpa, M. M., Huang, X.-J., Santarsiero, B. D., Chen, W.-L., Zhao, M., et al. (2016). Di-nor- and 17-Nor-Pimaranes from Icacina Trichantha. *J. Nat. Prod.* 79, 1815–1821. doi:10.1021/acs.jnatprod.6b00289

Horie, K., Inoue, Y., Sakai, M., Yao, Q., Tanimoto, Y., Koga, J., et al. (2015). Identification of UV-Induced Diterpenes Including a New Diterpene Phytoalexin, Phytocassane F, from Rice Leaves by Complementary GC/MS and LC/MS Approaches. *J. Agric. Food Chem.* 63, 4050–4059. doi:10.1021/acs.jafc.5b00785

Jansen, B. J. M., Schepers, G. C., and De Groot, A. (1989). The Stereoselective Synthesis of (±)-9βh-Pimara-7,19-Diene. *Tetrahedron* 45, 2773–2776. doi:10.1016/S0040-4020(01)80107-1

Jiang, Z.-Y., Yang, C.-T., Hou, S.-Q., Tian, K., Wang, W., Hu, Q.-F., et al. (2016). Cytotoxic Diterpenoids from the Roots of Aralia Melanocarpa. *Planta Med.* 82, 742–746. doi:10.1055/s-0042-104349

Kato, T., Aizawa, H., Tsunakawa, M., Sasaki, N., Kitahara, Y., and Takahashi, N. (1977). Chemical Transformations of the Diterpene Lactones Momilactones A and B. *J. Chem. Soc. Perkin Trans.* 1, 250–254. doi:10.1039/P19770000250

Kato, T., Kabuto, C., Sasaki, N., Tsunagawa, M., Aizawa, H., Fujita, K., et al. (1973). Momilactones, Growth Inhibitors from rice, Oryza Sativa L. *Tetrahedron Lett.* 14, 3861–3864. doi:10.1016/S0040-4039(01)87058-1

Li, G., Xu, Q.-L., He, C.-M., Zeng, L., and Wang, H.-F. (2014). Two New Anti-fungal Diterpenoids from the Husks of Oryza Sativa. *Phytochemistry Lett.* 10, 309–312. doi:10.1016/j.phytol.2014.10.023

Li, J. L., Wie, L. L., Chen, C., Liu, D., Gu, Y. Q., Duan-Mu, J. X., et al. (2020). Bioactive Constituents from the Bryophyta Hypnum Plumaeforme. *Chem. Biodiversity* 17, 1612–1630. doi:10.1002/cbdv.202000552

Lin, X., Pang, Y., Lu, F., Ding, C., Zeng, R., and Song, Y. (2019). Review on Momilactones of Key Allelochemicals in rice Allelopathy. *Guihaia* 39, 548–556. doi:10.11931/guihaia.gxzw201801016

Liu, N., Wang, S., and Lou, H. (2012). A New Pimarane-type Diterpenoid from moss Pseudoleskeella Papillosa (Lindb.) Kindb. *Acta Pharmaceutica Sinica B* 2, 256–259. doi:10.1016/j.apsb.2012.03.003

Meyer, W. L., Clemans, G. B., and Manning, R. A. (1975). Diterpenoid Total Synthesis, an A .Far. B .Far. C Approach. VII. Total Synthesis of DL-Sugiol, DL-Ferruginol, and DL-Nimbiol. *J. Org. Chem.* 40, 3686–3694. doi:10.1021/jo00913a015

Mohan, R. S., Yee, N. K. N., Coates, R. M., Ren, Y.-Y., Stamenkovic, P., Mendez, I., et al. (1996). Biosynthesis of Cyclic Diterpene Hydrocarbons in Rice Cell Suspensions: Conversion of 9,10-Syn-Labda-8(17),13-Dienyl Diphosphate to 9β-Pimara-7,15-Diene and Stemar-13-Ene. *Arch. Biochem. Biophys.* 330, 33–47. doi:10.1006/abbi.1996.0223

Monday Onakpa, M., Zhao, M., Gödecke, T., Chen, W.-L., Che, C.-T., Santarsiero, B. D., et al. (2014). Cytotoxic (9βH)-Pimarane and (9βH)-17-Norpimarane Diterpenes from the Tuber ofIcacina Trichantha. *Chem. Biodiversity* 11, 1914–1922. doi:10.1002/cbdv.201400151

Nozaki, H., Hayashi, K.-i., Nishimura, N., Kawaide, H., Matsuo, A., and Takaoka, D. (2007). Momilactone A and B as Allelochemicals from MossHypnum Plumaeforme: First Occurrence in Bryophytes. *Biosci. Biotechnol. Biochem.* 71, 3127–3130. doi:10.1271/bbb.70625

Okada, K., Kawaide, H., Miyamoto, K., Miyazaki, S., Kainuma, R., Kimura, H., et al. (2016). HpDTC1, a Stress-Inducible Bifunctional Diterpene Cyclase Involved in Momilactone Biosynthesis, Functions in Chemical Defence in the Moss Hypnum Plumaeforme. *Sci. Rep.* 6, 25316–25329. doi:10.1038/srep25316

On'Okoko, P., Vanhaelen, M., Vanhaelen-Fastré, R., Declercq, J. P., and Van Meerssche, M. (1985). Icacenone, a Furanoditerpene with a Pimarane Skeleton from Icacina Mannii. *Phytochemistry* 24, 2452–2453. doi:10.1016/S0031-9422(00)83067-8

Ravindar, K., Caron, P.-Y., and Deslongchamps, P. (2014). Anionic Polycyclization Entry to Tricycles Related to Quassinoids and Terpenoids: A Stereocontrolled Total Synthesis of (+)-Cassaine. *J. Org. Chem.* 79, 7979–7999. doi:10.1021/jo501122k

Shen, L., Liu, M., He, Y., Al Anbari, W. H., Li, H., Lin, S., et al. (2020). Novel Antimicrobial Compounds as Ophiobolin-type Sesterterpenes and Pimarane-type Diterpene from Bipolaris Species TJ403-B1. *Front. Microbiol.* 11, 856–868. doi:10.3389/fmicb.2020.00856

Sicherer-Roetman, A., Jansen, B. J. M., and De Groot, A. (1985). ChemInform Abstract: Investigations into the Total Synthesis of Momilactones. Stereoselective Preparation of (±)-4,4-Dinor-9βh-Pimara-7,19-Diene. *Chemischer Informationsdienst* 16, 193–202. doi:10.1002/chin.198551295

Sicherer-Roetman, A., Jansen, B. J. M., and De Groot, A. (1984). Stereospecific Preparation of (±)-4,4-Dinor-9βh-Pimara-7,15-Diene, a Model for the Total Synthesis of Momilactone Type Diterpenes. *Tetrahedron Lett.* 25, 2593–2596. doi:10.1016/S0040-4039(01)81239-9

Sun, M., Guo, B., Xu, M., Zhao, M., Onakpa, M. M., Wu, Z., et al. (2021). (9βH)- and 17-Nor-Pimaranes from Icacina Oliviformis. *J. Nat. Prod.* 84, 949–955. doi:10.1021/acs.jnatprod.9b01131

Tsunakawa, M., Ohba, A., Sasaki, N., Kabuto, C., Kato, T., Kitahara, Y., et al. (1976). Momilactone-c, a Minor Constituent of Growth Inhibitors in Rice Husk. *Chem. Lett.* 5, 1157–1158. doi:10.1246/cl.1976.1157

Xu, M.-M., Zhou, J., Zeng, L., Xu, J., Onakpa, M. M., Duan, J.-A., et al. (2021). Pimarane-derived Diterpenoids with Anti-Helicobacter pylori Activity from the Tuber of Icacina Trichantha. *Org. Chem. Front.* 8, 3014–3022. doi:10.1039/d1qo00374g

Yajima, A., Toda, K., Okada, K., Yamane, H., Yamamoto, M., Hasegawa, M., et al. (2011). Stereocontrolled Total Synthesis of (±)-3β-Hydroxy-9β-Pimara-7,15-Diene, a Putative Biosynthetic Intermediate of Momilactones. *Tetrahedron Lett.* 52, 3212–3215. doi:10.1016/j.tetlet.2011.04.044

Yee, N. K. N., and Coates, R. M. (1992). Total Synthesis of (+)-9,10-syn- and (+)-9,10-Anti-Copalol via Epoxy Trienylsilane Cyclizations. *J. Org. Chem.* 57, 4598–4608. doi:10.1021/jo00043a014

Yu, J., and Yu, B. (2015). Synthesis of the ABC Skeleton of the Aglycon of Echinoside A. *Chin. Chem. Lett.* 26, 1331–1335. doi:10.1016/j.cclet.2015.08.010

Zhao, M., Cheng, J., Guo, B., Duan, J., and Che, C.-T. (2018). Momilactone and Related Diterpenoids as Potential Agricultural Chemicals. *J. Agric. Food Chem.* 66, 7859–7872. doi:10.1021/acs.jafc.8b02602

Zhao, M., Onakpa, M. M., Chen, W.-L., Santarsiero, B. D., Swanson, S. M., Burdette, J. E., et al. (2015b). 17-Norpimaranes and (9βH)-17-Norpimaranes from the Tuber of Icacina Trichantha. *J. Nat. Prod.* 78, 789–796. doi:10.1021/np5010328

Zhao, M., Onakpa, M. M., Santarsiero, B. D., Chen, W.-L., Szymulanska-Ramamurthy, K. M., Swanson, S. M., et al. (2015a). (9βH)-Pimaranes and Derivatives from the Tuber of Icacina Trichantha. *J. Nat. Prod.* 78, 2731–2737. doi:10.1021/acs.jnatprod.5b00688

Zhou, J., Wu, Z., Guo, B., Sun, M., Onakpa, M. M., Yao, G., et al. (2020). Modified Diterpenoids from the Tuber of Icacina Oliviformis as Protein Tyrosine Phosphatase 1B Inhibitors. *Org. Chem. Front.* 7, 355–367. doi:10.1039/c9qo01320b

An Unexpected Inactivation of *N*-Heterocyclic Carbene Organic Catalyst by 1-Methylcyclopropylcarbaldehyde and 2,2,2-Trifluoroacetophenone

Yanling Chen[†], Jie Lv[†], Xuling Pan and Zhichao Jin*

State Key Laboratory Breeding Base of Green Pesticide and Agricultural Bioengineering, Key Laboratory of Green Pesticide and Agricultural Bioengineering, Ministry of Education, Guizhou University, Guiyang, China

An unprecedented inactivation process of the indanol-derived NHC catalysts bearing *N*-C$_6$F$_5$ groups is reported. An unexpected multi-cyclic complex product is obtained from the 3-component reaction with the 1-methylcyclopropyl-carbaldehyde, the 2,2,2-trifluoroacetophenone and the NHC catalyst. The absolute structure of the inactivation product is unambiguously assigned *via* X-ray analysis on its single crystals. The formation of the structurally complex product is rationalized through a multi-step cascade cyclization process.

Keywords: catalyst inactivation, N-heterocyclic carbene, organocatalysis, 3-component reaction, multi-step cascade cyclization

INTRODUCTION

Ever since the first report from Ukai and co-workers on the thiazolium salt promoted benzoin reaction in 1943 (Ukai et al., 1943), *N*-heterocyclic carbene (NHC) has been developed and used as robust organic catalyst for more than 70 years (Breslow, 1958; Sheehan and Hunneman, 1966; Enders et al., 1995; Rovis et al., 2002). Especially, NHC organocatalysis has seen fantastic development within the past two decades (Enders et al., 2007; Lupton et al., 2013; Glorius et al., 2014; Mahatthananchai and Bode, 2014; Nair et al., 2015; Rovis et al., 2015; Scheidt et al., 2018; Chi et al., 2020; Chi et al., 2021; Wang et al., 2017). Numerous catalytic activation modes have been established within this highly active research field with a huge number of reactions realized for quick and selective access to functional molecules with interesting synthetic or biological applications. Functional molecules such as aldehydes, carboxylic acids and their derivatives, imines, ketenes, and activated ketones can be efficiently activated by NHC organic catalysts *via* formation of (*aza*)-Breslow intermediates and go through addition reactions with various electrophiles or nucleophiles through electron-pair-transfer processes (Gu et al., 2017; Yao et al., 2019; Chen et al., 2020; Yao et al., 2020; Fu et al., 2021; Xue and Zheng, 2021). Due to the rich electron densities of the Breslow intermediates formed from the NHC catalysts and the aldehyde substrates, they can be selectively oxidized by external oxidants through single-electron-transfer (SET) processes and furnished radical reactions in both enantioselective and non-chiral fashion. Recently, a couple of carbon- and heteroatom-centered nucleophiles were found to be activated by chiral NHC catalysts *via* non-covalent interactions and smoothly participate in the enantioselective addition reactions with a diversity of electrophiles (Van Halbeek and Poppe, 1991; Enders et al., 1995; Regitz, 1996; Enders,
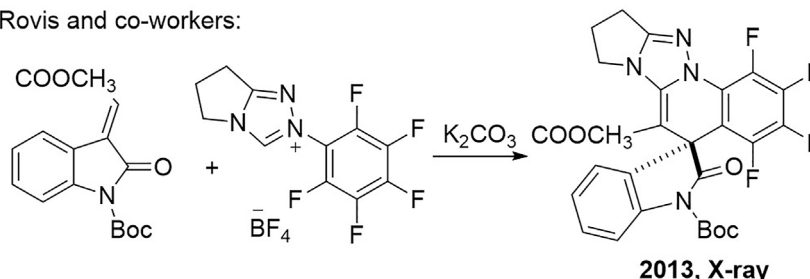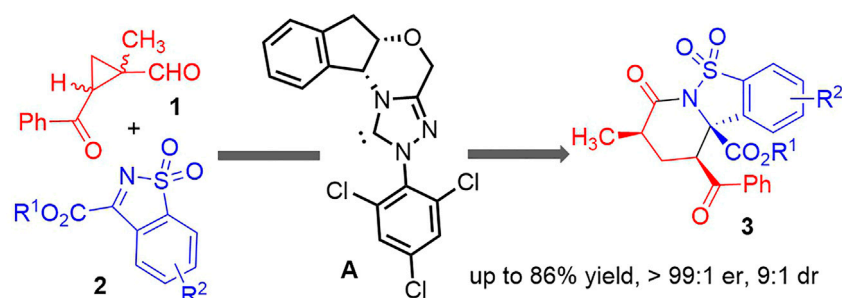
FIGURE 1 | Isolation and characterization of NHC-bounded intermediates and products. **(A)** Isolable breslow intermediates with full characterizations. **(B)** Stable NHC-bounded products from NHCs and electrophiles.

2003; Bastin et al., 2019). In all the NHC-catalyzed synthetic transformations we mentioned above, mechanistic studies *via* both experimental and computational methods have played critical roles in the development and innovations of the activation modes. Therefore, the observation and characterization of the critical intermediates and/or side reaction products to provide evidence for mechanistic studies are of great significance.

Investigations into the cross-interactions between the NHC organic catalysts and the reaction substrates are one of the effective approaches for the mechanistic studies in NHC organocatalytic reactions. Continuous endeavour has been made by organic chemists towards the isolation and characterization of the most basic Breslow intermediates since it was hypothesized by Breslow in 1958 (Breslow, 1958) (**Figure 1A**). For example, Berkessel and co-workers reported

in 2010 the full NMR spectra analysis of the ketone form of the Breslow intermediate generated from the triazolium salt-derived NHC catalyst and the propionic aldehyde (Berkessel et al., 2010). They successfully isolated the crystals of the typical Breslow intermediate from an imidazolium-typed NHC catalyst and the benzaldehyde and obtained its X-ray analytical spectrum in 2012 (Berkessel et al., 2012). An advanced reaction intermediate between the *α,β*-unsaturated Breslow intermediate and the chalcone substrate could also be isolated as stable crystals and their structures were unambiguously assigned *via* X-ray analysis in 2015 (Berkessel et al., 2015). The single crystals of the *aza*-analogues of the Breslow intermediate were obtained by Rovis and co-workers from a chiral indanol-derived NHC catalyst and an iminium salt in 2012 (Rovis et al., 2012). They can also apply the *aza*-Breslow intermediate analogues as the NHC catalyst precursors to
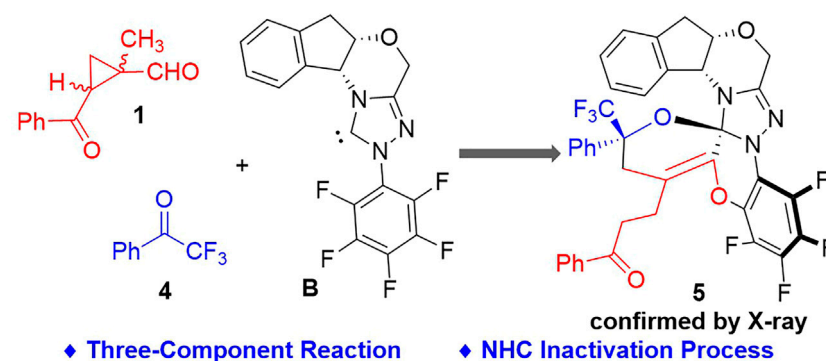
FIGURE 2 | Our studies on 1-methylcyclopropylcarbaldehyde activations with NHC organic catalysts. **(A)** Our previous work of the NHC-catalyzed (4 + 2) cycloaddition. **(B)** This work—inactivation of the NHC catalyst.

promote an intramolecular Stetter reaction in enantioselective fashion.

The isolation and characterization of the NHC-bounded reaction products from the inactivation of the NHC catalysts in the reaction system can also provide significant information on the cross interactions between the NHC catalysts and the reaction substrates. Although the formation of the NHC-bounded side reaction products might be sometimes observed during the investigations of various NHC organocatalytic transformations, to the best of our knowledge, there has been very limited reports on the characterization of those NHC-bounded reaction products (Berkessel et al., 2013; Berden et al., 2021). A representative study was from Rovis and co-workers in 2013, when they reported a cascade cyclization reaction between the triazolium NHC catalyst bearing an *N*-pentafluorophenyl (*N*-C$_6$F$_5$) group and the isatin-derived α,β-unsaturated ester substrate (Rovis et al., 2013) (**Figure 1B**). The spirocyclic product was characterized *via* X-ray analysis on the product crystals.

We have previously reported an NHC-catalyzed asymmetric (4 + 2) cycloaddition reaction between 1-methylcyclopropyl-carbaldehyde 1 (Chi et al., 2011; Mu et al., 2020; Tong et al., 2021; Wang et al., 2021) and the cyclic sulfonimides 2 (Xu et al., 2013; Wang et al., 2020a; Wang et al., 2020b; Liu et al., 2021) to give a variety of multi-functionalized fused cyclic products 3 in

TABLE 1 | Optimization of reaction conditions[a].

Entry	Base	Equivn. Of base	T (°C)	Solvent	Yield (%)[b]
1	Et$_3$N	1.0	30	THF	12
2	DBU	1.0	30	THF	21
3	Cs$_2$CO$_3$	1.0	30	THF	34
4	Cs$_2$CO$_3$	1.0	30	DCM	<5
5	Cs$_2$CO$_3$	1.0	30	CHCl$_3$	<5
6	Cs$_2$CO$_3$	1.0	30	MeCN	<5
7	Cs$_2$CO$_3$	0.8	30	THF	31
8	Cs$_2$CO$_3$	1.5	30	THF	27
9	Cs$_2$CO$_3$	1.0	50	THF	34

[a]*Unless otherwise specified, the reactions were carried using 1 (0.05 mmol), 4 (0.05 mmol), B·HBF$_4$ (0.05 mmol), base, 4 Å MS (50.0 mg), solvent (1.0 ml) at the given temperature for 6 h.*
[b]*Isolated yield of 5.*

FIGURE 3 | Proposed reaction mechanism for the formation of the product **5**.
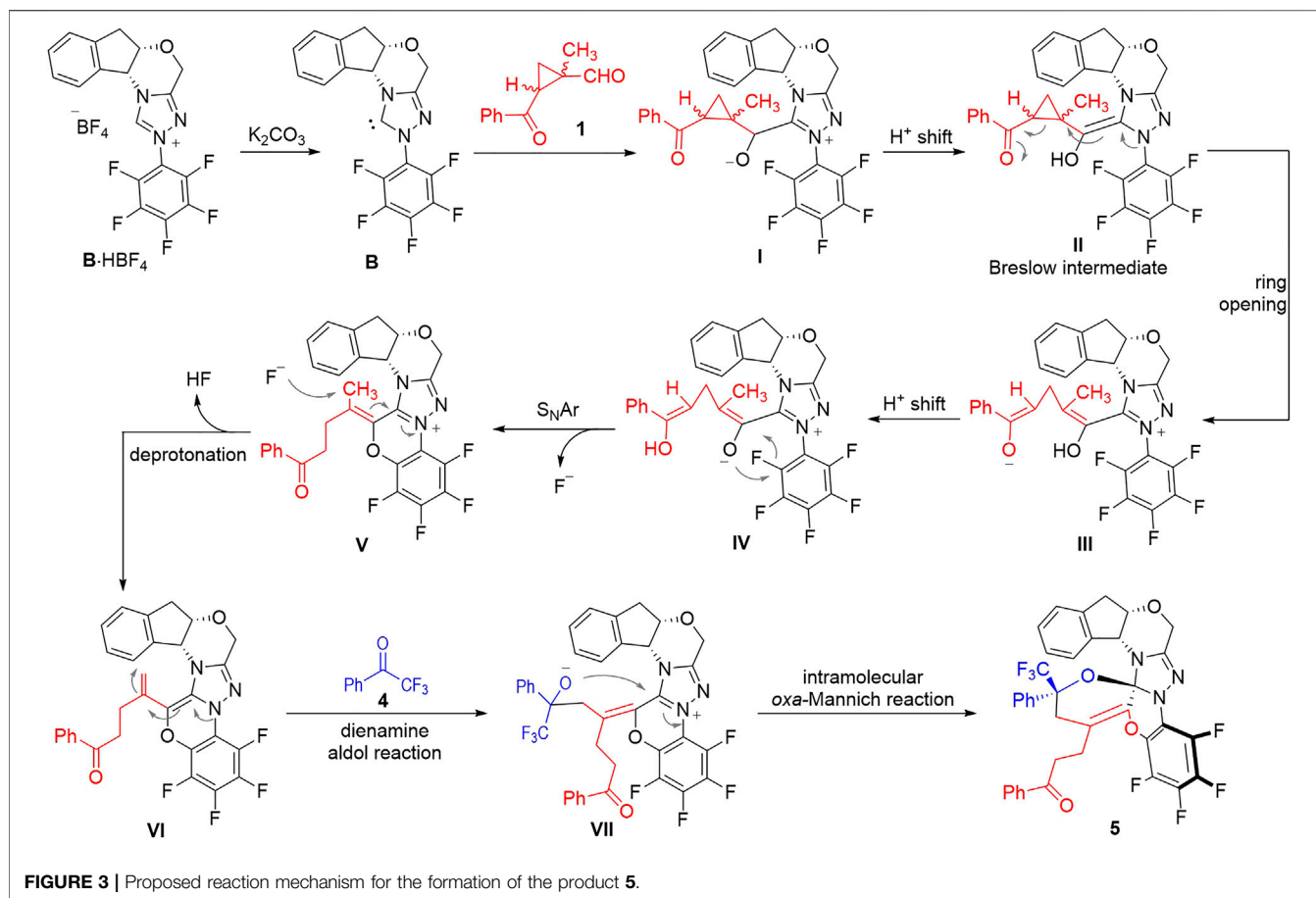
moderate to good yields with generally excellent enantio- and diastereoselectivities (Lv et al., 2021) (**Figure 2A**). Indanol-derived NHC catalysts bearing electron-deficient *N*-substituents were found effective for this transformation. However, during the evaluations of different chiral NHC catalysts, we noticed that switching the indanol-derived NHC catalyst **A** (Rovis et al., 2012) to the NHC catalyst **B** (Enders and Balensiefer, 2004) bearing an *N*-C₆F₅ group resulted in a significant drop of the product yields (from 72% with **A** to 36% with **B**), with multiple unidentifiable by-products formed in low yields.

After completion of our studies on the chiral NHC-catalyzed [4 + 2] cycloaddition reactions. We continue to focus on the side products formed with the NHC catalyst **B** bearing an *N*-C₆F₅ group (**Figure 2B**). To our delight, a crystalline product could be isolated from the reaction system consisted of the 1-methylcyclopropyl-carbaldehyde **1**, the 2,2,2-trifluoroaceto-phenone **4** (Su et al., 2017) and the NHC catalyst **B**. An unexpected crystal structure of **5** was assigned by X-ray analysis, with all the three components combined within one molecule.

RESULTS AND DISCUSSION

Having obtained the crystal structure of the NHC-bounded compound **5**, we went on to optimize the reaction condition

in order to improve the yield of the structural complex product **5** (**Table 1**). The raw materials of the 1-methylcyclopropyl-carbaldehyde **1**, the 2,2,2-trifluoroacetophenone **4** and the NHC catalyst **B** were initially stirred in THF at room temperature in the presence of a stoichiometric amout of Et₃N, with the product of **5** obtained in 12% yield (**Table 1**, entry 1). The yield of the target product **5** could be improved when switching Et₃N in to stronger bases such as DBU and Cs₂CO₃ (entries 2-3). Solvents other than THF we tested were not effective for this transformation (e.g., entries 4-6). The attempts to improve the reaction yield by adding more or less amount of basic additives were failed (entries 7-8). Further increasing the reaction temperature resulted in the formation of the target product with the same yield.

The formation of the structurally complex product **5** is rationalized through a multi-step cascade cyclization process among the three components of the 1-methylcyclopropyl-carbaldehyde **1**, the 2,2,2-trifluoroacetophenone **4** and the NHC catalyst **B** (**Figure 3**). After deprotonation of the NHC pre-catalyst, the free NHC **B** can attack the aldehyde **1** to give the adduct **I**, which can isomerize to give the Breslow intermediate **II** *via* an intramolecular proton shift process. The Breslow intermediate **II** can go through a ring-opening process to give the zwitter ionic intermediate **III** that is in equilibrium with the intermediate **IV** through intramolecular proton transfer processes.

The oxide anion of the intermediate **IV** can attack the electron-deficient pentafluorophenyl group to form a 6-membered ring *via* an intramolecular O-addition/elimination (S_NAr) process to give the intermediate **V**. The intermediate **V** bears an *α,β*-unsaturated iminium ion moiety that can easily be deprotonated by the F⁻ anion to form the dienamine intermediate **VI**. A dienamine aldol reaction between the intermediate **VI** and the 2,2,2-trifluoroacetophenone **4** gives the adduct **VII**, which can further cyclize to afford the final product **5** *via* an intramolecular *oxa*-Mannich reaction process.

It is worth noting that the formation of the structurally complex compound **5** is a highly stereospecific process. Only one diastereomer is observed in all the experiments we carried out. This is probably due to the steric match/mismatch effects provided by the chiral NHC scaffold we used in this transformation.

CONCLUSION

In summary, we have disclosed an unprecedented inactivation process of NHC organic catalysts bearing N-C$_6$F$_5$ groups. A structurally complex multi-cyclic compound was obtained from the 3-component reaction of the 1-methylcyclopropyl-carbaldehyde, the 2,2,2-trifluoroacetophenone and the NHC catalyst bearing an N-C$_6$F$_5$ group. The absolute structure of the complex product was unambiguously assigned *via* X-ray analysis on its single crystals. The current study can provide novel inspections into the possible pathways that are taking place in the reactions promoted by NHC catalysts bearing N-C$_6$F$_5$ groups. Further investigations into the interactions between the NHC organic catalysts and various reaction substrates are in progress in our laboratories.

DATA AVAILABILITY STATEMENT

The raw data supporting the conclusion of this article will be made available by the authors, without undue reservation.

AUTHOR CONTRIBUTIONS

YC and JL conducted most of the experiments and contributed equally to this work. XP contributed to some work in manuscript writing. ZJ conceptualized and directed the whole project. ZJ drafted the manuscript. All of the authors contributed in scientific discussions.

ACKNOWLEDGMENTS

SUPPLEMENTARY MATERIAL

The Supplementary Material for this article can be found online at: https://www.frontiersin.org/articles/10.3389/fchem.2022.875286/full#supplementary-material

REFERENCES

Bastin, S., Pallova, L., Morantin, M. E., Lafitte, T., Huynh, M., Barthes, C., et al. (2019). N-Heterocyclic Carbenes as Key Intermediates in the Synthesis of Fused, Mesoionic, Tricyclic Heterocycles. *Chem. Eur. J.* 25, 13030–13036. doi:10.1002/chem.201903242

Berden, G., Peckelsen, K., Thomulka, T., Martens, J., Paul, M., Oomens, J., et al. (2021). Breslow Intermediates (Amino Enols) and Their Keto Tautomers: First Gas-Phase Characterization by IR Ion Spectroscopy. *Chem. Eur. J.* 27, 2662–2669. doi:10.1002/chem.202003454

Berkessel, A., Elfert, S., Etzenbach-Effers, K., and Teles, J. H. (2010). Aldehyde Umpolung by N-Heterocyclic Carbenes: NMR Characterization of the Breslow Intermediate in its Keto Form, and a Spiro-Dioxolane as the Resting State of the Catalytic System. *Angew. Chem. Int. Edition* 49, 7120–7124. doi:10.1002/anie.200907275

Berkessel, A., Elfert, S., Yatham, V. R., Neudörfl, J.-M., Schlörer, N. E., and Teles, J. H. (2012). Umpolung by N-Heterocyclic Carbenes: Generation and Reactivity of the Elusive 2,2-Diamino Enols (Breslow Intermediates). *Angew. Chem. Int. Ed.* 51, 12370–12374. doi:10.1002/anie.201205878

Berkessel, A., Neudörfl, J.-M., Schlörer, N. E., and Yatham, V. R. (2015). Carbene Catalyzed Umpolung of α,β-enals: a Reactivity Study of Diamino Dienols vs. Azolium Enolates, and the Characterization of Advanced Reaction Intermediates. *Chem. Sci.* 6, 3706–3711. doi:10.1039/c5sc01027f

Berkessel, A., Yatham, V. R., Elfert, S., and Neudörfl, J.-M. (2013). Characterization of the Key Intermediates of Carbene-Catalyzed Umpolung by NMR Spectroscopy and X-ray Diffraction: Breslow Intermediates, Homoenolates, and Azolium Enolates. *Angew. Chem. Int. Ed.* 52, 11158–11162. doi:10.1002/anie.201303107

Breslow, R. (1958). On the Mechanism of Thiamine Action. IV.1 Evidence from Studies on Model Systems. *J. Am. Chem. Soc.* 80, 3719–3726. doi:10.1021/ja01547a064

Chen, F., Wang, H. J., Zhang, W., and Tang, P. (2020). Asymmetric Catalytic Hydrogenation of Imines and Enamines in Natural Product Synthesis. *Green. Synth. Catal.* 1, 2666–5549. doi:10.1016/j.gresc.2020.05.006

Chi, Y. R., Mo, J., Fang, X., and Lv, H. (2011). Formal Diels-Alder Reactions of Chalcones and Formylcyclopropanes Catalyzed by Chiral *N*-Heterocyclic Carbenes. *Org. Lett.* 13, 5366–5369. doi:10.1021/ol202250s

Chi, Y. R., Wang, H., Jin, Z., and Chen, X. (2020). N-Heterocyclic Carbene Organocatalysis: Activation Modes and Typical Reactive Intermediates. *Chin. J. Chem.* 38, 1167–1202. doi:10.1002/cjoc.202000107

Chi, Y. R., Wang, H., Jin, Z., and Yang, X. (2021). Development of Green and Low-Cost Chiral Oxidants for Asymmetric Catalytic Hydroxylation of Enals. *Green. Synth. Catal.* 2, 295–298. doi:10.1016/j.gresc.2021.05.002

Dirocco, D. A., and Rovis, T. (2012). Catalytic Asymmetric α-Acylation of Tertiary Amines Mediated by a Dual Catalysis Mode: N-Heterocyclic Carbene and Photoredox Catalysis. *J. Am. Chem. Soc.* 134, 8094–8097. doi:10.1021/ja3030164

Enders, D. (2003). Preparation and Application of 1,3,4-Triphenyl-4,5-Dihydro-1h-1,2,4-Triazol-5-Ylidene, A Stable Carbene. *Synthesis* 2003, 1292–1295. doi:10.1055/s-2003-3940910.1002/chin.200341135

Enders, D., and Balensiefer, T. (2004). Nucleophilic Carbenes in Asymmetric Organocatalysis. *Acc. Chem. Res.* 37, 534–541. doi:10.1021/ar030050j

Enders, D., Breuer, K., Raabe, G., Runsink, J., Teles, J. H., Melder, J.-P., et al. (1995). Preparation, Structure, and Reactivity of 1,3,4-Triphenyl-4,5-Dihydro-1h-1,2,4-Triazol-5-Ylidene, A New Stable Carbene. *Angew. Chem. Int. Ed. Engl.* 34, 1021–1023. doi:10.1002/anie.199510211

Enders, D., Niemeier, O., and Henseler, A. (2007). Organocatalysis by *N*-Heterocyclic Carbenes. *Chem. Rev.* 107, 5606–5655. doi:10.1021/cr068372z

Fu, Z. Q., Guo, J. C., Huang, J., and Zhang, Y. X. (2021). *N*-heterocyclic Carbene-Catalyzed [4 + 2] Annulation of Acetates and *β*-Silyl Enones: Highly Enantioselective Synthesis of *β*-Silyl *δ*-Lactones. *Chin. J. Org. Chem.* 41, 4467–4475. doi:10.6023/cjoc202105002

Glorius, F., Richter, C., Schedler, M., and Hopkinson, M. N. (2014). An Overview of *N*-Heterocyclic Carbenes. *Nature* 510, 485–496. doi:10.1038/nature13384

Gu, C., Du, G., Zhang, J., and Dai, B. (2017). Strecker Reaction of Ethyl Cyanoformate with Aldimines Catalyzed by *N*-Heterocyclic Carbene. *Chin. J. Org. Chem.* 37, 914–919. doi:10.6023/cjoc201610029

Liu, P., Li, X., He, J., Li, W., Yang, Z., Wei, Y., et al. (2021). TBAI-catalyzed Ring-Opening Sulfonylations of Benzothiazoles and Arylsulfonyl Hydrazides. *Green. Synth. Catal.* 2, 381–384. doi:10.1016/j.gresc.2021.08.006

Lupton, D. W., Candish, L., and Ryan, S. J.(2013). Acyl Anion Free *N*-Heterocyclic Carbene Organocatalysis. *Chem. Soc. Rev.* 42, 4906–4917. doi:10.1039/c3cs35522e

Lv, J., Xu, J., Pan, X., Jin, Z., and Chi, Y. R. (2021). Carbene-catalyzed Activation of Cyclopropylcarbaldehydes for Mannich Reaction and *δ*-lactam Formation: Remote Enantioselecitvity Control and Dynamic Kinetic Asymmetric Transformation. *Sci. China Chem.* 64, 985–990. doi:10.1007/s11426-021-9989-1

Mahatthananchai, J., and Bode, J. W. (2014). On the Mechanism of *N*-Heterocyclic Carbene-Catalyzed Reactions Involving Acyl Azoliums. *Acc. Chem. Res.* 47, 696–707. doi:10.1021/ar400239v

Mu, W., Dou, L., and Liu, W. (2020). Recent Progress On[3+2] Ring-Expansion Reaction of Cyclopropane with Unsaturated Compounds. *Chin. J. Org. Chem.* 40, 1150–1176. doi:10.6023/cjoc201910019

Nair, V., Biju, A. T., and Menon, R. S. (2015). Recent Advances in Employing Homoenolates Generated by *N*-Heterocyclic Carbene (NHC) Catalysis in Carbon-Carbon Bond-Forming Reactions. *Chem. Soc. Rev.* 44, 5040–5052. doi:10.1039/c5cs00162e

Regitz, M. (1996). Nucleophile Carbene: Eine Unglaubliche Renaissance. *Angew. Chem.* 108, 791–794. doi:10.1002/ange.19961080706

Rovis, T., Glover, G. S., Oberg, K. M., Dalton, D. M., and Zhao, X. (2013). SNAr-Derived Decomposition By-Products Involving Pentafluorophenyl Triazolium Carbenes. *Synlett* 24, 1229–1232. doi:10.1055/s-0033-1338842

Rovis, T., Oberg, K. M., and Dirocco, D. A. (2012). Isolable Analogues of the Breslow Intermediate Derived from Chiral Triazolylidene Carbenes. *J. Am. Chem. Soc.* 134, 6143–6145. doi:10.1021/ja302031v

Rovis, T., Read de Alaniz, J., and Kerr, M. S. (2002). A Highly Enantioselective Catalytic Intramolecular Stetter Reaction. *J. Am. Chem. Soc.* 124, 10298–10299. doi:10.1021/ja027411v

Rovis, T., Romanov-Michailidis, F., White, N. A., and Flanigan, D. M. (2015). Organocatalytic Reactions Enabled by *N*-Heterocyclic Carbenes. *Chem. Rev.* 115, 9307–9387. doi:10.1021/acs.chemrev.5b00060

Scheidt, K. A., Jaworski, A. A., and Murauski, K. J. R. (2018). A Continuing challenge: N-Heterocyclic Carbene-Catalyzed Syntheses of γ-butyrolactones. *Chem. Soc. Rev.* 47, 1773–1782. doi:10.1039/c7cs00386b

Sheehan, J. C., and Hunneman, D. H. (1966). Homogeneous Asymmetric Catalysis. *J. Am. Chem. Soc.* 88, 3666–3667. doi:10.1021/ja00967a049

Su, Y., Wu, L., Chong, S., Zhang, W., Huang, D., Wang, K., et al. (2017). Chiral Thiourea Catalyzed Asymmetric Henry Reaction: Construction of Stereogenic

Center Bearing a CF3 Group from 2,2,2-Trifluoroacetophenone Substrates. *Chin. J. Org. Chem.* 37, 936–942. doi:10.6023/cjoc201612006

Tong, M., Zhang, X., Wang, Y., and Wang, Z. (2021). Advances in Reactions of Iodonium Ylides. *Chin. J. Org. Chem.* 41, 126–143. doi:10.6023/cjoc202006021

Ukai, T., Tanaka, R., and Dokawa, T. (1943). A New Catalyst for the Acyloin Condensation. *J. Pharm. Soc. Jpn.* 63, 296–304. doi:10.1248/yakushi1881.63.6-296

Van Halbeek, H., and Poppe, L. (1991). Nuclear Magnetic Resonance of Hydroxyl and Amido, Protons of Oligosaccharides in Aqueous Solution: Evidence for A Strong Intramolecular Hydrogen Bond in Sialic Acid Residues. *J. Am. Chem. Soc.* 113, 363–365. doi:10.1021/ja00001a055

Wang, A., Zhou, Y., Xu, J., and Liu, H. (2017). Progress of Organic Reactions Catalyzed by *N*-Heterocyclic Carbenes. *Chin. J. Org. Chem.* 37, 2590–2608. doi:10.6023/cjoc201702041

Wang, H., Gu, S., Yan, Q., Ding, L., and Chen, F.-E. (2020a). Asymmetric Catalysis in Synthetic Strategies for Chiral Benzothiazepines. *Green. Synth. Catal.* 1, 12–25. doi:10.1016/j.gresc.2020.05.005

Wang, J., Blaszczyk, S. A., and Zhao, C. (2021). Asymmetric Reactions of *N*-Heterocyclic Carbene (NHC)-Based Chiral Acyl Azoliums and Azolium Enolates. *Green. Synth. Catal.* 2, 198–215. doi:10.1016/j.gresc.2021.03.003

Wang, P., Zhao, Q., Xiao, W., and Chen, J. (2020b). Recent Advances in Visible-Light Photoredox-Catalyzed Nitrogen Radical Cyclization. *Green. Synth. Catal.* 1, 42–51. doi:10.1016/j.gresc.2020.05.003

Xu, M.-H., Jiang, T., and Wang, H. (2013). Simple Branched Sulfur-Olefins as Chiral Ligands for Rh-Catalyzed Asymmetric Arylation of Cyclic Ketimines: Highly Enantioselective Construction of Tetrasubstituted Carbon Stereocenters. *J. Am. Chem. Soc.* 135, 971–974. doi:10.1021/ja3110818

Xue, X.-S., and Zheng, H. (2021). Mechanism and Selectivity of N-Heterocyclic Carbene-Catalyzed Desymmetrizing [4+1] and [4+2] Annulations + 1] and [4 + 2] Annulations.*Chin. Chin. J. Org. Chem.* 41, 2530–2531. doi:10.6023/cjoc202100047

Yao, C. S., Yang, W. H., Luo, X., and Li, S. (2019). An Efficient N-Heterocyclic Carbene (NHC)-Catalyzed Synthesis of Polysubstituted Cyclopentene.*Chin. J. Org. Chem.* 39, 140–1410. doi:10.6023/cjoc201812035

Yao, C., Xu, J., Luo, X., Yang, W., and Li, S. (2020). Efficient N-Heterocyclic Carbene-Catalyzed Cascade Synthesis of Functionalized Naphthopyranone. *Chin. J. Org. Chem.* 40, 470–547. doi:10.6023/cjoc201905034

Check for updates

Application of Fe Based Composite Catalyst in Biomass Steam Gasification to Produce Hydrogen Rich Gas

Liang Zhou[1], Zhiyong Yang[2], Deju Wei[2], Heng Zhang[3]* and Wei Lu[4]*

[1]School of Chemistry and Chemical Engineering, Guangxi University, Nanning, China, [2]School of Chemical Engineering, Guizhou Institute of Technology, Guiyang, China, [3]State Key Laboratory Breeding Base of Green Pesticide and Agricultural Bioengineering, Key Laboratory of Green Pesticide and Agricultural Bioengineering, State-Local Joint Laboratory for Comprehensive Utilization of Biomass, Ministry of Education, Center for Research and Development of Fine Chemicals, Guizhou University, Guiyang, China, [4]School of Mechanical Engineering, Guangxi University, Nanning, China

A series of composite catalysts with different Fe-based load amounts were prepared and applied to the experiment of biomass gasification assisted by steam. The structure of the catalyst was analyzed by XRD, SEM, TEM, N_2 adsorption-desorption, and H_2-TPR. The effect of the change of Fe load amounts on the catalytic activity was studied, and the optimal conditions of the gasification reaction were selected. The relationship between catalyst structure and catalytic capacity was clarified. The results showed that under the optimal reaction conditions, the catalyst showed better catalytic activity when Fe load amounts were 10%. The proportion of hydrogen in the gasification gas is as high as 42.2% and the hydrogen production is 27.65 g/kg. The tar content reaches the lowest value of 34.07g/Nm^3.

Keywords: biomass, gasification, Fe based catalyst, hydrogen rich gas, characterization

1 INTRODUCTION

At present, global warming and energy supply security have become major strategic issues of common concern all over the world (United Nations, 2020). With the rapid and sustained growth of China's economy, energy, resources, and environment have become serious constraints affecting future development. Vigorously developing renewable energy has important strategic significance (Wu et al., 2020; Huang et al., 2022). As a renewable energy, biomass is an important energy resource in China. It has played an important role in meeting energy demand, improving energy structure, reducing environmental pollution, and promoting economic and social development (Zhang et al., 2019a; Zhou et al., 2020). China is a largely agricultural country, which contains a lot of biomass energy, such as sawdust, straw, and firewood. Therefore, the development of biomass energy has broad prospects (Zhang et al., 2019b; Wu et al., 2021a; Choi et al., 2022).

Hydrogen energy has high combustion heat, no pollution, and wide sources, which are unmatched by traditional energy such as coal, oil, and natural gas (Ortiz and Gorri, 2021; Wu et al., 2021b). Gasification of biomass with the assistance of steam can produce hydrogen rich gas, which can be further processed and transformed to obtain chemical raw materials in short supply in China (Yang et al., 2020). In the gasification reaction, if there is a suitable gasification catalyst, it can not only improve the yield of hydrogen but also reduce the yield of tar produced by biomass gasification (Cortazar et al., 2021).

Common biomass gasification catalysts include Ni-based, alkali metal, mineral, and Fe-based catalysts (Demirba, 2002). Although the catalytic activity of Fe-based catalyst is not as good as that of Ni-based catalyst, its cracking ability of tar is comparable to that of calcined dolomite (Nordgreen et al., 2006). In addition, Fe-based catalysts have the advantages of low price, wide sources, and non-toxicity, which should be widely used. The oxidation states of Fe-based catalysts under different conditions are diverse, and Fe-based catalysts under different oxidation states have potential catalytic activity for biomass gasification.

Industrial wastes such as red mud, phosphogypsum, and coal gangue have almost no cost. Even after certain pretreatment, their price is much lower than that of traditional catalysts. In the field of biomass gasification, some scholars have studied red mud as a possible catalyst carrier (Wang et al., 2008; Li et al., 2021; Sun et al., 2021). Udomsirichakorn et al. (2013) applied quicklime (CaO) to steam gasification of pine sawdust in bubbling sludge bed and found that CaO has strong advantages in tar reforming and CO_2 capture. Madhukar and maharishi (Mahishi and Goswami, 2007) studied that in a simple batch gasifier, CaO is used to increase H_2 in the biomass gasification process and reduce CO_2 content in the gas. In recent years, several studies have shown that when CaO is applied to biomass gasification experiments, it plays not only the role of carbon dioxide adsorbent but also the role of gasification catalyst (Tang et al., 2015; Zhou et al., 2019).

Therefore, in this study, the corresponding composites were prepared from industrial waste residue red mud, phosphogypsum, coal gangue, and CaO, and then the composites were modified with Fe salt to produce a series of catalysts with different Fe loading. The catalyst showed good catalytic activity in the process of biomass catalytic gasification to produce hydrogen rich gas. Combined with multiple detection methods, the effect of the change of Fe content in Fe-based composite catalyst on the catalyst activity was studied, and the optimal conditions of the gasification reaction were selected.

2 EXPERIMENT

2.1 Reagents and Instruments
The biomass raw material used in this experiment is pine sawdust, which comes from the Earth transportation mineral products processing plant in Lingshou County, China. Before the experiment, the biomass raw materials were dried at 105°C for 5 h. Before the gasification experiment, the biomass is mixed with the corresponding catalyst, a certain amount of sodium silicate solution is added, extruded, and granulated into particles <0.5, 0.5–1.0, and 1.0–1.5 mm. The industrial analysis and elemental analysis of pine sawdust are shown in **Supplementary Table S1**. Red mud comes from Guizhou Chinalco Group Co., Ltd., phosphogypsum from Guizhou kaiphosphorus Group Co., Ltd., and coal gangue from saping coal mine, Xiuwen County, Guizhou. Other reagents are analytical pure and purchased from Aladdin reagent company.

The instruments used in this experiment mainly include: collector constant temperature heating magnetic stirrer (DF-101s); Full automatic industrial analyzer (KDGF-8000A); Element analyzer (Elemental vario El/micro cube); X-ray fluorescence spectrometer (Bruker SRS3400); Gas chromatograph (Zhongke spectrum SP-7820); X-ray diffractometer (Rigaku Smart Lab); SEM (Tescan mira lms); TEM (FEI Tecnai G2 F20); Automatic specific surface and pore size distribution analyzer (Quantachrome Autosorb-iQ); Temperature programmed adsorption instrument (FINESORB 3010A).

2.2 Gasification Unit
The fluidized bed equipment (**Figure 1**) used in this gasification experiment is self-assembled and built. The experimental system is a circulating system (a large amount of inert gas is filled as circulating gas before work), which is mainly composed of three small systems: gasification system, purification system, and gas storage system from left to right.

2.3 Analysis of Products
2.3.1 Qualitative and Quantitative of Gas Components
The volume of non-condensable gas is quantified by a wet flowmeter and then collected by a gas collection bag. The main components are H_2, CO, CH_4, CO_2 which are analyzed by gas chromatography.

2.3.2 Collect and Weigh the Tar and Char Produced in the Gasification
Use the reagent bottle containing acetone to recover the tar discharged from the lower part of the scrubber. After collection, mix excess anhydrous copper sulfate into the mixture and filter it to remove the water in the mixture. Pour the mixture into a 500 ml conical bottle and put it in a constant temperature water bath heater at 70°C until the acetone volatilizes completely and the residue is tar. The mass of tar is the mass of the heated conical bottle minus the mass of the empty bottle, which is calculated by the difference method.

Collect the solid produced in the experiment from the ash hopper and secondary cyclone separator. After deducting the amount of added catalyst, the remaining solid is weighed and marked as char.

2.4 Preparation of Fe Based Composite Catalyst
The chemical composition of red mud, phosphogypsum, and coal gangue is determined by the X-ray fluorescence spectrum. The chemical composition analysis is shown in **Table 1**.

2.4.1 Preparation Method of Fe Based Catalyst
1) Preparation of red mud phosphogypsum slurry.

Dry, crush and grind the red mud and phosphogypsum respectively, screen and select 100 mesh raw materials. Weigh a certain amount of phosphogypsum and red mud respectively, and the mass ratio of the two is 3:7 for use. Phosphogypsum is
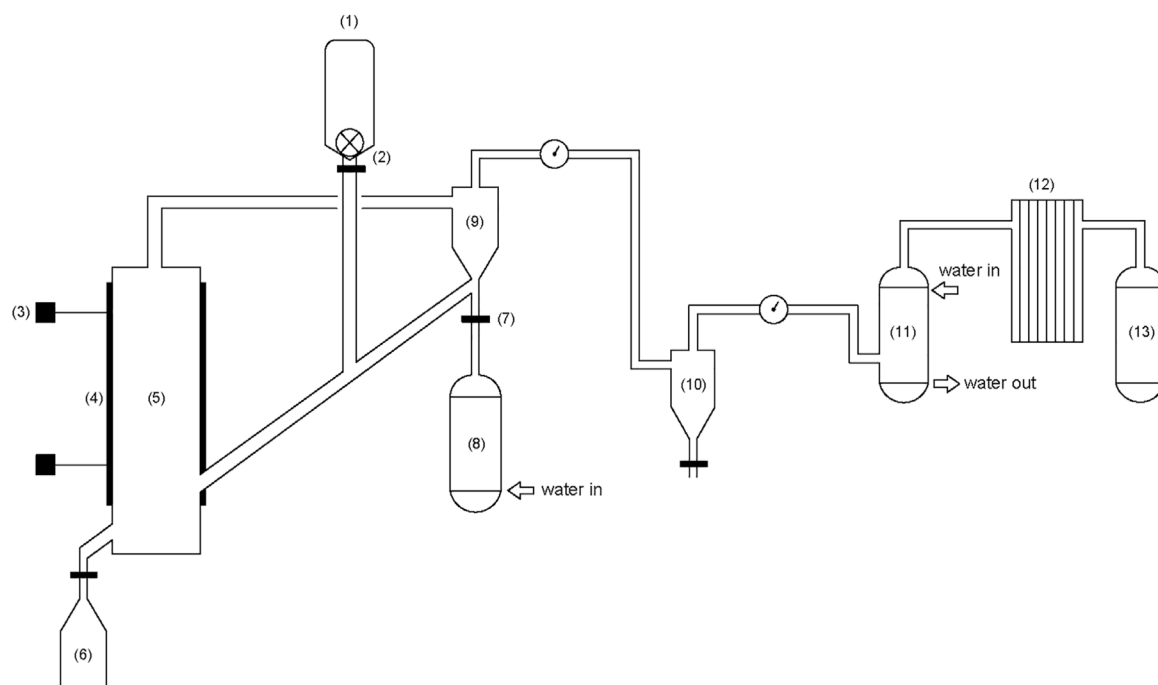
FIGURE 1 | Fluidized bed biomass steam gasification system. 1) Biomass hopper; 2) Stepping feeder; 3) Thermocouple; 4) Heater; 5) Gasifier; 6) Ash hopper; 7) Mass flowmeter; 8) Boiler; 9) Primary cyclone separator; 10) Secondary cyclone separator; 11) Scrubber; 12) Filter tower; 13) Gas collection device.

TABLE 1 | The chemical composition of industrial wastes (wt%).

Composition	SiO_2	Al_2O_3	Fe_2O_3	CaO	MgO	K_2O	Na_2O	TiO_2	SO_3	P_2O_5
Red mud	18.35	24.27	15.12	16.48	1.98	1.81	4.55	2.12	0.34	0.19
Phosphogypsum	12.32	1.89	0.76	26.7	0.28	0.66	0.21	0.23	36.33	0.88
Gangue	55.3	26.4	7.58	1.3	1.25	0.81	1.60	2.44	0.68	0.13

mixed with water to form a suspension, and red mud is gradually added to make it a uniformly mixed slurry.

2) Preparation of composites.

Weigh according to the ratio of slurry (dry basis mass)/CaO mass ratio of 7/3. Weigh the crushed coal gangue (100 mesh), and its mass is 10% of the dry basis mass of the slurry. Weigh sodium carbonate, and the mass is 3% of the total mass of the first several compounds (dry basis). Mix the weighed slurry with crushed CaO and coal gangue evenly. Use a certain amount of sodium carbonate dissolved in water as the foaming agent, add it to the mixed raw materials, add water and stir evenly, put it into a 100°C oven for constant temperature drying for 24 h, remove the water, put it in a muffle furnace, calcine at 1,000°C for 5 h. And then it is broken and passed through a 100 mesh sieve to obtain particles for the next step.

3) Preparation of Fe based composite catalysts.

In order to make the loading amount (weight percentage) of Fe in the composite catalyst 5%, 10%, and 15% respectively, the
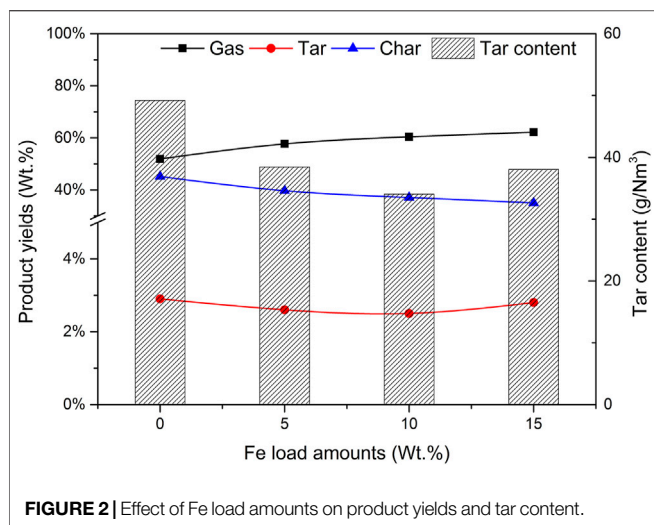
amount of Fe $(NO_3)_3 \cdot 9H_2O$ is calculated by using the mass of <0.5 mm composite particles prepared in the previous step. Weigh an appropriate amount of Fe $(NO_3)_3 \cdot 9H_2O$, prepare a solution with deionized water into a certain concentration, transfer the corresponding $FeNO_3$ solution, soak the particles prepared in the previous step, stand for 24 h, and put it into a 100°C oven for constant temperature drying for 24 h to evaporate the water. Then put the dried mixture into the muffle furnace, calcine it at 1,000°C for 5 h. Let it cool naturally in the muffle furnace, take it out, break it and screen it into particles less than 100 mesh for use, named catalyst a, b and c respectively.

2.5 Catalyst Performance Evaluation

Gas yield, tar yield, char yield, tar content, gas composition H_2, CO_2, CO, CH_4, and H_2 production are used as the criteria for evaluating the activity of the catalysts. The relevant calculation formula is as follows:

① Tar yield = tar mass/added absolute dry biomass raw material mass × 100%.
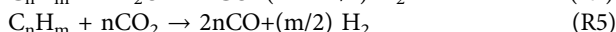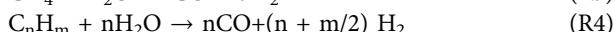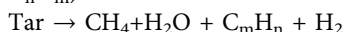② Char yield = char quality/added absolute dry biomass raw material mass × 100%.
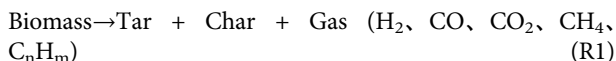
FIGURE 2 | Effect of Fe load amounts on product yields and tar content.

FIGURE 3 | Effect of Fe load amounts on gas composition and hydrogen production.

③ Gas yield = 100-Tar yield-Char yield.

④ Tar content (g/Nm^3) = tar quality (g)/dry gas volume (Nm^3).

⑤ H_2 production (g/kg) = weight of H_2 (g)/weight of biomass raw material (kg).

3 RESULTS AND DISCUSSION

Biomass gasification process is complex. The reaction process is different with the different process flow, reaction conditions, gasification medium, raw material properties, and other conditions. However, the basic reactions of these processes include biomass gasification reaction, reduction reaction, tar conversion reaction, and so on.

$$Biomass \rightarrow Tar + Char + Gas\ (H_2、CO、CO_2、CH_4、C_nH_m) \tag{R1}$$
$$Tar \rightarrow CH_4 + H_2O + C_mH_n + H_2 \tag{R2}$$
$$CH_4 + H_2O \rightarrow CO + 3H_2 \tag{R3}$$
$$C_nH_m + nH_2O \rightarrow nCO + (n + m/2)\ H_2 \tag{R4}$$
$$C_nH_m + nCO_2 \rightarrow 2nCO + (m/2)\ H_2 \tag{R5}$$
$$C + CO_2 \rightarrow 2CO \tag{R6}$$
$$C + H_2O \rightarrow CO + H_2 \tag{R7}$$
$$C + 2H_2O \rightarrow CO_2 + 2H_2 \tag{R8}$$
$$CO + H_2O \rightarrow CO_2 + H_2 \tag{R9}$$
$$CaO + CO_2 \rightarrow CaCO_3 \tag{R10}$$

3.1 Effect of Catalysts With Different Fe Load Amounts on Gasification Reaction

The Fe-based composite catalyst can effectively catalyze the gasification reaction of pine sawdust. When the mass fraction of Fe load amounts are 0%, 5%, 10%, and 15% respectively, the activity evaluation results of the prepared Fe-based composite catalyst are shown in **Figure 2**. Other conditions of the reaction are as follows: the mass ratio of

FIGURE 4 | XRD spectra of Fe based composite catalysts with different Fe load amounts.
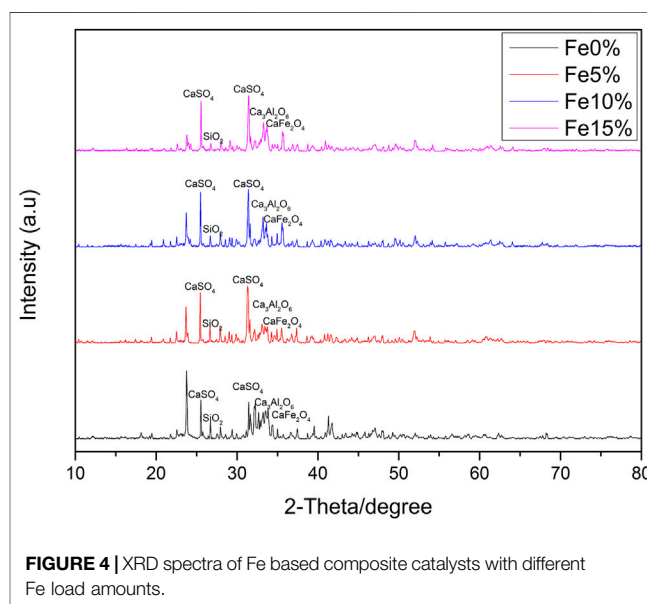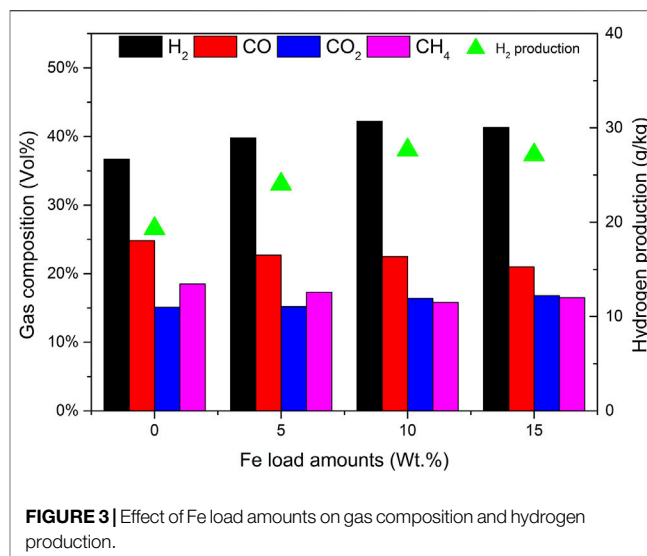
catalyst to biomass (CBR) is 1.2, the gasification reaction temperature is 650°C, the particle size of biomass is less than 0.5 mm, and the mass ratio of steam to biomass (SBR) is 1.0.

It can be seen from **Figure 2** that with the increase of Fe load amounts, the gas yield increases gradually, and the yields of tar and char also change. When the mass fraction of Fe is 10%, the gas yield is reaching 60.4%, and the yields of tar and char are 2.5% and 37.1% respectively.

Compared with composites with 0% Fe load and catalyst a, when the load amounts are low, the yields of tar and char are high. The reason is that the addition of the Fe base is conducive to tar reforming and char gasification. As the Fe load amounts increased to 15%, the percentage of H_2 in **Figure 3** did not increase, but decreased to 41.3%, so that the output of H_2 also
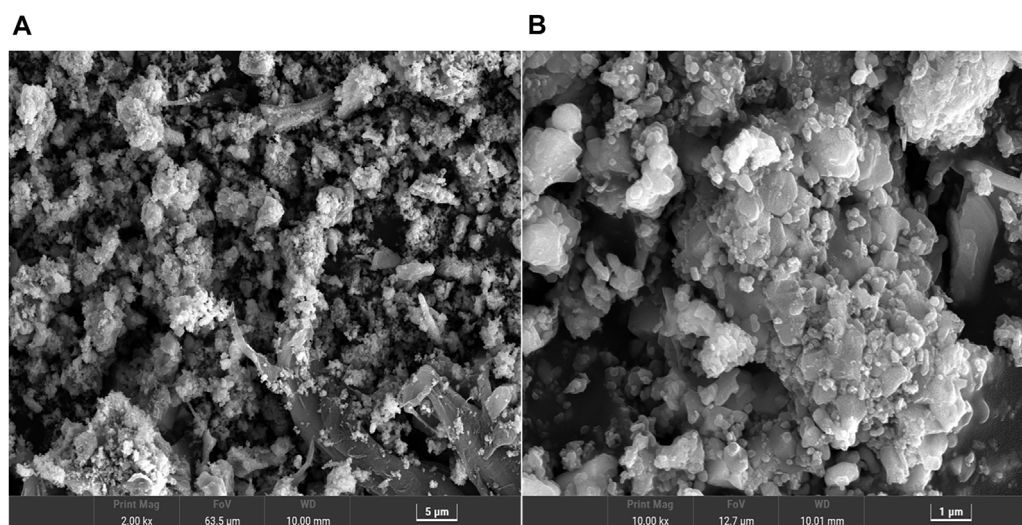
FIGURE 5 | SEM of catalyst b: **(A)** magnified 2000 times **(B)** magnified 10,000 times.

decreased. It does not seem that the higher the Fe load amounts, the better the catalytic efficiency. There is an optimal value in the experiment. The catalytic activities of catalysts a and c are significantly lower than those of catalyst b. Considering the catalytic efficiency and economic factors, the Fe-based loading of 10% is the most appropriate.

3.2 Characterization of Fe Based Composite Catalysts

3.2.1 XRD Characterization

Figure 4 shows the wide-angle XRD spectrum of Fe-based composite catalysts a, b and c. There are many diffraction peaks in the figure, indicating that the crystal form in the sample is relatively complex, and its main chemical components are $CaSO_4$, SiO_2, $Ca_3Al_2O_6$, $CaFe_2O_4$, and so on. Among the catalysts prepared by the impregnation method, the diffraction peak intensity of $CaFe_2O_4$ particles in catalyst a is the lowest. When the load amounts of Fe element increases to 15%, the intensity of $CaFe_2O_4$ diffraction peak increases, and the peak width narrows, indicating that $CaFe_2O_4$ particles increase with the increase of load amounts, dispersion of particles decreases, aggregation occurs and the reaction activity becomes worse. The diffraction peak intensity of catalyst b is weaker than that of catalyst c, indicating that the supported Fe-based compounds are better dispersed on the composites. It can be seen that the catalytic activity of Fe-based composite catalyst is b > c > a, which is in a certain compliance relationship with the diffraction peak intensity of $CaFe_2O_4$.

3.2.2 SEM Analysis

The working principle of SEM is to use the electron beam generated by cold field emission to scan the material surface, detect the secondary electrons and backscattered electrons generated by the electron beam excited surface, and determine the micromorphology of the sample surface. For the complex and rough sample surface, a clear image can be obtained. The structure and morphology of the prepared 10% Fe-loaded catalyst b were analyzed by scanning electron microscope. **Figure 5A** is an enlarged picture of 2000 times. The figure shows that the catalyst is a nanomaterial with a diameter of about 200–500 nm, which is united and gathered by many irregular particles. This nanoscale structure makes the solid catalyst generally have a large specific surface area so that the active sites of the reaction can be fully exposed, which is conducive to improving the catalytic activity of the catalyst. **Figure 5B** shows the image with a higher magnification of 10,000 times. At the same time, it can be observed that there are many small sheets with irregular shapes in the sample, which are bonded layer by layer to form relatively dense particles.

3.2.3 TEM Analysis

In order to further study the surface microstructure of catalyst b and verify the existence of its porous structure, catalyst b was characterized by TEM. The results are shown in **Figure 6A** (500 nm scale). It can be clearly observed that catalyst b is formed by stacking and agglomeration of crystal particles with different sizes and shapes. When further enlarged, as shown in **Figure 6B** (200 nm scale), it can be more clearly observed that the catalyst presents a vermicular disordered mesoporous structure. This porous structure may come from the ordered aggregation of materials. In addition, these connected holes are randomly connected, not orderly and regular linear shapes.

3.2.4 BET Analysis

The surface characteristics of Fe-based composite catalysts a, b and c were evaluated by the N_2 adsorption-desorption method. The results are listed in **Table 2**. It shows that the composite catalyst has a quite good specific surface area and pore structure. The high specific surface area and pore structure indicate that it
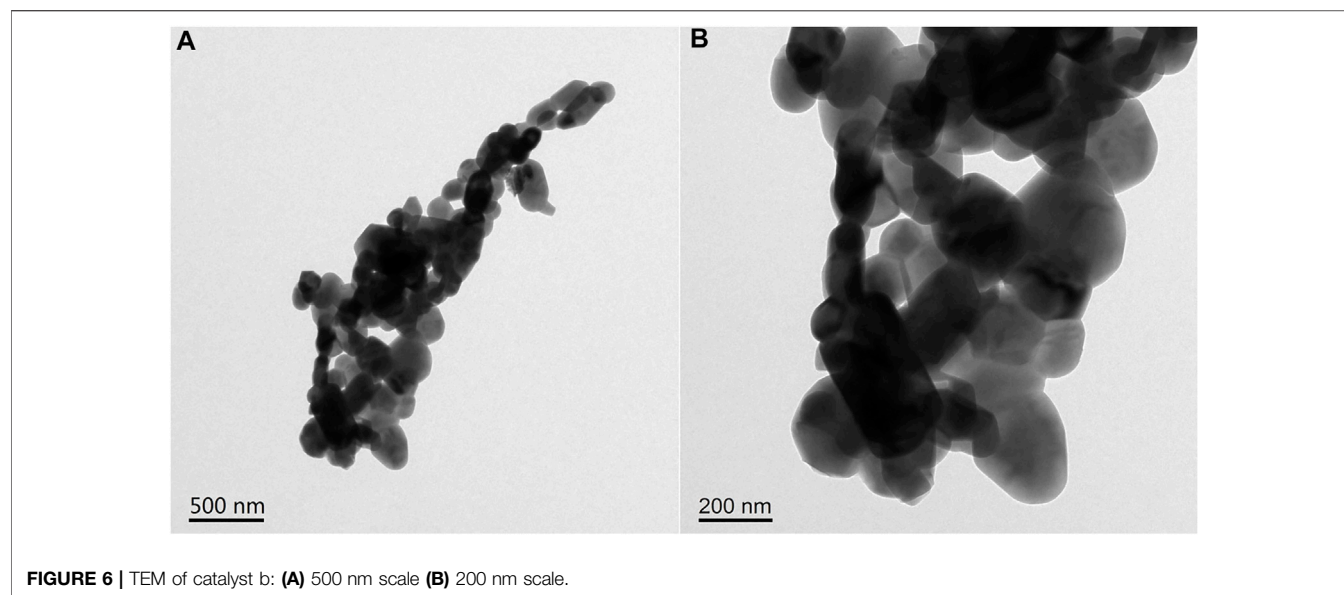
FIGURE 6 | TEM of catalyst b: **(A)** 500 nm scale **(B)** 200 nm scale.

TABLE 2 | Surface characteristics of Fe based composite catalyst.

Catalyst	Specific Surface area(m²/G)	Average Pore size(nm)	Pore volume(cm3/G)
a	229.5	537.2	0.40
b	225.3	519.6	0.35
c	220.1	484.5	0.33

FIGURE 7 | H$_2$-TPR characterization.

may have good catalytic activity and the feasibility of being a high-efficiency catalyst. With the increase of Fe load amounts, the average pore size and pore volume of catalysts a, b and c have a downward trend. It is speculated that Fe-based species are mainly successfully attached to the pore surface of the composite, which is more conducive to full contact with reactants and has the potential characteristics of excellent catalysts. At the same time, it can be seen that the Fe load amounts increase, the pores become smaller, and the Fe-based species agglomerate. These phenomena show that too much load amounts are not conducive to the catalytic activity.

3.2.5 TPR Characterization

Figure 7 shows the TPR curves of Fe-based composite catalysts a, b and c. The three composite catalysts have multiple H$_2$ reduction peaks. The reduction peak between 640°C, 661°C, 707°C can be attributed to the reduction of CaFe$_2$O$_4$ → Fe$_3$O$_4$ in the sample. The high-temperature reduction peak is between 712°C, 719°C, 721°C, which can be attributed to the continuous reduction of Fe$_3$O$_4$ → FeO/Fe (Cabello et al., 2014a; Cabello et al., 2014b). By comparing the TPR curves of Fe based composite catalysts with different Fe load amounts, it can be seen that the high-temperature peak of the sample with large Fe loading moves to the low-temperature direction, which is due to the simple substance formed after the metal oxide in the catalyst is reduced, hydrogen is adsorbed on the surface, and the activated hydrogen
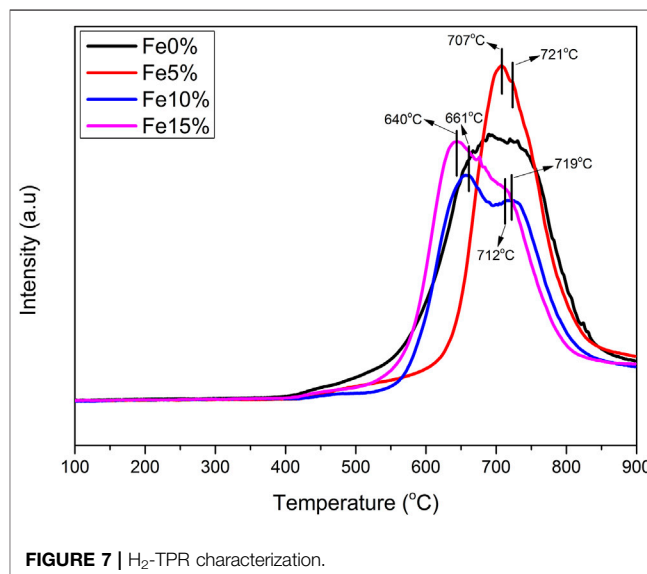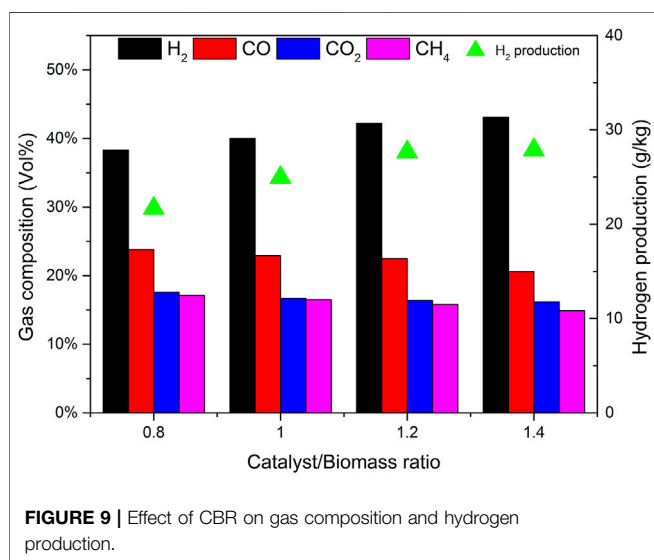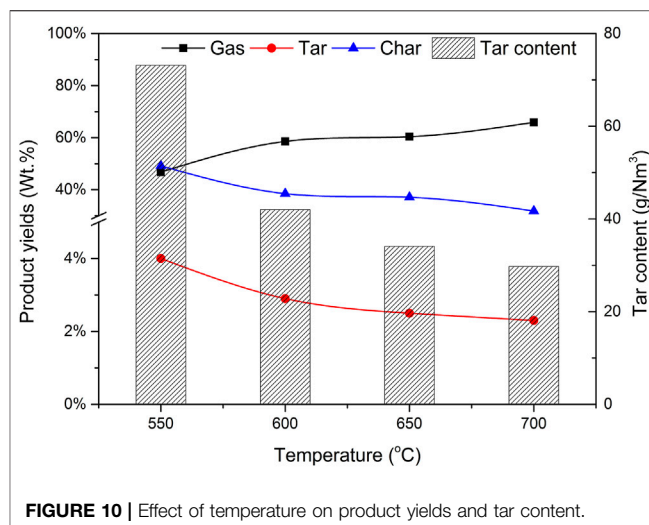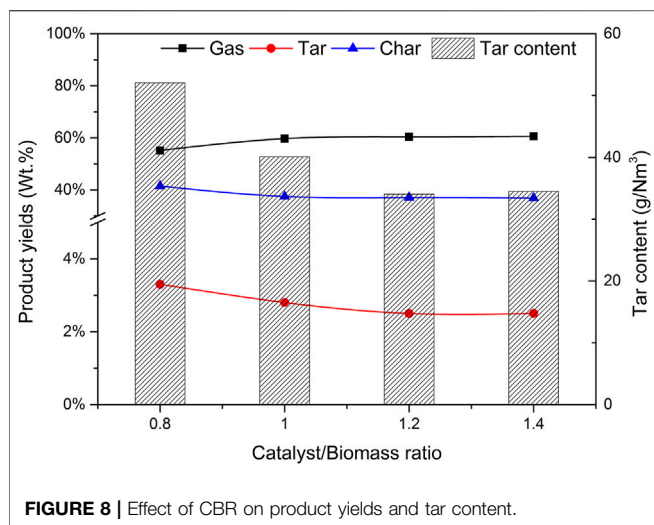
species reach the surface of the composite catalyst through overflow, It promotes the reduction of various metal elements in the sample at a lower temperature.

3.3 Effect of Mass Ratio of Catalyst b to Biomass (CBR) on Gasification

The selection of CBR is very important to the gasification process. The gasification conditions were selected as follows: catalyst b, reaction temperature 650°C, biomass particle size <0.5 mm, and SBR = 1.0. The gasification effects of CBR 0.8, 1.0, 1.2, and 1.4 were investigated.

Figure 8 shows the effect of CBR on each product component and tar content. During the increase of CBR from 0.8 to 1.4, the

FIGURE 8 | Effect of CBR on product yields and tar content.

FIGURE 10 | Effect of temperature on product yields and tar content.

FIGURE 9 | Effect of CBR on gas composition and hydrogen production.

percentage of gas increases significantly, while tar and char are gradually decreasing. The higher the CBR value, the higher the gas yield. This phenomenon can be explained that the reaction R10 is an exothermic reaction. When CaO captures CO_2, it will release heat, which may increase the temperature around biomass. This higher temperature is also conducive to the increase of tar cracking and char conversion. For the above reasons, when CBR = 1.2, the tar content reaches the lowest value of 34.07 g/Nm^3.

Figure 9 shows the effect of CBR on gas composition and H_2 production. When CBR increases from 0.8 to 1.2, the volume fraction of H_2 increases rapidly from 38.3% to 42.2%, and the volume fraction of CO decreases from 23.8% to 22.5%. CO_2 also shows a decreasing trend, and the volume fraction decreases from 17.4% to 16.4%. The volume fractions of CH_4 were relatively stable, maintained at about 16.5%. The increase of CBR increases the amount of H_2 and decreases the amount of CO. it can be explained that according to le Chatelier's principle if the partial

pressure of the product is less than that of the reactant, the reaction will move forward. The catalyst b contains CaO, which can absorb CO_2 and produce $CaCO_3$. The occurrence of reaction R10 will promote the positive movement of reaction R9, so it consumes CO and produces more H_2. If the CBR continues to increase from 1.2 to 1.4, the change tends to be gentle. It may be that the excess catalyst b fails to contact biomass particles, so it does not play a corresponding role. Therefore, there is an optimal value of 1.2 for the mass ratio of catalyst to biomass.

3.4 Effect of Temperature on Gasification

The selection of reaction temperature is very important to the gasification process. The gasification conditions are as follows: the CBR of catalyst b is 1.2, the particle size of biomass is less than 0.5 mm and the SBR is 1.0. The yield of each product (gas, tar, and char) and its effect on gas components were investigated when the reaction temperatures are 550, 600, 650, and 700°C respectively.

Figure 10 shows the effect of reaction temperature on the components of each product and tar content. When the reaction temperature is 550°C, the proportion of gas in the product is 46.8%. When the temperature rises, the percentage of gas increases, and the peak value reaches 65.9% when the temperature rises to 700°C. This is because the increase of reaction temperature is conducive to biomass pyrolysis, gasification, and gas catalytic reforming, resulting in increased gas production. The yield of tar and char has the opposite trend with temperature because at higher furnace temperature, tar cracking and transfer reaction will take place further reactions, such as R2, R7, and R8, resulting in more non-condensable gas, which is consistent with the research results of Li et al. (Li et al., 2007). Therefore, as the temperature increases from 550 to 700°C, the total output of gas products increases significantly.

The effect of reaction temperature on gas composition and H_2 production is shown in **Figure 11**. The reaction temperature increases from 550 to 650°C, and the volume fraction of H_2 increases from 36.5% to 42.2%. CO decreased from 27.6% to 22.5% and the volume fraction of CH_4 decreased slightly from 18.6% to 15.8%. This is because when water vapor is introduced,
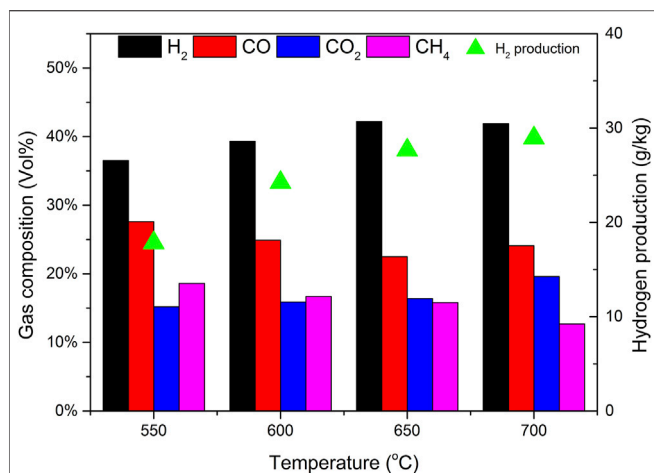
FIGURE 11 | Effect of temperature on gas composition and hydrogen production.
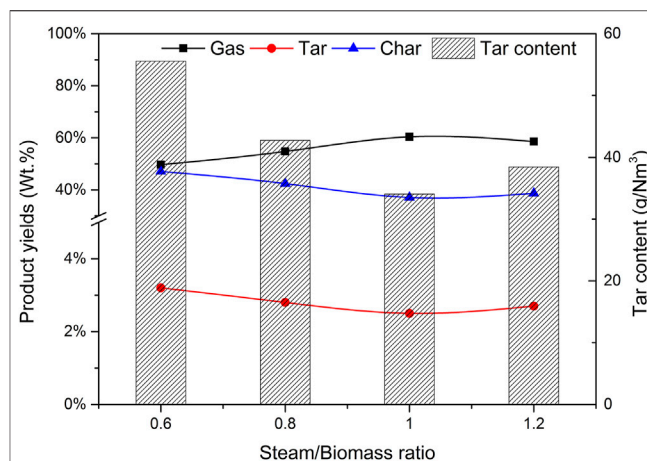

FIGURE 12 | Effect of SBR on product yields and tar content.

FIGURE 13 | Effect of SBR on gas composition and hydrogen production.

the temperature rise is conducive to some reactions related to water vapor in the process of biomass catalytic reforming, such as hydrocarbon conversion reactions R4 and R5, water vapor conversion reactions R7, and R8, and carbon monoxide conversion reaction R9 in the direction of H_2 generation. Therefore, with the increase of temperature, the content of H_2 in the gas increases rapidly. The carbon monoxide shift reaction R9 will also proceed violently in the direction of generating H_2. While the H_2 content increases rapidly, the fraction of CO decreases with the increase of temperature, and the content of CO_2 increases with the increase of temperature, from 15.2% to 16.4% gradually. However, the increase of temperature also promotes the reverse reaction of carbon dioxide reduction reaction R6 and reaction R10. Under the joint action of the three reactions, the increase of CO_2 is small. When the temperature continues to rise to 700°C, the high temperature further intensifies the reverse reaction of R10, further increases the content of CO_2 sharply, and even reduces the volume fraction of H_2 in the gas. Considering comprehensively, it is most suitable to set the reaction temperature at 650°C and the production of hydrogen has reached 27.65 g/kg.

3.5 Effect of Water Vapor/Biomass Ratio (SBR) on Gasification

Steam is also an important variable of biomass catalytic gasification. Using catalyst b as the catalyst, CBR is 1.2, the gasification reaction temperature is 650°C, biomass particle size <0.5 mm, the effects of steam/biomass ratio (SBR) of 0.6, 0.8, 1.0, and 1.2 on gasification results were studied.

Figure 12 depicts the effect of steam/biomass ratio (SBR) on the yield of pyrolysis reaction products and tar content. When SBR is less than 1.0, the gas yield increases with the increase of SBR, while the yield of tar and char shows the opposite trend. Wei et al. (Wei et al., 2007) found the same trend. This phenomenon can be attributed to the increased SBR, which provides more favorable conditions for tar cracking and carbon gasification.
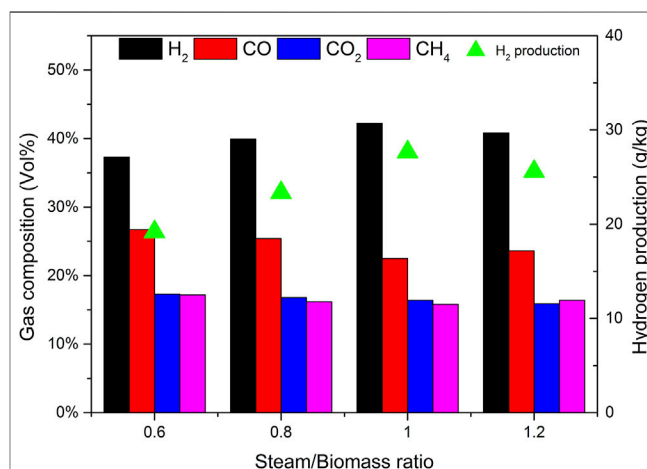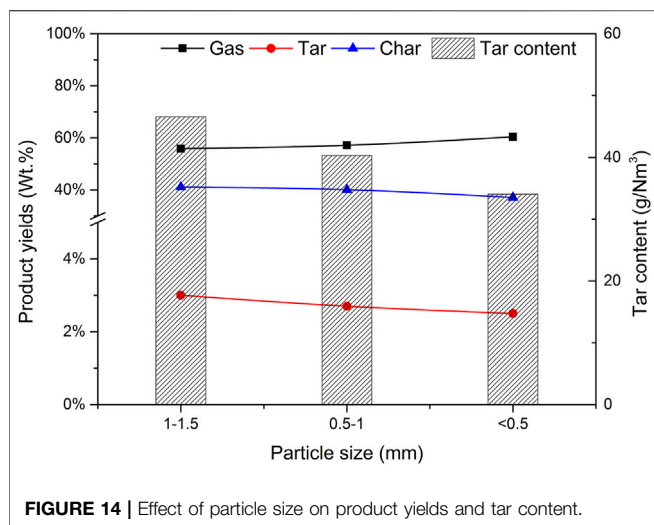
When SBR increased from 0.6 to 1.0, the gas yield increased from 49.7% to 60.4%, and the yields of tar and char decreased from 3.2% to 2.5% and 47.1.% to 37.1% respectively. These trends are highly consistent with other reports by researchers (Zhou et al., 2018). However, when too much steam is introduced and SBR is 1.2, the gas production rate decreases, which may be caused by the decrease of temperature in the furnace caused by the heat absorbed by excess water.

As can be seen from **Figure 13**, when SBR increases from 0.4 to 0.8, the H_2 content increases significantly, because the introduction of water vapor is conducive to tar cracking and char gasification, resulting in higher H_2 production. According to Le Chatelier's principle, the introduction of steam in the system will move the reactions R7, R8, and R9 in the positive direction to produce more hydrogen. When SBR is less than 1.0, the CO content decreases with the increase of water vapor, which is the direction of hydrocarbon conversion reactions R5 and R6, water vapor conversion reactions R8 and R9 to generate H_2 and reduce

FIGURE 14 | Effect of particle size on product yields and tar content.

**FIGURE 15 |** Effect of particle size on gas composition and hydrogen production.

CH_4 and other hydrocarbons. At the same time, in the carbon monoxide shift reaction R9, due to the increase of the amount of water vapor and the acceleration of the positive reaction speed, the content of CO_2 will increase, while the increased carbon dioxide will be absorbed by CaO in the catalyst. Therefore, in the process of increasing SBR, the content of CO_2 will decrease, which is also confirmed by Acharya's research (Acharya et al., 2010). It can be seen from **Figure 13** that the addition of an appropriate amount of steam can improve the yield and quality of gas, but when the steam is excessive, the quality of gas begins to decline. There is an optimal value of SBR, which is 1.0 in this experimental study.

3.6 Effect of Biomass Particle Size on Gasification

Using catalyst b as the catalyst, CBR was 1.2, the gasification reaction temperature was 650°C and SBR was 1.0. The effects of biomass particle size <0.5, 0.5–1, and 1.0–1.5 mm on gasification results were studied. **Figure 14** depicts the effect of biomass particle size on the yield of gasification products and tar content. As expected, with the increase of particle size, the gas yield decreases, while the yield of tar and char shows the opposite trend. These results are consistent with those obtained by Mohammed et al. (Mohammed et al., 2011). With the decrease of particle size, the surface area of biomass particles increases, which improves the heating rate of biomass particles and promotes the pyrolysis reaction of biomass. With the increase of biomass particle size, the heat transfer resistance increases, resulting in incomplete gasification and coking. Another reason is that the size of biomass particles affects the fluidization state in the gasifier. Under the same conditions, the pyrolysis diffusion of biomass particles is mainly controlled by the diffusion of a gas. Due to its large weight, larger particles are often difficult to diffuse and cannot effectively contact the catalyst, resulting in insufficient reaction R1 and low gasification degree (Zhang et al., 2007).

Figure 15 shows the effect of biomass particle size on gas composition and H_2 production. It can be seen that when the
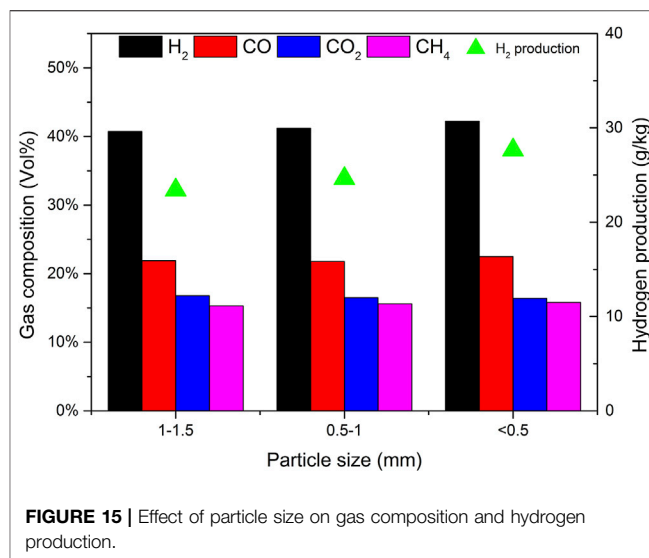
particle size decreases, the content of H_2, CO, and CH_4 increases, while the content of CO_2 decreases. When the biomass particle size decreases, it is conducive to the full contact between biomass and water vapor, and the reactions R7 and R8 are enhanced. More CO_2 is produced in the reaction process. Due to the existence of CaO in the catalyst, the biomass particles are small and in closer contact with the catalyst, which promotes the progress of reaction R10 and absorbs CO_2 more fully. In general, the particle size of biomass material has a certain impact on the gas production characteristics of steam catalytic gasification. As the particle size of the material decreases, the H_2 content in the generated gas increases. Compared with the influence of temperature and steam flux, the influence of material particle size is not very significant.

4 CONCLUSION

1) Three kinds of Fe-based composite catalysts with different loading were prepared. The analysis of catalytic activity for hydrogen production from biomass steam gasification showed that catalyst b with 10% Fe loading showed better activity than the other two catalysts.

2) XRD characterization shows that when the mass fraction of loading is 10%, Fe species are well dispersed on the carrier; N_2 adsorption and desorption showed that catalyst b had a large specific surface area and pore structure; The TPR analysis of catalyst b shows that Fe species are successfully loaded on the composites. Several characterization methods show that catalyst b has the potential for high catalytic activity.

3) By changing the reaction conditions, the optimal reaction conditions were selected, CBR = 1.2, temperature 650°C, SBR = 1.0, particle size <0.5 mm. Under these conditions, the gas yield reached 60.4%, and the tar yield and char yield decreased to 2.5% and 37.1% respectively. The proportion of hydrogen in the gas composition has also reached a high level of 42.2% and

the production of hydrogen has reached 27.65 g/kg. The tar content reaches the lowest value of 34.07 g/Nm^3.

DATA AVAILABILITY STATEMENT

The original contributions presented in the study are included in the article/**Supplementary Material**, further inquiries can be directed to the corresponding authors.

AUTHOR CONTRIBUTIONS

Conceptualization, Methodology, Formal analysis, Investigation, Writing—original draft preparation, LZ. Revising—manuscript, ZY. Figure drawing, DW. Writing—reviewing, Supervision, HZ. Project administration, Supervision, WL. All authors have read and agreed to the published version of the manuscript.

FUNDING

SUPPLEMENTARY MATERIAL

The Supplementary Material for this article can be found online at: https://www.frontiersin.org/articles/10.3389/fchem.2022.882787/full#supplementary-material

REFERENCES

Acharya, B., Dutta, A., and Basu, P. (2010). An Investigation into Steam Gasification of Biomass for Hydrogen Enriched Gas Production in Presence of CaO. *Int. J. Hydrogen Energ.* 35, 1582–1589. doi:10.1016/j.ijhydene.2009.11.109

Cabello, A., Abad, A., García-Labiano, F., Gayán, P., de Diego, L. F., and Adánez, J. (2014b). Kinetic Determination of a Highly Reactive Impregnated Fe2O3/Al2O3 Oxygen Carrier for Use in Gas-Fueled Chemical Looping Combustion. *Chem. Eng. J.* 258, 265–280. doi:10.1016/j.cej.2014.07.083

Cabello, A., Dueso, C., García-Labiano, F., Gayán, P., Abad, A., de Diego, L. F., et al. (2014a). Performance of a Highly Reactive Impregnated Fe2O3/Al2O3 Oxygen Carrier with CH4 and H2S in a 500Wth CLC Unit. *Fuel* 121, 117–125. doi:10.1016/j.fuel.2013.12.027

Choi, H. I., Sung, Y. J., Hong, M. E., Han, J., Min, B. K., and Sim, S. J. (2022). Reconsidering the Potential of Direct Microalgal Biomass Utilization as End-Products: A Review. *Renew. Sustain. Energ. Rev.* 155, 111930. doi:10.1016/j.rser.2021.111930

Cortazar, M., Santamaria, L., Lopez, G., Alvarez, J., Amutio, M., Bilbao, J., et al. (2021). Fe/olivine as Primary Catalyst in the Biomass Steam Gasification in a fountain Confined Spouted Bed Reactor. *J. Ind. Eng. Chem.* 99, 364–379. doi:10.1016/j.jiec.2021.04.046

Demirbaş, A. (2002). Gaseous Products from Biomass by Pyrolysis and Gasification: Effects of Catalyst on Hydrogen Yield. *Energ. Convers. Manage.* 43, 897–909. doi:10.1016/S0196-8904(01)00080-2

Huang, H., Hong, J., Wang, X., Richards, A., Zhang, J., and Qiao, B. (2022). A Spatiotemporal Analysis of the Driving Forces behind the Energy Interactions of the Chinese Economy: Evidence from Static and Dynamic Perspectives. *Energy* 239, 122104. doi:10.1016/j.energy.2021.122104

Li, J., Yan, R., Xiao, B., Wang, X., and Yang, H. (2007). Influence of Temperature on the Formation of Oil from Pyrolyzing Palm Oil Wastes in a Fixed Bed Reactor. *Energy Fuels* 21, 2398–2407. doi:10.1021/ef060548c

Li, X., Chang, G., Yang, L., and Wang, C. (2021). Enhancement of Coke Gasification by lignite and a Low-Cost Fe/red Mud Catalyst to Produce Syngas. *J. Energ. Inst.* 98, 116–123. doi:10.1016/j.joei.2021.06.004

Mahishi, M., and Goswami, D. (2007). An Experimental Study of Hydrogen Production by Gasification of Biomass in the Presence of a CO2CO2 Sorbent. *Int. J. Hydrogen Energ.* 32, 2803–2808. doi:10.1016/j.ijhydene.2007.03.030

Mohammed, M. A. A., Salmiaton, A., Wan Azlina, W. A. K. G., Mohammad Amran, M. S., and Fakhru'l-Razi, A. (2011). Air Gasification of Empty Fruit bunch for Hydrogen-Rich Gas Production in a Fluidized-Bed Reactor. *Energ. Convers. Manage.* 52, 1555–1561. doi:10.1016/j.enconman.2010.10.023

Nordgreen, T., Liliedahl, T., and Sjostrom, K. (2006). Metallic Iron as a Tar Breakdown Catalyst Related to Atmospheric, Fluidised Bed Gasification of Biomass. *Fuel* 85, 689–694. doi:10.1016/j.fuel.2005.08.026

Ortiz, A., and Gorri, D. (2021). Preface to the Special Issue on the Workshop: "Renewable Hydrogen Energy World" (ANQUE-ICCE 2019), June 20-21 2019, Santander, Spain". *Int. J. Hydrogen Energ.* 46, 17446. doi:10.1016/j.ijhydene.2021.02.169

Sun, R., Zhang, X., Wang, C., and Cao, Y. (2021). Co-carbonization of Red Mud and Waste Sawdust for Functional Application as Fenton Catalyst: Evaluation of Catalytic Activity and Mechanism. *J. Environ. Chem. Eng.* 9, 105368. doi:10.1016/j.jece.2021.105368

Tang, Q., Bian, H., Ran, J., Zhu, Y., Yu, J., and Zhu, W. (2015). Hydrogen-Rich Gas Production from Steam Gasification of Biomass Using CaO and a Fe-Cr Water-Gas Shift Catalyst. *Bioresources* 10, 220–227. doi:10.15376/biores.10.2.2560-2569

Udomsirichakorn, J., Basu, P., Salam, P. A., and Acharya, B. (2013). Effect of CaO on Tar Reforming to Hydrogen-Enriched Gas with In-Process CO2 Capture in a Bubbling Fluidized Bed Biomass Steam Gasifier. *Int. J. Hydrogen Energ.* 38, 14495–14504. doi:10.1016/j.ijhydene.2013.09.055

United Nations (2020). About the Sustainable Development Goals. Available at: : https://www.un.org/sustainabledevelopment/sustainable-development-goals/.

Wang, S., Ang, H. M., and Tadé, M. O. (2008). Novel Applications of Red Mud as Coagulant, Adsorbent and Catalyst for Environmentally Benign Processes. *Chemosphere* 72, 1621–1635. doi:10.1016/j.chemosphere.2008.05.013

Wei, L., Xu, S., Zhang, L., Liu, C., Zhu, H., and Liu, S. (2007). Steam Gasification of Biomass for Hydrogen-Rich Gas in a Free-Fall Reactor. *Int. J. Hydrogen Energ.* 32, 24–31. doi:10.1016/j.ijhydene.2006.06.002

Wu, H., Dai, W., Saravanamurugan, S., Li, H., and Yang, S. (2020). Endogenous X-C=O Species Enable Catalyst-free Formylation Prerequisite for CO2 Reductive Upgrading. *Green. Chem.* 22, 5822–5832. doi:10.1039/d0gc02142c

Wu, H., Li, H., and Fang, Z. (2021a). Hydrothermal Amination of Biomass to Nitrogenous Chemicals. *Green. Chem.* 23, 6675–6697. doi:10.1039/D1GC02505H

Wu, H., Zhang, L.-L., Wang, J., Jiang, Y., Li, H., Sudarsanam, P., et al. (2021b). Room-temperature Quasi-Catalytic Hydrogen Generation from Waste and Water. *Green. Chem.* 23, 7528–7533. doi:10.1039/D1GC02722K

Yang, S., Fan, F., Hu, J., and Wang, H. (2020). Particle-scale Evaluation of the Biomass Steam-Gasification Process in a Conical Spouted Bed Gasifier. *Renew. Energ.* 162, 844–860. doi:10.1016/j.renene.2020.08.009

Zhang, H., Li, H., Hu, Y., Venkateswara Rao, K. T., Xu, C., and Yang, S. (2019b). Advances in Production of Bio-Based Ester Fuels with Heterogeneous Bifunctional Catalysts. *Renew. Sustain. Energ. Rev.* 114, 109296. doi:10.1016/j.rser.2019.109296

Zhang, H., Li, H., Xu, C. C., and Yang, S. (2019a). Heterogeneously Chemo/Enzyme-Functionalized Porous Polymeric Catalysts of High-Performance for Efficient Biodiesel Production. *ACS Catal.* 9, 10990–11029. doi:10.1021/acscatal.9b02748

Zhang, R., Wang, Y., and Brown, R. C. (2007). Steam Reforming of Tar Compounds over Ni/olivine Catalysts Doped with CeO2. *Energ. Convers. Manage.* 48, 68–77. doi:10.1016/j.enconman.2006.05.001

Zhou, C., Chen, X., Zhang, W., Gao, F., and Liu, G. (2020). Physicochemical Properties and Energy Production Potential of Agricultural Residues in Anhui Province (Central China). *ACS Sustain. Chem. Eng.* 8, 18476–18483. doi:10.1021/acssuschemeng.0c05967

Zhou, L., Yang, Z., Tang, A., Huang, H., and Lu, W. (2019). Catalytic Steam-gasification of Biomass in a Fluidized Bed Reactor. *J. Chem. Technol. Biotechnol.* 94, 1460–1465. doi:10.1002/jctb.5896

Zhou, L., Yang, Z., Tang, A., Huang, H., Wei, D., Yu, E., et al. (2019). Steam-gasification of Biomass with CaO as Catalyst for Hydrogen-Rich Syngas Production. *J. Energ. Inst.* 92, 1641–1646. doi:10.1016/j.joei.2019.01.010

The handling editor YS declared a past co-authorship with the author YS.

In Situ Green Synthesis of Graphene Oxide-Silver Nanoparticles Composite with Using Gallic Acid

Yunhui Bao[1], Chunlian Tian[1], Huazhong Yu[1,2], Jian He[1,2], Ke Song[1,2], Jie Guo[1,2], Xianwu Zhou[1,2], Ou Zhuo[2] and Shima Liu[1,2]*

[1]Key Laboratory of Hunan Forest Products and Chemical Industry Engineering, Jishou University, Zhangjiajie, China, [2]College of Chemistry and Chemical Engineering, Jishou University, Jishou, China

The adoption of plant-derived natural products to synthesize metal nanoparticles and their complexes has the advantages of mild reaction conditions, environmental protection, sustainability and simple operation compared with traditional physical or chemical synthesis methods. Herein, silver nanoparticles (AgNPs) were *in situ* synthesized on the surface of graphene oxide (GO) by a "one-pot reaction" to prepare graphene oxide-silver nanoparticles composite (GO-AgNPs) based on using $AgNO_3$ as the precursor of AgNPs and gallic acid (GA) as the reducing agent and stabilizer. The size and morphology of GO-AgNPs were characterized by ultraviolet-visible spectrophotometer (Uv-vis), Fourier transform infrared spectroscopy (FT-IR), transmission electron microscope (TEM), X-ray diffractometer (XRD) and dynamic light scattering (DLS). The effects of pH, temperature, time and material ratio on the synthesis of GO-AgNPs were investigated experimentally. The results showed that ideal GO-AgNPs could be prepared under the conditions of pH = 9, 45°C, 2 h and the 2:1 of molar ratio of $AgNO_3$ to GA. The AgNPs within GO-AgNPs are highly crystalline spherical particles with moderate density on the surface of GO, and the size of AgNPs is relatively uniform and determined to be about 8.19 ± 4.21 nm. The research results will provide new ideas and references for the green synthesis of metal nanoparticles and their complexes using plant-derived natural products as the reducing agent and stabilizer.

Keywords: green synthesis, gallic acid, silver nanoparticles, graphene oxide, natural products

1 INTRODUCTION

In the past few decades, green chemistry has been greatly developed in many fields, especially in the field of green synthesis of metal nanoparticles and their complexes based on using natural plant products (Tortella et al., 2021). Due to the mild reducibility of some plant-derived natural products, some metal ions can be reduced to corresponding metal nanoparticles. And at the same time, the metal nanoparticles can be protected from oxidation. This kind of synthesis reaction also has the advantages of mild reaction conditions, environmental protection, sustainable and easily operation (Lee and Park, 2020). Therefore, the green synthesis of metal nanoparticles and their complexes using plant-derived natural products as the reducing agent and stabilizer has attracted much attention (Veisi et al., 2019).

Graphene oxide-silver nanoparticles composites (GO-AgNPs), as silver nanoparticles (AgNPs)-based composites, have excellent antibacterial, antifungal, catalytic, electrical and sensing properties,

and have been widely used in biological pollution control, plant protection, dye degradation, super capacitor and biosensors (Li and Liu, 2010; Liu, et al., 2016; He, et al., 2018). The combination of AgNPs and graphene oxide (GO), the hydrophilicity and stability of GO can effectively hinder the aggregation and dissociation of AgNPs (Jakhar and Sharma, 2020; Rohaizad, et al., 2020). According to existing research reports, in addition to using GO as a platform for AgNPs, there are polymers such as cellulose, lignin, and chitosan that are used to bind AgNPs, but their stability and hydrophilicity are not as good as GO (Pang, et al., 2021; Affes, et al., 2020; Yu, et al., 2020).

The current preparation methods of GO-AgNPs mainly include step-by-step deposition method and *in-situ* reduction method. Graphene oxide (GO) and AgNPs need to be synthesized separately when using the step-by-step deposition method. Generally, methods such as mechanical grinding, laser ablation, and thermal decomposition are used to reduce the size of bulk silver to obtain AgNPs (Meyers, et al., 2006), and then AgNPs are deposited on the GO sheet through interactions such as physical adsorption or electrostatic bonding (Karuppiah, et al., 2015; Pratheesya, et al., 2019; Liu, et al., 2020). The step-by-step deposition method has certain advantages in controlling the size and shape of AgNPs, but the operation is complicated, time-consuming, costly and generally requires expensive specialized equipment (Wang, et al., 2012; Stadler, et al., 2018).

Compared with the step-by-step deposition method, the *in-situ* reduction method has been widely adopted due to its simplicity and high efficiency (Wang, et al., 2016; Mariadoss, et al., 2020; Rohaizad, et al., 2020; Shubhadarshinee, et al., 2022). The synthesis of GO-AgNPs by *in situ* reduction method generally includes silver salts that are reduced to AgNPs by a reducing agent in a GO solution and directly adsorbed on the surface of GO. *In situ* reduction method is usually divided into chemical reduction method and biological reduction method based on the stabilizers and reductants. For GO-AgNPs synthesis, the chemical reduction method generally adopts polyvinylpyrrolidone (PVP), dimethylformamide (DMF) and Tween 80 as stabilizers, and uses aniline, sodium borohydride, hydration hydrazine and formaldehyde as reducing agents (Bao, et al., 2021; Darabdhara, et al., 2019; Kausar, et al., 2018), which are cumbersome and not environmentally friendly. These methods are cumbersome, not environmentally friendly, and generally have toxic substances adsorbed on the products, which limit the biomedical application of GO-AgNPs (Veisi, et al., 2019). Biosynthesis of AgNPs generally uses plant-derived natural products or microorganisms as stabilizers and reducing agents, wherein AgNPs are synthesized on the surface of GO. The biosynthesis method has received much attention owing to the advantages of high efficiency, convenience and environmental protection (Sahu, et al., 2019; Veisi, et al., 2019).

Gallic acid (3,4,5-trihydroxybenzoic acid, GA), a natural low-molecular-weight phenolic compound, exists in a variety of plants or fruits (such as tea, grapes, and gallnuts), and has a variety of biological activities including antibacterial, anticancer and antioxidant (Motloung, et al., 2020; Yetissin and Kurt, 2020). In addition, GA has the potential to be applied in the synthesis of certain metal nanoparticles (such as AgNPs and gold nanoparticles) due to its mild reducibility, in which GA acts as reducing agent and stabilizer (Ahani and Khatibzadeh, 2021; Jing, et al., 2021).

In the process of GA interacting with metal ions, GA is oxidized by losing two electrons and protons to form the corresponding quinone, and the metal ion is reduced to the corresponding metal nanoparticles. The formed metal nanoparticles achieve dispersion stability by continuing to interact with GA (Yoosaf, et al., 2007). However, the use of GA to *in situ* synthesize AgNPs on the surface of GO to prepare GO-AgNPs is rarely reported.

In this study, GA was used as the reducing agent and stabilizer for the synthesis of GO-AgNPs. AgNPs were *in situ* synthesized on the surface of GO by a "one-pot reaction" to prepare GO-AgNPs. Reaction parameters including pH of the synthesis mixtures, temperature, material ratio and time were investigated by orthogonal experiments. At the same time, the size and morphology of GO-AgNPs were characterized by ultraviolet-visible spectrophotometer (Uv-vis), transmission electron microscope (TEM), X-ray diffractometer (XRD) and dynamic light scattering (DLS).

2 MATERIALS AND METHODS

2.1 Materials

Graphite powder, sulfuric acid and potassium permanganate were obtained from Sigma-Aldrich (St. Louis, MO, United States). Hydrochloric acid was purchased from Titan (Shanghai, China). $AgNO_3$, gallic acid, sodium hydroxide and other reagents are purchased from Macklin (Shanghai, China). All aqueous solutions were prepared with deionized (DI) water from Milli-Q-Water (Heal Force, China).

2.2 The Preparation of GO and GO-AgNPs

GO was synthesized according to the modified Hummers method (Hummers and Offeman, 1958), and the whole synthesis process was divided into two parts: pre-oxidation and oxidation. Briefly, the graphite powder is first oxidized with $K_2S_2O_8$ and P_2O_5 in concentrated H_2SO_4, and the pre-oxidized graphite powder is obtained after post-treatment. Next, the graphite powder was re-oxidized with $KMnO_4$ in concentrated H_2SO_4, then the reaction was terminated with hydrogen peroxide, and finally the GO solution was prepared by washing, ultrasonication and dialysis, and stored at 4°C for later use.

Synthesis of GO-AgNPs: Take 3.4 ml of 1 mg/ml GO in a beaker, add 3.4 ml of 10 mM $AgNO_3$ and 3.2 ml of DI water after sonication for 15 min, and add 10 ml of 2 mM GA dropwise after mixing evenly. The pH of the solution was adjusted with 1 mol/L NaOH and 1 mol/L HCl, and the reaction temperature and time were controlled. After the completion of the reaction, the samples were centrifuged at 5,500 r/min for 10 min, washed with DI water for three times, and then resuspended GO- AgNPs with DI water.

Optimization of reaction pH: keep other reaction conditions unchanged, set up six groups of experiments, and use 1 mol/L NaOH and 1 mol/L HCl to adjust the pH of the reaction solution to 3, 5, 7, 9, 11, and 13, respectively.

FIGURE 1 | Schematic diagram of the synthesis of GO-AgNPs.
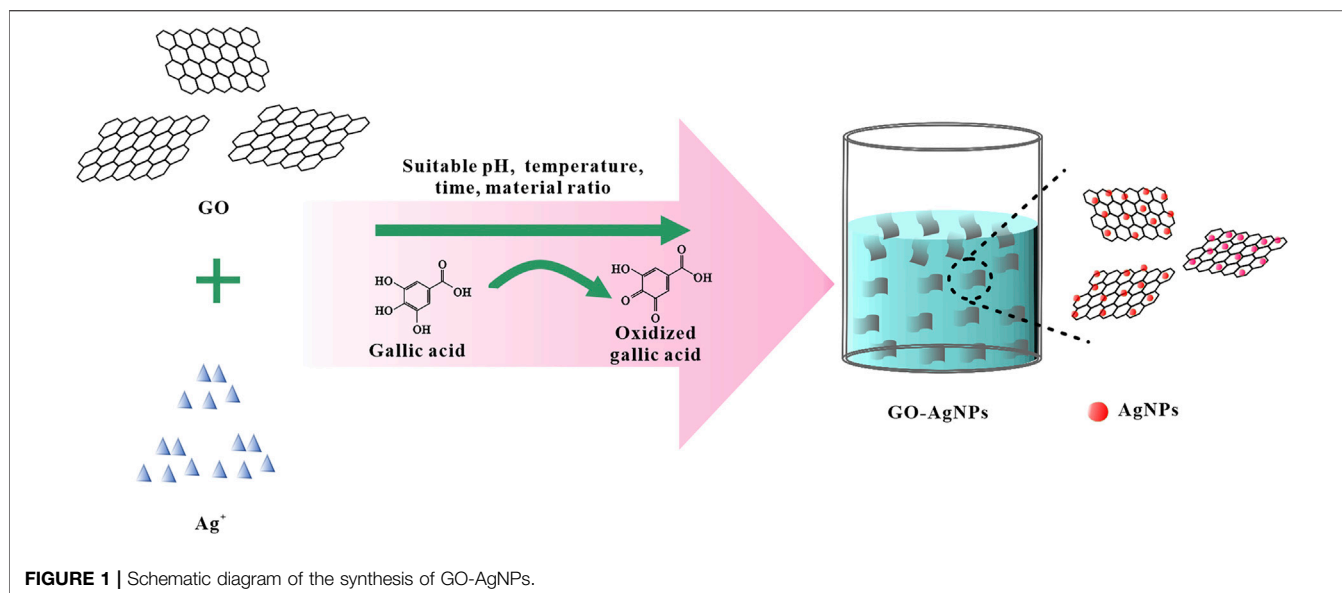
Optimization of reaction temperature: under the optimum reaction pH condition, keep other reaction conditions unchanged. Five groups of experiments were set up, and the reaction temperature was adjusted to 5, 25, 45, 65, and 85°C respectively.

Optimization of reaction time: under the optimum reaction pH and temperature conditions, keep other reaction conditions unchanged. Six groups of experiments were set up, and the reaction times were adjusted to 5, 15, 30 min, 1, 2 and 4 h.

Optimization of reaction material ratio: under the optimum reaction pH, temperature and time conditions, keep other reaction conditions unchanged. Set up six groups of experiments, and adjust the material ratio of $AgNO_3$ and GA to 1:4, 1:2, 1:1, 2:1, 4:1 and 8:1.

Synthesis of GO-AgNPs under optimal conditions: Keeping other reaction conditions unchanged, GO-AgNPs was synthesized again under the conditions of reaction pH of 9, temperature of 45°C, time of 2 h and the ratio of $AgNO_3$ to GA of 2:1.

2.3 Characterizations

The morphology of the GO-AgNPs was characterized by transmission electron microscopy (TEM, JEM-2100F, JEOL, Japan). The structure of the GO-AgNPs and GO was measured by Uv-vis spectrophotometer (Evolution 220, Thermofisher, United States), FTIR spectrophotometer (Nicolet iS10, Thermofisher, United States) and X-ray diffraction spectra (XRD, Bruker D8 Advance, Germany). The thickness and size of GO were characterized by atomic force microscopy (AFM, Multimode Nanoscope VIII Instrument Bruker, United States). The Zeta potential and average particle size of the GO-AgNPs was measured by Dynamic Light Scattering (DLS, ZS-90, Malvern, United Kingdom).
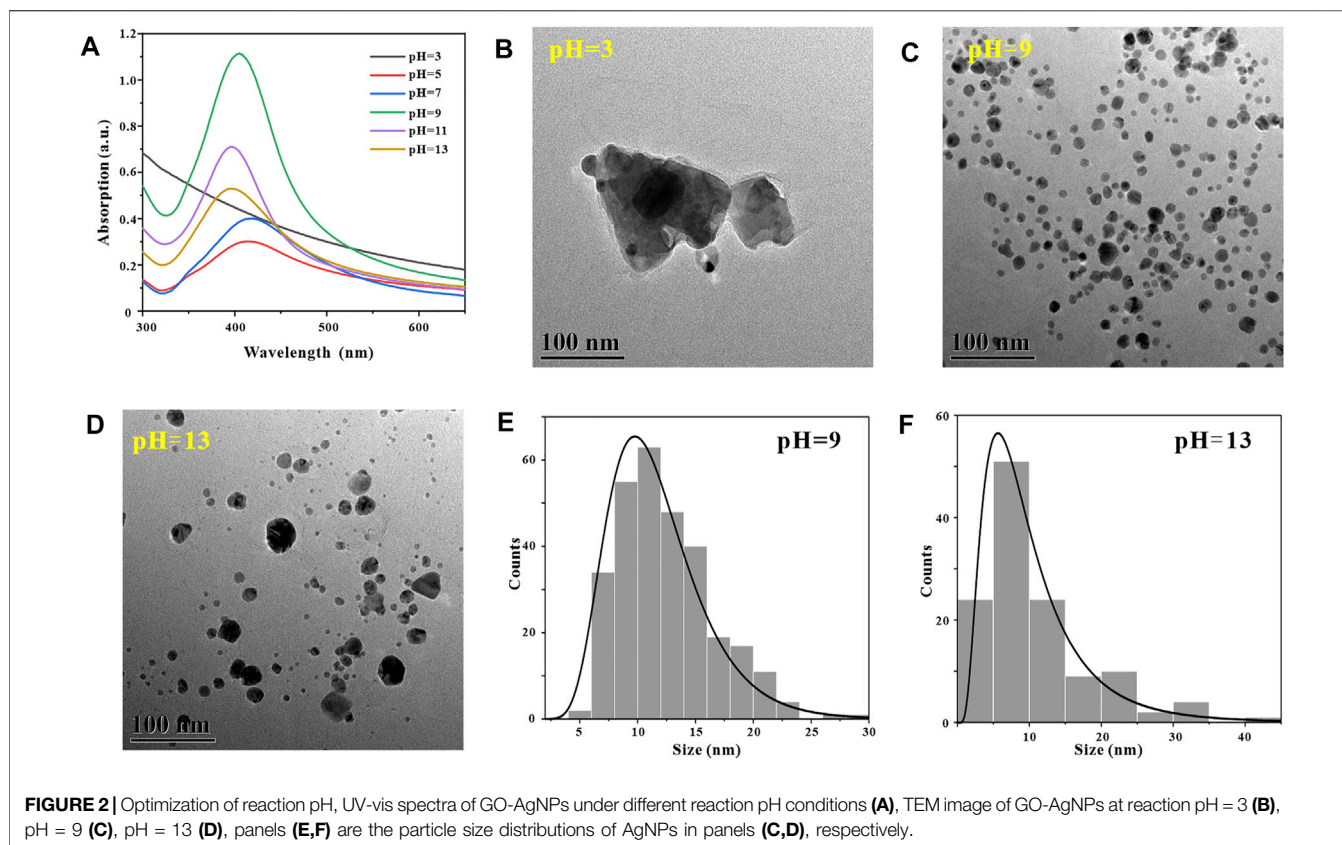
3 RESULTS AND DISCUSSION

3.1 The Synthesis of GO and GO-AgNPs

In this study, GO was first prepared by the modified Hummers method. By observing **Supplementary Figure S1**, it can be found that GO is a single-layer structure with a thickness of about 1 nm, and the size is concentrated between 0.3 and 3 μm. After preparing the GO, based on the mild reducibility of GA, GA was used as reducing agent and stabilizer, and $AgNO_3$ was used as the precursor of AgNPs. As a precursor, GO-AgNPs were prepared by *in-situ* synthesis of AgNPs on the surface of GO by a "one-pot method" (**Figure 1**). In this process, Ag^+ is reduced to AgNPs, and GA is oxidized. At the same time, orthogonal experiments were designed to study the effects of pH, temperature, time and material ratio of the synthesis reaction on the synthesis of GO-AgNPs, so as to determine the optimal reaction conditions for the synthesis of GO-AgNPs using GA.

3.2 Effects of Different Reaction Conditions on the Synthesis of GO-AgNPs
3.2.1 Reaction pH

Due to the surface plasmon resonance (SPR) of the AgNPs, corresponding characteristic absorption peaks appear in the Uv-vis spectrum. According to the Mie theory: The larger the particle size of the metal nanoparticles, the red-shift the absorption peak wavelength. The smaller the particle size, the blue-shift of the absorption peak wavelength, and the width of the half-peak of the absorption peak corresponds to the more concentrated or dispersed particle size distribution of the metal nanoparticles. In addition, the strength of the absorption peak represents the more or less the number of nanoparticles (Luo, et al., 2018). Therefore, the size, shape and number of AgNPs in GO-AgNPs can be preliminarily determined according

FIGURE 2 | Optimization of reaction pH, UV-vis spectra of GO-AgNPs under different reaction pH conditions **(A)**, TEM image of GO-AgNPs at reaction pH = 3 **(B)**, pH = 9 **(C)**, pH = 13 **(D)**, panels **(E,F)** are the particle size distributions of AgNPs in panels **(C,D)**, respectively.
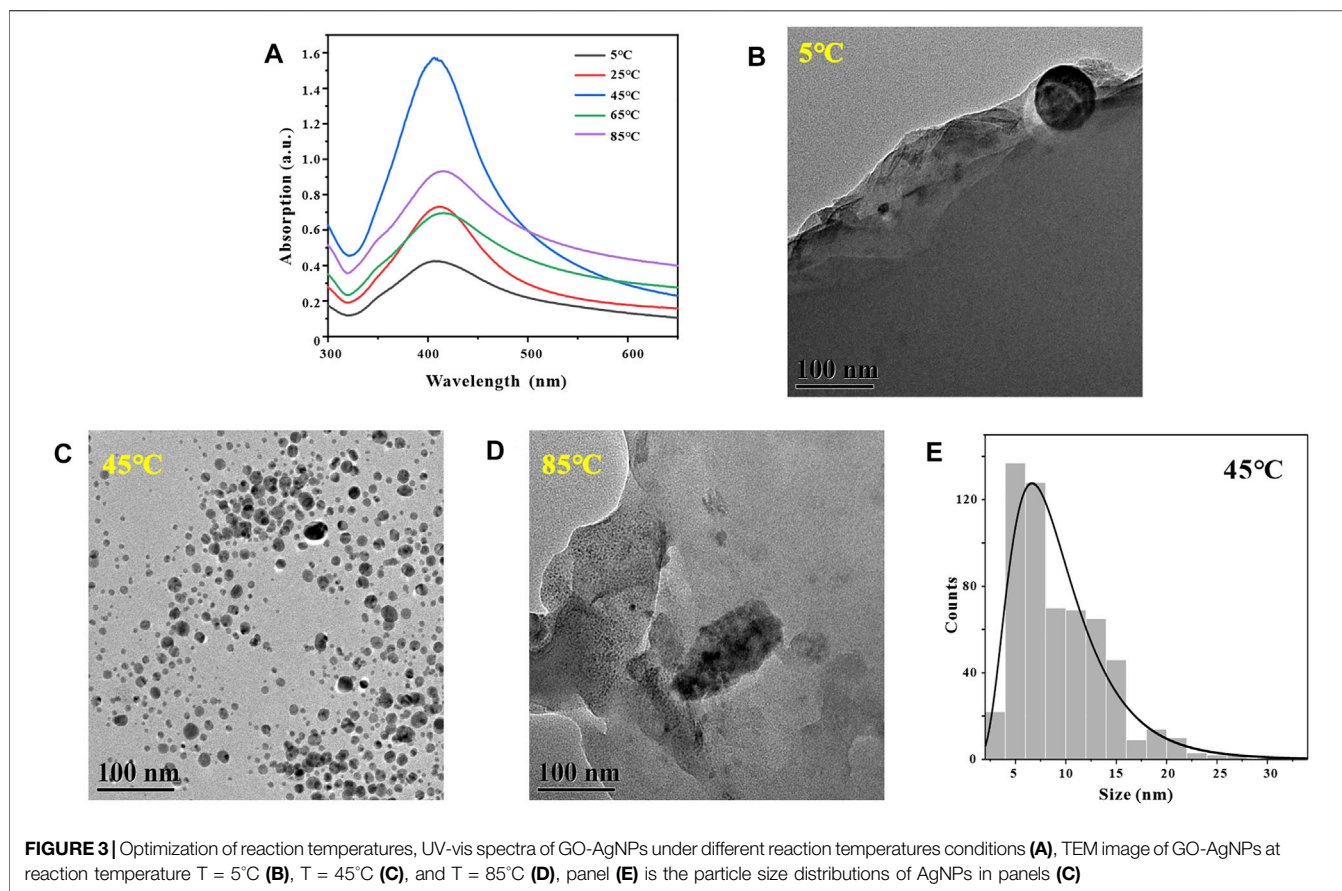
to the shape of the Uv-vis characteristic absorption peak of AgNPs.

In the process of synthesizing metal nanoparticles by reduction method, the reaction pH has a crucial influence on the synthesis success or failure of metal nanoparticles (Wu, et al., 2021). To explore the effect of reaction pH on the number and morphology of AgNPs in GO-AgNPs, we synthesized GO-AgNPs at reaction pH of 3, 5, 7, 9, 11, and 13, respectively, and subjected them to Uv-vis characterization analysis. By observing **Figure 2A**, it can be found that when the reaction pH is 3, there is no obvious AgNPs characteristic absorption peak in the Uv-vis spectrum of GO-AgNPs, indicating that almost no GO-AgNPs are generated in the reaction system at this time. When the reaction pH is 5–13, the characteristic absorption peaks of AgNPs in the figure are concentrated in the interval of 396–418 nm, indicating that spherical AgNPs is formed in the reaction system (Zhang, et al., 2014). When the reaction pH is 9, the characteristic absorption peak intensity of AgNPs in the figure is the highest, and the half-peak width is narrow, indicating that the number of AgNPs in GO-AgNPs is large and the particle size distribution is relatively concentrated. When the reaction pH is 13, the characteristic absorption peak intensity of AgNPs in the figure is low and the half-peak width is wide, indicating that the number of AgNPs in GO-AgNPs is small and the particle size distribution is relatively dispersed. Based on the UV-vis spectra of GO-AgNPs analysis, we can preliminarily determine that the optimal reaction pH for the synthesis of GO-AgNPs is 9.

In order to further confirm that the optimal reaction pH for the synthesis of GO-AgNPs is 9, we also used TEM to characterize and analyze GO-AgNPs. Through the TEM images of GO-AgNPs, the size, shape and density degree of AgNPs in GO-AgNPs can be visually observed. By observing **Figure 2B**, it can be found that when the reaction pH is 3, there are no AgNPs in the corresponding TEM image, but irregular impurities around 300 nm appear in the picture, which may be the agglomerates of GO in the reaction system. By observing **Figure 2C**, we can find that when the reaction pH is 9, a large number of spherical AgNPs appear in the corresponding TEM image, and the sizes are relatively concentrated, and the average particle size of AgNPs is 11.68 ± 4.11 nm (**Figure 2E**). By observing **Figure 2D**, we can find that when the reaction pH is 13, a small amount of spherical AgNPs appear in the corresponding TEM image, and the sizes are relatively dispersed, and the average particle size of AgNPs is 10.53 ± 7.83 nm (**Figure 2F**). Based on the above TEM characterization results of GO-AgNPs, it can be found that the optimal reaction pH for the synthesis of GO-AgNPs is 9, which is consistent with the Uv-vis characterization results of GO-AgNPs above.

3.2.2 Reaction Temperature
Similarly, in the process of synthesizing metal nanoparticles by reduction method, the reaction temperature has a crucial effect on the synthesis rate of metal nanoparticles (Stavinskaya, et al., 2019). After determining the optimal reaction pH for the

FIGURE 3 | Optimization of reaction temperatures, UV-vis spectra of GO-AgNPs under different reaction temperatures conditions **(A)**, TEM image of GO-AgNPs at reaction temperature T = 5°C **(B)**, T = 45°C **(C)**, and T = 85°C **(D)**, panel **(E)** is the particle size distributions of AgNPs in panels **(C)**

synthesis of GO-AgNPs using GA is 9, in order to explore the effect of reaction temperature on the number and morphology of AgNPs in GO-AgNPs. GO-AgNPs were synthesized under the conditions of temperature at 5, 25, 45, 65, and 85°C, respectively, and Uv-vis characterization analysis of GO-AgNPs was carried out. By observing **Figure 3A**, it can be found that when the reaction temperature is 5°C, in the Uv-vis spectrum of GO-AgNPs, the characteristic absorption peak of AgNPs has low intensity and wide half-peak width, indicating that the number of AgNPs in the GO-AgNPs is small and the particle size distribution is relatively dispersed. When the reaction temperature was 45°C, the characteristic absorption peak intensity of AgNPs in the figure was the largest, and the half-peak width was narrow, indicating that the number of AgNPs in GO-AgNPs was large and the particle size distribution was relatively concentrated. When the reaction temperature was 85°C, the characteristic absorption peak intensity of AgNPs in the figure was low and the half-peak width was wide, indicating that the number of AgNPs in GO-AgNPs was small and the particle size distribution was relatively dispersed. Based on the above analysis, we can preliminarily determine that the optimal reaction temperature for the synthesis of GO-AgNPs is 45°C.

In order to further confirm that the optimal reaction temperature for the synthesis of GO-AgNPs is 45°C, we also used TEM to characterize and analyze the GO-AgNPs. The size, shape, and density of AgNPs in GO-AgNPs can be intuitively

reflected by TEM images. By observing **Figure 3B**, it can be found that there are almost no AgNPs in the corresponding TEM image when the reaction temperature is 5°C. By observing **Figure 3C**, we can find that when the reaction temperature is 45°C, a large number of spherical AgNPs appear in the corresponding TEM image, and the size distribution is relatively concentrated, and the average particle size of AgNPs is 9.42 ± 4.59 nm (**Figure 3E**). By observing **Figure 3D**, we can find that there are almost no AgNPs in the corresponding TEM image when the reaction temperature is 85°C. Based on the above TEM and Uv-vis characterization results of GO-AgNPs, it can be determined that the optimal reaction temperature for the synthesis of GO-AgNPs is 45°C.

3.2.3 Reaction Time

Generally, in the process of synthesizing metal nanoparticles by reduction method, the length of reaction time will affect the synthesis amount and particle size distribution of metal nanoparticles (Khan, et al., 2022). After determining the optimal reaction pH and temperature for synthesizing GO-AgNPs using GA at 9 and 45°C, in order to explore the effect of reaction time on the number and morphology of AgNPs in GO-AgNPs. GO-AgNPs were synthesized under the reaction time of 5, 15, 30 min, 1, 2 and 4 h, respectively, and Uv-vis characterization analysis was performed on GO-AgNPs. By observing **Figure 5A**, it can be found that when the reaction time was 5 min, the characteristic absorption peak of AgNPs in
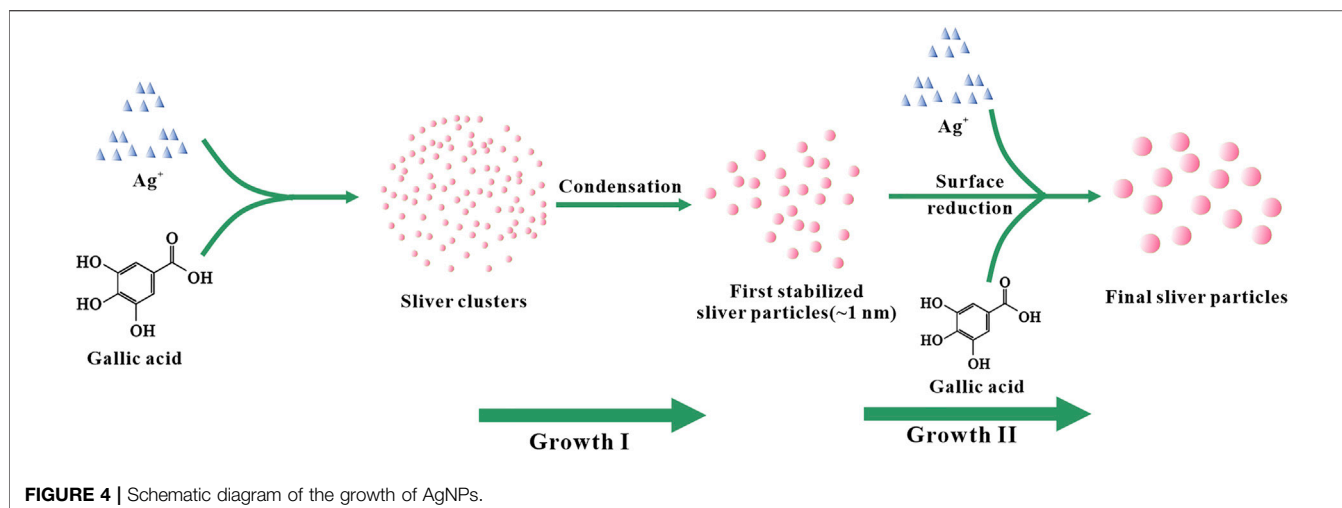
FIGURE 4 | Schematic diagram of the growth of AgNPs.

the Uv-vis spectrum of GO-AgNPs has a low intensity and a wide half-peak width, indicating that the number of AgNPs in GO-AgNPs is small and the particle size distribution is relatively dispersed. When the reaction time was 2 h, the characteristic absorption peak intensity of AgNPs in the figure was the highest, and the half-peak width was narrower, indicating that the number of AgNPs in GO-AgNPs was large and the particle size distribution was relatively concentrated. When the reaction time was 4 h, the characteristic absorption peak intensity of AgNPs in the figure was lower and the half-peak width was wider, indicating that the number of AgNPs in GO-AgNPs was small and the particle size distribution was relatively dispersed. Based on the above analysis, we can preliminarily determine that the optimal reaction time for the synthesis of GO-AgNPs is 2 h.

In order to further confirm that the optimal reaction time for the synthesis of GO-AgNPs is 2 h, we also used TEM to characterize and analyze GO-AgNPs, and used TEM images to visually observe the size, shape and density of AgNPs in GO-AgNPs. By observing **Figure 5B**, it can be found that when the reaction time is 5 min, the AgNPs in the corresponding TEM image are seriously aggregated and the particle size distribution is relatively dispersed, and the average particle size of AgNPs is 11.2 ± 4.59 nm (**Figure 5E**). By observing **Figure 5C**, we can find that when the reaction time is 2 h, there are more spherical AgNPs in the corresponding TEM image, and the sizes are relatively concentrated, and the average particle size of AgNPs is 11.28 ± 5.42 nm (**Figure 5F**).
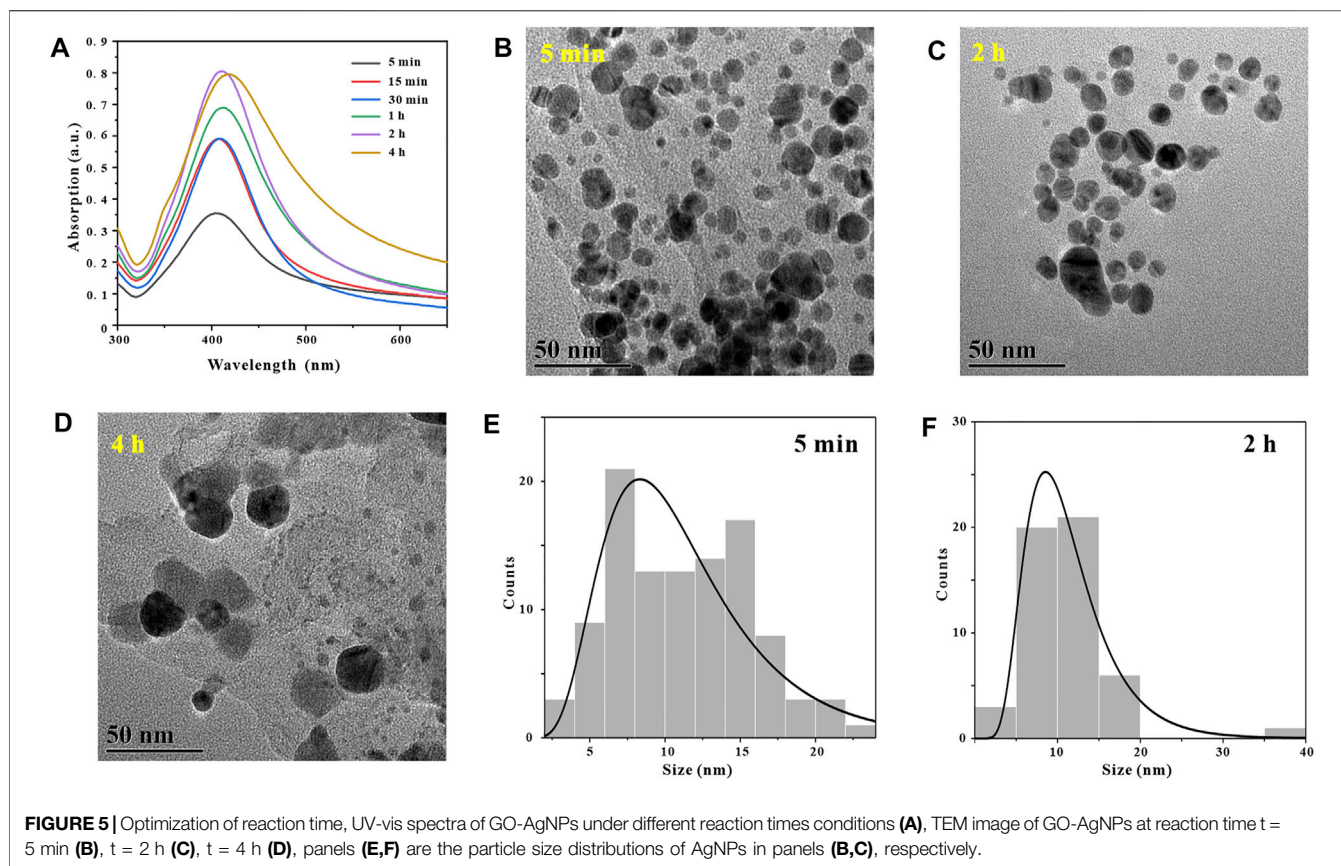
According to existing literature reports, the formation of AgNPs from Ag^+ can be roughly divided into two stages (**Figure 4**). On the one hand, Ag^+ is chelated with GA in the solution and further reduced to silver nuclei (Mafuné, et al., 2003). With the prolongation of the reaction time, the amount of silver nuclei gradually increases. The silver nuclei aggregated and formed small silver nanoclusters. At the same time, Ag^+ continues to aggregate on the surface of silver nanoclusters and is further reduced to Ag^0 through charge transfer, which causes the particle size of silver nanoclusters to increase and grow into larger silver nanoparticles. On the other hand, GA in the solvent also acts as a stabilizer, GA interacts with silver nanoclusters

to achieve regulation of the growth and stability of silver nanoclusters (Henglein and Giersig, 1999; Pillai and Kamat, 2004; Wang, et al., 2010; Thanh, et al., 2014).

By observing **Figure 5D**, we can find that when the reaction time is 4 h, the number of AgNPs in the corresponding TEM image is less, and the large particles are more, this is because the second stage of AgNPs growth will last longer with the extension of time. After a long time, the obtained AgNPs have larger particle size (**Figure 4**). Based on the above TEM characterization analysis results of GO-AgNPs, combined with the Uv-vis characterization analysis results of GO-AgNPs above, it can be determined that the optimal reaction time for the synthesis of GO-AgNPs is 2 h.

3.2.4 Reaction Material Ratio

In addtion, in the process of synthesizing metal nanoparticles by reduction method, the molar ratio of metal ions to reducing agent has an important influence on the synthesis success or failure of metal nanoparticles and the particle size (Mittal, et al., 2014). After determining that the optimal reaction pH for synthesizing GO-AgNPs from GA is 9, the temperature is 45°C and the time is 2 h, in order to explore the effect of the molar ratio of $AgNO_3$ to GA ($M_{AgNO3}:M_{GA}$) in the reaction system on GO-AgNPs. To investigate the effect of the number and morphology of AgNPs, we synthesized GO-AgNPs under the conditions of $M_{AgNO3}:M_{GA}$ at 1:4, 1:2, 1:1, 2:1, 4:1, and 8:1, respectively, and the GO-AgNPs was subjected to Uv-vis characterization analysis. By observing **Figure 6A**, it can be found that when $M_{AgNO3}:M_{GA}$ is 1:4, there is no obvious AgNPs characteristic absorption peak in the Uv-vis spectrum of GO-AgNPs, indicating that almost no GO-AgNPs was synthesized at this time. When the ratio of $M_{AgNO3}:M_{GA}$ is 2:1, the characteristic absorption peak intensity of AgNPs in the figure is higher, and the half-peak width is narrower, indicating that the number of AgNPs in GO-AgNPs is large and the particle size distribution is relatively concentrated. When $M_{AgNO3}:M_{GA}$ is 8:1, the characteristic absorption peak intensity of AgNPs in the figure is higher, but the half-peak width is wider, indicating that the number of AgNPs in GO-AgNPs at this time is quite large but the particle size distribution is relatively dispersed.

FIGURE 5 | Optimization of reaction time, UV-vis spectra of GO-AgNPs under different reaction times conditions **(A)**, TEM image of GO-AgNPs at reaction time t = 5 min **(B)**, t = 2 h **(C)**, t = 4 h **(D)**, panels **(E,F)** are the particle size distributions of AgNPs in panels **(B,C)**, respectively.

In order to further determine the optimal material ratio for the synthesis of GO-AgNPs, we also used TEM to characterize and analyze the GO-AgNPs. The size, shape, and density of AgNPs in GO-AgNPs can be visually observed by using TEM images. By observing **Figure 6B**, it can be found that when the ratio of $M_{AgNO3}:M_{GA}$ is 1:4, there are almost no AgNPs in the corresponding TEM image, and only some agglomerate impurities exist. By observing **Figure 6C**, we can find that when $M_{AgNO3}:M_{GA}$ is 2:1, there are more spherical AgNPs in the corresponding TEM image, and the size distribution is relatively concentrated, and the average particle size of AgNPs is 10.45 ± 4.22 nm (**Figure 6E**). By observing **Figure 6D**, we can find that when the $M_{AgNO3}:M_{GA}$ ratio is 8:1, the corresponding TEM image has a large number of AgNPs, but the particle size distribution is relatively dispersed, and the average particle size of AgNPs is 7.82 ± 4.25 nm (**Figure 6F**). Based on the above TEM characterization analysis results of GO-AgNPs, combined with the Uv-vis characterization analysis results of GO-AgNPs above, it can be determined that the optimal $M_{AgNO3}:M_{GA}$ for the synthesis of GO-AgNPs is 2:1.

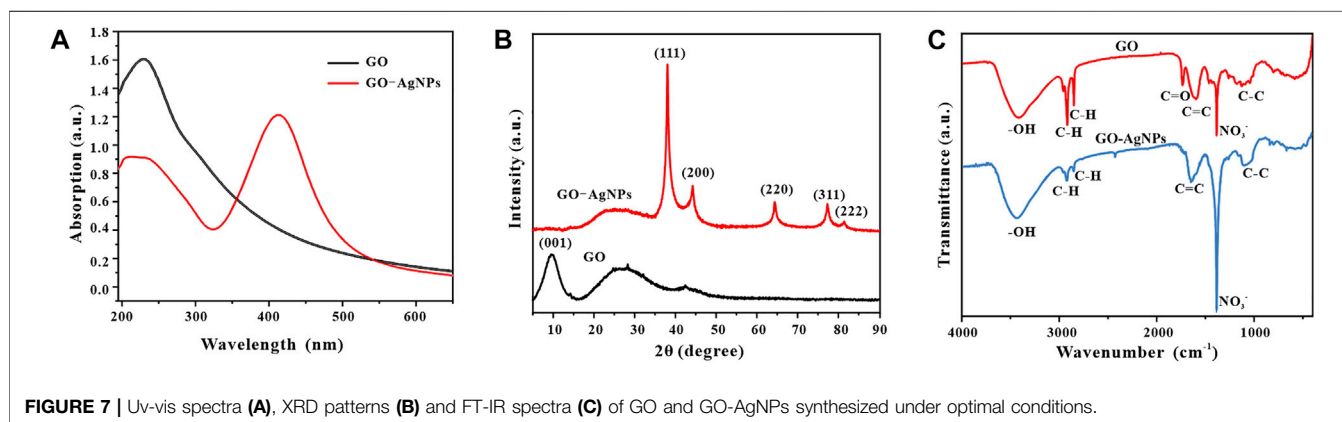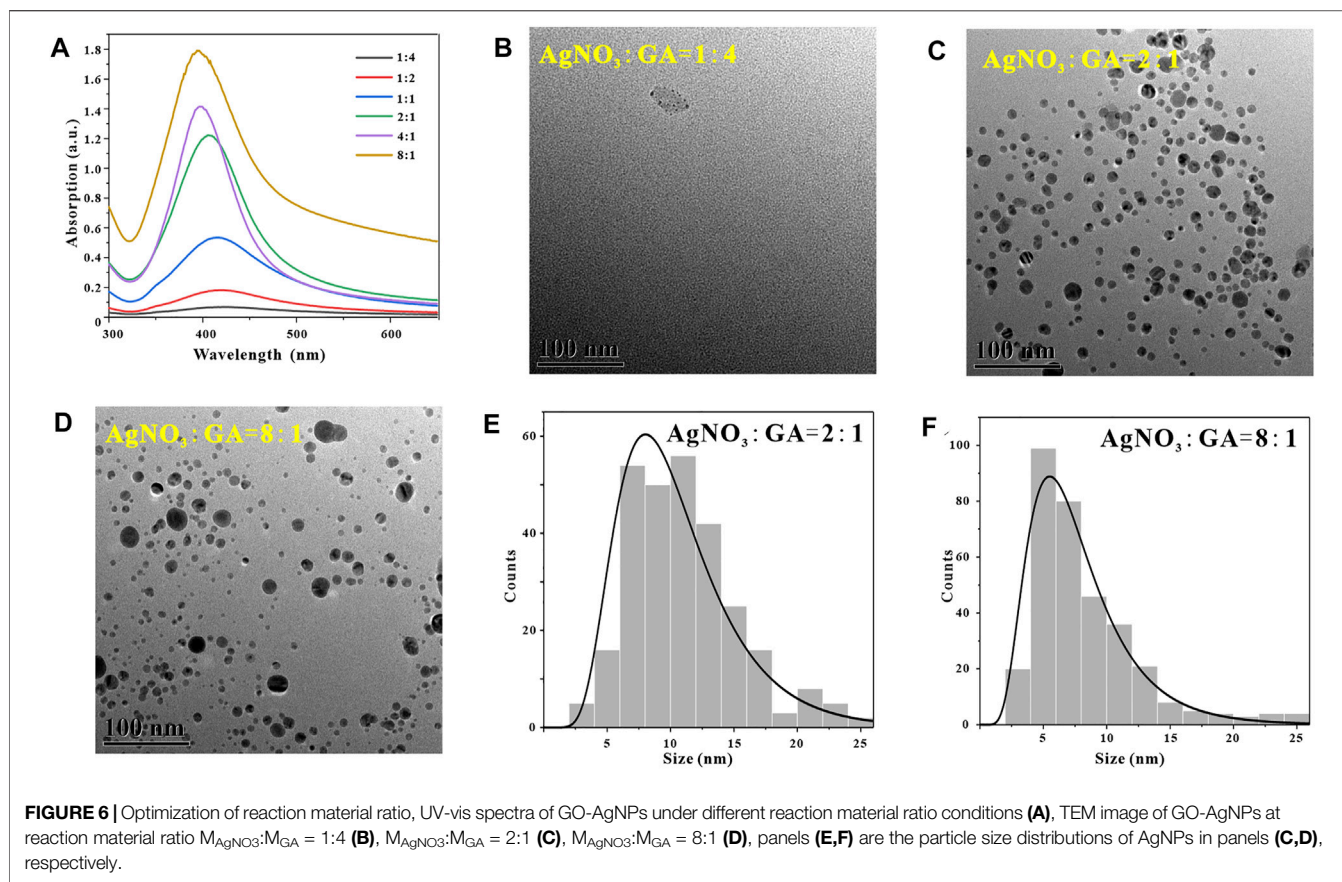## 3.3 Preparation and Characterization of GO-AgNPs Under Optimal Conditions
3.3.1 Uv-Vis Spectral Analysis
In order to verify the scientificity and reliability of the optimal synthesis conditions for GO-AgNPs in the previous article, we re-

prepared GO-AgNPs under the optimal synthesis conditions. The GO-AgNPs were systematically analyzed by Uv-vis, FT-IR, XRD, and TEM. First, the GO-AgNPs were characterized by Uv-vis (**Figure 7A**), and GO was introduced as a control. It was found that the Uv-vis spectrum of GO has an obvious absorption peak at 230 nm, representing the π→π⋆ transition of the C-C bond in GO (Sahu, et al., 2019). The Uv-vis spectra of GO-AgNPs have characteristic peaks at 230 and 410 nm, the former is the characteristic peak of GO, and the latter is the surface plasmon resonance peak of AgNPs. By comparing and analyzing the Uv-vis spectra of GO and GO-AgNPs, we can preliminarily prove the successful synthesis of AgNPs in GO-AgNPs.
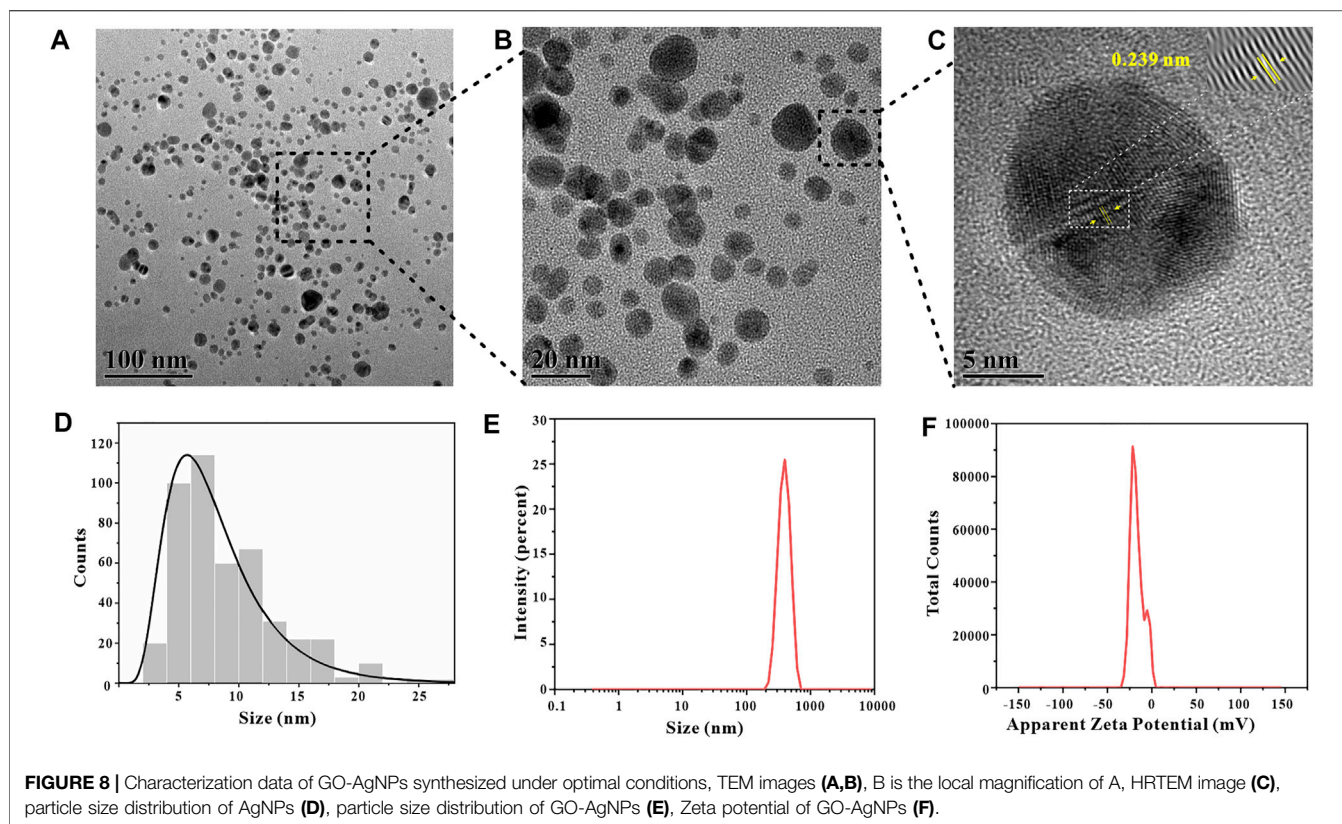
3.3.2 X-Ray Diffraction Analysis
To further confirm the successful synthesis of GO-AgNPs, we performed X-ray diffraction analysis of GO-AgNPs and added GO as a control, and the results are shown in **Figure 7B**. In the figure, GO has an obvious characteristic peak at 2θ = 9.5°, which corresponding to the (001) typical diffraction peak of GO (Zhang, et al., 2017). In the figure, GO-AgNPs showed obvious characteristic peaks at 2θ = 38.06°, 44.26°, 64.38°, 77.34°, and 81.5°, which corresponds to face-centered cubic (FCC) AgNPs (JCPDS No.04-0783) crystal structures of (111), (200), (220), (222), and (311) crystal planes (Chunfa, et al., 2018). At the same time, there are no other obvious impurity diffraction peaks in the spectrum, so it can be inferred that the prepared AgNPs particles

FIGURE 6 | Optimization of reaction material ratio, UV-vis spectra of GO-AgNPs under different reaction material ratio conditions **(A)**, TEM image of GO-AgNPs at reaction material ratio M_{AgNO3}:M_{GA} = 1:4 **(B)**, M_{AgNO3}:M_{GA} = 2:1 **(C)**, M_{AgNO3}:M_{GA} = 8:1 **(D)**, panels **(E,F)** are the particle size distributions of AgNPs in panels **(C,D)**, respectively.

FIGURE 7 | Uv-vis spectra **(A)**, XRD patterns **(B)** and FT-IR spectra **(C)** of GO and GO-AgNPs synthesized under optimal conditions.

are relatively pure and have few impurity particles. In addition, the diffraction peaks of GO-AgNPs are quite sharp, which indicates the good crystallinity of AgNPs in GO-AgNPs. It is worth noting that the peak of GO at 9.5° almost completely disappeared after binding with AgNPs. One possible reason is that the strong signal of AgNPs masks the signal of GO, and the other possible reason is the high degree of the exfoliation of GO after loading AgNPs. There is a large space between the lamellae, so there is no longer a corresponding diffraction peak (Yang, et al., 2011; Chen, et al., 2016; Liu, et al., 2020).

3.3.3 FT-IR Spectral Analysis

In order to demonstrate the synthesis of GO-AgNPs from multiple perspectives, we used FT-IR to analyze the GO-AgNPs by infrared spectroscopy and added GO as a control, and the results are shown in **Figure 7C**. It is well known that GO contains various oxygen functional groups, such as epoxy, hydroxyl, carbonyl, and carboxyl groups, and the characteristic vibrations of these groups can be clearly observed in the infrared spectrum of GO, with a wide range of 3,200 cm^{-1}–3,600 cm^{-1}. The peaks are formed by O-H stretching vibrations in alcohol and

FIGURE 8 | Characterization data of GO-AgNPs synthesized under optimal conditions, TEM images **(A,B)**, B is the local magnification of A, HRTEM image **(C)**, particle size distribution of AgNPs **(D)**, particle size distribution of GO-AgNPs **(E)**, Zeta potential of GO-AgNPs **(F)**.

carboxylic acid functional groups (Liu, et al., 2020). The peaks corresponding to $2,918 \, cm^{-1}$ and $2,849 \, cm^{-1}$ represent weak stretching vibrations of C-H in the alkyl group at the margin of GO (Yang, et al., 2011). The two peaks at $1734 \, cm^{-1}$ and $1,597 \, cm^{-1}$ represent the asymmetric stretching vibration of the carboxyl group in GO and the stretching vibration of C=C (Sedki, et al., 2015). In contrast, the peak intensity of GO-AgNPs nanocomposites decreased at $1734 \, cm^{-1}$ and increased at $1,639 \, cm^{-1}$, indicating that the connection between AgNPs and GO was via electrostatic attraction (Liu, et al., 2020). In addition, the peak at $1,384 \, cm^{-1}$ represents the stretching vibration of NO_3^-, and the presence of NO_3^- may be related to the addition of nitrate during the synthesis of GO and GO-AgNPs (Sundriyal and Bhattacharya, 2017).

3.3.4 TEM Analysis

In order to visually observe the morphology of GO-AgNPs, we used TEM to characterize and analyze GO-AgNPs. Since GO has a single-layer carbon atomic structure, it is difficult to observe in TEM images, but AgNPs on GO sheets are easy to observe (**Figures 8A,B**). It can be indicated a strong interaction between AgNPs and GO (Liu, et al., 2020). The high-resolution TEM (HRTEM) image of GO-AgNPs is shown in **Figure 8C**. Through the measurement, the interplanar spacing of AgNPs is 0.239 nm, which is consistent with the (111) interplanar spacing of metallic silver FCC phase, which is 0.23 nm. It is proved that the black dots in the figure are AgNPs particles. In addition, we also counted the particle size

distribution of 452 AgNPs particles through TEM images (**Figure 8D**) and calculated that the average particle size of AgNPs is 8.19 ± 4.21 nm.

3.3.5 DLS Analysis

Zeta potential is the potential generated by the distributed charges around the nanoparticle, and the Zeta potential of the nanoparticle is an vital indicator of its stability, and its numerical value directly shows the stability of the nanoparticle in colloidal suspension (Sahu, et al., 2019). The GO-AgNPs were characterized by DLS and the Zeta potential of the GO-AgNPs was measured to be −16.8 mV (Figure 8F). In terms of Zeta potential alone, it does not mean that GO-AgNPs have excellent stability, but apart from that, GO contains abundant oxygen-containing functional groups, has good hydrophilicity and stability, and can effectively hinder the aggregation precipitation of GO-AgNPs, bringing good stability to GO-AgNPs. In addition, by DLS characterization analysis, we also measured the average hydrated particle size of GO-AgNPs to be 455.9 ± 84.42 nm (Figure 8E).

4 CONCLUSION

In this study, GO-AgNPs was prepared by a "one-pot" reaction on the surface of GO, in which GA was adopted as reducing agent and stabilizer for the *in situ* green synthesis of AgNPs

due to its mild reducibility and stability to metal nanoparticles. The effects of reaction pH, temperature, time and material ratio on the synthesis of GO-AgNPs were investigated by orthogonal experiments. Combined with the characterization results of Uv-vis, FT-IR, TEM, XRD and DLS on GO-AgNPs, it was determined that the conditions of pH = 9, 45°C, 2 h and 2:1 of molar ratio of AgNO$_3$ to GA were the optimal reaction conditions for the synthesis of GO-AgNPs with using GA as reducing agent and stabilizer. The as-prepared AgNPs in GO-AgNPs were spherical particles with highly crystalline, and the spherical particles were moderately densely distributed on the surface of GO with a size of 8.19 ± 4.21 nm and a high particle size uniformity. The research results can provide a potential theoretical reference for the *in situ* green synthesis of metal nanoparticles and their complexes using plant-derived natural products as reducing agent and stabilizer.

DATA AVAILABILITY STATEMENT

The original contributions presented in the study are included in the article/**Supplementary Material**, further inquiries can be directed to the corresponding author.

AUTHOR CONTRIBUTIONS

YB conducted most of the experiments. SL conceptualized and directed the whole project. YB and SL drafted the manuscript. CT, HY, JH, KS, JG, XZ, and OZ revised the manuscript. All of the authors contributed in scientific discussions.

SUPPLEMENTARY MATERIAL

The Supplementary Material for this article can be found online at: https://www.frontiersin.org/articles/10.3389/fchem.2022.905781/full#supplementary-material

REFERENCES

Affes, S., Maalej, H., Aranaz, I., Kchaou, H., Acosta, N., Heras, Á., et al. (2020). Controlled Size Green Synthesis of Bioactive Silver Nanoparticles Assisted by Chitosan and its Derivatives and Their Application in Biofilm Preparation. *Carbohydr. Polym.* 236, 116063–116075. doi:10.1016/j.carbpol.2020.116063

Ahani, M., and Khatibzadeh, M. (2021). Green Synthesis of Silver Nanoparticles Using Gallic Acid as Reducing and Capping Agent: Effect of pH and Gallic Acid Concentration on Average Particle Size and Stability. *Inorg. Nano-met. Chem.* 52, 234–240. doi:10.1080/24701556.2021.1891428

Bao, Y., He, J., Song, K., Guo, J., Zhou, X., and Liu, S. (2021). Plant-Extract-Mediated Synthesis of Metal Nanoparticles. *J. Chem.* 2021, 1–14. doi:10.1155/2021/6562687

Chen, J., Sun, L., Cheng, Y., Lu, Z., Shao, K., Li, T., et al. (2016). Graphene Oxide-Silver Nanocomposite: Novel Agricultural Antifungal Agent against *Fusarium Graminearum* for Crop Disease Prevention. *ACS Appl. Mater. Inter.* 8, 24057–24070. doi:10.1021/acsami.6b05730

Chunfa, D., Fei, C., Xianglin, Z., Xiangjie, W., Xiuzhi, Y., and Bin, Y. (2018). Rapid and Green Synthesis of Monodisperse Silver Nanoparticles Using Mulberry Leaf Extract. *Rare Metal Mater. Eng.* 47, 1089–1095. doi:10.1016/s1875-5372(18)30125-5

Darabdhara, G., Das, M. R., Singh, S. P., Rengan, A. K., Szunerits, S., and Boukherroub, R. (2019). Ag and Au Nanoparticles/Reduced Graphene Oxide Composite Materials: Synthesis and Application in Diagnostics and Therapeutics. *Adv. Colloid Interf. Sci.* 271, 101991–102021. doi:10.1016/j.cis.2019.101991

He, K., Zeng, Z., Chen, A., Zeng, G., Xiao, R., Xu, P., et al. (2018). Advancement of Ag-Graphene Based Nanocomposites: An Overview of Synthesis and its Applications. *Small* 14, 1800871–1800883. doi:10.1002/smll.201800871

Henglein, A., and Giersig, M. (1999). Formation of Colloidal Silver Nanoparticles: Capping Action of Citrate. *J. Phys. Chem. B* 103, 9533–9539. doi:10.1021/jp9925334

Hummers, W. S., and Offeman, R. E. (1958). Preparation of Graphitic Oxide. *J. Am. Chem. Soc.* 80, 1339. doi:10.1021/ja01539a017

Jakhar, V., and Sharma, D. K. (2020). A Sustainable Approach for Graphene-Oxide Surface Decoration Using *Oxalis Corniculata* Leaf Extract-Derived Silver Nanoparticles: Their Antibacterial Activities and Electrochemical Sensing. *Dalton Trans.* 49, 8625–8635. doi:10.1039/d0dt01747g

Jing, Z., Li, M., Wang, H., Yang, Z., Zhou, S., Ma, J., et al. (2021). Gallic Acid-gold Nanoparticles Enhance Radiation-induced Cell Death of Human Glioma U251 Cells. *IUBMB Life* 73, 398–407. doi:10.1002/iub.2436

Karuppiah, C., Muthupandi, K., Chen, S.-M., Ali, M. A., Palanisamy, S., Rajan, A., et al. (2015). Green Synthesized Silver Nanoparticles Decorated on Reduced Graphene Oxide for Enhanced Electrochemical Sensing of Nitrobenzene in Waste Water Samples. *RSC Adv.* 5, 31139–31146. doi:10.1039/c5ra00992h

Kausar, A., Ilyas, H., and Siddiq, M. (2018). Aptitude of Graphene Oxide-Silver in Advance Polymer Nanocomposite: A Review. *Polymer-Plastics Technol. Eng.* 57, 283–301. doi:10.1080/03602559.2017.1326135

Khan, F., Shariq, M., Asif, M., Siddiqui, M. A., Malan, P., and Ahmad, F. (2022). Green Nanotechnology: Plant-Mediated Nanoparticle Synthesis and Application. *Nanomaterials* 12, 673–694. doi:10.3390/nano12040673

Lee, Y. J., and Park, Y. (2020). Graphene Oxide Grafted Gold Nanoparticles and Silver/Silver Chloride Nanoparticles Green-Synthesized by a *Portulaca Oleracea* Extract: Assessment of Catalytic Activity. *Colloids Surf. A: Physicochemical Eng. Aspects* 607, 125527–125536. doi:10.1016/j.colsurfa.2020.125527

Li, J., and Liu, C. y. (2010). Ag/Graphene Heterostructures: Synthesis, Characterization and Optical Properties. *Eur. J. Inorg. Chem.* 2010, 1244–1248. doi:10.1002/ejic.200901048

Liu, H., Hao, C., Nan, Z., Qu, H., Zhang, X., Zhang, Z., et al. (2020). Fabrication of Graphene Oxide and Sliver Nanoparticle Hybrids for Fluorescence Quenching of DNA Labeled by Methylene Blue. *Spectrochimica Acta A: Mol. Biomol. Spectrosc.* 243, 118802–118812. doi:10.1016/j.saa.2020.118802

Liu, H., Zhong, L., Yun, K., and Samal, M. (2016). Synthesis, Characterization, and Antibacterial Properties of Silver Nanoparticles-Graphene and Graphene Oxide Composites. *Biotechnol. Bioproc. E* 21, 1–18. doi:10.1007/s12257-015-0733-5

Luo, Y., Li, Y., Li, Y., Cheng, H., Kong, H., and Li, L. (2018). Optimization of Preparation Technology for Silver Nanoparticles Using Lemon Juice. *Sci. Technol. Food Ind.* 39, 194–199. doi:10.13386/j.issn10020306.2018.12.034

Mafuné, F., Kohno, J.-y., Takeda, Y., and Kondow, T. (2003). Nanoscale Soldering of Metal Nanoparticles for Construction of Higher-Order Structures. *J. Am. Chem. Soc.* 125, 1686–1687. doi:10.1021/ja021250d

Mariadoss, A. V. A., Saravanakumar, K., Sathiyaseelan, A., and Wang, M.-H. (2020). Preparation, Characterization and Anti-cancer Activity of Graphene

Oxide--silver N-anocomposite. *J. Photochem. Photobiol. B: Biol.* 210, 111984–111991. doi:10.1016/j.jphotobiol.2020.111984

Meyers, M. A., Mishra, A., and Benson, D. J. (2006). Mechanical Properties of Nanocrystalline Materials. *Prog. Mater. Sci.* 51, 427–556. doi:10.1016/j.pmatsci.2005.08.003

Mittal, A. K., Kumar, S., and Banerjee, U. C. (2014). Quercetin and Gallic Acid Mediated Synthesis of Bimetallic (Silver and Selenium) Nanoparticles and Their Antitumor and Antimicrobial Potential. *J. Colloid Interf. Sci.* 431, 194–199. doi:10.1016/j.jcis.2014.06.030

Motloung, D. M., Mashele, S. S., Matowane, G. R., Swain, S. S., Bonnet, S. L., Noreljaleel, A. E. M., et al. (2020). Synthesis, Characterization, Antidiabetic and Antioxidative Evaluation of a Novel Zn(II)-Gallic Acid Complex with Multi-Facet Activity. *J. Pharm. Pharmacol.* 72, 1412–1426. doi:10.1111/jphp.13322

Pang, Y., Chen, Z., Zhao, R., Yi, C., Qiu, X., Qian, Y., et al. (2021). Facile Synthesis of Easily Separated and Reusable Silver Nanoparticles/Aminated Alkaline Lignin Composite and its Catalytic Ability. *J. Colloid Interf. Sci.* 587, 334–346. doi:10.1016/j.jcis.2020.11.113

Pillai, Z. S., and Kamat, P. V. (2004). What Factors Control the Size and Shape of Silver Nanoparticles in the Citrate Ion Reduction Method? *J. Phys. Chem. B* 108, 945–951. doi:10.1021/jp037018r

Pratheesya, T., Harish., S, M., N., Sohila, S., and Ramesh, R. (2019). Enhanced Antibacterial and Photocatalytic Activities of Silver Nanoparticles Anchored Reduced Graphene Oxide Nanostructure. *Mater. Res. Express* 6, 074003–074015. doi:10.1088/2053-1591/ab1567

Rohaizad, A., Shahabuddin, S., Shahid, M. M., Rashid, N. M., Hir, Z. A. M., Ramly, M. M., et al. (2020). Green Synthesis of Silver Nanoparticles from *Catharanthus Roseus* Dried Bark Extract Deposited on Graphene Oxide for Effective Adsorption of Methylene Blue Dye. *J. Environ. Chem. Eng.* 8, 103955–103964. doi:10.1016/j.jece.2020.103955

Sahu, D., Sahoo, G., Mohapatra, P., and Swain, S. K. (2019). Dual Activities of Nano Silver Embedded Reduced Graphene Oxide Using Clove Leaf Extracts: Hg 2+ Sensing and Catalytic Degradation. *ChemistrySelect* 4, 2593–2602. doi:10.1002/slct.201803725

Sedki, M., Mohamed, M. B., Fawzy, M., Abdelrehim, D. A., and Abdel-Mottaleb, M. M. S. A. (2015). Phytosynthesis of Silver-Reduced Graphene Oxide (Ag-RGO) Nanocomposite with an Enhanced Antibacterial Effect Using *Potamogeton Pectinatus* Extract. *RSC Adv.* 5, 17358–17365. doi:10.1039/c4ra13117g

Shubhadarshinee, L., Jali, B. R., Barick, A. K., and Mohapatra, P. (2022). Preparation and Characterisation of Silver Nanoparticles/Graphene Oxide Hybrid Nanofiller Reinforced-Polyaniline. *Plastics, Rubber and Composites* 51, 72–84. doi:10.1080/14658011.2021.1939587

Stadler, D., Siribbal, S. M., Gessner, I., Öz, S., Ilyas, S., and Mathur, S. (2018). Asymmetric Attachment and Functionalization of Plasmonic Nanoparticles on Ceramic Interfaces. *J. Nanostruct Chem.* 8, 33–44. doi:10.1007/s40097-018-0252-y

Stavinskaya, O., Laguta, I., Fesenko, T., and Krumova, M. (2019). Effect of Temperature on Green Synthesis of Silver Nanoparticles Using Vitex Agnus-Castus Extract. *ChemJMold* 14, 117–121. doi:10.19261/cjm.2019.636

Sundriyal, P., and Bhattacharya, S. (2017). Polyaniline Silver Nanoparticle Coffee Waste Extracted Porous Graphene Oxide Nanocomposite Structures as Novel Electrode Material for Rechargeable Batteries. *Mater. Res. Express* 4, 35501–35513. doi:10.1088/2053-1591/aa.5ece

Thanh, N. T. K., Maclean, N., and Mahiddine, S. (2014). Mechanisms of Nucleation and Growth of Nanoparticles in Solution. *Chem. Rev.* 114, 7610–7630. doi:10.1021/cr400544s

Tortella, G., Rubilar, O., Fincheira, P., Pieretti, J. C., Duran, P., Lourenço, I. M., et al. (2021). Bactericidal and Virucidal Activities of Biogenic Metal-Based

Nanoparticles: Advances and Perspectives. *Antibiotics* 10, 783–805. doi:10.3390/antibiotics10070783

Veisi, H., Kavian, M., Hekmati, M., and Hemmati, S. (2019). Biosynthesis of the Silver Nanoparticles on the Graphene Oxide's Surface Using *Pistacia Atlantica* Leaves Extract and its Antibacterial Activity against Some Human Pathogens. *Polyhedron* 161, 338–345. doi:10.1016/j.poly.2019.01.034

Wang, R., Tang, J., Zhou, H., and Yu, Y. (2010). Research on Dispersion Stability of Nano Silver. *Metallic Funct. Mater.* 17, 17–21. doi:10.13228/j.boyuan.issn1005-8192.2010.01.00310.5188/ijsmer.17.93

Wang, X., Huang, P., Feng, L., He, M., Guo, S., Shen, G., et al. (2012). Green Controllable Synthesis of Silver Nanomaterials on Graphene Oxide Sheets via Spontaneous Reduction. *RSC Adv.* 2, 3816–3822. doi:10.1039/c2ra00008c

Wang, X., Zhu, C., Huang, Z., Hu, X., and Zhu, X. (2016). *In Situ* Synthesis of Pristine-Graphene/Ag Nanocomposites as Highly Sensitive Sers Substrates. *RSC Adv.* 6, 91579–91583. doi:10.1039/c6ra20085k

Wu, Y.-Z., Tsai, Y.-Y., Chang, L.-S., and Chen, Y.-J. (2021). Evaluation of Gallic Acid-Coated Gold Nanoparticles as an Anti-aging Ingredient. *Pharmaceuticals* 14, 1071–1084. doi:10.3390/ph14111071

Yang, Y.-K., He, C.-E., He, W.-J., Yu, L.-J., Peng, R.-G., Xie, X.-L., et al. (2011). Reduction of Silver Nanoparticles onto Graphene Oxide Nanosheets with N,N-Dimethylformamide and Sers Activities of GO/Ag Composites. *J. Nanopart. Res.* 13, 5571–5581. doi:10.1007/s11051-011-0550-5

Yetişsin, F., and Kurt, F. (2020). Gallic Acid (GA) Alleviating Copper (Cu) Toxicity in Maize (*Zea Mays* L.) Seedlings. *Int. J. Phytoremediation* 22, 420–426. doi:10.1080/15226514.2019.1667953

Yoosaf, K., Ipe, B. I., Suresh, C. H., and Thomas, K. G. (2007). *In Situ* Synthesis of Metal Nanoparticles and Selective Naked-Eye Detection of Lead Ions from Aqueous Media. *J. Phys. Chem. C* 111, 12839–12847. doi:10.1021/jp073923q

Yu, Z., Hu, C., Guan, L., Zhang, W., and Gu, J. (2020). Green Synthesis of Cellulose Nanofibrils Decorated with Ag Nanoparticles and Their Application in Colorimetric Detection of L-Cysteine. *ACS Sustain. Chem. Eng.* 8, 12713–12721. doi:10.1021/acssuschemeng.0c04842

Zhang, C.-y., Hao, R., Zhao, B., Fu, Y., Zhang, H., Moeendarbari, S., et al. (2017). Graphene Oxide-Wrapped Flower-like Sliver Particles for Surface-Enhanced Raman Spectroscopy and Their Applications in Polychlorinated Biphenyls Detection. *Appl. Surf. Sci.* 400, 49–56. doi:10.1016/j.apsusc.2016.12.161

Zhang, Z., Gao, X., and Jia, X. (2014). The Extraction of Sericin and its Application in Preparation of Nano-Silver Sol. *Textile Auxiliaries* 31, 16. doi:10.3969/j.issn.1004-0439.2014.06.005

Highly Efficient One-Step Conversion of Fructose to Biofuel 5-Ethoxymethylfurfural Using a UIO-66-SO₃H Catalyst

Kangyu Zhao[1], Yanping Xiang[1], Xiaoao Sun[1], Linjiao Chen[1], Jiafu Xiao[2]* and Xianxiang Liu[1]*

[1]National and Local Joint Engineering Laboratory for New Petro-chemical Materials and Fine Utilization of Resources, Key Laboratory of the Assembly and Application of Organic Functional Molecules of Hunan Province, Hunan Normal University, Changsha, China, [2]Hunan Provincial Key Laboratory for Synthetic Biology of Traditional Chinese Medicine, School of Pharmaceutical Sciences, Hunan University of Medicine, Huaihua, China

In this study, a novel sulfonic acid-modified catalyst for MOFs (UIO-66-SO₃H) was synthesized using chlorosulfonic acid as a sulfonating reagent and first used as efficient heterogeneous catalysts for the one-pot conversion of fructose into biofuel 5-ethoxymethylfurfural (EMF) in a cosolvent free system. The physicochemical properties of this catalyst were characterized by Fourier transform infrared spectroscopy (FT-IR), transmission electron microscopy (TEM), and powder X-ray diffraction (XRD). The characterization demonstrated that the sulfonic acid group was successfully grafted onto the MOF material and did not cause significant changes to its morphology and structure. Furthermore, the effects of catalyst acid amount, reaction temperature, reaction time, and catalyst dosage on reaction results were investigated. The results showed that the conversion of fructose was 99.7% within 1 h at 140°C, while the EMF yield reached 80.4%. This work provides a viable strategy by application of sulfonic acid-based MOFs for the efficient synthesis of potential liquid fuel EMF from renewable biomass.

Keywords: biomass, fructose, 5-ethoxymethylfurfural, catalysis, one-step conversion

INTRODUCTION

As the only renewable carbon resource with extensive distribution and abundant reserves in nature, biomass has become the most attractive potential energy to replace fossil fuels (Hu et al., 2015; Tang et al., 2019; Guo D. et al., 2020), especially in recent years, with the shortage of fossil resources and the environmental problems brought by the applications, the development of new methods for the conversion of biomass and its platform molecules into fuels and chemicals is a current priority (Liu et al., 2016; Venkata Mohan et al., 2016).

The products gained from biomass conversion mainly include polyols, furans, organic acids and their ester derivatives, short-chain alkanes, and other basic platform chemicals and new fuels. The large-scale utilization of these biomass conversion products will play a significant leading role in sustainable and healthy socio-economic development (Hommes et al., 2019; He 2021; Hoang and Pham, 2021). The acid-catalyzed conversion of biomass to biomass platform molecule 5-hydroxymethylfurfural (HMF) has been previously reported in some research and progress (Zhao et al., 2007; Guo H. et al., 2020; Liu et al., 2021; Yin et al., 2021), and its derivative 5-ethoxymethylfurfural (EMF) is also a potential fuel or fuel additive with excellent properties such as
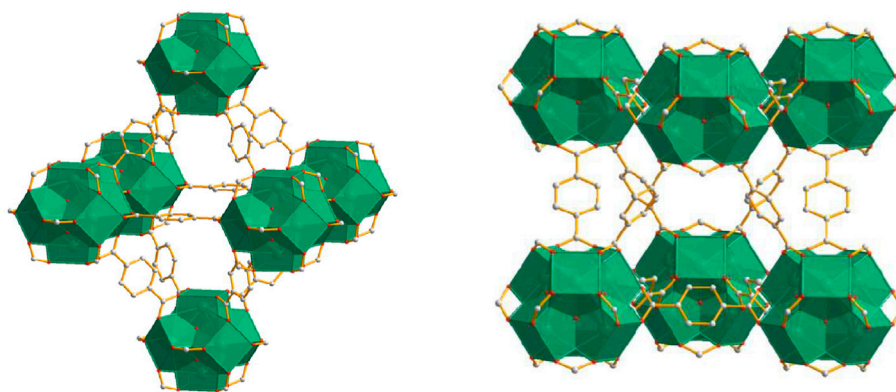
FIGURE 1 | Structure of UIO-66 (Guillerm et al., 2012; Olorunyomi et al., 2021). Gray and red balls represent carbon and oxygen atoms, respectively. Zirconium octahedral is in green. Hydrogen atoms are omitted for clarity.

high energy density and low toxicity, with energy density up to 8.7 kWh/L, even higher than ethanol (6.1 kWh/L), and has good oxidation properties when used as a fuel (Chen et al., 2019a; Guo D. et al., 2020). Currently, the main synthesis pathway of EMF is based on biomass sugar compounds (e.g., glucose, fructose, and cellulose), which are converted to EMF in an ethanol system through acid catalysis (Chen et al., 2019b; Dai et al., 2019; Zhang et al., 2020). Among them, fructose exists in large quantities in the free state in the pulp of fruits and honey and is a common biomass raw material. As a reaction substrate for the generation of EMF, unlike glucose and cellulose, fructose has a strong crystal structure, is easily soluble in conventional organic solvents, and has a higher yield than glucose and cellulose (Zhang et al., 2019). Meanwhile, the acidic catalyst has a crucial role in the synthesis of the EMF reaction, making the conversion process more complete and efficient. The catalysts reported in previous studies are zeolite catalysts, sulfonic acid-type solid acid catalysts, and heteropolyacids (Li et al., 2016; Liu et al., 2016; Kumari et al., 2019; Xiang et al., 2021). In particular, sulfonic acid-type catalysts have high protonic acid strength, which is beneficial for the synthesis of EMF. For instance, Zhang et al (2018) reported sulfonated organic hyper-cross-linked polymer (HCP)-based carbohydrate catalysts to yield 78.9% EMF, 15.4% HMF, and 4.6% ethyl levulinate (EL) in an ethanol-dimethyl sulfoxide system with fructose as feedstock. Yan et al (2022) found sulfonic acid-based annealed functionally biobased carbon microspheres loading polytetrafluoroethylene (A-BCMSs-SO$_3$H@PTFE) catalyst applied to the acid-catalyzed synthesis of liquid EMF. The yield of EMF could reach more than 36.6% after 72 h of the acid-catalyzed reaction. Manjunathan et al (2021) used the sulfonated hydrophobic mesoporous organic polymer (MOP-SO$_3$H) in the production of EMF by the one-pot method using fructose in an ethanol solvent. The conversion of fructose was 99.3%, and the EMF yield reached 72.2% at 100°C for 5 h. These results show that loading acid-functionalized sulfonic acid groups onto the carrier can produce sulfonic acid-based solid acid catalysts to improve the efficiency of fructose conversion to EMF

(Nakajima and Hara 2012). Therefore, finding a suitable, modified as well as stable performance carrier is a prerequisite for successful catalyst preparation.

Metal–organic framework (MOF) materials, developed rapidly in the last two decades, have a large ordered specific surface area, adjustable pore size, customizable functions, and a large number of active junctions (Herbst and Janiak 2017; Lv et al., 2019). As a new type of MOFs, UIO-66 has great stability and can exist stably in an acidic environment, and UIO-66 is a hydrophobic material with the molecular formula [Zr$_6$(OH)$_4$O$_4$(BDC)$_6$], which is a Zr$_6$-cluster as the central structural unit and 12 terephthalic acid (H$_2$BDC) as the ligand to form a three-dimensional topology of metal–organic backbone materials with the structure shown in **Figure 1** (Guillerm et al., 2012; Olorunyomi et al., 2021). Also, UIO-66 is a hydrophobic material which is well suited for the conversion of biobased feedstock (Lv et al., 2019; Oozeerally et al., 2021). It also inherits the characteristics of ordinary MOF materials such as large specific surface area, adjustable pore size, and easy modification, which is a good catalyst supporter.

Based on the aforementioned details, in this study, we report a sulfonic acid-functionalized UIO-66-type MOFs (UIO-66-SO$_3$H) prepared under mild conditions. The catalytic performance of these catalysts was investigated for selective preparation of EMF from fructose in the one-pot strategy. Also, the effects of reaction temperature, reaction time, catalyst dosage, and acid amount on the yield of EMF were also evaluated. In addition, the morphology and physicochemical properties of the catalysts were characterized and discussed.

EXPERIMENTAL

Materials

Terephthalic acid was purchased from Aladdin Industrial Corporation. 5-Hydroxymethylfurfural (HMF, 98%), 5-ethoxymethylfurfural (EMF, 97%), ethyl levulinate (EL, 99%), and zirconium octahydrate oxychloride were purchased from Macklin Biochemical Co., Ltd. Ethanol (≥99.8%), glacial acetic
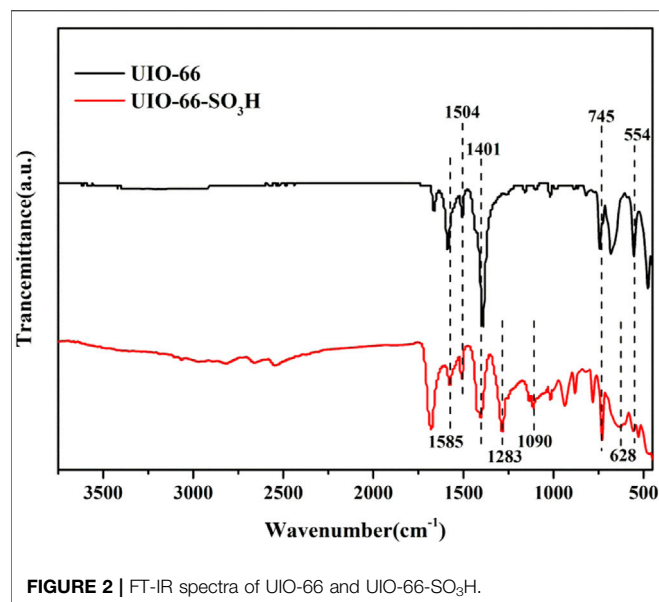
FIGURE 2 | FT-IR spectra of UIO-66 and UIO-66-SO$_3$H.

acid, N, N-dimethylformamide (DMF), and methylene chloride were obtained from Sinopharm Chemical Reagent Co., Ltd. Chlorosulfonic acid was purchased from Shanghai Jiuding Chemical Reagent Co., Ltd.

Catalyst Preparation

In a 100-ml round-bottom flask, 4.8 g ZrOCl$_2$·8H$_2$O (15 mmol), 2.4 g terephthalic acid (15 mmol), 50 ml DMF, and 6 ml acetic acid was mixed, and the mixture was then treated with ultrasound for 30 min. After that, the resultant mixture was kept under constant stirring at 120°C for 24 h, and the obtained white precipitate was washed with methanol and DMF several times. After drying, the mashy white solids were calcined in a muffle furnace to give UIO-66 (Ragon et al., 2014).

The as-prepared UIO-66 (1 g) was dispersed in 40 ml CH$_2$Cl$_2$ and stirred at 0°C for 30 min. Under vigorous magnetic stirring, ClSO$_3$H x mL in 10 ml CH$_2$Cl$_2$ was slowly added to the mixture. After the reaction continued for 4 h, the produced solid was filtered and washed with ethanol and then with deionized water and dried in a vacuum oven. The prepared catalysts are designated as UIO-66-SO$_3$H-x (x = 0.3, 0.5, 0.8, and 1.0 ml), and x represents the volume of chlorosulfonic acid added.

Fructose Degradation

The catalytic upgrading of fructose was carried out in a 50-ml autoclave with a Teflon liner. Typically, the Teflon liner was loaded with fructose (1 mmol, 0.180 g), ethanol (5 ml) as the reactant and solvent, and the UIO-66-SO$_3$H catalyst. Then, the reaction mixture was heated to the prescribed temperature for a desired reaction time with stirring. After finishing the reaction, the reactor was given an ice bath for rapid cooling to room temperature.

Then, the mixture products were diluted and filtered using a 0.22-μm syringe filter. The fructose and the formed products were analyzed using an Agilent 1260 HPLC chromatograph equipped

with refractive index and UV detectors. The external standard method was used to analyze the substrate conversion rate and selectivity of each product, and the calculation equation is as follows:

$$\text{Fructose conversion}\,(\%) = \left(1 - \frac{\text{Mole of Fructose}}{\text{Initial mole of Fructose}}\right) \times 100\%;$$

$$\text{EMF yield}\,(\%) = \frac{\text{Mole of EMF}}{\text{Initial mole of Fructose}} \times 100\%;$$

$$\text{HMF yield}\,(\%) = \frac{\text{Mole of HMF}}{\text{Initial mole of Fructose}} \times 100\%.$$

RESULTS AND DISCUSSION

Catalyst Characterization

The FT-IR spectra of the metal–organic framework material UIO-66 and catalyst UIO-66-SO$_3$H are shown in **Figure 2**, in which 1,585 cm^{-1} is the benzene ring skeleton stretching vibration peak; 1,504 cm^{-1} and 1,401 cm^{-1} are the absorption peaks corresponding to the structural unit $(Zr_6O_4)(OH)_4(CO_2)_n$ formed by coordination of terephthalic acid with zirconium nodes (Zaboon et al., 2018). The fingerprint region 745 cm^{-1} is the out-of-plane bending vibration of C-H; an absorption peak can be seen at 554 cm^{-1}, which is the Zr-O bond stretching vibration peak in the metal–organic skeleton. In the IR curve of UIO-66-SO$_3$H, 1,283 cm^{-1} and 1,090 cm^{-1} belong to the O=S=O symmetric stretching vibration peak and S-O stretching vibration peak, respectively; 628 cm^{-1} is the stretching vibration peak of the C-S bond (Chen T.-F. et al., 2019). Thus, the presence of sulfonic acid groups in the UIO-66-SO$_3$H catalyst was confirmed, indicating the successful preparation of sulfonic acid-functionalized materials.
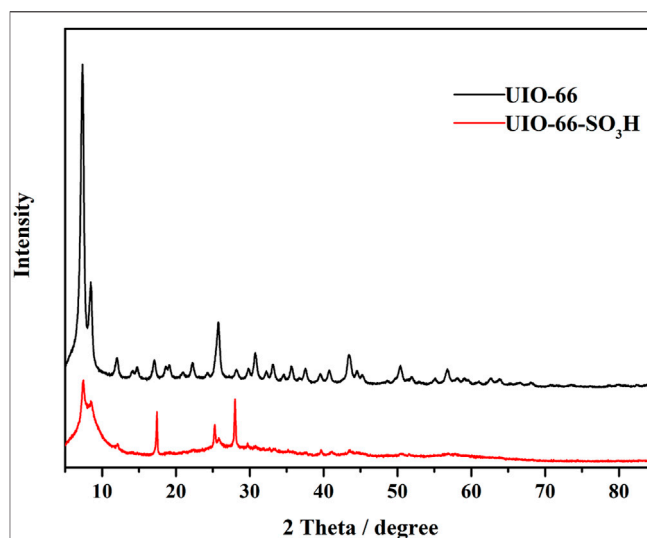

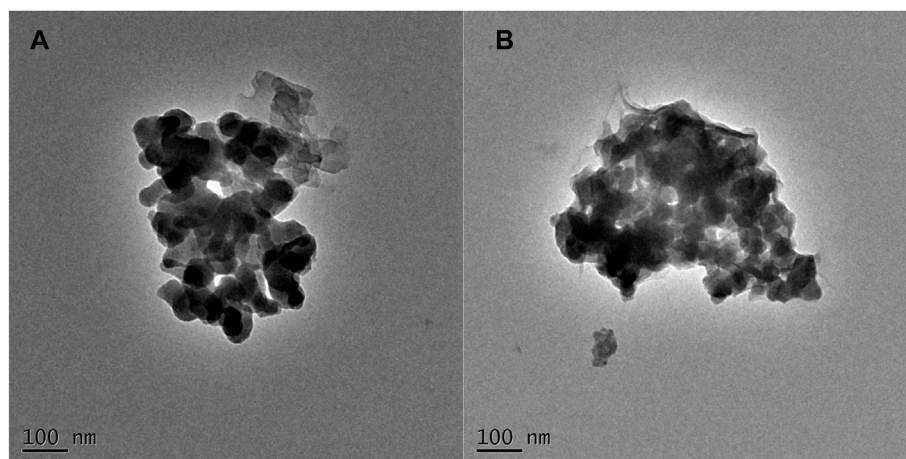**FIGURE 3 |** XRD patterns of UIO-66 and UIO-66-SO$_3$H.

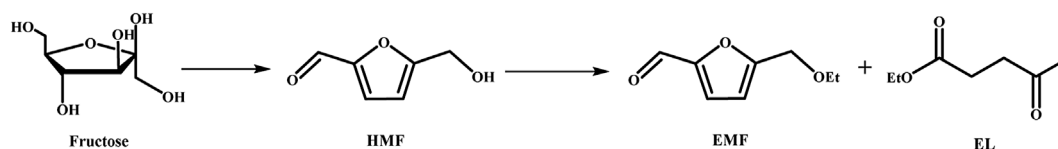FIGURE 4 | TEM image of UIO-66 (A) and UIO-66-SO₃H (B).

FIGURE 5 | Synthesis of EMF from fructose.

The XRD spectra of UIO-66 and UIO-66-SO$_3$H are shown in **Figure 3**, in which the XRD spectrum of UIO-66 is consistent with that in the literature. Some XRD peaks of the UIO-66-SO$_3$H catalyst were shifted, and the intensity of the peaks was significantly weakened compared with the UIO-66 sample, which is similar to the literature report. This was because during the introduction of strong Brønsted acidity into UIO-66, the chlorosulphonic acid impaired its crystallinity as well as the stability of the framework (Hu et al., 2016).

Figure 4 presents the transmission electron microscopy images of the samples, from which it can be observed that the morphology of both materials is similar and consist of particles of relatively uniform size. However, they are also in a more agglomerated state, which can be attributed to the particle size of the samples being around 50 nm, resulting in strong surface forces and agglomeration. The result of transmission electron microscopy revealed that the morphological characteristics of the UIO-66 material were hardly affected by the presence of the sulfonic acid group during the preparation of the catalyst.

Catalytic Performance

In this study, ethanol was used as the reactant and reaction medium, and the reaction was carried out in the order of fructose dehydration to produce HMF and ethyl alcohol etherification to produce EMF, and the ring-opening by-product EL was also generated (**Figure 5**).

For the sulfonation of the prepared metal–organic framework UIO-66, the same mass of UIO-66 added with different amounts

TABLE 1 | Acid content of UIO-66-SO₃H with different dosages of ClSO₃H.

Entry	Sample	Acid amount (mmol/g)
1	UIO-66-SO₃H-0.3	0.87
2	UIO-66-SO₃H-0.5	1.13
3	UIO-66-SO₃H-0.8	1.46
4	UIO-66-SO₃H-1.0	1.30

of the sulfonating agent resulted in different acid amounts of UIO-66-SO$_3$H catalysts as listed in **Table 1**. The UIO-66 (1 g) added with the volume of chlorosulfonic acid increased from 0.3 to 1.0 ml, and the acid amount of the catalytic material showed a roughly increasing trend. The highest acid amount of the catalyst was measured at 0.8 ml of chlorosulfonic acid, and the best catalytic effect was achieved with UIO-66-SO$_3$H showing a maximum acid amount of 1.46 mmol/g. To some extent, the acid amount of the catalyst increased with increasing concentration of the sulfonating agent. However, due to the gradual increase of the spatial site resistance and the damage to the catalyst structure caused by the addition of too much chlorosulfonic acid, further increase of the sulfonating agent did not increase the amount of acid, while the sulfonated materials were all effective in catalyzing the conversion of fructose to EMF. Accordingly, the effect of the acid amount of the catalyst on the catalytic activity is reflected in **Figure 6**. If the catalyst material was used without sulfonic acid groups, the target product is almost absent in the reaction solution, while the sulfonated
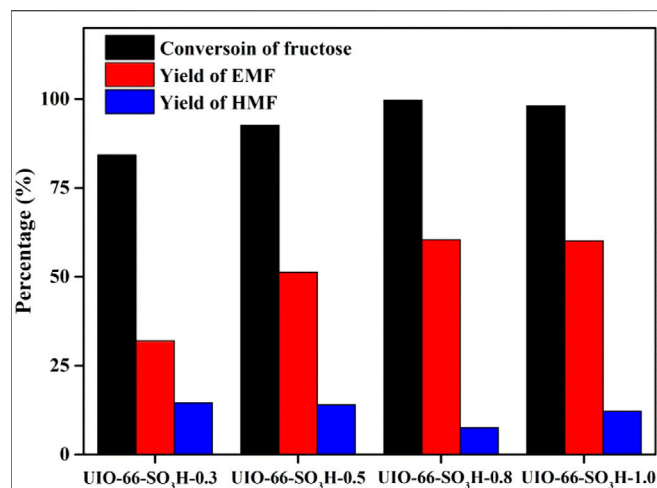
FIGURE 6 | Results of alcoholysis of fructose catalyzed by UIO-66-SO$_3$H with different acidity. Reaction conditions: 1 mmol fructose, 5 ml ethanol, 30 mg catalyst, 1 h, and 140°C.
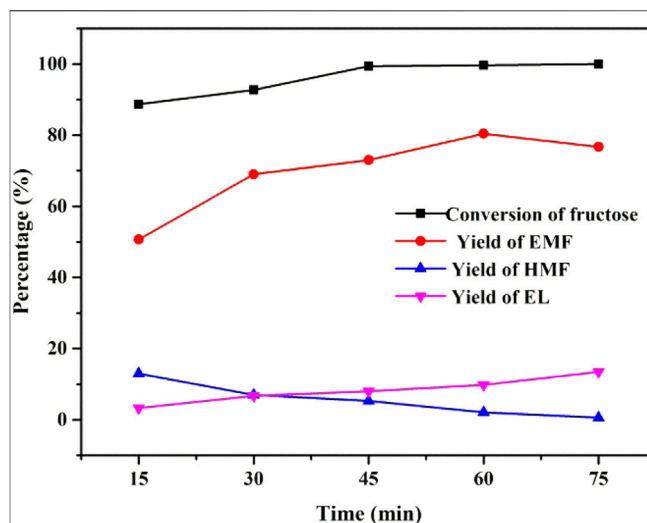

FIGURE 8 | Effect of reaction time on the alcoholysis of fructose. Reaction conditions: 1 mmol fructose, 5 ml ethanol, 30 mg catalyst, and 140°C.
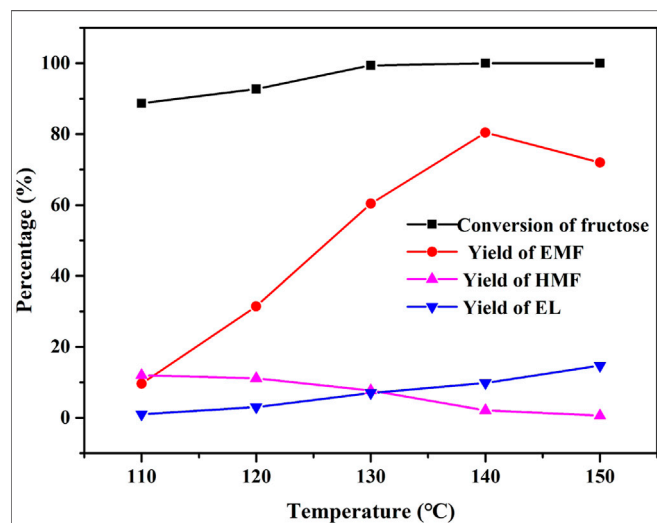

FIGURE 7 | Effect of reaction temperature on the alcoholysis of fructose. Reaction conditions: 1 mmol fructose, 5 ml ethanol, 30 mg catalyst, and 1 h.

Figure 7. As the reaction temperature was 110°C, the yield of both EMF and HMF was low, and a trace amount of EL was detected. With the increase in the reaction temperature, the fructose was gradually converted from 88.7% to complete conversion, indicating that the dehydration of fructose required higher temperature, and the etherification of HMF was easier than the dehydration of fructose into HMF. The yield of EMF increased significantly from 9.6 to 80.4% with the increase from 110 to 140°C, the yield of the intermediate product HMF decreased, and the byproduct EL showed a gradual increase. However, when the temperature was increased to 150°C, the yield of the target product EMF decreased due to the ring opening of the side reaction EMF, which might be due to the instability of EMF at higher reaction temperatures under acidic conditions, resulting in the generation of more ring-opening product EL. The increase in temperature was favorable to the conversion of fructose, and too high temperature promoted the decomposition of EMF into other products. Therefore, the optimal reaction temperature for this experiment was 140°C.

Figure 8 shows the effect of the reaction time of UIO-66-SO$_3$H-0.8 as a catalyst on the synthesis of EMF from fructose in the ethanol system at a reaction temperature of 140°C. It can be seen that the target product EMF yield increased relatively fast at the beginning of the reaction stage, reaching 69% within 30 min, and as the reaction time continued to extend, the yield of EMF reached the best yield of 80.4% at 1 h, followed by a slight decrease in the yield of EMF. The content of HMF gradually decreased with the extension of time and was gradually converted into EMF, while the yield of EL gradually increased. This result indicates that fructose conversion is a typical continuous reaction in the ethanol reaction system. The longer reaction time allowed the conversion of EMF to its byproduct EL. Since the long time was not favorable for the production of EMF, a reaction time of 1 h was chosen for the subsequent reaction.
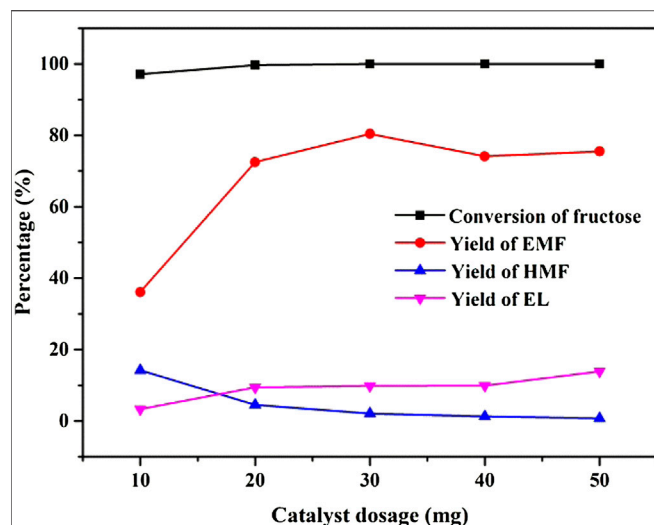
materials were all effective in catalyzing the conversion of fructose to EMF. Thus, it is evident that the acidity of the catalyst is crucial for this reaction. With the increase of the acid amount, the conversion of fructose gradually increased, and the yield of EMF also showed an increasing trend, and it can be concluded that the acid amount is closely related to the synthesis of the target product EMF yield. Based on the aforementioned conclusions, the effect of factors such as reaction temperature, time, and catalyst amount on fructose alcoholysis of UIO-66-SO$_3$H was further investigated systematically in this article.

The effect of reaction temperature in the range of 110–150°C on the conversion of fructose to EMF was investigated using UIO-66-SO$_3$H-0.8 as the catalyst, and the results are shown in

FIGURE 9 | Effect of catalyst dosage on the alcoholysis of fructose. Reaction conditions: 1 mmol fructose, 5 ml ethanol, 1 h, and 140°C.

Under the conditions of 180 mg of substrate, 140°C of reaction temperature, and 1 h of reaction time, the effects of catalyst dosages of 10 mg, 20 mg, 30 mg, 40 mg, and 50 mg on the conversion of fructose to synthesize EMF were investigated. As seen in **Figure 9**, under the condition of 10 mg catalyst dosage, the fructose was almost completely converted, and the EMF yield was 36.1%. It can be observed in the figures that the increase of catalyst dosage from 10 to 20 mg increased the yield of EMF by about double, which was 72.5%. The highest EMF yield was obtained when the catalyst dosage was 30 mg, while the yield decreased slightly when the catalyst dosage was 40 mg and more. Therefore, 30 mg was chosen as the best catalyst dosage.

In addition, the possible mechanism for catalyzed conversion of fructose to EMF is shown in **Figure 10**. Fructose is dehydrated, dehydrogenated, and dehydrated to produce HMF under acidic conditions. Then, the acid site on the catalyst surface protonated with hydroxyl oxygen in HMF to form carbocation, followed by ethanol attack on carbocation, and finally formed EMF after proton migration (Amarasekara et al., 2008; Ohara et al., 2010; Yan et al., 2022).
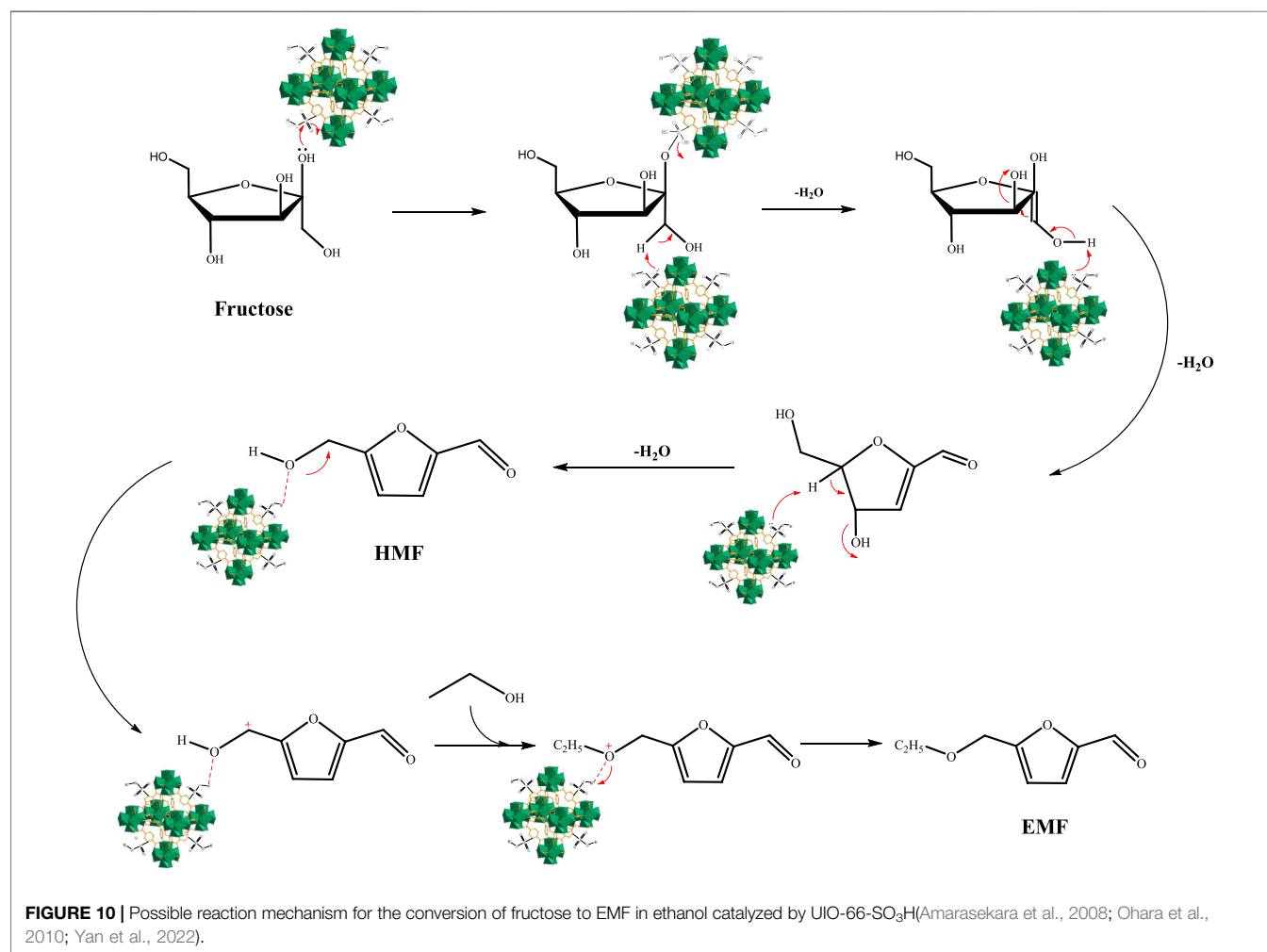

FIGURE 10 | Possible reaction mechanism for the conversion of fructose to EMF in ethanol catalyzed by UIO-66-SO$_3$H(Amarasekara et al., 2008; Ohara et al., 2010; Yan et al., 2022).

TABLE 2 | Catalytic performance of UIO-66-SO$_3$H compared to reported solid acid catalysts for the EMF synthesis from fructose.

Entry	Catalyst	Solvent	Time/h	T/°C	EMF yield/%	Reference
1	D0.5-SPC	Ethanol/THF	18	140	68.8	Dai et al. (2019)
2	MOP-SO$_3$H-0.6	Ethanol	5	100	72.2	Manjunathan et al. (2021)
3	Pd-Ru/MXene	Ethanol	2.5	120	82.0	Bharath et al. (2021)
4	UIO-66-SO$_3$H	Ethanol	1	140	80.4	This work

Comparison With Reported Catalysts

The literature related to the one-step conversion of fructose to EMF is presented in **Table 2**, which compares the catalytic activity of the catalyst prepared in this study, UIO-66-SO$_3$H, with other catalysts. For example, Dai et al. (2019) reported a solid organocatalyst, double hydrogen-bonded sulfonated polymer catalyst (D-SPC), to convert fructose to EMF in 18 h at 140°C with a maximum yield of 68.8%. Manjunathan et al., (2021) found a catalyst consisting of divinylbenzene (DVB) and sodium p-styrenesulfonate (SPSS) copolymerized with a sulfonated hydrophobic mesoporous organic polymer (MOP-SO$_3$H) catalyst, which was able to achieve an EMF yield of 72.2% under the conditions of a bulk catalyst-catalyzed reaction. Bharath et al., (2021) immobilized the ultra-small Pd–Ru nanoparticles on the surface of 2D MXene nanosheets to produce a catalyst (Pd-Ru/MXene), which was reacted at 120°C for 2.5 h and was able to obtain a final EMF yield of 82%. Compared with the previous two catalysts, the catalyst prepared in this study has good catalytic effect. Meanwhile, the UIO-66-SO$_3$H catalyst catalyzed the conversion of fructose to EMF in this experiment under lower conditions that were easily satisfied, and the reaction time was greatly reduced to achieve high catalytic effect.

CONCLUSION

In summary, we prepared the MOF material UIO-66 and functionalized it using chlorosulfonic acid under mild conditions to produce a series of sulfonic acid-functionalized MOF-based solid catalysts (UIO-66-SO$_3$H). The catalyst was characterized, and the corresponding results showed that the sulphonic acid group was successfully bonded to the benzene ring on the metal–organic framework. In addition, the acid amount of the catalyst could be adjusted by changing the amount of chlorosulfonic acid, and the highest acidity of the catalyst reached 1.46 mmol/g. The as-prepared heterogeneous catalyst

UIO-66-SO$_3$H showed efficient catalytic performance for the one-pot conversion of fructose to biofuel EMF under cosolvent-free conditions. The effect of different reaction conditions on the catalytic reaction was systematically investigated, and the EMF yield of 80.4% could be obtained under the optimum reaction conditions. Compared with those previously reported, the catalyst prepared in this work has the advantages of easy preparation, mild reaction conditions, and a good catalytic effect. It is expected that our catalytic system can be further applied for the efficient production of biofuel EMF in industrial applications.

DATA AVAILABILITY STATEMENT

The original contributions presented in the study are included in the article/Supplementary Material, further inquiries can be directed to the corresponding authors.

AUTHOR CONTRIBUTIONS

KZ: investigation, methodology, and writing–original draft preparation. YX: data curation and formal analysis. XS: validation. LC: methodology and visualization. JX: conceptualization, project administration, and writing–review and editing. XL: conceptualization, project administration, funding acquisition, and supervision.

FUNDING

REFERENCES

Amarasekara, A. S., Williams, L. D., and Ebede, C. C. (2008). Mechanism of the Dehydration of D-Fructose to 5-hydroxymethylfurfural in Dimethyl Sulfoxide at 150°C: an NMR Study. *Carbohydr. Res.* 343, 3021–3024. doi:10.1016/j.carres.2008.09.008

Bharath, G., Rambabu, K., Hai, A., Morajkar, P. P., Salkar, A. V., Hasan, S. W., et al. (2021). Highly Selective Etherification of Fructose and 5-hydroxymethylfurfural over a Novel Pd-Ru/MXene Catalyst for Sustainable Liquid Fuel Production. *Int. J. Energ. Res.* 45, 14680–14691. doi:10.1002/er.6743

Chen, B., Xu, G., Chang, C., Zheng, Z., Wang, D., Zhang, S., et al. (2019b). Efficient One-Pot Production of Biofuel 5-Ethoxymethylfurfural from Corn Stover: Optimization and Kinetics. *Energy Fuels* 33, 4310–4321. doi:10.1021/acs.energyfuels.9b00357

Chen, B., Xu, G., Zheng, Z., Wang, D., Zou, C., and Chang, C. (2019a). Efficient Conversion of Corn stover into 5-ethoxymethylfurfural Catalyzed by Zeolite USY in Ethanol/THF Medium. *Ind. Crops Prod.* 129, 503–511. doi:10.1016/j.indcrop.2018.12.027

Chen, T.-F., Han, S.-Y., Wang, Z.-P., Gao, H., Wang, L.-Y., Deng, Y.-H., et al. (2019c). Modified UiO-66 Frameworks with Methylthio, Thiol and Sulfonic Acid Function Groups: The Structure and Visible-Light-Driven Photocatalytic

Property Study. *Appl. Catal. B: Environ.* 259, 118047. doi:10.1016/j.apcatb.2019.118047

Dai, J., Liu, Z., Hu, Y., Liu, S., Chen, L., Qi, T., et al. (2019). Adjusting the Acidity of Sulfonated Organocatalyst for the One-Pot Production of 5-ethoxymethylfurfural from Fructose. *Catal. Sci. Technol.* 9, 483–492. doi:10.1039/c8cy02010h

Guillerm, V., Ragon, F., Dan-Hardi, M., Devic, T., Vishnuvarthan, M., Campo, B., et al. (2012). A Series of Isoreticular, Highly Stable, Porous Zirconium Oxide Based Metal-Organic Frameworks. *Angew. Chem. Int. Ed.* 51, 9267–9271. doi:10.1002/anie.201204806

Guo, D., Liu, X., Cheng, F., Zhao, W., Wen, S., Xiang, Y., et al. (2020a). Selective Hydrogenolysis of 5-hydroxymethylfurfural to Produce Biofuel 2, 5-dimethylfuran over Ni/ZSM-5 Catalysts. *Fuel* 274, 117853. doi:10.1016/j.fuel.2020.117853

Guo, H., Duereh, A., Su, Y., Hensen, E. J. M., Qi, X., and Smith, R. L. (2020b). Mechanistic Role of Protonated Polar Additives in Ethanol for Selective Transformation of Biomass-Related Compounds. *Appl. Catal. B: Environ.* 264, 118509. doi:10.1016/j.apcatb.2019.118509

He, X. (2021). A Novel Hybrid Digestion-Gasification Process Integrated with Membranes for Efficient Conversion of Biomass to Bio-Alcohols. *Green. Energ. Environ.* 6, 15–21. doi:10.1016/j.gee.2020.04.003

Herbst, A., and Janiak, C. (2017). MOF Catalysts in Biomass Upgrading towards Value-Added fine Chemicals. *CrystEngComm* 19, 4092–4117. doi:10.1039/c6ce01782g

Hoang, A.T, and Pham, V. (2021). 2-Methylfuran (MF) as a Potential Biofuel: A Thorough Review on the Production Pathway from Biomass, Combustion Progress, and Application in Engines. *Renew. Sustain. Energ. Rev.* 148, 111265. doi:10.1016/j.rser.2021.111265

Hommes, A., Heeres, H. J., and Yue, J. (2019). Catalytic Transformation of Biomass Derivatives to Value-Added Chemicals and Fuels in Continuous Flow Microreactors. *ChemCatChem* 11, 4671–4708. doi:10.1002/cctc.201900807

Hu, L., Tang, X., Wu, Z., Lin, L., Xu, J., Xu, N., et al. (2015). Magnetic Lignin-Derived Carbonaceous Catalyst for the Dehydration of Fructose into 5-hydroxymethylfurfural in Dimethylsulfoxide. *Chem. Eng. J.* 263, 299–308. doi:10.1016/j.cej.2014.11.044

Hu, Z., Lin, J., Ogiwara, N., Rodriguez, A., Peng, Y., Wang, Y., et al. (2016). A pH-Responsive Phase Transformation of a Sulfonated Metal-Organic Framework from Amorphous to Crystalline for Efficient CO2capture. *CrystEngComm* 18, 2803–2807. doi:10.1039/c6ce00369a

Kumari, P. K., Rao, B. S., Dhana Lakshmi, D., Sai Paramesh, N. R., Sumana, C., and Lingaiah, N. (2019). Tungstophosphoric Acid Supported on Mesoporouus Niobiumoxophosphate: an Efficient Solid Acid Catalyst for Etherification of 5-hydroxymethylfurfural to 5-ethoxymethylfurfural. *Catal. Today* 325, 53–60. doi:10.1016/j.cattod.2018.06.047

Li, H., Saravanamurugan, S., Yang, S., and Riisager, A. (2016). Direct Transformation of Carbohydrates to the Biofuel 5-ethoxymethylfurfural by Solid Acid Catalysts. *Green. Chem.* 18, 726–734. doi:10.1039/c5gc01043h

Liu, S., Zheng, W., Wen, X., Fang, Z., Li, H., Li, C., et al. (2022). Molecular Design and Experimental Study of Cellulose Conversion to 5-hydroxymethylfurfural Catalyzed by Different Ratios of Brønsted/Lewis Acid Ionic Liquids. *Carbohydr. Polym.* 278, 118936. doi:10.1016/j.carbpol.2021.118936

Liu, X., Li, H., Pan, H., Zhang, H., Huang, S., Yang, K., et al. (2016). Efficient Catalytic Conversion of Carbohydrates into 5-ethoxymethylfurfural over MIL-101-Based Sulfated Porous Coordination Polymers. *J. Energ. Chem.* 25, 523–530. doi:10.1016/j.jechem.2016.01.015

Lv, S.-W., Liu, J.-M., Li, C.-Y., Ma, H., Wang, Z.-H., Zhao, N., et al. (2019). Fabrication of Fe3O4@UiO-66-So3h Core-Shell Functional Adsorbents for Highly Selective and Efficient Removal of Organic Dyes. *New J. Chem.* 43, 7770–7777. doi:10.1039/c9nj01324e

Manjunathan, P., Upare, P. P., Lee, M., and Hwang, D. W. (2021). One-pot Fructose Conversion into 5-ethoxymethylfurfural Using a Sulfonated Hydrophobic Mesoporous Organic Polymer as a Highly Active and Stable Heterogeneous Catalyst. *Catal. Sci. Technol.* 11, 5816–5826. doi:10.1039/d1cy00883h

Nakajima, K., and Hara, M. (2012). Amorphous Carbon with SO3H Groups as a Solid Brønsted Acid Catalyst. *ACS Catal.* 2, 1296–1304. doi:10.1021/cs300103k

Ohara, M., Takagaki, A., Nishimura, S., and Ebitani, K. (2010). Syntheses of 5-hydroxymethylfurfural and Levoglucosan by Selective Dehydration of Glucose Using Solid Acid and Base Catalysts. *Appl. Catal. A: Gen.* 383, 149–155. doi:10.1016/j.apcata.2010.05.040

Olorunyomi, J. F., Liu, T., Ho, C.-K., Li, C.-Y. V., and Chan, K.-Y. (2021). Imparting UiO-66 with Fast Cation Exchange Property via Sulfonating Organic Linkers for Selective Adsorption. *Separat. Purif. Technol.* 260, 118219. doi:10.1016/j.seppur.2020.118219

Oozeerally, R., Burnett, D. L., Chamberlain, T. W., Kashtiban, R. J., Huband, S., Walton, R. I., et al. (2021). Systematic Modification of UiO-66 Metal-Organic Frameworks for Glucose Conversion into 5-Hydroxymethyl Furfural in Water. *ChemCatChem* 13, 2517–2529. doi:10.1002/cctc.202001989

Ragon, F., Horcajada, P., Chevreau, H., Hwang, Y. K., Lee, U.-H., Miller, S. R., et al. (2014). *In Situ* energy-dispersive X-ray Diffraction for the Synthesis Optimization and Scale-Up of the Porous Zirconium Terephthalate UiO-66. *Inorg. Chem.* 53, 2491–2500. doi:10.1021/ic402514n

Tang, Y., Cheng, Y., Xu, H., Wang, Y., Ke, L., Huang, X., et al. (2019). Binary Oxide Nanofiber Bundle Supported Keggin-type Phosphotungstic Acid for the Synthesis of 5-hydroxymethylfurfural. *Catal. Commun.* 123, 96–99. doi:10.1016/j.catcom.2019.02.015

Venkata Mohan, S., Nikhil, G. N., Chiranjeevi, P., Nagendranatha Reddy, C., Rohit, M. V., Kumar, A. N., et al. (2016). Waste Biorefinery Models towards Sustainable Circular Bioeconomy: Critical Review and Future Perspectives. *Bioresour. Technol.* 215, 2–12. doi:10.1016/j.biortech.2016.03.130

Xiang, Y., Wen, S., Tian, Y., Zhao, K., Guo, D., Cheng, F., et al. (2021). Efficient Synthesis of 5-ethoxymethylfurfural from Biomass-Derived 5-hydroxymethylfurfural over Sulfonated Organic Polymer Catalyst. *RSC Adv.* 11, 3585–3595. doi:10.1039/d0ra10307a

Yan, Y., Guo, H., Li, K., and Yan, L. (2022). Fabrication of Supported Acid Catalytic Composite Fibers by a Simple and Low-Cost Method and Their Application on the Synthesis of Liquid Biofuel 5-ethoxymethylfurfural. *Green. Energ. Environ.* 7, 165–171. doi:10.1016/j.gee.2020.06.028

Yin, Y., Ma, C. H., Li, W., and Liu, S. X. (2021). Solvent System and Conversion Mechanism of 5 over Line Hydroxymethylfurfural Preparation from Glucose. *Prog. Chem.* 33, 1856–1873. doi:10.7536/pc200852

Zaboon, S., Abid, H. R., Yao, Z., Gubner, R., Wang, S., and Barifcani, A. (2018). Removal of Monoethylene Glycol from Wastewater by Using Zr-Metal Organic Frameworks. *J. Colloid Interf. Sci.* 523, 75–85. doi:10.1016/j.jcis.2018.03.084

Zhang, J., Dong, K., Luo, W., and Guan, H. (2018). Catalytic Upgrading of Carbohydrates into 5-ethoxymethylfurfural Using SO3H Functionalized Hyper-Cross-Linked Polymer Based Carbonaceous Materials. *Fuel* 234, 664–673. doi:10.1016/j.fuel.2018.07.060

Zhang, L., Tian, L., Xi, G., Sun, R., and Zhao, X. (2020). Catalytic Valorization of Expired Fructan-Rich Food into the Biofuel 5-Ethoxymethylfurfural via a Restaurant Food Waste-Derived Carbonaceous Solid Acid. *Waste Biomass Valor.* 11, 6223–6233. doi:10.1007/s12649-019-00904-6

Zhang, Y., Li, B., Wei, Y., Yan, C., Meng, M., and Yan, Y. (2019). Direct Synthesis of Metal-Organic Frameworks Catalysts with Tunable Acid-Base Strength for Glucose Dehydration to 5-hydroxymethylfurfural. *J. Taiwan Inst. Chem. Eng.* 96, 93–103. doi:10.1016/j.jtice.2018.12.020

Zhao, H., Holladay, J. E., Brown, H., and Zhang, Z. C. (2007). Metal Chlorides in Ionic Liquid Solvents Convert Sugars to 5-hydroxymethylfurfural. *Science* 316, 1597–1600. doi:10.1126/science.1141199

Sustainable Approaches to Selective Conversion of Cellulose Into 5-Hydroxymethylfurfural Promoted by Heterogeneous Acid Catalysts: A Review

Yuanyong Yao*, Shixue Chen and Meng Zhang

School of Material and Chemical Engineering, Tongren University, Tongren, China

5-Hydroxymethylfurfural (5-HMF) as a triply catalytic product is a value-added refining chemical in industry production. 5-HMF as biomass feedstock enables to be transformed into other high-value industrial compounds, such as 2,5-furandicarboxylic acid (FDCA), 5-hydroxymethyl-2-furancarboxylic acid (HMFCA), 5-formyl-2-furancarboxylic acid (FFCA), 2,5-diformylfuran (DFF), 2,5-bis(aminomethyl)furan (BAMF), and 2,5-dimethylfuran (DMF). Hence, catalytic conversion of biomass into 5-HMF has been given much more attention by chemists. In this review, some latest studies about the conversion of cellulose to 5-HMF have been introduced systematically. Solid acids such as heterogeneous catalysts have been widely applied in the conversion of cellulose into 5-HMF. Therefore, some novel solid acids with Brønsted and/or Lewis acidic sites, such as sulfonated solid acids, carbon-based acids, and zeolite particles employed for biomass conversions are listed.

Keywords: 5-Hydroxymethylfurfural, cellulose, biomass resources, solid acids, selective conversion, heterogeneous acid catalysis

1 INTRODUCTION

With the progressive increase in consumption of unsustainable resources (e.g., crude oil, coal, and natural gas), the global energy crisis has been much of an emergency (Kittner et al., 2017; Wang et al., 2018; Sadhukhan et al., 2018; Ng et al., 2021). Many fossil fuels are exhausting rapidly with high emission of exhaust gases (e.g., carbon dioxide, sulfur dioxide, and nitric oxides); simultaneously, social and environmental problems such as acid rain and greenhouse effect are becoming more and more serious (Zhang et al., 2015; Venkata Mohan et al., 2016; Zhao et al., 2018; Li et al., 2020). At present, the promising strategy for improving the current issues of multicarbon energy *via* developing and searching for an alternative to fossil-based fuels has garnered much attention (Li et al., 2019a; Li et al., 2019b; Zhang H. et al., 2019; Nabil et al., 2021; Meng et al., 2022). Bioorganic carbon substances acting as sustainable and renewable biomass resources have a promising prospect for constructing a carbon-neutral society because of their abundance and wide existence in biological organisms, including straw, wood, and cotton as agroforestry biomass (Tan J. et al., 2021; De et al., 2020; Danish and Ahmad., 2018; Gazi, 2019; Zhang et al., 2021). In recent decades, biomass resources have been validated to be used as renewable and sustainable biomass materials, which are capable of being a pioneer in the field of alleviating resource shortage (Li et al., 2013; Li et al., 2014; Liu et al., 2015; Tareen et al., 2019; Kang et al., 2020). Lignocellulosic biomass is the most abundant content of renewable and sustainable biomass materials, considering further a building block for biomass

FIGURE 1 | Compositions of lignocellulosic biomass.
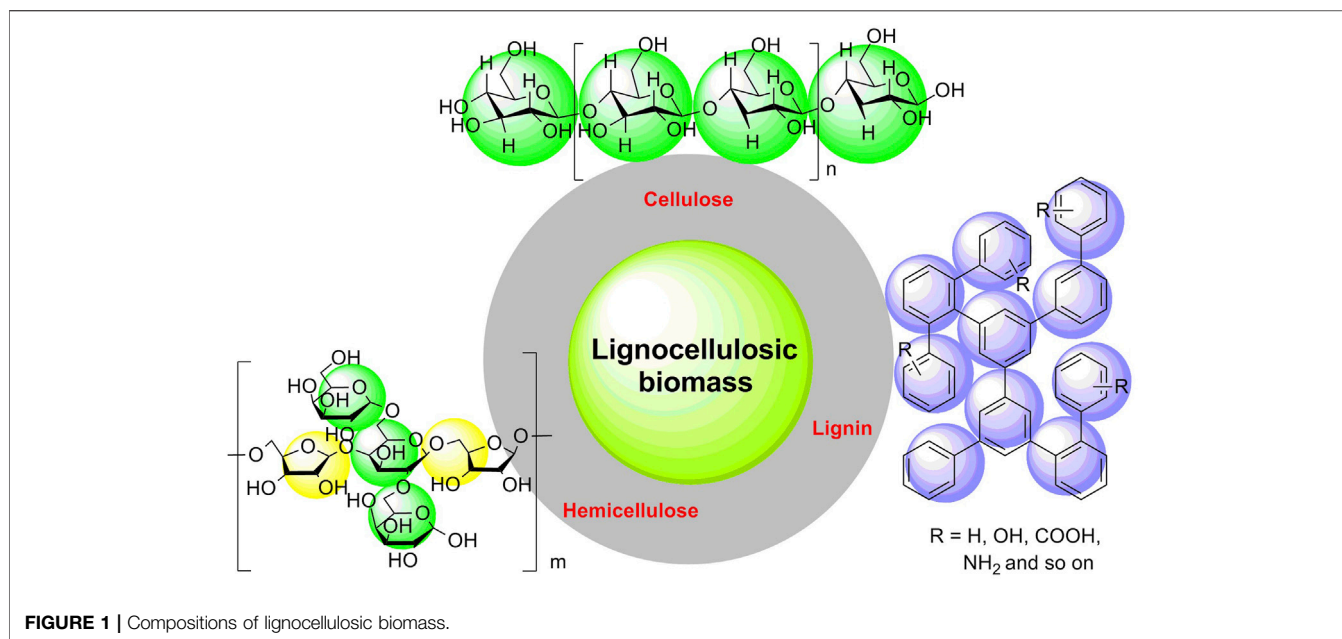
resources (Tian et al., 2018; Mahajan et al., 2020). Because of its abundance, diversity, and inexpressiveness in merits, lignocellulosic biomass has a promising prospect for replacing fossil-based fuels in refining industrial production (Sánchez et al., 2019; Shen et al., 2020; Haldar et al., 2021). In essence, lignocellulosic biomass is a complicated bio-based substance including cellulose (30–50 wt%), hemicelluloses (20–40 wt%), and lignin (10–20 wt%) (**Figure 1**) (Sarip et al., 2016; Silva et al., 2018; Zhao et al., 2020). Cellulose is a polymer of glucose with varying degrees of polymerization; hemicellulose is a heteropolymer of pentose and glucose linked by β-1, 4-glycosidic bonds; lignin mainly consists of amorphous aromatic macromolecules (Cao et al., 2019; Mansora et al., 2019; Yang et al., 2020). In recent years, tremendous practical applications for cellulose converted selectively into some high value-added chemicals through multistep promotions have been focused (Li et al., 2017; Li X. et al., 2018; Wang H. et al., 2019; Slak et al., 2022), for instance, the efficient conversion of cellulose into levulinic acid by using cellulase-mimetic mesoporous solid acid (Shen et al., 2017), selective conversion of bio-based hemicellulose prehydrolysate to high-value succinic acid (Dalli et al., 2017), one-pot chemoenzymatic transformation of furfuryl alcohol from biomass (Qin and He., 2020), catalytic pyrolysis of cellulose into furan by solid acid catalysts (Nb_2O_5, γ-Al_2O_3, ZSM-5, and TS-1) (Zhu et al., 2021; Huang X. et al., 2022), and one-pot production of 5-hydroxymethylfurfural from cellulose using Brønsted-type catalysts (Al-SBA-15) (Shirai et al., 2017). Moreover, in pharmaceutical preparation, microcrystalline cellulose is a commonly used drug excipient, which is good for active drug molecules to be absorbed in the small intestine (Gadge, 2020; Benabbas et al., 2021). So, cellulose is a well-recognized commercial chemical.

More significantly, 5-hydroxymethylfurfural (5-HMF), a high value-added chemical, is a selective dehydration product of monosaccharides (e.g., glucose and fructose) or acid-catalyzed dehydration/hydrolysis of cellulose, which can become a versatile bio-carbon platform compound for upgrading other valuable refining industrial chemicals (Heo et al., 2021; Meng et al., 2022). 5-HMF is essentially a furfural derivative bearing hydroxymethyl (–CH_2OH) and aldehyde group (CH = O) distributed at 1, 4-positions of the furan ring, which can be responsible for upgrading 5-HMF into value-added chemicals via oxidation and/or reduction. In the commercial survey, the 5-HMF's market share will be predicted to reach up to EUR 55 million in 2024 (MarketWatch, 2019). Hence, 5-HMF as a refining chemical product devotes a great contribution to sustainable biorefinery, and 5-HMF as a core stock presents a powerful tool in the synthesis of antihypertensive, antidepressant, antianxiety, and anti-inflammatory drugs (Espro et al., 2021).

For the past few years, selectively catalytic conversions of cellulose into refining high-value chemical of 5-HMF over various potent solid acids have been paid much more attention (Flores-Velázquez et al., 2020; Liu G. et al., 2022; Liu S. et al., 2022). Many efficient solid acids as catalysts with novel carbon frameworks have been developed and utilized in selective biomass conversions. The related investigations on some protocols for cellulose converted into 5-HMF loading heterogeneous solid acids have been only briefly documented and discussed in previous published reviews (Shen et al., 2020; Xu et al., 2020; Tempelman et al., 2021; Slak et al., 2022). In this review, numerous recent applications of the selective conversions for cellulose into 5-HMF as a high value-added industrial chemical are emphasized via heterogeneous catalysis. Moreover, solid acids as potent heterogeneous catalysts comprising Brønsted and/or Lewis acidic sites are discussed in affecting the selective conversion of cellulose into 5-HMF. Therefore, summarizing heterogeneous solid acid catalysts with novel frameworks enables us to further understand their role in the selective conversion of cellulose.
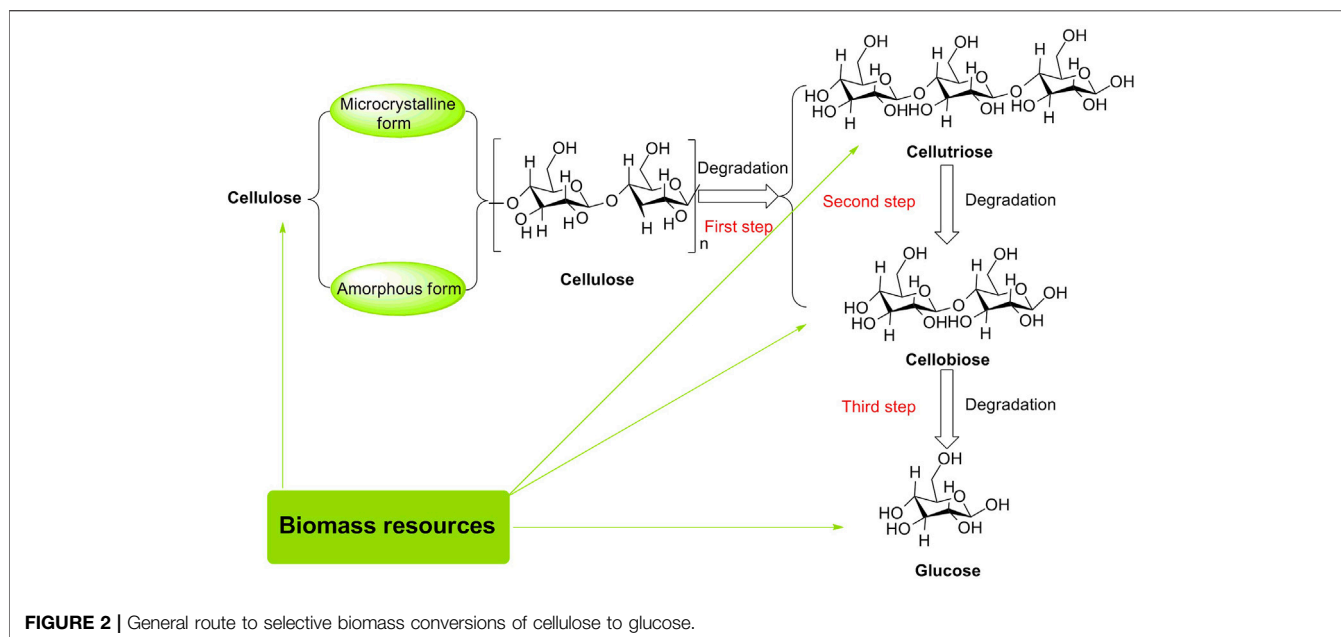
FIGURE 2 | General route to selective biomass conversions of cellulose to glucose.

2 CELLULOSE BIOMASS

Cellulose, one of the major components of lignocellulosic biomass, is composed of D-glucose linked by β-1,4-glycosidic bonds, having 30–50 wt% in quantity (Qi et al., 2018; Zhao et al., 2020; Vanderfleet et al., 2021). Conventionally, cellulose has both microcrystalline and amorphous forms (Haan et al., 2007; Wang et al., 2021). Microcrystalline cellulose as a stable carbohydrate with a robust crystalline structure is not sensitive to acidic conditions, as compared to amorphous cellulose without a densely packed region that can form an ordered matrix. Herein, it is worthy to be noted that the formation of the ordered matrix for polysaccharides can effectively inhibit the contact of acids with 1, 4-glycosidic bonds in the bulk phase (Heinze, 2015; Tkachenko et al., 2021). For instance, the hydrolysis of microcrystalline cellulose into glucose in the presence of solid acids (e.g., sulfonated active carbon (AC-SO_3H), magnetic solid acid (Fe_3O_4-SBA-SO_3H), and macroporous resin Amberlyst 15) was just tolerated to be 40.5, 21, and 15% in yields of glucose, respectively (Onda et al., 2009; Lai et al., 2011). To the best of our knowledge, D-glucose is a product of complete hydrolysis of cellulose; additional hydrolysates of cellobiose and cellotriose are products of partially hydrolyzed cellulose (Guo et al., 2019; Lehrhofer et al., 2022). They are usually utilized as the main feedstock for the preparation of high value-added industrial chemicals because of multiple hydroxyl groups present in their molecular skeletons. These hydroxyl groups are reckoned as efficient reaction sites that enable interaction with Brønsted/Lewis acidic sites originating from potent solid acid catalysts (**Figure 2**). Therefore, the interaction between cellulose/cellobiose/cellotriose/D-glucose and acid catalysts is beneficial for the 1, 4-glycosidic bond/C-O bond to be broken down and hydroxyl groups to be dehydrated in biomass conversions.

3 5-HYDROXYMETHYLFURFURAL AND ITS REACTIVITY

3.1 Overview of 5-Hydroxymethylfurfural

5-HMF is a selective transformation product of cellulose (polysaccharide) through consecutive acidic hydrolysis, isomerization, and dehydration, which, at the same time, has been awarded to be the promising candidate of the "top 10 + 4" bio-based key platform compounds by the U.S. Department of Energy because it is capable of being a bridge between biomass feedstock and value-added industrial chemicals (Hu et al., 2020; Thoma et al., 2020). 5-HMF is a five-membered heterocyclic compound comprising one furan ring as the parental skeleton and one hydroxymethyl and aldehyde group located at 2, 5 positions that is permitted to be converted efficiently into various high-quality fuels and value-added chemicals by the oxidation and/or reduction reactions for the hydroxymethyl and/or aldehyde group(s).

3.2 Reactivity of 5-Hydroxymethylfurfural

The oxidation/reduction of 5-HMF can yield furanic derivatives such as 2, 5-furandicarboxylic acid (FDCA), 5-hydroxymethyl-2-furancarboxylic acid (HMFCA), 5-formyl-2-furancarboxylic acid (FFCA), 2, 5-diformylfuran (DFF), 2, 5-bis(aminomethyl)furan (BAMF), (tetrahydrofuran-2, 5-diyl)dimethanol (THFDM), 2, 5-dimethyl furan (DMF), and 5-methylfuran-2-carbaldehyde (MFC), which undergo oxidation/reduction of formyl and/or hydroxymethyl group(s) of 5-HMF to various extents (**Figure 3**).

3.2.1 Reactivity for Oxidation
As taken, for example, the refining chemical of HMFCA was afforded through the selective aerobic oxidation for the formyl moiety of 5-HMF in the presence of Ag/ZrO_2 catalysts, with more than 98% in yield (Schade et al., 2018). In the preparation of

FIGURE 3 | Transformation of 5-HMF into its derivatives.
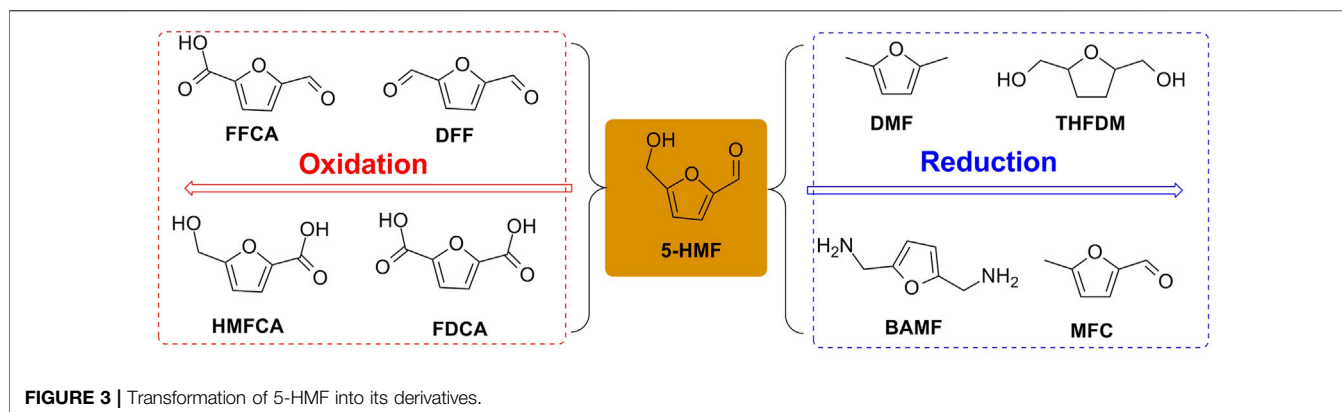
FFCA oxidized selectively from 5-HMF, CuO-CeO$_2$, Ru/Al$_2$O$_3$, and MnO$_2$–NaHCO$_3$ mixed oxides were, respectively, used as a cheap and stable catalyst for catalytic conversion of 5-HMF into FFCA, and with the aid of diatomic oxygen as the oxidant in aqueous solution; the selectivity and conversion for FFCA showed good performance through the selective chemical oxidation (Ventura et al., 2016; Danielli da Fonseca Ferreira et al., 2018; Hayashi et al., 2019). Furthermore, the accessible approach to the selective oxidation of 5-HMF into DFF proceeded well by means of a Mn-based heterogeneous catalyst, with >99% selectivity and 100% conversion (Chen et al., 2019; Ke et al., 2019). As well, the photosensitive catalyst of WO$_3$/g-C$_3$N$_4$ used as an electronic donator under visible light illumination could initiate catalytic oxidation of the 5-HFM solution at a certain concentration, retaining 87% in the selectivity of DFF (Wu et al., 2017). With a similar effect to photochemical oxidation, electrochemical oxidation becomes another available access from 5-HMF to FDCA. Bimetallic NiFe-layered double-hydroxide nanosheets loaded on carbon fiber paper and nickel boride decorated on the surface of Ni foam as electrodes were, respectively, testified to be potent in the electrochemical oxidation of 5-HMF into FDCA, with the yields of 99 and 98%, and excellent selectivity and conversions (Barwe et al., 2018; Liu et al., 2018). Based on the aforementioned experimental facts, it is definitely confirmed that the chemical oxidation of 5-HMF is indeed an effective gateway to the synthesis of further valuable refining chemicals in industrial production.

3.2.2 Reactivity for Reduction

In terms of reduction for 5-HMF, the promising green solvent of DMF used as a "second-generation biofuel" is obtained by catalytic hydrogenation of 5-HMF (Rothamer and Jennings, 2012; Nishimura et al., 2014). In the investigation of direct hydrogenation of 5-HMF to DMF, a series of noble (Ru-, Pt-, and Pd-based) and non-noble (Ni- and Co-based) metal complexes are usually utilized to be potent Lewis acid sites in designing novel solid acids. In 2019, the reduction of 5-HMF into DMF was smoothly promoted by non-/noble metal-based solid acids, assisting hydrogen gas as a hydrogen source (Wang X. et al., 2019). In the same year, the Co-based metal catalyst of Co-(ZnO-ZnAl$_2$O$_4$) gave a 74% yield of DMF converted from 5-HMF (An S. et al., 2019). Simultaneously, the developed Co–graphene

nanoparticle employed in the hydrogenation of 5-HMF to DMF was estimated definitely to be validated in the conversion of 5-HMF into DMF (Yang et al., 2019). Excitingly, 97% conversion of 5-HMF and 93% selectivity of DMF were successfully achieved by the utilization of the bimetallic Cu–Fe complex as a non-noble metal catalyst (Solanki and Rode, 2019). Significantly, the application of a non-noble bimetallic Cu–Ni electrode for the electrocatalytic reduction of 5-HMF into DMF was also in effect with the achievement of 91% conversion and 88% Faradic efficiency (Zhang Y. R. et al., 2019). Moreover, the commercial and valuable chemical BAMF prepared from 5-HMF as a feedstock was smooth to be on the run through the application of the combination of Ru/Nb$_2$O$_5$ and [Ru(CO)ClH(PPh$_3$)$_3$]/xantphos system (Komanoya et al., 2017). Afterward, the heterogeneous Ru-based catalyst reported by Pingen et al. was utilized for the one-pot amination of HMF to BAMF, exhibiting to be potent solid acid, with a 90% in yield of BAMF (Pingen et al., 2018).

All in all, the refining chemical of 5-HMF is a crucial building block for the synthesis of deeply high value-added chemicals in industry production and is also a significant selective catalyzed hydrolysis/dehydration product of cellulose. In recent years, the merits of 5-HMF as a feedstock utilized for upgrading high value-added industrial chemicals have appeared obviously in biomass conversions. However, the difficulty of selective conversion of cellulose into 5-HMF is still a necessity to be overcome, especially for the development of highly efficient catalysts for large-scale productions.

4 THE GENERAL PATHWAY FOR CONVERSION OF CELLULOSE INTO 5-HYDROXYMETHYLFURFURAL BY ACID CATALYSTS

With the microcrystalline or amorphous form of cellulose coming up, it is usually utilized as a biomass raw material for the synthesis of various refining chemicals such as glucose, fructose, and 5-HMF. The selective conversion of cellulose into D-glucose is essentially a crucial step for other high valuable refining chemicals obtained from lignocellulosic biomass (Inoue et al., 2021; Yao,
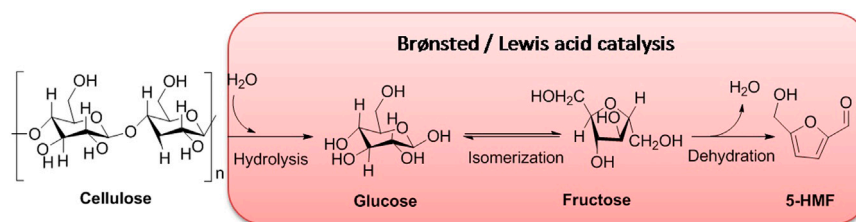
SCHEME 1 | Plausible pathway of 5-HMF converted from cellulose by solid acids.

2022). D-glucose as the complete hydrolysate of cellulose, with a six-membered ring framework, is flexible to be isomerized into a five-membered ring skeleton of fructose under acidic conditions. The intermediate of fructose bearing five hydroxyl groups in the conversion of cellulose can be transformed readily to 5-HMF by autocatalytic systems under heating surroundings. Certainly, the autocatalytic system in determining the conversion and selectivity of 5-HMF is closely related to the reaction temperature, being in direct proportion at a certain range. Nevertheless, the excessive temperature limits the conversion and selectivity of 5-HMF (Bocanegra et al., 2021; Lyu et al., 2022).

Catalysis is an effective strategy for producing refining industrial chemicals from biomass feedstock, which is able to lower the active energy of the reaction system and improve reaction conditions, as well as promote conversion and selectivity (Lange, 2021; Witzel et al., 2021). Catalysts acting as initiators of catalysis can be divided into homogeneous and heterogeneous coordinators (Bai et al., 2021; Taipabu et al., 2021). In the conversion of cellulose into 5-HMF, although homogeneous acid catalysts such as enzymes, mineral salts or acids, and supercritical water can overcome the resistance to degradation of cellulose for preparation of high-value chemicals, serious drawbacks for product separation, corrosion hazard, waste fluids, and severe reacting conditions are emerged obviously (Güell et al., 2015; Wang et al., 2021a; Chai et al., 2021). As compared to homogeneous acid catalysts, heterogeneous acid catalysts showing many merits, such as efficient conversion and selectivity, flexible separation, and low toxicity, have been extensively and popularly applied to industrial production and scientific research (Huo et al., 2015; Sun et al., 2016; Tan X. et al., 2021). To further understand the role of a heterogeneous acid catalyst in biomass conversions, exploring the mechanism of product 5-HMF converted from cellulose is favorable for novel catalyst design and improvement of hydrothermal conversion for biomass. As far as we know, a number of acid catalysts promoting the conversion of biomass are being on the same catalytic pathway involving Brønsted acid catalysis and Lewis acid catalysis (**Scheme 1**).

4.1 Brønsted Acid Catalysis
In Brønsted acid catalysis, Brønsted acids are often considered to be potential catalysts in catalysis because of enabling the release of hydrogen ions (H^+) in an aqueous solution via dissociation. H^+ can protonate oxygen atom(s) in the 1, 4-glycosidic bond and/or pyranose ring. Subsequently, by undergoing the half-chair

conformational isomerization of the oxygen atom neighboring C_1 position of the anhydroglucose unit, it can bring about the formation of carbenium ion, presenting the cleavage of the C-O bond. Finally, in the presence of a water molecule, the carbenium ion interacted with the water molecule, enabling to reconstruct of the anomeric center to form D-glucose. After the formation of D-glucose, the isomerization of D-glucose into fructose occurs successively in acidic surroundings (**Scheme 2**) (Rinaldi and Schüth, 2009; Van Putten et al., 2013; Yamabe et al., 2013; Kang et al., 2018; Zhao et al., 2021). In this process, the critical intermediate of 1, 2-enediol is formed via a 1, 2-hydride shift that occurred in glucose. And then, as following steps of two 1, 2-eliminations, one 1, 4-elimination, and a ring closure in 1, 2-enediol, the promising production of 5-HMF is converted successfully from cellulose. Totally, the aforementioned pathway of 5-HMF converted from cellulose can be summarized by the following steps: 1) the protonation of oxygen atoms in the 1, 4-glycosidic bond and/or pyranose ring; 2) the cleavage of carbon–oxygen bond; 3) nucleophilic attack of water; 4) isomerization of glucose into fructose; and 5) successive dehydration (Zhao et al., 2021).

4.2 Lewis Acid Catalysis
In comparison with Lewis acid catalysis, Lewis acids inhering empty orbits can accept electron pairs in chemical concepts (Marqués et al., 2021). In other words, acidic sites of Lewis acids are capable of being transformed into Brønsted acidic sites by combination with pairs of electrons donated from protic solvent, which can be responsible for the isomerization of glucose into fructose (Delidovich and Palkovits., 2015; Xu et al., 2017). In previous research studies, Lewis acidic sites of catalysts utilized for the aldose–ketose isomerization were conducted well because they could effectively promote the formation of enol intermediates (Charmot and Katz, 2010; Choudhary et al., 2013). Therefore, the general mechanism for Lewis acid-catalyzed isomerization can be summarized in two steps: one is the enolization of aldose, and the other is the 1, 2-hydride shift, both of which favor the isomerization of aldose into ketose. Moreover, in terms of glucose–fructose isomerization with Lewis acid, the isomerization promoted by Lewis acid (M_xL_y) should first follow the interaction of L of M_xL_y with H of hydroxyl groups attached to the glucose skeleton. Afterward, under heating conditions, the formation of the five-membered complex occurs immediately, resulting from the coordination between M

SCHEME 2 | Brønsted acid-catalyzed hydrolysis mechanism of cellulose into 5-HMF.
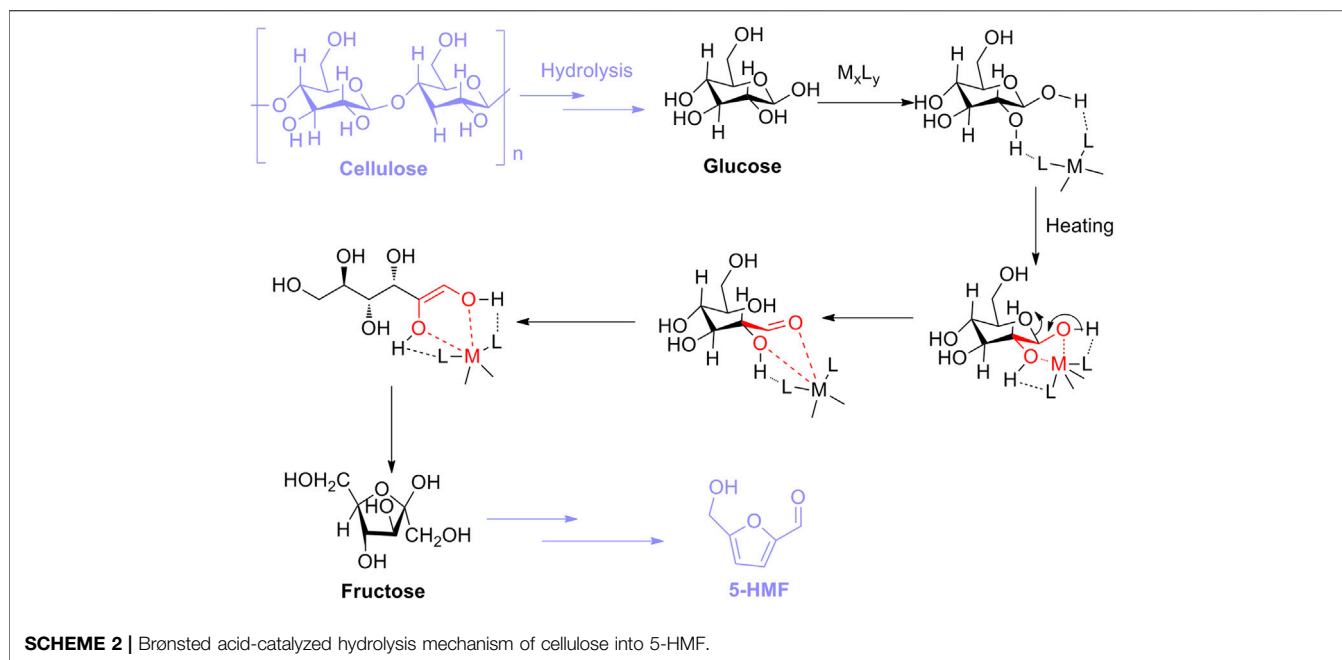
(Lewis acidic site) and two oxygen atoms (electron donors) in glucose. Then, the complex is authorized to be transformed into the corresponding enol intermediate through undergoing ring opening, which is subsequently isomerized into fructose. Eventually, as for the step of 5-HMF converted from fructose as an isomer of glucose, fructose is permitted to be directly dehydrated into 5-HMF with the assistance of the Brønsted acidic site (**Scheme 3**) (Hu et al., 2009; Zhao et al., 2021).

# 5 APPLICATIONS OF ACID CATALYSTS TO CONVERSIONS OF CELLULOSE BIOMASS INTO 5-HYDROXYMETHYLFURFURAL

Based on the aforementioned propositions of general pathways for conversions of cellulose into 5-HMF by Brønsted and Lewis acids, numerous heterogeneous acid catalysts with novel frameworks incorporating Brønsted and/or Lewis acidic sites have been emerging consecutively, such as sulfonated solid acid catalysts (Brønsted acidic sites), carbon-based acid catalysts (Brønsted acidic sites), M-zeolite acid catalysts (Lewis acidic sites), and heteropoly acid catalysts (Brønsted and/or Lewis acidic sites). Simultaneously, numerous achievements regarding biomass conversions have adequately convinced us that heterogeneous novel acid catalysts have a good promising prospect in biomass conversions.

5.1 Resin-Based Sulfonated Solid Acid Catalysts

Resin-based sulfonated solid acids as potent heterogeneous catalysts have achieved good results in biomass conversions, resulting from the presence of sulfonic groups (-SO$_3$H) on the

frameworks of catalysts. The sulfonic groups are essentially Brønsted acidic sites, with strong acidity. In recent years, some novel resin-based sulfonated acid catalysts have been reported in the application of biomass conversions to high-value chemicals, with good results. The novel Cl-containing resin-based solid acid catalyst (Cl$_{0.3}$-S-R) bearing with -Cl and -SO$_3$H was synthesized by a simple hydrothermal method through the polymerization of *o*-chlorophenol and *p*-hydroxybenzenesulfonic with formaldehyde. Sulfonated solid acid with 1.47 mmol/g SO$_3$H density on the external surface was thought to be an effective catalyst for corn stover conversion to 5-HMF and furfural production. Notably, cellulose is a major component of corn stover. In experimental results, the Cl-containing sulfonated acid catalyst exhibited a superior catalytic activity in the catalytic transformation of corn stover to 5-HMF in a 1,4-dioxane/H$_2$O biphasic system, yielding a product of 5-HMF in a yield of 43.8% and the by-product of furfural in a yield of 38.1% (**Figure 4**) (Yang et al., 2021).

Afterward, with the assistance of microwave irradiation, employment of the catalyst SC-FAR-800 to the selective conversions of fructose, glucose, cellobiose, and cellulose into 5-HMF was exhibited to be in effect to varying extent, with the yields of 5-HMF being on 89.35, 38.17, 42.6, and 14.73%, respectively, indicating that fructose is a more appropriate feedstock for the synthesis of 5-HMF (**Figure 5**) (Huang T. et al., 2022). Moreover, the SC-FAR-800 is a furfuryl alcohol resin-based sulfonated acid catalyst, containing multiple sulfonic acid moieties with an acid density of 3.43 mmol/g. Moreover, by the techniques of SEM and BET, the irregular mesoporous structure of the sulfonated solid acid SC-FAR-800 was observed to be a specific surface area of 32.56 m^2/g, an average pore size of 0.018 cm^3/g, and a pore volume of 3.25 nm, which could be accountable for the efficient conversions of biomass.

SCHEME 3 | Lewis acid-catalyzed hydrolysis mechanism of cellulose into 5-HMF.
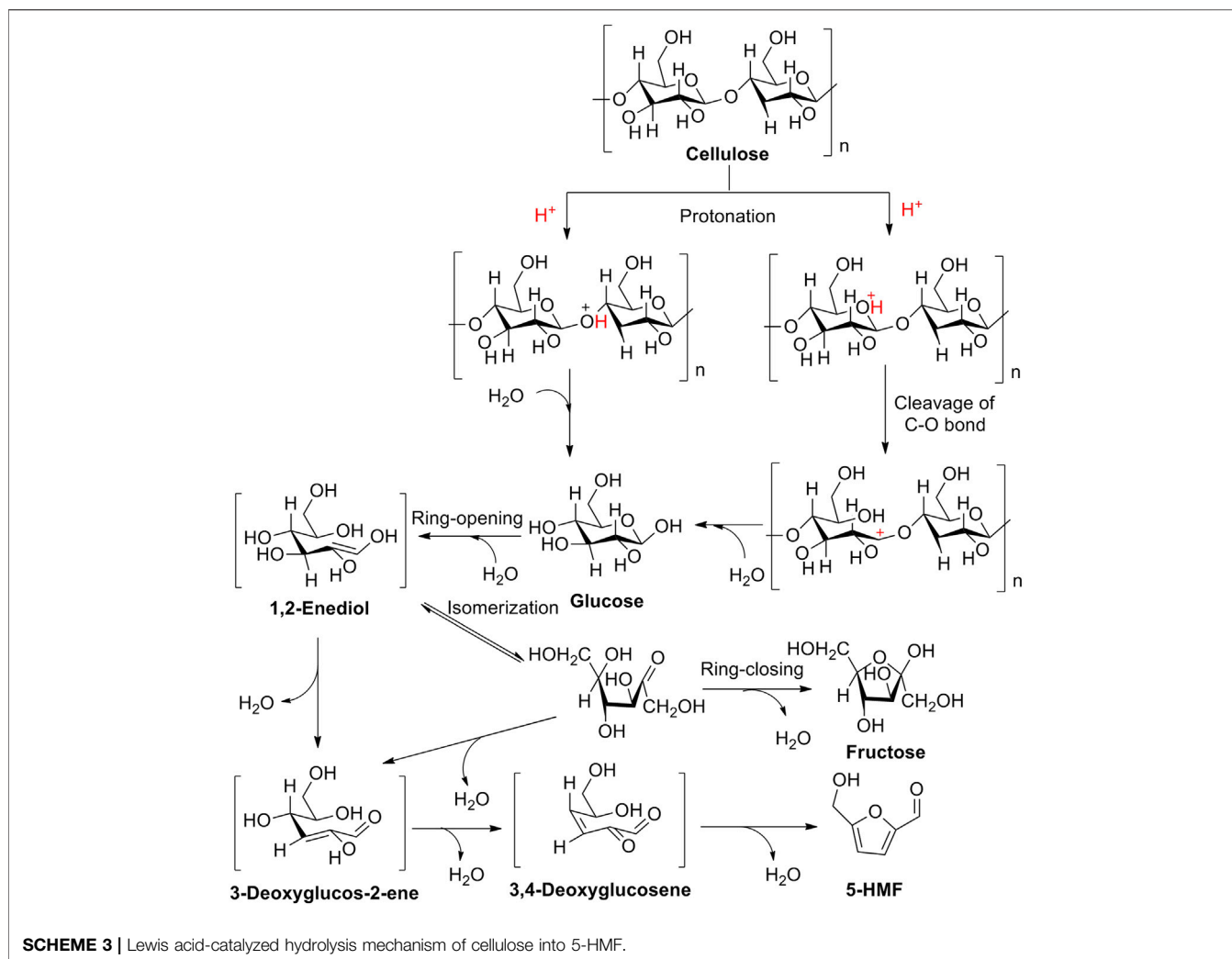
5.2 Carbon-Based Acid Catalysts

Carbon is the most basic element in bio-organism. Carbon-based materials such as activated carbon (AC), graphite, hydrothermal carbon, graphene, and carbon nanotube (CNT) have been in popularity in the design of novel functional carbon-based materials because carbon-based materials as potential supporters are capable to be in charge of the construction of novel frameworks. The novel Nb–carbon composite is a class of bifunctional carbon-based catalysts in possession of varying amounts of Brønsted and Lewis acid sites, which are able to be prepared by means of the hydrothermal carbonization method. Relying on the determination of catalytic activity for the hydrolysis and dehydration of cellulose, the agglomerated particle of Nb/C-50 can effectively enhance the selectivity of 5-HMF, which was achieved with a 53.3% yield of 5-HMF in a THF/ H_2O biphasic system at 170°C for 8 h (**Figure 6**) (Li Z. et al., 2018).

With the development of effective approaches to conversions of biomass, the eco-friendly and energy-efficient methods for cellulose conversion to 5-HMF were developed using modified activated carbon (AC) immobilized with metal ions. Activated

carbon (AC) is a common carbon-based material. Via the treatment of diluted acid H_2SO_4, H_3PO_4, and HCl, it can, respectively, gain modified activated carbon supporters (ACS, ACP, and ACH). These supporters undergoing the immobilization of metal ions (M^{+n} = Cr^{+3}, Fe^{+3}, Cu^{+2}, Zn^{+2}, K^+, and Al^{+3}) in aqueous media were successfully transformed into carbon-based catalysts M-ACS/ACP/ACH. In the identification of catalytic activity, a potent metal carbon-based Cr-ACS catalyst was identified to be effective for 5-HMF conversion from cellulose, assisting ionic liquid [Bmim]Cl as a medium. Of course, it is emphasized here that immobilized metal ions can effectively improve Lewis acidic sites on the surface of catalysts (Tyagi et al., 2018).

In the same year, the supporter of graphite-like mesoporous carbon material Sibunit had been documented by Gromov et al. (2018). Virtually, the supporter is also a carbon-based material. As a result of its inherent mesoporous properties, the carbon Sibunit treated by the following procedures of sulfonation, oxidation, and additional reaction for all the oxidized carbons sulfonated at 200°C was developed for the successive solubilization, hydrolysis, and dehydration of cellulose into 5-
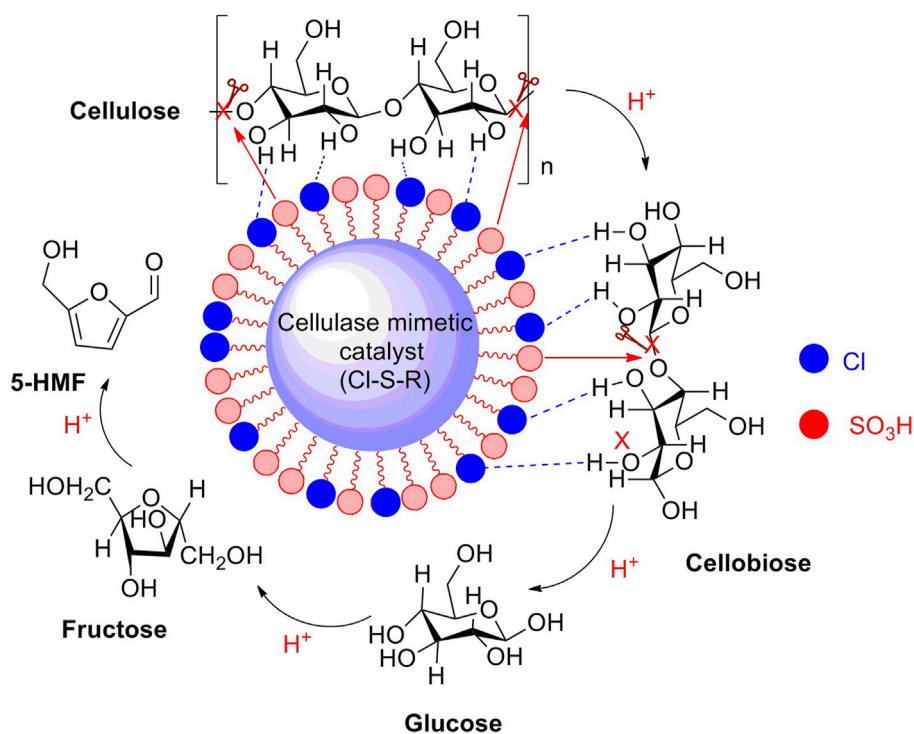
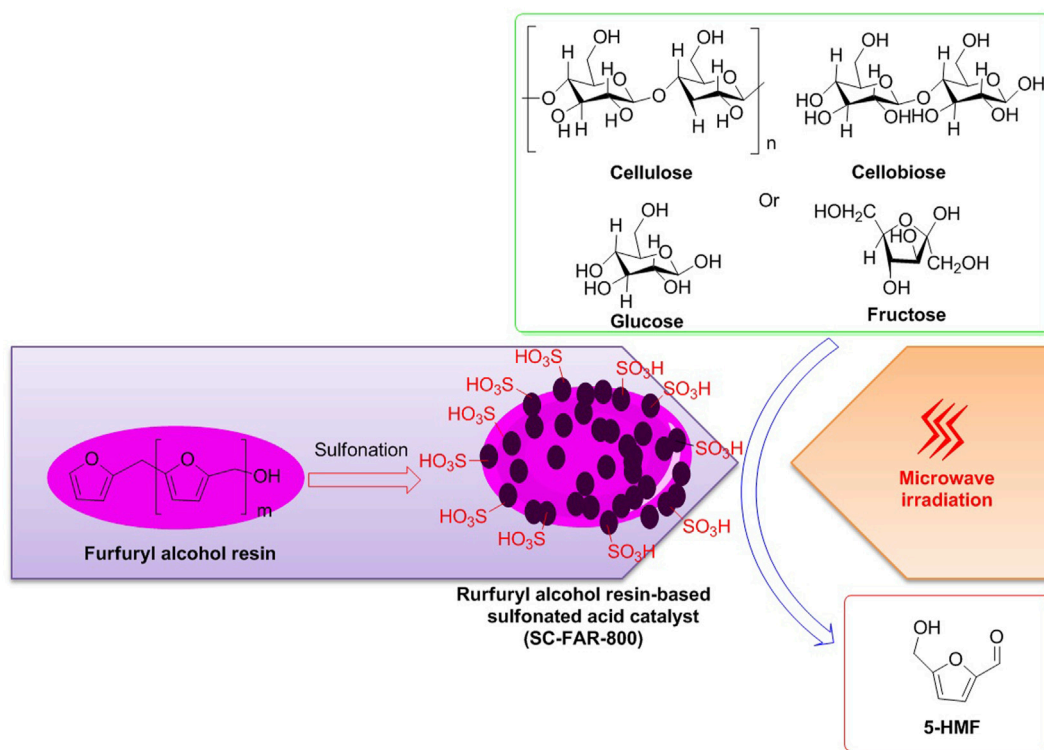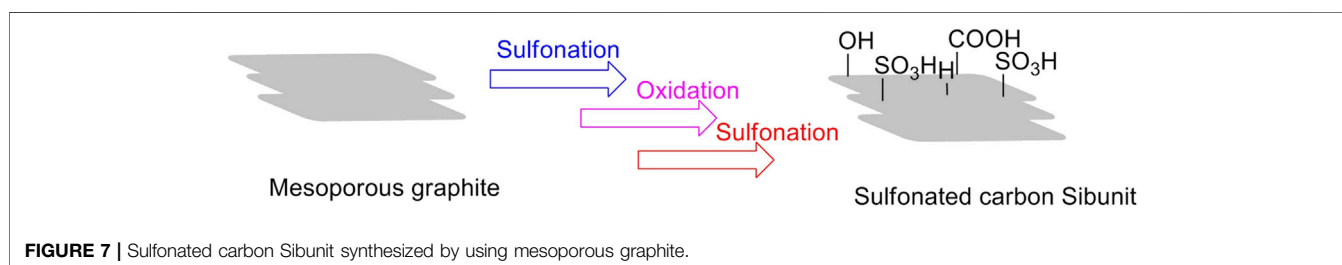**FIGURE 4 |** Route of cellulose converted into 5-HMF promoted by a solid acid catalyst (Cl$_{0.3}$-S-R).
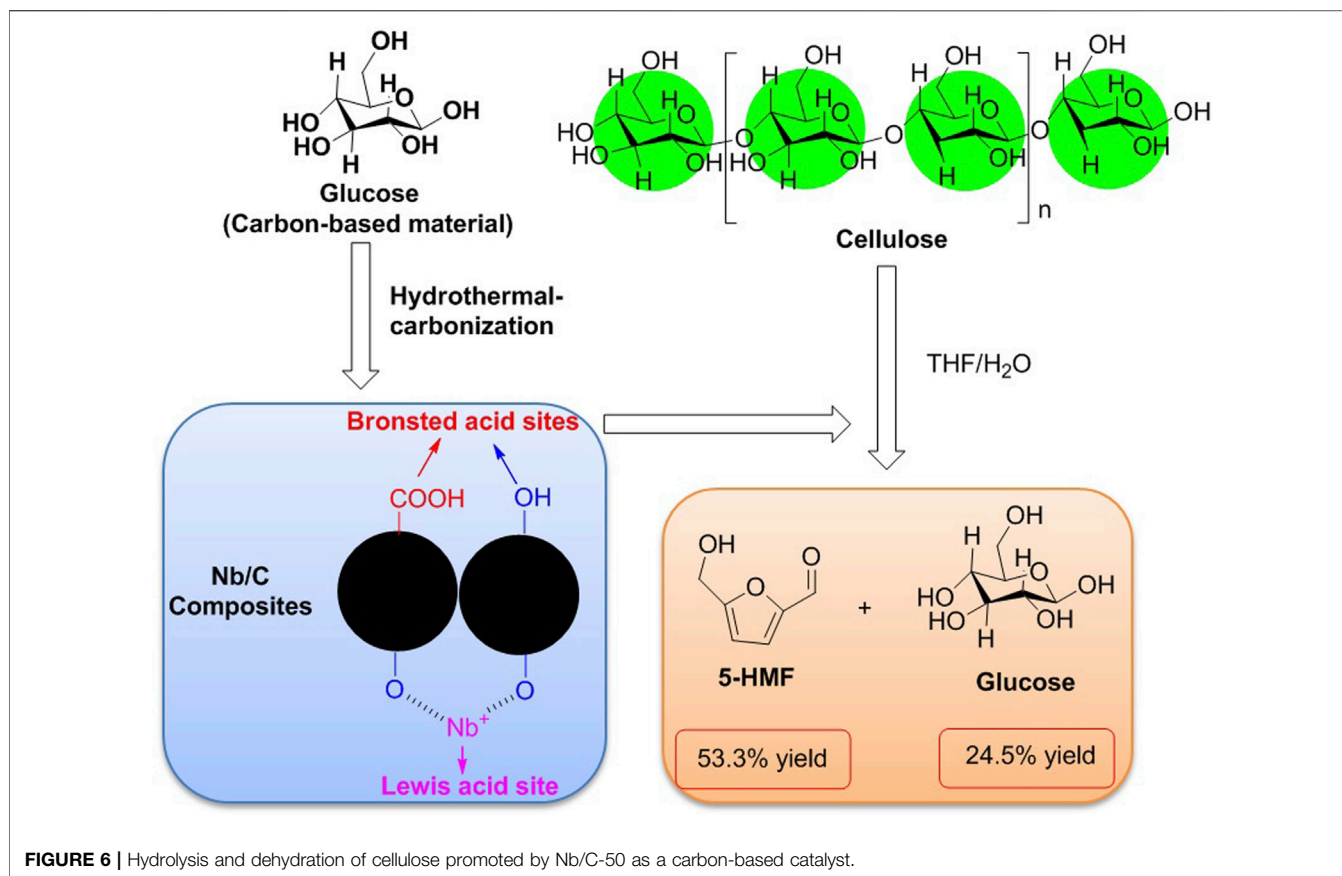

FIGURE 5 | Catalyst SC-FAR-800 employed for biomass conversions into 5-HMF, with the assistance of microwave irradiation.

FIGURE 6 | Hydrolysis and dehydration of cellulose promoted by Nb/C-50 as a carbon-based catalyst.

FIGURE 7 | Sulfonated carbon Sibunit synthesized by using mesoporous graphite.

HMF in a one-pot reaction. The depolymerization of microcrystalline cellulose began at 180°C in water, in the presence of sulfonated carbon Sibunit solid acid. The main product 5-HMF could be achieved with the maximum yield of 22%, which was possibly ascribed to the formation of acidic groups (sulfuric, phenolic, and carboxylic groups) on the external surface of the carbon Sibunit (**Figure 7**) (Gromov et al., 2018).

Similarly, novel supporters of hydrothermal carbons (HTCs) as sugar-derived carbon materials prepared from monosaccharides are allowed to be obtained by suitable hydrothermal carbonizations (including reaction temperature and time). Subsequently, the resulting HTCs following the sulfonation can be transformed into potential novel carbon-based solid acids. The carbon-based acid (HTC220-6-SO$_3$H) acting as a representative example was afforded through the

hydrothermal carbonization of glucose for 6 h at 220°C, and subsequently the sulfonation for 15 h at 150°C. The HTC220-6-SO$_3$H solid acid acting as a novel catalyst exhibited relatively high catalytic activity for the selective hydrolysis of cellulose and dehydration of fructose, indicating that sulfuric acidity (Brønsted acidity) can be responsible for the conversion to glucose and 5-HMF, with 43.63 and 20.29% yields of glucose and 5-HMF, respectively (Wataniyakula et al., 2018).

Bio-carbon is one of the most promising carbon-based materials. Cellulose, acting as a representative bio-carbon, is usually considered to be a biomass raw feedstock for biomass conversions and an effective supporter for carbon-based catalysts. In recent studies, the supporter of cellulose *via* moderate formylation was facilely developed for cellulose formate (CF) production. The CF production with a special net-like structure
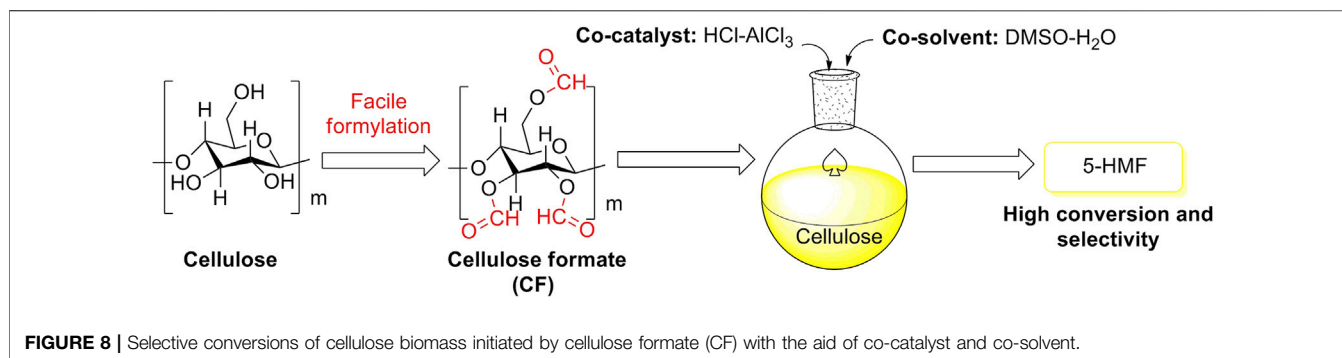
FIGURE 8 | Selective conversions of cellulose biomass initiated by cellulose formate (CF) with the aid of co-catalyst and co-solvent.

TABLE 1 | Comparison of the cellulose to 5-HMF catalyzed by $FeCl_3$, $RuCl_3$, $TiCl_3$, and VCl_3 in the biphasic system (with or without NaCl in aqueous phase). (Jin et al., 2021)

Cat	Conditions	NaCl addition (%)	Organic phase	Cellulose conversion (%)	5-HMF selectivity (%)	5-HMF yield (%)
$FeCl_3$	220C/20 min	35%	Butanol	97.3	75.2	73.2
		0	Butanol	97.3	62.0	60.3
		0	MIBK	97.3	55.3	53.8
		0	Hexanol	97.3	53.0	51.6
$RuCl_3$	220C/30 min	35%	Butanol	95.2	87.5	83.3
		0	Butanol	95.2	67.8	64.6
		0	MIBK	95.2	64.6	61.4
		0	Hexanol	95.2	61.8	58.8
VCl_3	220C/40 min	35%	Butanol	88.6	80.5	71.3
		0	Butanol	88.6	62.7	55.6
		0	MIBK	88.6	59.5	52.7
		0	Hexanol	88.6	56.9	50.4
$TiCl_3$	220C/40 min	35%	Butanol	90.8	79.7	72.4
		0	Butanol	90.8	66.4	60.3
		0	MIBK	90.8	64.2	58.7
		0	Hexanol	90.8	61.9	56.2

Note: MIBK is methyl isobutyl ketone; catalyst loading: 0.125 mol/L.

and a high degree of formyl substitution was successfully applied to the selective conversions of cellulose biomass, assisting co-catalyst of HCl-AlCl₃ and co-solvent of DMSO-H₂O (**Figure 8**) (Jin et al., 2021). The exhibitions of conversion and selectivity to 5-HMF appeared to be excellent, as compared to monomeric glucose as another bio-carbon supporter (**Table 1**).

5.3 Zeolite Catalysts

To the best of our knowledge, the framework of zeolite presents a promising constitution for a novel solid catalyst. In general, once non-/noble metal ions are inhered on the external surface of a zeolite structure, the catalytic activity of metal–zeolite material will be effectively improved, due to the enhancement of pore volumes and Lewis acidic sites on the external surface of the metal–zeolite occurred. In 2020, the access gateway of non-/noble metal ions (Cu^{+2} and Cr^{+3}) loaded on the external surface of ZSM-5 zeolite particles to the establishment of Cu-Cr-based zeolite was achieved by means of the ion exchange method. The highly crystalline Cu–Cr/ZSM-5 zeolite applied to the catalytic conversion of glucose into 5-HMF was smoothly initiated under suitable conditions, with good performance in conversion and selectivity (Chung et al., 2020).

Catalytic activity is always the key index for evaluating the performance of catalysts. Some classic zeolites of HY, Hβ,

H-mordenite, and HZSM-5 as conventional solid catalysts are further discussed in catalytic activities for biomass conversions. In 2021, Zheng et al. (2021) reported on selective conversions of cellulose and starch over classic zeolites. The experimental results indicated that Hβ zeolite having appropriate Brønsted and Lewis acid sites becomes an effective promoter for furfural conversion from cellulose and starch. Simultaneously, HY zeolite with weak acidity is a flexible access to the transformation of 5-HMF from starch. H-mordenite and HZSM-5 zeolites bearing fewer Lewis acid sites on their external surfaces enable to inhibit the isomerization from glucose to fructose. On the whole, the generation of 5-HMF is closely correlated to the acid properties of zeolites. Simultaneously, it is confirmed that the acidity of zeolites can determine the target product formation.

Furthermore, the multifunctional zeolite catalyst (Ru/HY-SO₃H) was developed by the introduction of Lewis and Brønsted acidic sites on the surface of zeolite for the selective cellulose conversion to 5-HMF, which was successfully prepared under metal immobilization and sulfonation (Wang et al., 2021b). Under light illumination and low temperature (120°C), the Ru/HY-SO₃H, with the help of an ionic liquid/methyl isobutyl ketone biphasic medium, was capable of being a potent solid acid catalyst for the production of 5-HMF converted from cellulose. More
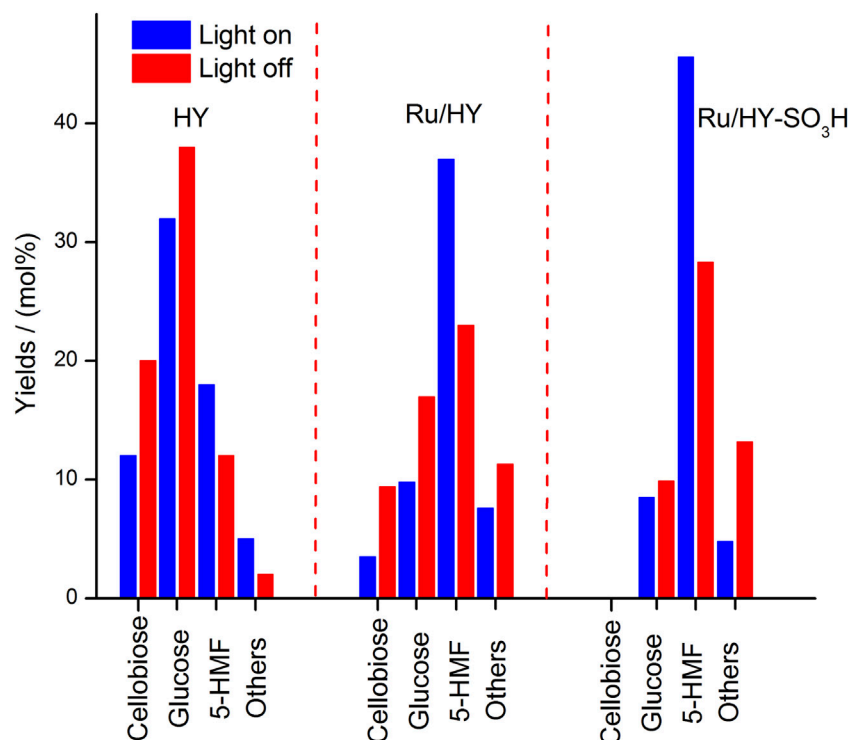
FIGURE 9 | Performance on cellulose conversion over zeolite catalysts (Ru/HY-SO$_3$H, Ru/HY, and HY) with/without light irradiation in a biphasic system.

significantly, the external surface of Ru/HY-SO$_3$H irradiated by high-intensity light could be initiated on the plasmon resonance effect for the direct cellulose conversion, with a 48.4% yield of 5-HMF as selective production. Nevertheless, as compared to precursors of Ru/HY-SO$_3$H, the promotions for selective conversion to 5-HMF by HY and Ru/HY were being on less in yields under the same conditions (**Figure 9**). It is implied that the formation of the plasmon resonance effect on the external surface of Ru/HY-SO$_3$H can enhance more acidic sites for the selective conversion of microcrystalline cellulose.

Pham et al. (2020) disclosed a series of bifunctional sulfonated mesoporous silica materials used for the conversion of cellulose into 5-HMF in the Teflon-lined stainless steel reactor. These mesoporous silica catalysts (Zr-MCM-41) synthesized following the *in situ* method and sulfonation were given varied Brønsted acidic sites, which were identified by NH$_3$-TPD analysis. Under heating for 2 h at 170°C, the sulfonated acid of S-15Zr-MCM-41 (73.44 wt% in silicon, 14.78 wt% in zirconium, and 11.78 wt% in sulfur) was allowed to be 70.2 and 16.4% in the conversion of cellulose and selectivity of 5-HMF, which were more than MCM-41 without sulfonation being on the conversion and selectivity of 15.2 and 1.3%.

5.4 Heteropoly Acids

Heteropoly acids (HPAs) are a type of unique combination of hydrogen cations and polyoxometalate anions, which are composed of transition metal–oxygen anion clusters. Stable heteropoly acid (HPA) with strong Brønsted acidity and mild

Lewis acidity is reckoned as an effective solid acid that is significant for the efficient conversion of renewable biomass to valuable chemicals. In 2015, a novel ionic crystal of metal-based HPA was emerged in the conversion of monosaccharides into 5-HMF. Cs$_2$[Cr$_3$O(OCC$_2$H$_5$)$_6$(H$_2$O)$_3$]$_2$[α-SiW$_{12}$O$_{40}$] acting as an HPA ionic crystal was witnessed to be a novel heterogeneous acid catalyst, with identifying components (W, 49.37; Cr, 6.83; Cs, 5.85; Si, 0.61 wt.%), in the dehydration of fructose or glucose into 5-HMF. The effects for fructose or glucose selectively dehydrated into 5-HMF were being on desirable results that were, respectively, 86 and 56% in yields of 5-HMF in DMSO media. In further investigation, the experimental results were demonstrated that lower Brønsted acidity of the HPA ionic crystal profits for the stabilization of 5-HMF with weak polarity, which may be a rational explanation for better catalytic performance of the HPA ionic crystal, as compared to conventional HPA (H$_4$SiW$_{12}$O$_{40}$) (Yi et al., 2015). In 2020, a novel strategy for synthesizing a series of temperature-responsive HPA catalysts (Ch$_n$H$_{5-n}$CeW$_{12}$O$_{40}$, n = 1–5) was proposed by Lai et al. The Ce-based HPA of ChH$_4$CeW$_{12}$O$_{40}$ was responsible for one-pot production of 5-HMF from cellulose, with the achievement of 67.5% in yield in a biphasic system (**Figure 10**) (Lai et al., 2020).

In addition, in terms of catalytic dehydration of fructose to 5-HMF by HPA, the newly plausible pathway for PW$_{12}$-ILs-C$_4$-HNS-catalyzed dehydration process of fructose to 5-HMF in DMSO was proposed by An Z. et al. (2019) (**Scheme 4**) (An Z. et al., 2019).
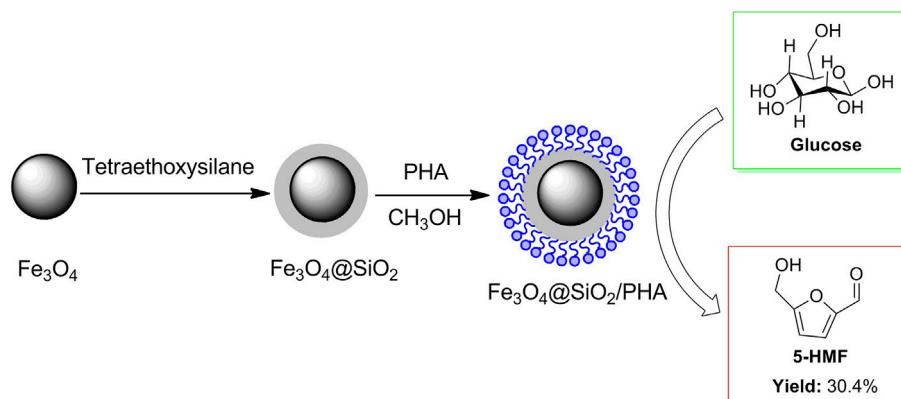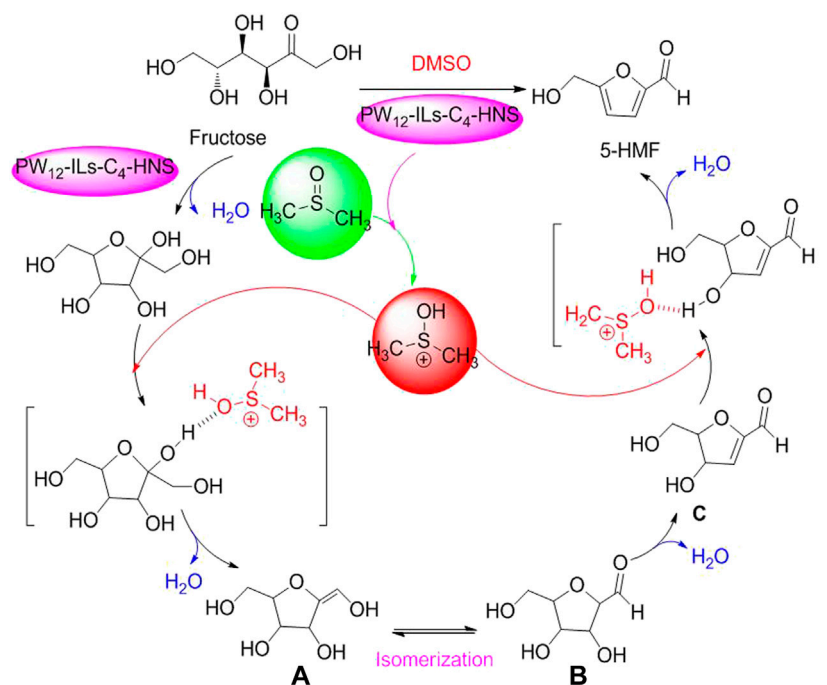
FIGURE 10 | Synthesis and application of Fe$_3$O$_4$@SiO$_2$/PHA in glucose conversion.

SCHEME 4 | Proposed mechanism for selective conversion of fructose into 5HMF with the assistance of DMSO.

As shown in **Scheme 3**, the media molecule of DMSO is first activated by an active proton originating from PW$_{12}$-ILs-C$_4$-HNS. Then, the interactions between the activated DMSO and fructose happened through the formation of hydrogen bonds. With the release of H$_2$O, the intermediate of enol **A** is formed. Enol **A** is transformed to corresponding aldehyde **B** (2, 5-anhydro-D-mannose) via isomerization. Afterward, the dehydrated product **C** is authorized to transform into 5-HMF via successive dehydration in the presence of PW$_{12}$-ILs-C$_4$-HNS and activated DMSO. PW$_{12}$-ILs-C$_4$-HNS as a novel PHA is a multicomponent solid acid, composed of phosphotungstic acid (H$_3$PW$_{12}$O$_{40}$) and organosilica ((EtO)$_3$ Si-ILs-C$_4$) via

immobilization to form corresponding organosilica hollow nanospheres. In terms of the organosilica hollow nanospheres, it was clearly figured out that H$_3$PW$_{12}$O$_{40}$ of PW$_{12}$-ILs-C$_4$-HNS HPA is a Brønsted acid site, enabling strong electrostatic interactions with ILs. In practical biomass conversion application, the PW$_{12}$-ILs-C$_4$-HNS PHA exhibited excellent catalytic capacity and selectivity for acid-catalyzed dehydration of fructose to 5-HMF, under the conditions of DMSO as good media and heating for 2 h at 100°C. Moreover, the data of 93.7 % yield of 5-HMF and over six catalytic cycles were adequately witnessed that PW$_{12}$-ILs-C$_4$-HNS PHA is a cost-effective and environmentally benign catalyst (An S. et al., 2019). Similarly,

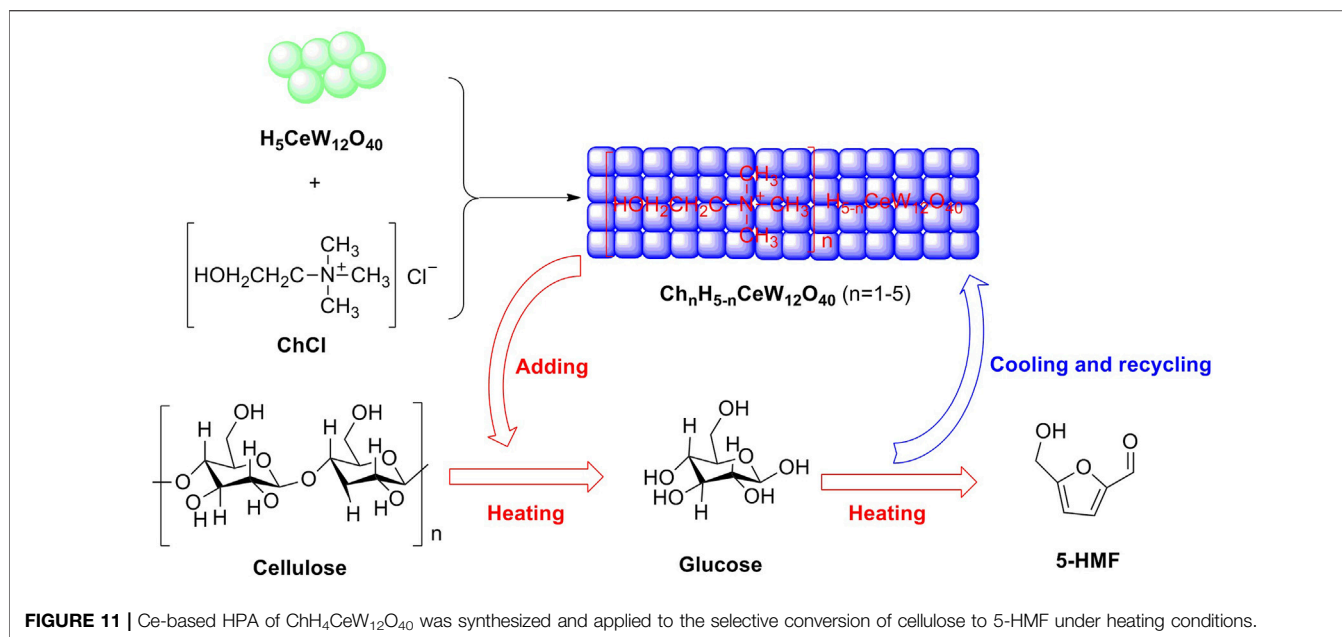**FIGURE 11 |** Ce-based HPA of $ChH_4CeW_{12}O_{40}$ was synthesized and applied to the selective conversion of cellulose to 5-HMF under heating conditions.

glucose as a common monosaccharide, used as biomass feedstock to be upgraded into high value-added chemicals, has attracted extensive attention (Han et al., 2018; Li X. et al., 2018; Wei and Wu., 2018). The establishment of HPW-Nb_2O_5 calcined at 300°C to the selective conversion of glucose into 5-HMF was promptly documented in 2020 (Siqueira Mancilha Nogueira et al., 2020). The HPW-Nb_2O_5 was prepared through the combination of Nb_2O_5 (HY-340) as a support with $H_3PW_{12}O_{40}$ as an active phase and subsequently calcination at 300°C. In optimizing reaction conditions, reaction temperature, reaction media, substrate concentration, and catalyst amount as essential factors were evaluated via Taguchi's L_{16} experimental design. As a result, glucose at a concentration of 50g/L was allowed to be efficiently converted to 5-HMF (40.8% in yield), loading the HPW-Nb_2O_5 PHA (5%, w/v), with acetone–water media (1:1, v/v in ratio) at 160°C.

5.5 Other Solid Acids

In addition to aforementioned heterogeneous solid acids, other solid acids are still able to exhibit excellent catalytic activity for biomass conversions. The 2Al/SBA-15 catalyst containing 9.70 wt % in Al with a high amount of medium acid sites was permitted to be synthesized by means of the atomic implantation method. Because of the incorporation of appropriate Al amount into the framework of SBA-15, solid acid could present medium and strong acidic sites. Moreover, the catalytic activity and selectivity for the 2Al/SBA-15 were testified in the degradation of cotton cellulose to 5-HMF under mild hydrothermal conditions, with the performance of 2Al/SBA-15 in cellulose transformation with 5-HMF yield and selectivity of 68.5 and 62.1%, which was better than that of 3Al/SBA-15 (12.56 wt% in Al) with 46.03 and 64.49% in yield and selectivity of 5-HMF. The cause might be attributed to the formation of Al_2O_3 particles covering the acid sites created after the second Al layer deposition (Pham et al., 2019).

D-glucose, a complete hydrolysate of cellulose, is usually used as biomass raw material to synthesize refining industrial substances in biomass conversions. Actually, the conversion of glucose into 5-HMF is a crucial intermediate step for cellulose being converted to 5-HMF. Considering the convenient separation of a catalyst from the mixture, a magnetic solid acid $Fe_3O_4@SiO_2/PHA$ was prepared by phosphotungstic acid (Brønsted acid) supported on magnetic nanoparticles (Fe_3O_4) coated by SiO_2 (**Figure 11**) (Wang Y. et al., 2019). The magnetic solid acid in possession of good recovery by an external magnet could be on the run for four cycles in the glucose conversion to 5-HMF, without catalytic activity declining significantly.

In addition, heterogeneous catalysis asks for the catalyst and catalytic substrate to be in a varying phases and interacted on the external surface of the catalyst. Briefly, the catalyst is disabled to be dissolved in the solvent in the catalytic system. Therefore, inorganic metal salts are considered to be potential heterogeneous catalysts in the organic solvent. In 2019, an efficient strategy for one-pot conversion of microcrystalline cellulose into 5-HMF was introduced by the employment of non-/noble metal salts (e.g., $FeCl_3$, $RuCl_3$, VCl_3, $TiCl_3$, $MoCl_3$, and $CrCl_3$) in a biphasic system. The catalytic results demonstrated that $RuCl_3$ as a potent catalyst exhibits excellent performance in the selectivity and conversion, with 83.3 and 87.5% in yield and selectivity of 5-HMF, in the NaCl aqueous/butanol biphasic system. Notably, the decrystallization and cleavage of 1, 4-glycosidic bonds in cellulose were able to be promoted through the interaction between transition metal chloride and cellulose, and subsequently, the consecutive isomerization, dehydration, and elimination of glucose being transformed into 5-HMF occurred (Yan et al., 2019).

In the same year, a hydrothermal solid acid $(Yb_6(BDC)_7(OH)_4(H_2O)_4)$ containing both bridging hydroxyls and metal-coordinated waters was introduced by Burnett et al. in glucose biomass conversions. The stable ytterbium metal–organic

framework in possession of Brønsted and Lewis acid sites was considered to be a bifunctional catalyst, by which the conversion of glucose to 5-HMF was achieved successfully with 70% in selectivity in aqueous media (Burnett et al., 2019). With a similarity to the promotion of glucose into 5-HMF by $Yb_6(BDC)_7(OH)_4(H_2O)_4$ in water, transition metal–oxide nanosheet aggregates, such as $HNbWO_6$, HNb_3O_8, and $HTiNbO_5$, were prepared by means of successive exfoliation and aggregation of layered metal oxides, which were good for yielding 5-HMF under hydrothermal conditions. In the conversion performance for 5-HMF, the catalytic capacities of these aggregated nanosheets were much better than that of ion-exchange resins and H-form zeolites under the same conditions. Meanwhile, it found that $HNbWO_6$ nanosheets with an acid amount of 0.34 mmol/g exhibited higher selectivity for glucose conversion in the H_2O–toluene biphasic system than fructose conversion (Takagaki, 2019). As a developing catalytic pathway of biomass conversion, a catalytic fast pyrolysis of cellulose biomass yielding value-added platform chemical 5-HMF was initiated over zirconium–tin mixed metal oxides (ZrO_2–SnO_2). The ZrO_2–SnO_2 metal oxide with 15 wt% Zr loading was mainly in charge of the increase in 5-HMF yield and selectivity, in a catalyst-to-cellulose ratio of 2/1, at 350°C as a pyrolysis temperature. In testifying the catalytic scope of ZrO_2-SnO_2-15 as a catalyst, various saccharides, such as cellobiose, maltose, glucose, and mannose, used as biomass stocks for selective conversion to 5-HMF were, respectively, evaluated under the same conditions. The conversion results indicated that the effects for the 5-HMF yield of glucose and mannose are slightly different, with 5-HMF yields of 12.16 wt% and 11.07 wt%. Maltose and cellobiose are deemed to be a dimer of amylose and cellulose, including, respectively, α- and β-O-4 glycosidic bonds. In their selectively catalytic pyrolysis, the yield of selective product 5-HMF from maltose and cellobiose were, respectively, 14.63 wt% and 14.21 wt% over ZrO_2-SnO_2-15 catalysts, which may be more conductive for α- and β-O-4 glycosidic bonds (Li Y. et al., 2021).

6 CONCLUSION AND OUTLOOK

More efficient biomass conversions into various refining chemicals become a hot topic of lower carbon energy regeneration and sustainability. Cellulose is the most abundant bio-based component in lignocellulosic biomass, with both microcrystalline and amorphous forms. Microcrystalline cellulose with a robust crystalline structure composed of β-1, 4-glycosidic bonds of D-glucose is limited to be automatically hydrolyzed into simple monosaccharides (e.g., glucose and fructose) in an aqueous solution. So, the degradation of cellulose becomes a difficulty in biomass conversions. High value-added chemicals (e.g., 5-HMF, THF, furfuryl alcohol, and levulinic acid) are the focus of renewable and sustainable biomass conversions all the time. The industrial production of 5-HMF acting as a monosaccharide derivative becomes a building block for biomass conversion, which can be responsible for a bridge between cellulose biomass and deeply refining high-value chemicals (e.g., FDCA, HMFCA, FFCA, DFF, BAMF, THFDM, DMF, and MFC). At present, the efficient strategy

for selective conversion of cellulose biomass into 5-HMF should be attributed to acid-catalyzed dehydration/hydrolysis of cellulose in the presence of a potent acid catalyst. In this review, we summarize and discuss some catalytic strategies for acid-catalyzed dehydration/hydrolysis of cellulose into 5-HMF over varying novel solid acids. On the basis of Brønsted acid catalysis/Lewis acid catalysis, the strategies for selective conversion of cellulose into 5-HMF loading varying novel solid acids are categorized into the following: (I) employment of sulfonated solid acid catalysts to the selective conversion of cellulose biomass into 5-HMF, (II) carbon-based acids with novel frameworks utilized to the synthesis of value-added chemical of 5-HMF, (III) 5-HMF converted from cellulose occurred on the external surface of zeolite catalysts, and (IV) selective acid-catalyzed transformation into 5-HMF from cellulose biomass by other heterogeneous solid acids. Totally, powerful solid acid as a heterogeneous catalyst employed for the selective conversion of cellulose biomass into 5-HMF is undoubtedly effective access to biomass conversions in the laboratory.

To the best of our knowledge, the reactivity of 5-HMF has been well recognized by chemists. The functional groups (-CH_2OH and C=O) located on the furan ring of 5-HMF are facilitated to be transformed into expected moieties to afford corresponding high value-added chemicals, via selectively catalytic oxidation/reduction. Nevertheless, it requires well that related oxidant/reductant with powerful selectivity and catalytic capacity are well developed. 5-HMF is widely regarded as a promising candidate for well-known bio-based platform compounds. Relying on its functional groups' oxidation/reduction, various furfuryl derivatives are permitted to be afforded to support the development of renewable and sustainable biomass resources. Therefore, in the current multicarbon energy crisis, 5-HMF is capable of being a pioneer for developing lower carbon energy. In future works involving biomass conversion, considering complicated components of raw biomass resources, designing a well-tolerated/-selective heterogeneous acid catalyst is still a necessity for biomass conversions with high selectivity on large-scale production.

In summary, the objective of this review is to disclose available strategies for 5-HMF selectively converted from cellulose biomass, opportunities and challenges faced by various solid acid catalysts in the heterogeneous catalysis system and to provide reactivity of 5-HMF (oxidation and reduction) upgrading into varying refining high-value chemicals and some Brønsted/Lewis acid catalysis theory for guiding future biomass development.

AUTHOR CONTRIBUTIONS

YY and SC were in charge of writing the manuscript. SC contributed equally to this work. MZ was in charge of drawing Figures and Schemes.

FUNDING

REFERENCES

An, S., Wang, Z., Zhang, H., Miras, H. N., and Song, Y. F. (2019). Self-Organization of Ionic Liquid-Modified Organosilica Hollow Nanospheres and Heteropolyacids: Efficient Preparation of 5-HMF under Mild Conditions. *Chem.Cat.Chem* 11 (10), 2526–2536. doi:10.1002/cctc.201900285

An, Z., Wang, W., Dong, S., and He, J. (2019). Well-distributed Cobalt-Based Catalysts Derived from Layered Double Hydroxides for Efficient Selective Hydrogenation of 5-hydroxymethyfurfural to 2,5-methylfuran. *Catal. Today* 319, 128–138. doi:10.1016/j.cattod.2018.03.052

Bai, S.-T., De Smet, G., Liao, Y., Sun, R., Zhou, C., Beller, M., et al. (2021). Homogeneous and Heterogeneous Catalysts for Hydrogenation of CO2 to Methanol under Mild Conditions. *Chem. Soc. Rev.* 50 (7), 4259–4298. doi:10.1039/D0CS01331E

Barwe, S., Weidner, J., Cychy, S., Morales, D. M., Dieckhöfer, S., Hiltrop, D., et al. (2018). Electrocatalytic Oxidation of 5-(Hydroxymethyl)furfural Using High-Surface-Area Nickel Boride. *Angew. Chem. Int. Ed.* 57, 11460–11464. doi:10.1002/anie.201806298

Benabbas, R., Sanchez-Ballester, N. M., Bataille, B., Sharkawi, T., and Soulairol, I. (2021). Development and Pharmaceutical Performance of a Novel Co-processed Excipient of Alginic Acid and Microcrystalline Cellulose. *Powder Technol.* 378, 576–584. doi:10.1016/j.powtec.2020.10.027

Burnett, D. L., Oozeerally, R., Pertiwi, R., Chamberlain, T. W., Cherkasov, N., Clarkson, G. J., et al. (2019). A Hydrothermally Stable Ytterbium Metal-Organic Framework as a Bifunctional Solid-Acid Catalyst for Glucose Conversion. *Chem. Commun.* 55, 11446–11449.

Cao, W., Li, J., Martí-Rosselló, T., and Zhang, X. (2019). Experimental Study on the Ignition Characteristics of Cellulose, Hemicellulose, Lignin and Their Mixtures. *J. Energ. Inst.* 92 (5), 1303–1312. doi:10.1016/j.joei.2018.10.004

Chai, Y., Dai, W., Wu, G., Guan, N., and Li, L. (2021). Confinement in a Zeolite and Zeolite Catalysis. *Acc. Chem. Res.* 54 (13), 2894–2904. doi:10.1021/acs.accounts.1c00274

Charmot, A., and Katz, A. (2010). Unexpected Phosphate Salt-Catalyzed Hydrolysis of Glycosidic Bonds in Model Disaccharides: Cellobiose and Maltose. *J. Catal.* 276, 1–5. doi:10.1016/j.jcat.2010.08.006

Chen, L., Yang, W., Gui, Z., Saravanamurugan, S., Riisager, A., Cao, W., et al. (2019). MnOx/P25 with Tuned Surface Structures of Anatase-Rutile Phase for Aerobic Oxidation of 5-hydroxymethylfurfural into 2,5-diformylfuran. *Catal. Today* 319, 105–112. doi:10.1016/j.cattod.2018.05.049

Choudhary, V., Pinar, A. B., Lobo, R. F., Vlachos, D. G., and Sandler, S. I. (2013). Comparison of Homogeneous and Heterogeneous Catalysts for Glucose-To-Fructose Isomerization in Aqueous media. *ChemSusChem* 6, 2369–2376. doi:10.1002/cssc.201300328

Chung, N. H., Oanh, V. T., Thoa, L. K., and Hoang, P. H. (2020). Catalytic Conversion of Glucose into 5-hydroxymethyl Furfural over Cu-Cr/ZSM-5 Zeolite. *Catal. Lett.* 150, 170–177. doi:10.1007/s10562-019-02922-4

Dalli, S. S., Tilaye, T. J., and Rakshit, S. K. (2017). Conversion of wood-based Hemicellulose Prehydrolysate into Succinic Acid Using a Heterogeneous Acid Catalyst in a Biphasic System. *Ind. Eng. Chem. Res.* 56 (38), 10582–10590. doi:10.1021/acs.iecr.7b01708

Danielli da Fonseca Ferreira, A., Dorneles de Mello, M., and da Silva, M. A. P. (2018). Catalytic Oxidation of 5-Hydroxymethylfurfural to 2,5-Furandicarboxylic Acid over Ru/Al2O3 in a Trickle-Bed Reactor. *Ind. Eng. Chem. Res.* 58, 128–137. doi:10.1021/acs.iecr.8b05602

Danish, M., and Ahmad, T. (2018). A Review on Utilization of wood Biomass as a Sustainable Precursor for Activated Carbon Production and Application. *Renew. Sustain. Energ. Rev.* 87, 1–21. doi:10.1016/j.rser.2018.02.003

De, S., Mishra, S., Poonguzhali, E., Rajesh, M., and Tamilarasan, K. (2020). Fractionation and Characterization of Lignin from Waste rice Straw: Biomass Surface Chemical Composition Analysis. *Int. J. Biol. Macromolecules* 145, 795–803. doi:10.1016/j.ijbiomac.2019.10.068

Delidovich, I., and Palkovits, R. (2015). Structure-performance Correlations of Mg-Al Hydrotalcite Catalysts for the Isomerization of Glucose into Fructose. *J. Catal.* 327, 1–9. doi:10.1016/j.jcat.2015.04.012

Den Haan, R., Rose, S. H., Lynd, L. R., and van Zyl, W. H. (2007). Hydrolysis and Fermentation of Amorphous Cellulose by Recombinant saccharomyces Cerevisiae. *Metab. Eng.* 9, 87–94. doi:10.1016/j.ymben.2006.08.005

Espro, C., Paone, E., Mauriello, F., Gotti, R., Uliassi, E., Bolognesi, M. L., et al. (2021). Sustainable Production of Pharmaceutical, Nutraceutical and Bioactive Compounds from Biomass and Waste. *Chem. Soc. Rev.* 50, 11191–11207. doi:10.1039/D1CS00524C

Flores-Velázquez, V., Córdova-Pérez, G. E., Silahua-Pavón, A. A., Torres-Torres, J. G., Sierra, U., Fernández, S., et al. (2020). Cellulose Obtained from Banana Plant Waste for Catalytic Production of 5-HMF: Effect of Grinding on the Cellulose Properties. *Fuel* 265, 116857–116867. doi:10.1016/j.fuel.2019.116857

Gadge, G. G. (2020). An Overview: Natural Polymers and Their Applications. *Rese. Jour. Pharmaceut. Dosag. Form. Technol.* 12 (2), 131–136. doi:10.5958/0975-4377.2020.00023.3

Gazi, S. (2019). Valorization of wood Biomass-Lignin via Selective Bond Scission: A Minireview. *Appl. Catal. B: Environ.* 257, 117936–117953. doi:10.1016/j.apcatb.2019.117936

Gromov, N. V., Medvedeva, T. B., Taran, O. P., Bukhtiyarov, A. V., Aymonier, C., Prosvirin, I. P., et al. (2018). Hydrothermal Solubilization-Hydrolysis-Dehydration of Cellulose to Glucose and 5-hydroxymethylfurfural over Solid Acid Carbon Catalysts. *Top. Catal.* 61, 1912–1927. doi:10.1007/s11244-018-1049-4

Güell, E. J., Maru, B. T., Chimentão, R. J., Gispert-Guirado, F., Constantí, M., and Medina, F. (2015). Combined Heterogeneous Catalysis and Dark Fermentation Systems for the Conversion of Cellulose into Biohydrogen. *Biochem. Eng. J.* 101, 209–219. doi:10.1016/j.bej.2015.06.004

Guo, K., Guan, Q., Xu, J., and Tan, W. (2019). Mechanism of Preparation of Platform Compounds from Lignocellulosic Biomass Liquefaction Catalyzed by Bronsted Acid: a Review. *J. Bioresour. Bioprod.* 4 (4), 202–213. doi:10.12162/jbb.v4i4.009

Haldar, D., and Purkait, M. K. (2021). A Review on the Environment-Friendly Emerging Techniques for Pretreatment of Lignocellulosic Biomass: Mechanistic Insight and Advancements. *Chemosphere* 264, 128523. doi:10.1016/j.chemosphere.2020.128523

Han, B., Zhao, P., He, R., Wu, T., and Wu, Y. (2018). Catalytic Conversion of Glucose to 5-Hydroxymethylfurfural over B2O3 Supported Solid Acids Catalysts. *Waste Biomass Valor.* 9 (11), 2181–2190. doi:10.1007/s12649-017-9971-4

Hayashi, E., Yamaguchi, Y., Kamata, K., Tsunoda, N., Kumagai, Y., Oba, F., et al. (2019). Effect of MnO2 Crystal Structure on Aerobic Oxidation of 5-Hydroxymethylfurfural to 2,5-Furandicarboxylic Acid. *J. Am. Chem. Soc.* 141, 890–900. doi:10.1021/jacs.8b09917

Heinze, T. (2015). "Cellulose: Structure and Properties," in *Cellulose Chemistry and Properties: Fibers, Nanocelluloses and Advanced Materials. Advances in Polymer Science*. Editor O. Rojas (Cham: Springer), Vol. 271, 1–52. doi:10.1007/12_2015_319

Heo, J. B., Lee, Y.-S., and Chung, C.-H. (2021). Seagrass-based Platform Strategies for Sustainable Hydroxymethylfurfural (HMF) Production: toward Bio-Based Chemical Products. *Crit. Rev. Biotechnol.* 41 (6), 902–917. doi:10.1080/07388551.2021.1892580

Hu, L., Wu, Z., Jiang, Y., Wang, X., He, A., Song, J., et al. (2020). Recent Advances in Catalytic and Autocatalytic Production of Biomass-Derived 5-hydroxymethylfurfural. *Renew. Sustain. Energ. Rev.* 134, 110317–110374. doi:10.1016/j.rser.2020.110317

Hu, S., Zhang, Z., Song, J., Zhou, Y., and Han, B. (2009). Efficient Conversion of Glucose into 5-hydroxymethylfurfural Catalyzed by a Common Lewis Acid SnCl4 in an Ionic Liquid. *Green. Chem.* 11, 1746–1749. doi:10.1039/B914601F

Huang, T., Zhou, Y., Zhang, X., Peng, D., Nie, X., Chen, J., et al. (2022). Conversion of Carbohydrates into Furfural and 5-hydroxymethylfurfural Using Furfuryl Alcohol Resin-Based Solid Acid as Catalyst. *Cellulose* 29, 1419–1433. doi:10.1007/s10570-021-04375-8

Huang, X., Ren, J., Ran, J.-Y., Qin, C.-L., Yang, Z.-Q., and Cao, J.-P. (2022). Recent Advances in Pyrolysis of Cellulose to Value-Added Chemicals. *Fuel Process. Technol.* 229, 107175–107192. doi:10.1016/j.fuproc.2022.107175

Huo, Z.-B., Liu, J.-K., Yao, G.-D., Zeng, X., Luo, J., and Jin, F.-M. (2015). Efficient Hydrothermal Conversion of Cellulose into Methane over Porous Ni Catalyst. *Appl. Catal. A: Gen.* 490, 36–41. doi:10.1016/j.apcata.2014.10.058

Inoue, R., Agutaya, J. K. C. N., Quitain, A. T., Sasaki, M., Cocero, M. J., and Kida, T. (2021). Supercritical CO2-subcritical H2O System: a green Reactive Separation Medium for Selective Conversion of Glucose to 5-hydroxymethylfurfural. *J. Supercrit. Fluids* 168, 105079–105089. doi:10.1016/j.supflu.2020.105079

Jin, C., Xiang, N., Zhu, X., E, S., Sheng, K., and Zhang, X. (2021). Selective 5-hydroxymethylfurfural Production from Cellulose Formate in DMSO-H2o media. *Appl. Catal. B: Environ.* 285, 119799–119809. doi:10.1016/j.apcatb.2020.119799

Kang, S., Fu, J., and Zhang, G. (2018). From Lignocellulosic Biomass to Levulinic Acid: a Review on Acid-Catalyzed Hydrolysis. *Renew. Sustain. Energ. Rev.* 94, 340–362. doi:10.1016/j.rser.2018.06.016

Kang, Y., Yang, Q., Bartocci, P., Wei, H., Liu, S. S., WuZhou, Z. H., et al. (2020). Bioenergy in China: Evaluation of Domestic Biomass Resources and the Associated Greenhouse Gas Mitigation Potentials. *Renew. Sustain. Energ. Rev.* 127, 109842–109887. doi:10.1016/j.rser.2020.109842

Ke, Q., Jin, Y., Ruan, F., Ha, M. N., Li, D., Cui, P., et al. (2019). Boosting the Activity of Catalytic Oxidation of 5-hydroxymethylfurfural to 2,5-diformylfuran over Nitrogen-Doped Manganese Oxide Catalysts. *Green. Chem.* 21, 4313–4318. doi:10.1039/C9GC01041F

Kibria Nabil, S., McCoy, S., and Kibria, M. G. (2021). Comparative Life Cycle Assessment of Electrochemical Upgrading of CO2 to Fuels and Feedstocks. *Green. Chem.* 23, 867–880. doi:10.1039/D0GC02831B

Kittner, N., Lill, F., and Kammen, D. M. (2017). Energy Storage Deployment and Innovation for the Clean Energy Transition. *Nat. Energ.* 2, 17125–17130. doi:10.1038/nenergy.2017.125

Komanoya, T., Kinemura, T., Kita, Y., Kamata, K., and Hara, M. (2017). Electronic Effect of Ruthenium Nanoparticles on Efficient Reductive Amination of Carbonyl Compounds. *J. Am. Chem. Soc.* 139, 11493–11499. doi:10.1021/jacs.7b04481

Lai, D.-m., Deng, L., Li, J., Liao, B., Guo, Q.-x., and Fu, Y. (2011). Hydrolysis of Cellulose into Glucose by Magnetic Solid Acid. *ChemSusChem* 4, 55–58. doi:10.1002/cssc.201000300

Lai, F., Yan, F., Wang, P., Wang, S., Li, S., and Zhang, Z. (2020). Highly Efficient Conversion of Cellulose into 5-hydroxymethylfurfural Using Temperature-Responsive ChnH5-nCeW12O40 (N = 1-5) Catalysts. *Chem. Eng. J.* 396, 125282–125293. doi:10.1016/j.cej.2020.125282

Lange, J.-P. (2021). Performance Metrics for Sustainable Catalysis in Industry. *Nat. Catal.* 4 (3), 186–192. doi:10.1038/s41929-021-00585-2

Lehrhofer, A. F., Goto, T., Kawada, T., Rosenau, T., and Hettegger, H. (2022). The *In Vitro* Synthesis of Cellulose - A Mini-Review. *Carbohydr. Polym.* 285, 119222–119231. doi:10.1016/j.carbpol.2022.119222

Li, H., Guo, H., Fang, Z., Aida, T. M., and Smith, R. L. (2020). Cycloamination Strategies for Renewable N-Heterocycles. *Green. Chem.* 22, 582–611. doi:10.1039/C9GC03655E

Li, H., Guo, H., Su, Y., Hiraga, Y., Fang, Z., Hensen, E. J. M., et al. (2019a). N-formyl-stabilizing Quasi-Catalytic Species Afford Rapid and Selective Solvent-free Amination of Biomass-Derived Feedstocks. *Nat. Commun.* 10, 699–711. doi:10.1038/s41467-019-08577-4

Li, H., He, X., Zhang, Q., Chang, F., Xue, W., Zhang, Y., et al. (2013). Polymeric Ionic Hybrid as Solid Acid Catalyst for the Selective Conversion of Fructose and Glucose to 5-hydroxymethylfurfural. *Energ. Technol.* 1, 151–156. doi:10.1002/ente.201200041

Li, H., Li, Y., Fang, Z., and Smith, R. L. (2019b). Efficient Catalytic Transfer Hydrogenation of Biomass-Based Furfural to Furfuryl Alcohol with Recyclable Hf-Phenylphosphonate Nanohybrids. *Catal. Today* 319, 84–92. doi:10.1016/j.cattod.2018.04.056

Li, H., Zhang, Q., Bhadury, P., and Yang, S. (2014). Furan-type Compounds from Carbohydrates via Heterogeneous Catalysis. *Coc* 18, 547–597. doi:10.2174/13852728113176660138

Li, H., Zhao, W., and Fang, Z. (2017). Hydrophobic Pd Nanocatalysts for One-Pot and High-Yield Production of Liquid Furanic Biofuels at Low Temperatures. *Appl. Catal. B: Environ.* 215, 18–27. doi:10.1016/j.apcatb.2017.05.039

Li X., X., Peng, K., Xia, Q., Liu, X., and Wang, Y. (2018). Efficient Conversion of Cellulose into 5-hydroxymethylfurfural over Niobia/carbon Composites. *Chem. Eng. J.* 332, 528–536. doi:10.1016/j.cej.2017.06.105

Li, Y., Hu, B., Naqvi, S. R., Zhang, Z. X., Li, K., and Lu, Q. (2021). Selective Preparation of 5- Hydroxymethylfurfural by Catalytic Fast Pyrolysis of Cellulose Over Zirconium-Tin Mixed Metal Oxides. *J. Anal. Appl. Pyrolysis.* 155, 105103–105109. doi:10.1016/j.jaap.2021.105103

Li Z., Z., Su, K., Ren, J., Yang, D., Cheng, B., Kim, C. K., et al. (2018). Direct Catalytic Conversion of Glucose and Cellulose. *Green. Chem.* 20 (4), 863–872. doi:10.1039/C7GC03318D

Liu, G., Xie, Y., Wei, C., Liu, C., Song, F., Sun, X., et al. (2022). Synergistic Catalysis of Species in Molten Salt Hydrate for Conversion of Cellulose to 5-hydroxymethylfurfural. *Biomass and Bioenergy* 158, 106363–106379. doi:10.1016/j.biombioe.2022.106363

Liu, J., Li, H., Liu, Y.-C., Lu, Y.-M., He, J., Liu, X.-F., et al. (2015). Catalytic Conversion of Glucose to 5-hydroxymethylfurfural over Nano-Sized Mesoporous Al2O3-B2o3 Solid Acids. *Catal. Commun.* 62, 19–23. doi:10.1016/j.catcom.2015.01.008

Liu, S., Zheng, W., Wen, X., Fang, Z., Li, H., Li, C., et al. (2022). Molecular Design and Experimental Study of Cellulose Conversion to 5-hydroxymethylfurfural Catalyzed by Different Ratios of Brønsted/Lewis Acid Ionic Liquids. *Carbohydr. Polym.* 278, 118936–118952. doi:10.1016/j.carbpol.2021.118936

Liu, W.-J., Dang, L., Xu, Z., Yu, H.-Q., Jin, S., and Huber, G. W. (2018). Electrochemical Oxidation of 5-Hydroxymethylfurfural with NiFe Layered Double Hydroxide (LDH) Nanosheet Catalysts. *ACS Catal.* 8, 5533–5541. doi:10.1021/acscatal.8b01017

Lyu, X., Li, H., Xiang, H., Mu, Y., Ji, N., Lu, X., et al. (2022). Energy Efficient Production of 5-hydroxymethylfurfural (5-HMF) over Surface Functionalized Carbon Superstructures under Microwave Irradiation. *Chem. Eng. J.* 428, 131143–131152. doi:10.1016/j.cej.2021.131143

Mahajan, J. S., O'Dea, R. M., Norris, J. B., Korley, L. T. J., and Epps, T. H. (2020). Aromatics from Lignocellulosic Biomass: a Platform for High-Performance Thermosets. *ACS Sustain. Chem. Eng.* 8 (40), 15072–15096. doi:10.1021/acssuschemeng.0c04817

Mansora, A. M., Lima, J. S., Anib, F. N., Hashima, H., and Hoa, W. S. (2019). Characteristics of Cellulose, Hemicellulose and Lignin of MD2 Pineapple Biomass. *Chem. Eng.* 72 (1), 79–84. doi:10.3303/CET1972014

MarketWatch (2019). *5-Hydroxymethylfurfural (5-HMF) Market Sales Volume, Analysis, Size, Share, Growth, Trends and Forecast 2019-2025.* doi:10.1039/D0CS00041H

Marqués, P. S., Londi, G., Yurash, B., Nguyen, T.-Q., Barlow, S., Marder, S. R., et al. (2021). Understanding How Lewis Acids Dope Organic Semiconductors: a "Complex" story. *Chem. Sci.* 12 (20), 7012–7022. doi:10.1039/D1SC01268A

Meng, Y., Yang, S., and Li, H. (2022). Electro- and Photocatalytic Oxidative Upgrading of Bio-based 5-Hydroxymethylfurfural. *ChemSusChem* 2022, e202102581. doi:10.1002/cssc.202102581

Ng, K. H., Lai, S. Y., Cheng, C. K., Cheng, Y. W., and Chong, C. C. (2021). Photocatalytic Water Splitting for Solving Energy Crisis: Myth, Fact or Busted? *Chem. Eng. J.* 417, 128847. doi:10.1016/j.cej.2021.128847

Nishimura, S., Ikeda, N., and Ebitani, K. (2014). Selective Hydrogenation of Biomass-Derived 5-hydroxymethylfurfural (HMF) to 2,5-dimethylfuran (DMF) under Atmospheric Hydrogen Pressure over Carbon Supported PdAu Bimetallic Catalyst. *Catal. Today* 232, 89–98. doi:10.1016/j.cattod.2013.10.012

Onda, A., Ochi, T., and Yanagisawa, K. (2009). Hydrolysis of Cellulose Selectively into Glucose over Sulfonated Activated-Carbon Catalyst under Hydrothermal Conditions. *Top. Catal.* 52, 801–807. doi:10.1007/s11244-009-9237-x

Pham, S. T., Nguyen, B. M., Le, G. H., Sapi, A., Mutyala, S., Szenti, I., et al. (2020). Role of Brønsted and Lewis Acidic Sites in Sulfonated Zr-MCM-41 for the Catalytic Reaction of Cellulose into 5-hydroxymethyl Furfural. *Reac. Kinet. Mech. Cat.* 130, 825–836. doi:10.1007/s11144-020-01799-4

Pham, S. T., Nguyen, M. B., Le, G. H., Pham, T. T. T., Quan, T. T. T., Nguyen, T. D., et al. (2019). Cellulose Conversion to 5 Hydroxymethyl Furfural (5-HMF) Using Al-Incorporated SBA-15 as Highly Efficient Catalyst. *J. Chem.* 2019, 1–8. doi:10.1155/2019/5785621

Pingen, D., Schwaderer, J. B., Walter, J., Wen, J., Murray, G., Vogt, D., et al. (2018). Diamines for Polymer Materials via Direct Amination of Lipid- and Lignocellulose-Based Alcohols with NH3. *ChemCatChem* 10, 3027–3033. doi:10.1002/cctc.201800365

Qi, B., Vu, A., Wickramasinghe, S. R., and Qian, X. (2018). Glucose Production from Lignocellulosic Biomass Using a Membrane-Based Polymeric Solid Acid Catalyst. *Biomass and Bioenergy* 117, 137–145. doi:10.1016/j.biombioe.2018.07.017

Qin, L.-Z., and He, Y.-C. (2020). Chemoenzymatic Synthesis of Furfuryl Alcohol from Biomass in Tandem Reaction System. *Appl. Biochem. Biotechnol.* 190, 1289–1303. doi:10.1007/s12010-019-03154-3

Ramírez Bocanegra, N., Rivera De la Rosa, J., Lucio Ortiz, C. J., Cubillas González, P., Greenwell, H. C., Badillo Almaráz, V. E., et al. (2021). Catalytic Conversion

of 5-hydroxymethylfurfural (5-HMF) over Pd-Ru/FAU Zeolite Catalysts. *Catal. Today* 360, 2–11. doi:10.1016/j.cattod.2019.11.032

Rinaldi, R., and Schüth, F. (2009). Acid Hydrolysis of Cellulose as the Entry point into Biorefinery Schemes. *ChemSusChem* 2, 1096–1107. doi:10.1002/cssc.200900188

Rothamer, D. A., and Jennings, J. H. (2012). Study of the Knocking Propensity of 2,5-Dimethylfuran-Gasoline and Ethanol-Gasoline Blends. *Fuel* 98, 203–212. doi:10.1016/j.fuel.2012.03.049

Sadhukhan, J., Martinez-Hernandez, E., Murphy, R. J., Ng, D. K. S., Hassim, M. H., Siew Ng, K., et al. (2018). Role of Bioenergy, Biorefinery and Bioeconomy in Sustainable Development: Strategic Pathways for Malaysia. *Renew. Sustain. Energ. Rev.* 81, 1966–1987. doi:10.1016/j.rser.2017.06.007

Sánchez, J., Curt, M. D., Robert, N., and Fernández, J. (2019). Biomass Resources. *The Role of Bioenergy in the Bioeconomy* 2019, 25–111. doi:10.1016/B978-0-12-813056-8.00002-9

Sarip, H., Sohrab-Hossain, M., Azemi, M., and Allaf, K. (2016). A Review of the thermal Pretreatment of Lignocellulosic Biomass towards Glucose Production: Autohydrolysis with DIC Technology. *BioResources* 11 (4), 10625–10653. doi:10.15376/biores.11.4.10625-1065310.15376/biores.11.4.9311-9324

Schade, O. R., Kalz, K. F., Neukum, D., Kleist, W., and Grunwaldt, J.-D. (2018). Supported Gold- and Silver-Based Catalysts for the Selective Aerobic Oxidation of 5-(hydroxymethyl)furfural to 2,5-furandicarboxylic Acid and 5-Hydroxymethyl-2-Furancarboxylic Acid. *Green. Chem.* 20, 3530–3541. doi:10.1039/C8GC01340C

Shen, F., Smith, R. L., Jr, Li, L., Yan, L., and Qi, X. (2017). Eco-friendly Method for Efficient Conversion of Cellulose into Levulinic Acid in Pure Water with Cellulase-Mimetic Solid Acid Catalyst. *ACS Sustain. Chem. Eng.* 5 (3), 2421–2427. doi:10.1021/acssuschemeng.6b02765

Shen, G., Andrioletti, B., and Queneau, Y. (2020). Furfural and 5-(hydroxymethyl) furfural: Two Pivotal Intermediates for Bio-Based Chemistry. *Curr. Opin. Green Sustain. Chem.* 26, 100384–100395. doi:10.1016/j.cogsc.2020.100384

Shirai, H., Ikeda, S., and Qian, E. W. (2017). One-pot Production of 5-hydroxymethylfurfural from Cellulose Using Solid Acid Catalysts. *Fuel Process. Technol.* 159, 280–286. doi:10.1016/j.fuproc.2016.10.005

Silva, V., Ratti, R. P., Sakamoto, I. K., Andrade, M. V. F., and Varesche, M. B. A. (2018). Biotechnological Products in Batch Reactors Obtained from Cellulose, Glucose and Xylose Using Thermophilic Anaerobic Consortium. *Renew. Energ.* 125, 537–545. doi:10.1016/j.renene.2018.02.124

Siqueira Mancilha Nogueira, J., Alves Silva, J. P., Mussatto, S. I., and Melo Carneiro, L. (2020). Synthesis and Application of Heterogeneous Catalysts Based on Heteropolyacids for 5-hydroxymethylfurfural Production from Glucose. *Energies* 13 (3), 655. doi:10.3390/en13030655

Slak, J., Pomeroy, B., Kostyniuk, A., Grilc, M., and Likozar, B. (2022). A Review of Bio-Refining Process Intensification in Catalytic Conversion Reactions, Separations and Purifications of Hydroxymethylfurfural (HMF) and Furfural. *Chem. Eng. J.* 429, 132325–132341. doi:10.1016/j.cej.2021.132325

Solanki, B. S., and Rode, C. V. (2019). Selective Hydrogenation of 5-HMF to 2,5-DMF over a Magnetically Recoverable Non-noble Metal Catalyst. *Green. Chem.* 21, 6390–6406. doi:10.1039/C9GC03091C

Sun, R., Zheng, M., Pang, J., Liu, X., Wang, J., Pan, X., et al. (2016). Selectivity-switchable Conversion of Cellulose to Glycols over Ni-Sn Catalysts. *ACS Catal.* 6, 191–201. doi:10.1021/acscatal.5b01807

Taipabu, M. I., Viswanathan, K., Wu, W., and Nagy, Z. K. (2021). Production of Renewable Fuels and Chemicals from Fats, Oils, and Grease (FOG) Using Homogeneous and Heterogeneous Catalysts: Design, Validation, and Optimization. *Chem. Eng. J.* 424, 130199–130218. doi:10.1016/j.cej.2021.130199

Tan, J., Li, Y., Tan, X., Wu, H., Li, H., and Yang, S. (2021). Advances in Pretreatment of Straw Biomass for Sugar Production. *Front. Chem.* 9, 696030–696057. doi:10.3389/fchem.2021.696030

Tan, X., Sudarsanam, P., Tan, J., Wang, A., Zhang, H., Li, H., et al. (2021). Sulfonic Acid-Functionalized Heterogeneous Catalytic Materials for Efficient Biodiesel Production: a Review. *J. Environ. Chem. Eng.* 9 (1), 104719–104742. doi:10.1016/j.jece.2020.104719

Tareen, W. U. K., Dilbar, M. T., Farhan, M., Ali Nawaz, M., Durrani, A. W., Memon, K. A., et al. (2019). Present Status and Potential of Biomass Energy in Pakistan Based on Existing and Future Renewable Resources. *Sustainability* 12 (1), 249–288. doi:10.3390/su12010249

Tempelman, C. H. L., Oozeerally, R., and Degirmenci, V. (2021). Heterogeneous Catalysts for the Conversion of Glucose into 5-hydroxymethyl Furfural. *Catalysts* 11, 861–881. doi:10.3390/catal11070861

Thoma, C., Konnerth, J., Sailer-Kronlachner, W., Solt, P., Rosenau, T., and van Herwijnen, H. W. G. (2020). Current Situation of the Challenging Scale-Up Development of Hydroxymethylfurfural Production. *ChemSusChem* 13 (14), 3544–3564. doi:10.1002/cssc.v13.1410.1002/cssc.202000581

Tian, S.-Q., Zhao, R.-Y., and Chen, Z.-C. (2018). Review of the Pretreatment and Bioconversion of Lignocellulosic Biomass from Wheat Straw Materials. *Renew. Sustain. Energ. Rev.* 91, 483–489. doi:10.1016/j.rser.2018.03.113

Tkachenko, T., Sheludko, Y., Yevdokymenko, V., Kamenskyh, D., Khimach, N., Povazhny, V., et al. (2021). Physico-chemical Properties of Flax Microcrystalline Cellulose. *Appl. Nanosci.* 5, 1–14. doi:10.1007/s13204-021-01819-2

Tyagi, U., Anand, N., and Kumar, D. (2018). Synergistic Effect of Modified Activated Carbon and Ionic Liquid in the Conversion of Microcrystalline Cellulose to 5-Hydroxymethyl Furfural. *Bioresour. Technol.* 267, 326–332. doi:10.1016/j.biortech.2018.07.035

Van Putten, R.-J., Van Der Waal, J. C., De Jong, E., Rasrendra, C. B., Heeres, H. J., and de Vries, J. G. (2013). Hydroxymethylfurfural, a Versatile Platform Chemical Made from Renewable Resources. *Chem. Rev.* 113, 1499–1597. doi:10.1021/cr300182k

Vanderfleet, O. M., and Cranston, E. D. (2021). Production Routes to Tailor the Performance of Cellulose Nanocrystals. *Nat. Rev. Mater.* 6, 124–144. doi:10.1038/s41578-020-00239-y

Venkata Mohan, S., Nikhil, G. N., Chiranjeevi, P., Nagendranatha Reddy, C., Rohit, M. V., Kumar, A. N., et al. (2016). Waste Biorefinery Models towards Sustainable Circular Bioeconomy: Critical Review and Future Perspectives. *Bioresour. Technol.* 215, 2–12. doi:10.1016/j.biortech.2016.03.130

Ventura, M., Aresta, M., and Dibenedetto, A. (2016). Selective Aerobic Oxidation of 5-(Hydroxymethyl)furfural to 5-Formyl-2-Furancarboxylic Acid in Water. *ChemSusChem* 9, 1096–1100. doi:10.1002/cssc.201600060

Wang, A., Berton, P., Zhao, H., Bryant, S. L., Kibria, M. G., and Hu, J. (2021). Plasmon-enhanced 5-hydroxymethylfurfural Production from the Photothermal Conversion of Cellulose in a Biphasic Medium. *ACS Sustain. Chem. Eng.* 9, 16115–16122. doi:10.1021/acssuschemeng.1c04592

Wang, A., Li, H., Pan, H., Zhang, H., Xu, F., Yu, Z., et al. (2018). Efficient and green Production of Biodiesel Catalyzed by Recyclable Biomass-Derived Magnetic Acids. *Fuel Process. Technol.* 181, 259–267. doi:10.1016/j.fuproc.2018.10.003

Wang, H., Zhu, C., Li, D., Liu, Q., Tan, J., Wang, C., et al. (2019). Recent Advances in Catalytic Conversion of Biomass to 5-hydroxymethylfurfural and 2, 5-dimethylfuran. *Renew. Sustain. Energ. Rev.* 103, 227–247. doi:10.1016/j.rser.2018.12.010

Wang, X., Liang, X., Li, J., and Li, Q. (2019). Catalytic Hydrogenolysis of Biomass-Derived 5-hydroxymethylfurfural to Biofuel 2, 5-dimethylfuran. *Appl. Catal. A: Gen.* 576, 85–95. doi:10.1016/j.apcata.2019.03.005

Wang, Y., Hu, Z., Fan, G., Yan, J., Song, G., and Li, J. (2019). Catalytic Conversion of Glucose to 5-(Hydroxymethyl)furfural over Phosphotungstic Acid Supported on SiO2-Coated Fe3O4. *Waste Biomass Valor.* 10, 2263–2271. doi:10.1007/s12649-018-0242-9

Wang, Y., Kiziltas, A., Drews, A. R., Tamrakar, S., Blanchard, P., and Walsh, T. R. (2021a). Dynamical Water Ingress and Dissolution at the Amorphous-Crystalline Cellulose Interface. *Biomacromolecules* 22 (9), 3884–3891. doi:10.1021/acs.biomac.1c00690

Wang, Y., Wang, M., Li, Y., and Liu, Q. (2021b). Homogeneous Manganese-Catalyzed Hydrogenation and Dehydrogenation Reactions. *Chem* 7 (5), 1180–1223. doi:10.1016/j.chempr.2020.11.013

Wataniyakul, P., Boonnoun, P., Quitain, A. T., Sasaki, M., Kida, T., Laosiripojana, N., et al. (2018). Preparation of Hydrothermal Carbon as Catalyst Support for Conversion of Biomass to 5-hydroxymethylfurfural. *Catal. Commun.* 104, 41–47. doi:10.1016/j.catcom.2017.10.014

Wei, W., and Wu, S. (2018). Experimental and Kinetic Study of Glucose Conversion to Levulinic Acid in Aqueous Medium over Cr/HZSM-5 Catalyst. *Fuel* 225, 311–321. doi:10.1016/j.fuel.2018.03.120

Witzel, S., Hashmi, A. S. K., and Xie, J. (2021). Light in Gold Catalysis. *Chem. Rev.* 121 (14), 8868–8925. doi:10.1021/acs.chemrev.0c00841

Wu, Q., He, Y., Zhang, H., Feng, Z., Wu, Y., and Wu, T. (2017). Photocatalytic Selective Oxidation of Biomass-Derived 5-hydroxymethylfurfural to 2,5-

diformylfuran on Metal-free G-C3n4 under Visible Light Irradiation. *Mol. Catal.* 436, 10–18. doi:10.1016/j.mcat.2017.04.012

Xu, C., Paone, E., Rodríguez-Padrón, D., Luque, R., and Mauriello, F. (2020). Recent Catalytic Routes for the Preparation and the Upgrading of Biomass Derived Furfural and 5-hydroxymethylfurfural. *Chem. Soc. Rev.* 49 (13), 4273–4306. doi:10.1039/d0cs00041h

Xu, S., Zhang, L., Xiao, K., and Xia, H. (2017). Isomerization of Glucose into Fructose by Environmentally Friendly Fe/β Zeolite Catalysts. *Carbohydr. Res.* 446-447, 48–51. doi:10.1016/j.carres.2017.05.006

Yamabe, S., Guan, W., and Sakaki, S. (2013). Three Competitive Transition States at the Glycosidic Bond of Sucrose in its Acid-Catalyzed Hydrolysis. *J. Org. Chem.* 78, 2527–2533. doi:10.1021/jo3027565

Yan, L., Ma, R., Wei, H., Li, L., Zou, B., and Xu, Y. (2019). Ruthenium Trichloride Catalyzed Conversion of Cellulose into 5-hydroxymethylfurfural in Biphasic System. *Bioresour. Technol.* 279, 84–91. doi:10.1016/j.biortech.2019.01.120

Yang, F., Mao, J., Li, S., Yin, J., Zhou, J., and Liu, W. (2019). Cobalt-graphene Nanomaterial as an Efficient Catalyst for Selective Hydrogenation of 5-hydroxymethylfurfural into 2,5-dimethylfuran. *Catal. Sci. Technol.* 9, 1329–1333. doi:10.1039/C9CY00330D

Yang, J., An, X., Liu, L., Tang, S., Cao, H., Xu, Q., et al. (2020). Cellulose, Hemicellulose, Lignin, and Their Derivatives as Multi-Components of Bio-Based Feedstocks for 3D Printing. *Carbohydr. Polym.* 250, 116881–116897. doi:10.1016/j.carbpol.2020.116881

Yang, T., Chen, D., Li, W., and Zhang, H. (2021). Efficient Conversion of Corn stover to 5-hydroxymethylfurfural and Furfural Using a Novel Acidic Resin Catalyst in Water-1, 4-dioxane System. *Mol. Catal.* 515, 111920–111928. doi:10.1016/j.mcat.2021.111920

Yao, Y. (2022). Sustainable Approaches to Selective Hydrolysis of Cellulose with Robust Crystalline Structure into Glucose Promoted by Heterogeneous Acid Catalysts. *Biomass, Biofuels, Biochemicals* 2022, 309–338. doi:10.1016/B978-0-12-824417-7.00003-0

Yi, X., Delidovich, I., Sun, Z., Wang, S., Wang, X., and Palkovits, R. (2015). A Heteropoly Acid Ionic crystal Containing Cr as an Active Catalyst for Dehydration of Monosaccharides to Produce 5-HMF in Water. *Catal. Sci. Technol.* 5 (4), 2496–2502. doi:10.1039/C4CY01555J

Zhang, A.-N., Zhao, H.-B., Cheng, J.-B., Li, M.-E., Li, S.-L., Cao, M., et al. (2021). Construction of Durable Eco-Friendly Biomass-Based Flame-Retardant Coating for Cotton Fabrics. *Chem. Eng. J.* 410, 128361–128370. doi:10.1016/j.cej.2020.128361

Zhang, H., Li, H., Hu, Y., Venkateswara Rao, K. T., Xu, C., and Yang, S. (2019). Advances in Production of Bio-Based Ester Fuels with Heterogeneous Bifunctional Catalysts. *Renew. Sustain. Energ. Rev.* 114, 109296. doi:10.1016/j.rser.2019.109296

Zhang, H., Zhou, Q., Chang, F., Pan, H., Liu, X.-F., Li, H., et al. (2015). Production and Fuel Properties of Biodiesel from Firmiana Platanifolia L.F. As a Potential Non-food Oil Source. *Ind. Crops Prod.* 76, 768–771. doi:10.1016/j.indcrop.2015.08.002

Zhang, Y.-R., Wang, B.-X., Qin, L., Li, Q., and Fan, Y.-M. (2019). A Non-noble Bimetallic alloy in the Highly Selective Electrochemical Synthesis of the Biofuel 2,5-dimethylfuran from 5-hydroxymethylfurfural. *Green. Chem.* 21, 1108–1113. doi:10.1039/C8GC03689F

Zhao, D., Su, T., Wang, Y., Varma, R. S., and Len, C. (2020). Recent Advances in Catalytic Oxidation of 5-hydroxymethylfurfural. *Mol. Catal.* 495, 111133–111151. doi:10.1016/j.mcat.2020.111133

Zhao, W., Chi, X., Li, H., He, J., Long, J., Xu, Y., et al. (2018). Eco-friendly Acetylcholine-Carboxylate Bio-Ionic Liquids for Controllable N-Methylation and N-Formylation Using Ambient CO2 at Low Temperatures. *Green. Chem.* 21, 567–577. doi:10.1039/C8GC03549K

Zhao, Y., Lu, K., Xu, H., Zhu, L., and Wang, S. (2021). A Critical Review of Recent Advances in the Production of Furfural and 5-hydroxymethylfurfural from Lignocellulosic Biomass through Homogeneous Catalytic Hydrothermal Conversion. *Renew. Sustain. Energ. Rev.* 139, 110706–110732. doi:10.1016/j.rser.2021.110706

Zheng, H.-y., Zhao, Z.-l., Xiao, L.-q., Zhao, W.-s., Liang, X.-b., Xue, Y.-f., et al. (2021). Catalytic Conversion of Cellulose and Starch to Furfural over Zeolites. *J. Fuel Chem. Technol.* 49 (9), 1261–1269. doi:10.1016/S1872-5813(21)60083-X

Zhu, Y., Li, W., Huang, Y., Zheng, Y., Wang, D., Ye, Y., et al. (2021). Catalytic Pyrolysis of Cellulose over Solid Acidic Catalysts: an Environment-Friendly Method for Furan Production. *Biomass Conv. Bioref.* 11 (6), 2695–2702. doi:10.1007/s13399-020-00812-z

Green Photocatalysis of Organic Pollutants by Bimetallic Zn-Zr Metal-Organic Framework Catalyst

Xiaojuan Zhang [1,2,3], Rongfei Yu [1], Dandan Wang [1], Weihua Li [2,3] and Yutao Zhang [1,2,3]*

[1]School of Chemistry and Chemical Engineering, Anshun University, Anshun, China, [2]University Rural Revitalization Research Center in Guizhou, Anshun, China, [3]Engineering Technology Center of Control and Remediation of Soil Contamination of Guizhou Science and Technology Department, Anshun, China

A series of bimetallic Zn-Zr metal-organic frameworks (Zn-Zr MOFs) with different Zn:Zr molar ratios has been synthesized *via* a green hydrothermal method. The structures and morphologies of these photocatalysts have been characterized and analyzed by FTIR, XRD, SEM, and nitrogen adsorption-desorption. The prepared Zn-Zr MOFs had large specific surface areas and pore volumes, favoring the adsorption of pollutant molecules, which in turn led to an improved photocatalytic effect. The photocatalytic activities of the Zn-Zr MOFs under visible light irradiation have been studied towards rhodamine B (RhB) as a target pollutant. The extent of degradation of RhB in a 40 mg/L aqueous solution reached 97.4%. The optimal photocatalyst could also degrade other dyes, suggesting a certain degree of universality.

1 INTRODUCTION

With the development of economy and society, and growing demand for industrial chemicals are accompanied by the increasing extent of environmental pollution. It has engendered an urgent need for the use of green catalytic methods to remove the organic molecules from industrial wastewater (Shanmuganathan et al., 2021). Among the various types of industrial wastewater, that from the printing and dyeing industries is some of the hardest to treat, being characterized by high volume, high content of organic pollutants, and high salinity (Kan et al., 2020). As the main pollutants in printing and dyeing wastewater, dyes are among the most important chemical species that need to be removed in wastewater treatment (Banerjee and Dastidar, 2005). Several dyeing wastewater treatment technologies have hitherto been devised, such as chemical oxidation, coagulation, and photocatalytic degradation, of which the latter is playing an increasingly important role in the field of water treatment (Xue and Zhu, 2019). The photocatalytic degradation of organic materials under light illumination has proven to be an efficient approach for wastewater treatment due to the simple treatment process, low cost, and environmental benignity (Yin et al., 2021). To date, ZnO, TiO$_2$, SnO$_2$, BiFeO$_3$, and other photocatalysts have been designed and applied to degrade dye molecules in dyeing wastewater [such as rhodamine B (RhB), methyl orange (MO), Congo red (CR), acridine orange (AO), and methylene blue (MB)]. However, these photocatalysts have various disadvantages, such as fast recombination rates of photogenerated electrons and holes, relatively poor photocatalytic performance, low specific surface areas, and a tendency for agglomeration, which limit their practical application (Yang et al., 2021; Li et al., 2021).

Metal-organic frameworks (MOFs), as new crystalline porous materials, are attracting widespread attention in the field of photocatalysis due to their rich and tunable components, porous structures,

large surface areas, uniform distributions of metal sites, and tunable optical absorption abilities (Zhao and Cai, 2021). Although single-metal MOFs have been reported to show a certain photocatalytic activity, they have poor photosensitivity and weak spectral absorption (Huang et al., 2021). Nevertheless, single-metal MOFs can be doped or composited with other metals to improve the photocatalytic activity. Baten et al. prepared MIL-53 (Fe) doped with Fe^{2+}, which showed excellent photocatalytic activity for the degradation of MB (Baten et al., 2021). Wang et al. synthesized a highly efficient bifunctional Cu-MOF photocatalyst, over which MB was almost completely degraded within 5 h (Wang et al., 2019). In this study, Zn-Zr metal-organic frameworks (Zn-Zr MOFs) have been synthesized by a one-pot hydrothermal method. The structures and morphologies of Zn-Zr MOF photocatalysts with different Zn:Zr molar ratios have been studied. The photocatalytic properties of Rhodamine B (RhB) of Zn-Zr MOFs with different Zn:Zr molar ratios and single-metal MOFs have been compared and analyzed. In additon, the photocatalytic degradations of CR, NR, AO, MB, and MG over Zn-Zr MOFs-1 have been studied, with the aim of providing reference data for the industrial treatment of dyeing wastewater. The ultimate purpose of this research was to prepare photocatalysts through simple synthetic methods that were active under sunlight irradiation for the degradation of environmental pollutants. To this end, we have focused on the synthesis of bimetallic MOF composites, the photocatalytic performances which were superior to those of the single-metal MOFs.

2 MATERIALS AND METHODS

2.1 Materials and Techniques

Zinc (II) nitrate hexahydrate ($Zn(NO_3)_2 \cdot 6H_2O$), zirconium (IV) chloride ($ZrCl_4$), terephthalic acid (H_2BDC), Congo red (CR), acridine orange (AO), methylene blue (MB), and malachite green (MG) were obtained from Shanghai Aladdin Biochemical Technology Co., Ltd. Rhodamine B (RhB), neutral red (NR), N,N-dimethylformamide (DMF), and anhydrous ethanol were obtained from Chemical Reagent Co., Ltd. The above reagents were analytically pure. They were used without any further pretreatments or purifications. Deionized (DW, 18.25 MΩ) was used to prepare all solutions.

Powder X-ray diffraction (XRD) patterns of various samples were recorded on an automated X-ray diffractometer (XRD, Bruker D8 Advance, Germany) employing Cu-K_α radiation ($\lambda = 1.54060$ Å), and scanning the 2θ range 10–80°. The morphologies of the photocatalysts were examined by scanning electron microscopy (SEM, Hitachi SU 8100, Japan). The surface functional groups present on the samples were identified by Fourier-transform infrared (FTIR) spectroscopy (Perkin-Elmer 100, Shanghai). Parameters of the pore distribution and specific surface area were determined by the Brunauer-Emmett-Teller (BET) method by recording N_2 adsorption–desorption isotherms at 77 K (Quadrasorb evo™, United States). Variations in solution dye concentrations were monitored using a UV/Vis spectrophotometer (UV-5200PC, Shanghai). The visible light
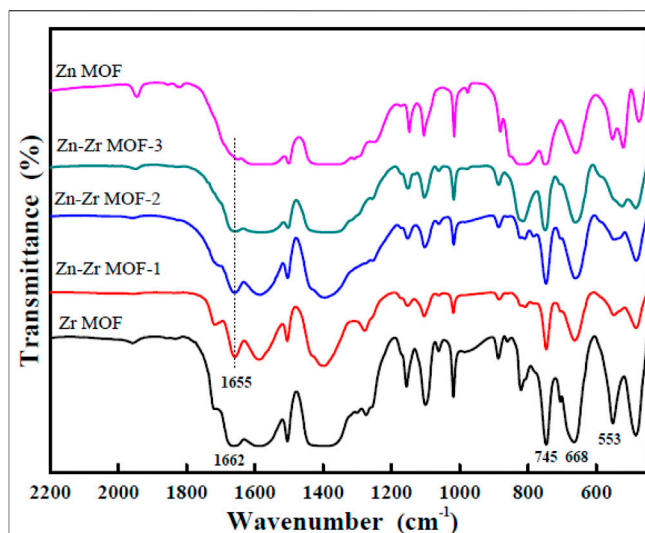

FIGURE 1 | FTIR spectra of Zr MOF, Zn MOF, and Zn-Zr MOFs with different Zn:Zr molar ratios.

source for photocatalytic degradation experiments was a xenon lamp (HSX-F300, Beijing).

2.2 Synthesis of Photocatalysts

$Zn(NO_3)_2 \cdot 6H_2O$ and $ZrCl_4$ in Zn:Zr molar ratios of 1:1.5, 2:1, and 3:0.5 were dissolved in absolute ethanol (10 ml) to give solution A. H_2BDC (0.66 g) was dissolved in absolute ethanol (10 ml) to give solution B. Solutions A and B were then simultaneously dropped into DMF (10 ml) under magnetic stirring. The mixture was stirred at room temperature for 1 h, and then transferred to an autoclave, which was maintained at 150°C for 6 h. After allowing the autoclave to cool to room temperature, the precipitate was collected by centrifugation. It was washed three times each with DMF and deionized water and dried at 60°C for 12 h to afford the Zn-Zr metal-organic framework (Zn-Zr MOF). For Zn:Zr molar ratios of 1:1.5, 2:1, and 3:0.5, the Zn-Zr MOFs are denoted as Zn-Zr MOF-1, Zn-Zr MOF-2, and Zn-Zr MOF-3, respectively. A Zr metal-organic framework without Zn (Zr MOF) and a Zn metal-organic framework without Zr (Zn MOF) were synthesized by the same method. All MOF materials were stored in a dry box.

2.3 Photocatalytic Activity Experiments

Rhodamine B (RhB) was used as the target pollutant for the investigation of photocatalytic activity. To evaluate the photocatalytic performances of the synthesized samples, they were deployed at 40 ppm in aliquots (50 ml) of aqueous RhB solution. Each mixture was stirred for 30 min in a darkroom to achieve adsorption-desorption equilibrium. It was then irradiated with simulated sunlight from a 300 W xenon lamp under continuous stirring.

At intervals of 15 min during the irradiation, the absorbance of RhB was recorded by a UV/Vis spectrophotometer. The efficiency of dye degradation was calculated according to the degradation percentage (**Eq. 1**):
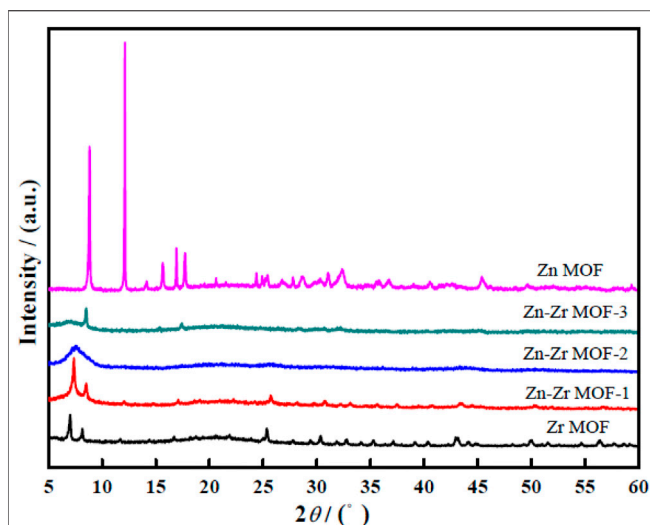
FIGURE 2 | XRD patterns of Zr MOF, Zn MOF, and Zn-Zr MOFs with different Zn:Zr molar ratios.

$$RhB(\%) = (1 - C/C_0) \times 100\% = (1 - A/A_0) \times 100\% \qquad (1)$$

where C_0 is the initial concentration of the dye, A_0 is the initial absorbance of the dye, and C and A are the concentration of the dye and the corresponding absorbance at time t.

3 RESULTS AND DISCUSSION

3.1 Structural Characterization of Composite Materials

3.1.1 FTIR Measurements

The FTIR spectra of Zr MOF, Zn MOF, and Zn-Zr MOFs with different Zn:Zr molar ratios are presented in **Figure 1**. It could be seen that the peak positions of each of the Zn-Zr MOF composites were consistent, and that the characteristic peaks of the Zr MOF and the Zn MOF were retained. This indicated the integrity and stability of the structures of the Zn-Zr MOF composites. The absorption bands in the range $1,200$–$600\ cm^{-1}$ could be attributed to antisymmetric and symmetric stretching vibrations of the carboxylate groups of terephthalate. The bands at $745\ cm^{-1}$ and $668\ cm^{-1}$ could be ascribed to stretching vibrations of O-H and C-H bonds of terephthalate. The absorption peak at $553\ cm^{-1}$ was a characteristic vibration peak of Zr-O. Notably, for the Zr MOF sample, the characteristic peak at $1,662\ cm^{-1}$ could be attributed to the vibration absorption of the C=O bond in carboxylate, and this peak was shifted to lower wavenumber at $1,655\ cm^{-1}$ when the second metal Zn was introduced into the MOF. This was consistent with Zn being coordinated by the carboxylate (Wang et al., 2021). Furthermore, the intensities of the characteristic absorption peaks of the Zr MOF were weakened, especially of that at $553\ cm^{-1}$, when the molar proportion of Zn was increased, consistent with successful synthesis of the Zn-Zr MOF.

3.1.2 Powder XRD Measurements

Figure 2 presents the XRD patterns of Zr MOF, Zn MOF, and Zn-Zr MOFs with different Zn:Zr molar ratios. The peaks at $2\theta = 7.0°$ and $8.2°$ could be indexed to the (111) and (002) crystal planes, respectively, of the Zr MOF phase structure (Kandiah et al., 2010). For Zn MOF, an obvious diffraction peak was seen at $2\theta = 8.8°$. The XRD patterns indicated that the synthesized Zr MOF and Zn MOF had good crystallinity. For Zn-Zr MOF-1, the characteristic diffraction peaks were observed at $2\theta = 7.3°$ and $8.5°$, slightly displaced from those of Zr MOF, but still clearly consistent. For Zn-Zr MOF-2, however, only a broad peak at $2\theta = 7.3°$ was seen, and for Zn-Zr MOF-3 only the peak at $2\theta = 8.5°$ was seen, with that at $2\theta = 7.3°$ having disappeared. Evidently, the crystal structure of Zr MOF was gradually modified by the introduction of Zn (Chen et al., 2021). Compared with Zr MOF, the peaks of the Zn-Zr MOF composites were obviously weakened or disappeared, but there were no obvious new peaks that could be attributed to discrete Zn or Zr compounds. This implied the successful synthesis of Zn-Zr MOF composites with a uniform distribution of Zn and Zr. As would be expected, the XRD pattern of Zn-Zr MOF-1 most closely resembled that of Zr MOF.

3.1.3 SEM Measurements

SEM images of Zr MOF, Zn MOF, and Zn-Zr MOFs with different Zn:Zr molar ratios are shown in **Figure 3**. As can be seen from **Figure 3D**, Zn MOF consisted of irregular blocks of random aggregates with smooth surfaces. **Figure 3E** shows that Zr MOF adopted a layered and lamellar structure with rough surfaces. As can be seen from **Figures 3A–C**, the morphologies and structures of the Zn-Zr MOFs with different Zn:Zr molar ratios progressively changed. **Figure 3A** shows that the structure of Zn-Zr MOF-1 consisted of small spheres made up of small particles of size about 100 nm. The SEM image of Zn-Zr MOF-2 (**Figure 3B**) revealed a structure comprising small particles, some of which aggregate into blocks. **Figure 3C** showed that Zn-Zr MOF-3 formed an irregular sheet structure with a smooth surface. It transpired that Zn-Zr MOF-2 and Zn-Zr MOF-3 could not efficiently photocatalyze the degradation of pollutants, because the surfaces of their structures were not sufficiently exposed. The SEM images revealed that the Zn:Zr molar ratio directly affected the assembly and hence the crystal structures of the Zn-Zr MOFs. This was corroborated by the N_2 adsorption-desorption isotherms of the samples (*vide infra*) and the XRD measurements (*vide supra*). Based on the accumulated results, Zn-Zr MOF-1 was selected for physical adsorption studies.

3.1.4 N_2 Adsorption-Desorption Isotherms

N_2 adsorption-desorption was performed to further investigate the pore structure parameters of Zn-Zr MOFs with different Zn: Zr molar ratios. The results were presented in **Figure 4** and **Table 1**. As could be seen in **Figures 4A–C**, the adsorption–desorption isotherms of the Zn-Zr MOF-1 sample showed type I/IV isotherms, indicative of microporous and mesoporous. For comparison, Zn-Zr MOF-2 and Zn-Zr MOF-
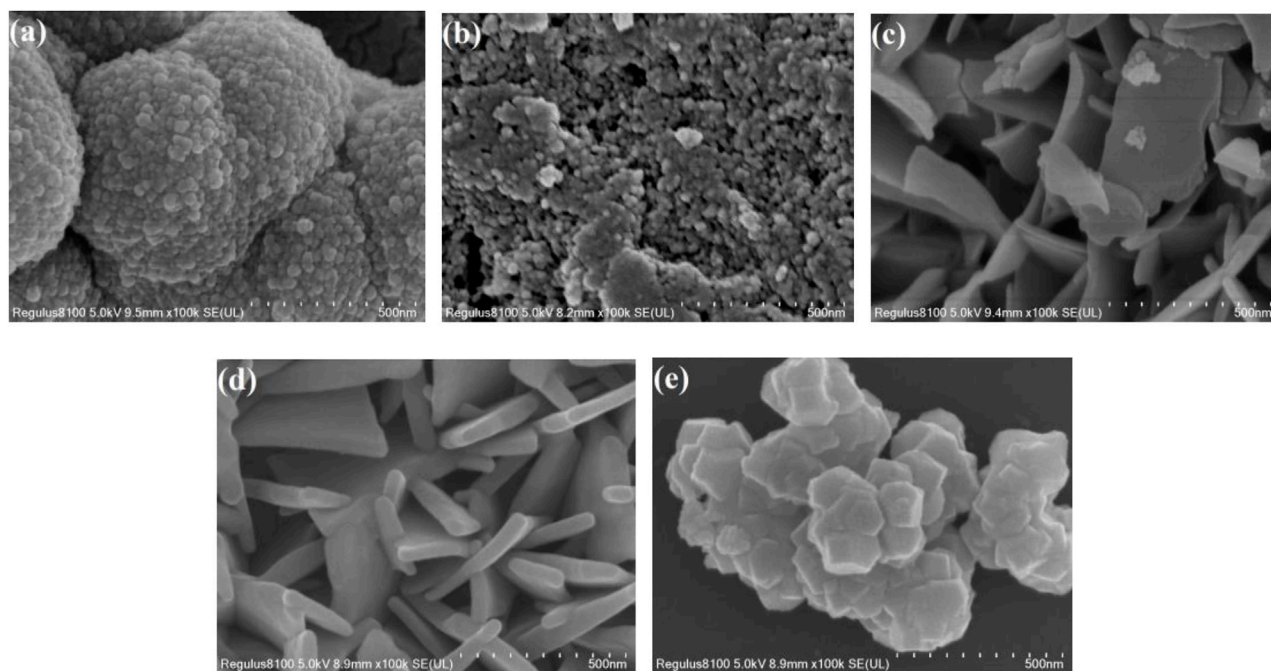
FIGURE 3 | SEM images of Zn-Zr MOF-1 **(A)**, Zn-Zr MOF-2 **(B)**, Zn-Zr MOF-3 **(C)**, Zn MOF **(D)**, and Zr MOF **(E)**.

2 samples revealed a type-IV shape pattern with an obvious hysteresis loop, which suggested that mesopores exist. As expected, from **Table 1**, the BET surface area and mean pore volume of Zn-Zr MOF-1 (460.4 m^2/g, 0.27 cm^3/g) were found to be larger than those of Zn-Zr MOF-2 (254.11 m^2/g, 0.12 cm^3/g) or Zn-Zr MOF-3 (294.94 m^2/g, 0.24 cm^3/g), indicating more pores in the former. Meanwhile, the average pore sizes of Zn-Zr MOF-1, Zn-Zr MOF-2, and Zn-Zr MOF-3 were evaluated as 2.35, 7.69, and 3.35 nm, respectively. The results showed that different Zn:Zr ratios modified the pores. The characterization data showed that larger specific surface area and pore volume increased the adsorption performance of the material, promoted contact between the pollutant and catalyst, and hence improved the catalytic efficiency. It was generally believed that the greater the surface area of a catalyst, the greater the number of active sites thereon (Wang et al., 2015), favoring molecular diffusion and binding of the reactant. Since the catalytic reaction was a surface-controlled process, the photocatalytic activity was improved and the separation efficiency of photogenerated electrons and holes was enhanced (Wu et al., 2021). Therefore, the structural characteristics of Zn-Zr MOF-1 may be envisaged as beneficial for the removal of organic pollutants from water.

3.2 Photocatalytic Performance Study of the MOFs Towards RhB Degradation

The catalytic performances of the MOFs were evaluated by carrying out the photodegradation of RhB over Zr MOF, Zn MOF, and Zn-Zr MOFs. In order to eliminate the self-degradation effect of RhB in the photoreaction system, a blank degradation experiment on RhB was carried out

under visible light irradiation without any catalyst. As could be observed from **Figure 5**, essentially no degradation of RhB occurred under visible light in the absence of a catalyst. Similarly, RhB showed almost no degradation in the presence of the Zn-Zr MOF catalyst but with the exclusion of light. As expected, the degradation of RhB increased with increasing reaction time in the presence of different photocatalysts under visible light irradiation. Zn MOF proved to be the least effective photocatalyst. The extent of degradation of RhB over Zn MOF at 0.6 g/L was just 10.3% after 60 min. This implied a high proclivity for electron-hole recombination under light irradiation, due to a slow rate of electron transfer and relatively poor absorption of visible light. Nevertheless, there was still a certain degree of degradation, mainly due to the photosensitivity of RhB (Liang et al., 2018). The photodegradation performance of Zr MOF was superior to that of Zn MOF, but inferior to those of the Zn-Zr MOFs, degrading 59.9% of RhB at a loading of 0.6 g/L within 60 min. The Zn-Zr MOF-1 composite showed the best RhB photodegradation performance, degrading 97.4% of RhB at a loading of 0.6 g/L within 60 min. The photocatalytic activities of the Zn-Zr MOFs with different Zn:Zr molar ratios were clearly higher than those of the single-metal MOFs, which may be attributed to some suppression of electron-hole recombination and improved absorption intensity in the visible light region (Li, 2021). However, it appeared that excessive Zn hinders the response of bimetallic Zn-Zr MOF catalysts to visible light. The photodegradation rates of RhB over Zr MOF, Zn MOF, and Zn-Zr MOFs with different Zn:Zr molar ratios were quantitatively evaluated using a kinetic rate model (Zhang et al., 2021), and the results were shown in
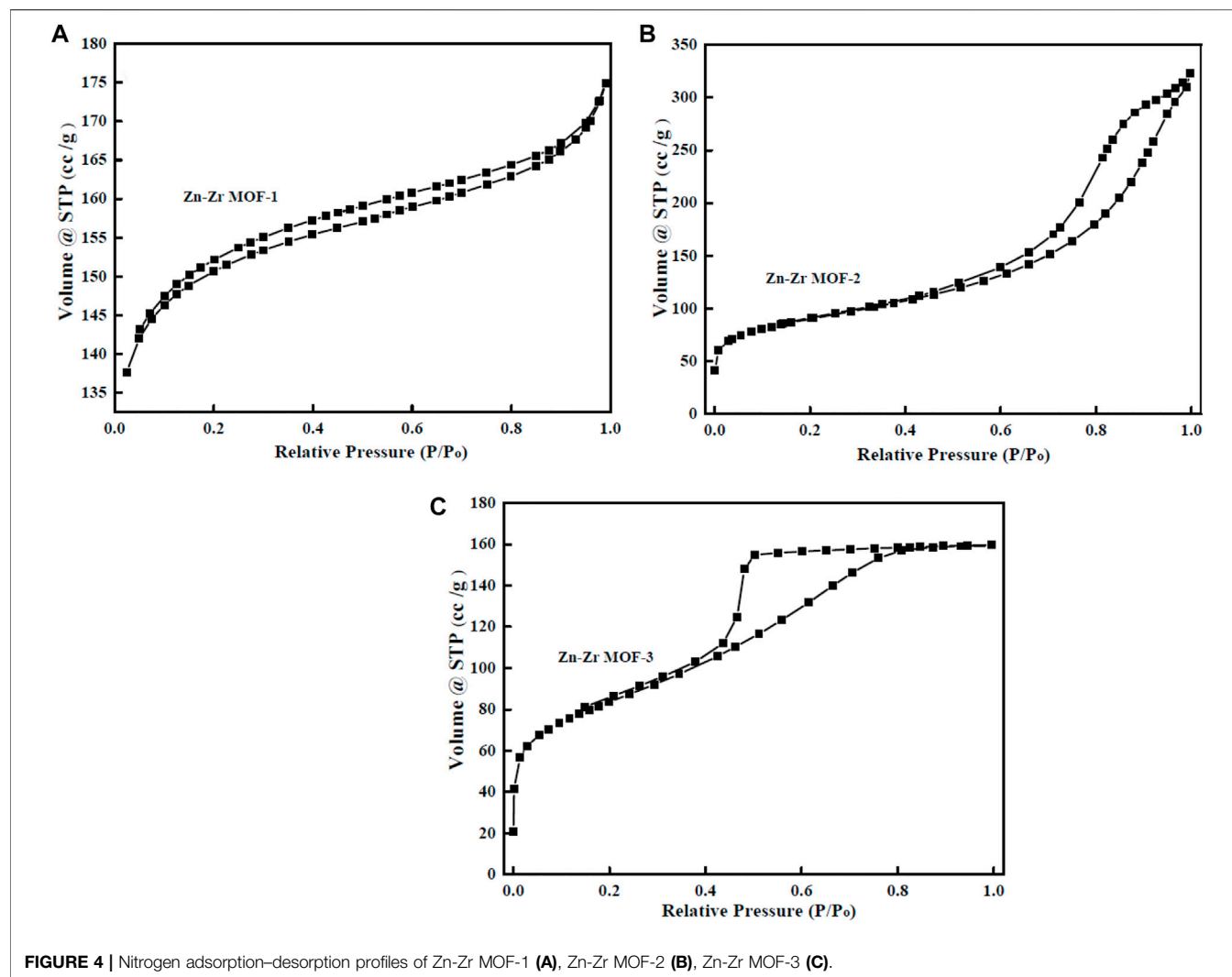
FIGURE 4 | Nitrogen adsorption–desorption profiles of Zn-Zr MOF-1 **(A)**, Zn-Zr MOF-2 **(B)**, Zn-Zr MOF-3 **(C)**.

TABLE 1 | BET surface areas and total pore volumes of the synthesized samples.

Sample	BET surface area (m^2/g)	Pore volume (cm^3/g)	Pore size (nm)
Zn-Zr MOF-1	460.4	0.27	2.35
Zn-Zr MOF-2	254.1	0.12	7.69
Zn-Zr MOF-3	294.9	0.24	3.35

Figure 5B and **Table 2**. The results of kinetic studies on the degradation of RhB over the different photocatalysts showed that the correlation coefficients were 0.8784, 0.9741, 0.9625, 0.8036, 0.9880 for linear plots of Zn MOF, Zr MOF, Zn-Zr MOF-1, and Zn-Zr MOF-2 and Zn-Zr MOF-3 respectively, indicating the process follows a pseudo-first-order model. The apparent rate constant k over Zn-Zr MOF-1 was 0.0627 min^{-1}, around 4.0 times higher than that over Zr MOF and 36.9 times higher than that over Zn MOF. The apparent rate constant over Zn-Zr MOF-1 was about 1.7 times that over Zn-Zr MOF-2 and 2.1 times that over Zn-Zr MOF-3, which may be attributed to the abovementioned observations concerning

the surface morphology and structure and the higher specific surface area and pore volume of Zn-Zr MOF-1.

3.3 Effect of Photocatalyst Dosage on RhB Degradation

In view of the results obtained in the preceding section, the Zn-Zr MOF-1 sample with Zn:Zr molar ratio 1:1.5 was selected to further investigate the effects of various factors on its photocatalytic activity. First, the effect of varying the loading amount of Zn-Zr MOF-1 photocatalyst in the RhB solution was investigated, keeping all other operating variables constant. The
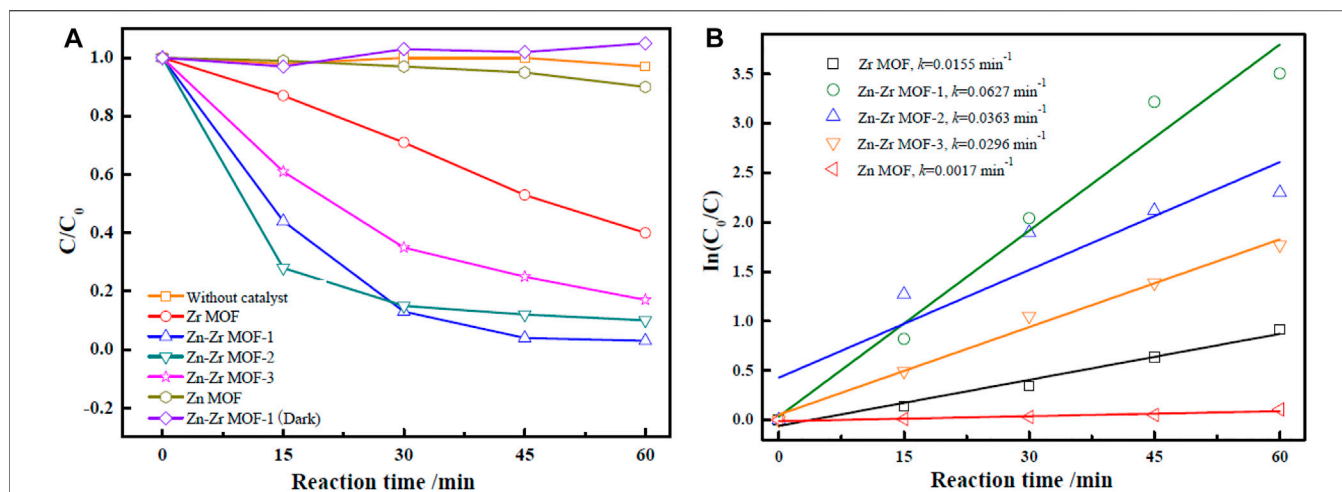
FIGURE 5 | Photocatalytic degradation curves **(A)** and first-order kinetic degradation rates **(B)** of RhB with different catalysts under visible light irradiation.

TABLE 2 | Kinetic parameters of the pseudo-first order for RhB degradation under visible light irradiation.

Dye	Sample	Pseudo-first order	
		k	R^2
RhB	Zn MOF	0.0017	0.8784
RhB	Zr MOF	0.0155	0.9741
RhB	Zn-Zr MOF-1	0.0627	0.9625
RhB	Zn-Zr MOF-2	0.0363	0.8036
RhB	Zn-Zr MOF-3	0.0296	0.9880
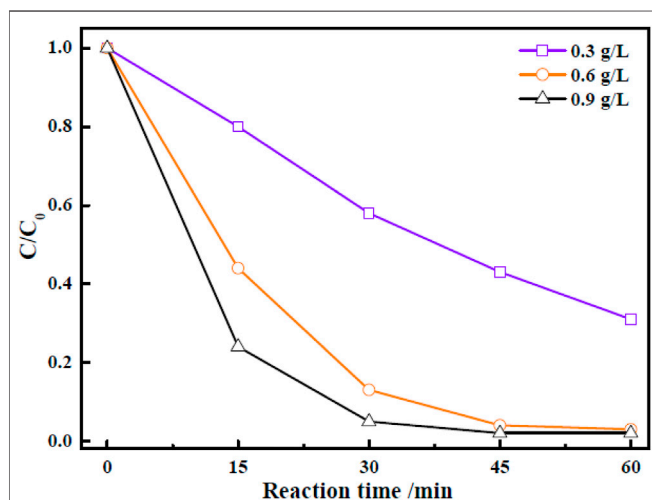
FIGURE 6 | Effect of catalyst loading on the photocatalytic degradation of RhB under visible light irradiation.

FIGURE 7 | Effect of different concentrations of RhB on its photocatalytic degradation under visible light irradiation.

relevant results were displayed in **Figure 6**. It could be seen that the amount of degradation of RhB within 30 min increased with increasing loading of the photocatalyst, within a certain range, presumably due to the provision of more active sites. The extents
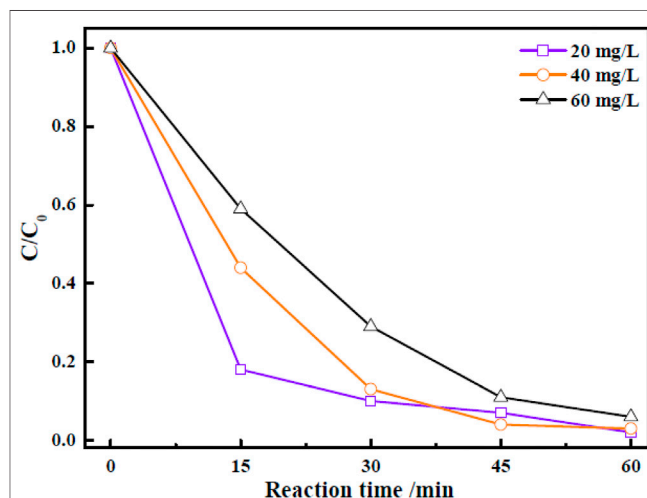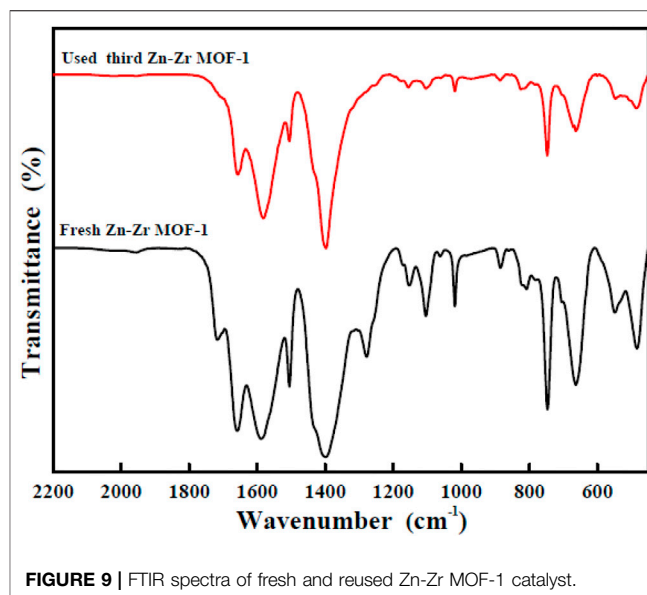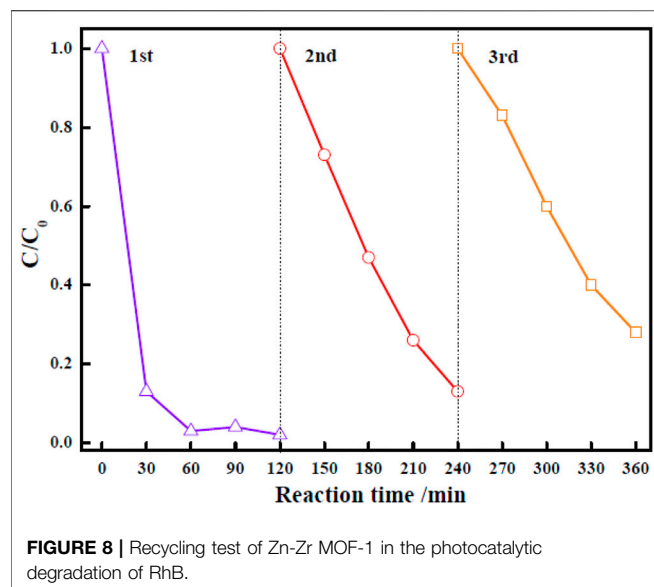
of RhB degradation were 57.5, 97.4, and 98.1% after 60 min with Zn-Zr MOF-1 loadings of 0.3 g/L, 0.6 g/L, and 0.9 g/L, respectively. It could be observed from **Figure 6** that there was no obvious change in the final degree of degradation of RhB when the catalyst loading was increased from 0.6 g/L to 0.9 g/L, which may possibly be attributed to a light shielding effect between particles (Liu et al., 2020). At the same time, a high catalyst loading in the degradation process would introduce a new environmental concern to the water supply ecology. Therefore, the Zn-Zr MOF-1 dosage was selected as 0.6 g/L.

## 3.4 Effect of the Initial RhB Concentration

The effect of initial dye concentration on the photocatalytic performance of Zn-Zr MOF-1 catalyst was studied. In these experiments, other operating factors, such as the solution pH, light source, and catalyst loading, were all kept constant. The

FIGURE 8 | Recycling test of Zn-Zr MOF-1 in the photocatalytic degradation of RhB.

FIGURE 9 | FTIR spectra of fresh and reused Zn-Zr MOF-1 catalyst.

results of the assessment of the photocatalytic efficiency of Zn-Zr MOF-1 catalyst at various initial concentrations of RhB dye (20, 40, and 60 mg/L) were presented in **Figure 7**. It could be seen that the extent of photocatalytic degradation of RhB after 30 min decreased as its initial concentration was increased. The extent of photocatalytic degradation of an organic dye depended upon the available surface area of the photocatalyst, the production of various radicals, and the ability of these radicals to react with the dye molecules (Bagherzadeh et al., 2020) Here, an increase in the initial dye concentration reduced the mean length of the penetration path of incident photons in the solution. As a result, the likelihood of incident photons reaching the surface of the photocatalyst to produce electron–hole pairs was suppressed. After 60 min, the degrees of degradation of RhB at concentrations of 20 mg/L, 40 mg/L, and 60 mg/L were 98.1, 97.4, and 94.4%, respectively, indicating that Zn-Zr MOF-1 showed a good degradation effect towards RhB at different concentrations, and hence a certain practical application potential.

3.5 Reusability and Stability of Zn-Zr MOF-1 Composite

For practical evaluation of the large-scale application of Zn-Zr MOF-1 photocatalyst, its reusability and stability in the photodegradation of RhB were investigated. Specifically, it was applied over three successive cycles. After each degradation process, the particles of the photocatalyst powder were separated. They were then collected from the reaction mixture by centrifugation, washed with ethanol and water, and oven-dried at 70°C. They were then applied in the next degradation cycle. The results of RhB degradation efficiency over Zn-Zr MOF-1 over three runs were presented in **Figure 8**. It could be seen that the degree of degradation of RhB was 97.7% in the first run, 86.8% in the second run, and 72.0% in the third run, indicating a loss of degradation efficiency over the three cycles. The decrease in RhB degradation efficiency in the course of reuse may be due in part to

FIGURE 10 | Photocatalytic degradation curves of different dyes over Zn-Zr MOF-1.
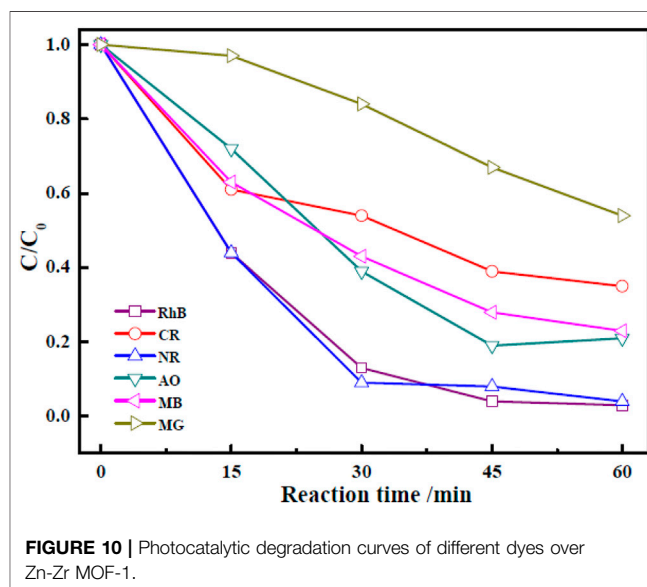
a small amount of catalyst being lost from the system during each recovery step (Duan et al., 2021). On the other hand, it may also be attributed to a loss of active sites on the catalyst surface. Pollutants or degradation products adsorbed on the material would gradually accumulate with increasing number of reaction cycles, progressively blocking more sites. Therefore, the relative reusability and stability of the Zn-Zr MOF-1 composite in photodegradation of the RhB was concluded. The FTIR spectra of Zn-Zr MOF-1 before and after three cycles of usage in the degradation of RhB were displayed in **Figure 9**. It could be seen that the spectrum remained essentially unchanged, albeit with a slight decrease in peak intensity. These results emphasized that a stable structure of the composite was maintained during the photocatalytic degradation process of RhB.

TABLE 3 | Degradation RB dyes by different photocatalysts as-synthesized.

Photocatalyst	Dye	Dye concentration	Photocatalyst concentration	Light source	Radiation time (min)	Degradation	Ref.
TiO_2	RhB	—	40 mg/40 ml	Visible	300	62.20	Huerta-Flores et al. (2019)
$ZnTiO_3$	RhB	0.1 mM	4 g/L	Visible	210	55.00	Meng et al. (2019)
$ZnTiO_3@TiO_2$	RhB	—	40 mg/40 ml	Visible	300	87.50	Huerta-Flores et al. (2019)
$ZnTiO_3@S$	RhB	10 ppm	0.03 g/30 ml	Solar	180	94.74	Tavakoli-Azar et al. (2020)
Cu-MOF	RhB	—	15 mg/40 ml	Visible	300	94.50	Wang et al. (2019)
$Sn O_2$/RCs	RhB	40 mg/L	0.9 g/L	Visible	120	95.56	Shi et al. (2021)
Zn-Zr MOF-1	RhB	40 mg/L	0.6 g/L	Visible	60	97.40	This work

3.6 Photocatalytic Degradation of Other Dyes by Zn-Zr MOF-1

It was crucial to study the photocatalytic degradation of other organic dyes to assess the applicability of the photocatalyst. Therefore, photocatalytic degradations of CR, NR, AO, MB, and MG by Zn-Zr MOF-1 were studied, according to the optimum experimental conditions of catalytic degradation of RHB by Zn-Zr MOF-1, which the initial concentration of dye is 40 mg/L, the photocatalyst concentration is 0.6 g/L and the illumination time is 60 min and the results were shown in **Figure 10**. The photocatalytic degradation effect of Zn-Zr MOF-1 on NR was similar to that on RhB, reaching 95.9% after 60 min. Zn-Zr MOF-1 also showed good degradation effects towards AO and MB, amounting to 79.2 and 76.7%, respectively, after 60 min of illumination. However, the degrees of degradation of CR and MG were low, which may be related to the chemical structures of these dyes. Overall, the results demonstrated that the synthesized Zn-Zr MOF-1 photocatalyst could be used to degrade different organic dyes with reasonably good universality.

3.7 Photocatalytic Degradation RB Dyes by Different Photocatalysts As-Synthesized

The degradation percentage of dyes of RB by different photocatalysts under visible light listed in **Table 3**. As can be seen, the catalytic degradation rate of RHB by Zn-Zr MOF-1 synthesized in this paper was significantly higher than that of TiO_2, $ZnTiO_3$ and $ZnTiO_3$, which had comprehensive significant advantages in terms of catalyst dosage and catalytic degradation time. Comparing with $ZnTiO_3@S$ Cu MOF and SnO_2/RCS, Zn-Zr MOF-1 also had certain advantages in the photocatalytic degradation effect of RHB, which mainly reflected in the characteristics of less catalyst dosage and shorter catalytic degradation time of Zn-Zr MOF-1.

4 CONCLUSION

A series of bimetallic Zn-Zr MOF photocatalysts has been synthesized by a hydrothermal method. Compared with the single-metal MOFs, the photocatalytic activity of bimetallic Zn-Zr MOF is significantly improved. The effects of different Zn:Zr molar ratios on the structures and morphologies of the MOFs have been studied. The results showed that when the Zn:Zr molar ratio was 1:1.5, the surface morphology and structure of the Zn-Zr MOF were relatively uniform, and it had a high specific surface area and large pore volume, providing more reactive sites for the substrate. Under visible light irradiation, the extent of degradation of RhB by Zn-Zr MOF-1 reached 97.4% within 60 min, and the photocatalyst also showed good photocatalytic degradation activity towards other dyes. The results of this study may provide reference data for industrial organic wastewater treatment.

DATA AVAILABILITY STATEMENT

The original contributions presented in the study are included in the article/Supplementary Material, further inquiries can be directed to the corresponding author.

AUTHOR CONTRIBUTIONS

XZ was in charge of designing the experiments and writing the manuscript. RY and DW was in charge of methodology and formal analysis. WL and YZ were in charge of revising the manuscript. YZ was in charge of project administration.

FUNDING

REFERENCES

Bagherzadeh, S. B., Kazemeini, M., and Mahmoodi, N. M. (2020). A Study of the DR_{23} Dye Photocatalytic Degradation Utilizing a Magnetic Hybrid Nanocomposite of MIL-53(Fe)/CoFe$_2$O$_4$: Facile Synthesis and Kinetic Investigations. *J. Mol. Liq.* 301, 112427. doi:10.1016/j.molliq.2019.112427

Banerjee, S., and Dastidar, M. G. (2005). Use of Jute Processing Wastes for Treatment of Wastewater Contaminated with Dye and Other Organics. *Bioresour. Technol.* 96 (17), 1919–1928. doi:10.1016/j.biortech.2005.01.039

Baten, S. H., Yang, T. Y., Li, Z. Y., and Wu, M. H. (2021). Preparation of Ferrous-Doped MIL-53(Fe) Photo-Fenton Catalyst and its Application in Dyeing and Printing Wastewater Treatment. *Text. Aux.* 38 (7), 36–40. doi:10.3969/j.issn.1004-0439.2021.07.009

Chen, S., Xu, X., Gao, H., Wang, J., Li, A., and Zhang, X. (2021). Fine-tuning the Metal Oxo Cluster Composition and Phase Structure of Ni/Ti Bimetallic MOFs for Efficient CO2 Reduction. *J. Phys. Chem. C* 125, 9200–9209. doi:10.1021/acs.jpcc.1c03239

Duan, X. Y., Xu, J. H., He, M. Q., and Zhang, X. Q. (2021). Preparation of 2D Graphite Phase Carbon Nitride Nanosheets and Their Photocatalytic Performance. *Fine Chem.* 38 (1), 83–90. doi:10.26918/d.cnki.ghngc.2020.000810

Huang, F., Li, Q., Luo, S., Yan, A. H., Xu, Y. F., and Xiong, X. (2021). Preparation and Photocatalytic Activity of ZnIn$_2$S$_4$/MIL-125 Nanocomposites. *J. Chin. Ceram. Soc.* 49 (6), 1167–1175. doi:10.14062/j.issn.0454-5648.20200657

Huerta-Flores, A. M., Sánchez-Martínez, D., del Rocío Hernández-Romero, M., Zarazúa-Morín, M. E., and Torres-Martínez, L. M. (2019). Visible-light-driven BaBiO3 Perovskite Photocatalysts: Effect of Physicochemical Properties on the Photoactivity towards Water Splitting and the Removal of Rhodamine B from Aqueous Systems. *J. Photochem. Photobiol. A Chem.* 368, 70–77. doi:10.1016/j.jphotochem.2018.09.025

Kan, H., Soklun, H., Yang, Z., Wu, R., Shen, J., Qu, G., et al. (2020). Purification of Dye Wastewater Using Bicarbonate Activated Hydrogen Peroxide: Reaction Process and Mechanisms. *Sep. Purif. Technol.* 232, 115974. doi:10.1016/j.seppur.2019.115974

Kandiah, M., Nilsen, M. H., Usseglio, S., Jakobsen, S., Olsbye, U., Tilset, M., et al. (2010). Synthesis and Stability of Tagged UiO-66 Zr-MOFs. *Chem. Mat.* 22 (24), 6632–6640. doi:10.1021/cm102601v

Li, L. Z. (2021). Preparation Andphotocatalytic Degradation of ZnO Graphene Composites. *J. Funct. Mater.* 52 (5), 5140–5144. doi:10.3969/j.issn.1001-9731.2021.05.021

Li, N., Zhang, W., Li, G. X., and Zhao, Y. (2021). Research Progress of TiO$_2$ Photocatalysts. *Fine Chem.* 38 (11), 2181–2188. 2258. doi:10.13550/j.jxhg.20210582

Liang, H. Y., Zou, H., Hu, S. Z., Li, J. Z., and Tian, Y. W. (2018). Preparation and Photocatalytic Performance of G-C$_3$n$_4$ Composites Hybridized with Bi$_2$O$_2$CO$_3$2D Nanosheets. *J. Mol. Catal.* 32 (2), 152–162.

Liu, T. Y., Gong, Y. T., Zhao, J., and Wang, M. (2020). Study on the Degradation of Rhodamine B by Co$_3$O$_4$/g-C$_3$n$_4$ Composite Photocatalys. *Ind. Water Treat.* 40 (2), 92–95.

Meng, J., Lan, Z., Lin, Q., Chen, T., Chen, X., Wei, X., et al. (2019). Cubic-like BaZrO3 Nanocrystals with Exposed {001}/{011} Facets and Tuned Electronic Band Structure for Enhanced Photocatalytic Hydrogen Production. *J. Mat. Sci.* 54, 1967–1976. doi:10.1007/s10853-018-2995-8

Shanmuganathan, V., Santhosh Kumar, J., Pachaiappan, R., and Thangadurai, P. (2021). Transition Metal Ion-Doped In2O3 Nanocubes: Investigation of Their Photocatalytic Degradation Activity under Sunlight. *Nanoscale Adv.* 3 (2), 471–485. doi:10.1039/d0na00694g

Shi, Q. Y., Zhang, J., Guo, Y. F., Gong, H., and Zhang, W. K. (2021). Photocatalytic Degradation of Rhodamine B by SnO$_2$/reticulated Carbon Composite. *ActaScientiae Circumstantiae* 12, 1–14. doi:10.13671/j.hjkxxb.2021.0194

Tavakoli-Azar, T., Mahjoub, A. R., Sadjadi, M. S., Farhadyar, N., and Sadr, M. H. (2020). Improving the Photocatalytic Performance of a Perovskite ZnTiO3 through ZnTiO3@S Nanocomposites for Degradation of Crystal Violet and Rhodamine B Pollutants under Sunlight. *Inorg. Chem. Commun.* 119, 108091. doi:10.1016/j.inoche.2020.108091

Wang, Y., Sun, H., Duan, X., Ang, H. M., Tadé, M. O., and Wang, S. (2015). A New Magnetic Nano Zero-Valent Iron Encapsulated in Carbon Spheres for Oxidative Degradation of Phenol. *Appl. Catal. B Environ.* 172-173, 73–81. doi:10.1016/j.apcatb.2015.02.016

Wang, Y., Li, Q., Guan, B. B., and Fan, Z. L. (2019). A Dual Functional Copper-MOF towards Dyes via Physical Adsorption and Chemical Photodegradation. *Dye. Finish.* 45 (11), 17–22. 42.

Wang, Y., Tang, W., Li, X., and Wei, D. (2021). Improving the Electrocatalytic Activity of NiFe Bimetal-Organic Framework toward Oxygen Evolution Reaction by Zr Doping. *Electrochimica Acta* 381, 138292. doi:10.1016/j.electacta.2021.138292

Wu, Q., Siddique, M. S., and Yu, W. (2021). Iron-nickel Bimetallic Metal-Organic Frameworks as Bifunctional Fenton-like Catalysts for Enhanced Adsorption and Degradation of Organic Contaminants under Visible Light: Kinetics and Mechanistic Studies. *J. Hazard. Mater.* 401, 123261. doi:10.1016/j.jhazmat.2020.123261

Xue, F. H., and Zhu, B. Y. (2019). Study on the Treatment Technology of Dye Wastewater. *Environ. Dev.* 31, 91–93.

Yang, S. X., Zhong, W. Y., Li, C. X., Su, Q., Xu, B., He, G., et al. (2021). Photochemical Fabrication and Performance of Polyaniline Nanowire/SnO2 Composite Photocatalyst. *Chem. J. Chin. Univ.* 42 (6), 1942–1951. doi:10.7503/cjcu20200573

Yin, N., Liu, C. L., and Zhang, J. (2021). Preparation and Photocatalytic Property of MoO$_3$/g-C$_3$n$_4$ Composite. *Inorg. Chem. Ind.* 52 (10), 161–165. doi:10.11962/1006-4990.2019-0568

Zhang, Y. Q., Li, X. L., Zhao, Z. J., Wang, Y. J., Yuan, X. Z., Zhang, J., et al. (2021). Ascorbic Acid Modified Br-Doped G-C$_3$n$_4$ Photocatalytic Degradation of Pollutants. *China Environ. Sci.* 41 (11), 5160–5168. doi:10.19674/j.cnki.issn1000-6923.20210527.004

Zhao, D., and Cai, C. (2021). Cerium-based UiO-66 Metal-Organic Framework for Synergistic Dye Adsorption and Photodegradation: A Discussion of the Mechanism. *Dyes Pigments* 185, 108957. doi:10.1016/j.dyepig.2020.108957

Research Progress and the Development Trend of the Utilization of Crop Straw Biomass Resources in China

Wei Yang[1,2], Xiaohua Li[1,2] and Yutao Zhang[2,3]*

[1]College of Resources and Environmental Engineering, Anshun University, Anshun, China, [2]University Rural Revitalization Research Center in Guizhou, Anshun, China, [3]College of Chemistry and Chemical Engineering, Anshun University, Anshun, China

The utilization of crop straw biomass resources is highly emphasized by governments and academia in recent decades. Based on the core databases of the literature in China National Knowledge Infrastructure (CNKI) academic journals, CiteSpace software is used to analyze and process the hotspots, and this study proposed the primary coverage and evolutionary trends of research on the utilization of crop straw resources. The thesis proposes the research development trend for improving the institutional mechanism of the utilization of crop straw resources, strengthening technology research and development, exploring the economic model of green cycle agriculture, accelerating the construction of the industrial system, and designing new paths of resource utilization in multiple ways, which helps estimate the development trend of the utilization of crop straw resources and provide inspiration and direction for future research and practices.

Keywords: crop straw biomass, resource utilization, progress, development trend, CiteSpace

INTRODUCTION

The effective utilization of crop straw biomass is an important basis for the development of green agriculture and directly affects the construction of the rural ecological environment (Nie, 2021). It is a significant topic of common concern about how to efficiently use and scientifically treat it in all countries nowadays, and academics have carried out multifaceted research on this problem at home and abroad. Developed agricultural countries attach great importance to the resource utilization of straw and have carried out a series of studies on the usage methods (Champagne, 2008; Arthur and Baidoo, 2011). For example, in the United States, 45 million tons of wheat straw was utilized each year. Special funds were set up by the Department of Agriculture and Energy to research biomass fuels such as straw, and they have built 16 ethanol refineries, and certain government subsidies were given to them (Zhu and Yu, 2012). In Japan, 75% of straw is returned to the field every year or processed into roughage for cattle and sheep. The Japanese government pays great attention to developing and upgrading the straw utilization technology (Liu, 2014), and the law stipulates that straw must be recycled (Jia, 2015). In Denmark, the development of direct-fired biomass power generation is outstanding. They have built 13 straw power plants, and straw power generation accounts for 81% of the total renewable energy in the country (Fu, 2007). In Europe and the US, the way and amount of crop straw returned are clearly defined in the law in order to promote the standardization of crop straw utilization (Zhu, 2014), and they achieved good performance. For example, in Canada, about 67% and 73% of crop straw are recycled in Canada and England, respectively (Zhu, 2014). China is a large agricultural country with more than 1.4 billion people and a

country with large straw production each year. Data show that China produced about 700 million tons of crop straw in 2012 (Chen et al., 2012), accounting for 18% of total agricultural organic waste (Zhou et al., 2017), and the number increased to 827 million tons in 2017 (Cong et al., 2019). With the increase in huge pressure of straw biomass disposal, people are increasingly concerned about this issue (Chen and Shi, 2017). China's government attaches great importance to the utilization of crop straw resources. Domestic research on straw resource utilization is slightly delayed compared to other developed countries, and over the years, the governments have issued a series of documents to prohibit straw burning and promote diversified utilization pathways to accelerate straw utilization. However, squander of straw also can be observed sometimes for economic benefits and labor costs (Wen et al., 2018). Research results show that China's crop straw is utilized in various ways, and it is used to generate energy (Liu et al., 2020), forage (Duan, 2018), fertilizer (Ma and Dong, 2020), raw material, and base material (Wu et al., 2010). The main approach is to return the straw to the field (Bi et al., 2009). In 2008, straw harvested from 26.76 million hm^2 was returned to the field (Bi, 2010), but the utilization of straw resources, especially the industrial development, is still limited. The technical system is still immature, and a series of problems need to be resolved (Liu et al., 2011). Therefore, a systematic analysis of crop straw resource utilization hotspots, content, and the current situation can help in studying and judging the development trend of straw resource utilization and provide inspiration and direction for future research and practice.

Based on the CNKI database, core journal papers database, using CiteSpace software, and graphical compilation, the authors mapped and analyzed the progress and trends of crop straw resource utilization research in China. The authors summarized and sorted out the main research hotspots to judge the future development trend of research on straw utilization.

DATA SOURCES AND RESEARCH METHODS

Data Sources

The main subject of this article is the utilization of crop straw resources. The literature studies that the author has studied are core papers in the CNKI database, and these papers are indexed by the source journals from SCI, EI, core journal Peking University, CSSCI, and CSCD. The author set the search terms as *the utilization of crop straw resource*, *the utilization of crop straw feed*, *the utilization of crop straw energy*, *the utilization of raw material*, *the utilization of crop straw fertilizer*, *crop straw base utilization*, or *crop straw industrial utilization* with all years.

The index results showed that from 1994 to 2022, 135 articles studied the straw utilization from core journals in the CNKI database. The author removed four articles from the first online journals and eight articles from other volumes that were not part of the research papers. Eventually, 123 relevant literature studies from 2002 to 2021 were pitched to analyze and study.

Research Methodology

CiteSpace software is commonly used in academic research because it enables readers to study the literature on a specific topic in scientific research in a visual way to obtain a scientific knowledge map in terms of layout structure, change pattern, publication time, subject area, author institution, and research level (Hu et al., 2022). In this study, CiteSpace software combined with fuzzy clustering analysis and correlation analysis is used to explore the research hotspots, main contents, evolutionary trends, and their correlations with the utilization of crop straw resources. The author analyzed the intrinsic connections of research hotspots at different stages and then studied the development direction of future research.

RESEARCH HOTSPOTS AND EVOLUTION TRENDS

Research Hotspots

The keywords or subject terms can reflect the core content and research hot spots of the study perfectly (Shi and Tong, 2018). The authors analyzed the high-frequency keyword co-occurrence with CiteSpace software and summarized the hot spots of the research of crop resource utilization in each period. These keywords include *the utilization of crop straw fodder, biomass energy utilization, resource utilization, lignin degradation, biofermentation, straw gasification, base material utilization, industrial utilization, rational utilization, industrial chain, farmers' willingness,* and *livestock carrying capacity*. In summary, they focused on high-frequency co-occurring words such as resource utilization, energy, forage utilization, fertilizer utilization, industrial raw material, base material utilization, and circular economy, reflecting the research hotspots of crop resource utilization in the last decade.

Evolution Trends

The keywords or subject terms in the relevant literature were analyzed for emergent terms (**Figure 1**) to determine the development and new directions in the field of the research of crop straw resource utilization. The author used the time-zone function of CiteSpace software to explore the emergent terms to determine the emerging trends of research topics. **Figure 1** shows the top nine emergent terms in the last 10 years: the first one is energy utilization with 1.5544 intensity from 2008 to 2010. The second one is straw fertilization with 1.5259 intensity from 2006 to 2009. The following terms are fodderization from 2014 to 2016, straw fodder from 2018 to 2021, agricultural waste from 2009 to 2013, resourcization from 2009 to 2010, crops from 2015 to 2016, straw burning from 2014 to 2015, and raw material from 2014 to 2015. The intensity of straw burning and straw raw materialization is the lowest. Straw burning causes severe environmental pollution, and how to reduce pollution induced by CO_2 emissions and make straw into a propellant for ecological civilization and ecological environment construction is still a problem to be solved.

At present, straw is used as raw materials for industrial and agricultural utilization. Agricultural utilization mainly includes
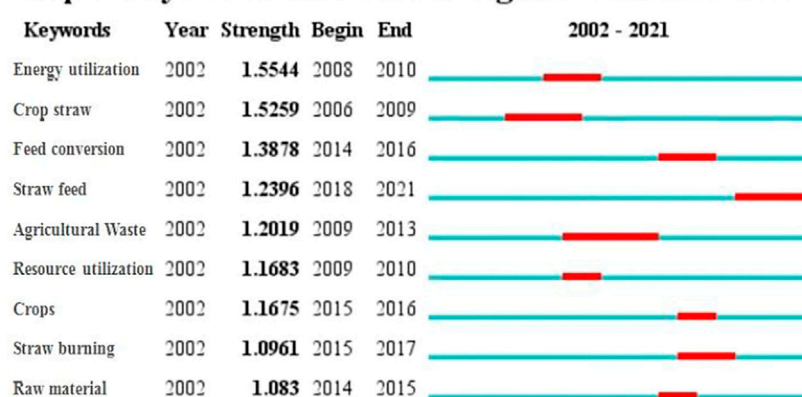
Top 9 Keywords with the Strongest Citation Bursts

Keywords	Year	Strength	Begin	End	2002 - 2021
Energy utilization	2002	1.5544	2008	2010	
Crop straw	2002	1.5259	2006	2009	
Feed conversion	2002	1.3878	2014	2016	
Straw feed	2002	1.2396	2018	2021	
Agricultural Waste	2002	1.2019	2009	2013	
Resource utilization	2002	1.1683	2009	2010	
Crops	2002	1.1675	2015	2016	
Straw burning	2002	1.0961	2015	2017	
Raw material	2002	1.083	2014	2015	

FIGURE 1 | Top nine high-frequency emergent words.

TABLE 1 | Pathway of crop straw resource utilization.

Entry	Utilization Approach	Technical Connotations	Application Area	Evaluation	Reference
1	Utilization as fertilizers	Straw is decomposed into an organic fertilizer or returned to the field directly.	Organic fertilizer	Enhance soil fertility and increase yield. Ecological effects under different tillage conditions are unclear.	Ding et al. (2010)
2	Utilization as forage	Straw is used as fodder directly or silage into forage that can be easily digested by animals.	Forage for livestock	After physical, chemical, and biological processing, straw has a higher value, but the operation process is complicated.	Wang et al. (2009)
3	Utilization as energy generation material	Straw is burned directly or converted to heat, gas, electricity, and other forms of energy.	Used to generate biogas and power; liquefaction, solidification, and carbonization of straw	The technology is imperfect for low overall utilization, high cost, and secondary pollution.	Xiao et al. (2010)
4	Utilization as industrial raw materials	Straw is rich in cellulose and is processed as a raw material for industrial production.	Plate, paper, packaging materials, starch extraction, and production of thermal insulation material	Resource-saving and environment friendly with bright prospects	Fan and Zhou, (2004)
5	Utilization as base material	Straw is used as strain culture, seedling, and lawn substrate.	Substrate for edible fungi, flower seedling base material, and lawn base material	Drives the growth of straw utilization scale effectively.	Shi et al. (2016)

being used as the planting substrate of edible fungi and flowers. However, this utilization is at a relatively low level at this stage with immature technology and low effectiveness, so there are still many issues to be further explored.

Main Research Content

Based on the analysis of the occurrence time and frequency of keywords, the main research contents of agricultural straw resource utilization were divided into five utilization approaches (**Table 1**).

1) Fertilization of Straw

Returning straw to the field improves soil fertility well because crop straw is rich in organic matter and minerals (Yang et al., 2011), making good natural suitability and economic benefits (Chen et al., 2020). Crop straw can be returned to the field directly or indirectly. Direct return mainly includes burying rice or cornstalk in the field, mixing corn straw within the plow layer, mulching corn in the field, and rototilling rice straw in the field (Han and Zou, 2018). Indirect return involves crop straw composting (Zhang et al., 2016), making biogas and its by-product fertilizer utilization (Zhao et al., 2017), combining straw utilization with farming (Shi, 2018), straw carbonization (Wu et al., 2015), straw substrate fertilization, and other technical models (Zhang, 2017), while indirect return to the farmland is faced with difficulties such as cost increase caused by the input of agricultural implements, machinery and labor, difficulty in storage, and pollution in the fermentation process.

2) The Straw Utilization of Forage

The utilization of straw for feed, especially studying the development of the food-saving livestock industry and promoting China's food security guarantee, is an important measure of sustainable agricultural development. Straw feed processing

methods mainly include straw bulking, ammonification, pellet feed, straw silage, straw compaction, and straw microstorage. The integration and optimization of the aforementioned technologies are effective means to promote the utilization of straw for feed. Technological progress is mainly achieved through the optimization of the main body, process, facilities, and auxiliary parts. (Qi et al., 2013).

3) The Straw Utilization of Energy

At present, straw energy utilization modes mainly include straw to biogas, straw centralized gas supply, straw power generation, and straw solidification molding (Li et al., 2010).

The utilization of biomass to generate energy is an important source of energy in the future. There are various ways of energy utilization, but the utilization technology needs to be further explored. At present, the main modes of straw energy utilization include biogas production, straw-fired cogeneration, and densified corn stover briquetting fuel (Li et al., 2010).

Practice shows that the efficiency of straw-fired cogeneration is low while the cost is high (Li et al., 2010). Currently, fuel enterprises in operation are mainly small- and medium-sized enterprises, which need to be improved in scale utilization and market recognition (Guo and Wand, 2017). The research shows that in the process of straw energy utilization, the cost of straw includes the input of raw material purchase, transportation, collection, and loading, which is generally high (Han and Zou, 2018). To promote straw energy utilization, many studies should be solved in the future to decrease the cost.

4) Straw Raw Materialization and Base Materialization Utilization

Straw is rich in lignocellulose and can be used as raw material for industrial products after a series of processes. This process can save resources and increase income at the same time. Raw materialization of straw is a process in which crop straw is transformed into lightweight synthetic panels, functional flooring, wooden doors or windows, and other construction materials for usage. Crop straw is used as a substrate generally for flowers, seedlings, and microbial strains (Li, 2014). Some scholars have concluded that straw materials can be used as building insulation, which has the advantage of reducing CO_2 emissions and saving energy (Ma and Dong, 2010). However, the proportion of straw used as raw material for industrial products is still relatively small, and the technology of straw materialization needs to be improved to increase the scale of raw material utilization.

RESEARCH CONCLUSIONS AND DEVELOPMENT TRENDS

Conclusion of the Study

This study tries to estimate the utilization of crop straw resources in China by analyzing the research hotspot, research content, and the evolution trend of research direction using CiteSpace software. The results showed that the research frequency of crop straw resource utilization is on the rise, and the number of articles increased from 2002 to 2021, and the high-frequency co-occurring words with crop straw resource utilization mainly involve energy utilization, straw fertilization, straw fodder, straw resourcization, straw burning, and raw materialization, reflecting the research hotspot in different periods. In addition, the main content includes the straw utilization as fertilizer, forage, energy, raw materialization, and base materialization. Last, from the perspective of the evolution trend of research content, the research content gradually changes from increasing the utilization rate of straw resources to improving the level of the utilization technique.

Development Trend

The implementation of a series of national strategies such as new countryside construction, beautiful countryside construction, territorial space planning and rural revitalization, efficient utilization of resources, ecological environment protection, and high-quality economic development has become the theme of China's development. Based on the analysis of the current predicament and research progress of crop straw resource utilization, the authors assume that more attention should be paid to the following area:

1) The systems and mechanisms should be improved for using crop straw as resources. Under the leadership of the government, professional teams were organized to conduct in-depth research; the policy obstacles in the utilization of crop straw as resources were clarified, and targeted policies about financial support, technical assistance, incentive system, and performance assessment for the utilization of crop straw as resources were formulated.

2) Research on the resourcization technique of crop straw should be strengthened. The backward technology of straw recycling results in high production costs and small scale of straw-consuming enterprises. Strengthening the technical level of straw industrial utilization is the most important task at present.

3) It is necessary to adhere to the concept of carbon peak and carbon neutrality to explore the green circular agricultural economic model. Governments should promote the recycling of crop straws, especially the economical and intensive utilization of straw resources, and explore the suitable mode of green agriculture and recycling agriculture.

4) The construction of an industrial system should be accelerated for the utilization of crop straw resources. Countries all over the world, especially developed countries, should guide the exploration of diversified industrial utilization of crop straw, such as fertilizer, energy, feed, and raw material. The straw resource utilization industrial system should be constructed to get rid of crop straw resource utilization of small scale and low benefit predicament.

5) The utilization paths of crop straw are designed in diverse ways. In view of the needs of rural revitalization, beautiful countryside construction, and territorial space planning in the new era, a diversified design of the crop straw resource utilization path is carried out so as to explore a low-carbon

and high-efficient regional straw resource utilization path tailored to local conditions.

The raw data supporting the conclusions of this manuscript will be made available by the authors, without undue reservation, to any qualified researcher.

AUTHOR CONTRIBUTIONS

WY was in charge of designing the experiments and writing the manuscript. WY, XL, and YZ were in charge of revising the manuscript. YZ was in charge of project administration.

REFERENCES

Arthur, R., and Baidoo, M. F. (2011). Harnessing Methane Generated from Livestock Manure in Ghana, Nigeria, Mali and Burkina Faso. *Biomass Bioenergy* 35, 4648–4656. doi:10.1016/j.biombioe.2011.09.009

Bi, Y. Y., Gao, C. Y., and Wang, Y. J. (2009). Estimation of Straw Rresources in China. *Trans. CSAE* 25 (12), 211–217.

Bi, Y. Y. (2010). *Study on Straw Resources Evaluativn and Utilisation in China*. Beijing: Chinese Academy of Agricultural Sciences.

Champagne, P. (2008). Bioethanol from Agricultural Waste Residues. *Environ. Prog.* 27, 51–57. doi:10.1002/ep.10242

Chen, L., Li, X., Wen, W., Jia, J., Li, G., and Deng, F. (2012). The Status, Predicament and Countermeasures of Biomass Secondary Energy Production in China. *Renew. Sustain. Energy Rev.* 16 (8), 6212–6219. doi:10.1016/j.rser.2012.07.006

Chen, W. H., and Shi, X. X. (2017). Application and Research Status of Agricultural and Forestry Waste in China. *Mod. Agric. Sci. Technol.* 18, 148–149.

Chen, Y. F., Xia, X. G., and Yang, L. (2020). Straw Return Is the Realistic Way of Straw Resource Utilization. *Soil Fertilizer Sci. China* 6, 299–307.

Cong, H. B., Yao, Z. L., and Zhao, L. X. (2019). Distribution of Crop Straw Resource and its Industrial Systemand Utilization Path in China. *Trans. CSAE* 35 (22), 132–140.

Ding, Y., Peng, Z. M., and Xia, J. L. (2010). Domestic Comparison and Analysis of a Typical Straw Machinery. *Chin. Agric. Mech.* 03, 43–46.

Duan, G. R. (2018). Discussion on Feed Processing Technology of Crop Straw Based on Nutrition Economics. *China feed* 16, 13–16.

Fan, F., and Zhou, M. H. (2004). Make the Use of Straw Resource as Industrial Raw and Processed Materials. *China Resour. Compr. Util.* 04, 13–17.

Fu, B. Q. (2007). Development and Utilization of Straw Biomass Energy in Denmark. *Popular Util. Electr.* 7, 20–21.

Guo, K., and Wang, Q. (2017). *Overview of Development Status of Biomass Briquette Fuel in Jiangsu Province,Science and Technology Economic Guide*, 6, 60–62.

Han, X., and Zou, W. X. (2018). Effects and Suggestions of Black Soil Protection and Soil Fertility Increase in Northeast China. *Bull. Chin. Acad. Sci.* 33 (2), 206–212.

Hu, L. N., Zhang, J. F., and Xing, J. (2022). Research Hotspot and Evolution Trend of Green Economic Efficiency at Home and Abroad-Visual Analysis Based on CiteSpace. *J. Commer. Econ.* 04, 189–192.

Jia, L. (2015). *The Effects of Straw Return on Water Quality of Paddy Field*. Mianyang: Southwest University of Science and Technology, 2015.

Li, L. M., Yu, C. J., and Bai, J. S. (2010). Current Situation of Straw Direct Combustion Power Generation Technology in China. *Chem. Industry Eng. Prog.* 29 (Suppl. 1), 84–90.

Liu, H. X. (2014). Application of Straw Abroad. *North. Hortic.* 10, 142.

Liu, J. P., Ju, M. T., and Liu, Y. H. (2011). The Analysis of China's Utilization Technology of Agricultural Straw and Development of Biomass Industry. *Ecol. Econ.* 05, 136–141.

Liu, T. L., Zhao, L. X., and Meng, H. B. (2020). Reserch and Optimization of Evaluation Methords for Straw Energy Utilization Technology. *Environ. Eng.* 38 (08), 195–200.

Ma, Y. Y., and Dong, M. (2020). Analysis on the Farmers' Straw Resource Disposal Behavior and the Influencing Factors in Ecologically Fragile Areas. *Ecol. Econ.* 36 (06), 118–123.

Nie, X. D. (2021). *Research on Utilization of Crop Straw Resources in Tianjin*. Tianjin: Tianjin Agricultural University, 2015.

Qi, F., Zhou, X. Q., and Bao, S. S. (2013). Expression and Evaluation Method of Integrated Modes for Protected Horticulture Engineering. *Trans. CSAE* 29 (8), 195–202.

Shi, S. X., and Tong, P. S. (2018). Ananalysis of Ecological Security of the Urban Agglomeration Development Trend Based on CiteSpace Econometric Analysis. *Acta Ecol. Sin.* 38 (22), 8234–8246.

Shi, Z. L. (2018). Current Situation of Utilization of Straw Resources in China and Relevant Countermeasures and Suggestions. *World Environ.* 05, 16–18.

Shi, Z. L., Wang, F., and Li, X. (2016). The Discussion on Concept and Definition of Straw Substrate Utilization. *Soil Fertilizer Sci. China* 06, 152–155.

Wang, Y. J., Wang, B. R., and Zhang, Q. G. (2009). Ways and Suggestions of Straw Resource Utilization. *J. Henan Agric. Sci.* 07, 23–23+42.

Wen, C. B., Qian, F. J., and Liu, P. (2018). Situation and Evaluation of Agricultural Straw Resource Utilization. *Ecol. Econ.* 34 (02), 147–150+157.

Wu, W. X., Sun, X., and Dong, D. (2015). *Soil Environmental Effects of Biomass Carbon*. Beijing: Science Press, 1995.

Wu, Y. P., Zhang, L. W., and Cui, G. Q. (2010). Investigation and Thoughts on the Cmprehensive Utilization of Crop Stalk Resource in Henan Province. *J. Henan Agric. Univ.* 44 (03), 352–359.

Xiao, T. Q., He, C. X., and Ling, X. J. (2010). Research on Current Situation and Countermeasures of Comprehensive Utilization of Crop Straw Resources in China. *World Agric.* 12, 31–33+36.

Yang, F., Li, R., and Cui, Y. (2011). Effect of Straw Returning on Improving Soil Fertility and Increasing Crop Yield in Southern China. *Soil Fertilizer Sci. China* 01, 10–14.

Zhang, C. P. (2017). Production Technology of Edible Fungi Cultivated with Straw Based Materials in Anda City, Heilongjiang Province. *Chin. Hortic. Abstr.* 8, 175–176.

Zhang, Y. F., Teng, X., Li, Z. H., Wen, J., Li, Q., and Gao, X. (2016). Research Progress of Corn Stalk Compost and its Influencing Factors. *J. Jilin Agric. Univ.* 38 (5), 613–618.

Zhao, L. X., Meng, H. B., and Shen, Y. J. (2017). Investigation and Development Analysis of Planting-Breeding Circulating Agriculture Ecosystem in Northern Plains in China. *Trans. CSAE* 33 (18), 1–10.

Zhou, Z. R. (2012). A Theoretical Study of the Sustainable Use of Biomass Energy by Rural Households in China[C].Mems. *Nano Smart Syst.* 1-6, 2905–2909.

Zhu, J. C. (2014). *Study on the Problem of Shanxi Agricultural Wastes Resource Utilization*. Yangling: Northwest A&F University, 2014.

Zhu, Z. Y., and Yu, L. M. (2012). Effects of Fuel Ethanol Production by Maize on the Agricultural Products Market in U.S. *Food Nutr. China* 18 (6), 48–51.

Green Solvents for Lipid Extraction From Microalgae to Produce Biodiesel

Xiaofang Liu[†], Dayong Yu[†], Hangyu Luo and Can Li*

Guizhou Provincial Key Laboratory for Rare Animal and Economic Insects of the Mountainous Region, College of Biology and Environmental Engineering, Guiyang University, Guiyang, China

Microalgae are considered as the third-generation feedstock for biodiesel production, and lipid extraction plays a significant role in efficient production of biofuels. Numerous technologies including chemical, mechanical, and biological have been achieved but high efficiency and potential application on an industrial scale are still needed. This review discusses the factors that influence biodiesel quality and the relative green and sustainable solvents for lipid extraction.

Keywords: microalgae, biodiesel, lipid extraction, deep eutectic solvents, green solvent

INTRODUCTION

With the concern that fossil fuels have caused global warming and an energy crisis, there is a need to diminish the dependence on it and explore renewable energy. Biodiesel is considered as a potential alternative to petro-diesel as it is non-toxic, biodegradable, has an enhanced cetane number, higher flash point, is renewable, and is produced by transesterification of renewable feedstocks, resulting in monoalkyl esters from fatty acids (Meher et al., 2004; Hoekman et al., 2012; Fazal et al., 2013; Pan et al., 2022) In the past 2 decades, three generations of biodiesels have been investigated and each generation had advantages and disadvantages over different feedstocks. **Table 1** provided the summary of the generations of biodiesels. High-efficiency converted algae for biodiesel urgently needs to be explored.

THE PRODUCTION OF BIODIESEL FROM MICROALGAE

Fuel Properties Parameters of Biodiesels

Generally, factors including the viscosity, oxidation stability, cetane number (CN), cold filter plugging point, flash point, saponification value (SV), energy density, and density of biodiesel are determined by the fatty acid composition, which plays a crucially important role in biodiesel qualities. How to optimize the parameters with technologies to enhance quality during the production process is a key question.

Fatty acids are comprised of unsaturated, namely mono-unsaturated (denoted as Cn:1) and polyunsaturated (Cn:2 or 3), and saturated (Cn:0) fatty acids. Viscosity increases along with the chain length and fatty acid saturability. Transesterification, also called alcoholysis, of the algae oil to the corresponding fatty ester (biodiesel) is the most promising approach to the high viscosity problem (Demirbas, 2009). Better oxidation stability, meanwhile, requires a high level of fatty acid saturation (Graboski and McCormick, 1998). CN increases with the enhancement in chain length and fatty acid saturation level (İçingür and Altiparmak, 2003; Knothe, 2005). The higher the saturation degree is, the poorer the cold filter plugging point is (Ramos et al., 2009). A shorter chain length provides a lower flash point and the density will be high when the polyunsaturation level is high (Karmakar et al., 2010). Fatty acid methyl esters with a carbon chain length from 12 to 20 are identified as

TABLE 1 | Differences of three generations of biodiesel.

Biodiesel	Feedstock	Advantage	Disadvantage	Processing Technology	Ref
First Generation	Edible Plant Seeds	Relative high yield	negative impact on the arable land, food and environment	Esterification and Transesterification of oils	Ahmad et al. (2011) Mancaruso et al. (2011)
Second Generation	Non-edible Plant Seeds, Waste Cooking Oil, Lignocellulosic Feedstocks Animal Fats	environmentally friendly, higher cetane number, clean and renewable properties	inabundant reserves, poor property in cold temperatures, greater amount of saturated fatty acids	Esterification and transesterification of oils/seeds (utilises organic catalyst/ additives)	Ahmad et al. (2011) Bhuiya et al. (2014)
Third Generation	Algae (especially Microalgae)	high growth rate and lipid contents, lower demand for water and land, High efficiency in fixing CO_2	dependence on light, complex and inexpensive procedures to produce biodiesel	Cultivation, harvesting, lipid extraction, transesterification	Ahmad et al. (2011) Alaswad et al. (2015) Saladini et al. (2016)

biodiesel. The SV indicates the chain length of triglycerides and explains the content of free fatty acids, high levels of which can be reduced by acid catalysts (Srivastava and Prasad, 2000; Aransiola et al., 2010).

The Influence of Reaction Factors on Biodiesel Derived From Microalgae

The effect of water content mainly refers to the handled dry and original wet algal biomass (Atadashi et al., 2012) to produce biodiesel. The presence of water plays a crucial part in triglyceride hydrolyzing to free fatty acid (FFA) resulting in soap and emulsions formation, hence the water content control is lower than 0.05% (w/w) (Sanford et al., 2009). Another dimension, a high water content of up to about 98%, generates the hydrated shell around algal cells affecting energy as well as mass transfer (Martinez Guerra et al., 2018), furthermore, posing difficulty in the extraction of lipids.

Although homogeneous acid and base catalysts exhibit high efficiency and universality, the separation is tough and requires further neutralization. Although homogenous base-catalyzed reaction is 400 times quicker than the acid-catalyzed reaction, acidic catalysts are normally used for the feedstocks with high contents of FFAs and water (Aransiola et al., 2010), while the alkaline ones are very sensitive to them, affecting the introduction to the laboratory and the industrial popularly (Frascari et al., 2008). A heterogeneous catalyst is easily separated, reducing the cost of catalyst recovery (Tran et al., 2017; Zhang et al., 2019), and the inexpensive basic catalyst including calcium oxide, calcium hydroxide, and magnesium oxide also reduce the environmental impact (Zhang et al., 2010).

Biodiesel can be synthesized from algae through a traditional two-step method (oil extracted from the algae and then transesterified into biodiesel) or an *in-situ* approach (extraction of oil, esterification of FFAs, and transesterification of triglycerides occur simultaneously)

(Sara et al., 2016; Martinez-Guerra et al., 2018; Al-Ameri and Al-Zuhair, 2019). The former requires a long time, a large reactor, and an even higher investment, while the latter offers an efficient method, which simplifies the production process, minimizes the dosage of solvents, and can give improved biodiesel yield.

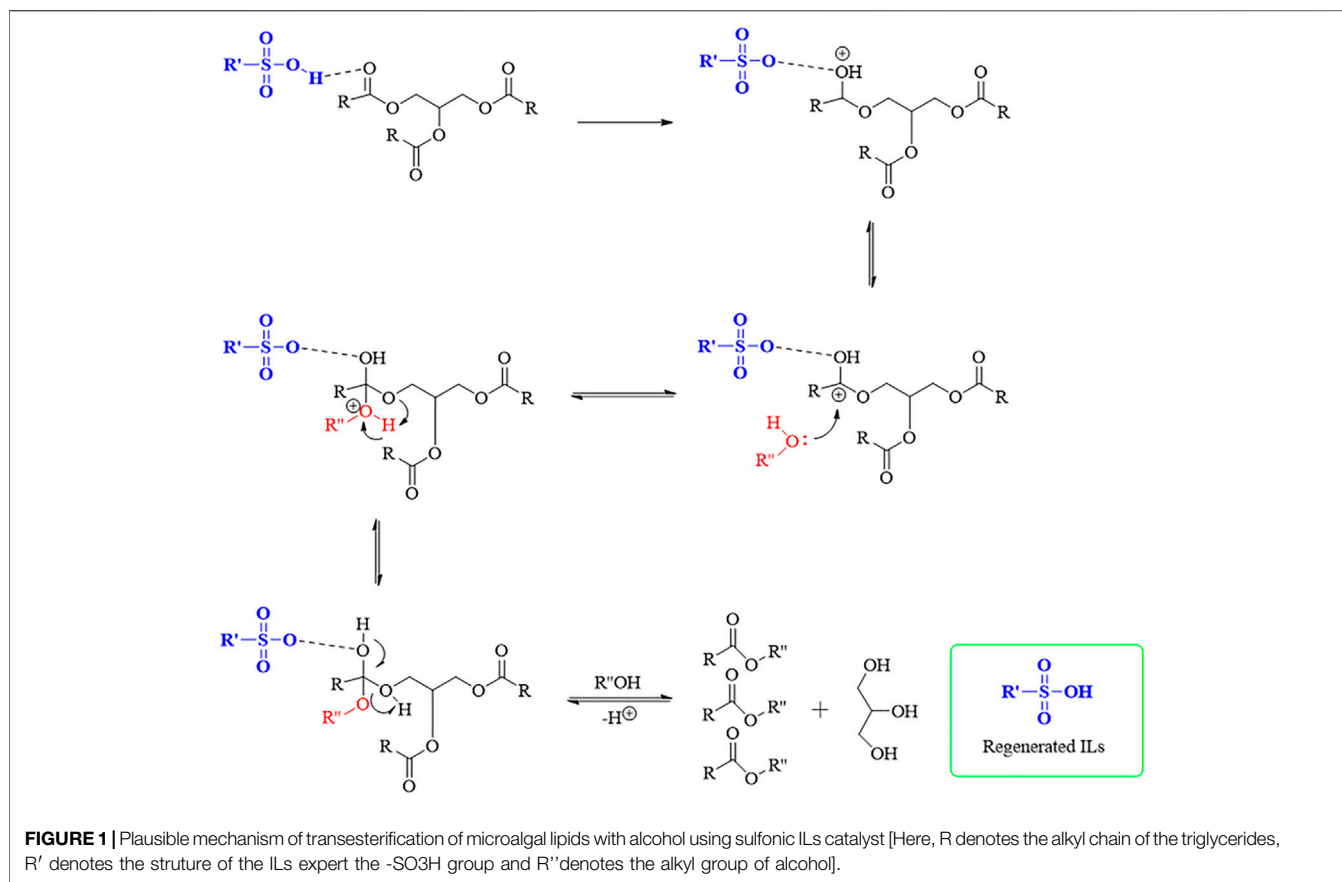## THE IONIC LIQUIDS FOR ENHANCING LIPID RECOVERY FOR BIODIESEL PREPARATION

Ionic liquids (ILs) are widely known as green organic solvents and are non-aqueous salt composed of organic cations and organic or inorganic anions melting at low temperatures (<100°C). ILs are suitable for lipid extraction owing to the major advantages:

1)eco-friendly in nature (Zhao et al., 2019); 2)non-volatile and non-flammable (Vekariya, 2017; Harris et al., 2018); 3) good thermal and chemical stability (Khiratkar et al., 2018); 4)synthetic flexibility (Kim et al., 2012); and 5)immiscibility with organic solvents (Li et al., 2013).

The plausible mechanism of the transesterification of microalgal lipids with alcohol using sulfonic ILs catalyst is shown in **Figure 1**.

Conventional Ionic Liquids

The research explored the lipid extraction effect of [Bmim][MeSO$_4$] from *Chlorella vulgaris* combined with ultrasound pre-treatment and drew a comparison to the traditional Soxhlet method and Bligh and Dyer's method. Results demonstrated that IL exhibited 2-fold and 1.6-fold higher lipid extraction than the classic approaches (Kim et al., 2013). Similarly, Choi compared the lipid extraction yield of *Chlorella vulgaris* by the mixture of ILs, with the assistance of organic solvents. They confirmed that lipid extraction yield was enhanced using IL mixtures, which was ascribed to the synergistic effects with different anions (Choi et al., 2014). The introduction of ILs on

FIGURE 1 | Plausible mechanism of transesterification of microalgal lipids with alcohol using sulfonic ILs catalyst [Here, R denotes the alkyl chain of the triglycerides, R′ denotes the struture of the ILs expert the -SO3H group and R''denotes the alkyl group of alcohol].

wet algal biomass has proven to be the easiest and most efficient method of lipid extraction (Orr and Rehmann, 2016). Furthermore, the poly-ILs catalyst with a large surface area and abundant mesopores have also been investigated for biodiesel preparation (Bian et al., 2020). The combination of magnetic nanoparticles (MNPs) and ILs was used to separate microalgae from the aqueous phase with 99% efficiency and 99% lipids extraction efficiency under ILs/hexane, respectively (Egesa and Plucinski 2022).

Due to ILs' unrealistic application at an industrial scale due to costs and environmental impact, limited articles are available in the literature on the synthesis of biodiesel (Motlagh et al., 2019). ILs have been confirmed to not be harmful for humans, but the preparation routes involve processes that require expensive, toxic, and volatile reagents (Harris et al., 2018; Singh and Savoy, 2020).

Deep Eutectic Solvents

DESs are generally comprised of organic salts (such as choline chloride, choline acetate, quaternary ammonium salt, or phosphonium salt) and hydrogen-bond donors (HBD) (such as amides, amines, alcohols, and carboxylic acids) that are stable in hydrogen bond interactions, with a melting point lower than that of anionic and cationic counterparts (Zhang et al., 2010; Durand et al., 2013). As a novel class of renewable solvents, DESs emerge with several benefits including low-cost synthesis, non-toxicity, low volatility, and high biodegradability (Zhang et al., 2010; Radošević et al., 2015).

The investigation reported that the cell wall of *Chlorella* sp. and *Chlorococcum* sp. contains α-cellulose, hemicellulose, protein, lipid, and ash (Loos and Meindl, 1982). tThe combination of DESs and α-cellulose, hemicellulose, affords new hydrogen bonds that could damage the microalgae cells to enhance the lipid extraction. Three different DESs, aqueous choline chloride-oxalic acid (aCh-O), aqueous choline chloride-ethylene glycol (aCh-EG), and aqueous urea-acetamide (aU-A), were applied to pretreated *Chlorella* sp. and the lipid recovery rate of biomass was evaluated. Results demonstrated that the lipid recovery rate was enhanced from 52.0% of a blank control group to 80.9, 66.9, and 75.3% of the biomass treated by aCh-O, aCh-EG, and aU-A, respectively (Lu et al., 2016). There a consistent conclusion obtained when DESs are treated on wet and unbroken (water content is 65–67%) with *Chlorella* sp. and *Chlorococcum* sp. (GN38) through one-step and two-step methods (Pan et al., 2017).

CONCLUSION AND PERSPECTIVES

The review discusses the factors that influence biodiesel quality and conversion of microalgal. It is necessary to adjust these technical parameters with analysis to ensure the feasibility of biodiesel production. The main aims of green solvents for extraction should be eco-friendliness, less dosage of solvent, increasing the quality of the product without byproducts, and saving energy. The

efficient DESs with suitable organic salts and HBD to extract lipid are in demand. Microalgae research and development are expansive and synthesis technology for biodiesel from microalgae still requires much investigation. The life cycle analysis of the existing processes will be beneficial for commercial application.

AUTHOR CONTRIBUTIONS

XL and DY jointly conceived the article and discussed the outline. XL wrote the manuscript. DY and HL have made preliminary

revisions to the manuscript. CL and XL coordinated the entire content of the manuscript and made detailed revisions.

FUNDING

REFERENCES

Ahmad, A. L., Yasin, N. H. M., Derek, C. J. C., and Lim, J. K. (2011). Microalgae as a Sustainable Energy Source for Biodiesel Production: A Review. *Renew. Sustain. Energy Rev.* 15, 584–593. doi:10.1016/j.rser.2010.09.018

Al-Ameri, M., and Al-Zuhair, S. (2019). Using Switchable Solvents for Enhanced, Simultaneous Microalgae Oil Extraction-Reaction for Biodiesel Production. *Biochem. Eng. J.* 141, 217–224. doi:10.1016/j.bej.2018.10.017

Alaswad, A., Dassisti, M., Prescott, T., and Olabi, A. G. (2015). Technologies and Developments of Third Generation Biofuel Production. *Renew. Sustain. Energy Rev.* 51, 1446–1460. doi:10.1016/j.rser.2015.07.058

Aransiola, E., Betiku, E., Layokun, S., and Solomon, B. (2010). Production of Biodiesel by Transesterification of Refined Soybean Oil. *Int. J. Biol. Chem. Sci.* 4 (2), 58132. doi:10.4314/ijbcs.v4i2.58132

Atadashi, I. M., Aroua, M. K., Abdul Aziz, A. R., and Sulaiman, N. M. N. (2012). The Effects of Water on Biodiesel Production and Refining Technologies: a Review. *Renew. Sustain. Energy Rev.* 16, 3456–3470. doi:10.1016/j.rser.2012.03.004

Bhuiya, M. M. K., Rasul, M. G., Khan, M. M. K., Ashwath, N., Azad, A. K., and Hazrat, M. A. (2014). Second Generation Biodiesel: Potential Alternative To-Edible Oil-Derived Biodiesel. *Energy Procedia* 61, 1969–1972. doi:10.1016/j.egypro.2014.12.054

Bian, Y., Zhang, J., Liu, C., and Zhao, D. (2020). Synthesis of Cross-Linked Poly Acidic Ionic Liquids and its Application in Biodiesel Production. *Catal. Lett.* 150, 969–978. doi:10.1007/s10562-019-02988-0

Choi, S.-A., Oh, Y.-K., Jeong, M.-J., Kim, S. W., Lee, J.-S., and Park, J.-Y. (2014). Effects of Ionic Liquid Mixtures on Lipid Extraction from Chlorella Vulgaris. *Renew. Energy* 65, 169–174. doi:10.1016/j.renene.2013.08.015

Demirbas, A. (2009). Production of Biodiesel from Algae Oils. *Energy Source. Part A* 31, 163–168. doi:10.1080/15567030802093955

Durand, E., Lecomte, J., and Villeneuve, P. (2013). Deep Eutectic Solvents: Synthesis, Application, and Focus on Lipase-catalyzed Reactions. *Eur. J. Lipid Sci. Technol.* 115 (4), 379–385. doi:10.1002/ejlt.201200416

Egesa, D., and Plucinski, P. (2022). Efficient Extraction of Lipids from Magnetically Separated Microalgae Using Ionic Liquids and Their Transesterification to Biodiesel. *Biomass Convers. bior.* doi:10.1007/s13399-022-02377-5

Fazal, M. A., Haseeb, A. S. M. A., and Masjuki, H. H. (2013). Investigation of Friction and Wear Characteristics of Palm Biodiesel. *Energy Convers. Manag.* 67, 251–256. doi:10.1016/j.enconman.2012.12.002

Frascari, D., Zuccaro, M., Pinelli, D., and Paglianti, A. (2008). A Pilot-Scale Study of Alkali-Catalyzed Sunflower Oil Transesterification with Static Mixing and with Mechanical Agitation. *Energy fuels.* 22, 1493–1501. doi:10.1021/ef700584h

Graboski, M. S., and McCormick, R. L. (1998). Combustion of Fat and Vegetable Oil Derived Fuels in Diesel Engines. *Prog. Energy Combust. Sci.* 24, 125–164. doi:10.1016/s0360-1285(97)00034-8

Harris, J., Viner, K., Champagne, P., and Jessop, P. G. (2018). Advances in Microalgal Lipid Extraction for Biofuel Production: a Review. *Biofuels, Bioprod. Bioref.* 12 (6), 1118–1135. doi:10.1002/bbb.1923

Hoekman, S. K., Broch, A., Robbins, C., Ceniceros, E., and Natarajan, M. (2012). Review of Biodiesel Composition, Properties, and Specifications. *Renew. Sustain. Energy Rev.* 16, 143–169. doi:10.1016/j.rser.2011.07.143

Içingür, Y., and Altiparmak, D. (2003). Effect of Fuel Cetane Number and Injection Pressure on a DI Diesel Engine Performance and Emissions. *Energy Convers. Manag.* 44, 389–397. doi:10.1016/S0196-8904(02)00063-8

Karmakar, A., Karmakar, S., and Mukherjee, S. (2010). Properties of Various Plants and Animals Feedstocks for Biodiesel Production. *Bioresour. Technol.* 101, 7201–7210. doi:10.1016/j.biortech.2010.04.079

Khiratkar, A. G., Balinge, K. R., Patle, D. S., Krishnamurthy, M., Cheralathan, K. K., and Bhagat, P. R. (2018). Transesterification of castor Oil Using Benzimidazolium Based Brønsted Acid Ionic Liquid Catalyst. *Fuel* 231, 458–467. doi:10.1016/j.fuel.2018.05.127

Kim, Y.-H., Choi, Y.-K., Park, J., Lee, S., Yang, Y.-H., Kim, H. J., et al. (2012). Ionic Liquid-Mediated Extraction of Lipids from Algal Biomass. *Bioresour. Technol.* 109, 312–315. doi:10.1016/j.biortech.2011.04.064

Kim, Y.-H., Park, S., Kim, M. H., Choi, Y.-K., Yang, Y.-H., Kim, H. J., et al. (2013). Ultrasound-assisted Extraction of Lipids from Chlorella Vulgaris Using [Bmim][MeSO4]. *Biomass Bioenergy* 56, 99–103. doi:10.1016/j.biombioe.2013.04.022

Knothe, G. (2005). Dependence of Biodiesel Fuel Properties on the Structure of Fatty Acid Alkyl Esters. *Fuel Process. Technol.* 86, 1059–1070. doi:10.1016/j.fuproc.2004.11.002

Li, H., He, X., Zhang, Q., Chang, F., Xue, W., Zhang, Y., et al. (2013). Polymeric Ionic Hybrid as Solid Acid Catalyst for the Selective Conversion of Fructose and Glucose to 5-hydroxymethylfurfural. *Energy Technol.* 1, 151–156. doi:10.1002/ente.201200041

Loos, E., and Meindl, D. (1982). Composition of the Cell Wall of Chlorella Fusca. *Planta* 156 (3), 270–273. doi:10.1007/BF00393735

Lu, W., Alam, M. A., Pan, Y., Wu, J., Wang, Z., and Yuan, Z. (2016). A New Approach of Microalgal Biomass Pretreatment Using Deep Eutectic Solvents for Enhanced Lipid Recovery for Biodiesel Production. *Bioresour. Technol.* 218, 123–128. doi:10.1016/j.biortech.2016.05.120

Mancaruso, E., Sequino, L., and Vaglieco, B. M. (2011). First and Second Generation Biodiesels Spray Characterization in a Diesel Engine. *Fuel* 90 (9), 2870–2883. doi:10.1016/j.fuel.2011.04.028

Martinez-Guerra, E., Howlader, M. S., Shields-Menard, S., French, W. T., and Gude, V. G. (2018). Optimization of Wet Microalgal FAME Production from Nannochloropsis Sp. Under the Synergistic Microwave and Ultrasound Effect. *Int. J. Energy Res.* 42, 1934–1949. doi:10.1002/er.3989

Meher, L., Vidyasagar, D., and Naik, S. (2004). Technical Aspects of Biodiesel Production by Trans- Esterification—A Review. *Renew. Sustain. Energy Rev.* 10, 248–268. doi:10.1016/j.rser.2004.09.002

Orr, V. C. A., and Rehmann, L. (2016). Ionic Liquids for the Fractionation of Microalgae Biomass. *Curr. Opin. Green Sustain. Chem.* 2, 22–27. doi:10.1016/j.cogsc.2016.09.006

Pan, H., Xia, Q., Li, H., Wang, Y., Shen, Z., Wang, Y., et al. (2022). Direct Production of Biodiesel from Crude *Euphorbia Lathyris* L. Oil Catalyzed by Multifunctional Mesoporous Composite Materials. *Fuel* 309, 122172. doi:10.1016/j.fuel.2021.122172

Pan, Y., Alam, M. A., Wang, Z., Huang, D., Hu, K., Chen, H., et al. (2017). One-step Production of Biodiesel from Wet and Unbroken Microalgae Biomass Using Deep Eutectic Solvent. *Bioresour. Technol.* 238, 157–163. doi:10.1016/j.biortech.2017.04.038

Radošević, K., CvjetkoBubalo, M., GaurinaSrček, V., Grgas, D., LandekaDragičević, T., and RadojčićRedovniković, I. (2015). Evaluation of Toxicity and

Biodegradability of Choline Chloride Based Deep Eutectic Solvents. *Ecotx. Environ. Safe.* 112, 46–53. doi:10.1016/j.ecoenv.2014.09.034

Ramos, M. J., Fernández, C. M., Casas, A., Rodríguez, L., and Pérez, Á. (2009). Influence of Fatty Acid Composition of Raw Materials on Biodiesel Properties. *Bioresour. Technol.* 100, 261–268. doi:10.1016/j.biortech. 2008.06.039

Rezaei Motlagh, S., Harun, R., Awang Biak, D., Hussain, S., Wan Ab Karim Ghani, W., Khezri, R., et al. (2019). Screening of Suitable Ionic Liquids as Green Solvents for Extraction of Eicosapentaenoic Acid (EPA) from Microalgae Biomass Using COSMO-RS Model. *Molecules* 24, 713. doi:10.3390/ molecules24040713

Saladini, F., Patrizi, N., Pulselli, F. M., Marchettini, N., and Bastianoni, S. (2016). Guidelines for Emergy Evaluation of First, Second and Third Generation Biofuels. *Renew. Sustain. Energy Rev.* 66, 221–227. doi:10.1016/j.rser.2016. 07.073

Sanford, S. D., White, J. M., Shah, P. S., Wee, C., Valverde, M. A., and Meier, G. R. (2009). Feedstock and Biodiesel characteristics report. *Renew. Energy Group. Rep.*

Sara, M., Brar, S. K., and Blais, J. F. (2016). Comparative Study between Microwave and Ultrasonication Aided *In Situ* Transesterification of Microbial Lipids. *RSC Adv.* 6, 56009–56017. doi:10.1039/c6ra10379k

Singh, S. K., and Savoy, A. W. (2020). Ionic Liquids Synthesis and Applications: an Overview. *J. Mol. Liq.* 297, 112038. doi:10.1016/j.molliq.2019.112038

Srivastava, A., and Prasad, R. (2000). Triglycerides-based Diesel Fuels. *Renew. Sustain. Energy Rev.* 4, 111–133. doi:10.1016/s1364-0321(99)00013-1

Tran, D.-T., Chang, J.-S., and Lee, D.-J. (2017). Recent Insights into Continuous-Flow Biodiesel Production via Catalytic and Non-catalytic Transesterification Processes. *Appl. Energy* 185, 376–409. doi:10.1016/j. apenergy.2016.11.006

Vekariya, R. L. (2017). A Review of Ionic Liquids: Applications towards Catalytic Organic Transformations. *J. Mol. Liq.* 227, 44–60. doi:10.1016/j.molliq.2016.11.123

Zhang, H., Li, H., Hu, Y., Venkateswara Rao, K. T., Xu, C., and Yang, S. (2019). Advances in Production of Bio-Based Ester Fuels with Heterogeneous Bifunctional Catalysts. *Renew. Sustain. Energy Rev.* 114, 109296. doi:10.1016/j.rser.2019.109296

Zhang, J., Chen, S., Yang, R., and Yan, Y. (2010). Biodiesel Production from Vegetable Oil Using Heterogenous Acid and Alkali Catalyst. *Fuel* 89, 2939–2944. doi:10.1016/j.fuel.2010.05.009

Zhao, W., Chi, X., Li, H., He, J., Long, J., Xu, Y., et al. (2019). Eco-friendly Acetylcholine-Carboxylate Bio-Ionic Liquids for Controllable N-Methylation and N-Formylation Using Ambient CO2 at Low Temperatures. *Green Chem.* 21, 567–577. doi:10.1039/c8gc03549k

![frontiers | Frontiers in Chemistry]

Titanate Nanotubes-Based Heterogeneous Catalyst for Efficient Production of Biomass Derived Chemicals

Shuolin Zhou[1]*, Lu Wu[1], Junzhuo Bai[1], Xianxiang Liu[2]*, Min Lei[1], Min Long[1] and Keying Huang[1]

[1]School of Elementary Education, Changsha Normal University, Changsha, China, [2]National and Local Joint Engineering Laboratory for New Petro-Chemical Materials and Fine Utilization of Resources, Key Laboratory of the Assembly and Application of Organic Functional Molecules of Hunan Province, College of Chemistry and Chemical Engineering, Hunan Normal University, Changsha, China

The development of efficient heterogeneous catalytic system to convert plentiful biomass to renewable bio-chemicals is urgent need. Titanate nanotubes-based materials obtained from hydrothermal treatment have been reported as low-cost and efficient catalytic materials in chemical syntheses for bio-based chemicals production with interesting catalytic performance. This mini-review expressly revealed the significance and potential of using titanate nanotubes based material as sustainable and environmentally benign solid catalysts/supports for synthesis of various bio-based chemicals, including glycerol-derived solketal, jet fuel range alkanes precursors, biomass-derived esters, aldehydes, aromatic compounds and so on. From the current knowledge on titanate nanotubes-based material via hydrothermal method here summarized, the future lines of research in the field of catalysis/supports for bio-based chemicals production are outlined.

Keywords: titanate nanotubes, bio-based chemicals, catalytic reaction, supports, solid acid (base) catalyst

INTRODUCTION

At the present moment, fossil fuels are the primary sources of energy for humankind. However, the use of fossil fuels often associated with the concerns, such as price fluctuation, long-term availability, and growing environmental effects (Brockway et al., 2019). Besides, the quest for global energy and chemicals needs will be in high demand due to the rapidly developments of economic and socioeconomic. Hence, transforming renewable energy into alternative fuels and chemicals is an essential and indispensable pathway (Gielen et al., 2019; Stančin et al., 2020). Biomass is an abundant renewable and cleaner resource, which can be converted into a wide range of various fuel grade molecules and bio-chemicals as alternatives to fossil-derived products (Li et al., 2017; Schutyser et al., 2018; Okolie et al., 2021; Ashokkumar et al., 2022). In this situation, new chemical technology and efficient catalysts to convert plentiful biomass to renewable bio-chemicals is urgent need.

Titanate nanotubes (TNTs), a typical of Ti-based material, have attracted extensive researches due to its novel properties such as chemical stability, large surface area, non-toxicity, and relatively hydrophobic nature, which have shown great potential not only as catalysts but also as supports. A lot of literatures have described the synthesis of titanate nanotubes by various methods such as hydrothermal treatment (Kasuga et al., 1998; Kasuga et al., 1999), template-assisted method
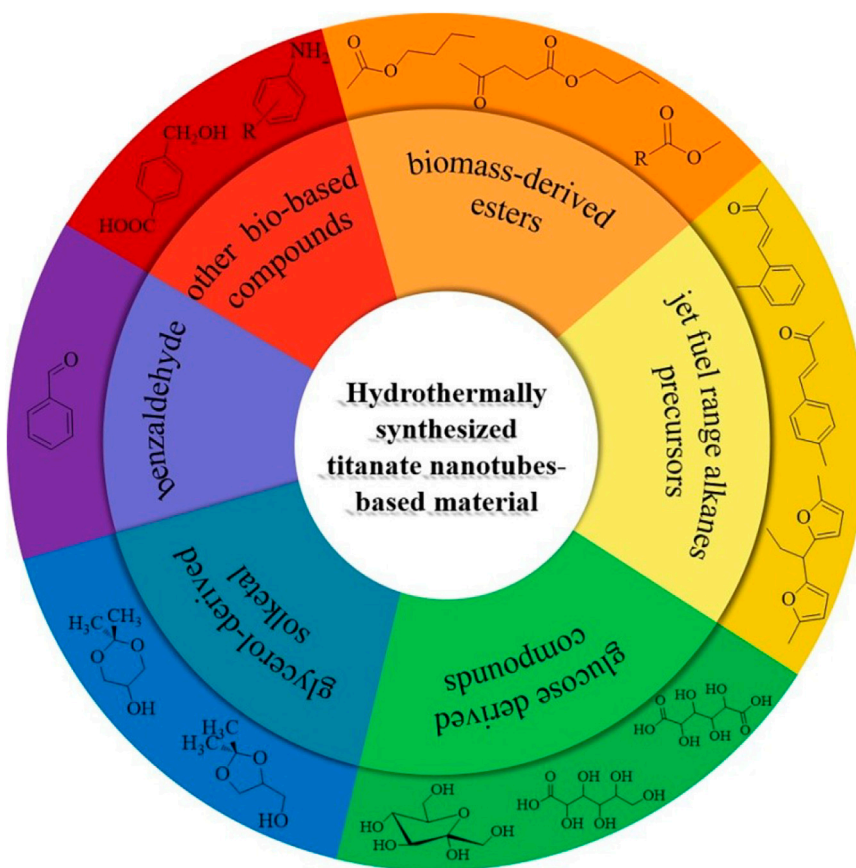
FIGURE 1 | The schematic of production of typical biomass derived chemicals over titanate nanotubes-based catalyst.

(Zhang et al., 2001), and the anodizing of titanium metal (Gong et al., 2001). It is worth noted that TNTs obtained by hydrothermal treatment of TiO_2 nanoparticles in the absence of a template and at low temperature (120–150°C), which has received significant attention (Bavykin et al., 2006). In recent years, many articles and reviews have covered the applications of hydrothermally synthesized TNTs materials in photoelectrochemial reactions (Arifin et al., 2021), photocatalytic (Ji et al., 2022), dye-sensitized solar cells (Madurai Ramakrishnan et al., 2020; Souza et al., 2021), adsorbents (Li et al., 2021) and other interesting applications (Yao et al., 2020). In addition, the structural, optical, thermal and morphological properties of TNTs synthesized by conventional hydrothermal method were systematically discussed in other reviews (Ou and Lo, 2007; Muniyappan et al., 2017; Rempel et al., 2021).

Kitano and co-workers found that the TNTs exhibited excellent catalytic performance in Friedel-Crafts alkylation and the 5-hydroxymethylfurfural production (Kitano et al., 2010). This finding may potentially open up new catalytic applications of the titanate nanotubes for organic transformations and biomass conversion. In the past few years, some studies have been reported the use of TNTs in various acid (base) catalyzed organic chemical transformation (Kitano et al., 2013; Wada

et al., 2013; Li et al., 2015; Reddy et al., 2015). This mini-review focuses on TNTs based material as solid catalysts/supports with the potential application for the bio-based chemicals production (**Figure 1**).

BIOMASS DERIVED CHEMICALS PRODUCTION

Production of Glycerol-Derived Solketal

The acetalization reaction has been widely studied because they are important and efficient processes to convert aldehydes or ketones into high-valued compounds. The glycerol-derived solketal as oxygenated compound may be incorporate into additive for standard diesel fuel as well as decrease the emission of hydrocarbons and particulate species (Talebian-Kiakalaieh et al., 2018). De Carvalho et al. reported the acetalization of glycerol using the protonated titanate nanotubes as a solid catalyst (de Carvalho et al., 2017). The synthesis time of TNTs and the role of structure on the catalytic performance were systematically investigated. The best performance towards glycerol conversion was achieved by the TNTs synthesized at 72 h with high textural, morphological and acidity properties. The glycerol conversion was 44.4% and the

TABLE 1 | Structural properties of various titanate nanotubes-based acid catalysts.

Catalyst	S_{BET} (m²/g)	Pore Volume (cm³/g)	Mesopore Diameter (nm)	Acidity (mmol/g)	Ref.
HTNT48	313	0.81	9.0	0.24	de Carvalho et al. (2017)
HTNT72	182	0.74	11.5	0.33	de Carvalho et al. (2017)
Co-TNT	236	0.84	11.8	0.093	Coelho et al. (2016); Gomes et al. (2018)
Ni-TNT	222	0.84	12.6	0.103	Coelho et al. (2016); Gomes et al. (2018)
Pt-TNT	182	0.64	12.2	0.261	Coelho et al. (2016); Gomes et al. (2018)

selectivity toward the desired products (solketal and acetal) was observed to be more than 98% at 50°C and an acetone/glycerol molar ratio of 1. Decoration of transition and rare earth metal nanoparticles on titanate nanotubes has a considerable effect on the number of Brønsted and Lewis acidity sites (Camposeco et al., 2016; Wada et al., 2016). These researches demonstrated that various metals (Ag, Au, Ce, Fe, Mn, Pd, Pt, V, W and Nb) obviously improve the Brønsted acidity of TNTs except for La; some metals such as Pt, Mn and W could enhance Lewis acidity of TNTs; the addition of transition metals (V, Mn, W and Fe) increased remarkably the total acidity of TNTs. In another study, TNTs incorporated with metals (Pt, Co, Ni) were synthesized and applied in acetalization of glycerol with acetone (Gomes et al., 2018). Interestingly, the Pt-containing titanate nanotubes (Pt-TNT) catalyst has high catalytic activity, affording 46.7% of glycerol conversion with 10% selectivity to solketal, whereas the Co and Ni-incorporated titanate nanotubes exhibited relativity low catalytic activity (glycerol conversion <5%). Structural properties of various titanate nanotubes-based acid catalysts are listed **Table 1**. The suitable tuning of pore-structure and proper surface acidity of Pt-TNT were contributed to the resulting in a stable solid for this reaction (Gomes et al., 2018). It is noteworthy that leaching of Co and Ni species is reported as the main mechanism for the catalyst deactivation for Co-containing titanate nanotubes and Ni-containing titanate nanotubes. This demonstrated that the catalytic activity and recyclability of TNTs could be tuned by incorporation of a suitable metal.

Jet Fuel Range Alkanes Precursors Synthesis

Aldol condensation approach is the very important for synthesis of high-quality bio-fuels (He et al., 2021). Protonated titanate nanostructures used as solid acid catalysts exhibited the excellent catalytic activity in the condensation reaction between various benzaldehyde derivatives and cyclohexanone (Sluban et al., 2017). A higher conversion rate was obtained over TNTs as compared to titanate nanoribbons, demonstrating the beneficial role of nanotube morphology. The catalyst showed a remarkable stability since no significant decrease in the catalytic activity in five cycles. In addition, protonated titanate nanotubes did not require any activation prior to the reaction. Recently, protonated titanate nanotubes catalyst displayed much higher activity for acid-catalyzed aldol condensation of methyl benzaldehyde and acetone, two platform compounds obtained from lignocelluloses (Timothy et al., 2020). Around 76% yield of jet fuel precursors,

namely 4-(o-tolyl)but-3-en-2-one, was obtained under the optimum reaction conditions. After the hydrodeoxygenation (HDO) of jet fuel precursors in cyclohexane under mild conditions (403K, 5MPa, 2 h), high yields (~ 90%) of dicycloalkanes were achieved. They discovered the catalytic activity of protonated titanate nanotubes was higher than TiO₂ P25 and titanate nanowire under the same conditions. It is suggested that the special nanotube morphology, bigger surface area, higher acid site amount and acid strength could be considered as the reasons for the good catalytic performance of protonated titanate nanotube. It is also found that the protonated titanate nanotubes catalyst was stable and could be repeatedly used for five runs without significant deactivation.

The protonated titanate nanotubes as a good solid catalyst was applied for the hydroxyalkylation/alkylation (HAA) of 2-methylfuran (2-MF) with n-butanal from lignocelluloses to synthesize diesel and jet fuel range alkanes precursors. Compared to other inorganic solid acids such as SO_4^{2-}/ZrO_2, ZrP and H-ZSM-5, protonated titanate nanotubes has higher catalytic activity, giving 77% yield of HAA product under mild reaction conditions (Li et al., 2015). The protonated titanate nanotubes was also effective for the catalytic HAA of 2-MF with other lignocellulosic carbonyl compounds, such as furfural, acetone and mesityl oxide. The outstanding catalytic performance of protonated titanate nanotubes for the HAA of 2-MF and n-butanal can be explained by the following reasons: 1) the protonated titanate nanotubes has higher specific surface area, which is beneficial for the adsorption of reactants, 2) the transformation of commercial TiO₂ P25 to protonated titanate nanotubes leads to the higher acidity (the amount of acid sites and the generation of strong acid sites), and 3) the generation of Brønsted acid sites may be beneficial to the HAA reaction of 2-MF and n-butanal.

Preparation of Biomass-Derived Esters

Some researchers have suggested that the sodium titanate nanotubes is an efficient heterogenous base catalyst in the transesterification reactions, which is the most common route for biodiesel production (Hernández-Hipólito et al., 2014). Recently, the sodium titanates were used as catalysts in the transesterification of pure and cooked oils into biodiesel (Zaki et al., 2019). The biodiesel yield was found to be 95.9% at 80°C for 2 h; the authors discovered that the catalyst showed high activity for cooked oil conversion, with yields of 96.0, 96.0, and 93.58% for the first, second, and third uses of oil, respectively. The authors found that the transesterification reaction preferentially

proceeded via dual-site Langmuir-Hinshelwood mechanism with the aid of the Density Functional Theory (DFT), Monte Carlo (MC) simulation, and molecular dynamics simulation. Furthermore, the transesterification reaction kinetics followed a pseudo-first-order kinetics model. Simiarlly, the sodium titanate catalysts were prepared by sol–gel hydrothermal method, and the synthesis parameters of sodium titanates on the catalysts activity in soybean oil conversion to biodiesel were discussed using a factorial design (Machorro López et al., 2021). Combing the characterization results and catalytic results, the authors pointed out that trititanate was the most efficient in the conversion of soybean oil to biodiesel, achieving around 80% conversion. Doping metal ions on sodium titanate nanotubes may be an important strategy to improve the catalytic acitivity. For example, sodium titanate nanotubes doped with potassium proved as a efficient catalyst for transesterification of soybean oil with methanol (Hernández-Hipólito et al., 2015; Martínez-Klimova et al., 2016). Recently, the promoting role of sodium carbonate addition to sodium titanate nanotubes were reported (Martínez-Klimov et al., 2020). Incorporation of Na_2CO_3 (3–10 wt%) to sodium titanate nanotubes can increase the amount of strong basic sites in the catalysts. A synergetic effect between Na_2CO_3 and sodium titanate nanotubes was proposed for the increase in the amount of strong basic sites, resulting in an excellent catalytic performance in transformation of triglycerides to methyl esters (97% yield). Interestingly, in other important studies, lipase immobilized onto the sodium titanate nanotubes have recently been employed in the fatty acid methyl esters production (Nady et al., 2020; El-Kady et al., 2021). The immobilized lipase gave a high fatty acid methyl esters yield of 83.5% at short time of 90 min and showed the enhanced recycling stability for ten consecutive cycles.

Esterification is the most common reaction for biomass conversion and high-valued chemicals production (Zhang et al., 2019). Xu et al. found the catalytic performance of the titanate nanotubes is significantly higher than titanate nanosheets and layered H_2TiO_7 in esterification of acetic acid with n-butanol (Xu et al., 2020). The authors proposed that the surface acid characteristics and confinement effect were responsible for the high catalytic activity of titanate nanotubes. This clearly reveals that the microstructure is important to the catalytic activity. The finite amount of catalytic sites on the TNTs, however, would hamper in practical applications. It is noteworthy that TNTs prepared by hydrothermal method with abundant hydroxyl groups. Thus, the potential to modify TiO_2 nanotubes to incorporate organosulfonic acid groups open new perspectives for their use as solid acid catalysts in a variety of reactions. Our groups reported various titanate nanotubes-bonded organosulfonic acid catalysts for the esterification of biomass-derived levulinic acid with n-butyl alcohol (Zhou et al., 2018; Zhou et al., 2019; Zhou et al., 2022a). Up to 98.9% yield of n-butyl levulinate was obtained under the optimal reaction conditions. In these hybrid catalysts the acid sites are covalently linked on titanate nanoutbes, therefore, they showed an excellent reusability with a slight decrease in several runs. On the other hand, the incorporation of organic groups on the TNTs can tune surface hydrophobicity property. Recently, in order to recycle

heterogeneous acid catalysts from the reaction mixture, a new solid acid catalyst $Fe_3O_4@TNTs-SO_3H$ was successfully synthesized and applied to esterification of renewable levulinic acid to fuel additive n-butyl levulinate (Mao et al., 2020). This catalyst was demonstrated to show high catalytic activity, affording n-butyl levulinate with a yield of 94.6% under optimum conditions; the catalyst could be reused for 6 times. It is believed that titanate nanotubes can be rationally designed via post-synthesis strategy to prepare solid acid catalysts with excellent performance.

The alcoholysis process has been reported as a highly reactive method for conversion of lignocellulose to valuable chemicals (Zhu et al., 2017). Sulfonic acid functionalized TiO_2 nanotubes were prepared by the sulphonation reaction of hydrothermally synthesized Titanate nanotubes using chlorosulfonic acid as the sulfating agent in our recent work (Zhou et al., 2022b). About 79.9% yield of n-butyl levulinate was achieved in the alcoholysis of the furfuryl alcohol with n-butanol under mild conditions. In addition, the catalysts showed a stable catalytic performance after four consecutive cycles. The covalently linked –SO_3H groups on the TNTs surface was responsible for the stability of catalyst.

Synthesis of Glucose Derived Compounds

Kumar and co-workers have recently reported a sodium titanate nanotubes as a potential Lewis base catalyst for large-scale demonstration of glucose isomerization to fructose in aqueous media (Kumar et al., 2018). In this work, the glucose conversion could be reached with 31.26% fructose yield and 65.26% selectivity under relatively lower operating conditions for 15 min or less. They found that the presence of large basic sites in sodium titanate nanotubes was contribute to the higher glucose conversion. Additionally, the catalyst could be effciently recycled and regenerated by a simple NaOH treatment. On the contray, protonated titanate nanotubes was reported as solid acid catalyst for conversion of glucose into HMF via isomerization and dehydration process, giving the moderate yield of HMF (Kitano et al., 2010). Recently, protonated titanate nanotubes exhibit relatively high catalytic performance for isomerizaiton of alpha pinene, an inexpensive and important essential oil which is widely used in the synthesis of various fine chemicals (Huang et al., 2020). Hence, it is believed that the protonated titanate nanotubes/sodium titanate nanotubes can be uesed as acid or base catalyst in different types of isomerization reactions for bio-based chemicals production.

More importantly, TNTs are regarded as an attractive support material because they exhibit large surface area, high surface hydroxyl density, high ion-exchange capacity and the good stability. Recently, the catalytic performance of Au-Pd nanoparticles prepared by colloidal synthesis and immobilised on titanate nanotubes in the selective oxidation of glucose to gluconic and glucaric acids has been studied by Khawaji et al. under relatively mild conditions (Khawaji et al., 2019). They found that Au-rich catalysts favored deep oxidation to glucaric acid while Pd-rich catalysts displayed the formation of gluconic acid. It is suggested that the bimetallic composition of Au and Pd on TNTs could be tuned to enhance the production of either gluconic acid or glucaric acid.

Selective Oxidation of Benzyl Alcohol to Benzaldehyde

The selective oxidation is potentially key reaction in the biomass conversion and value-added chemicals production (Nasrollahzadeh et al., 2020). The selective oxidation of benzyl alcohol, a typical biomass derivative, to corresponding carbonyl compounds has been received much attention. A highly active Au-Pd on titanate nanotubes (Au-Pd/Ti-NT) catalyst has been produced by using colloidal synthesis and immobilisation on sodium-free Ti-nanotubes (Khawaji and Chadwick, 2017). The catalyst has markedly superior catalytic activity (turn over frequency>19,000 h^{-1}) for the selective oxidation of benzyl alcohol compared with similar catalysts reported in the literature such as Au-Pd catalysts supported on Ti-NTs prepared by adsorption as well as conventional Au-Pd/TiO$_2$ prepared by impregnation. The authors claimed that the superior catalytic activity of the catalyst is attributed to the high metal dispersion on the external surfaces of titanate nanotubes, the narrow particle size distribution, and the high degree of Au-Pd mixed alloying. Moreover, the effect of the catalyst preparation method on the selective oxidation catalytic activity of Au-Pd supported on titanate nanotubes (Au-Pd/Ti-NT) was further investigated (Khawaji and Chadwick, 2019). The most active Au-Pd/Ti-NT catalyst for the selective oxidation of benzyl alcohol is shown to be that prepared using colloidal synthesis and immobilization with PVA as a stabilizer, which has markedly superior catalytic activity compared to catalysts prepared by deposition-precipitation, adsorption, and dry impregnation methods. Therefore, it is very importance to select a synthesis method to obtain optimal catalytic performance. Besides, the morphology and physiochemical properties of the support were also found to play a crucial role for catalytic oxidation activity, selectivity, and stability (Khawaji and Chadwick, 2018; Khawaji and Chadwick, 2020). Furthermore, exploring the utilization of TNTs-based material as a photocatalyst for selective oxidation of benzyl alcohol will be desirable under ambient conditions (Yang et al., 2016).

Production of Other Bio-Based Chemicals

Hydrogenation reactions are considered as valuable and key technologies in biomass conversion processes (Li et al., 2019). Titanate nanotubes supported Pd was applied to hydrogenation of 4-carboxy-benzaldehyde, displaying a better catalytic performance than the commercial Pd/C catalyst (Liu et al., 2018). Meanwhile, Torres' group reported the selective hydrogenation of nitrobenzenes over gold nanoparticles supported on titania nanotubes in liquid phase at room temperature (Torres et al., 2018). It was found that the selectivity towards p-substituted anilines reached 90% for all substrates in their study. Recently, other nobel metals, such Pt and Pd, confined on titanate nanotubes also performed well for the hydrogenation of nitroarenes and other substituted-nitroarenes (Shanmugaraj et al., 2022). These works indicated that the TNTs has the hollow tubular structure, the abundant –OH groups and strong metal–support interaction which renders them excellent supports for preparing TNT-supported catalysts

for hydrogenation of various compounds to high-value chemicals.

Transforming of CO$_2$ conversion into hydrocarbons recently has received significant attention (Díaz de León et al., 2019). A ternary hybrid catalyst, poly (ethyleneimine)-tethered Ir complex catalyst immobilized in titanate nanotubes were applied to hydrogenation of CO$_2$ to formic acid under the relatively mild conditions (Kuwahara et al., 2017). Kuwahara et al. stated that the ability of TNTs to efficiently capture CO$_2$ and to stabilize PEI, where Na$^+$-type TNTs with higher basic property provides more productive effect, which are responsible for the high catalytic performances. Recently, the catalytic activity of rhodium supported on titanate nanotubes was evaluated by *in situ* infrared study in the synthesis of formic acid *via* CO$_2$ hydrogenation (Ruiz-García et al., 2019). For this catalyst a turn over frequency (TOF) of 7.2 × 10^{-2} h^{-1} was obtained at 90°C and atmospheric pressure. Furthermore, the authors provided the evidence of active surface species bonded to support sites and to rhodium sites via *in-situ* studies. Besides, photocataytic CO$_2$ conversion to hydrocarbon fuel using TiO$_2$ based material is another important strategy (Razzaq and In, 2019).

CONCLUSION

In summary, titanate nanotubes-based heterogeneous catalyst prepared via hydrothermal method have been critically outlined and discussed in this mini-review as a promising catalyst/support for bio-based chemicals production. Titanate nanotubes can be modified by a variety of metal or non-metal dopants or be functionalized by organic surface modification to increase the acid and/or base properties of titanate nanotubes, thereby enhancing the catalytic activity and selectivity. Their very interesting properties make them promising catalysts for use in various reactions, such as acetalization/condensation, hydroxyalkylation/alkylation, transesterification, esterification, alcoholysis and isomerization for production of biomass derived chemicals. The described titanate nanotubes-based heterogeneous catalyst with different catalytic properties can be utilized as low-cost, efficient, sustainable and versatile materials. Enlightened by the hollow tubular structure, confinement effect and strong metal–support interaction, much works on the rational design of multifunctional catalyst for selective oxidation and hydrogenation reaction are ongoing. Although these catalysts have some advantages such as simple separation, and recycling, it would be highly desirable to keep the catalysts intrinsic characteristics that will enhance the catalytic stability of titanate nanotubes-based material under extreme environment. Therefore, except for traditional catalyst characterization, a combination of *in situ* catalytic studies and theoretical calculations and simulations are also helpful to provide valuable information toward the structure-activity relationships of titanate nanotubes-based catalysts. This review is also expected to act as a key reference to researchers for developing advanced titanate nanotubes-based catalysts in large scale applications for bio-based chemicals production with resulting in significant developments.

AUTHOR CONTRIBUTIONS

SZ: Conceptualization, writing-original draft preparation, project administration. LW: Investigation. JB: Conceptualization. XL: Project administration, supervision. MeL: Conceptualization. MiL: Conceptualization. KH: Conceptualization.

FUNDING

REFERENCES

Arifin, K., Yunus, R. M., Minggu, L. J., and Kassim, M. B. (2021). Improvement of TiO_2 Nanotubes for Photoelectrochemical Water Splitting: Review. *Int. J. Hydrogen Energy* 46, 4998–5024. doi:10.1016/j.ijhydene.2020.11.063

Ashokkumar, V., Venkatkarthick, R., Jayashree, S., Chuetor, S., Dharmaraj, S., Kumar, G., et al. (2022). Recent Advances in Lignocellulosic Biomass for Biofuels and Value-Added Bioproducts - a Critical Review. *Bioresour. Technol.* 344, 126195. doi:10.1016/j.biortech.2021.126195

Bavykin, D. V., Friedrich, J. M., and Walsh, F. C. (2006). Protonated Titanates and TiO_2 Nanostructured Materials: Synthesis, Properties, and Applications. *Adv. Mat.* 18, 2807–2824. doi:10.1002/adma.200502696

Brockway, P. E., Owen, A., Brand-Correa, L. I., and Hardt, L. (2019). Estimation of Global Final-Stage Energy-Return-On-Investment for Fossil Fuels with Comparison to Renewable Energy Sources. *Nat. Energy* 4, 612–621. doi:10.1038/s41560-019-0425-z

Camposeco, R., Castillo, S., Mejia-Centeno, I., Navarrete, J., and Rodriguez-Gonzalez, V. (2016). Behavior of Lewis and Brönsted Surface Acidity Featured by Ag, Au, Ce, La, Fe, Mn, Pd, Pt, V and W Decorated on Protonated Titanate Nanotubes. *Microporous Mesoporous Mater.* 236, 235–243. doi:10.1016/j.micromeso.2016.08.033

Coelho, D. C., Oliveira, A. C., Filho, J. M., Oliveira, A. C., Lucredio, A. F., Assaf, E. M., et al. (2016). Effect of the Active Metal on the Catalytic Activity of the Titanate Nanotubes for Dry Reforming of Methane. *Chem. Eng. J.* 290, 438–453. doi:10.1016/j.cej.2016.01.051

de Carvalho, D. C., Oliveira, A. C., Ferreira, O. P., Filho, J. M., Tehuacanero-Cuapa, S., and Oliveira, A. C. (2017). Titanate Nanotubes as Acid Catalysts for Acetalization of Glycerol with Acetone: Influence of the Synthesis Time and the Role of Structure on the Catalytic Performance. *Chem. Eng. J.* 313, 1454–1467. doi:10.1016/j.cej.2016.11.047

Díaz de León, J. N., Rodríguez, J. R., Rojas, J., Esqueda-Barrón, Y., Cardenas, L., Ramesh Kumar, C., et al. (2019). New Insight on the Formation of Sodium Titanates 1D Nanostructures and its Application on CO_2 Hydrogenation. *Front. Chem.* 7, 750. doi:10.3389/fchem.2019.00750

El-Kady, K., Raslan, M., and Zaki, A. H. (2021). Effect of Different TiO_2 Morphologies on the Activity of Immobilized Lipase for Biodiesel Production. *ACS Omega* 6, 35484–35493. doi:10.1021/acsomega.1c04942

Gielen, D., Boshell, F., Saygin, D., Bazilian, M. D., Wagner, N., and Gorini, R. (2019). The Role of Renewable Energy in the Global Energy Transformation. *Energy Strategy Rev.* 24, 38–50. doi:10.1016/j.esr.2019.01.006

Gomes, I. S., de Carvalho, D. C., Oliveira, A. C., Rodríguez-Castellón, E., Tehuacanero-Cuapa, S., Freire, P. T. C., et al. (2018). On the Reasons for Deactivation of Titanate Nanotubes with Metals Catalysts in the Acetalization of Glycerol with Acetone. *Chem. Eng. J.* 334, 1927–1942. doi:10.1016/j.cej.2017.11.112

Gong, D., Grimes, C. A., Varghese, O. K., Hu, W., Singh, R. S., Chen, Z., et al. (2001). Titanium Oxide Nanotube Arrays Prepared by Anodic Oxidation. *J. Mat. Res.* 16, 3331–3334. doi:10.1557/jmr.2001.0457

He, J., Qiang, Q., Liu, S., Song, K., Zhou, X., Guo, J., et al. (2021). Upgrading of Biomass-Derived Furanic Compounds into High-Quality Fuels Involving Aldol Condensation Strategy. *Fuel* 306, 121765. doi:10.1016/j.fuel.2021.121765

Hernández-Hipólito, P., García-Castillejos, M., Martínez-Klimova, E., Juárez-Flores, N., Gómez-Cortés, A., and Klimova, T. E. (2014). Biodiesel Production with Nanotubular Sodium Titanate as a Catalyst. *Catal. Today* 220-222, 4–11. doi:10.1016/j.cattod.2013.09.003

Hernández-Hipólito, P., Juárez-Flores, N., Martínez-Klimova, E., Gómez-Cortés, A., Bokhimi, X., Escobar-Alarcón, L., et al. (2015). Novel Heterogeneous Basic Catalysts for Biodiesel Production: Sodium Titanate Nanotubes Doped with Potassium. *Catal. Today* 250, 187–196. doi:10.1016/j.cattod.2014.03.025

Huang, G., Zhou, S., Liu, J., Su, S., and Yin, D. (2020). Highly-selective Solvent-free Catalytic Isomerization of α-pinene to Camphene over Reusable Titanate Nanotubes. *RSC Adv.* 10, 10606–10611. doi:10.1039/d0ra01093f

Ji, H., Ni, J., Zhao, D., and Liu, W. (2022). Application of Titanate Nanotubes for Photocatalytic Decontamination in Water: Challenges and Prospects. *ACS Est. Eng.* doi:10.1021/acsestengg.1c00451

Kasuga, T., Hiramatsu, M., Hoson, A., Sekino, T., and Niihara, K. (1998). Formation of Titanium Oxide Nanotube. *Langmuir* 14, 3160–3163. doi:10.1021/la9713816

Kasuga, T., Hiramatsu, M., Hoson, A., Sekino, T., and Niihara, K. (1999). Titania Nanotubes Prepared by Chemical Processing. *Adv. Mat.* 11, 1307–1311. doi:10.1002/(sici)1521-4095(199910)11:15<1307::aid-adma1307>3.0.co;2-h

Khawaji, M., and Chadwick, D. (2017). Au-Pd Bimetallic Nanoparticles Immobilised on Titanate Nanotubes: A Highly Active Catalyst for Selective Oxidation. *ChemCatChem* 9, 4353–4363. doi:10.1002/cctc.201700851

Khawaji, M., and Chadwick, D. (2018). Au–Pd NPs Immobilised on Nanostructured Ceria and Titania: Impact of Support Morphology on the Catalytic Activity for Selective Oxidation. *Catal. Sci. Technol.* 8, 2529–2539. doi:10.1039/c7cy02329d

Khawaji, M., and Chadwick, D. (2019). Selective Catalytic Oxidation over Au-Pd/ titanate Nanotubes and the Influence of the Catalyst Preparation Method on the Activity. *Catal. Today* 334, 122–130. doi:10.1016/j.cattod.2018.11.080

Khawaji, M., and Chadwick, D. (2020). Selective Oxidation Using Au-Pd Catalysts: Role of the Support in the Stabilization of Colloidal Au-Pd NPs. *Catal. Today* 348, 203–211. doi:10.1016/j.cattod.2019.08.036

Khawaji, M., Zhang, Y., Loh, M., Graça, I., Ware, E., and Chadwick, D. (2019). Composition Dependent Selectivity of Bimetallic Au-Pd NPs Immobilised on Titanate Nanotubes in Catalytic Oxidation of Glucose. *Appl. Catal. B Environ.* 256, 117799. doi:10.1016/j.apcatb.2019.117799

Kitano, M., Nakajima, K., Kondo, J. N., Hayashi, S., and Hara, M. (2010). Protonated Titanate Nanotubes as Solid Acid Catalyst. *J. Am. Chem. Soc.* 132, 6622–6623. doi:10.1021/ja100435w

Kitano, M., Wada, E., Nakajima, K., Hayashi, S., Miyazaki, S., Kobayashi, H., et al. (2013). Protonated Titanate Nanotubes with Lewis and Brønsted Acidity: Relationship between Nanotube Structure and Catalytic Activity. *Chem. Mat.* 25, 385–393. doi:10.1021/cm303324b

Kumar, S., Nepak, D., Kansal, S. K., and Elumalai, S. (2018). Expeditious Isomerization of Glucose to Fructose in Aqueous Media over Sodium Titanate Nanotubes. *RSC Adv.* 8, 30106–30114. doi:10.1039/c8ra04353a

Kuwahara, Y., Fujie, Y., and Yamashita, H. (2017). Poly(ethyleneimine)-tethered Ir Complex Catalyst Immobilized in Titanate Nanotubes for Hydrogenation of CO_2 to Formic Acid. *ChemCatChem* 9, 1906–1914. doi:10.1002/cctc.201700508

Li, H., Huang, Y., Liu, J., and Duan, H. (2021). Hydrothermally Synthesized Titanate Nanomaterials for the Removal of Heavy Metals and Radionuclides from Water: A Review. *Chemosphere* 282, 131046. doi:10.1016/j.chemosphere.2021.131046

Li, H., Li, Y., Fang, Z., and Smith, R. L. (2019). Efficient Catalytic Transfer Hydrogenation of Biomass-Based Furfural to Furfuryl Alcohol with Recyclable Hf-Phenylphosphonate Nanohybrids. *Catal. Today* 319, 84–92. doi:10.1016/j.cattod.2018.04.056

Li, H., Zhao, W., and Fang, Z. (2017). Hydrophobic Pd Nanocatalysts for One-Pot and High-Yield Production of Liquid Furanic Biofuels at Low Temperatures. *Appl. Catal. B Environ.* 215, 18–27. doi:10.1016/j.apcatb.2017.05.039

Li, S., Li, N., Li, G., Li, L., Wang, A., Cong, Y., et al. (2015). Protonated Titanate Nanotubes as a Highly Active Catalyst for the Synthesis of Renewable Diesel and Jet Fuel Range Alkanes. *Appl. Catal. B Environ.* 170-171, 124–134. doi:10.1016/j.apcatb.2015.01.022

Liu, J., Du, W., Li, Z., and Yang, A. (2018). Preparation of TiO$_2$ Nanotube Supported Pd for the Hydrogenation of 4-Carboxy-Benzaldehyde. *Catal. Lett.* 148, 2472–2479. doi:10.1007/s10562-018-2469-2

Machorro López, J. J., Lázaro, A. L., Rodriguez-Valadez, F. J., and Espejel-Ayala, F. (2021). Synthesis of Sodium Titanate Catalysts Using a Factorial Design for Biodiesel Production. *Environ. Prog. Sustain. Energy* 40, e13475. doi:10.1002/ep.13475

Madurai Ramakrishnan, V., Muthukumarasamy, N., Balraju, P., Pitchaiya, S., Velauthapillai, D., and Pugazhendhi, A. (2020). Transformation of TiO$_2$ Nanoparticles to Nanotubes by Simple Solvothermal Route and its Performance as Dye-Sensitized Solar Cell (DSSC) Photoanode. *Int. J. Hydrogen Energy* 45, 15441–15452. doi:10.1016/j.ijhydene.2020.04.021

Mao, F.-F., Zhao, W., Tao, D.-J., and Liu, X. (2020). Highly Efficient Conversion of Renewable Levulinic Acid to N-Butyl Levulinate Catalyzed by Sulfonated Magnetic Titanium Dioxide Nanotubes. *Catal. Lett.* 150, 2709–2715. doi:10.1007/s10562-020-03177-0

Martínez-Klimov, M. E., Ramírez-Vidal, P., Roquero Tejeda, P., and Klimova, T. E. (2020). Synergy between Sodium Carbonate and Sodium Titanate Nanotubes in the Transesterification of Soybean Oil with Methanol. *Catal. Today* 353, 119–125. doi:10.1016/j.cattod.2019.08.027

Martínez-Klimova, E., Hernández-Hipólito, P., and Klimova, T. E. (2016). Biodiesel Production with Nanotubular Sodium Titanate Doped with Potassium as a Catalyst. *MRS Adv.* 1, 415–420. doi:10.1557/adv.2015.52

Muniyappan, S., Solaiyammal, T., Sudhakar, K., Karthigeyan, A., and Murugakoothan, P. (2017). Conventional Hydrothermal Synthesis of Titanate Nanotubes: Systematic Discussions on Structural, Optical, Thermal and Morphological Properties. *Mod. Electron. Mater.* 3, 174–178. doi:10.1016/j.moem.2017.10.002

Nady, D., Zaki, A. H., Raslan, M., and Hozayen, W. (2020). Enhancement of Microbial Lipase Activity via Immobilization over Sodium Titanate Nanotubes for Fatty Acid Methyl Esters Production. *Int. J. Biol. Macromol.* 146, 1169–1179. doi:10.1016/j.ijbiomac.2019.09.240

Nasrollahzadeh, M., Shafiei, N., Nezafat, Z., Soheili Bidgoli, N. S., and Soleimani, F. (2020). Recent Progresses in the Application of Cellulose, Starch, Alginate, Gum, Pectin, Chitin and Chitosan Based (Nano)catalysts in Sustainable and Selective Oxidation Reactions: A Review. *Carbohydr. Polym.* 241, 116353. doi:10.1016/j.carbpol.2020.116353

Okolie, J. A., Mukherjee, A., Nanda, S., Dalai, A. K., and Kozinski, J. A. (2021). Next-generation Biofuels and Platform Biochemicals from Lignocellulosic Biomass. *Int. J. Energy Res.* 45, 14145–14169. doi:10.1002/er.6697

Ou, H., and Lo, S. (2007). Review of Titania Nanotubes Synthesized via the Hydrothermal Treatment: Fabrication, Modification, and Application. *Sep. Purif. Technol.* 58, 179–191. doi:10.1016/j.seppur.2007.07.017

Razzaq, A., and In, S.-I. (2019). TiO$_2$ Based Nanostructures for Photocatalytic CO$_2$ Conversion to Valuable Chemicals. *Micromachines* 10, 326. doi:10.3390/mi10050326

Reddy, B. R. P., Reddy, P. V. G., and Reddy, B. N. (2015). Efficient Solvent Free Synthesis of Tertiary α-aminophosphonates Using H2Ti3O7nanotubes as a Reusable Solid-Acid Catalyst. *New J. Chem.* 39, 9605–9610. doi:10.1039/c5nj01914a

Rempel, A. A., Valeeva, A. A., Vokhmintsev, A. S., and Weinstein, I. A. (2021). Titanium Dioxide Nanotubes: Synthesis, Structure, Properties and Applications. *Russ. Chem. Rev.* 90, 1397–1414. doi:10.1070/rcr4991

Ruiz-García, J. R., Fierro-Gonzalez, J. C., Handy, B. E., Hinojosa-Reyes, L., De Haro Del Río, D. A., Lucio-Ortiz, C. J., et al. (2019). An *In Situ* Infrared Study of CO$_2$ Hydrogenation to Formic Acid by Using Rhodium Supported on Titanate Nanotubes as Catalysts. *ChemistrySelect* 4, 4206–4216. doi:10.1002/slct.201900361

Schutyser, W., Renders, T., Van den Bosch, S., Koelewijn, S.-F., Beckham, G. T., and Sels, B. F. (2018). Chemicals from Lignin: An Interplay of Lignocellulose Fractionation, Depolymerisation, and Upgrading. *Chem. Soc. Rev.* 47, 852–908. doi:10.1039/c7cs00566k

Shanmugaraj, K., Bustamante, T. M., de León, J. N. D., Aepuru, R., Mangalaraja, R. V., Torres, C. C., et al. (2022). Noble Metal Nanoparticles Supported on Titanate Nanotubes as Catalysts for Selective Hydrogenation of Nitroarenes. *Catal. Today* 392-393, 93–104. doi:10.1016/j.cattod.2021.09.003

Sluban, M., Cojocaru, B., Parvulescu, V. I., Iskra, J., Cerc Korošec, R., and Umek, P. (2017). Protonated Titanate Nanotubes as Solid Acid Catalyst for Aldol Condensation. *J. Catal.* 346, 161–169. doi:10.1016/j.jcat.2016.12.015

Souza, A. P. S., Almeida, A. F. L., Freire, F. N. A., Nunes, V. F., and de Lima, F. M. Titanates Nanotubes and Nanoribbons Applied in Dye-Sensitized Solar Cells, R. F. d. Nascimento, V. d. O. S. Neto, P. B. A. Fechine, and P. d. T. C. Freire, in *Nanomaterials and Nanotechnology. Materials Horizons: From Nature to Nanomaterials*, Springer Singapore, Singapore, 2021, pp. 339–373.doi:10.1007/978-981-33-6056-3_11

Stančin, H., Mikulčić, H., Wang, X., and Duić, N. (2020). A Review on Alternative Fuels in Future Energy System. *Renew. Sustain. Energy Rev.* 128, 109927. doi:10.1016/j.rser.2020.109927

Talebian-Kiakalaieh, A., Amin, N. A. S., Najaafi, N., and Tarighi, S. (2018). A Review on the Catalytic Acetalization of Bio-Renewable Glycerol to Fuel Additives. *Front. Chem.* 6, 573. doi:10.3389/fchem.2018.00573

Timothy, A. A., Han, F., Li, G., Xu, J., Wang, A., Cong, Y., et al. (2020). Synthesis of Jet Fuel Range High-Density Dicycloalkanes with Methyl Benzaldehyde and Acetone. *Sustain. Energy Fuels* 4, 5560–5567. doi:10.1039/d0se01110j

Torres, C. C., Jiménez, V. A., Campos, C. H., Alderete, J. B., Dinamarca, R., Bustamente, T. M., et al. (2018). Gold Catalysts Supported on TiO 2 -nanotubes for the Selective Hydrogenation of P -substituted Nitrobenzenes. *Mol. Catal.* 447, 21–27. doi:10.1016/j.mcat.2017.12.039

Wada, E., Kitano, M., Nakajima, K., and Hara, M. (2013). Effect of Preparation Conditions on the Structural and Acid Catalytic Properties of Protonated Titanate Nanotubes. *J. Mat. Chem. A* 1, 12768–12774. doi:10.1039/c3ta13015k

Wada, E., Kitano, M., Yamamoto, K., Nakajima, K., Hayashi, S., and Hara, M. (2016). Synthesis of Niobium-Doped Titanate Nanotubes as Solid Acid Catalysts. *Catal. Sci. Technol.* 6, 4832–4839. doi:10.1039/c6cy00044d

Xu, C., He, J., Zhang, W., Cui, H., Zhu, J., and Hu, L. (2020). Effect of Microstructures on the Acidity and Catalytic Performance for H 2 Ti 3 O 7 Nanomaterials. *ChemistrySelect* 5, 10081–10089. doi:10.1002/slct.202002739

Yang, J., Shen, X., Wei, J., Zhang, L., Zhao, D., and Yao, B. (2016). Selective Oxidation of Alcohols on Hydrogen Titanate Nanotubes under Visible Light Irradiation: Relationship between Nanostructure and Catalytic Activity. *Catal. Sci. Technol.* 6, 7604–7614. doi:10.1039/c6cy01345g

Yao, Y., Zuo, M., Shao, P., Huang, X., Li, J., Duan, Y., et al. (2020). Oxidative Desulfurization of 4,6-dimethyldibenzothiophene over Short Titanate Nanotubes: A Non-classical Shape Selective Catalysis. *J. Porous Mat.* 27, 331–338. doi:10.1007/s10934-019-00809-8

Zaki, A. H., Naeim, A. A., and El-Dek, S. I. (2019). Sodium Titanate Nanotubes for Efficient Transesterification of Oils into Biodiesel. *Environ. Sci. Pollut. Res.* 26, 36388–36400. doi:10.1007/s11356-019-06602-z

Zhang, H., Li, H., Hu, Y., Venkateswara Rao, K. T., Xu, C., and Yang, S. (2019). Advances in Production of Bio-Based Ester Fuels with Heterogeneous Bifunctional Catalysts. *Renew. Sustain. Energy Rev.* 114, 109296. doi:10.1016/j.rser.2019.109296

Zhang, M., Bando, Y., and Wada, K. (2001). Sol-gel Template Preparation of TiO$_2$ Nanotubes and Nanorods. *J. Mat. Sci. Lett.* 20, 167–170. doi:10.1023/a:1006739713220

Zhou, S., Lei, M., Bai, J., Liu, X., Wu, L., Long, M., et al. (2022a). Titania Nanotubes-Bonded Sulfamic Acid as an Efficient Heterogeneous Catalyst for the Synthesis of N-Butyl Levulinate. *Front. Chem.* 10, 894965. doi:10.3389/fchem.2022.894965

Zhou, S., Jiang, D., Liu, X., Chen, Y., and Yin, D. (2018). Titanate Nanotubes-Bonded Organosulfonic Acid as Solid Acid Catalyst for Synthesis of Butyl Levulinate. *RSC Adv.* 8, 3657–3662. doi:10.1039/c7ra12994g

Zhou, S., Lai, J., Liu, X., Huang, G., You, G., Xu, Q., et al. (2022b). Selective Conversion of Biomass-Derived Furfuryl Alcohol into N-Butyl Levulinate over Sulfonic Acid Functionalized TiO$_2$ Nanotubes. *Green Energy & Environ.* 7, 257–265. doi:10.1016/j.gee.2020.09.009

Zhou, S., Liu, X., Lai, J., Zheng, M., Liu, W., Xu, Q., et al. (2019). Covalently Linked Organo-Sulfonic Acid Modified Titanate Nanotube Hybrid Nanostructures for the Catalytic Esterification of Levulinic Acid with N-Butyl Alcohol. *Chem. Eng. J.* 361, 571–577. doi:10.1016/j.cej.2018.12.111

Zhu, S., Guo, J., Wang, X., Wang, J., and Fan, W. (2017). Alcoholysis: A Promising Technology for Conversion of Lignocellulose and Platform Chemicals. *ChemSusChem* 10, 2547–2559. doi:10.1002/cssc.201700597

Conflict of Interest: The authors declare that the research was conducted in the absence of any commercial or financial relationships that could be construed as a potential conflict of interest.

Advantages of publishing in Frontiers

OPEN ACCESS
Articles are free to read
for greatest visibility
and readership

FAST PUBLICATION
Around 90 days
from submission
to decision

HIGH QUALITY PEER-REVIEW
Rigorous, collaborative,
and constructive
peer-review

TRANSPARENT PEER-REVIEW
Editors and reviewers
acknowledged by name
on published articles

Frontiers
Avenue du Tribunal-Fédéral 34
1005 Lausanne | Switzerland

Visit us: www.frontiersin.org
Contact us: frontiersin.org/about/contact

REPRODUCIBILITY OF RESEARCH
Support open data
and methods to enhance
research reproducibility

DIGITAL PUBLISHING
Articles designed
for optimal readership
across devices

FOLLOW US
@frontiersin

IMPACT METRICS
Advanced article metrics
track visibility across
digital media

EXTENSIVE PROMOTION
Marketing
and promotion
of impactful research

LOOP RESEARCH NETWORK
Our network
increases your
article's readership